

Astronomy and Astrophysics Library

Eugene F. Milone
William J.F. Wilson

Solar System Astrophysics

Planetary Atmospheres and the Outer
Solar System

Second Edition



Astronomy and Astrophysics Library

SERIES EDITORS

G. BÖRNER, *Garching, Germany*

A. BURKERT, *München, Germany*

W.B. BURTON, *Charlottesville, VA, USA and Leiden, The Netherlands*

A. COUSTENIS, *Meudon, France*

M.A. DOPITA, *Canberra, Australia*

B. LEIBUNDGUT, *Garching, Germany*

G. MEYNET, *Sauverny, Switzerland*

I. ROBSON, *Edinburgh, United Kingdom*

P. SCHNEIDER, *Bonn, Germany*

V. TRIMBLE, *College Park, MD, and Irvine, CA, USA*

D. WARD-THOMPSON, *Lancashire, England*

For further volumes:
<http://www.springer.com/series/848>

Eugene F. Milone • William J.F. Wilson

Solar System Astrophysics

Planetary Atmospheres and the Outer
Solar System

Second Edition



Springer

Eugene F. Milone
Professor Emeritus
Dept. Physics & Astronomy
University of Calgary
Calgary, Alberta
Canada

William J.F. Wilson
Senior Instructor Emeritus
Dept. Physics & Astronomy
University of Calgary
Calgary, Alberta
Canada

Cover Illustration: "Mysterium Cosmographicum" by David R. Mourtisen

ISSN 0941-7834 ISSN 2196-9698 (electronic)
ISBN 978-1-4614-9089-0 ISBN 978-1-4614-9090-6 (eBook)
DOI 10.1007/978-1-4614-9090-6
Springer New York Heidelberg Dordrecht London

Library of Congress Control Number: 2013949767

© Springer Science+Business Media New York 2014

This work is subject to copyright. All rights are reserved by the Publisher, whether the whole or part of the material is concerned, specifically the rights of translation, reprinting, reuse of illustrations, recitation, broadcasting, reproduction on microfilms or in any other physical way, and transmission or information storage and retrieval, electronic adaptation, computer software, or by similar or dissimilar methodology now known or hereafter developed. Exempted from this legal reservation are brief excerpts in connection with reviews or scholarly analysis or material supplied specifically for the purpose of being entered and executed on a computer system, for exclusive use by the purchaser of the work. Duplication of this publication or parts thereof is permitted only under the provisions of the Copyright Law of the Publisher's location, in its current version, and permission for use must always be obtained from Springer. Permissions for use may be obtained through RightsLink at the Copyright Clearance Center. Violations are liable to prosecution under the respective Copyright Law.

The use of general descriptive names, registered names, trademarks, service marks, etc. in this publication does not imply, even in the absence of a specific statement, that such names are exempt from the relevant protective laws and regulations and therefore free for general use.

While the advice and information in this book are believed to be true and accurate at the date of publication, neither the authors nor the editors nor the publisher can accept any legal responsibility for any errors or omissions that may be made. The publisher makes no warranty, express or implied, with respect to the material contained herein.

Printed on acid-free paper

Springer is part of Springer Science+Business Media (www.springer.com)

Preface

Preface to the First Edition

This work is appearing in two parts because its mass is the result of combining detailed exposition and recent scholarship. Book I, dealing mainly with the inner solar system, and Book II, mainly on the outer solar system, represent the combined, annually updated, course notes of E. F. Milone and W. J. F. Wilson for the undergraduate course in solar system astrophysics that has been taught as part of the Astrophysics Program at the University of Calgary since the 1970s. The course, and so the book, assumes an initial course in astronomy and first-year courses in mathematics and physics. The relevant concepts of mathematics, geology, and chemistry that are required for the course are introduced within the text itself.

Solar System Astrophysics is intended for use by second- and third-year astrophysics majors, but other science students have also found the course notes rewarding. We therefore expect that students and instructors from other disciplines will also find the text a useful treatment. Finally, we think the work will be a suitable resource for amateurs with some background in science or mathematics. Most of the mathematical formulae presented in the text are derived in logical sequences. This makes for large numbers of equations, but it also makes for relatively clear derivations. The derivations are found mainly in Chaps. 2–6 in the first volume, *Background Science and the Inner Solar System*, and in Chaps. 10 and 11 in the second volume, *Planetary Atmospheres and the Outer Solar System*. Equations are found in the other chapters as well but these contain more expository material and recent scholarship than some of the earlier chapters. Thus, Chaps. 8 and 9, and 12–16 contain some useful derivations, but also much imagery and results of modern studies.

The first volume starts with a description of historical perceptions of the solar system and universe, in narrowing perspective over the centuries, reflecting the history (until the present century, when extra-solar planets again have begun to broaden our focus). The second chapter treats the basic concepts in the geometry of the circle and of the sphere, reviewing and extending material from introductory astronomy courses, such as spherical coordinate transformations. The third chapter

then reviews basic mechanics and two-body systems, orbital description, and the computations of ephemerides, then progresses to the restricted three-body and n -body cases, and concludes with a discussion of perturbations. The fourth chapter treats the core of the solar system, the Sun, and is not a bad introduction to solar or stellar astrophysics; the place of the Sun in the galaxy and in the context of other stars is described, and radiative transport, optical depth, and limb-darkening are introduced. In Chap. 5, the structure and composition of the Earth are discussed, the Adams–Williamson equation is derived, and its use for determining the march of pressure and density with radius described. In Chap. 6, the thermal structure and energy transport through the Earth are treated, and in this chapter the basic ideas of thermodynamics are put to use. Extending the discussion of the Earth’s interior, Chap. 7 describes the rocks and minerals in the Earth and their crystalline structure. Chapter 8 treats the Moon, its structures, and its origins, making use of the developments of the preceding chapters. In Chap. 9, the surfaces of the other terrestrial planets are described, beginning with Mercury. In each of the three sections of this chapter, a brief historical discussion is followed by descriptions of modern ground-based and space mission results, with some of the spectacular imagery of Venus and Mars. The chapter concludes with a description of the evidence for water and surface modification on Mars. This concludes the discussion of the inner solar system.

The second volume begins in Chap. 10 with an extensive treatment of the physics and chemistry of the atmosphere and ionosphere of the Earth and an introduction to meteorology, and this discussion is extended to the atmospheres of Venus and Mars. Chapter 11 treats the magnetospheres of these planets, after a brief exposition of electromagnetic theory. In Chap. 12, we begin to treat the outer solar system, beginning with the gas giants. The structure, composition, and particle environments around these planets are discussed, and this is continued in Chap. 13, where the natural satellites and rings of these objects are treated in detail, with abundant use made of the missions to the outer planets. In Chap. 14, we discuss comets, beginning with a historical introduction that highlights the importance of comet studies to the development of modern astronomy. It summarizes the ground- and space-based imagery and discoveries, but makes use of earlier derivations to discuss cometary orbits. This chapter ends with the demise of comets and the physics of meteors. Chapter 15 treats the study of meteorites and the remaining small bodies of the solar system, the asteroids (*aka* minor planets, planetoids), and the outer solar system “Kuiper Belt” objects, and the closely related objects known as centaurs, plutinos, cubewanos, and others, all of which are numbered as asteroids. The chapter ends with discussions of the origin of the solar system and of debris disks around other stars, which point to widespread evidence of the birth of other planetary systems. Finally, in Chap. 16, we discuss the methods and results of extra-solar planet searches, the distinctions among stars, brown dwarfs, and planets, and we explore the origins of planetary systems in this wider context.

At the end of nearly every chapter we have a series of challenges. Instructors may use these as homework assignments, each due 2 weeks after the material from that chapter were discussed in class; we did! The general reader may find them helpful as focusing aids.

Preface to the Second Edition

As in the first edition, we maintain the two-volume bifurcation of the inner and outer regions of the solar system. In the first volume, we again begin with a historical overview but expand the horizon to include glimpses of extra-solar planetary systems. The basic mathematics, mechanics, geophysics, thermodynamics, chemistry, astrophysics, and mineralogical principles required for a sound introduction to space science have been revised with improved illustrations and examples drawn from wider sources. In Chap. 4, we have added descriptions of the features of the active Sun. Chapter 8, on the Moon, has been updated with results of probes of water at the poles and a fresh discussion of the Moon's origin. In Chap. 9, the Messenger mission has provided vital new details about Mercury, and the history of the study of Venus has been expanded. The Mars section includes results from the Curiosity mission and a description of current views of the search for life in the Viking mission. The crustal changes in Mars since its formation, and an enlarged discussion of climate changes, expand that section further. Similar expansions of the chapters of the second volume have vastly expanded the discussions of atmospheres, magnetospheres, the gas and ice giants of the outer solar system and their moons and ring systems. The discussion of meteors and meteorite impacts has been enlivened by recent events, and a deepening understanding of the role played by disks in the early history of planetary formation. The burgeoning field of extrasolar planets has been reflected in the vastly increased discussion in the last chapter, with the increasing knowledge of the properties of extrasolar planets and their more massive siblings, the brown dwarfs. The dynamical interactions being studied with increasingly sophisticated software simulations have greatly illuminated the likely dynamical development of the solar system. As in all such investigations, present questions have been and are being answered, but new puzzles arise, and it is the anticipation of the new adventures required to explain them that makes this field truly exciting.

Calgary, Alberta, Canada

Eugene F. Milone
William J.F. Wilson

Acknowledgments

These volumes owe their origin to more than 30 years of solar system classes in the Astrophysics Program at the University of Calgary, called, at various times, Geophysics 375, Astrophysics 301, 309, and 409. Therefore, we acknowledge, first, the students who took these courses and provided feedback. It is also a pleasure to thank the following people for their contributions:

David R. Mouritsen, formerly of Calgary and now in Toronto, provided for Chap. 1 and our covers an image of his original work of art, an interpretation of Kepler's *Mysterium Cosmographicum*, in which the orbits of the planets are inscribed within solid geometric figures.

In Chap. 3, the Bradstreet and Steelman software package *Binary Maker 3* was used to create an image to illustrate restricted three-body solutions.

University of Calgary Professor Emeritus Alan Clark gave us an image of an active region and detailed comments on the material of Chap. 4 for both editions; Dr. Rouppe van der Voort of the University of Oslo provided high-quality images of two other active region figures, for Chap. 4; the late Dr. Richard Tousey of the US Naval Research Laboratory provided slides of some of the images, subsequently scanned for Chap. 4; limb-darkened spectral distribution plots were provided by Dr. Robert L. Kurucz, of the Harvard-Smithsonian Center for Astrophysics; Dr. Charles Wolff, of Goddard Space Flight Center, NASA, reviewed the solar oscillations sections and provided helpful suggestions for both editions; Dr. David H. Hathaway, Marshall space Flight Center, NASA, provided permission to use his solar cycle sunspot area graphic.

Dr. David Eaton of the Geoscience Department of the University of Calgary made available for Chap. 5 his seismogram image of the major Japanese earthquake of 2011.

Mr. Gerhard Brunthaler provided inspiration for the derivation of the contribution of tidal heating to the Earth's interior heat budget in Chap. 6.

Dr. D.J. Stevenson provided helpful criticism of our lunar origins figures, and Dr. Robin Canup kindly prepared panels of her lunar simulations for our Fig. 8.13.

Dr. James A. Slavin, of the Dept. Atmospheric, Oceanic and Space Sciences, University of Michigan, critiqued our discussion of Mercury's magnetosphere in Chap. 11.

Dr. Andrew Yau provided excellent notes as a guest lecturer in Asph 409 on the Martian atmosphere and its evolution, which contributed to our knowledge of the material presented in Chaps. 9, 10, and 11; similarly, lectures by Professor J. S. Murphree of the University of Calgary illuminated the magnetospheric material described in Chap. 11. For the second edition, Professor David Knudsen of the University of Calgary critiqued our expanded Chap. 11.

NASA's online photo gallery provided many of the images in Chaps. 8, 9, 12, 13, 14, and some of those in Chap. 15; additional images were provided by the Naval Research Laboratory (of both the Sun and the Moon). Some of these and other images involved work by other institutions, such as the U.S. Geological Survey, the Jet Propulsion Laboratory, Arizona State Univ., Cornell, the European Space Agency, the Italian Space Agency (ASI), CICLOPS, CalTech, Univ. of Arizona, Space Science Institute, Boulder, the German Air and Space Center (DLR), Brown University, the Voyagers and the Cassini Imaging Teams, the Hubble Space Telescope, University of Maryland and the Deep Impact mission team, the Minor Planet Center, Applied Physics Laboratory of the Johns Hopkins University, and the many individual sources, whether cited in captions or not, who contributed their talents to producing these images.

We also acknowledge with thanks and gratitude the help of Prof. S. van Gasselt, Inst. Geologische Wissenschaften, Freie Univ., Berlin and Ms. Stefanie Potts, Sekretariat Planetologie, for their kindness in providing and enabling our use of Fig. 9.51, and Ms. Nadia Imbert-Vier of ESA for her helpful and timely responses for permission to use ESA images.

Dr. John Trauger provided a high-resolution UV image of Saturn and its auroras for Chap. 12, and Dr. Chris Arridge (Univ. College London) provided helpful suggestions for our magnetospheric effects in the Saturn system in Chap. 12. Dr. Stuart Eves provided an important reference to William Herschel's reports of his observations for Chap. 13.

Dr. William Reach, Caltech, provided an infrared mosaic image of Comet Schwassmann-Wachmann 3, and Mr. John Mirtle of Calgary provided many of the comet images for Chap. 14, including those of Comets 109P/Swift-Tuttle, C/1995 O1 (Hale-Bopp), C/Hyakutake, Lee, C/Ikeya-Zhang, Brorsen-Metcalf, and Machholz; Professor Michael F. A'Hearn of the University of Maryland for his critique of the comet content of Chap. 14. Univ. of Calgary Prof. Emer. Alan Clark and Dr. William Livingstone, KPNO, Tucson, provided images of meteors. Mr. Mike Hankey of the American Meteor Society provided useful sources of recent fireball frequency data.

Dr. Allan Treiman, of the Lunar and Planetary Institute, Houston, was kind enough to provide background material on the debate over the ALH84001 organic life question, mentioned in Chap. 15. Mr. Matthias Busch made available his *Easy-Sky* images of asteroid family distributions, and the Minor Planet Center

provided the high-resolution figures of the distributions of the minor planets in the inner and outer solar system.

Dr. Charles Lineweaver, University of New South Wales, provided a convincing illustration for the brown dwarf desert, illustrated in Chap. 16; University of Calgary graduate student Michael Williams provided several figures from his MSc thesis on the extra-solar planet HD 209458b, the first to be found transiting a star, for Chap. 16.

Mr. Alexander Jack assisted in updating and improving the readability of equations and text in some of the early chapters, and he and Ms. Veronica Jack assisted in developing the tables of the extra-solar planets and their stars for Chap. 16 in both editions.

Adapted Figs. 5.23 and 11.3 appear with the permission of Elsevier; adapted Figs. 10.34 and 10.35 by permission of Oxford University Press; and adapted Fig. 13.12 by permission of Cambridge University Press. The images in Figs. 9.31, 9.36, 9.38, 9.48, 9.50, and 9.52a, b are courtesy of NASA, the Jet Propulsion Laboratory—Caltech, and Malin Space Science Systems. For more information concerning the images provided courtesy of Malin Space Science Systems, contact Malin Space Science Systems at www.msss.com. Re materials provided courtesy of the American Association for the Advancement of Science (AAAS), namely, the adapted Figs. 8.2, 8.8, 11.40a–d, and 14.12b; Table 14.3; and Dr. Canup’s newly supplied Fig. 8.13,” readers may view, browse, and/or download material for temporary copying purposes only, provided these uses are for noncommercial personal purposes. Except as provided by law, this material may not be further reproduced, distributed, transmitted, modified, adapted, performed, displayed, published, or sold in whole or in part, without prior written permission from the publisher.

In addition, we thank the many authors, journals, and publishers who have given us permission to use their figures and tabular material or adaptations thereof, freely. Finally, it is also a pleasure to thank Springer editors Dr. Hans Koelsch, Dr. Harry Blom, and their associates, Christopher Coughlin, Brian Halm, and Jennifer Satten, for their support for this project.

Contents

10 Planetary Atmospheres	337
10.1 Atmospheric Constituents	337
10.2 Atmospheric Structure	340
10.2.1 Pressure Variation with Height	340
10.2.2 Temperature Variation with Height	344
10.3 Circulation in the Atmosphere	349
10.3.1 Centrifugal and Coriolis Forces	349
10.3.2 Physical Effects of the Centrifugal and Coriolis Forces	352
10.3.3 Pressure Gradient Force	354
10.3.4 Friction	355
10.3.5 Geostrophic Balance and Geostrophic Winds	356
10.3.6 Thermal Effects	357
10.3.7 Global Circulation	360
10.4 Atmospheric Effects on the Heat Budget	367
10.4.1 The Earth	367
10.4.2 Mars	371
10.4.3 Venus	374
10.5 Planetary Circulation Effects	377
10.5.1 Circulation and the Coriolis Force	377
10.5.2 Meridional (N–S) Circulation	378
10.5.3 Zonal (E–W) Circulation	380
10.5.4 Other Considerations	385
10.5.5 Chemical Cycles	389
10.5.6 Excess Radiation	394
Challenges	395
References	396

11 Planetary Ionospheres and Magnetospheres	399
11.1 Earth: Ionospheric Layers	399
11.1.1 The F Layer	399
11.1.2 The E Layer	403
11.1.3 The D Layer	404
11.1.4 Reflection of Radio Waves	406
11.2 Atmospheric and Ionospheric Chemistry on Mars and Venus	407
11.2.1 Neutral Atmosphere of Mars	407
11.2.2 Neutral Atmosphere of Venus	408
11.2.3 Ionosphere of Mars	409
11.2.4 Ionosphere of Venus	410
11.2.5 Atmospheric Escape Mechanisms	411
11.3 Solar Wind	416
11.4 Maxwell's Equations and the Plasma Frequency	417
11.4.1 Maxwell's Equations	417
11.4.2 Application to a Polarized Wave	420
11.5 The Earth's Magnetosphere	423
11.5.1 Forces Acting on Charged Particles	425
11.5.2 \vec{E} Uniform and Time-Independent; $\vec{B} = 0$	427
11.5.3 \vec{B} Uniform and Time-Independent; $\vec{E} = 0$	428
11.5.4 Guiding Center	429
11.5.5 Diamagnetism	430
11.5.6 $\vec{E} \times \vec{B}$ Drift and Field-Aligned Currents	431
11.5.7 $\vec{E} \times \vec{B}$ Drift with Collisions	434
11.5.8 Polarization Drift	435
11.5.9 Gradient and Curvature Drift	437
11.6 Electric Currents in the Ionosphere and Magnetosphere	439
11.6.1 The Ionospheric Dynamo	439
11.6.2 Boundary Current	440
11.6.3 Ring Current	441
11.6.4 Magnetic Storms	448
11.6.5 Magnetospheric Convection	449
11.6.6 The Magnetotail Current Sheet	451
11.6.7 Coupling Between the Magnetosphere and the Ionosphere	452
11.6.8 Magnetospheric Substorms	454
11.7 Magnetospheres of Mercury, Venus, and Mars	458
11.7.1 Mercury	458
11.7.2 Venus	462
11.7.3 Mars	467
Challenges	470
References	472

12 The Giant Planets	475
12.1 Jupiter	478
12.1.1 Visible Phenomena	478
12.1.2 Jovian Atmospheric Structure	483
12.2 Saturn	486
12.3 Uranus	490
12.4 Neptune	492
12.5 Internal Pressures	494
12.6 Excess Radiation	496
12.7 Ionospheres of the Giant Planets	497
12.8 The Jovian Magnetosphere	498
12.8.1 Inner Magnetosphere of Jupiter	500
12.8.2 Middle Magnetosphere of Jupiter	501
12.8.3 Outer Magnetosphere of Jupiter	502
12.8.4 Jovian Aurorae	503
12.8.5 Interaction with Io	503
12.9 Saturn's Magnetosphere	511
12.9.1 Neutral and Ionic Content	512
12.9.2 Magnetospheric Currents	513
12.9.3 Radiation Belts	514
12.9.4 Saturn Kilometric Radiation (SKR)	515
Challenges	516
References	516
13 Satellite and Ring Systems	521
13.1 Satellites	521
13.1.1 The Moons of Mars	528
13.1.2 The Moons of Jupiter	535
13.1.3 The Moons of Saturn	548
13.1.4 Uranian Moons	563
13.1.5 Neptunian Moons	564
13.1.6 Pluto-Charon	567
13.2 Origins of Ring Systems	570
13.3 Ring Structures	572
13.3.1 Jovian Rings	572
13.3.2 Saturnian Rings	575
13.3.3 Uranian Rings	578
13.3.4 Neptunian Rings	581
13.3.5 Nature and Possible Origins of the Ring Structures	582
13.4 Orbital Stability of the Moons	586
13.4.1 Satellite Stability	586
13.4.2 Conjectures about Pluto	587
13.5 Origins of the Moons	590
Challenges	590
References	591

14 Comets and Meteors	597
14.1 Comets in History	597
14.1.1 Early History	597
14.1.2 Tycho Brahe and the Comet of 1577	598
14.1.3 Later Historical Studies	600
14.2 Comet Designations	601
14.3 Cometary Orbits	603
14.4 Typical and Historically Important Comets	609
14.5 Cometary Structure	612
14.6 Cometary Composition	614
14.7 Induced Magnetospheres of Comets	622
14.8 Origins of Comets	625
14.8.1 Formation of the Nucleus	625
14.8.2 Origin of the Present Distribution of Comets	625
14.9 Cometary Demise	628
14.10 Meteor Showers	630
14.11 Individual Meteors	632
14.11.1 Basic Meteor Phenomena and Circumstances	632
14.11.2 Meteor Heating and Incandescence	633
14.12 Micrometeorites	639
14.13 Dust Destinies	640
14.13.1 Radiation Pressure	640
Challenges	643
References	643
15 Meteorites, Asteroids and the Age and Origin of the Solar System	647
15.1 Stones from Heaven	647
15.1.1 Categories and Nomenclature of Meteorites	648
15.1.2 Petrographic Categories	650
15.1.3 Meteorite Groupings and Subgroupings	652
15.2 Undifferentiated Meteorites: The Chondrites	657
15.2.1 Defining the Chondrites	657
15.2.2 Carbonaceous Chondrites	659
15.2.3 Ordinary Chondrites	660
15.2.4 Enstatites	660
15.2.5 The R Group	661
15.2.6 Former Members, from the IAB Clan	661
15.2.7 Origins of the Chondrites	661
15.3 Differentiated Silicate-Rich Meteorites	662
15.3.1 The Igneous Clan	663
15.3.2 Other DSR Meteorites	664
15.4 Iron Meteorites	667

15.5	Ages and Origins of Meteorites	669
15.5.1	Radiometric Ages	669
15.5.2	Gas Retention Ages	672
15.5.3	Cosmic Ray Exposure Ages	673
15.5.4	Case Study: The Zagami SNC Basaltic Shergottite	673
15.6	Other Sources of Evidence for Meteoritic Origins	674
15.7	Parent Bodies and the Asteroids	676
15.7.1	The Discovery of Ceres	676
15.7.2	Nomenclature	677
15.7.3	Groups of Asteroids and Families of Orbits	681
15.7.4	Dimensions and Masses of Asteroids	686
15.7.5	Case Study: (4) Vesta	690
15.7.6	Asteroids and Meteorites	696
15.8	Implications for the Origin of the Solar System	701
15.9	The Solar Nebula	701
15.10	The Proto-Planetary Disk	704
	Challenges	706
	References	707
16	Extra-Solar Planetary Systems	713
16.1	Historical Perspective	713
16.2	Methods to Find “Small”-Mass Companions	742
16.2.1	Radial Velocity Variations of the Visible Component	743
16.2.2	Transit Eclipses	747
16.2.3	Astrometric Variations	750
16.2.4	Gravitational Lensing	753
16.2.5	Direct Imaging and Spectroscopy	755
16.2.6	Pulsar Timings	756
16.2.7	Indirect Effects	757
16.3	Definitions of Planets and Brown Dwarfs	758
16.4	Extra-Solar Planets Detected or Awaiting Confirmation	761
16.4.1	HD 209458b	764
16.4.2	The Multi-planet System of ν Andromedae	767
16.4.3	The Multi-planet System of 55 Cancri	767
16.4.4	The Multi-planet System of Kepler 11	768
16.4.5	The Multi-planet System of HD 69830	769
16.4.6	The Multi-planet System of Gliese J 876	770
16.4.7	The ϵ Eridani System	770
16.4.8	The TrES-1 System	771
16.4.9	The WASP-17 System	772

16.4.10 The Closely Packed Planetary System of Kepler 32	774
16.4.11 Approaching Another Milestone in Extrasolar Planet Research: The Search for α Cen Bb	775
16.5 Origins of Brown Dwarfs and Planets	776
Challenges	781
References	782
Index	797

Chapter 10

Planetary Atmospheres

10.1 Atmospheric Constituents

The constituents of a planetary atmosphere are determined in a general way by the likelihood that a given constituent will be retained, rather than lost by evaporation into space over long periods of time. This likelihood is determined by three factors: (1) the equilibrium temperature of the planet, because the hotter the atmosphere, the larger the mean kinetic energy of its molecules,

$$E = \frac{3}{2} kT \quad (10.1)$$

where $k = 1.3806488(13) \times 10^{-23}$ J/K is the Boltzmann constant, T is the equilibrium temperature in kelvin, and the number in parentheses is the uncertainty in the last two digits of the constant; (2) the molecular weight, m , of each atmospheric constituent, because equipartition of energy requires that more massive particles have smaller mean velocities,

$$E = \frac{1}{2} mv^2 \quad (10.2)$$

and (3) the planet's escape velocity,

$$v_{esc} = \sqrt{\frac{2GM}{R}} \quad (10.3)$$

where M and R are the planetary mass and radius, respectively. In a region of atmosphere in thermal equilibrium,¹ the distribution of the number of molecules

¹A system is in thermal equilibrium if its temperature is spatially uniform (the same temperature throughout the system) and is constant in time.

vs. the speed at which they are moving at any instant is said to be *Maxwellian* (See Schlosser et al. 1991/1994, Fig. 18.1).

The *molecular weight* of any species of molecule can be written

$$m = \mu m_u \quad (10.4)$$

where $m_u = (1/12)[m(^{12}\text{C})] = 1.660538921(73) \times 10^{-27}$ kg is the unit atomic mass, and the dimensionless quantity μ is expressed in units of m_u . It is not uncommon to refer to μ as the *molecular weight*, the units of m_u being understood.

From (10.1), (10.2) and (10.4), the root mean square speed of any constituent can be written in terms of μ as

$$v = \sqrt{\frac{3kT}{m}} = 157.94 \sqrt{\frac{T}{\mu}} \text{ m/s} \quad (10.5)$$

A very massive planet will retain even the lightest gases over a wide range of temperatures. Quite generally, if $v/v_{esc} = 1/3$, the atmosphere can be expected to be lost in weeks; if $v/v_{esc} = 1/4$, 10,000 years; if $v/v_{esc} = 1/5$, 10^8 years; and if $v/v_{esc} = 1/6$, it can be considered retained for eons, or billions of years (Gy), assuming no major departure from the assumed equilibrium planetary temperature over this interval of time.

From (10.3) and (10.5), the lower limit for the molecular weight of a molecule that can be *retained* is

$$\mu \geq \left(157.94 \frac{\sqrt{T}}{(v_{esc}/6)} \right)^2 = 8.980 \times 10^5 \frac{T}{v_{esc}^2} \quad (10.6)$$

From (6.35) of Milone and Wilson (2014), the equilibrium temperature for an assumed black body, rapidly rotating planet is:

$$T = \left\{ L_\odot (1 - A) / [16\pi\sigma r^2] \right\}^{\frac{1}{4}} = 1.078 \times 10^8 [(1 - A)/r^2]^{\frac{1}{4}} \text{ K}$$

where A is the bolometric albedo, $\sigma = 5.671 \times 10^{-8} \text{ W m}^{-2} \text{ K}^{-4}$ is the Stefan–Boltzmann constant, r is the distance from the sun in meters, and the solar luminosity is $L_\odot = 3.845 \times 10^{26} \text{ W}$ (Cox 2000, p. 340).

For a particular molecule to be retained over a significant fraction of the solar system's lifetime (assuming the equilibrium temperature correctly indicates the effective mean temperature of the planet, and there is no significant change in this temperature over this interval),

$$\begin{aligned}\mu &\geq 8.980 \times 10^5 \times 1.078 \times 10^8 \frac{[(1-A)/r^2]^{1/4}}{2GM/R} \\ &= 7.254 \times 10^{23} \frac{R}{M} \left(\frac{1-A}{r^2} \right)^{1/4}\end{aligned}\quad (10.7)$$

where r , R , M , and $G = 6.67428(67) \times 10^{-11} \text{ N m}^2/\text{kg}^2$ are in SI units. The corresponding numerical constant for a slowly rotating planet is greater by a factor $2^{\frac{1}{4}} = 1.189$. Finally, with R and M in units of the Earth's radius and mass ($6.378 \times 10^6 \text{ m}$, $5.972 \times 10^{24} \text{ kg}$, respectively) and a in au,² (10.7) becomes

$$\mu \geq 2.002 \frac{R/R_{\oplus}}{M/M_{\oplus}} \left(\frac{1-A}{a^2} \right)^{1/4} \quad (10.8)$$

As an example, for the Earth, $A \approx 0.307$, $\mu > \sim 2 \times 0.91 = 1.82$, provided T is correctly given by (10.7); i.e., $\langle T_{\oplus} \rangle = T_{\text{eq}} = 254 \text{ K}$. In point of fact, the Earth is slightly warmer because of its atmosphere, so that $\langle T_{\oplus} \rangle = 288 \text{ K}$. Using this value directly in (10.6), one obtains, $\mu = 2.07$.

Thus, the Earth is marginally unable to retain hydrogen at present, but should have retained helium (${}^4\text{He}$, $\mu \sim 4$). Nevertheless, the abundance of ${}^4\text{He}$ in the Earth's atmosphere is much less than would be expected if all of its primordial helium were still present. In fact, the small amount present is equal to the amount being outgassed into the atmosphere every $\sim 10^6$ years from α -decay of uranium and thorium in the Earth's crust and mantle (Lie-Svendsen and Rees 1996). (An alpha particle is a ${}^4\text{He}$ nucleus, and α -decay involves the ejection of a ${}^4\text{He}$ nucleus from an unstable atom.) This is a rapid rate of supply compared to the age of the Earth, so if there is not a comparable loss rate then there would be much more ${}^4\text{He}$ in the atmosphere than we find. Thermal escape is insufficient, so other loss mechanisms are required. The two most promising are outflow of He^+ along open magnetic field lines around the geomagnetic poles (planetary magnetospheres are discussed in Chap. 11) and exothermic charge exchange with atmospheric nitrogen, $\text{He}^+ + \text{N}_2 \rightarrow \text{N}_2^+ + \text{He}$. In the latter process, the He can gain enough kinetic energy to escape, and being neutral is not constrained by the magnetic field lines.

See Schlosser et al. (1991/1994, pp. 94–97) for further discussion of the species of molecules retainable in planetary atmospheres.

One of the more interesting concepts in planetary physics is the probability of escape of gases from the sub-solar region, where the instantaneous temperature is much higher than the global or even hemispherical average. How do we know if the evaporation from this location alone is the determining factor?

²for the astronomical unit, the semi-major axis of the Earth's orbit, defined by the IAU in 2012 formally as exactly equal to 149,597,870,700 m.

The answer probably lies in the *mean free path* of a molecule on the surface of a planet. The term refers to the average distance a molecule travels before colliding with another molecule. If a molecule receives sufficient energy for it to escape, how long does it take before it collides with another molecule? The problem and the solutions to it are described in, for example, Jeans' (1952) *Kinetic Theory of Gases*. The probability of collision depends strongly on the atmospheric density. In the hypothetical case where all molecules are stationary except one, it can be shown that the mean distance, d , which that one travels between collisions may be written

$$d = \frac{1}{\pi nR^2} \quad (10.9)$$

where n is the number density [the number of particles (in this case, molecules) per unit volume], and R is a characteristic distance about equal to the mean radius of a molecule. If, on the other hand, all molecules are moving and the gas is in thermal equilibrium then the molecular speeds correspond to a Maxwellian distribution.³ In this case, the mean free path of a molecule depends on its speed; e.g., if the molecule is moving very quickly, then the other molecules are essentially at rest by comparison and d is given by (10.9). Averaged over molecules of all speeds in a Maxwellian distribution, the mean free path is

$$\frac{1}{\sqrt{2}\pi nR^2} \quad (10.10)$$

This number is about 6×10^{-8} m at sea level in the Earth's atmosphere, or about $320R$ (Jeans 1952 pp. 44–49).

Thus, a great many collisions may occur prior to escape, the angle of alteration of direction in each collision being a further variable, and, at each collision, energy may be lost as well as gained; obviously, it will be easier to escape in a less dense environment.

Next we discuss the structure of atmospheres, and the behavior of pressure with height.

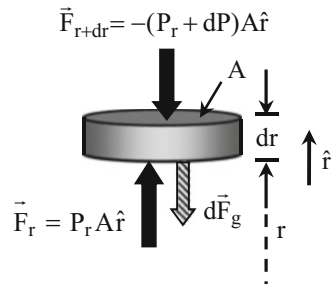
10.2 Atmospheric Structure

10.2.1 Pressure Variation with Height

For an atmosphere to be a reasonably permanent feature of a planet, the atmosphere must be in hydrostatic equilibrium, i.e., it should neither accelerate outward nor

³A Maxwellian distribution gives the number of atoms or molecules vs. speed in a gas in thermal equilibrium.

Fig. 10.1 Mechanical equilibrium of a parcel of air in a stationary atmosphere



collapse inward. Here, we will assume that the atmosphere can be approximated by spherical symmetry, e.g., only the radial components of force vectors are non-zero.

Figure 10.1 shows a free-body diagram for a small parcel of gas in such an atmosphere, in the form of a short cylinder of thickness dr , cross-section A , volume $dV = Adr$, density ρ , and mass $dm = \rho dV$, located at a distance r from the center of the planet. The unit vector, \hat{r} , signifies the positive radial direction; subscripts r or $r + dr$ specify radial location.

For hydrostatic equilibrium, the forces acting on this pillbox-shaped parcel must add to zero:

$$\vec{F}_r + \vec{F}_{r+dr} + d\vec{F}_g = 0 \quad (10.11)$$

[N.B: The “+” symbols in (10.11) are addition operators, not signs of quantities. Vectors are defined by only two attributes: magnitude and direction.] From Fig. 10.1, and with $M(r)$ being the total mass interior to radius r ,

$$d\vec{F}_g = -g dm \hat{r} = -g \rho dV \hat{r} = -g \rho A dr \hat{r} = -\frac{GM(r)}{r^2} \rho A dr \hat{r} \quad (10.12)$$

$$\vec{F}_r = P_r A \hat{r} \quad (10.13)$$

$$\vec{F}_{r+dr} = -P_{r+dr} A \hat{r} = -(P_r + dP) A \hat{r} \quad (10.14)$$

[For any two vectors, \vec{A} and \vec{B} , if $\vec{B} = -\vec{A}$ then \vec{B} has the same magnitude as \vec{A} and the opposite direction. Thus, the “-” symbols in (10.12) and (10.14) and the implied “+” sign in (10.13) show how the three force vectors in (10.11) are directed relative to the chosen unit vector, \hat{r} .] Substituting (10.12)–(10.14) into (10.11) and taking vector components in the radial direction gives

$$P_r A - (P_r + dP)A - g \rho A dr = 0 \quad (10.15)$$

[Vector components are scalars with magnitude and sign, with the radial component being positive in the direction of $\hat{\mathbf{r}}$ (upward in Fig. 10.1) and negative in the direction opposite to $\hat{\mathbf{r}}$ (downward in Fig. 10.1). Because the individual quantities in (10.15) are magnitudes, the signs of the components appear explicitly in the equation.] Solving for dP ,

$$dP = -g\rho dr = -\frac{dF_g}{A} \quad (10.16)$$

The quantities g and ρ are positive, so dP is negative when dr is positive, i.e., pressure decreases outward in the atmosphere. The *pressure gradient* is the rate of change of pressure with distance, so

$$\frac{dP}{dr} = -g\rho \quad (10.17)$$

also known as the *equation of hydrostatic equilibrium*.

The pressure can also be expressed in terms of the *perfect gas law*, which provides an *equation of state*:

$$P = nkT \quad (10.18)$$

Here, n is again the number density, related to the density and the mean molecular weight, m , of the atmosphere through the relation

$$n = \rho/m \quad (10.19)$$

Then from (10.4),

$$P = \rho kT/m = \rho kT/\mu m_u \quad (10.20)$$

From (10.17), substituting for ρ from (10.20), we then get for the pressure gradient

$$\frac{dP}{dr} = -\frac{\mu m_u g P}{kT} \quad (10.21)$$

from which we obtain the differential equation

$$\frac{dP}{P} = -\frac{\mu m_u g}{kT} dr \quad (10.22)$$

The integrated solution to (10.22) is

$$\ln \frac{P}{P_0} = -\frac{\mu m_{\text{u}} g}{kT} (r - r_0) \quad (10.23)$$

or

$$\frac{P}{P_0} = \exp \left\{ -\frac{\mu m_{\text{u}} g}{kT} (r - r_0) \right\} \quad (10.24)$$

where r_0 is a reference height (e.g., the base of the atmosphere) and P_0 is the pressure at $r = r_0$.

The *pressure scale height* is defined as

$$H = \frac{kT}{\mu m_{\text{u}} g} \quad (10.25)$$

Equation (10.25) can be expressed in terms of the universal gas constant, $R = 8.3144621(75) \text{ J mol}^{-1} \text{ K}^{-1}$, using the relationship $R = kN_A$. Here, $N_A = 6.02214129(27) \times 10^{23} \text{ mol}^{-1}$ is Avogadro's number, the number of particles (e.g., atoms or molecules) in one mole.

Then

$$H = \frac{RT}{\mu m_{\text{u}} N_A g} = (10^3 \text{ mol kg}^{-1}) \frac{RT}{\mu g} \quad (10.25a)$$

The factor in parentheses in (10.25a) may be combined with R to obtain a new constant (commonly and somewhat confusingly also written R ; check its units if in doubt!), $R = 8314.4621(75) \text{ J kg}^{-1} \text{ K}^{-1}$; then

$$H = \frac{RT}{\mu g} \quad (10.26)$$

Then, letting $h = r - r_0$, we get the *pressure scale height equation*,

$$P = P_0 e^{-h/H} \quad (10.27)$$

Equation (10.27) has been used to compute the mean molecular weight for outer planet atmospheres. In particular, the occultation of a star by Jupiter or another planet provides such an opportunity. The geometry, technique, and many results are reviewed by Elliott and Olkin (1996). A similar opportunity is provided by the occultation of an orbiting spacecraft passing behind the planet's atmosphere, as seen from Earth. Radio waves in the GHz range interact differently with the neutral and ionized components of the atmosphere, allowing the effects of ionization to be subtracted out and thus providing information about the neutral components (and

vice versa); see, e.g., Jenkins et al. (1994). As the planet progressively covers the star, astronomers at various sites on the Earth measure the optical depth along the line traversed by the starlight through the planet's atmosphere as a function of time. The *optical depth* is a measure of the absorptive/scattering properties of an atmosphere; an optical depth of one corresponds to the distance required for the transmitted light to decrease in intensity by a factor e . The curve of optical depth vs. time can be converted to a curve of refractive index vs. depth vertically into the atmosphere. Refractive index in turn depends on the number density of absorbers, n , as does the atmospheric pressure by (10.18), $P = nkT$, so that the index of refraction demonstrates similar behavior to pressure as the occultation proceeds. The refractivity scale height allows a determination of the pressure scale height, and from that the mean molecular weight of the atmosphere. In practice, the temperature and therefore pressure scale height vary with height through the atmosphere, and this variation is not generally known, so the profiles are compared to those predicted from atmospheric models with a number of parameters that are adjusted to achieve best fits. An example of the usefulness of an occultation for determining an atmosphere's mean molecular weight is given in Sect. 12.1.1.

10.2.2 Temperature Variation with Height

The temperature structure of a planetary atmosphere, as for the interior, is reached through a consideration of the heat flow.

We consider an atmosphere in which heat flow is dominated by *adiabatic convection*, i.e., parcels of air convect without exchanging heat with their surroundings.

The adiabatic relation between pressure and density in an ideal gas is

$$P = \text{const } \rho^\gamma \quad \text{or} \quad PV^\gamma = \text{const} \quad (10.28)$$

where $\gamma = c_p/c_V$ is a quantity known as the *ratio of specific heats* (discussed below). Writing $n = N/V$, where N is the number of particles in volume V , we may solve the perfect gas law (10.18) for V to obtain

$$V = \frac{NkT}{P} \quad (10.29)$$

Then from (10.28) and (10.29),

$$P \left(\frac{NkT}{P} \right)^\gamma = \text{const} \quad (10.30)$$

or

$$(Nk)^\gamma T^\gamma P^{1-\gamma} = \text{const} \quad (10.31)$$

Finally,

$$T = \text{const}' P^{(\gamma-1)/\gamma} \quad (10.32)$$

We have shown that P depends on the altitude above the ground; we can now expect T to have such a dependence also.

The *heat capacity*, C , of a system is the heat input per unit temperature increase, i.e., the heat required to raise the temperature of the system by 1° :

$$C \equiv \frac{dQ}{dT} \quad (10.33)$$

Two types of heat capacity are particularly useful:

1. Heat capacity at constant pressure, P ,

$$C_P \equiv \left(\frac{dQ}{dT} \right)_P = \text{const}$$

2. Heat capacity at constant volume, V ,

$$C_V \equiv \left(\frac{dQ}{dT} \right)_V = \text{const}$$

If heat is added to a gas, the change shows up as an increase in internal energy and as work done,

$$dQ = dU + P dV \quad (10.34)$$

In (10.34), known as the differential form of the *first law of thermodynamics*, dQ is the heat entering the system, dU is the change in the internal energy of the gas, and $P dV$ is the work done by the gas on its surroundings.

We now apply (10.34) to three different processes in a planetary atmosphere.

First, in an *adiabatic* process, such as occurs during adiabatic convection, no heat enters or leaves a parcel of gas as it convects, i.e., $dQ = 0$. Equation (10.34) then shows that, in an adiabatic process, any work done by expansion of the gas is carried out at the expense of internal energy:

$$P dV = -dU \quad (10.35)$$

Second, if a process occurs at constant volume (referred to as an *isochoric* process), then no work is done and (10.34) gives

$$dQ = dU \quad (10.36)$$

that is, the heat goes into raising the internal energy because no expansion is permitted. The definition of C_V then gives

$$C_V = \left(\frac{dQ}{dT} \right)_{V=\text{const}} = \frac{dU}{dT} \quad (10.37)$$

for a process at constant volume.

Third, in an *isobaric* process, when the pressure is constant and the volume is allowed to change, (10.34) gives

$$C_P = \left(\frac{dQ}{dT} \right)_{P=\text{const}} = \frac{dU}{dT} + P \frac{dV}{dT} \quad (10.38)$$

Now noting from (10.37) that dU/dT equals C_V , we arrive at

$$C_P = C_V + P \frac{dV}{dT} \quad (10.39)$$

We now write the equation of state, (10.18), $P = nkT$, as

$$PV = NRT \quad (10.40)$$

where now N is the number of mol⁴ and R is the *molar gas constant*,⁵ which has the value

$$\begin{aligned} 8.3144621(75) \text{ J mol}^{-1} \text{ K}^{-1} &\cong 1.987 \text{ kcal kmol}^{-1} \text{ K}^{-1} \\ &\cong 0.08208 \text{ L atm mol}^{-1} \text{ K}^{-1} \end{aligned}$$

We can differentiate (10.40) to get

$$P \frac{dV}{dT} + V \frac{dP}{dT} = NR \quad (10.41)$$

⁴Or *moles*, gram-molecular weights or the mass equivalent of Avogadro's number ($6.02214129 (27) \times 10^{23}$) of molecules of this species. The latest values for physical constants, generally accepted worldwide, may be found on the National Institute for Standards and Technology (NIST) Website, <http://physics.nist.gov/cuu/Constants/>. At current writing (May 2013), these are the 2010 CODATA recommended values, where CODATA is the Committee on Data for Science and Technology.

⁵Or *universal gas constant*. See also Sect. 10.2.1.

Then for a process at constant pressure,

$$P \frac{dV}{dT} = NR \quad (10.42)$$

and (10.39) becomes

$$C_P = C_V + NR \quad (10.43)$$

We now define the *specific heat capacity*, also called the *specific heat*, c , by either

$$c \equiv \frac{C}{N} = \frac{1}{N} \frac{dQ}{dT} \quad \text{molar specific heat}$$

or

$$c \equiv \frac{C}{m} = \frac{1}{m} \frac{dQ}{dT} \quad \text{specific heat per unit mass}$$

depending on context. Equation (10.43) then shows that the molar specific heats are related by

$$c_P = c_V + R \quad (10.44)$$

The specific heat of an ideal gas depends on the number of degrees of freedom, g , of its particles (N.B.: this g is **not** gravitational acceleration). In general, the molar specific heats are given by

$$c_V = (g/2)R, \quad c_P = [(g/2) + 1]R$$

so the ratio of specific heats is

$$\gamma \equiv \frac{c_P}{c_V} = \frac{\left(\frac{g}{2} + 1\right)R}{\left(\frac{g}{2}\right)R} = \frac{g+2}{g} \quad (10.45)$$

In an ideal, monatomic gas the particles have only the three translational degrees of freedom in the x , y , and z directions, so $g = 3$ and

$$c_V = (3/2)R, \quad c_P = (5/2)R$$

For the light diatomic gases H₂, N₂, CO and O₂, the molecules have at least five degrees of freedom: three translational and two rotational (about the two axes perpendicular to the long axis of the molecule). If temperatures are high enough, vibration adds a sixth. Thus at the lower temperatures,

$$c_V = (5/2)R, \quad c_P = (7/2)R$$

Consequently,

$$\gamma = \frac{5}{3} \quad \text{for a monatomic gas}$$

and $\gamma = \frac{7}{5} = 1.4 \quad \text{for a diatomic gas}$

For polyatomic gases and chemically active gases (e.g., CO₂, NH₃, CH₄, Cl₂, and Br₂), C_P and C_V , and thus c_P and c_V , vary with temperature in a different way for each gas.

From (10.41) we have

$$P dV = NR dT - V dP \quad (10.46)$$

and from (10.37),

$$dU = C_V dT \quad (10.47)$$

Then (10.34) becomes

$$dQ = (C_V + NR) dT - V dP \quad (10.48)$$

In the adiabatic case, $dQ = 0$, and, using the relation $C_P - C_V = NR$ from (10.43), we find

$$C_P dT = V dP \quad (10.49)$$

When a parcel of gas rises through a displacement dr , the pressure change within the parcel is given by (10.16). Substituting from (10.16) and replacing r by the distance, h , above a reference level in the atmosphere (recall $h = r - r_0$) we obtain

$$C_P dT = -V g \rho dh \quad (10.50)$$

Dividing by $V\rho = m$ and using the specific heat per unit mass, $c_P = C_P/m$, we get

$$dT/dh = -g/c_P = -\Gamma \quad (10.51)$$

where Γ is known as the *adiabatic lapse rate*. If the air is dry, the symbol Γ_d is used. Equation (10.51) shows the explicit dependence of the temperature on

altitude for an adiabatically convecting atmosphere that we mentioned earlier in this section.

In the Earth's atmosphere, $g = 9.81 \text{ m/s}^2$, $c_P = 1,005 \text{ J/kg K}$, and

$$\Gamma_d = 0.00976 \text{ K/m} = 9.76 \text{ K/km} \quad (10.51a)$$

Later we will compare the temperature structures and *mixing ratios*⁶ of the atmospheres of the Earth, Venus, and Mars.

For a wet atmosphere,

$$c_{P(\text{water vapor})}w + c_{P(\text{dry air})}(1 - w)$$

where w is the ratio of the mass of water vapor to the total mass of air for a given volume of air.

Because $c_{P(\text{moist air})} > c_{P(\text{dry air})}$, the variation of T with height is smaller for moist air than for dry air. A lucid and still topical expansion of this discussion can be found in Seinfeld and Pandis (1998, esp., Chap. 14).

10.3 Circulation in the Atmosphere

10.3.1 Centrifugal and Coriolis Forces

In a rotating frame, such as a planet, there are “apparent” or “virtual” forces and motions that arise solely because of the motion of the frame. These are often referred to as *fictitious forces*.

(In this section, **boldface type** in equations is used to denote vectors.) Consider a displacement vector, \mathbf{r} , fixed in a frame of reference, Σ' , which is rotating with an angular velocity, $\boldsymbol{\Omega}$, with respect to an inertial (non-rotating) frame, Σ , as illustrated in Fig. 10.2. By virtue of the rotation of Σ' , the tip of the vector \mathbf{r} will appear to be moving with a linear velocity

$$\mathbf{v}_\Sigma = \boldsymbol{\Omega} \times \mathbf{r} \quad (10.52)$$

when viewed from frame Σ .

⁶The fraction by volume (or mass or number of moles) of one component compared to all others; if it is a gas, compared to all other gases but not including liquid or solid particle forms.

Fig. 10.2 A vector, \mathbf{r} , fixed in a rotating frame of reference, Σ' , and viewed from an inertial frame, Σ

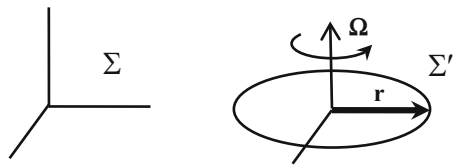
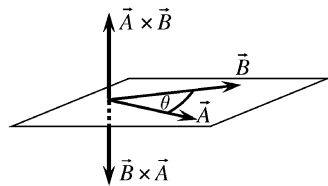


Fig. 10.3 The vector cross-product



The quantity $\boldsymbol{\Omega} \times \mathbf{r}$ is a vector cross-product, and is itself a vector, the magnitude of which equals the product of the magnitudes of the two vectors times the sine of the angle between them:

$$|\boldsymbol{\Omega} \times \mathbf{r}| = \boldsymbol{\Omega} r \sin \theta \quad (10.53)$$

and the direction of which is perpendicular to both vectors, as given by the “right-hand rule” (see Fig. 10.3):

Point the fingers of your right hand along the first vector in the cross-product, then orient your hand so you can curl your fingers from the first vector to the second vector. Your thumb now points in the direction of the cross-product.

If in Fig. 10.2 the vector \mathbf{r} changes with time as viewed from frame Σ' , the effect as viewed from frame Σ will be

$$(\mathbf{D}\mathbf{r})_\Sigma = (\mathbf{D}\mathbf{r})_{\Sigma'} + \boldsymbol{\Omega} \times \mathbf{r} \quad (10.54)$$

where D is the operator $D = d/dt$.

Equation (10.54) gives the relationship between the velocity vectors,

$$\mathbf{v}_\Sigma = \mathbf{v}_{\Sigma'} + \boldsymbol{\Omega} \times \mathbf{r} \quad (10.55)$$

In the example above, $\mathbf{v}_{\Sigma'} = 0$.

In fact, the rate of change of any vector, \mathbf{A} , as seen in Σ is the rate of change in Σ' plus the cross-product with the angular velocity vector, $\boldsymbol{\Omega}$:

$$(\mathbf{D}\mathbf{A})_\Sigma = (\mathbf{D}\mathbf{A})_{\Sigma'} + \boldsymbol{\Omega} \times \mathbf{A} \quad (10.56)$$

Thus the variation of the velocity vector is, from either (10.55) or (10.56),

$$(D\mathbf{v}_\Sigma)_\Sigma = (D\mathbf{v}_\Sigma)_{\Sigma'} + \boldsymbol{\Omega} \times \mathbf{v}_\Sigma \quad (10.57)$$

The quantity on the left-hand side is the acceleration observed by an observer in the inertial frame, Σ .

Substituting (10.55) into (10.57), we find

$$(D\mathbf{v}_\Sigma)_\Sigma = (D\mathbf{v}_{\Sigma'})_{\Sigma'} + 2(\boldsymbol{\Omega} \times \mathbf{v}_{\Sigma'}) + \boldsymbol{\Omega} \times (\boldsymbol{\Omega} \times \mathbf{r}) \quad (10.58)$$

Then defining $\mathbf{a} = (D\mathbf{v})_\Sigma$, $\mathbf{a}' = (D\mathbf{v}_{\Sigma'})_{\Sigma'}$, and $\mathbf{v}' = \mathbf{v}_{\Sigma'}$, we obtain

$$\mathbf{a} = \mathbf{a}' + 2\boldsymbol{\Omega} \times \mathbf{v}' + \boldsymbol{\Omega} \times (\boldsymbol{\Omega} \times \mathbf{r}) \quad (10.59)$$

where primes denote quantities measured in the rotating frame. If our vectors actually describe the position, velocity, and acceleration of a particle, then multiplying by the particle's mass, we arrive at the force equation:

$$\mathbf{F} = \mathbf{F}' + 2m\boldsymbol{\Omega} \times \mathbf{v}' + m\boldsymbol{\Omega} \times (\boldsymbol{\Omega} \times \mathbf{r}) \quad (10.60)$$

or, from the standpoint of an observer in the moving frame,

$$\mathbf{F}' = \mathbf{F} - 2m\boldsymbol{\Omega} \times \mathbf{v}' - m\boldsymbol{\Omega} \times (\boldsymbol{\Omega} \times \mathbf{r}) \quad (10.61)$$

The second term on the right-hand side,

$$\mathbf{F}'_{\text{Cor}} = -2m\boldsymbol{\Omega} \times \mathbf{v}' \quad (10.62)$$

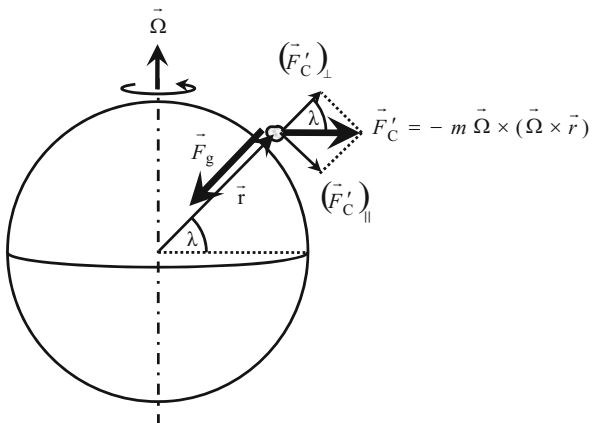
is the *Coriolis force*, and the third,

$$\mathbf{F}'_C = -m\boldsymbol{\Omega} \times (\boldsymbol{\Omega} \times \mathbf{r}) \quad (10.63)$$

the *centrifugal force*. The Coriolis and centrifugal forces are so-called *fictitious forces* that are apparent to a non-inertial observer rotating with the planet. Some experimentation with the right-hand rule, and remembering the minus sign in the equation, will show that the centrifugal force is directed perpendicularly outward from the rotation axis of the planet.

The practical consequences of these terms will be examined next.

Fig. 10.4 The centrifugal force, \vec{F}'_C , on a parcel of air in the atmosphere of a rotating planet, and its components parallel and perpendicular to the planetary surface. λ is the latitude of the parcel



10.3.2 Physical Effects of the Centrifugal and Coriolis Forces

10.3.2.1 The Centrifugal Force

Figure 10.4 shows a parcel of air in the atmosphere of a rotating planet. The view is that of an inertial observer in space, but we analyze the forces as experienced by a non-inertial observer on the planet's surface. The gravitational force on the parcel, $F_g = mg$ (where m is the mass of the parcel), acts directly toward the center of the planet, whereas applying the right-hand rule in Fig. 10.4 shows that the centrifugal force, F'_C , acts radially outward from the planet's rotation axis. (Here we retain the primed notation for “fictitious” forces that exist only in the rotating frame.)

From Fig. 10.4, the apparent weight of the parcel (i.e., the upward force needed to prevent the parcel from falling) has magnitude

$$(F_g)_{\text{eff}} = F_g - (F'_C)_{\perp} = F_g - F'_C \cos \lambda \quad (10.64)$$

where λ is the latitude of the parcel. Then using (10.52) and (10.63),

$$(F_g)_{\text{eff}} = mg - m \frac{v^2}{r} \cos \lambda = m \left(g - \frac{v^2}{r} \cos \lambda \right) \equiv mg_{\text{eff}} \quad (10.65)$$

where

$$g_{\text{eff}} \equiv g - \frac{v^2}{r} \cos \lambda \quad (10.66)$$

is the effective gravitational acceleration (or *effective gravity*) at the parcel's location. Rotation thus reduces the apparent weight and apparent acceleration due to gravity

on a rotating planet. [In (10.65) and (10.66), g and g_{eff} are the magnitudes of the gravitational acceleration and effective gravitational acceleration, respectively.]

The component vector $(\vec{F}'_C)_{||}$ in Fig. 10.4 causes the parcel of air to drift toward the equator, creating an equatorial bulge. The consequent *rotational flattening* can be seen in images of Jupiter and Saturn as in Figs. 12.1 and 12.9, for example. The process is self-limiting, because the bulge in turn creates pressure gradient forces that oppose $(F'_C)_{||}$. $(F'_C)_{||}$ is larger at a given latitude for faster-rotating planets, so faster-rotating planets are more rotationally flattened.

10.3.2.2 The Coriolis Force

From (10.62), the Coriolis force on any object depends on its velocity, \mathbf{v}' , relative to the rotating reference frame of the planet. For a planet with a solid surface, e.g., a terrestrial planet, we can take \mathbf{v}' as relative to the horizon plane at a point on the surface.

Some experimentation applying the right-hand rule (Sect. 10.3.1) to the cross-product in (10.62) combined with appropriate diagrams (see Fig. 10.5 for an example) shows that:

1. An object at rest in the rotating frame (e.g., at rest relative to the Earth's surface) experiences no Coriolis force.
2. An object exactly on the equator experiences no Coriolis force when moving due north or south, because $\Omega \parallel \mathbf{v}'$. If moving in any other compass direction, it experiences no Coriolis force parallel to the surface because Ω and \mathbf{v}' are both in the plane of the surface.
3. In both hemispheres, an object moving toward the (nearest) pole experiences a Coriolis force toward the east, and an object moving toward the equator experiences a Coriolis force toward the west.
4. In both hemispheres, an object moving due east experiences a Coriolis force perpendicularly outward from the planet's rotation axis; the component parallel to the surface therefore causes the object to veer toward the equator. For an object moving due west, the Coriolis force is perpendicularly inward toward the rotation axis and the object veers toward the pole.

Case (3), above, can be understood intuitively when analyzed in the inertial frame (e.g., in the view from space shown in Fig. 10.5). Consider objects at rest relative to the surface of the rotating planet. The linear speed eastward of such objects when measured in the inertial frame is greater for objects closer to the equator because they are further from the rotational axis. In the absence of other constraints, when the object moves poleward it finds itself above points on the ground that are closer to the rotational axis and moving eastward more slowly than itself. Consequently, it drifts toward the east relative to the ground below. An object moving toward the equator finds itself moving over points on the ground that are

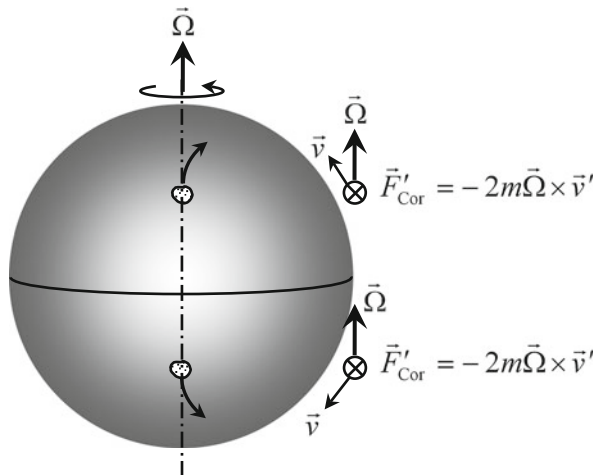


Fig. 10.5 The vectors on the right show the planetary angular velocity, $\vec{\Omega}$, the velocity, \vec{v} , and the Coriolis force, \vec{F}'_{Cor} (into the page) on a poleward-moving parcel of air on the limb of a rotating planet, as viewed from space. The *curved arrows* on the central longitude show the resulting motion of the parcel of air *relative to the planet's surface*, in the absence of other constraints. The northern parcel veers right (east) and the southern veers left (also east)

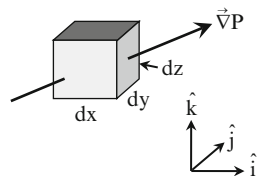
moving faster than itself, and it therefore drifts toward the west relative to the ground below. (For an object moving parallel to the ground or a projectile returning to the ground, the effect is actually stronger than suggested by this intuitive description because of conservation of angular momentum. As a parcel of air moves poleward it also approaches the rotation axis, so its eastward speed increases in the inertial frame while the ground speed below it decreases. If it moves toward the equator then it also moves away from the rotation axis, and its eastward speed decreases while the ground speed increases.)

Cases (3) and (4) can be summarized by saying that the Coriolis force causes moving objects to veer toward the right in the northern hemisphere and toward the left in the southern, regardless of (northward or southward) direction of travel.

10.3.3 Pressure Gradient Force

Pressure varies horizontally as well as vertically in planetary atmospheres, and the resulting horizontal forces drive winds and atmospheric circulation. Occasionally these winds can be extreme. In Hurricane Wilma (2005), a Category 5 hurricane in the northwestern Caribbean, the surface atmospheric pressure at peak intensity was 1,004 mb outside the hurricane and 882 mb at the center of the eye, the latter being the lowest value ever found for an Atlantic-basin hurricane since record-keeping began in 1851. The resulting peak sustained surface wind speed was 160 knots,

Fig. 10.6 A small volume of air in a region of pressure gradient in a planetary atmosphere



or 300 km/h. Fortunately, these peak values occurred over open water, but Wilma was still very intense during landfall (Pasch et al. 2006). The lowest sea-level pressure recorded to date was 870 mb in the eye of Typhoon Tip on Oct 12, 1979, when it was 840 km NW of Guam. The typhoon at that time was more than 2,000 km diameter with winds up to 305 km/h.

In Fig. 10.6, a small parcel of air of volume $dx dy dz$ is situated in a region of a planetary atmosphere containing a pressure gradient. We place the lower front left corner at (x,y,z) , so the right-hand face is at $x + dx$, the back face at $y + dy$, and the top face at $z + dz$. The pressure gradient vector, expressed as $\vec{\nabla}P$, where the del (or grad) operator is defined as

$$\vec{\nabla} \equiv \frac{\partial}{\partial x} \hat{i} + \frac{\partial}{\partial y} \hat{j} + \frac{\partial}{\partial z} \hat{k}$$

is oriented in an arbitrary direction relative to the x,y,z coordinate axes. The force component, dF_x , in the x -direction on this parcel of air is

$$dF_x = P_x dA - P_{x+dx} dA = -(P_{x+dx} - P_x) dy dz \equiv -dP_x dy dz$$

where P_x and P_{x+dx} are the pressures at positions x and $x + dx$, respectively, and $dA = dy dz$ is the cross-sectional area perpendicular to the x -axis. The change in pressure over distance dx is $dP_x = \partial P / \partial x dx$, so we can write

$$dF_x = -\frac{\partial P}{\partial x} dx dy dz$$

Applying a similar procedure to the y and z -directions gives

$$d\vec{F} = -\left(\frac{\partial}{\partial x} \hat{i} + \frac{\partial}{\partial y} \hat{j} + \frac{\partial}{\partial z} \hat{k}\right) P dx dy dz = -\vec{\nabla}P dx dy dz \quad (10.67)$$

It follows that the pressure gradient force is opposite in direction to the pressure gradient.

10.3.4 Friction

Friction has an important influence on winds and circulation in the lowest 1 km of air above the ground.

Fig. 10.7 Variation of wind speed with altitude, due to friction. Not to scale

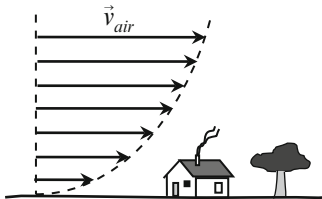


Fig. 10.8 Isobars, forces, and wind near high and low-pressure areas in the northern hemisphere of a planetary atmosphere (see text)

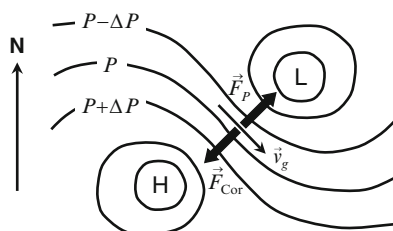
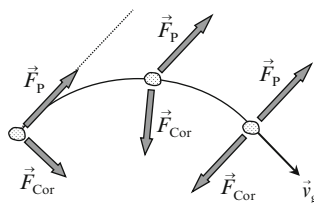


Fig. 10.9 Establishment of geostrophic balance for a parcel of air in the northern hemisphere, initially moving in the direction of the pressure gradient force (see text)



Within about 1 m of the ground the source of friction is molecular viscosity; above 1 m it is small-scale eddies. As suggested in Fig. 10.7, the effect of friction is to limit wind speed progressively closer to the ground.

10.3.5 Geostrophic Balance and Geostrophic Winds

Figure 10.8 shows a schematic representation of high- and low-pressure areas in the northern hemisphere of a planetary atmosphere, with illustrative *isobars* (lines of constant pressure). \vec{F}_P is the pressure gradient force, directed from high to low pressure; \vec{F}_{Cor} is the Coriolis force, directed perpendicular to the air motion; and \vec{v}_g is the geostrophic wind, defined and discussed below.

In Fig. 10.9, a parcel of air initially begins traveling in the direction of the pressure gradient force. Immediately, it feels a Coriolis force perpendicular to its direction of motion, causing it to veer to the right in the northern hemisphere or to the left in the southern. It continues to veer as long as the total force has a component perpendicular to the wind direction; consequently, the circulation can reach steady state only when the Coriolis and pressure gradient forces exactly balance.

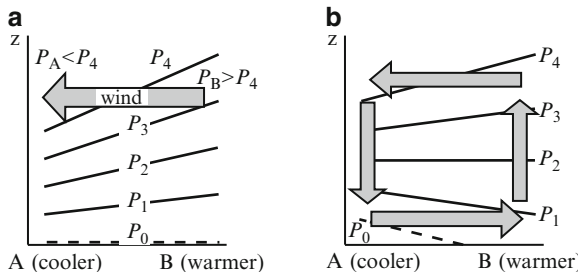


Fig. 10.10 Isobars above a region of uneven temperature ($T_A < T_B$), and the resulting winds. (a) Upper-level wind assuming a horizontal isobar at ground level. (b) Mass transport from B to A by the upper-level wind tilts the lower-level isobars, resulting in a return flow near ground level

Because of the constraint that the pressure gradient force is always perpendicular to the isobars, the resulting wind direction must be parallel to the isobars (Figs. 10.8 and 10.9). This balance of Coriolis and pressure gradient forces is referred to as *geostrophic balance*, and the resulting wind is a *geostrophic wind*.

It is also worth noting that the more compressed the isobars, the stronger the pressure gradient force, the stronger the required Coriolis force, and therefore the stronger the geostrophic wind.

10.3.6 Thermal Effects

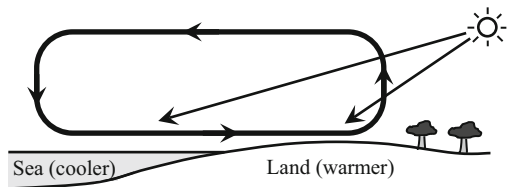
10.3.6.1 Thermal Circulation

A horizontal temperature gradient between one part of a planetary atmosphere and another creates a pressure gradient force that in turn creates a wind. We will look first at distance scales small enough to ignore the Coriolis force (e.g., a few hundred meters), so that the wind direction is in the direction of the pressure gradient.

To see how thermal circulation arises, consider the following thought experiment for a region on the Earth. Consider a vertical cross-section through a volume of calm air above level ground that is at a uniform temperature, T_0 . Because the air is calm and the ground temperature is uniform, the pressure scale height, H , is also uniform, as per (10.25) or (10.26), and the isobars are horizontal. The ground is thus both an *isotherm* (line of constant temperature) and an isobar, which we define to be at pressure P_0 .

Now allow the air temperature to fall at some location, A, and rise at some other location, B, i.e., $T_A < T_B$. Then by (10.25), $H_A < H_B$. At this point in our experiment the mass of air above each point on the ground remains unchanged, so there is still a horizontal isobar at pressure P_0 at ground level; but because of the larger scale height at B, the isobars are as in Fig. 10.10a. At *any given altitude*, the pressure will be higher above B than above A, and the horizontal pressure gradient will drive a wind from the warmer to the cooler region (B to A), as indicated by the arrow in Fig. 10.10a.

Fig. 10.11 Thermal circulation and the daytime sea breeze. The flow is reversed at night



The transport of mass from B to A by this wind increases the air mass above A and decreases it above B, causing the air pressure at ground level to rise at A and fall at B. This makes the lower-altitude isobars tilt in the opposite direction from those at higher altitudes. The upper level flow from the warmer to the cooler region is then matched by a return flow from the cooler to the warmer region at low level. These in turn are joined by warm air rising at B and cool air falling at A, creating a complete *thermal circulation* pattern, as in Fig. 10.10b.

An example of thermal circulation is the sea breeze created by solar heating of the land and the water at a seashore, illustrated in Fig. 10.11. The land has lower heat capacity compared to the water, and so can be heated more quickly by sunlight. From Figs. 10.10b and 10.11, on a hot day with otherwise no wind, people on the beach enjoy a cool breeze coming from the water. At night, although there may be few people on the beach to notice, the land cools faster than the water and the circulation reverses: the breeze at night is directed from the land to the water.

10.3.6.2 The Thermal Wind

When the scale is larger than in Fig. 10.11, the Coriolis force can no longer be ignored. Horizontal temperature gradients then affect the geostrophic balance and the direction of the geostrophic wind.

Figure 10.12 illustrates isobars at ground level in the vicinity of high and low-pressure regions. For simplicity we assume level ground. The geostrophic wind at ground level, $(\vec{v}_g)_0$, is parallel to the isobars. In the absence of a temperature gradient, the isobars above ground level will be parallel to the ground and the direction of the geostrophic wind will be the same at all altitudes.

Now consider the region between the two isotherms T_1 and T_2 (dashed lines) in Fig. 10.12, with $T_1 < T_2$. Figure 10.13a plots pressure vs. altitude, z , above a line that follows the P_0 isobar (dotted line) in Fig. 10.12, so that ground level is a line of constant pressure (cf. Fig. 10.10a). At altitudes above the ground the sloping isobars create a pressure gradient force, $(\vec{F}_P)_T$, parallel to the ground-level isobars of Fig. 10.12. The subscript, T , indicates that $(\vec{F}_P)_T$ is produced by the horizontal temperature gradient. $(\vec{F}_P)_T$ is zero at ground level because the isobar is horizontal, and increases progressively as the isobars steepen with altitude.

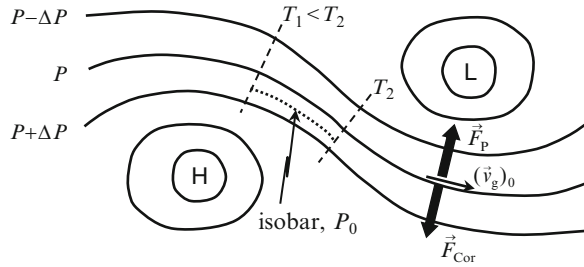


Fig. 10.12 Isobars, forces, and wind near high and low-pressure areas in a planetary atmosphere (see text)

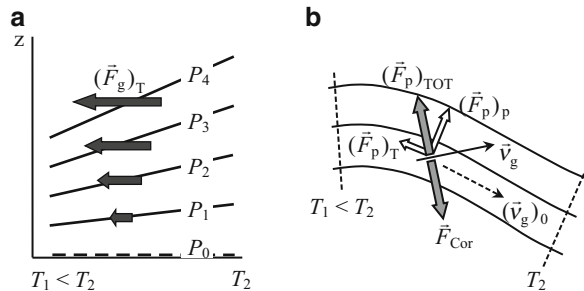


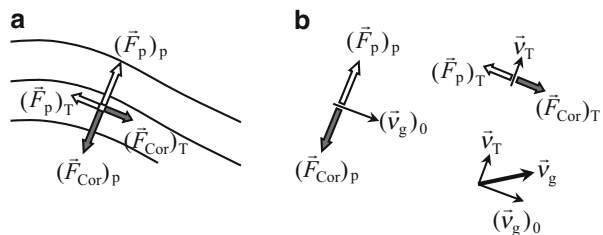
Fig. 10.13 (a) Isobars above a region with a temperature gradient ($T_1 < T_2$) and the resulting thermal component of the pressure gradient force, $(\vec{F}_P)_T$ (arrows). (b) Geostrophic wind, \vec{v}_g , at altitude $z > 0$ compared to $(\vec{v}_g)_0$ at ground level, in a region of temperature gradient

$(\vec{F}_P)_T$ adds vectorially to the original pressure gradient force, which we now call $(\vec{F}_P)_p$, created by the high and low-pressure areas, as shown in Fig. 10.13b. As described in Fig. 10.9, the Coriolis force, \vec{F}_{Cor} , causes the wind to veer until the net force on an air parcel is zero; i.e., until the geostrophic wind (always perpendicular to \vec{F}_{Cor}) is perpendicular to $(\vec{F}_P)_{\text{TOT}} = (\vec{F}_P)_p + (\vec{F}_P)_T$ rather than to $(\vec{F}_P)_p$ alone.

Thus, in the northern hemisphere, if the geostrophic wind blows from a colder to a warmer region, it veers to the left at any altitude $z > 0$, compared to its direction at ground level ($z = 0$), with the amount of veer increasing with increasing altitude. In the southern hemisphere it would veer to the right. If the wind blows from a warmer to a colder region these directions would be reversed: to the right in the northern hemisphere and to the left in the southern.

A more common way of describing the same effect is to picture the wind at altitude as consisting of two components: a purely geostrophic component (parallel to the isobars), which remains constant with altitude and equal to the geostrophic

Fig. 10.14 (a) Components of the pressure gradient force and the Coriolis force on a parcel of air. (b) The corresponding wind components and the resultant geostrophic wind



wind at ground level, $(\vec{v}_g)_0$, and a *thermal wind*, \vec{v}_T (also a wind component), which blows in a direction such that the Coriolis force on it, $(\vec{F}_{Cor})_T$, is opposite to $(\vec{F}_P)_T$, as shown in Fig. 10.14b. The thermal wind increases with increasing altitude, making the resulting geostrophic wind, \vec{v}_g , veer increasingly away from $(\vec{v}_g)_0$ as altitude increases.

The thermal wind direction can always be predicted from the isotherms by the fact that \vec{v}_T is directed so that the colder region is to the left of the wind vector in the northern hemisphere and to the right in the southern. $(\vec{v}_g)_0$ can also be predicted from the isobars, because it is directed so that the lower pressure is to the left of the vector in the northern hemisphere, and to the right in the southern.

10.3.7 Global Circulation

10.3.7.1 The Observed Surface Pattern

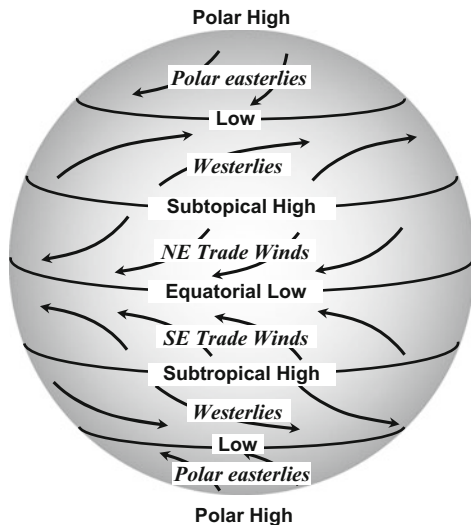
Figure 10.15 shows the major features of the global circulation pattern on the surface of the Earth. The pattern shown is highly smoothed and averaged, and the latitudes are very approximate. The actual pattern on any given day is more complicated. The features also shift north and south somewhat with the seasons, as the direction of illumination by the Sun changes through the year.

The pattern is characterized by alternating high and low-pressure belts, with winds dominantly in one direction in the region between any two belts. (Note that, by tradition, winds are named for the direction *from* which they blow, not the direction *towards* which they blow, i.e., the *westerlies* blow *from* the west, and the *north-east trade winds* blow *from* the north-east (toward the south-west).)

The trade winds got their name because they “blow trade,” that is, they blow a constant course or direction. This made them very useful to sailing ships carrying trade goods over the world’s oceans.

The westerlies are much more variable and unreliable, to the detriment of some sailing ships that did not make it back home.

Fig. 10.15 Global circulation pattern on the Earth



The area from which the westerlies and the trade winds diverge (the subtropical high) is a region of calm or light winds, and is often called the *horse latitudes*.

In the area near the equator where the NE and SE trade winds converge and the air rises toward the upper troposphere, surface winds not surprisingly tend to be light. This region is often called the *doldrums*; or, more technically, the *inter-tropical convergence zone* (ITCZ). The origin of the word “doldrums” is not known, but it may have been created by contrasting the dullness of, for example, being sick, with the liveliness of having a tantrum. A person getting better from the “flu” would be recovering from the “dull-drums.” By extension, any becalmed ship was said to be in the doldrums, and eventually the name became a geographical location, applying to the region of ocean where ships were most often becalmed.

The warm air of the NE trade winds picks up moisture from the ocean and then loses it to condensation as the air rises in the ITCZ. Thus the ITCZ often shows up in satellite photographs of the Earth as a band of clouds near the equator.

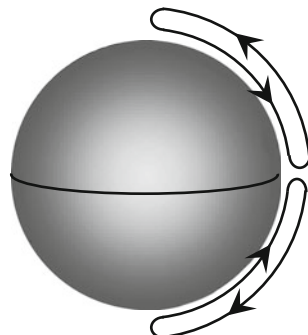
In the following sections, we will use the forces and processes described above to try to account for the circulation pattern in Fig. 10.15, and then go on to other topics.

10.3.7.2 The Hadley Cell

The basic pattern of westerlies and trade winds was known by the 1600s from data provided by mariners. The cause, however, was unknown. Edmund Halley⁷ (of Halley’s Comet fame) suggested in 1686 that the trade winds resulted from

⁷1656–1742.

Fig. 10.16 Hypothetical single Hadley cells extending from the equator to the poles



solar heating at the equator, making the air rise and forcing other air to flow toward the equator from the tropics to replace it. This accounted nicely for the component toward the equator, but not for the easterly component (toward the west).

The English scientist, George Hadley (1685–1768), in 1735, extended Halley's explanation to create a complete circulation cell and suggested that the Earth's rotation deflected the air toward the west. This was 100 years before Gaspar G. Coriolis (1792–1843) of France derived the Coriolis force mathematically, in 1835.

The *Hadley cell* is a thermal circulation cell like that causing a sea breeze, but on a global scale. A single Hadley cell on the Earth might (but doesn't!) extend from the equator to the pole in each hemisphere, as shown in Fig. 10.16. The air would be heated at the equator, rise, move toward the colder poles for the reasons described in Sect. 10.3.6, cool there, sink, and return to the equator along the Earth's surface. With a single Hadley cell in each hemisphere, we would have:

Southward-moving surface air which veers toward the west, creating the polar easterlies and the trade winds;

A low-pressure area where the air is heated at the equator and a high-pressure area where the air cools at the poles.

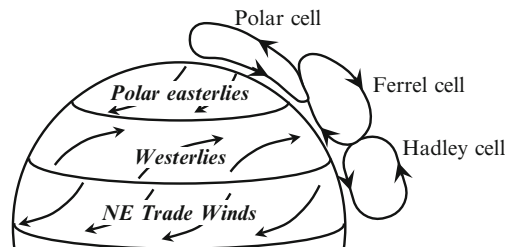
Each cell would also carry warm air from the equator to the pole and cooler air from the pole to the equator, balancing the radiant energy surplus at the equator and the radiant energy deficit at the pole. However, a single Hadley cell in each hemisphere does not account for the subtropical high-pressure belts, the mid-latitude low-pressure belts, or the westerlies.

10.3.7.3 The Ferrel and Polar Cells

The Coriolis force makes the single Hadley cell described in Sect. 10.3.7.2 break up into three cells, as indicated in Fig. 10.17. In each cell, the surface winds veer toward the right to create the polar easterlies, westerlies, and NE trade winds. The high-altitude winds also veer toward the right, and are therefore in the opposite sense to the surface winds.

By about 30°N and S latitude, the upper air from the equator has lost much of its northward component and has time to cool and sink. The descending flow splits, as

Fig. 10.17 The Coriolis force causes each Hadley cell in Fig. 10.16 to break up into three cells. Not to scale



shown in Fig. 10.17. Some air flows south, completing the Hadley cell, while some flows north to create a new cell, the *Ferrel cell*, named for William Ferrell (1817–1891).

The warmer and cooler temperatures where the air rises and sinks, respectively, create the equatorial low and the subtropical highs (respectively) in Fig. 10.17, as discussed in Sect. 10.3.7.1.

At about 60°N and S latitude, the surface air from the poles has lost much of its southward component and has time to warm and rise. The warmer temperature creates the mid-latitude low-pressure belt. The rising flow splits, as shown in Fig. 10.17. Some air flows north, completing the polar cell, while some flows south, joining the Ferrel cell.

The Hadley and polar cells are thermally driven. The Ferrel cell is thermally indirect (sometimes referred to as *parasitic*) and is driven by the other two cells.

Figure 10.18 illustrates the observed seasonal variation in the mean meridional (north–south) circulation pattern in the northern hemisphere between winter and summer. (The word *meridional* refers to the north–south direction, i.e., along a meridian of longitude, whereas *zonal* refers to the east–west direction, along a line of latitude.)

The northern- and southern-hemisphere Hadley cells are of similar strength near the equinoxes. Both cells move north in the northern summer and south in the southern summer (northern winter), with the winter-hemisphere Hadley cell dominating the circulation and the summer-hemisphere cell becoming much weaker (Fig. 10.18). In southern summer, the northern cell carries ~5 times the flow of the southern, whereas in northern summer the southern cell straddles the equator from ~30° S to >10° N and carries 10–15 times the flow of the northern.

The polar cell is very weak, and does not show up in Fig. 10.18.

10.3.7.4 Eddie Motions in the Westerlies

A large-scale view such as that in Fig. 10.15 ignores small-scale features that can in fact be important in the poleward transport of heat by the atmosphere. In the westerlies in particular, uneven heating and cooling of the atmosphere, caused, e.g., by the differing heat capacities of continents and oceans, produces *baroclinic instabilities*.

Specifically, baroclinic instabilities occur when the isobaric surfaces are inclined to the isothermal surfaces (Sect. 10.3.6). These instabilities perturb the generally westerly mid-latitude flow, creating large-scale waves. Eddies associated with these

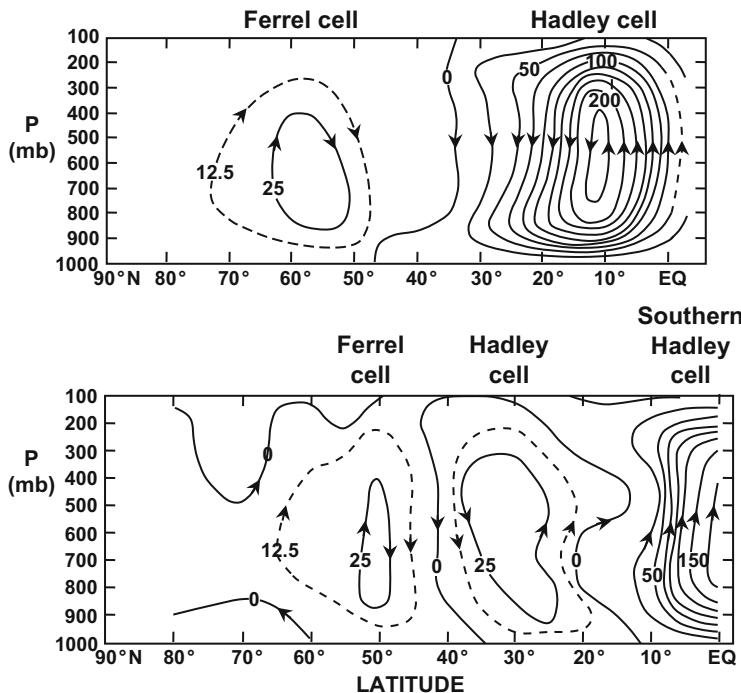


Fig. 10.18 Zonally averaged meridional circulation as a function of latitude and altitude during northern winter (*upper chart*) and northern summer (*lower*). Numbers on flow lines represent mass flux in units of 25×10^6 tons/s, i.e., the mass transported in the channel between any two adjacent, solid streamlines is 25×10^6 tons/s. See Fig. 10.22 for an approximate conversion chart between pressure and altitude. (After Iribarne and Cho 1980, Fig. VII-22, p. 179)

waves show up as high and low-pressure areas, the former usually lying equatorward of the flow and the latter lying poleward. As indicated schematically in Fig. 10.19 for the northern hemisphere, the alternating northward and southward flow results in a net transport of heat poleward.

10.3.7.5 Air Masses and Fronts

An *air mass*⁸ is a large volume of air having reasonably unified properties (e.g., temperature, moisture content). A *front* is a boundary between two air masses.

On the Earth, there are three basic types of air mass in terms of temperature: *polar*, *mid-latitude*, and *tropical*, as illustrated schematically in Fig. 10.20. Each of these in turn can be divided into two categories in terms of moisture content: *maritime* (moist) and *continental* (dry) air masses.

⁸Not to be confused with *air mass* in astronomical extinction, which is the thickness of a column of air normalized to the zenith value.

Fig. 10.19 Poleward transport of heat by eddy and wave motion in a planetary atmosphere, illustrated for the northern hemisphere

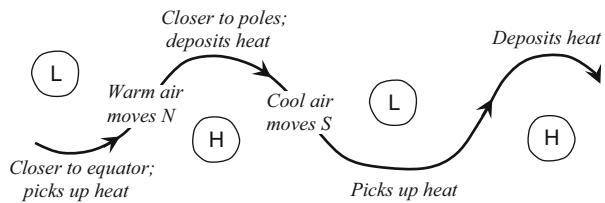
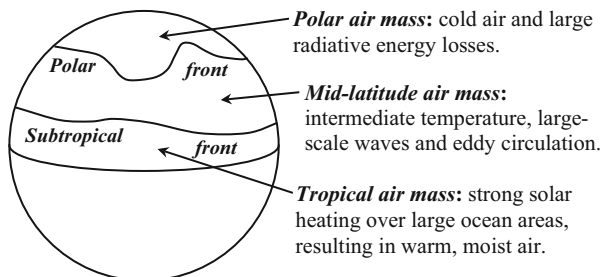


Fig. 10.20 Air masses and fronts in the Earth's atmosphere. A corresponding division occurs in the southern hemisphere



10.3.7.6 Jet Streams

A *jet stream* is a narrow, high-velocity stream of air in the upper troposphere or the stratosphere. Here, we describe in some detail the formation of the *polar jet stream*, formed by the strong horizontal temperature gradient across the polar front. The weaker *subtropical jet stream* forms by a similar process at the more diffuse subtropical front.

Figure 10.21 shows a meridional cross-section of the Earth's atmosphere. The view is facing east, with the North Pole on the left and the equator on the right. The polar and subtropical jet streams, marked by J_p and J_s , respectively, are located at the discontinuities between the tropical and middle and the middle and polar tropopausees.

The strong horizontal temperature gradient across the polar front is evident in Fig. 10.21 where, e.g., the temperature on a horizontal line through the polar front at 4 km altitude rises toward the south from -25 to -15 °C.

In the northern hemisphere, a horizontal temperature gradient produces a thermal wind directed with the colder air on the left and the warmer air on the right (Sect. 10.3.6.2). The reverse would be true in the southern hemisphere. Thus the wind becomes stronger westerly (toward the east) as altitude increases through the troposphere in both hemispheres. The effect is strongest where the horizontal temperature gradient is strongest, near the polar front. A similar effect occurs at the subtropical front, but because the front is more diffuse, the subtropical jet stream is weaker.

Figure 10.22 shows a zonally averaged cross-section of the Earth's atmosphere from the North Pole to the South Pole during the northern summer (left) and northern winter (right). The mean zonal winds are marked. Along the surface of the Earth, the wind directions correspond to the trade winds (easterly winds, i.e., *from* the east), the westerlies, and the polar easterlies. However, the winds swing

Fig. 10.21 Meridional cross-section of the Earth's atmosphere, showing zonal mean temperatures ($^{\circ}\text{C}$) in the northern hemisphere on January 1, 1956. The positions of the polar (J_p) and subtropical (J_s) jet streams and the polar and subtropical fronts are marked. The subtropical front is much more diffuse than the polar front. (After Iribarne and Cho 1980, Fig. VII-26, p. 185)

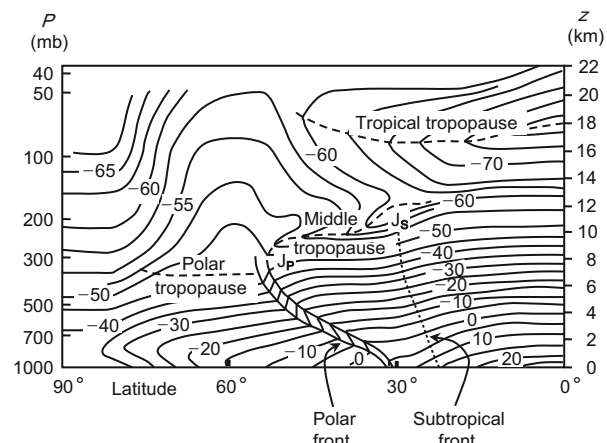
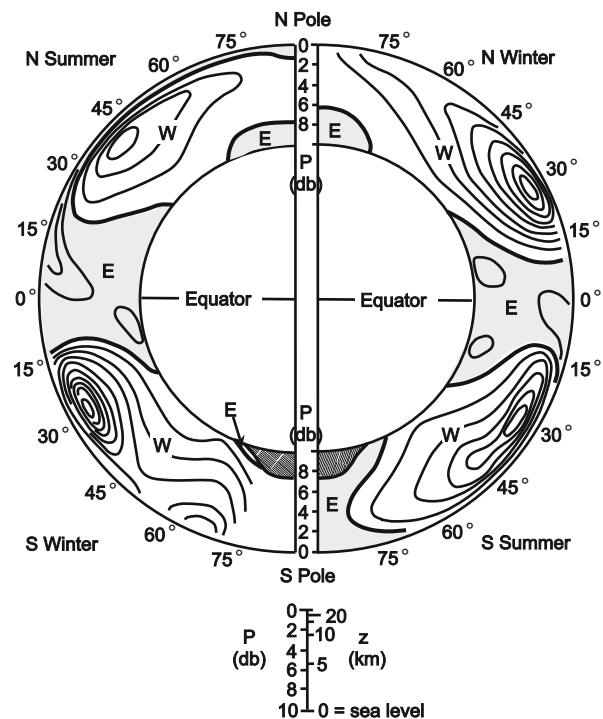


Fig. 10.22 Zonally averaged wind distribution from sea level (inner circle) to the top of the atmosphere (outer circle), during northern summer (left) and northern winter (right). Heavy contours = 0 m/s; contour interval = 5 m/s. Regions of easterly (E) and westerly (W) winds are marked. The hatched area near the bottom is Antarctica. An approximate conversion chart is shown from pressure to altitude (1 db = 0.1 bar). (After Iribarne and Cho 1980, Fig. VII-23, p. 180.)



more and more westerly as altitude increases, with the strongest westerly winds occurring near the 200 mb level (about 12 km altitude) in the upper troposphere. These are quite localized and indicate the polar jet streams.

Comparing the two sides of the diagram, it is evident that each jet is strongest during winter in its hemisphere. The entire circulation pattern also shifts northward

during northern summer and southward during southern summer, responding to the changing position of the sub-solar point over the year.

We next discuss the interaction between planetary atmospheres and surfaces.

10.4 Atmospheric Effects on the Heat Budget

Figure 10.23 shows the variation of temperature with altitude in the atmospheres of the Earth, Venus, and Mars. The four main divisions in the Earth's atmosphere are labeled.

10.4.1 The Earth

By far the dominant source of heat for the Earth's atmosphere is the Sun, which approximates very closely a black body of 5,800 K. The energy flux incident on the Earth is thus almost entirely short wavelength (UV, visible and near-IR, $\lambda \leq 2 \mu\text{m}$); see, e.g., Milone and Wilson 2014, Sect. 4.4.4 for further discussions of blackbody flux, and Sect. 6.3 for the effect of solar radiation on Earth.

The *solar constant* for the Earth (the radiant power from the Sun per square meter perpendicular to the Sun's rays at the Earth's mean distance of 1 au, measured outside the Earth's atmosphere) is $\sim 1,368$ (Cox 2000, p. 340 gives 1,365–1,370), W/m^2 . The globally and temporally averaged energy flux intercepted by the Earth then equals solar constant $\times \pi r^2 / 4\pi r^2 = 342 \text{ W/m}^2$, where r is the radius of the Earth and $4\pi r^2$ is the surface area of a sphere. For long-term thermal stability, the Earth must reflect or radiate this same globally and temporally averaged energy flux back into space.

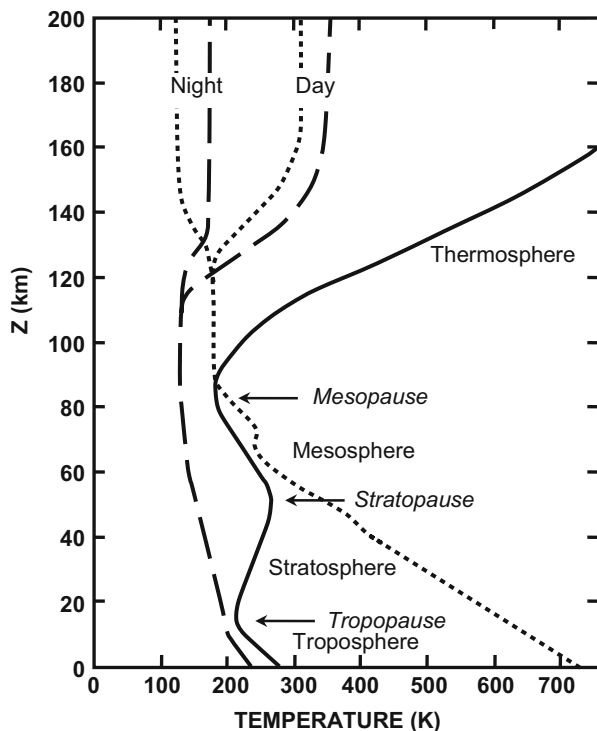
On average, of every 100 units of energy incident, approximately 31 are reflected or scattered back to space and 69 are absorbed: three in the stratosphere (primarily by ozone), 17 by cloud droplets, water vapor, dust, and carbon dioxide in the troposphere, and 49 by the ground.

The absorbed energy flux maintains the Earth at a globally and temporally averaged equilibrium temperature near 288 K, for which the emitted black body radiation is almost entirely at long wavelengths ($5 \mu\text{m} \leq \lambda \leq 20 \mu\text{m}$). Given the same 100 units incident as above, 12 units are radiated directly to space by the ground, 48 are radiated by water vapor and carbon dioxide in the troposphere, and nine are radiated by the clouds; thus the 69 units absorbed from the sun are balanced by 69 units radiated back to space.

10.4.1.1 Troposphere of the Earth

The primary absorbers in the troposphere are water vapor and carbon dioxide, which absorb efficiently at $\lambda \geq 5 \mu\text{m}$. Thus, the troposphere allows most of the incoming solar radiation to pass through to the ground, but absorbs most of the IR

Fig. 10.23 Thermal structure of the atmospheres of the Earth (solid line), Venus (dotted), and Mars (dashed). The atmospheric layers are labeled for the Earth



radiated upward by the ground. (The 12 units radiated directly to space, mentioned above, are only a small fraction of the flux radiated by the ground.) Absorption in lower layers reduces the flux to higher layers, resulting in a temperature that decreases with height, z , above the ground, i.e., the lapse rate from (10.51) in Sect. 10.2.2,

$$\Gamma = -\frac{dT}{dz} \quad (10.68)$$

is positive in the troposphere. The observed average lapse rate in the troposphere is about $6.5 \text{ }^{\circ}\text{C}/\text{km}$; however, the value at specific locations can deviate significantly from this, even becoming negative (temperature increasing with altitude) in a region of temperature inversion.

If the lapse rate becomes greater than the adiabatic lapse rate then convection begins and the lapse rate decreases to the adiabatic value. As a convecting parcel of air rises, it expands due to decreasing air pressure and cools; falling parcels are compressed and heat up. Consequently, the adiabatic lapse rate is always positive ($dT/dz < 0$). (See Challenge 9.1 for an environmental example.)

The adiabatic lapse rate for dry air (*dry adiabatic lapse rate*, DALR or Γ_d , cf. Sect. 10.2.2) is constant at $9.76 \text{ }^{\circ}\text{C}/\text{km}$ from (10.51a). If, on the other hand, the

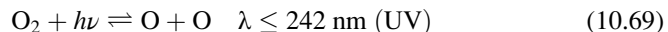
air is saturated, then moisture condenses as the air rises and cools, and evaporates as the air descends and heats. The latent heat of condensation offsets the temperature change, resulting in a *saturated adiabatic lapse rate* (SALR) of typically about 4.9 °C/km. Condensation does not occur if the air is not saturated, so air can be treated as dry until the saturation point (or *dew point*) is reached.

The *environmental lapse rate* refers to the lapse rate that would exist if there were no convection. In a gravitationally bound gas, whether a planetary atmosphere or a stellar atmosphere or interior, the lapse rate (usually referred to as the *temperature gradient* in a stellar interior) always equals the smaller of the environmental and the adiabatic values of the lapse rate. Thus if the environmental lapse rate is less than the adiabatic lapse rate for the moisture content of the air, then the air is stable against convection. If the environmental lapse rate rises above the adiabatic lapse rate, then the air becomes convective.

Most of the Earth's troposphere is dry (i.e., unsaturated), so comparing the values above shows that the lapse rate in the Earth's troposphere is normally sub-adiabatic, and convection is transient and localized.

10.4.1.2 Stratosphere and Mesosphere

Ozone production occurs between approximately 30 and 60 km altitude, primarily by the photodissociation reactions



(where ν is frequency, $h = 6.62608 \times 10^{34}$ Js is Planck's constant, and $h\nu$ represents the energy of the photon) and secondarily by collisions,



Here, M represents a third atom or molecule, the collision of which is required to conserve energy and momentum.

The rate of ozone production is determined by a number of competing factors, two of which are:

1. The probability of three-body collisions increases with decreasing altitude because of increasing atmospheric density
2. The supply of UV photons decreases with decreasing altitude because an increasing amount has already been absorbed at higher altitudes

Ozone is formed mainly between about 30 and 60 km altitude, where three-body collisions are sufficiently probable and the UV radiation is sufficiently intense.

Ozone is unstable and is destroyed by photochemical reactions involving O₂, NO_x, and the HO₂ radical. Although maximum ozone production occurs between 30 and 60 km altitude, its maximum concentration occurs between 10 and 25 km, depending on latitude (lower at higher latitudes), because of transport to lower altitudes where its destruction is less likely.

The temperature in the stratosphere and mesosphere is determined by the relative rates of energy deposition and loss. Energy deposition is primarily by absorption of near-UV ($170 \text{ nm} < \lambda < 300 \text{ nm}$) by ozone. Energy loss is primarily radiation by CO₂, an efficient emitter of IR. In the stratosphere the ozone concentration is high enough that radiative losses by CO₂ are relatively small, and temperature increases with increasing altitude as the UV intensity increases; whereas in the mesosphere the ozone concentration becomes very low, so absorption of solar UV is relatively low while radiative cooling through IR emission by CO₂ is relatively more important, and temperature decreases with increasing altitude. Because the lapse rate in the stratosphere is negative and therefore always less than the adiabatic value, the stratosphere is convectively stable.

10.4.1.3 Thermosphere

Above about 80 km altitude, absorption of far-UV radiation by NO, O₂, O, N, and N₂ partially ionizes and substantially heats the atmosphere. Heat is also deposited by solar x-rays, solar and galactic cosmic rays, and meteoroids.

The energy deposition rate depends on the number density of absorbers, which increases with decreasing altitude, and the number density of UV photons, which decreases with decreasing altitude due to absorption at higher altitudes. The primary heat sink is conduction to the lower atmosphere with subsequent IR emission. As a result of these competing factors, the temperature increases upward from the mesopause to approximately 150 km altitude in the thermosphere. Above this level the rate of energy deposition decreases with increasing altitude, but the atmospheric density is too low for efficient heat loss by conduction, and the thermospheric temperature continues to increase to an altitude of about 200–300 km, above which the atmosphere is approximately isothermal.

The temperature in the isothermal region is highly dependent on solar energy, exhibiting a strong diurnal variation and a dependence on solar activity. Daytime temperatures are in the approximate range of 1,000–2,000 K, depending on solar activity, and 500–1,500 K at night.

The ionization rate also depends on atmospheric density and UV photon flux, and peaks at around 300 km altitude. The ionosphere is thus located in the upper thermosphere.

Because the lapse rate is negative, the thermosphere is convectively stable.

10.4.1.4 Exosphere

The *exosphere* is the outer part of the thermosphere, where the density is low enough that the mean free path of a molecule (the mean distance between collisions), L_{mfp} , is greater than the pressure scale height, H . Under these conditions collisions are rare, and particles follow ballistic trajectories.

It is from the exosphere that escape of atmospheric constituents to space takes place. If the particle speed is less than the escape speed, $v < v_{\text{esc}}$, the particle remains gravitationally bound to the Earth, whereas if $v > v_{\text{esc}}$ then the particle can escape. Root mean square particle speeds are related to temperature by

$$v = \sqrt{\frac{3kT}{m}} = 157.94 \sqrt{\frac{T}{\mu}} \text{ m/s} \quad (10.5)$$

so lighter particles have higher mean speeds and escape at a higher rate, as shown in Sect. 10.1.

The base of the exosphere (the *exobase*) is defined as the altitude at which $L_{\text{mfp}} = H$, and is located at about 500–600 km altitude.

Satellites in low Earth orbit, such as the International Space Station and the Hubble Space Telescope, orbit near the exobase. Although a very good vacuum in normal terrestrial terms, the particle density is high enough that the orbit decays slowly and the satellite has to be boosted to a higher orbit occasionally. For comparison, the first manned space capsules to orbit the Earth, Yuri Gagarin's Vostok 1, Gherman Titov's Vostok 2, and John Glenn's Friendship 7, orbited at altitudes of about 200–300 km.

The properties of the lower atmospheres of the Earth, Venus, and Mars are compared in Table 10.1.

10.4.2 Mars

The thermal structure of the Martian atmosphere is illustrated in Fig. 10.23 (dashed lines). Because of the low thermal inertia of the atmosphere and surface (Sect. 10.5.4.2) and the planet's axial tilt and orbital eccentricity, the Martian atmosphere is subject to large diurnal, annual, and equator-pole temperature variations. The curve in Fig. 10.23 represents a highly smoothed profile above the equator.

Because the Martian atmosphere lacks significant free oxygen, ozone is unable to form in any appreciable quantity and the temperature maximum associated with the stratopause on Earth does not occur. The Martian atmosphere is then divided into three primary levels, the troposphere, a combined stratosphere and mesosphere (often called the *stratomesosphere*), and the thermosphere.

Table 10.1 Properties of the lower atmospheres of Earth, Venus, and Mars

Property	Earth	Venus	Mars ^a
Major constituents (mole fraction)	N ₂ : 0.781 O ₂ : 0.209 ⁴⁰ Ar: 0.00934 H ₂ O: 0–4 × 10 ^{−2} CO ₂ : 2–4 × 10 ^{−4}	CO ₂ : 0.965 N ₂ : 0.035 SO ₂ : 150 ppm ⁴⁰ Ar: 70 ppm CO: 26 ppm H ₂ O: 20–30 ppm	CO ₂ : 0.953 N ₂ : 0.027 ⁴⁰ Ar: 0.016 O ₂ : 0.0013 CO: 0.0007 H ₂ O: < 3 × 10 ^{−4}
Mean molecular weight, μ	28.96 (dry air)	43.44	43.49
Surface pressure	1.013 bar	95 bar	6–10 mbar
Mean surface temperature	288 K	730 K	220 K
Surface density	1.225 kg/m ³	65 kg/m ³	0.012 kg/m ³
Pressure scale height at surface	8.43 km	15.75 km	11.3 km
Solar constant	1,368 W/m ²	2,620 W/m ²	594 W/m ²
Fraction of incident solar energy absorbed	0.7	0.23	0.86
Absorbed solar flux, averaged over the planet	242 W/m ²	151 W/m ²	127 W/m ²
Major absorber of solar energy	Ground (but above 100 km for EUV)	Clouds and above (2.5 % reaches the ground)	Ground
$\Gamma_{\text{adiabatic}}$ (troposphere)	9.76 °C/km (dry); 4.9 °C/km (wet)	8 °C/km	4.4 °C/km
Γ_{observed} (troposphere)	6.5 °C/km	8 °C/km	Varies with dust content

^aThe atmospheric properties of Mars vary seasonally at any given location due to sublimation of CO₂ at the polar caps

10.4.2.1 Troposphere

The Martian troposphere forms in a similar way to that on Earth: absorption of solar radiation by the ground followed by absorption of the IR radiation from the ground by (on Mars) the CO₂-rich atmosphere.

The Martian atmosphere, however, differs from that of both the Earth and Venus in that it always contains silicate dust, raised from the surface by winds. Silicate dust is very effective at absorbing solar radiation. The dust in turn heats the atmosphere, producing a generally stable (sub-adiabatic) lapse rate (Table 10.1).

Dust devils (small, dust-laden whirlwinds) are common in the afternoon (Fig. 10.24), increasing the low-altitude dust content. Stronger winds can produce localized dust storms. When Mars is near perihelion (spring and early summer in the southern hemisphere), the winds can become strong enough to create dust storms that envelope the entire planet. Thus, the amount of dust present in the atmosphere varies considerably with time and location. The tropospheric lapse rate varies with the dust content, generally being greatest (convectively least stable)



Fig. 10.24 Mars Reconnaissance Orbiter photograph of a Martian dust devil on a late spring afternoon in Amazonis Planitia. The image is 640 m in width, and north is up. The whirlwind has a diameter of 30 m, and, from the shadow length and known sun angle, it extends from the ground to >800 m altitude. The wind speed is unknown, but speeds up to ~70 km/h have been measured in other dust devils. A westerly breeze at about 250 m altitude causes the plume to bend in a delicate arc toward the east. Image PIA15116; credit: NASA/JPL-Caltech/University of Arizona

at night and early morning, and least (convectively most stable) in the afternoon. In the afternoon, the lapse rate can be negative, with the minimum temperature at ground level.

The height of the troposphere varies considerably with ground temperature, and thus with latitude and season.

10.4.2.2 Mesosphere

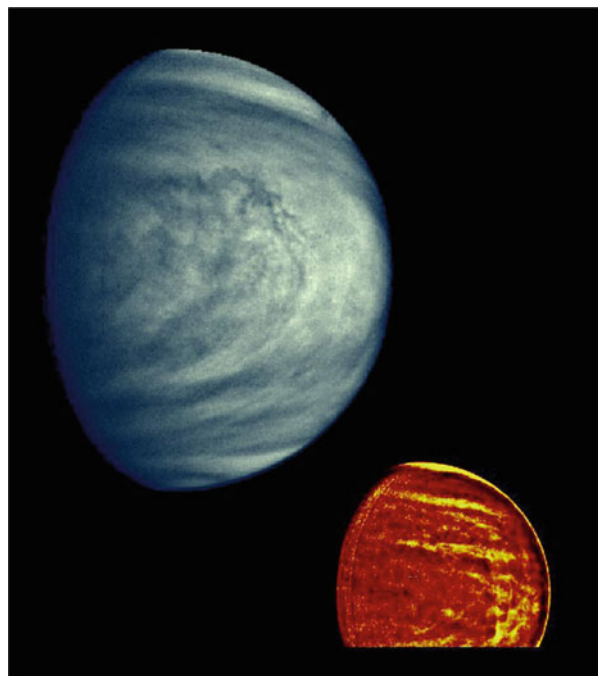
As noted above, the lack of ozone on Mars means that there is no distinction between the stratosphere and the mesosphere, and the temperature is roughly constant at about 130 K from the top of the troposphere to the base of the thermosphere.

The lack of an ozone or other such absorbing layer means that the Martian surface, during the daytime, is continuously bathed in sterilizing ultraviolet radiation.

10.4.2.3 Thermosphere

Solar EUV is absorbed by CO₂ above ~100 km altitude, producing a hot outer atmosphere (the thermosphere) as on Earth. However, CO₂ also emits IR efficiently, and is thus a good refrigerant. As a result, thermospheric temperatures on Mars vary from around 170 K at night to 300–370 K in the daytime, compared to 500–1,500 K and 1,000–2,000 K, respectively, for the Earth.

Fig. 10.25 Venus' cloud layer as observed by the Hubble Space Telescope. *Top:* The cloud tops as viewed through the violet filter. The bright region at right center is the subsolar point. *Bottom:* Cloud patterns located several kilometers below the visible cloud tops, as viewed in the near infrared. Image PIA00073; credit: NASA/JPL



10.4.3 Venus

Information about Venus' atmosphere has been obtained from telescopes on Earth (radio and infrared), orbiting spacecraft, fly-bys (e.g., *Galileo* on its way to Jupiter), probes descending to the surface, and balloon-borne instruments released in the atmosphere. Two views by the Hubble Space Telescope are shown in Fig. 10.25.

The atmosphere is characterized by a permanent H_2SO_4 haze layer between ~ 30 – 50 km altitude, above which is a layer of dense H_2SO_4 clouds between ~ 50 and 70 km altitude that completely obscures the ground at optical wavelengths. Between the haze layer and the ground, the air is relatively transparent.

Viewed from above, as in Fig. 10.25, the cloud layer can be divided into three distinct regions in terms of latitude:

- A broad, relatively-uniform region between $\sim 60^\circ$ N and $\sim 60^\circ$ S.
- A *polar collar* (or *cold collar*) encircling each pole at cloud level between ~ 60 and 70° latitude in both hemispheres, with a temperature minimum of ~ 220 K compared to ~ 230 – 240 K at the same altitude at mid-latitudes and in the polar vortex. The temperature gradients create a local peak in zonal wind speeds; i.e., a jetstream.

- A *polar vortex* covering the area within each polar collar, but not quite centered on the pole. The polar vortex is similar in appearance to a terrestrial hurricane, but three to four times larger.

The thermal structure of the Venus' atmosphere is illustrated in Fig. 10.23 (dotted lines). Because (1) the massive atmosphere provides a high thermal inertia (Sect. 10.5.4.2), (2) the rotation axis is almost perpendicular to the plane of the orbit, and (3) the orbital eccentricity is almost zero, the temperature profile below the thermosphere changes little with time.

10.4.3.1 Troposphere

Only 2.5 % of the incoming solar radiation reaches and is absorbed by the surface of Venus, but the thick CO₂-rich atmosphere is so efficient at absorbing the IR emitted by the ground that, in order for the small fraction that finds its way back to space to equal the amount absorbed by the surface, the surface temperature has to rise to 730 K.

The dry adiabatic lapse rate for an ideal gas is, from (10.51),

$$(\Gamma_d)_i = - \left(\frac{dT}{dz} \right)_i = \frac{g}{(c_P)_i} \quad (10.73)$$

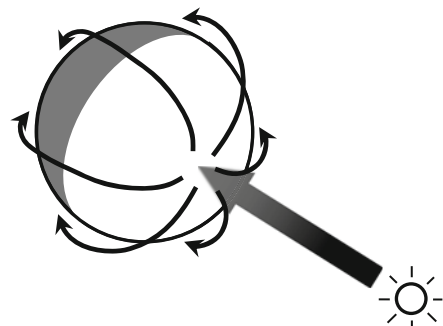
where $g = 8.87 \text{ m/s}^2$ at the surface of Venus, c_P is the specific heat at constant pressure, and the subscript i denotes values obtained assuming an ideal gas. $(c_P)_i$ is temperature dependent, and equals 1,134 J/kg K for CO₂ at 730 K. Equation (10.73) then gives $(\Gamma_d)_i = 7.82 \text{ K/km}$. However, a triatomic atmosphere generally departs noticeably from an ideal gas, and to obtain the actual dry adiabatic lapse rate, Γ_d , we must multiply $(\Gamma_d)_i$ by a conversion factor, $\Phi \equiv \Gamma_d / (\Gamma_d)_i$. Φ is computed numerically; for CO₂ at 90 bars pressure and 730 K, $\Phi = 1.033$. Then $\Gamma_d = 8.08 \text{ K/km}$.

The observed value of Γ in Table 10.1 and the approximately steady tropospheric profile in Fig. 10.23 suggest that Venus' atmosphere is close to adiabatic throughout most of the troposphere. Specifically, measurements during descent by the Russian *Venera* landers and the four atmospheric probes released by the American *Pioneer Venus* craft indicate that the lowest 23 km of the troposphere and a narrow region near 55 km have adiabatic temperature gradients. The other parts of the troposphere appear to be subadiabatic.

10.4.3.2 Mesosphere

Venus' atmosphere, like that of Mars, lacks ozone in any appreciable quantity, and the troposphere and thermosphere are separated by a roughly isothermal mesosphere at about 200 K.

Fig. 10.26 Subsolar-to-antisolar flow pattern on Venus and Mars



10.4.3.3 Thermosphere

The dayside thermospheric profile of Venus is similar to that of Mars (Fig. 10.23): absorption of solar EUV by CO₂ above ~100 km altitude accompanied by CO₂ infrared emission, producing a thermospheric dayside temperature near 300 K.

The thermosphere of Venus differs from that of Mars and Earth in several important ways arising from the much slower rotation period of the upper atmosphere: 4 days at the cloud tops and 6 days in the thermosphere. Because these are much shorter than the 243-day (retrograde) sidereal and 117-day synodic rotation periods of the solid planet, the atmosphere is said to *super rotate* (Sect. 10.5.3.2.3); but thermospheric gases on Venus spend six times longer on the nightside than on Mars or the Earth, and the temperature drops to a little over 100 K (Fig. 10.23). For this reason the nightside thermosphere on Venus is often referred to as the *cryosphere* (“cold sphere”).

The day-night thermospheric temperature difference translates into a much larger pressure scale height on the dayside, and therefore a larger atmospheric pressure on the dayside than at the same altitude on the nightside (recall Fig. 10.10).

This pressure difference creates a subsolar to antisolar pressure gradient force, strongest at the terminator. The dominant circulation pattern in the thermosphere is therefore a flow from the dayside to the nightside, symmetric about an axis approximately from the subsolar to the antisolar point, as illustrated in Figs. 10.26 and 10.27c. The subsolar to antisolar cell is completed by a return flow in the mesosphere at ~80–90 km altitude. For steady state, the return flow must carry the same mass per unit time as the direct flow, but because of the greater density at this altitude the speed and cross-section of the return flow are much smaller.

Instruments on *Venus Express* have detected a previously-unexpected warm layer in the nightside mesosphere of Venus, in which the temperature within ~15° of the antisolar point increases with altitude to ~230 K at 100 km before decreasing to 100 K at 140 km (Bertaux et al. 2007). Lower but still elevated temperatures are seen at greater angles from the antisolar point. This warm layer is believed to be caused by compression and adiabatic heating of the descending gas in the subsolar to antisolar cell. It is not clear yet whether this layer is a permanent or intermittent feature.

A subsolar to antisolar circulation pattern also occurs in the upper atmosphere of Mars.

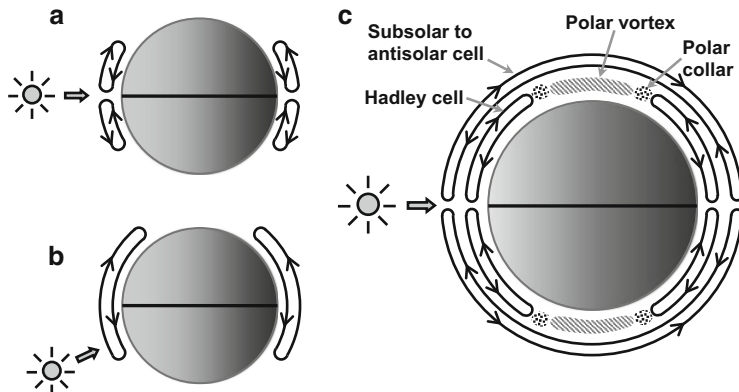


Fig. 10.27 Hadley cells on Mars and Venus. (a) Martian equinox: Two Hadley cells, one on each side of the equator. (b) Martian winter solstice for the upper hemisphere: A single Hadley cell with the rising branch $\sim 30^\circ$ S and the descending branch $\sim 50\text{--}60^\circ$ N. (c) Venus: Two solar-driven Hadley cells at cloud level, and a subsolar to antisolar cell in the thermosphere above it (inspired by Fig. 2 of Svedhem et al. 2007). The Hadley cells are symmetric about the polar axis, whereas the subsolar to antisolar cell is symmetric about an axis approximately from the subsolar point to the antisolar point, as indicated in Fig. 10.26)

10.5 Planetary Circulation Effects

10.5.1 Circulation and the Coriolis Force

Basically, circulation in planetary atmospheres is driven by solar heating and modified by planetary spin, topography, and surface friction. Table 10.2 compares some characteristics of circulation in the atmospheres of the Earth, Venus, and Mars.

The *Rossby number*, Ro , equal to the ratio of inertial acceleration ($a = F/m$, due to “real” forces acting) to Coriolis acceleration, a_{COR} , provides a measure of the effectiveness of the Coriolis force (away from the equator):

$$Ro \equiv \frac{a_{\text{inertial}}}{a_{\text{COR}}} = \frac{\left(\frac{dv}{dt}\right)}{\left(\frac{4\pi v \sin \lambda}{\tau}\right)} \quad (10.74)$$

where v is the speed of an air mass over the ground, λ , the latitude,⁹ and τ the planetary spin period (seconds). In the case of circular (e.g., cyclonic) motion of radius r , $dv/dt = v^2/r$, and $2\pi/\tau$ is the planetary angular speed of rotation, Ω .

⁹In other parts of Solar System Astrophysics, we have used the conventional astronomical notation of (λ, ϕ) for longitude and latitude, respectively, but in this context, we use λ for latitude in accord with planetary science literature.

Table 10.2 Circulation in the atmospheres of Earth, Venus, and Mars

Earth, Mars	Venus
Atmospheric circulation is driven from below by solar heating of the ground	Atmospheric circulation is driven from above by absorption of solar energy in and above the clouds
Rapid spin: ~24 h	Slow spin: (-)243 ^d sidereal period

Then $Ro = v/(2 \Omega r \sin \lambda)$. If $Ro < < 1$ then $a_{\text{COR}} >> a_{\text{inertial}}$ and the Coriolis force is strong; if $Ro > > 1$ then $a_{\text{COR}} << a_{\text{inertial}}$ and the Coriolis force is weak. Observed values in the lower 10 km of the atmospheres of the Earth, Venus, and Mars at 45° latitude are approximately:

Earth and Mars: $Ro = 0.1$ (“strong” Coriolis force)

Venus: $Ro = 10\text{--}50$ (“weak” Coriolis force)

10.5.2 Meridional (N-S) Circulation

The primary element of meridional circulation is the Hadley cell (Sect. 10.3.7.2), driven by solar heating near the equator and radiative cooling closer to the poles. The situation for the Earth is described in Sect. 10.3.7.

The meridional circulation on Mars resembles that on the Earth (e.g., Forget et al. 1999a), but is more exaggerated because of the low thermal inertia of the land and thin atmosphere, and the absence of the high thermal inertia (and consequent moderating effect) of oceans. As on Earth, for a relatively short period near each equinox there are two Hadley cells of similar strength, located on either side of the equator (illustrated schematically in Fig. 10.27a). During the rest of the year, approximately centered on each solstice, the winter-hemisphere cell intensifies and expands at the expense of the summer-hemisphere cell to form a single, dominant Hadley cell that (in the case of Mars) straddles the equator (Fig. 10.27b).

Figure 10.28 shows the zonally-averaged meridional circulation during (a) early northern summer and (b) early southern summer. At lower altitudes in northern summer (Fig. 10.28a), the southern Hadley cell has expanded northward across the equator at the expense of the northern Hadley cell, which is weakly visible at ~60–80° N. Weak Ferrell and polar cells are also visible at far southern latitudes. In southern summer (Fig. 10.28b), the northern cell has expanded southward at the expense of the southern cell, which is weakly visible at high southern latitudes, with a weak Ferrell cell visible at high northern latitudes. The black dot on each horizontal axis shows the latitude of the subsolar point. At altitudes above ~20–40 km in both of Fig. 10.27a, b, the dominant Hadley cell extends from pole to pole, with the southern summer cell being the stronger of the two.

Solar heating of the Martian atmosphere occurs not only by absorption and emission of radiation by the ground, but also by absorption and emission of radiation within the atmosphere by CO₂ gas, CO₂ ice particles, airborne dust,

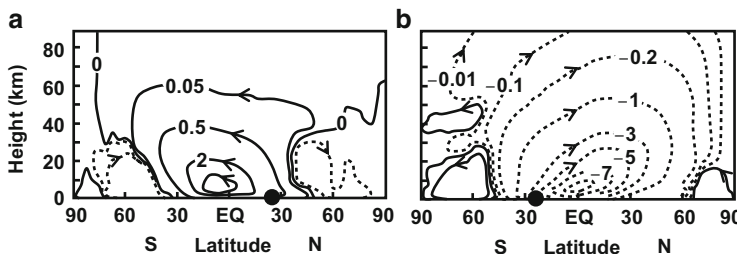


Fig. 10.28 Zonally-averaged meridional stream functions on Mars, temporally averaged over the first 30 days after the respective summer solstice in (a) early northern summer and (b) early southern summer. The numbers on the stream functions give the rate of mass transport (unit: 10^9 kg s^{-1}) between the given stream function and the zero stream function. The black dot on each horizontal axis shows the latitude of the subsolar point. From the general circulation model of the Laboratoire de Météorologie Dynamique in Paris and the sub-Department of Atmospheric Oceanic and Planetary Physics at Oxford University (Forget et al. 1999a), adapted from their Figs. 7 and 8)

water vapor, and water ice particles. An example of the effect of absorption within the atmosphere can be seen in Fig. 10.28: if the only important factor were absorption and emission by the ground, one might expect the ascending branch of the Hadley cell to be confined to latitudes close to the subsolar point (black dots in Fig. 10.28); but in fact the ascending branch extends considerably poleward of this point because of strong thermal forcing from absorption of solar radiation by airborne dust (Forget et al. 1999b).

At the current position of Mars' polar axis in its precessional cycle, perihelion occurs shortly before southern summer solstice. Consequently, because of the relatively large eccentricity of Mars' orbit, solar heating is ~44 % stronger during the southern summer, strengthening the dominant Hadley cell compared to that during the northern summer. The stronger Hadley cell then provides a positive feedback mechanism in which the increased circulation raises more dust into the atmosphere, and this in turn increases the absorption of solar radiation, which further strengthens the Hadley cell. The mechanism appears to involve the dust devils that appear in southern summer lifting enough dust into the atmosphere that, with the resulting increase in solar heating, ground winds become strong enough to lift the dust directly (Forget et al. 1999b). The process can then be self-sustaining until solar heating diminishes toward the southern autumn equinox. The atmosphere during northern summer is much less dusty.

Richardson and Wilson (2002) have suggested that the Martian topographical dichotomy (Sect. 9.3.2.1 of Milone and Wilson 2014) has a stronger effect than the orbital parameters in determining the relative strength of the northern summer and southern summer Hadley cells. The effect occurs in part because, if we consider air along a horizontal isobar, then even if all points on the planet were at the same temperature, the southern highland surface is closer to our chosen isobar than the northern lowland surface (i.e., the highlands form an elevated heat source for the air), so a parcel of air above the highland surface would be warmer and less dense than a

parcel on the same isobar above the lowland surface. Given the actual summer/winter temperature differences, this effect amplifies the dominant Hadley cell during southern summer and diminishes it during northern summer. The uphill slope from the lowlands to the highlands also plays a role.

The effect of topography vs. orbital parameters is important in terms of the evolution of the Martian climate, because the topography remains constant over time whereas the Martian orbital parameters interact with each other on timescales of tens of thousands of years (the Milankovic cycles); e.g., in \sim 11,500 years, perihelion will occur near the northern summer solstice. This would reverse the dominance of the southern summer vs. northern summer cells if the orbital parameters are more important, but leave it unchanged if topography is more important.

In the case of Venus, most of the absorption of solar energy takes place in and above the clouds. The main Hadley cell is therefore located at cloud level (the “driver cell”), with poleward flow at the cloud tops and equatorward flow near the cloud base. Because of the large Rossby number, it extends from the equator to the edge of the polar collar at \sim 60° latitude in each hemisphere (Fig. 10.27c). Measurements suggest a second, thermally indirect cell below the cloud level (not shown in Fig. 10.27c), driven by the cloud-level cell, and a third, thermally direct cell between the second cell and the ground. Other features in Fig. 10.27c are discussed in Sect. 10.5.3.2.

Figure 10.30b shows the meridional velocity at cloud level in the southern hemisphere due to the Hadley cell. The meridional flow is toward the south pole (negative velocity) at \sim 10 m/s at the cloud tops. The return flow at the cloud base is slower, in part because of the greater atmospheric density, and is not detected in the figure within uncertainty (<5 m/s).

10.5.3 Zonal (E–W) Circulation

Large-scale zonal flow on the Earth arises initially from deflection of the meridional flow by the Coriolis force. Thermal winds arising from temperature gradients, as well as topography, perturb this zonal flow and create large-scale waves, eddies, and jet streams (Sects. 10.3.2–10.3.6 and 10.3.7.4–10.3.7.6).

10.5.3.1 Mars

Figure 10.29a shows zonally-averaged isotherms on Mars in early southern summer. Adiabatic heating of the air in the descending branch of the dominant Hadley cell in Fig. 10.28b creates the temperature inversion (temperature increasing with height) over the north pole in Fig. 10.29a. The resulting steep isotherms produce strong meridional temperature gradients between approximately 30° and 80° N latitude in Fig. 10.29a.

In Fig. 10.29b this meridional temperature gradient has created a westerly (zonal) flow with speeds near ground level of less than about 20 m/s, and a westerly

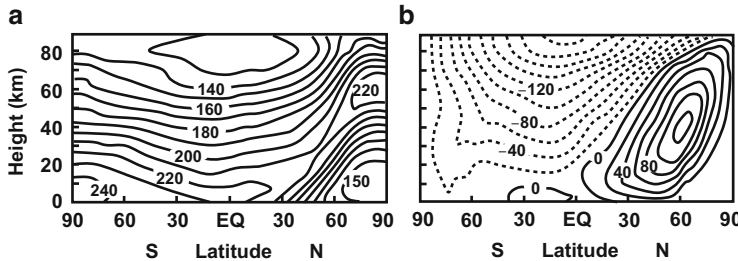


Fig. 10.29 (a) Zonally-averaged temperatures and (b) the corresponding zonally-averaged zonal winds as a function of latitude and altitude in early southern summer on Mars, temporally averaged over the first 30 days from the southern summer solstice. Temperatures are in K and velocities in m/s, with westerly winds positive (*solid lines*). From the general circulation model of the Laboratoire de Météorologie Dynamique in Paris and the sub-Department of Atmospheric Oceanic and Planetary Physics at Oxford University (Forget et al. 1999a, adapted from their Fig. 7)

jet near 60° N latitude extending into the mesosphere with speeds up to about 120 m/s. During northern summer the temperature inversion is at high southern latitudes, with corresponding steep isotherms and westerly jet. As on Earth, baroclinic waves arise in the westerly flow; thus on Mars these will be found only at mid-latitudes in the winter hemisphere.

10.5.3.2 Venus

10.5.3.2.1 Atmospheric Superrotation

The atmosphere between the base of the haze layer and the base of the thermosphere at ~ 120 km altitude *superrotates*, i.e., the atmosphere moves in the same direction as the planetary rotation (retrograde, east-to-west), but much faster than the solid planet (e.g., Sánchez-Lavega et al. 2008). Figure 10.30, adapted from Fig. 2 of Sánchez-Lavega et al. (2008), shows temporally- and longitudinally-averaged zonal and meridional velocities in the southern hemisphere at three different altitudes, ~ 47 km near the cloud base, ~ 61 km within the clouds, and ~ 66 km near the cloud tops. In the northern hemisphere, zonal velocities are approximately symmetrical with those shown in Fig. 10.30a and meridional velocities are approximately antisymmetrical with those in Fig. 10.30b (see Peralta et al. 2007).

Zonal wind speeds at low to mid-latitudes in Fig. 10.30a are approximately constant with latitude: 102 ± 10 m/s from the equator to $\sim 55^{\circ}$ S on the dayside, 60 ± 10 m/s from the equator to $\sim 65^{\circ}$ S at 61 km on the nightside, and very similar at 47 km on the dayside. By comparison, the rotational speed at the equator is 1.8 m/s; i.e., at the equator, the air at the cloud tops is moving almost 60 times faster than the planet under it. Consequently, the atmosphere over the equator circles the rotation axis in only 4 days at this altitude, or 3 days at 55° latitude, a much shorter

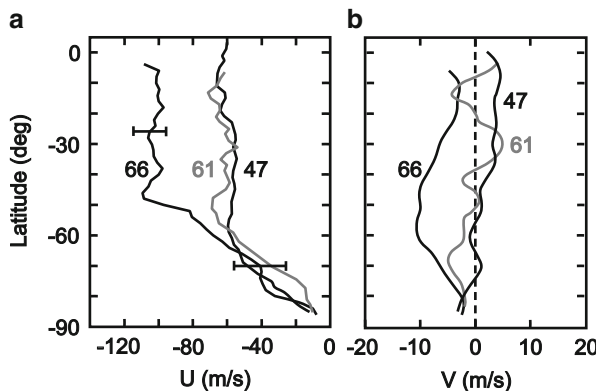


Fig. 10.30 (a) Zonal (E-W) and (b) meridional (N-S) wind velocities at the cloud base ($\sim 44\text{--}48$ km altitude, labeled in the plots by the median altitude, “47”), within the clouds at $58\text{--}64$ km altitude (“61”), and at the cloud tops ($62\text{--}70$ km altitude, “66”) in the southern hemisphere of Venus, from ESA’s *Venus Explorer* spacecraft. The altitude in kilometers is shown by the number beside each plot (the 61-km plot is in gray). Representative error bars are shown for the 66-km altitude plot in (a). The uncertainty in the 66-km plot in (b) is $\pm \sim 9$ m/s. The 61- and 47-km altitude plots are within uncertainty of each other on both graphs. Adapted from Fig. 2 of Sánchez-Lavega et al. (2008)

time than the 243-day sidereal rotation period of the planet. This is the atmospheric superrotation.

Wind shear (change of wind speed with altitude) appears to be minimal in the lower cloud levels, but is considerable in the upper levels (8 ± 2 m/s per km).

Poleward of $55\text{--}65^\circ$ latitude in Fig. 10.30a, the zonal wind speed drops linearly with latitude to zero at the poles, with no detectable vertical wind shear. The polar vortex thus appears to be strongly vertically coherent at $\sim 45\text{--}70$ km altitude.

Zonal wind speeds decrease with altitude above the clouds, becoming ~ 65 m/s in the thermosphere.

10.5.3.2.2 Cyclostrophic Balance

On the Earth, with its 24-h rotation period, wind direction and speed on a large scale are determined by geostrophic balance, where the pressure gradient force on a parcel of air is balanced by the Coriolis force (Sect. 10.3.5).

Venus, however, rotates much more slowly. As a result, the Rossby number for Venus is about 23 (Sect. 10.5.1), the Coriolis force is negligible, and geostrophic balance does not occur. Instead, the superrotating winds on Venus are in *cyclostrophic balance*, where in a horizontal plane (in a reference frame rotating with the planet) the pressure gradient force on a parcel of air is balanced by the centrifugal force.

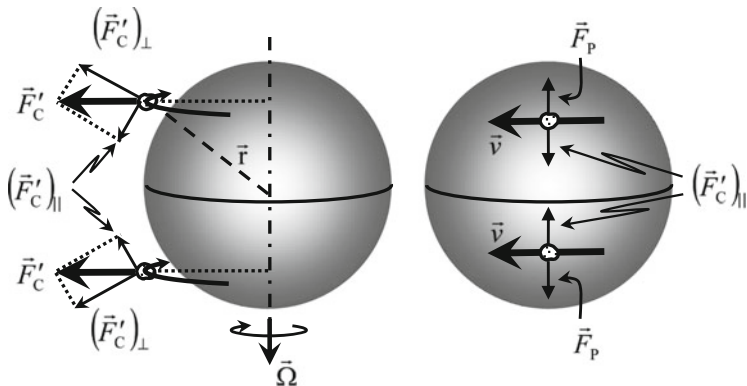


Fig. 10.31 (a) On the left: The centrifugal force, \vec{F}'_C , on parcels of air in the atmosphere of Venus, and its components parallel and perpendicular to the planetary surface. (b) Right: Cyclostrophic balance: the pressure gradient force, \vec{F}_p , is balanced by the parallel component of the centrifugal force. The resulting cyclostrophic wind, \vec{v} , is parallel to the equator

Figure 10.31a shows the centrifugal force, $\vec{F}'_C = -m\vec{\Omega}(\vec{\Omega} \times \vec{r})$, on two parcels of air in the atmosphere of Venus, as Venus rotates (retrograde) about its axis. \vec{F}'_C is directed perpendicularly outward from the rotation axis, and can be separated into components perpendicular to and parallel to the planetary surface, as indicated.

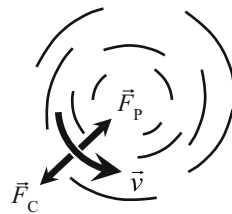
The perpendicular component of the centrifugal force reduces the effective gravity and increases the pressure scale height, i.e., the atmosphere expands vertically compared to the non-rotating case, to maintain pressure equilibrium.

The horizontal component points toward the equator for both air parcels shown, causing the air to move closer to the equator. This in turn increases the atmospheric pressure at the equator and creates a poleward-pointing pressure gradient force. The process continues until the pressure gradient force and the horizontal component of the centrifugal force balance, as indicated in Fig. 10.31b. This is cyclostrophic balance.

Cyclostrophic balance is familiar on the Earth in intense tropical cyclones, where the pressure gradient force toward the low-pressure area at the center (the eye) is so large that the Coriolis force is negligible by comparison ($Ro >> 1$). The rotating cyclone contracts, spinning up to conserve angular momentum, until the pressure gradient force is balanced by the centrifugal force, as illustrated in Fig. 10.32.

Note: On Venus, the winds are relatively light in the lowest scale height above the ground (containing more than half the mass of the atmosphere). Wind velocities measured at ground level by the Soviet *Venera* landers were 0.3–1 m/s. Because of the slow wind speeds and the slow planetary spin, the circulation in the lowest scale height is not expected to be either geostrophic or cyclostrophic.

Fig. 10.32 Cyclostrophic balance in an intense tropical cyclone on the Earth



10.5.3.2.3 Atmospheric Angular Momentum

A superrotating atmosphere has a greater angular momentum, L , than if it were simply corotating with the planet. The Earth's atmosphere superrotates at mid-latitudes (westerly jets), but this is partly offset by sub-rotation (retrograde compared to the planetary surface) near the equator due to easterly winds (the surface trade winds and stratospheric easterly summer jet). Also, the mass of the atmosphere is much less than on Venus, and the jets are localized in latitude.

One can gain some appreciation for the amount of superrotation in the atmosphere of Venus by looking at the excess atmospheric angular momentum over that required for corotation: $3.4 \times 10^{28} \text{ kg m}^2/\text{s}$ for Venus, or about 200 times that of the Earth's atmosphere ($1.6 \times 10^{26} \text{ kg m}^2/\text{s}$). Because of the more massive atmosphere of Venus, the excess atmospheric angular momentum per unit atmospheric mass is $7.1 \times 10^7 \text{ m}^2/\text{s}$, or about twice that of the Earth ($3.0 \times 10^7 \text{ m}^2/\text{s}$). To appreciate superrotation, however, it may be more instructive to express the excess atmospheric angular momentum as a fraction of the planetary angular momentum: 1.6×10^{-3} for Venus, or about 60,000 times that for the Earth (2.7×10^{-8}).

The angular momentum of the Earth's atmosphere changes by several tens of percent over short timescales, due to motions of atmospheric masses. The resulting angular momentum transfer between the atmosphere and the solid planet causes fluctuations (increases and decreases) of the order of milliseconds in the length of the day.

Measurements of zonal wind speeds on Venus made at different times indicate that similar angular momentum fluctuations may occur in Venus' atmosphere. Fluctuations of 20 % or more would result in fluctuations on the order of hours in the length of the day on Venus.

Maintaining superrotation in Venus' atmosphere is a concern, because the faster, high-level regions and the slower, lower-level regions exert drag forces on each other. This tends to slow the air at the higher levels and speed it up at the lower levels, producing a transfer of angular momentum downward. Superrotation can be maintained only if there is a competing process transferring angular momentum upward to the cloud level. Although the specific process has not been definitively identified, recent models suggest that meridional circulation in the Hadley driver cell (Fig. 10.27c) coupled with planetary-scale waves and eddies transport angular momentum equatorward in the lower and middle atmosphere (Hoshino et al. 2011;

Yamamoto and Takahashi 2004). Rising air near the equator (Fig. 10.27c) then transports the angular momentum upward.

10.5.3.2.4 Superrotation vs. Other Circulation Patterns

At mid-latitudes on the Earth, the zonal (geostrophic) wind dominates the meridional (Ferrel) flow, so the westerlies are from the west rather than the southwest. In the tropics the zonal and meridional (Hadley) flows are more equal, so the trade winds north of the equator are from the NE, and south of the equator from the SE.

On Venus, the zonal flow (superrotation) by far dominates the meridional flow everywhere from the cloud tops down except for the lowest scale height, so the flow is primarily parallel to the equator. The Hadley flow at cloud level still exists, however, and is important in the maintenance of the superrotation (Sect. 10.5.3.2.3).

Above the cloud tops, the thermospheric circulation is dominated by the subsolar to antisolar flow (Sect. 10.4.3.3), and the 65 m/s superrotation simply rotates the axis of the subsolar to antisolar flow in Fig. 10.26 somewhat from midnight toward morning (or noon toward evening). A transition region occurs the mesosphere where the zonal flow from superrotation decreases with altitude while the subsolar to antisolar flow increases.

10.5.4 Other Considerations

10.5.4.1 Latent Heat

Latent heat is the heat absorbed or released during a phase change. This is an important component of the atmospheric thermodynamics of the Earth, e.g., as saturated air rises and cools, the heat released by the condensation of water vapor to form cloud droplets reduces the adiabatic lapse rate to 4.9 °C/km, compared to 9.76 °C/km for dry air (Sect. 10.4.1.1). Latent heat is also important to the formation and maintenance of hurricanes and other weather systems.

Latent heat is not important for atmospheric circulation on Mars and Venus. Mars lacks liquid water on its surface; the very small quantity of water vapor in its atmosphere is maintained primarily by exchange with the water ice in the residual northern polar cap. Precipitable water vapor in the Martian atmosphere is equivalent to a depth of only micrometers of water on the Martian surface. Venus lacks surface water in any form, and *Venera* and *Pioneer Venus* measurements suggest a mole fraction of water vapor in the atmosphere 10–20 times less than that on the Earth.

10.5.4.2 Thermal Inertia

Massive absorbers exhibit *thermal inertia*, i.e., a large heat transfer produces only a small temperature change. They thus act as a heat reservoir, and reduce the temperature variations in a planetary atmosphere.

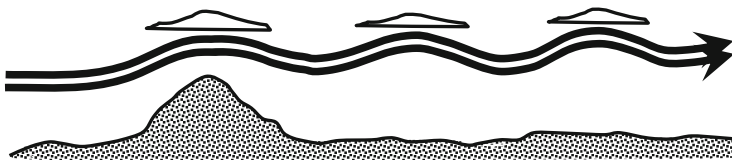


Fig. 10.33 Air flow over a mountain, illustrating oscillations at the Brunt-Väisälä frequency. Clouds often form when the air rises and cools, and evaporate when it sinks and heats, thus outlining the tops of the waves

The primary heat reservoir on the Earth is the ocean. On Venus, a similar function is provided by the massive lower atmosphere, which is about 50 times denser than on Earth and more than five times deeper (Fig. 10.23). As a result there is very little diurnal temperature variation in the troposphere (<1 K at 30° latitude) or the mesosphere, and only a small temperature decrease from the equator to the poles (5–15 K, compared to 45 K for the Earth and 90 K for Mars).

Mars, with no oceans and only a thin atmosphere, lacks an efficient atmospheric heat reservoir. The low thermal inertia results in strong diurnal and equator-pole temperature variations.

10.5.4.3 Brunt-Väisälä Frequency

When a parcel of air is displaced vertically in a convectively stable region of a planetary atmosphere it returns to its starting point, but overshoots and then oscillates up and down like a mass on a spring. The frequency of oscillation is the *Brunt-Väisälä frequency*, which also shows up as the buoyant frequency of solar oscillations [Milone and Wilson 2014, equation (4.47)].

If the period of oscillation is short compared to the damping time (e.g., damping by radiative cooling), then the oscillation is approximately undamped, and combined with horizontal flow produces atmospheric waves as illustrated schematically in Fig. 10.33. These waves are often visible as wave-like cloud patterns in the atmospheres of the Earth and Mars.

10.5.4.4 Diffusion and Mixing in Planetary Atmospheres

For a planetary atmosphere of any given overall composition, the actual composition at any given height is determined by the interaction of two competing factors:

Mixing: “stirs” the atmosphere and tends to produce a uniform composition, i.e., a composition which is constant with height.

Diffusion: lighter gases diffuse to greater heights than heavier gases because of their larger scale height; if diffusion acted alone then the composition would change with height, with lighter gases becoming increasingly dominant with increasing height in the atmosphere.

Table 10.3 Comparative composition of the lower atmospheres of the Earth, Venus, and Mars^a

Planet	Gas	Mole fraction	Major source	Major sink
Earth	N ₂	0.781	Biology	Biology
	O ₂	0.209	Biology	Biology
	⁴⁰ Ar	0.0093	Outgassing (⁴⁰ K)	—
	H ₂ O	<0.04	Evaporation	Condensation
	CO ₂	0.00034	Biology, combustion	Biology
Venus	CO ₂	0.965	Outgassing	CaCO ₃ formation?
	N ₂	0.035	Outgassing	—
	CO	0.00002	Photochemistry (from CO ₂)	Photooxidation
	SO ₂	0.00015	Photochemistry	CaSO ₄ formation
	⁴⁰ Ar	0.000033	Outgassing (⁴⁰ K)	—
	O ₂	Undetected in the lower atmosphere	—	—
Mars	CO ₂	0.953	Evaporation, outgassing	Condensation
	N ₂	0.027	Outgassing	Escape as N
	⁴⁰ Ar	0.016	Outgassing (⁴⁰ K)	—
	O ₂	0.0013	Photochemistry (from CO ₂)	Photoreduction
	CO	0.0007	Photochemistry (from CO ₂)	Photooxidation

^aFrom Prinn and Fegley (1987, Tables 1, 2, and 3)

Table 10.3 provides a comparison of the mole fractions of the most abundant components of the lower atmospheres of the Earth, Venus, and Mars, with the major sources and sinks.

10.5.4.4.1 Diffusion

An ideal gas, to which a planetary atmosphere may be approximated for most purposes, is a gas of non-interacting particles, and therefore also non-interacting chemical species. The pressure at any point in the atmosphere is

$$P = nkT \quad (10.18)$$

where n is the number density. The *partial pressure*, P_i , of any species i (e.g., oxygen, O₂) in the gas equals the total pressure which that species would exert if all other molecules were removed, i.e.,

$$P_i = n_i kT \quad (10.75)$$

The total number density of the gas equals the sum of the individual number densities, so

$$P = nkT = \left(\sum_i n_i \right) kT = \sum_i (n_i kT) = \sum_i P_i \quad (10.76)$$

Equation (10.76) shows that, for a mixture of ideal gases, each molecular species contributes a partial pressure proportional to its abundance, and the total pressure is equal to the sum of the partial pressures.

If mixing were to cease in a fully mixed atmosphere, each chemical species would proceed to diffuse upward or downward to establish its own scale height,

$$H_i = \frac{kT}{\mu_i m_{ug}} \quad (10.77)$$

where μ_i is the molecular weight of species i . Once this process is complete, the atmosphere is said to be in *diffusive equilibrium*.

The partial pressure of species i as a function of altitude, h , above any given reference level is, from (10.27),

$$P_i = P_0^i e^{-\frac{h}{H_i}} \quad (10.78)$$

where P_0^i is the pressure of species i at the reference level. If the atmosphere is in thermal equilibrium, then at any given altitude the components all have the same temperature. The scale height is then inversely proportional to the molecular weight, i.e., lighter gases have larger scale heights: the partial pressure of heavier gases decreases with increasing altitude faster than that of lighter gases, and for an atmosphere in diffusive equilibrium the composition shifts progressively toward lighter species as altitude increases.

10.5.4.4.2 Diffusion vs. Mixing

As seen above, diffusion tends to produce a composition gradient in the atmosphere, whereas convection and other atmospheric circulation tend to mix species, producing a uniform composition (zero composition gradient). Which process dominates at any given altitude depends on the relative timescales for diffusion and mixing. We define the *diffusion time*, τ_D , as the time needed for diffusion to produce a significant change in composition, and the *mixing time*, τ_m , as the time needed for mixing to produce a significant change in composition. The diffusion time is given approximately by

$$\tau_D = 10^{-13} n \text{ seconds} = 3 \times 10^{-21} n \text{ years} \quad (10.79)$$

where n is the total number density (m^{-3}) at any given altitude.

In the troposphere, $n \sim 10^{25} \text{ m}^{-3}$ and by (10.79) $\tau_D \sim 30,000$ years. The mixing time due to convection and circulation is $\tau_m \sim 1$ month; therefore, mixing by far dominates diffusion and the troposphere is well-mixed (uniform composition).

In the stratosphere, $n \sim 10^{23} \text{ m}^{-3}$ and $\tau_D = 300$ years. The lapse rate is negative (temperature increases with altitude) so there is no convection, but strong winds give $\tau_m \sim 10$ years. Therefore, mixing again dominates diffusion, and the stratosphere is well-mixed.

In the mesosphere, n decreases from $\sim 10^{21} \text{ m}^{-3}$ at the stratopause to $\sim 10^{20} \text{ m}^{-3}$ at the mesopause, giving $\tau_D \sim 3$ and 0.3 years (3.5 months), respectively. The mixing time due to convection is $\tau_m \sim 1$ month, so the mixing again dominates diffusion over most of the mesosphere, and the mesosphere is well-mixed except at the top, where diffusion begins to become important.

In the thermosphere, $n \sim 10^{13} \text{ m}^{-3}$ at 100 km altitude, and $\sim 10^{10} \text{ m}^{-3}$ at 200 km, giving $\tau_D \sim 10$ days at 100 km and 1 h at 200 km. The thermospheric lapse rate is negative so there is no convection, and the mixing times are long. Thus diffusion dominates mixing in the thermosphere.

10.5.4.4.3 The Homopause

The *homopause*, or *turbopause*, is defined as the altitude at which the diffusion time equals the mixing time, $\tau_D = \tau_m$. This occurs at about 100 km altitude on the Earth. On Venus, the homopause altitude varies with time between ~ 125 and 135 km, and on Mars it is at ~ 125 km altitude. Below the homopause is the *homosphere*, where mixing produces a homogeneous composition, and above it is the *heterosphere*, where diffusion produces a composition gradient (heterogeneous composition).

Even in the homosphere, however, local production and loss can be rapid enough to alter the abundance of selected species, e.g., ozone.

10.5.5 Chemical Cycles

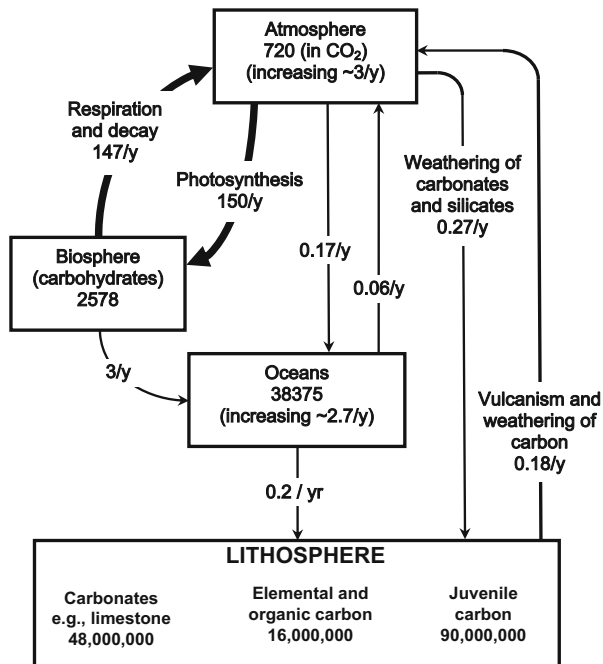
A planetary atmosphere is part of an interacting system that includes the solid planet and, where they exist, oceans, other surface liquids, and life. Here we look briefly at several important cycles in this system.

10.5.5.1 Carbon Cycle (Earth)

Figure 10.34 shows the terrestrial atmospheric carbon cycle. Juvenile carbon is carbon from the interior of the Earth, being released for the first time in the Earth's history. Almost all of this is in the form of CO_2 from volcanism along mid-ocean ridges.

The largest reservoir of carbon is lithospheric rock, such as limestone. However, the greatest rates of transfer are between the atmosphere and the biosphere by respiration, plant photosynthesis, and decay of organic material. The retention time for carbon (in the form of CO_2) in the atmosphere may be found from

Fig. 10.34 The terrestrial carbon cycle. The arrows show the rates of transfer of carbon between the various carbon reservoirs (boxes). Thick arrows show the dominant paths. The unit for all numbers is 10^{12} kg of carbon. The atmospheric carbon content, in the form of CO_2 , is increasing because of the burning of fossil fuels (not shown). (After Wayne 2000, Fig. 1.4, p. 19; by permission of Oxford University Press)



$$\tau = \frac{\text{supply}}{\text{rate of loss}} = \frac{720 \times 10^{12} \text{ kg of C}}{150 \times 10^{12} \text{ kg of C/y}} \cong 5 \text{ y} \quad (10.80)$$

Thus, atmospheric carbon is recycled every 5 years.

10.5.5.2 Oxygen Cycle (Earth)

By far the dominant source of free oxygen in the Earth's atmosphere is photosynthesis; consequently, the oxygen cycle is governed by the biosphere-atmosphere cycle shown by thick arrows in Fig. 10.34. The overall reaction for photosynthesis is $\text{CO}_2 \rightarrow \text{C} + \text{O}_2$, so the removal of 150×10^{12} kg of carbon from the atmosphere releases

$$150 \times 10^{12} \frac{\text{kg C}}{\text{y}} \times \frac{32}{12} = 400 \times 10^{12} \frac{\text{kg O}_2}{\text{y}}$$

into the atmosphere. The amount of oxygen in the Earth's atmosphere is 1.2×10^{18} kg, and from Fig. 10.34 the rates of removal and replenishment are approximately equal, so from (10.80) the retention time for oxygen in the Earth's atmosphere is approximately

$$\frac{1.2 \times 10^{18} \text{ kg of O}_2}{400 \times 10^{12} \text{ kg of O}_2/\text{y}} \approx 3000 \text{ y}$$

This compares to only a few years for carbon. The rates of removal of C and O₂ from the atmosphere are of the same order of magnitude, differing only by a factor of 32/12, so the much larger retention time for oxygen is due almost entirely to the much larger amount of free oxygen in the atmosphere (Table 10.3).

10.5.5.3 Nitrogen Cycle (Earth)

Nitrogen (N₂) is the most abundant component of the Earth's atmosphere, taking up a mole fraction of 0.78 (Table 10.3). It is chemically quite inert and does not participate in the cycles of other nitrogen compounds, such as ammonia (NH₃) or nitrous oxide (N₂O).

The fact that Venus and Mars, which lack life, have atmospheres composed almost entirely of CO₂, with N₂ taking up <4 % (Table 10.3), indicates that the N₂ in the Earth's atmosphere must be almost entirely biogenic in origin. Figure 10.35 shows the basic cycles involved. The major source of N₂ is denitrifying bacteria in soils and the oceans that convert ammonium and nitrate compounds into N₂; the major sinks are (1) nitrogen-fixing bacteria (e.g., in the root nodules of legumes) that convert atmospheric N₂ into NH₄⁺, NO₃⁻, and organic nitrogen and (2) lightning and combustion, in which N₂ reacts with free O₂ to produce the oxides NO, NO₂, etc.

If life were to cease on the Earth, then lightning and combustion would provide the major sinks for atmospheric N₂. However, combustion would cease when the supply of organic material was depleted, and both lightning and combustion would become ineffective with the loss of free O₂ from photosynthesis. Thus abiotic removal rates would be much smaller than today, and the retention time for N₂ in the atmosphere is expected to be of the order of a Gy.

10.5.5.4 Sulfur Cycle (Earth)

Figure 10.36 shows the major sources and sinks in the terrestrial sulfur cycle. The quantities involved are significantly less certain than for the carbon and oxygen cycles, e.g., more recent estimates for some quantities are, in the same units, volcanoes 7; decay 58 over land and 48 over the ocean; and industry 100 (Goody 1995; Wayne 2000).

The mixing ratio for SO₂ in the terrestrial atmosphere is 167 ppt (parts per trillion or parts per 10¹²), and that of H₂S is variable, but between 0 and 100 ppt. The corresponding amounts of these sulfur compounds present in the atmosphere are then much smaller than the amounts transferred per year, indicating very short retention times of days or even hours.

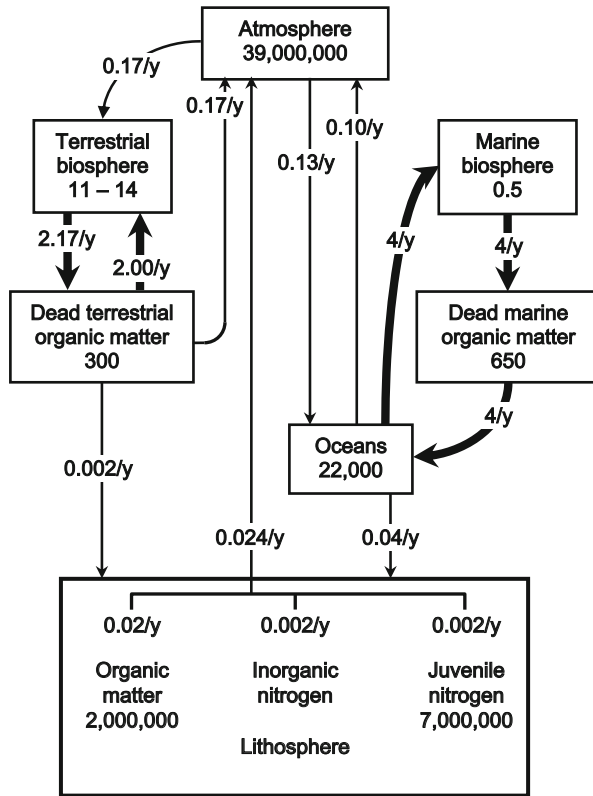


Fig. 10.35 The terrestrial nitrogen cycle; see Fig. 10.34 for explication. The unit for all numbers is 10^{12} kg of nitrogen. (After Wayne 2000, Fig. 1.6, p. 26; by permission of Oxford University Press)

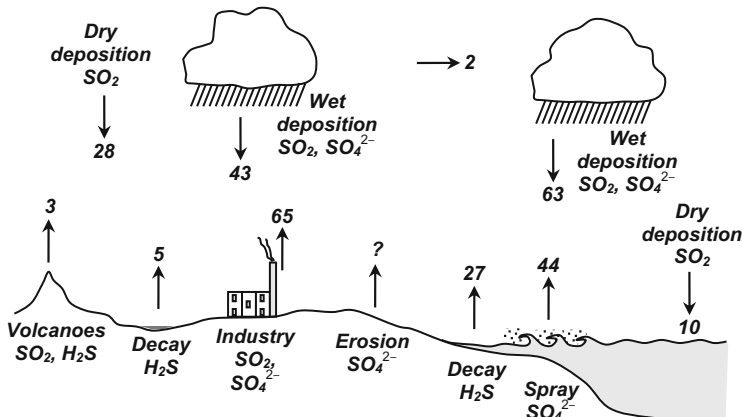


Fig. 10.36 Major sources and sinks of sulfur in the terrestrial atmosphere. The unit for all numbers is 10^9 kg of sulfur per year. The main compounds transferred are indicated in each case. Sources and sinks over land are shown on the left, and over oceans on the right. (After Iribarne and Cho 1980, Fig. II-5, p. 33)

Two more sulfur-containing gases are important in the chemistry of sulfur in the Earth's atmosphere: carbonyl sulfide (COS) is thought to be the most abundant sulfur gas in the troposphere at 500 ppt, and carbon disulfide (CS₂) is present in variable concentrations of 2–120 ppt. Volcanic eruptions contribute some portion of these gases, and oxidation of CS₂ also appears to produce COS, but in general their sources are not known at the present time, or even whether the dominant sources are natural or anthropogenic.

COS survives long enough to reach the stratosphere where it is oxidized to produce sulfate ions SO₄²⁻ and sulfuric acid (H₂SO₄), the latter principally in droplet form. This sulfuric acid aerosol layer tends to concentrate in a layer near 20 km altitude, called the *Junge layer*.

10.5.5.5 Sulfur Cycle (Venus)

Figure 10.37 shows the major reactions in the sulfur cycle on Venus. The cycle depends in part on the presence of free atomic oxygen in the upper atmosphere, and this is readily produced by photolysis of CO₂:



The recombination reaction



is spin-forbidden and slow, so although a considerable amount is lost to recombination to O₂, enough O remains to maintain the cycle.

An important component of the cycle is the production of sulfuric acid vapor in the upper atmosphere:

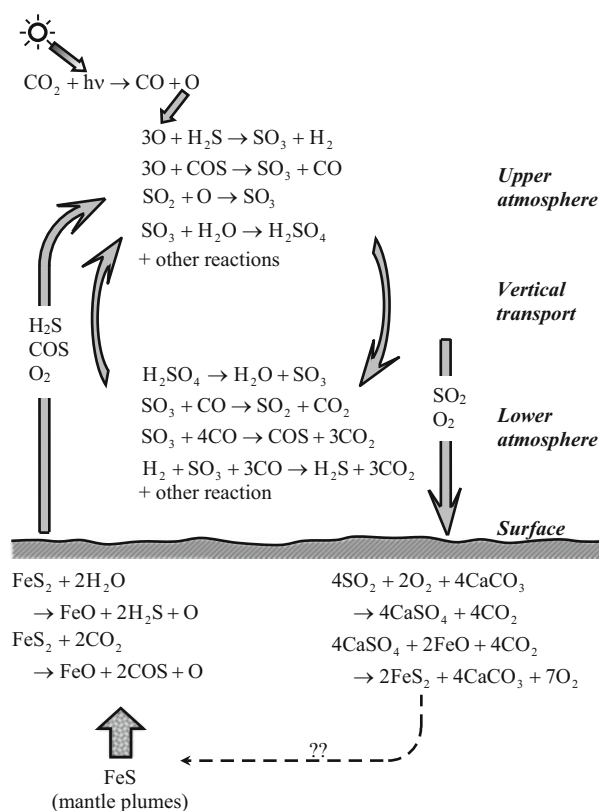


The temperature in the region 50–60 km altitude is low enough that the H₂SO₄ vapor readily condenses to form very concentrated droplets of sulfuric acid. The resulting sulfuric acid clouds are much more reflective than water-droplet clouds, and blanket the entire planet, giving Venus a very uniform optical albedo of 0.84.

10.5.5.6 Thermospheric Chemistry of Neutrals (Earth)

Two important thermospheric reactions are photodissociation ($AB + h\nu \rightarrow A + B$) and photoionization ($AB + h\nu \rightarrow AB^+ + e^-$), where $h\nu$ represents the energy of the absorbed photon, and e^- is a free electron.

Fig. 10.37 Sulfur cycle on Venus. Major chemical reactions are shown, and the vertical transport that links them



These reactions do not proceed directly. Instead, the absorbed photon energy creates an excited molecule, AB^* , which can decay by any allowed route; dissociation and ionization are just two of these routes. (Collisional de-excitation, or quenching, would be another route, but it is much less important at the low density of the thermosphere.)

Table 10.4 lists several decay routes of interest in a planetary atmosphere.

10.5.6 Excess Radiation

Up to now we have discussed the energy budget of the terrestrial planets. The temperatures of Venus and Earth are currently higher than their equilibrium temperatures, as we noted in earlier chapters, but this is understood in terms of greenhouse effects. One of the continuing mysteries of the solar system is the energy excess of the emission of the outer planets: three of the four giant planets appear to radiate more energy than they receive from the Sun. The sources of this energy may not be the same in each of Jupiter, Saturn, and Neptune; Uranus, which

Table 10.4 Products of molecular photoexcitation in the thermosphere

Reactants	Paths	Products	Description
$AB + h\nu \rightarrow$	AB^*		<i>Photoexcitation</i>
	\downarrow	$A + B^*$	<i>Dissociation</i> into two neutrals: one in the ground state; one in an excited state
	\rightarrow	$AB^+ + e^-$	<i>Ionization</i>
	\rightarrow	$AB + h\nu$	<i>Radiative de-excitation</i>
	\rightarrow	AB^\ddagger	<i>Intramolecular energy transfer: luminescence</i> if by an allowed transition; <i>phosphorescence</i> if by a forbidden transition
	$+CD \rightarrow$	$AB + CD^*$	<i>Intermolecular energy transfer: radiationless transition</i> to a different excited state of the same molecule.
	$+M \rightarrow$	$AB + M$	<i>Quenching</i> : the electronic excitation energy of AB^* is degraded to vibrational, rotational, or translational energy by collision with another molecule
	$+EF \rightarrow$	$AE + BF$	<i>Chemical reaction</i> mediated by the electronic excitation of AB^*

should be more closely related to Neptune than to the other two giants, does not show any excess radiation. The thermal emission is independent of the non-thermal radiation which has its origin in the magnetospheres (see Chap. 11), and which in origin is relatively well understood.

Of the possible sources of heat, primordial heat is a possibility, but bulk contraction (conversion of the potential energy of the planets' material into kinetic energy as it falls toward the center) is not favored at present because the liquid must resist compression.

Another related mechanism, however, involves selective "fall out" of some material—such as the "rain" of helium in the interior. This mechanism is thought to be especially important in Saturn, where the composition of the outer atmosphere seems to be deficient in helium relative to that of the Sun. In the case of Neptune, the excess may be due to a greenhouse effect, but here involving the gas methane in the very outer atmospheric layer.

Challenges

- [10.1] The phenomenon of the Chinook in Western Canada, the Föhn in Switzerland, and the Sirocco around the Mediterranean, involves a warm wind at lower elevations on the leeward side of mountains, with a higher temperature than is found at comparable elevations on the windward side of the mountains. Explain the physical basis for the phenomenon. (Hint: Consult the end of Sect. 10.2)

- [10.2] From (10.63), find the magnitude of the centrifugal force on an object of mass m on the surface of a planet as a function of Ω , r , and the object's latitude, λ . Also find the magnitude of the horizontal component of this force. At what latitude is the horizontal component largest?
- [10.3] From (10.62), find the magnitude of the Coriolis force on an object of mass m travelling horizontally at speed v on the surface of the Earth, as a function of Ω , r , v , and the object's latitude, λ , if the object is travelling (a) due north, (b) due east, and (c) at an azimuth angle α measured eastward from north. In part (c), α will also be in the equation. [Hint: Decompose the velocity into component vectors northward and eastward.] Illustrate the subsequent trajectory of a rocket fired due north from the equator.
- [10.4] Compute the relative magnitude of the Coriolis effect on Earth, Venus, and Mars. That is, derive the results of Sect. 10.5.1.
- [10.5] Derive (10.7) and (10.8), including the numerical constants in those equations.
- [10.6] Compute the tropospheric pressure scale heights for Venus, Earth, and Mars.
- [10.7] Consulting Sects. 10.1 and 10.2 and Fig. 10.23, discuss the retention of water vapor on the terrestrial planets.

References

- Bertaux, J.-L., Vandaele, A.-C., Koralev, O., Villard, E., Fedorova, A., Fussen, D., Quémérais, E., Belyaev, D., Mahieux, A., Montmessin, F., Muller, C., Neefs, E., Nevejans, D., Wilquet, V., Dubois, J.P., Hauchecorne, A., Stepanov, A., Vinogradov, I., Rodin, A., the SPICAV/SOIR team: A warm layer in Venus' cryosphere and high-altitude measurements of HF, HCl, H₂O and HDO. *Nature* **450**, 646–649 (2007)
- Cox, A.N. (ed.): *Allen's astrophysical quantities*, 4th edn. Springer, New York (2000)
- Elliott, J.L., Olkin, C.B.: Probing Planetary Atmospheres with Stellar Occultations. *Annu. Rev. Earth Planet. Sci.* **24**, 89–123 (1996)
- Forget, F., Hourdin, F., Fournier, R., Hourdin, C., Talagrand, O.: Improved General Circulation Models of the Martian Atmosphere from the Surface to above 80 km. *J. Geophys. Res.* **104**, 24,155–24,175 (1999a)
- Forget, F., Hourdin, F., Hourdin, C., and Talagrand, O. Simulations of the martian seasonal dust cycle with a general circulation model, 4th International Conference on Mars, abstract 6206, (1999b)
- Goody, R.: *Principles of atmospheric physics and chemistry*. Oxford University Press, New York (1995)
- Hoshino, N., Fujiwara, H., Takagi, M., Takahashi, Y., Kasaba, Y.: Characteristics of planetary-scale waves simulated by a new Venusian mesosphere and thermosphere general circulation model. *Icarus* **217**, 818–830 (2011)
- Iribarne, J.V., Cho, H.-R.: *Atmospheric physics*. D. Reidel, Boston (1980)
- Jeans, J.: *An introduction to the kinetic theory of gases*. The University Press, Cambridge (1952). Reprinting of 1st Ed., 1940
- Jenkins, J.M., Steffes, P.G., Hinson, D.P., Twicken, J.D., Tyler, G.L.: Radio Occultation Studies of the Venus Atmosphere with the Magellan Spacecraft: 2. Results from the October 1991 Experiments. *Icarus* **110**, 79–94 (1994)
- Lie-Svendsen, Ø., Rees, M. H. Helium escape from the terrestrial atmosphere: the ion outflow mechanism. *J Geophys Res* **101**, No. A2, 2435–2443 (1996)

- Milone, E.F., Wilson, W.J.F.: Solar system astrophysics: background science and the inner solar system. Springer, New York (2014)
- Pasch, R.J., Blake, E.S., Cobb, H.D. III, and Roberts, D.P. 12 January 2006. Tropical Cyclone Report Hurricane Wilma 15–25 October 2005 (National Hurricane Center)
- Peralta, J., Hueso, R., Sánchez-Lavega, A.: A reanalysis of Venus winds at two cloud levels from Galileo SSI images. *Icarus* **190**, 469–477 (2007)
- Prinn, R.G., Fegley Jr., B.: The atmospheres of Venus, Earth, and Mars: a critical comparison. *Ann. Rev. Earth Planet. Sci.* **15**, 171–212 (1987)
- Richardson, M.I., Wilson, R.J.: A topographically forced asymmetry in the Martian circulation and climate. *Nature* **416**, 298–301 (2002)
- Sánchez-Lavega, A., Hueso, R., Piccioni, G., Drossart, P., Peralta, J., Pérez-Hoyos, S., Wilson, C. F., Taylor, F.W., Baines, K.H., Luz, D., Erard, S., and Lebonnois, S. Variable winds on Venus mapped in three dimensions. *Geophys Res Lett* **35**, doi:10.1029/2008GL033817 (2008)
- Schlosser, W., Schmidt-Kaler, T.H., Milone, E.F.: Challenges of astronomy: hands-on experiments for the sky and laboratory. Springer-Verlag, New York (1991/1994)
- Seinfeld, J.H., Pandis, S.N.: Atmospheric chemistry and physics: from air pollution to climate change. Wiley, New York (1998)
- Svedhem, H., Titov, D.V., Taylor, F.W., Witasse, O.: Venus as a more earth-like planet. *Nature* **629–632** (2007)
- Wayne, R.P.: Chemistry of atmospheres. Oxford University Press, Oxford (2000)
- Yamamoto, M., Takahashi, M.: Dynamics of Venus' Superrotation: The Eddy Momentum Transport Processes Newly Found in a GCM. *Geophys. Res. Lett.* **31**, L09701 (2004). doi:[10.1029/2004GL019518](https://doi.org/10.1029/2004GL019518)

Chapter 11

Planetary Ionospheres and Magnetospheres

11.1 Earth: Ionospheric Layers

Sunlight interacts with planetary atmospheres to produce excited atoms and ions, and the ions interact with each other and with neutral atoms to produce unique, altitude-dependent populations. As with other aspects of the terrestrial planets, we know the ionosphere of the Earth best, so we start with it. Figure 11.1 shows the electron density and ionospheric layers in the Earth's ionosphere. During the daytime, the D layer forms and the F layer separates into two parts, F₁ and F₂; at night the D layer disappears, and the F layers merge into a single layer.

11.1.1 The F Layer

The F layer is created primarily by solar EUV radiation in the wavelength range $10 \text{ nm} < \lambda < 80 \text{ nm}$.

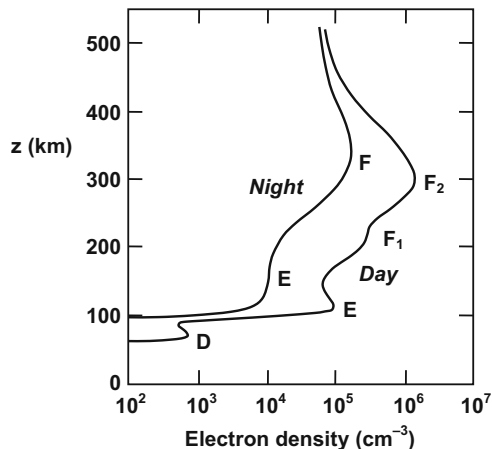
11.1.1.1 Atoms and Ions in the F Layer

The dominant neutral atoms are O and N₂. Atomic oxygen is much more abundant than O₂ in the F region because most of the O₂ has undergone *photodissociation* (or *photolysis*):



where, as an aid, we list the mechanism after the reaction.

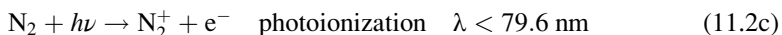
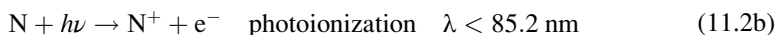
Fig. 11.1 Electron density vs. altitude in the Earth's ionosphere. Typical curves and ionospheric layers are shown for night and day. The curves vary considerably with solar activity, sunspot number, and time of year. From Iribarne and Cho (1980), Fig. I-7, p. 10



11.1.1.2 Production Mechanisms

The dominant ions are primarily O^+ with smaller amounts of O_2^+ , NO^+ , N^+ . The production of the ions is due to several reactions. The dominant (source) reactions are as follows:

A. The primary¹ reactions, the process, and the wavelength range are



B. The secondary reactions are



Most of the N_2^+ produced in the primary reactions is thus removed by the secondary reactions.

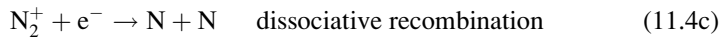
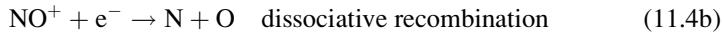
¹ The words “primary” and “secondary” refer to the sequence of events, not to relative importance, i.e., the primary reactions have to occur first, in order for the secondary reactions to occur.

11.1.1.3 Loss Mechanisms

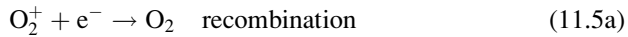
The loss mechanisms (sinks) of the ions are as follows:

A. Molecular ions

The most common process is dissociative recombination, where the electron recombines with a molecule, dissociating it into two neutral atoms in the process:

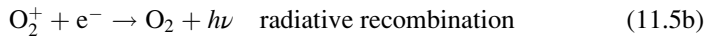


Dissociative recombination is required instead of simple recombination, e.g.,



because recombination is an exothermic process: energy is released. $\text{O}_2^+ + \text{e}^- \rightarrow \text{O}_2$ would leave the O_2 with an excess of energy that in fact would dissociate the molecule.

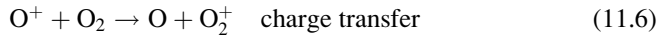
Radiative recombination, e.g.,



has a low probability and can be ignored compared to dissociative recombination.

B. Atomic ions

Simple recombination of electrons with atomic ions does not occur for the same reason described earlier for molecules: the recombination is an exothermic process, and the excess energy given to the atom by the recombination is sufficient to eject the electron again. The principal loss mechanism for atomic ions is charge transfer to a molecule



followed by molecular dissociative recombination:



11.1.1.4 Ion Concentration vs. Altitude

The concentration of a given species of ion at any given altitude in the ionosphere depends on the following:

- A. The production rate, which depends on the concentration of the “source” species (there will be, for instance, little O^+ if there is little atomic O to be ionized) and

the amount of ionizing radiation present, which decreases with decreasing altitude because of absorption at higher altitudes.

- B. The loss rate, which depends on (among other things) the density of air, because collisions which remove ions through such processes as electron recombination and charge transfer are less frequent at lower densities.
- C. The rate of vertical diffusion. Each species of ion tends to redistribute itself according to its own pressure scale height (Sect. 10.5.4.4), resulting in fractionation because lower mass ions have larger scale heights. We can describe two separate regimes, one below and the other above the peak of the F₂ region at 300 km altitude:
 - 1. $h < 300$ km altitude. Here, the density is “high,” so the mean ionic lifetime is “short,” and any ions produced are destroyed before they can diffuse to a different altitude. Therefore, below 300 km altitude, the ion concentrations at any given level are controlled primarily by local production and loss. This condition is called *photochemical equilibrium*.
 - 2. $h > 300$ km altitude. Here, the density is “low,” so the mean ionic lifetime is “long,” and ions have time to diffuse to different altitudes before they are destroyed. Thus the ion concentrations above 300 km altitude are controlled primarily by *diffusion*, producing an exponential decrease in the number density of each ion with altitude, according to the scale height.
- D. Horizontal transport. The Earth’s magnetic field, \vec{B} , is directed into the ground in the north polar region (e.g., Fig. 11.23), and the magnetospheric processes described in Sect. 11.6.5 create an electric field, \vec{E} , from the dawn side of the pole toward the dusk side (see Fig. 11.31). Patches of ionization created in the polar cusp (Fig. 11.23) at F layer altitudes can then undergo $\vec{E} \times \vec{B}$ drift (Sect. 11.5.6) at speeds up to several km/s from there into high latitudes on the nightside. $\vec{E} \times \vec{B}$ drift and related magnetospheric and ionospheric processes are described in detail in Sects. 11.5 and 11.6.

11.1.1.5 Charge Separation

The same processes of diffusion as apply above 300 km altitude and of photochemical equilibrium as apply below 300 km control the concentration of free electrons. Because of their small mass, their scale height is almost infinite compared to the positive ions, and their diffusion produces a vertical charge separation in the ionosphere above 300 km. This *ambipolar diffusion* (diffusion resulting in a charge separation) creates an upward force on the positive ions (especially H⁺), lifting them to higher altitudes, so that the scale heights for any ion is about twice the scale height of the equivalent neutral atom.

11.1.2 The E Layer

The E layer is distinct from the F layer by virtue of being created by different wavelengths of solar radiation:

F: primarily $10 \text{ nm} < \lambda < 80 \text{ nm}$

E: primarily $80 \text{ nm} < \lambda < 102.6 \text{ nm}$

and is characterized by a different population of neutral atoms and ions.

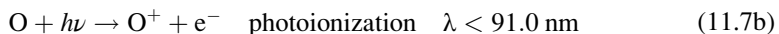
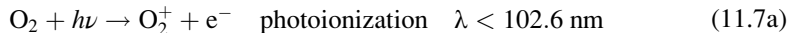
11.1.2.1 Atoms and Ions in the E Layer

The dominant neutrals are N_2 , O_2 , and O. Because of UV absorption in the F layer, there is less photodissociation of O_2 in the E layer; so O is less abundant than N_2 and O_2 in all but the highest parts of the E region. The dominant ions are NO^+ and O^+ .

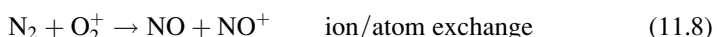
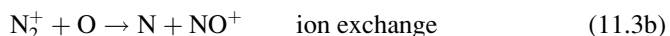
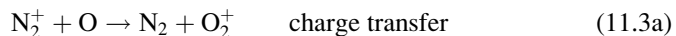
11.1.2.2 Production Mechanisms

The production of ions is due to photoionization and other processes: O_2 is more important in the E layer than in the F layer, but otherwise the reactions are similar.

A. The primary reactions (*i.e.*, those that need to occur first) are photoionizations:



B. The secondary reactions are as follows:

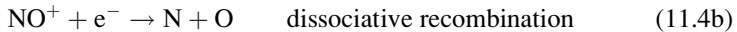


As in the F layer, the secondary reactions remove most of the N^+ in favor of O_2^+ and NO^+ .

11.1.2.3 Loss Mechanisms

The loss mechanisms for ions of the E layer are



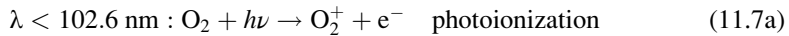
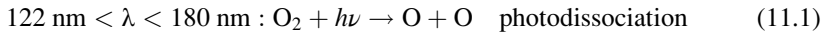


(11.4b) is the most important charge neutralization step in the E layer. Also, (11.9) is much more important than (11.4b) in the E layer because the concentration of neutral NO is much greater than the concentration of free electrons.

The E layer is in photochemical equilibrium during daytime, with diffusion and other motions also becoming important at night.

11.1.3 The D Layer

The D layer is shielded by the E and F layers above it. Most of the ionizing radiation has been absorbed by photodissociation and photoionization of O₂ in the E and F layers; particularly



11.1.3.1 Dominant Ions

The dominant ions in the D layer are NO⁺ (~80 % by number) and O₂ (~20 % by number), plus small but important amounts of other positive and negative molecular ions.

Ionization in the D region comes mainly from four sources:

1. “Windows” in the range 102.6 nm < λ < 122 nm, in which radiation reaches down to as low as 70 km. These windows include the Lyman-alpha (Lyα) emission line at λ = 121.6 nm.
2. Solar X rays in the upper D region, from the quiet (undisturbed) Sun.
3. Cosmic rays in the lower D region. Cosmic rays are particles (electrons, protons, etc.) arriving at the Earth from the Sun (solar cosmic rays) and sources beyond the solar system (galactic cosmic rays). Most of the electrons are stopped by collisions higher in the atmosphere, but energetic auroral electrons can reach the D region, e.g., during magnetospheric substorms (Sect. 11.6.8). Solar energetic protons, which have typical energies in the 100 s of MeV, can penetrate to the D region at high latitudes.
4. Solar X rays of λ < 0.6 nm during disturbed conditions, especially from solar flares.

11.1.3.2 Production Mechanisms

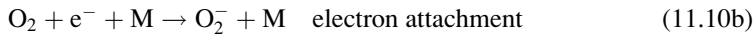
Production (source) of ions in the D layer is through

- A. Primary reactions, which produce mainly NO^+ , O_2^+ , and O_2^- .



(Ionization of NO by Ly α photons is the main reason for the existence of the D layer.)

Negative ions also form, by electron attachment in a three-body collision:



where M is any molecule or atom. Simple attachment, viz., $\text{O}_2 + \text{e}^- \rightarrow \text{O}_2^-$, cannot occur because the reaction $\text{O}_2 + \text{e}^-$ is exothermic, and the excess energy ejects the electron again unless a third body carries off the energy excess. The third body also allows both energy and momentum to be conserved. Radiative recombination ($\text{O}_2 + \text{e}^- \rightarrow \text{O}_2^- + h\nu$) is too slow to be important.

Negative ions are important only in the D region, because the probability of three-body collisions depends strongly on the density. In the E and F regions, the density is so low that three-body collisions are extremely rare, and negative ions are essentially absent.

- B. Secondary reactions:

NO^+ , O_2^+ and O_2^- react with a large variety of neutral molecules. As a result, the D layer is a complex system of many ionic species, such as H_3O^+ and O_2^+ , and NO_3^- , as well as “cluster ions,” such as $\text{H}_3\text{O}^+ \cdot \text{H}_2\text{O}$ and $\text{NO}_3^-(\text{H}_2\text{O})_n$ (where the subscript n is a small integer) that form when neutral molecules become attached to an ionized molecule.

11.1.3.3 Loss Mechanisms

The loss of ions in the D layer is primarily through dissociative recombinations.

Production and loss in the D layer occur much faster than mixing or diffusion. The concentration of each ion at each altitude in the D region is therefore controlled by photochemical equilibrium.

An important consequence of this photochemical equilibrium is that, with the rapidity of loss processes and the removal of solar ionizing radiation, the D layer disappears at night.

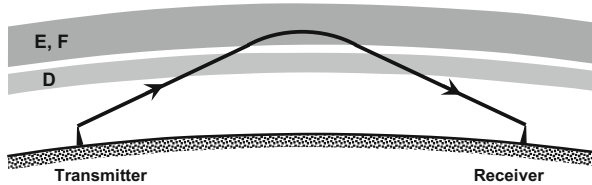


Fig. 11.2 Illustration of the refraction of radio waves by the Earth's ionospheric E and F layers. The diagram is a composite of two scenarios: during the daytime, the waves are absorbed in the D layer and do not reach the receiving antenna, whereas at night the D layer disappears and long-distance reception occurs

11.1.4 Reflection of Radio Waves

The E and F layers permit long-distance radio communication by reflecting radio waves back to the Earth, particularly in the standard commercial AM broadcast band (approximately 500–1,700 kHz) and short wave regions.

Radio waves are emitted by oscillating electric currents in the transmitting antenna. The inverse process takes place in reception: the incoming radio wave creates an oscillating electric current in the receiving antenna.

A similar process happens in the ionosphere. An incoming radio wave encountering a free electron makes the electron oscillate. The oscillating electron in turn behaves as a small transmitting antenna and emits a radio wave of the same frequency as the incoming wave. Each free electron therefore acts as a combination receiver and re-transmitter.

The overall process is complex (see Sect. 11.4), but the result is that the path of the radio wave is bent back toward the Earth; that is, the wave is “reflected” by the ionosphere, as Fig. 11.2 illustrates.

To be reflected by the E and F layers, however, radio waves have to pass twice through the D layer: once on the way up and once on the way back down.

The density in the D layer is high enough that the oscillating electrons collide with the surrounding molecules, removing energy from the electrons and increasing the random motion of the molecules. The electrons as a result are unable to retransmit efficiently, reducing the intensity of the radio beam. Thus, energy is taken from the radio waves and converted to heat in the D layer, with the result that the radio waves are absorbed rather than reflected.

During daytime, the D layer limits the commercial AM band to line-of-sight distances. At night, however, the D layer disappears, allowing long-distance reception.

Intense solar flares produce very energetic particles, which can reach the Earth within half an hour after the start of the flare and can penetrate to the D layer. The enhanced ionization in the D layer can then produce radio blackouts by disrupting long-distance radio communication.

11.2 Atmospheric and Ionospheric Chemistry on Mars and Venus

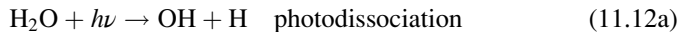
11.2.1 Neutral Atmosphere of Mars

The mixing ratios² of H, H₂, O, O₂, CO, and CO₂ in the Martian atmosphere are shown as a function of altitude in Fig. 11.3. Some of these are also listed in Table 11.1, for the lower atmosphere. The dominant component at all altitudes below 200 km is CO₂, with a mixing ratio of 0.953 in the troposphere.

Because of the thinness of the Martian atmosphere, solar UV penetrates to the ground, and the chemistry of the neutral atmosphere is therefore dominated by photodissociation (photolysis) of CO₂, producing atomic oxygen:



However, as Fig. 11.3 shows, molecular O₂ is much more abundant than atomic O below 100 km altitude. The O₂ is created by OH radicals derived from water, such as OH (hydroxyl) from



[where the superscript (*) signifies an excited state] reacting with atomic oxygen:

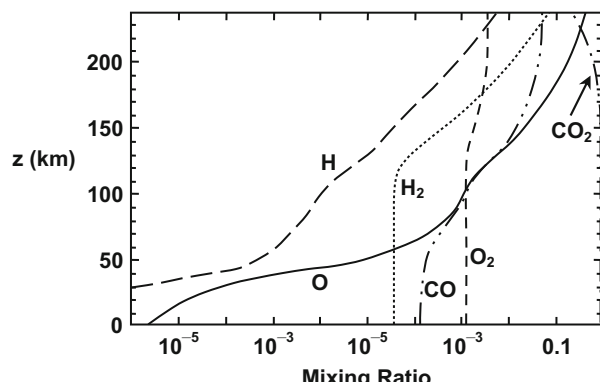


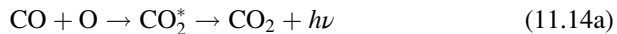
Fig. 11.3 Mixing ratios of H, H₂, O, O₂, CO, and CO₂ in the Martian atmosphere, as a function of altitude, z. Adapted from Nair et al. 1994, Fig. 3(a), p. 133, with permission

² Mixing ratio is defined in Footnote 3, Sect. 10.2.2.

Table 11.1 Comparison of the number densities of neutrals and ions in the Martian ionosphere (~130 km altitude)

Species	Number density (cm^{-3})	
	Neutral (CO_2, O_2)	Ion ($\text{CO}_2^+, \text{O}_2^+$)
CO_2	4×10^{10}	1.5×10^4
O_2	5×10^7	10^5

Without an opposing oxidizing process to convert CO back to CO_2 , (11.11) and (11.13) would produce the observed CO abundance in less than 3 years, and a mostly CO and O_2 atmosphere in about 2,000 years. Figure 11.3 shows that this has not happened. The oxidizing process cannot be direct recombination with O, either by



or by



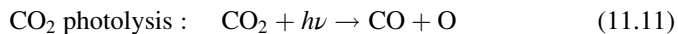
because radiative de-excitation of CO_2^+ is too slow to compete with (11.11), and (11.14b) is spin-forbidden. However, Mars has significant quantities of water. Various chemical reactions produce OH (hydroxyl) from water, including (11.12a) and (11.12b). The OH then reacts with CO rapidly enough to compete with CO_2 photolysis:



11.2.2 Neutral Atmosphere of Venus

Venus' clouds shield the regions below them from solar UV radiation, so photochemistry occurs at and above the cloud tops.

The major steps are similar to those on Mars, specifically,



Reaction (11.16) replaces (11.13) because Venus lacks significant water.

Reaction (11.17) is required because, in similar fashion to Mars, (11.11) and (11.16) would produce the observed O_2 abundance in only a few years and the observed CO abundance in about 200 years. The result should be a mostly CO and O_2 atmosphere from the cloud tops upward. This is true for the highest levels of Venus' atmosphere, but near the cloud tops the concentrations of CO and O_2 are only 45 and 1 ppm, respectively.

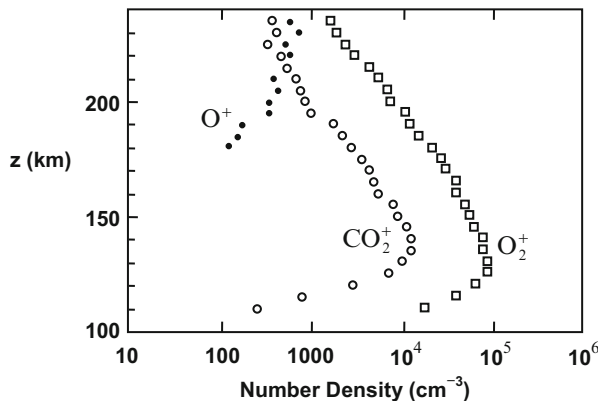


Fig. 11.4 Ion density profiles in the Martian ionosphere. Open squares are O_2^+ ; open circles are CO_2^+ ; and dots are O^+ . Because each ion contributes one free electron, the electron density is slightly greater than the density of O_2^+ . After Chen et al. (1978), Fig. 6, p. 3875); copyright 1978, American Geophysical Union. Modified by permission of American Geophysical Union

Venus differs from Mars in that the CO:O₂ ratio is about 45:1 on Venus, compared to about 1:10 on Mars (Fig. 11.3). Thus, an efficient reaction is needed on Venus to break the O–O bond of O₂. The solution is not clear, but several reaction cycles involving chlorine and/or sulfur appear likely.

11.2.3 Ionosphere of Mars

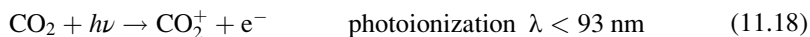
11.2.3.1 Dominant Ions

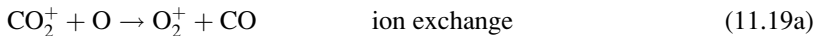
The dominant ion in the Martian ionosphere is O₂⁺, with smaller amounts of CO₂⁺ and O⁺ (Fig. 11.4).

It should be noted that, even in the region of greatest ion density (~130 km altitude), ions are a very small minority of the particles present. A similar situation applies to the ionospheres of the Earth and Venus. Table 11.1 lists some representative values.

11.2.3.2 Production Mechanisms

Production is due to the reactions

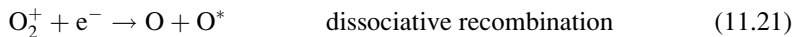




Not surprisingly, the primary ionospheric reaction is photoionization of CO_2 . However, CO_2^+ is not the dominant ion (Fig. 11.4), because (11.19a) and (11.19b) convert most of the CO_2^+ to O^+ and O_2^+ , and (11.20) then converts most of the O^+ to O_2^+ .

11.2.3.3 Loss Mechanisms

The most important charge-neutralization reaction is dissociative recombination of the domination:



11.2.4 Ionosphere of Venus

11.2.4.1 Dominant Ions

The dominant ions in the ionosphere of Venus are different at different altitudes, as on Earth:

Low altitudes (110–200 km): O_2^+ and NO^+

High altitudes (>200 km): O^+

Other ions present include C^+ , CO^+ , CO_2^+ , N^+ , N_2^+ , H^+ , He^+ .

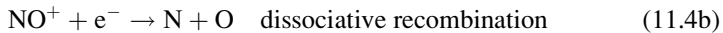
Below 170 km, the ionosphere is in photochemical equilibrium, i.e., abundances are determined by local production and loss. Above 170 km, abundances are determined primarily by diffusion.

11.2.4.2 Production and Loss Mechanisms

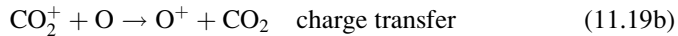
Reactions (11.18)–(11.20) apply on Venus as on Mars. In addition, one of the loss reactions for O_2^+ is the major source for NO^+ :



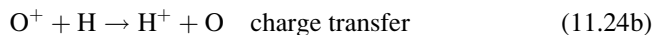
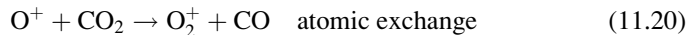
The NO^+ also contributes to the production neutral O:



Production of O⁺ is by



Loss of O⁺ is by



Reactions (11.19b) and (11.20) emphasize the importance of CO₂ on Venus.

11.2.5 Atmospheric Escape Mechanisms

11.2.5.1 Jeans Escape

The particles (atoms or molecules) of a gas in thermal equilibrium (in which case the gas has a well-defined temperature, T) are said to have a thermal, or *Maxwellian*, distribution of speeds. At and above the exobase (the base of the exosphere, Sect. 10.4.1.4), those particles in the Maxwellian distribution that are travelling upward with speeds above escape speed, v_{esc} , will escape. This type of atmospheric loss is called *Jeans escape*, and gives rise to the evaporation phenomenon discussed in connection with long-term retention in Sect. 10.1.

The flux of escaping particles (m⁻² s⁻¹) is given by

$$\Phi_J = n_x \frac{v_{th}}{2\sqrt{\pi}} P_{esc} = n_x \frac{v_0}{4} P_{esc} \quad (11.25)$$

(e.g., Hunten 1982, and references therein), where a subscript “ x ” signifies a value at the exobase, $v_{th} = \sqrt{2kT_x/m}$ is the most probable particle speed, $v_0 = \sqrt{8kT_x/(\pi m)}$ is the mean of the magnitudes of the particle speeds, k is Boltzmann’s constant, T_x and n_x are the temperature and particle density (m⁻³), respectively, at the exobase (the exosphere is isothermal, whereas density decreases with altitude), m is the mass per particle, $P_{esc} = (1 + \lambda_J) \exp(-\lambda_J)$ is the probability of escape, λ_J is the *Jeans parameter*, equal to the magnitude of the ratio of the gravitational energy, $E_{grav} = GMm/r$, of a particle to its thermal energy, $E_{th} = kT$, at the exobase,

$$\lambda_J \equiv \left| \frac{E_{grav}}{E_{th}} \right| = \frac{GMm}{kT_x r_x} = \frac{r_x}{H_x} = \left(\frac{v_{esc}}{v_{th}} \right)^2 \quad (11.26)$$

(see Problem 1 in the Challenges section at the end of this chapter), G is the universal gravitational constant, M is the planetary mass, r_x is the radial distance of the exobase from planetary center, $H_x = kT_x/(mg)$ is the pressure scale height at the exobase [cf. (10.26)], and g is the gravitational acceleration at the exobase. A correction factor, B ($0.5 \leq B \leq 0.8$), is sometimes included in (11.25) to allow for the depression of the high-velocity tail of the Maxwellian distribution by the escape of high-velocity particles (Hunten 1982).

The quantities v_{th} , v_o and P_{esc} , and therefore also Φ_J , all decrease with increasing particle mass, m . ($\lambda_J \propto m$ but, for large λ_J , the value of P_{esc} is dominated by the $\exp(-\lambda_J)$ factor.) Thus, for a given element, Jeans escape results in isotope fractionation: lighter isotopes become increasingly depleted as a function of time relative to heavier isotopes. Nonthermal loss mechanisms (Sect. 11.2.5.3) also contribute, and can in fact dominate, isotope fractionation. This effect makes isotope ratios a useful probe for investigating atmospheric history.

Another useful relation can be found from the fact that the mean free path, L_{mfp} , equals the total density scale height (i.e., including all species), H_{total} , at the exobase. H_{total} is related to the total number density (all species), n_{total} , and the mean collisional cross section, σ , by $L_{mfp} = 1/(n_{total}\sigma)$. It then follows that, at the exobase,

$$n_{x,total} H_{x,total} \sigma = 1 \quad (11.27)$$

On Venus, the exobase altitude is ~ 200 km, where the dominant species is atomic oxygen, followed by CO and then several other species including atomic hydrogen. Because of its large scale height, H becomes the major species after O at higher levels in the exosphere. The temperature is 275 K in the dayside thermosphere and 100 K in the nightside cryosphere. Number densities vary over the solar cycle; taking a number density for hydrogen of $n_x \sim 6 \times 10^{10} \text{ m}^{-3}$, (11.25) and (11.26) give, for H in the dayside exosphere, $\lambda_J = 22.87$, $P_{esc} = 2.8 \times 10^{-9}$, $\Phi_J = 1.0 \times 10^5 \text{ m}^{-2} \text{ s}^{-1}$, and a total loss rate of H from the dayside exosphere by Jeans escape of $2\pi r_x^2 \Phi_J = 2.5 \times 10^{19} \text{ s}^{-1}$.

As noted above, loss rates decrease strongly with increasing λ_J when λ_J is large. On the dayside, (11.26) gives $\lambda_J = 46$ for deuterium and 366 for atomic O, and on the nightside, $\lambda_J = 66.88$ for atomic hydrogen (giving a nightside hydrogen loss rate $< 10^4 \text{ s}^{-1}$). Thus, Jeans escape on Venus is by far dominated by H atoms from the dayside exosphere.

In the case of Mars, there is considerable uncertainty in the temperature and hydrogen density at the exobase (e.g., Chaufray et al. 2008). From *Mars Express* observations of Lyman α scattering by the hydrogen corona, Chaufray et al. (2008) use radiative transfer models to derive the H density profile and temperature (isothermal) in the exosphere, and, from that, the temperature and H density at

the exobase (200 km altitude). Assuming that exospheric H is characterized by a single temperature, they obtain $T_x = 200\text{--}250\text{ K}$ and a hydrogen number density $n_x \sim 1\text{--}4 \times 10^{11}\text{ m}^{-3}$. Using $T_x = 225\text{ K}$ and $n_x \sim 2.1 \times 10^{11}\text{ m}^{-3}$, we get $\lambda_J \sim 6.41$, $P_{esc} \sim 1.2 \times 10^{-2}$, and $\Phi_J \sim 1.4 \times 10^{12}\text{ m}^{-2}\text{ s}^{-1}$. Their assumption of spherical symmetry means that T_x is an average over the planet, so the total loss rate of H from the exosphere by Jeans escape is $4\pi r_x^2 \Phi_J \sim 2.2 \times 10^{26}\text{ s}^{-1}$. This loss rate is seven orders of magnitude greater than for Venus. The exospheric temperatures of the two planets are reasonably similar, so the difference arises from Venus' greater mass and gravitational acceleration.

As will be seen in Sects. 11.7.2.3 and 11.7.3.2, Jeans escape of H atoms from Venus is negligible compared to other, nonthermal mechanisms, whereas Jeans escape dominates the loss of H from Mars. On both planets, Jeans escape of O, O₂ and CO₂ is negligible.

11.2.5.2 Hydrodynamic Escape

In Jeans escape, atmospheric loss is governed by individual particle motion, and the loss rate can be described by kinetic theory. The rate of Jeans escape decreases with increasing atomic or molecular mass, causing isotope ratios to change.

If the loss rate becomes large enough, the lightest and therefore fastest-moving particles will drag the other particles along with them, and the escape is described by fluid mechanics. This latter condition is called *hydrodynamic escape*, sometimes referred to as *blow-off*. In detail, the lighter particles diffuse through the heavier particles, thus also transferring momentum to them (Hunten et al. 1987). Everything then moves outward, with relative speeds given by diffusion theory. Because all particles flow outward together (or almost together), hydrodynamic escape leaves isotope ratios essentially unchanged.

Jeans escape and hydrodynamic escape can be seen as two end-members of a single atmospheric loss process, with the particular description depending on the relative magnitudes of E_{grav} and E_{th} ; i.e., on the value of λ_J . The loss is by Jeans escape for large λ_J and by hydrodynamic escape for small λ_J . Intermediate cases ($\lambda_J \sim 2$) are often called *slow hydrodynamic escape*, and are more difficult to model.

The solar wind (Sect. 11.3) is described by hydrodynamic escape within a few solar radii of the solar photosphere, and the Earth's polar wind (Sect. 11.2.5.3(g), below) can be treated hydrodynamically, but otherwise hydrodynamic escape is not important for planetary atmospheres in the present solar system. However, it may have been important in some cases in the early solar system; e.g., Venus may have had abundant water early in its life, in the form of a primitive atmosphere laden with water vapor because of the high temperature. In this case, photodissociation of H₂O could have led to hydrodynamic escape until the water content dropped below some low level.

Both Jeans escape and hydrodynamic escape are thermal mechanisms. We now turn to nonthermal mechanisms.

11.2.5.3 Nonthermal Loss Mechanisms

Nonthermal processes are those that do not produce a thermal, or Maxwellian, distribution of speeds; e.g., an exothermic chemical reaction may produce atoms or ions with a narrow range of speeds or energies. If these speeds are much higher than the characteristic local thermal (Maxwellian) speed, then they are referred to as *suprothermal* atoms or ions.

Escape requires speeds greater than or equal to v_{esc} : 10–11 km/s for Venus and the Earth, or 5 km/s for Mars. These escape speeds correspond to particle energies of 0.5–0.6 eV per atomic mass unit for Venus and the Earth (1 eV = 1 electronvolt = 1.602×10^{-19} J), or 0.13 eV/u for Mars. If these were mean energies in a thermal distribution, then, by $E \sim kT$, 0.5 eV/u would correspond to a temperature increment of $\sim 6,000$ K for each atomic mass unit; i.e., characteristic temperatures of $6,000$ K \times 1 for H and $6,000$ K \times 16 = 96,000 K for O, much higher than the actual exospheric temperatures of ~ 300 K for Venus or 1,000 K for the Earth. Similarly, 0.13 eV/u corresponds to $\sim 1,500$ K for H or 24,000 K for O, compared to the Martian exospheric temperature of ~ 200 K. Nonthermal processes therefore have to create significant quantities of suprothermal atoms/ions to influence atmospheric loss.

Not all suprothermal atoms have sufficient energy to escape. Because of their high energies, they have a very large scale height and create a high-altitude corona around the planet. “Hot” (i.e., high-energy) H and O coronae have been observed around Venus, the Earth, and Mars.

The important nonthermal loss mechanisms are listed below (Hunten 1982). In this list, an asterisk denotes a high kinetic energy.

a. Charge exchange:



Ions are constrained by the magnetic field of the planet, whereas neutrals are not. Charge exchange therefore converts fast ions which cannot escape into fast neutrals which can, while the thermal neutral is converted into a thermal ion. The fast neutrals that do not escape help populate the hot H and O coronae.

(11.28) is the dominant loss mechanism for the Earth: Characteristic temperatures for plasmaspheric and ionospheric protons and deuterons are $\sim 2,000$ –10,000 K, compared ~ 750 –1,750 K for exospheric neutrals.

b. Dissociative recombination:



(11.21) releases 2.5 eV of kinetic energy to each oxygen atom; then, by (10.2), each oxygen atom has a speed $v = 5.5 \text{ km/s}$, equal to the escape speed from Mars. Oxygen is abundant in terrestrial planet exospheres, so (11.21) is an important source of energetic atomic oxygen on Earth, Venus and Mars. It also indirectly produces energetic H and D by elastic energy transfer collisions [(11.36)].

c. Impact dissociation and photodissociation:



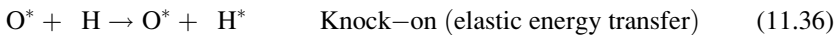
The e may be a photoelectron or an accelerated electron. In this and the previous mechanism, it is also possible for much of the photon or electron energy to go into electronic or vibrational excited states of the product atoms or molecules, reducing the kinetic energy available for escape. These H^* , N^* and O^* would then contribute to their respective coronae.

d. Ion-neutral reaction:



(11.34) yields 0.6 eV, but much of this energy is likely to go into vibrational excitation of the OH. In this case, most of the H will enter the H corona rather than escaping.

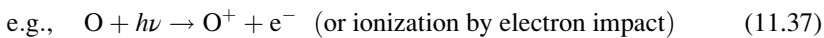
e. Sputtering and knock-on:



Sputtering refers to a backsplash of atoms caused by the impact of an energetic incident particle. It is usually thought of in terms of impacts on solid surfaces, such as sputtering of atoms and ions from the lunar surface by impacting solar wind particles, but also occurs with particles striking planetary atmospheres. In this case, multiple secondary collisions result in some particles travelling backward. Knock-on refers to forward acceleration of impacted particles.

Incident ions are usually the agents of sputtering, but only because the required speeds are seldom achieved by neutral atoms.

f. Solar wind pickup:



A neutral planetary corona can extend beyond the planetary magnetosphere into the solar wind, because neutral atoms are not constrained by magnetic fields. If such an atom is ionized as described above, then it suddenly finds itself as a charged particle in a moving magnetic field (the interplanetary magnetic field embedded in the solar wind). It therefore experiences a motional electric field that causes it to drift at the solar wind speed in the solar wind direction (see Sect. 11.5.6); i.e., it is picked up and carried off by the solar wind. These ions are referred to as *pickup ions*.

This loss mechanism also occurs on satellites in a planetary magnetospheric wind.

g. Ion escape:

e.g., escape of H^{+*} along open magnetic field lines. This process is important in the Earth's polar regions, where the magnetic field lines are open to the magnetotail (Sect. 11.5). The flux of ions is called the *polar wind*.

h. Plasma waves:

At high altitudes where the density is low enough for the plasma to be essentially collisionless, plasma waves involving broad-band, low-frequency electric-field oscillations in the range <1 Hz to several hundred Hz can accelerate ions to energies of tens to hundreds of eV, and even up to several keV (André and Yau 1997). A collisionless plasma is required to avoid losses by collisions and charge exchange. Several types of interactions can occur; e.g., resonant energy transfer from the waves to the ions when the plasma wave frequency is close to the gyrofrequency of the ions. The average global escape rate at Earth is ~ 1 kg/s (Knudsen 2013, *personal communication*).

Plasma wave acceleration is important in the dayside polar cusp (Fig. 11.23), creating a feature known as the cusp ion fountain that spews ions of all masses into the magnetosphere, and similar heating takes place on the night side, particularly near the poleward boundary of the auroral oval (Knudsen 2013, *personal communication*).

11.3 Solar Wind

The solar wind is composed of charged particles (electrons and positive ions) streaming out from the Sun. More than 99 % of the ions are H^{+} and ${}^4He^{2+}$, and the rest are ${}^3He^{2+}$, C, O, and other ions. Of the H^{+} and ${}^4He^{2+}$, 95–96 % is H and 3.5–4.5 % is He.

The solar wind behaves as a highly conducting medium, so the relative numbers of electrons and ions maintain charge neutrality.

There is a region of acceleration close to the Sun where the particles are accelerated from low speeds to about 400 km/s (Table 11.2). Thereafter, the speed is approximately constant.

Table 11.2 Typical solar wind values

r	$1.03R$	$1.5R$	$10R$	1 AU
$n_{\text{ion}} (\text{m}^{-3})$	2×10^{11}	1×10^{11}	2×10^9	5×10^6
$T (\text{K})$	1.7×10^6	10^6	4×10^5	4×10^4
$B (\text{T})$	10^{-4}	5×10^{-5}	10^{-6}	4×10^{-9}
$v (\text{km/s})$	0.6	3	300	400

For uniform expansion at constant speed, the number density of particles will decrease as one over the surface area, i.e., $n \propto r^{-2}$. In particular, if r is the distance from the Sun in AU, then the number density of ions is given by

$$n_{\text{ion}} (\text{m}^{-3}) = \frac{5 \times 10^6}{r^2 (\text{AU})} \quad (11.38)$$

Variations in these values are produced by high-speed jets ($\sim 600 \text{ km/s}$) of steady flow from coronal holes and by transient events including ejections by eruptive prominences, solar flares, and other active phenomena on the Sun.

The solar wind can be detected at great distances from the Sun, as discovered by *Voyager I*, which has just reached the region of sharply decreased solar wind, the edge of the heliosphere, $\sim 126 \text{ au}$ from the Sun.

11.4 Maxwell's Equations and the Plasma Frequency

A *plasma* is an ionized medium consisting of ions and free electrons. If in a plasma the charges of one sign are displaced relative to those of the other sign, creating a charge separation, the restoring force causes the charges to oscillate relative to each other at the *plasma frequency*, f_0 . The behavior of electromagnetic waves traveling through a plasma depends on how the frequency, f , of the waves relates to f_0 . We will now examine this dependence, making use of Maxwell's powerful formulation of electromagnetism.

11.4.1 Maxwell's Equations

Two of Maxwell's equations for free space may be written as follows (Griffiths 1999, p. 130):

$$\dot{\mathbf{B}} = -\vec{\nabla} \times \mathbf{E} \quad (11.39)$$

$$\dot{\mathbf{D}} + \mathbf{J} = -\vec{\nabla} \times \mathbf{H} \quad (11.40)$$

where

$$\mathbf{B} = \mu_o \mathbf{H} \quad (11.41)$$

$$\mathbf{D} = \epsilon_0 \mathbf{E} \quad (11.42)$$

$$\mathbf{J} = \sum_k N_k q_k \mathbf{v}_k \quad (11.43)$$

In (11.43), the summation is over all species of charge carriers (electrons and each type of ion), N_k is the number density of the k th species, q_k is the charge (with sign) of the k th species, and \mathbf{v}_k is the mean or drift velocity of the k th species. In this section, we use N in order to reserve n for the refractive index.

Other symbols are

\mathbf{B} = magnetic flux density, unit: tesla³ ($1 \text{ T} = 1 \text{ Wb/m}^2 = 1 \text{ kg s}^{-2} \text{ A}^{-1}$);

\mathbf{E} = electric field strength or electric intensity,
unit: $\text{N/C} = \text{V/m} = \text{m kg s}^{-3} \text{ A}^{-1}$;

\mathbf{H} = magnetic field strength, unit: A/m ;

\mathbf{D} = electric displacement, unit: C/m^2 ;

\mathbf{J} = current density, unit: A/m^2 ;

e = magnitude of the charge on the electron = $1.602177 \times 10^{-19} \text{ C}$;

ϵ_0 = permittivity of free space = $8.85 \times 10^{-12} \text{ F/m}$;

μ_0 = permeability of free space = $4\pi \times 10^{-7} \text{ N/A}^2$;

$\vec{\nabla}$ = gradient or del operator, $\vec{\nabla} \equiv \frac{\partial}{\partial x} \hat{\mathbf{i}} + \frac{\partial}{\partial y} \hat{\mathbf{j}} + \frac{\partial}{\partial z} \hat{\mathbf{k}}$.

Our task will be to obtain from (11.39) to (11.43) an equation involving only the electric field and its derivatives and to use this equation to study the interaction of the electric vector of a wave with an ionized medium. In particular, we will consider a medium that is charge-neutral, and \mathbf{J} is dominated by a single species of charge carrier of charge q . In this case, (11.43) can be replaced with:

$$\mathbf{J} = N q \mathbf{v} \quad (11.43a)$$

The result will, for example, be applicable to the ionosphere, where the mobility of electrons is much greater than that of the ions. In this case, $q = -e$ is the charge on an electron, and \mathbf{v} is in the direction of motion of the electrons.

Step 1: Take the curl⁴ of (11.39) and the time derivative of (11.41), and substitute the latter into the former to obtain

³ The SI unit of magnetic flux is the weber: $1 \text{ Wb} = 1 \text{ weber} = 1 \text{ T m}^2$. \mathbf{B} is therefore the magnetic flux density; i.e., the magnetic flux per unit area: $1 \text{ T} = 1 \text{ Wb/m}^2$.

⁴ The curl of any vector field, \vec{F} , written $\vec{\nabla} \times \vec{F}$, is a measure of rotation in the field. [A vector field is a representation of a vector quantity that (in general) has a different magnitude and direction at each point in space; e.g., the magnetic flux density, \vec{B}]. An intuitive way to think of curl is to imagine the vector field as representing flow vectors in a fluid. If a little paddlewheel placed at some point rotates as the fluid flows past it, then the vector field has non-zero curl at that point.

$$\mu_0 \vec{\nabla} \times \dot{\mathbf{H}} = -\vec{\nabla} \times \vec{\nabla} \times \mathbf{E} \quad (11.44)$$

Step 2: Substitute (11.43a) into (11.40), and take the time derivative of (11.42) to eliminate $\dot{\mathbf{D}}$ to obtain

$$\epsilon_0 \dot{\mathbf{E}} + Nq\mathbf{v} = \vec{\nabla} \times \mathbf{H} \quad (11.45)$$

Step 3: Differentiate (11.45) and multiply through by μ_0 to get

$$\mu_0 \epsilon_0 \ddot{\mathbf{E}} + \mu_0 Nq\dot{\mathbf{v}} = \mu_0 \vec{\nabla} \times \dot{\mathbf{H}} \quad (11.46)$$

Step 4: Substitute (11.44) into the right-hand side of (11.46) to obtain

$$\mu_0 \epsilon_0 \ddot{\mathbf{E}} + \mu_0 Nq\dot{\mathbf{v}} = -\vec{\nabla} \times \vec{\nabla} \times \mathbf{E} \quad (11.47)$$

Step 5: Use the identity

$$-\vec{\nabla} \times \vec{\nabla} \times \mathbf{E} = \nabla^2 \mathbf{E} + \vec{\nabla} (\vec{\nabla} \cdot \mathbf{E}) \quad (11.48)$$

to obtain

$$\mu_0 \epsilon_0 \ddot{\mathbf{E}} + \mu_0 Nq\dot{\mathbf{v}} = \nabla^2 \mathbf{E} + \vec{\nabla} (\vec{\nabla} \cdot \mathbf{E}) \quad (11.49)$$

Generally, the *divergence* of \mathbf{E} is $\vec{\nabla} \cdot \mathbf{E} = Q/\epsilon_0$ (*Gauss's law*), where Q is the net charge. In the case of multiple charge species, $Q = \sum_k N_k q_k$. For charge neutrality, $\vec{\nabla} \cdot \mathbf{E} = 0$.

The electron current is produced by the \mathbf{E} field initially, therefore the force is electrostatic, and Newton's second law ($\sum \mathbf{F} = m\mathbf{a}$) gives

$$q\mathbf{E} = m\dot{\mathbf{v}} \quad (11.50)$$

where $m = 9.10838 \times 10^{-31}$ kg is the mass of the electron. Whence,

Step 6: Substitute (11.50) into (11.49) to obtain

$$\mu_0 \epsilon_0 \ddot{\mathbf{E}} + \mu_0 \frac{Ne^2}{m} \mathbf{E} = \nabla^2 \mathbf{E} \quad (11.51)$$

where we have used $q = -e$. Now we are in a position to apply Maxwell's equations to a radio wave passing through the ionosphere.

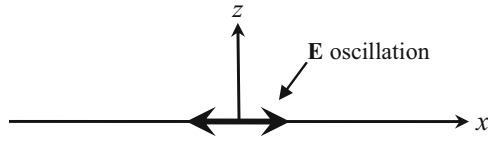


Fig. 11.5 A polarized electromagnetic wave traveling in the z -direction, with its electric field oscillation in the x -direction

11.4.2 Application to a Polarized Wave

Assume now that a polarized wave ascends vertically (in the z or $\hat{\mathbf{k}}$ unit vector direction), with the \mathbf{E} -field polarized in the x or $\hat{\mathbf{i}}$ direction, as illustrated in Fig. 11.5.

Adopt a trial solution to (11.51) of the form

$$\mathbf{E} = E_x \hat{\mathbf{i}} = E_0 \exp\left[j\omega\left(t - \frac{nz}{c}\right)\right] \hat{\mathbf{i}} \quad (11.52)$$

where $j = \sqrt{-1}$ and $n = c/v$ is the index of refraction. The last term in (11.52) is equal to

$$\left(\frac{n}{c}\right) \omega z = 2\pi f \left(\frac{n}{c}\right) z = 2\pi f \frac{z}{v} = 2\pi \frac{z}{\lambda} \quad (11.53)$$

where we make use of the relation $v = f\lambda$.

Insert (11.52) into (11.51) and define $\alpha \equiv j\omega (t - nz/c)$ to obtain

$$-\mu_0 \epsilon_0 \omega^2 E_0 \exp[\alpha] \hat{\mathbf{i}} + \frac{\mu_0 Ne^2}{m} E_0 \exp[\alpha] \hat{\mathbf{i}} = -\frac{\omega^2 n^2}{c^2} E_0 \exp[\alpha] \hat{\mathbf{i}}$$

or

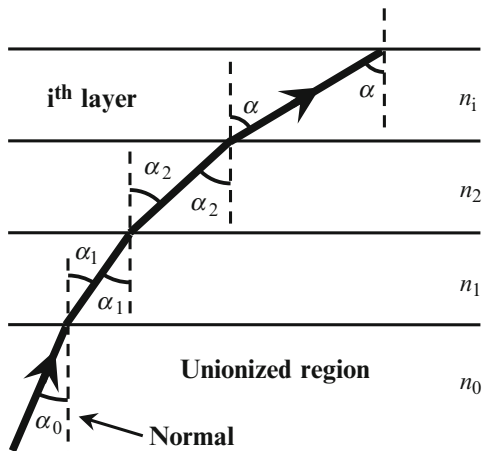
$$-\mu_0 \epsilon_0 \omega^2 + \frac{\mu_0 Ne^2}{m} = -\frac{\omega^2 n^2}{c^2} \quad (11.54)$$

Solving for n and using $c^2 = 1/(\mu_0 \epsilon_0)$, we obtain the dispersion relation for an ionizing medium:

$$n^2 = 1 - \frac{Ne^2}{m \epsilon_0 \omega^2} \quad (11.55)$$

or, recalling that $\omega = 2\pi f$,

Fig. 11.6 Refraction of an electromagnetic wave in a layered ionosphere of decreasing refractive index, n_i



$$n^2 = 1 - \frac{f_0^2}{f^2} \quad (11.56)$$

where

$$f_0^2 = \left(\frac{1}{2\pi} \right)^2 \left[\frac{Ne^2}{m\epsilon_0} \right] \quad (11.57)$$

defines the *plasma frequency*, f_0 . From (11.56) and (11.57), we have

1. For a vacuum, $f_0 = 0$ and $n = 1$; or, for $N > 0$,
2. n is real and $0 < n < 1$ for $f > f_0$;
3. $n = 0$ for $f = f_0$; and
4. n is imaginary for $f < f_0$.

We now look at some consequences of (11.56) and (11.57) for an electromagnetic wave of frequency f propagating from an unionized region into a region of increasing ionization, e.g., upward into a planetary ionosphere from below or downward from space (cf. Figs. 11.1, 11.2, and 11.4).

In Fig. 11.6, a hypothetical ionosphere is divided into layers of constant electron density, N , with N increasing in successive layers upward from $N_0 = 0$ in the region below the ionosphere. An electromagnetic wave of frequency f in the region below the ionosphere (refractive index n_0) encounters the ionosphere at an incident angle α_0 , refracts into the first layer (refractive index n_1) at an angle of refraction α_1 , the second layer (refractive index n_2) at angle α_2 , and the i th layer (refractive index n) at angle α .

Because in (11.57) $f_0 \propto \sqrt{N}$ it follows from (11.57) that $n < 1$ and decreases with increasing N . Thus, n decreases upward in Fig. 11.6 and, from Snell's law [(11.58), below], the wave refracts away from the normal, as shown.

From Snell's law,

$$n_1 \sin \alpha_1 = n_0 \sin \alpha_0 = \text{const} \quad (11.58)$$

$$n_2 \sin \alpha_2 = n_1 \sin \alpha_1 \quad (11.59)$$

Therefore,

$$n_2 \sin \alpha_2 = n_0 \sin \alpha_0 = \text{const} \quad (11.60)$$

Continuing this argument to the i th layer and dropping the subscript for the i th layer, we get

$$n \sin \alpha = n_0 \sin \alpha_0 = \text{const} \quad (11.61)$$

Thus, as long as the wave is able to reach the i th layer, the angle of refraction there depends only on the refractive indices n_0 and n and the incident angle α_0 and is independent of the characteristics of the ionosphere in the intervening layers. The result is also independent of the thickness of the layers, so we can take the limit as the thickness approaches zero, i.e., (11.61) applies also to continuous media (real ionospheres).

We now note that for a wave entering the ionosphere from space (vacuum), $n_0 = 1$; and for a wave entering from below, the ion density is low enough that n_0 can again be taken as (very close to) 1.

It is apparent from Fig. 11.6 that if α reaches a value $\pi/2$ then the wave can proceed no further and is reflected (internal reflection). Setting $\alpha_{\max} = \pi/2$ and $n_0 = 1$ in (11.61) gives

$$n = \sin \alpha_0 \quad (11.62)$$

i.e., for a given incident angle, the wave will be reflected if the minimum refractive index in the ionosphere is less than $n = \sin \alpha_0$. Define f_0^{peak} to be the maximum plasma frequency in the ionosphere, in the layer of maximum electron density. Then, from (11.56), a wave will be transmitted through the ionosphere only if its frequency exceeds a critical frequency, f_c , given by

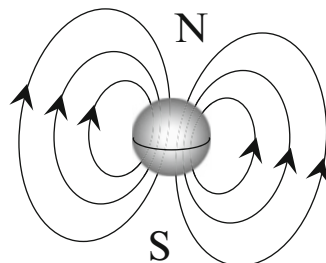
$$n^2 = 1 - \frac{(f_0^{\text{peak}})^2}{f_c^2} = \sin^2 \alpha_0 = 1 - \cos^2 \alpha_0 \quad (11.63)$$

or

$$f_c = \frac{f_0^{\text{peak}}}{\cos \alpha_0} = f_0^{\text{peak}} \sec \alpha_0 \quad (11.64)$$

For normal incidence ($\alpha_0 = 0$), $\cos \alpha_0 = \sec \alpha_0 = 1$, so from (11.64)

Fig. 11.7 The Earth's intrinsic dipolar magnetic field (Not to scale)



$$f_c = f_0^{\text{peak}} \quad (\text{normal incidence}) \quad (11.65)$$

Thus, from (11.56), the wave reflects at the first point (if any) where the refractive index is

$$n = \sqrt{1 - \left(\frac{f_0^{\text{peak}}}{f_c}\right)^2} = 0$$

It follows that electromagnetic waves cannot propagate in a region of imaginary refractive index.

11.5 The Earth's Magnetosphere

A planet's magnetosphere is the region of space around the planet occupied by its magnetic field. The magnetosphere constrains the motions of charged particles (electrons and ions) within it, sometimes producing very strong electric fields, electric potential differences, and electric currents and is itself shaped by the charged particles within it and by the solar wind.

We begin with a discussion of the Earth's magnetosphere, as illustrative of processes that take place in planetary magnetospheres in general.

The intrinsic magnetic field of the Earth, created by a self-exciting dynamo in the molten metallic core, is approximately dipolar, as illustrated schematically in Fig. 11.7. The dipole moment is currently 8×10^{22} amp m², but varies secularly. The minimum value⁵ over the last 3,000 years was 7.7×10^{22} amp m² in ~900 AD

⁵The magnetic field configuration at the Earth's surface at earlier times can be determined from archaeomagnetic and paleomagnetic data; e.g., the last time a clay hearth was heated above the Curie point and cooled again, the magnetic orientation of iron in the clay aligned itself with the magnetic field of the Earth at that time and location. Lake sediments have also been used, because iron in the sediments aligns itself with the local magnetic field as the material settles.

and the maximum was 10.4×10^{22} amp m² in ~100 BC (Korte and Constable 2011). The magnetic axis is tilted by ~11° relative to the rotation axis and also offset by 515 km radially from the rotation axis toward ~140° E longitude (2009 values, Olson and Deguen 2012) and ~50 km N of the equator, resulting in an offset between the geomagnetic poles and the geographic poles. These values also change secularly. As of the present writing, the north geomagnetic pole is in the Canadian arctic, but wanders with time, and is currently showing signs of migrating to Siberia.

By convention, magnetic field lines point away from a magnetic north (N) pole and toward a magnetic south (S) pole; but also by convention, the geomagnetic poles are labeled according to the geographic hemisphere (N or S) in which they occur. As Fig. 11.7 illustrates, with the magnetic field lines entering the Earth at the North Pole and leaving at the South Pole, these conventions result in the geomagnetic north pole actually being a magnetic south pole and vice versa.

(Historically, the “north” pole of a magnet or compass needle was called the “north-seeking” pole, i.e., the pole that seeks the geographic, or actually geomagnetic, north pole.)

If left to itself, the Earth’s dipole field would extend to infinity in all directions. However, the flow of solar wind plasma and *interplanetary magnetic field* (IMF) past the Earth modifies the dipole field as shown in Fig. 11.8.

The *magnetopause* in Fig. 11.8 is the boundary between the Earth’s magnetic field and the IMF, i.e., the magnetosphere is the region inside the magnetopause. The solar wind is supersonic, but the solar wind particles are slowed to subsonic speeds by their interaction with the Earth. The *bow shock* marks this transition from supersonic to subsonic flow. Between the bow shock and the magnetopause is a region of subsonic solar wind particles and IMF called the *magnetosheath*. Since disturbances cannot propagate upstream in supersonic flow, the bow shock marks the furthest extent of influence of the Earth’s magnetic field.

As is evident in Fig. 11.8, the solar wind substantially compresses the dipole field on the upstream side of the Earth, while on the downstream side, viscous interaction between the solar wind and the magnetospheric plasma stretches the Earth’s magnetosphere into a long *magnetotail*, through processes described below. Because of this stretching, magnetic field lines in the magnetotail are approximately parallel to a warped central plane called the *neutral sheet*. Continuity requires that the magnetic field lines above and below join through the neutral sheet; thus, on the neutral sheet the component of magnetic field parallel to the sheet is zero (this characteristic defines the neutral sheet) and the perpendicular component is extremely weak. Therefore, the neutral sheet can be regarded as a plane of essentially zero magnetic field.

The interaction of charged particles in both the magnetospheric plasma and the solar wind with the Earth’s magnetic field produces large-scale currents, as illustrated in Fig. 11.9.

We now develop some of the basic physics of the interaction of charged particles with magnetic fields, as it applies to the Earth’s magnetosphere in Fig. 11.8 and the currents in Fig. 11.9.

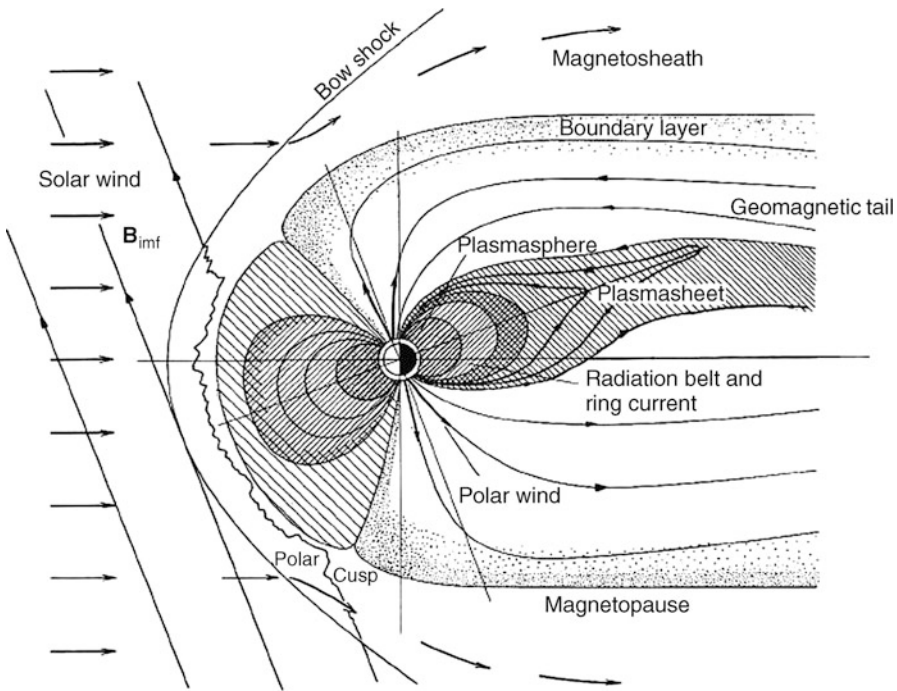


Fig. 11.8 Schematic diagram of the Earth's magnetosphere in the noon-midnight plane. The basic particle and magnetic field features are representative of other internally generated planetary magnetospheres, although the details may be different (from Parks 1991, Fig. 1.3, p. 8, reproduced with the author's permission.)

11.5.1 Forces Acting on Charged Particles

11.5.1.1 The Lorentz Force

The Lorentz force on a charged particle is the vector sum of the electric and magnetic forces:

$$\vec{F} = q\vec{E} + q\vec{v} \times \vec{B} = q(\vec{E} + \vec{v} \times \vec{B}) \quad (11.66)$$

where

q = electric charge on the particle

\vec{E} = electric field vector

\vec{v} = velocity of the particle

\vec{B} = magnetic field vector

The magnetic force points in the direction of the cross product as given by the right-hand rule (Sect. 10.3.1) if q is positive, and in the opposite direction if q is negative.

Solar wind-induced electric currents flowing in the magnetosphere

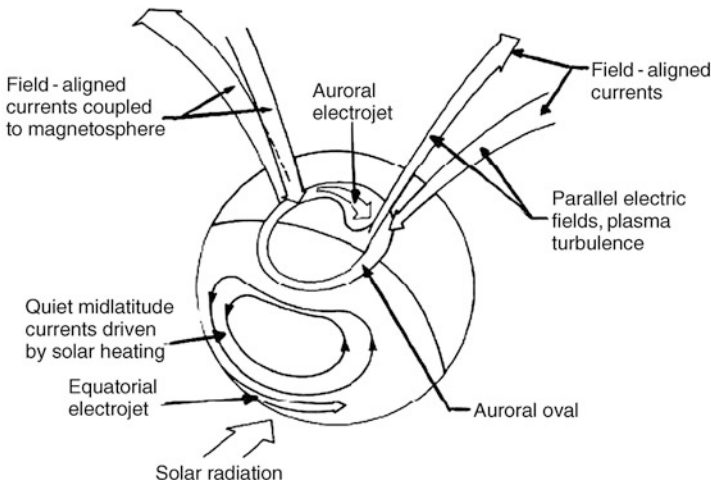
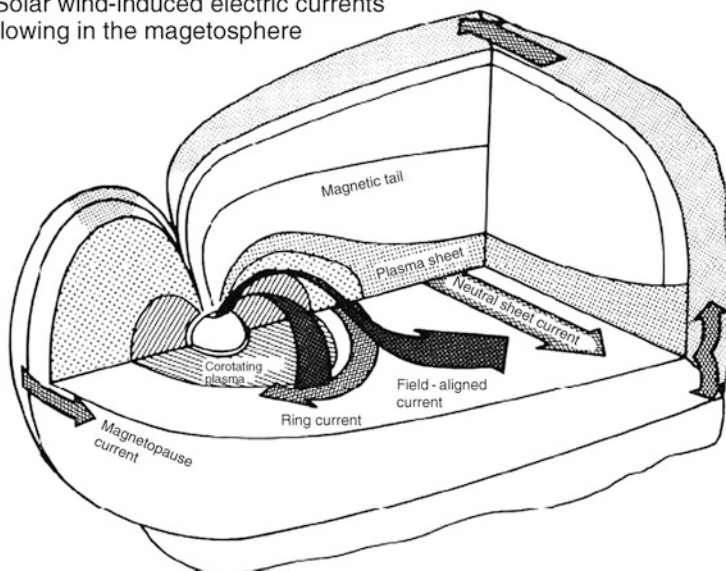
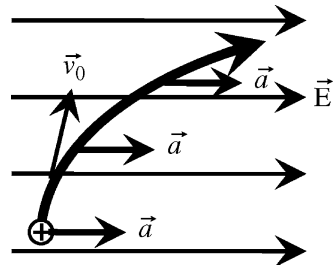


Fig. 11.9 Schematic diagrams showing where currents flow in the Earth's magnetosphere and ionosphere (from Parks 1991, Fig. 7.1, p. 244, reproduced with the author's permission.)

Equation (11.66) shows that

- A. electric fields affect all charges, moving or at rest.
- B. magnetic fields affect only moving charges.
- C. the electric force is parallel or antiparallel to \vec{E} .
- D. the magnetic force is perpendicular to both \vec{v} and \vec{B} .

Fig. 11.10 Acceleration of a charged particle by a uniform electric field



11.5.1.2 The Gravitational Force

$$\vec{F} = m\vec{g} \quad (11.67)$$

The gravitational force on a charged particle is usually insignificant when electric and/or magnetic fields are present, but there are times when it must be included.

We now apply (11.66) to several situations relevant to the Earth's magnetosphere.

11.5.2 \vec{E} Uniform and Time-Independent; $\vec{B} = 0$

With $\vec{B} = 0$, (11.1) becomes

$$\vec{F} = q\vec{E} \quad (11.68)$$

If other forces are negligible, then the acceleration of a particle of charge q and mass m is, from Newton's second law (the vector sum of all forces on an object equals the object's mass times its acceleration),

$$\vec{a} = \frac{q\vec{E}}{m} \quad (11.69)$$

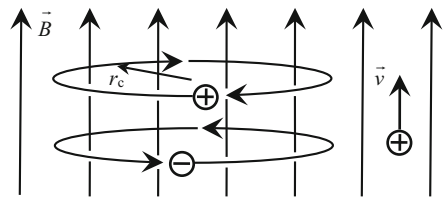
Thus the electric force acting by itself accelerates particles in a direction parallel or antiparallel to the electric field, sometimes producing very large speeds.

With \vec{E} constant and uniform, finding the motion of a charged particle is a straightforward constant-acceleration kinematics problem (projectile motion) as in Fig. 11.10 and is solved the same way as for a rock thrown off a cliff without air resistance. The solution in the direction parallel to \vec{E} is

$$v_{||} = (v_0)_{||} + \left(\frac{qE}{m} \right) t \quad (11.70)$$

$$x_{||} = (x_0)_{||} + (v_0)_{||} t + \frac{1}{2} \left(\frac{qE}{m} \right) t^2 \quad (11.71)$$

Fig. 11.11 Electric charges moving perpendicular to uniform magnetic field lines execute gyromotion; charges moving parallel to the field lines maintain constant velocity



11.5.3 \vec{B} Uniform and Time-Independent; $\vec{E} = 0$

With $\vec{E} = 0$, (11.66) becomes

$$\vec{F} = q\vec{v} \times \vec{B} \quad (11.72)$$

The cross-product ensures that $\vec{F} \perp \vec{v}$ at all times; consequently, the speed, $v = |\vec{v}|$, cannot change. The perpendicular force, however, produces a continuously changing direction of travel; thus the particle's velocity changes with no change in speed.

Case 1. If $\vec{v} \perp \vec{B}$, then the magnetic force acts centripetally to produce uniform circular motion (*gyromotion* or *cyclotron motion*) in a plane perpendicular to \vec{B} . The radius of gyromotion, r_c , is variously called the *Larmor radius*, *radius of gyration*, *gyroradius*, or *cyclotron radius*.

Because in (11.72) the direction of \vec{B} depends on the sign of q , charges of opposite sign gyrate in opposite directions. Figure 11.11 illustrates this motion for particles of equal mass and speed but opposite charge.

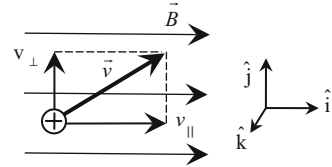
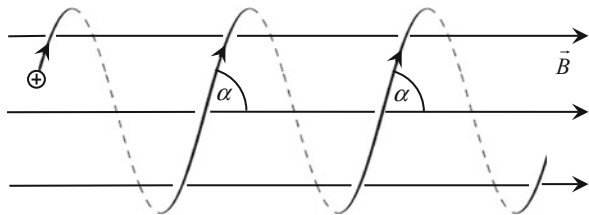
Centripetal acceleration is given by $a = v^2/r$, so if the magnetic force is the only force acting, and with $\vec{v} \perp \vec{B}$, Newton's second law ($\mathbf{F} = m\mathbf{a}$) becomes

$$qvB = m \frac{v^2}{r_c} \quad (11.73)$$

Solving for r_c gives

$$r_c = \frac{mv}{qB} \quad (11.74)$$

Case 2. If $\vec{v} \parallel \vec{B}$ (Fig. 11.11) then $\vec{F} = q\vec{v} \times \vec{B} = 0$. Thus a charged particle moving parallel to a uniform magnetic field feels no $\vec{v} \times \vec{B}$ force and continues to move in a straight line at a constant speed, parallel to \vec{B} , unless acted on by some other (non-magnetic) force.

Fig. 11.12 \vec{v} not $\parallel \vec{B}$ **Fig. 11.13** Helical path with constant pitch angle, for a charged particle moving in a uniform magnetic field

Case 3. If \vec{v} is neither perpendicular nor parallel to \vec{B} , as in Fig. 11.13, then we can break \vec{v} into components v_{\perp} perpendicular and v_{\parallel} parallel to \vec{B} . Using the unit vectors $\hat{i}, \hat{j}, \hat{k}$ defined in Fig. 11.12,

$$\vec{F} = q\vec{v} \times \vec{B} = q(v_{\parallel}\hat{i} + v_{\perp}\hat{j}) \times B\hat{i} = -qv_{\perp}B\hat{k} \quad (11.75)$$

because $\hat{i} \times \hat{i} = 0$. Thus the force is due entirely to v_{\perp} , producing gyromotion with a gyroradius

$$r_c = \frac{mv_{\perp}}{qB} \quad (11.76)$$

Because the force has no component parallel to \vec{B} , v_{\parallel} , remains constant. The particle thus moves at constant speed parallel or antiparallel to the magnetic field lines while executing circular motion perpendicular to the field lines.

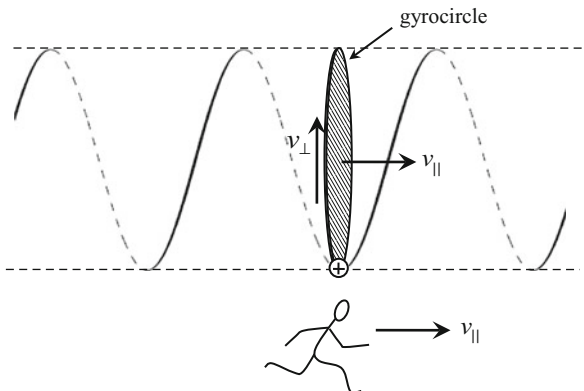
The resulting path is a *helix*, as shown in Fig. 11.13. The angle, α , between \vec{v} and \vec{B} is called the *pitch angle* of the helix and is constant in a uniform magnetic field.

11.5.4 Guiding Center

The guiding center concept is useful in many situations involving single particles, and in multi-particle situations where the individual particles act independently. It has limitations, however; for example, it is not so useful when the particles act collectively as a fluid.

The guiding center description is based on the idea (illustrated in Fig. 11.14) that a particle “spiralizing” along magnetic lines of force executes purely circular motion

Fig. 11.14 Guiding center concept



as seen by someone moving with a vector velocity equal to v_{\parallel} . Thus the particle moves in a gyrocircle, while the center of the gyrocircle is guided in a particular direction at a particular speed by the magnetic field lines.

We now apply the gyrocircle and guiding center concepts to various situations relevant to planetary magnetospheres.

11.5.5 Diamagnetism

A charged particle executing gyromotion is equivalent to a ring of electric current of radius r_c . Conventional current is taken to be in the direction of positive charge flow or opposite to the direction of negative charge flow, as indicated in Fig. 11.15. Because positive and negative charges gyrate in opposite directions, the conventional current, I , and the resulting induced magnetic field directions are the same for both positive and negative charges, as shown in Fig. 11.15.

The application of the right-hand rule for currents,

point the thumb of the right hand along the direction of conventional current; then the fingers curl around the current in the direction of the induced magnetic field,

or for current loops,

curl the fingers of the right hand around the current loop in the direction of conventional current; then the thumb points in the direction of the induced magnetic field inside the loop,

in Fig. 11.15 shows that, *within* each current loop, the induced magnetic field opposes the external magnetic field, whereas *outside* (but in the same plane as) the gyromotion, the induced field is in the same direction as the external field. These characteristics identify gyromotion as *diamagnetic*.

Fig. 11.15 Diamagnetic currents and induced magnetic fields

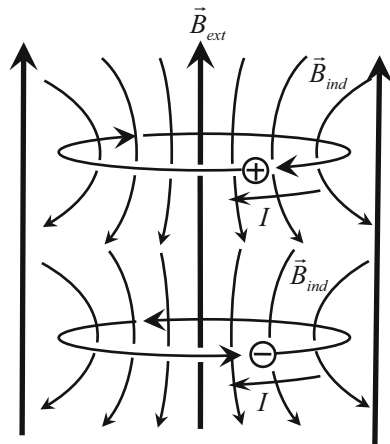
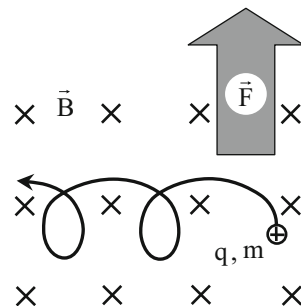


Fig. 11.16 $\vec{F} \times \vec{B}$ drift



11.5.6 $\vec{E} \times \vec{B}$ Drift and Field-Aligned Currents

In Fig. 11.16, a particle of charge q and mass m has been released at rest in a uniform, time-independent magnetic field, \vec{B} . In addition to the magnetic force, the particle is also subject to a constant force, \vec{F} , acting in a direction perpendicular to \vec{B} . This force might arise, for example, from a uniform electric or gravitational field in the same region of space.

As illustrated schematically in Fig. 11.16, the particle will initially accelerate in the direction of \vec{F} . This produces a magnetic force perpendicular to the motion, causing the particle to deviate more and more from its initial direction until it is moving perpendicular to \vec{F} .

Up to this point there is a component of the particle's motion in the direction of \vec{F} , so \vec{F} does positive work on the particle, the particle's speed increases, and by (11.74) the curve has an ever-increasing radius. After this point the magnetic force deviates the particle's motion back against \vec{F} , the work done on the particle by \vec{F} becomes negative, the particle's speed decreases, and the particle moves in a curve

of ever-decreasing radius until the motion is again perpendicular to \vec{F} . Both forces continue to act, and the subsequent motion is cyclic as illustrated schematically in Fig. 11.16. (Note that the curve in Fig. 11.16 is flat, and not a helix seen in perspective.)

Thus the motion is somewhat counter-intuitive: the force acting on the charged particle causes the particle to drift in a direction perpendicular to both \vec{F} and \vec{B} . Applying the right-hand rule in Fig. 11.16 shows that a positive charge drifts in the direction of $\vec{F} \times \vec{B}$. A mathematical analysis (see the problems at the end of this chapter) gives the drift velocity, \vec{v}_D , as

$$\vec{v}_D = \frac{\vec{F} \times \vec{B}}{qB^2} \quad (11.77)$$

If the force is gravitational, then

$$\vec{v}_D = \frac{m\vec{g} \times \vec{B}}{qB^2} = \frac{\vec{g} \times \vec{B}}{(q/m)B^2} \quad (11.78)$$

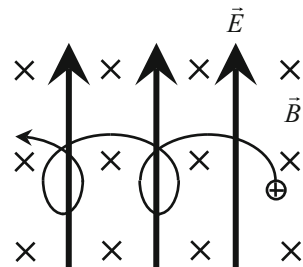
Thus the drift speed depends on the charge-to-mass ratio of the particle; also, because of the factor q in the equation, charges of opposite sign drift in opposite directions, producing a current.

If the force arises from an electric field, \vec{E} , in a region of space having crossed electric and magnetic fields (Fig. 11.17), then

$$\vec{v}_D = \frac{q\vec{E} \times \vec{B}}{qB^2} = \frac{\vec{E} \times \vec{B}}{B^2} \quad (11.79)$$

The resulting motion is called $\vec{E} \times \vec{B}$ drift and is perpendicular to both \vec{E} and \vec{B} (in the $\vec{E} \times \vec{B}$ direction). From (11.79), \vec{v}_D is independent of both q and m , so positive and negative charges drift in the same direction and (if there is charge neutrality and the charges have equal mobility) $\vec{E} \times \vec{B}$ drift does not produce a current.

The curves in Figs. 11.16 and 11.17 are examples of a *trochoid*, the curve traced by a point on the outer edge of a wheel that rolls with or without slippage; e.g., on a side-wheeler steamboat plying a lake, the rim of the paddlewheel turns faster than the boat moves forward, so a person standing on the lakeshore sees the outer edge of each paddle move forward in a long arc at the top, then dip into the water and drop back, producing the loops of the trochoid. If the wheel rolls on a solid surface without slipping, such as the wheel of a bicycle or automobile, the part of the wheel in contact with the ground is momentarily stationary and the loops in Fig. 11.17 degenerate to cusps (points). The resulting curve is a *cycloid*.

Fig. 11.17 $\vec{E} \times \vec{B}$ drift

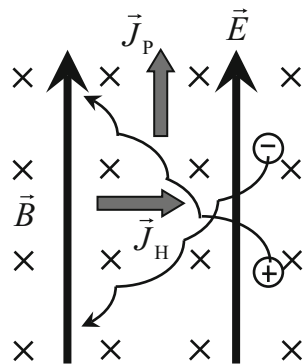
These analogies suggest that the guiding center concept remains valid for $\vec{E} \times \vec{B}$ drift: like a point on the paddlewheel, the particle moves at constant speed around a gyrocircle while the gyrocircle is guided in the $\vec{E} \times \vec{B}$ direction at the drift velocity, \vec{v}_D .

If \vec{E} is not perpendicular to \vec{B} then take components E_{\parallel} parallel to \vec{B} and E_{\perp} perpendicular to \vec{B} . E_{\perp} causes $\vec{E} \times \vec{B}$ drift perpendicular to the magnetic field, but (for charge neutrality and charges of equal mobility) no current. E_{\parallel} accelerates charges of opposite sign in opposite directions along the magnetic field lines, producing a current parallel to the magnetic field, i.e., a *field-aligned current*. E_{\parallel} creates a potential difference, $V = E_{\parallel}\ell$, over any distance ℓ along a field line, so magnetic field lines in planetary magnetospheres act like conductors in electric circuits. This idea will be developed further later in this chapter.

Now return to Fig. 11.11 and consider it from a new viewpoint. In Fig. 11.11, there is no electric field, the magnetic field is at rest relative to the observer, and the positive ion in the upper left trajectory in the figure is executing simple gyromotion around the magnetic field lines. This ion has some (and always the same) velocity \vec{v}_0 toward the left every time it is on the near side of the gyrocircle.

Now consider this ion from the viewpoint of a different observer who is moving toward the left at constant velocity \vec{v}_0 . This observer will see the ion momentarily at rest every time the ion is on the near side of the gyrocircle in Fig. 11.11, and will also see the gyrocenter dropping back (moving toward the right in the figure) at velocity $-\vec{v}_0$. The figure described by the ion as seen by this observer is therefore a cycloid, as described above; i.e., the ion appears to be undergoing $\vec{E} \times \vec{B}$ drift (to the right in the figure) as seen by this observer. An observer at rest relative to the magnetic field measures an electric field of zero (because the gyrocircle is closed), but an observer moving relative to the magnetic field measures a non-zero electric field (because the gyrocircle is open: a cycloid). This electric field is called a *motional electric field*, and is given by $\vec{E} = \vec{v}_0 \times \vec{B} = -\vec{v}_B \times \vec{B}$, where \vec{v}_B is the velocity of the magnetic field as seen by the moving observer. (This is the same motional electric field that is generated between the wingtips of an aircraft that is flying with its wings perpendicular to the Earth's magnetic field lines.) It is left as an exercise for the reader to verify (e.g., from the right-hand rule) that the motional electric field created by the observer's motion is in the correct direction to give an $\vec{E} \times \vec{B}$ drift to the right in Fig. 11.11 as seen by the moving observer.

Fig. 11.18 $\vec{E} \times \vec{B}$ drift with collisions. \vec{J}_P is the Pedersen current, and \vec{J}_H is the Hall current



11.5.7 $\vec{E} \times \vec{B}$ Drift with Collisions

In a collisionless plasma, $\vec{E} \times \vec{B}$ drift does not produce a current if there is charge neutrality (Sect. 11.5.6). However, the lower ionosphere is sufficiently dense for collisions to be important, and each collision allows the charge to restart its motion under the influence of the electric field. As shown in Fig. 11.18, charges of opposite sign drift in opposite directions parallel or antiparallel to \vec{E} while they continue to undergo $\vec{E} \times \vec{B}$ drift in the same direction perpendicular to \vec{E} . The former of these two drifts gives rise to a current, referred to in the ionosphere as the *Pedersen current*, parallel to \vec{E} .

In a collision-dominated plasma, $\vec{E} \times \vec{B}$ drift also creates a current, despite charge neutrality, because the smaller gyroradii and higher speeds of the electrons give them greater mobility than the ions. The resulting *Hall current* is perpendicular to both \vec{E} and \vec{B} , but opposite to the $\vec{E} \times \vec{B}$ direction (Fig. 11.18). The Pedersen and Hall currents will be important when discussing ionospheric currents and aurorae (Sect. 11.6.7).

The energy given to the ions and electrons of the plasma by the electric field is dissipated as heat through collisions of the plasma particles with (primarily) neutral ionospheric atoms, since neutrals far outnumber ions in the ionosphere. This process, in which the work done on the plasma particles by the electric field is dissipated as heat, is referred to as *ohmic losses* or *joule heating*. If in Fig. 11.18 a particle of species i (i.e., an ion or an electron) and charge q_i moves through a displacement $d\vec{l}$ along the path in time dt , then the infinitesimal quantity of work done on this particle by the electric field in time dt is

$$\delta W = d\vec{l} \cdot \vec{F} = q_i d\vec{l} \cdot \vec{E} \quad (11.80)$$

The rate of joule heating (= power dissipated, P_i) by any species i per unit volume is then

$$P_i = n_i \delta W / dt = n_i q_i d\vec{\ell} \cdot \vec{E} / dt = n_i q_i \vec{v}_i \cdot \vec{E} = \vec{J}_i \cdot \vec{E} \quad (11.81)$$

where n_i , \vec{v}_i and $\vec{J}_i = n_i q_i \vec{v}_i$ are the number density, velocity and current density of species i , respectively. (Note that in Fig. 11.18 we have assumed that the neutral medium is at rest; therefore, \vec{E} is the electric field measured in the rest frame of the neutral medium.) The total current density and power dissipated are $\vec{J} = \sum \vec{J}_i$ and

$$P = \sum P_i = \vec{J} \cdot \vec{E} \quad (11.82)$$

The treatment above assumes that the neutral gas remains at rest in the chosen reference frame and the plasma particles move through it. In fact, momentum transfer requires that some energy from the electric field is converted to bulk motion of the neutral gas; thus, the result above gives an upper limit to the amount of joule heating. Nevertheless, the dot product shows that only the component of \vec{J} parallel to \vec{E} contributes to joule heating; i.e., the Pedersen current is dissipative, because $\vec{J} \cdot \vec{E} > 0$ and the Hall current is dissipationless, because $\vec{J} \cdot \vec{E} = 0$.

Joule heating can be considerable in the ionosphere. Within an active aurora, it can amount to tens or even hundreds of kilowatts per square kilometer of sky within active aurorae (Knudsen, D. J. 2013, *private communication*). Figure 11.19 shows an active aurora on the Earth, photographed from the International Space Station.

For an alternative treatment of this topic in the reference frame of the plasma, where the dissipation turns out to be by friction between the plasma and the gas rather than by joule heating (i.e., the relationship is not simply $\vec{J} \cdot \vec{E}$), see Vasylunas and Song (2005).

11.5.8 *Polarization Drift*

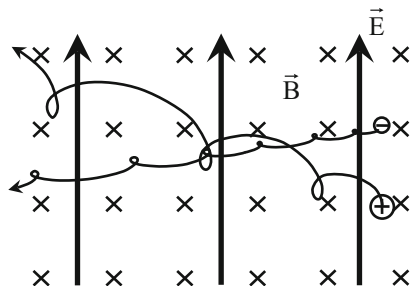
We now examine the situation where \vec{B} is uniform in space and constant in time and \vec{E} is uniform in space and constant in direction, but changes in magnitude with time, i.e., $d\vec{B}/dt = 0$ but $d\vec{E}/dt \neq 0$. Figure 11.20 illustrates the case where E increases with time.

Both particles in Fig. 11.20 undergo $\vec{E} \times \vec{B}$ drift toward the left, but because \vec{E} is increasing in strength, each particle's kinetic energy at the midpoint of any cycle is insufficient to allow it to return to its initial level in the diagram at the end of the cycle. Positive charges therefore drift parallel to \vec{E} and negative charges drift antiparallel to \vec{E} while both undergo $\vec{E} \times \vec{B}$ drift perpendicular to \vec{E} and \vec{B} . The drift parallel or antiparallel to \vec{E} is called *polarization drift*.



Fig. 11.19 Aurora over the southern Indian Ocean, photographed from the International Space Station on September 17, 2011. Although aurorae are usually seen only at high northern and southern latitudes, this one occurred during a geomagnetic storm, resulting from a coronal mass ejection that left the Sun on September 14, 2011. Credit: NASA/Goddard Space Flight Center

Fig. 11.20 Polarization drift $\parallel \vec{E}$ with $\vec{E} \times \vec{B}$ drift $\perp \vec{E}$

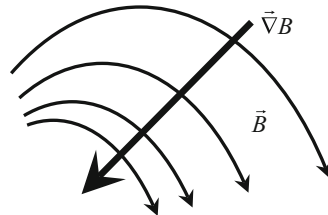


In this case, the drift velocity of the guiding center consists of two components:

1. \vec{v}_D , the $\vec{E} \times \vec{B}$ drift velocity perpendicular to \vec{E} and \vec{B} , described in Sect. 11.5.6; but note that v_D is increasing with time because E is increasing with time, so from (11.79) the cycles in Fig. 11.20 become increasingly stretched.
2. \vec{v}_P , the polarization drift velocity parallel or antiparallel to \vec{E} , given by

$$\vec{v}_P = -\frac{m}{qB^2} \left(\frac{d\vec{v}_D}{dt} \right) \times \vec{B} \quad (11.83)$$

Fig. 11.21 Curvature and gradient in an inhomogeneous magnetic field



It follows from (11.79) and (11.83) that

$$\vec{v}_P = -\frac{m}{qB^2} \frac{d\vec{E}}{dt} \quad (11.84)$$

Polarization drifts are in opposite directions for opposite charges, so polarization drift produces a current parallel to \vec{E} .

11.5.9 Gradient and Curvature Drift

We now investigate inhomogeneous, time-independent magnetic fields, in the absence of electric fields.

It is unusual for a magnetic field to be uniform. Figure 11.21 provides a schematic illustration of a more typical magnetic field (e.g., a magnetic dipole field): the field lines are curved, and the magnetic field strength, B , increases toward the center of curvature.

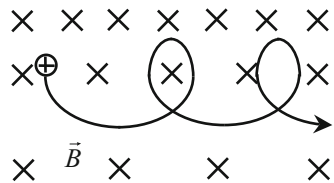
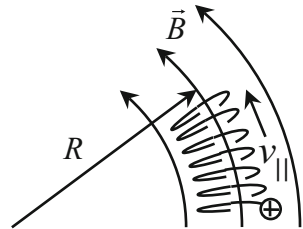
Thus, real magnetic fields generally show both curvature and gradient.

11.5.9.1 Gradient Drift

Figure 11.22 illustrates schematically a region of space containing a magnetic field gradient. Here, we temporarily neglect curvature. From (11.74), the gyroradius is smaller where B is greater and *vice versa*, so a positive particle follows a trochoid, as shown. A negative particle initially traveling downward will curve to the left in Fig. 11.22, so positive and negative charges drift in opposite directions and gradient drift produces a current.

If the magnetic field gradient is small ($\Delta B \ll B$ over a gyroradius) then \vec{B} is approximately uniform over the gyrocircle and the guiding center concept is still valid: the particle moves in a gyrocircle which does not quite close on itself, resulting in a drift of the guiding center perpendicular to both \vec{B} and $\vec{\nabla}B$. Taking the y -axis in the direction of the gradient (upward in Fig. 11.22), the drift speed is

$$v_{\nabla B} = \frac{mv_\perp^2}{2qB^2} \frac{\partial B}{\partial y} \quad (11.85)$$

Fig. 11.22 Gradient drift**Fig. 11.23** Curvature drift

11.5.9.2 Curvature Drift

Figure 11.23 illustrates a hypothetical magnetic field which has curvature, but no gradient. Charged particles follow helical paths along the field lines, as indicated. Because we are neglecting the field gradient, there is no gradient drift in Fig. 11.23. However, the particles can follow a curved field line only if there is a centripetal force

$$F_{\text{cent}} = \frac{mv_{||}^2}{R} \quad (11.86)$$

acting on them, directed toward the center of curvature. This force must arise from the motion of the particle and, in fact, is created by a drift of the particle across the field lines with a drift speed v_C (where “C” signifies *curvature drift*). Then from (11.72),

$$\vec{F}_{\text{cent}} = q\vec{v}_C \times \vec{B} \quad (11.87)$$

From the right-hand rule, with q positive in Fig. 11.23, $\vec{F}_{\text{cent}} = \vec{v}_C$ must be out of the page to give a force toward the center of curvature. From (11.87), negative charges drift into the page, so curvature drift in Fig. 11.23 produces a current out of the page. This result is independent of which direction the particle follows along the field line (upward or downward in Fig. 11.23), because the direction of the centripetal force must be toward the center of curvature in both cases.

The curvature drift speed is given by

$$v_C = \frac{mv_{\parallel}^2}{qB^2} \frac{\partial B}{\partial y} \quad (11.88)$$

In fact, in a curved magnetic field the field strength increases toward the center of curvature, so gradient and curvature drift act together. Compare Fig. 11.23 to Fig. 11.22 (rotated by some appropriate angle) to see that the gradient drift in Fig. 11.23 is then also out of the page, and the gradient and curvature drift speeds add. The resulting total drift speed, referred to here as $v_{C\nabla B}$, is

$$v_{C\nabla B} = v_C + v_{\nabla B} = \frac{m}{qB^2} \left(v_{\parallel}^2 + \frac{1}{2}v_{\perp}^2 \right) \frac{\partial B}{\partial y} \quad (11.89)$$

We now discuss various current systems that arise from the interactions described in Sect. 11.5.

11.6 Electric Currents in the Ionosphere and Magnetosphere

11.6.1 The Ionospheric Dynamo

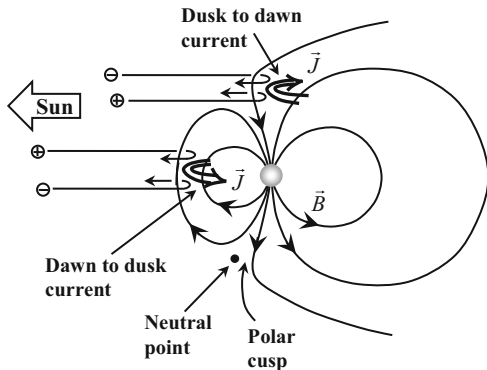
11.6.1.1 The S_q (“Solar Quiet”) Current System

The S_q current system is caused primarily by solar heating, and to a smaller extent by solar tides. The atmosphere over a given region of the Earth expands as it is heated in the morning and contracts as it cools later in the afternoon. This motion drives ionospheric electrons and ions across magnetic field lines, generating currents in the ionosphere (Fig. 11.9). The resulting current pattern remains at rest as seen from the Sun, as the Earth rotates under it.

The term “solar quiet” refers to the absence of solar activity (e.g., at solar minimum) such as solar flares, which can modify the current pattern.

Any current system creates magnetic fields, and these modify the observed magnetic field at a given location on the Earth. Thus, as an observer’s location rotates under the ionospheric current system, the observer sees a daily variation in the magnetic field.

Fig. 11.24 Schematic illustration of the interaction of solar wind particles with the Earth's magnetosphere, and the formation of the Chapman-Ferraro boundary current. In reality, the radius of gyration of positive ions is much greater than that of electrons. The view is from the dusk side of the Earth



11.6.1.2 The L_q (“Lunar Quiet”) Current System

The L_q current system is caused primarily by lunar tides and remains at rest as seen from the Moon as the Earth rotates under it.

Of the atmospheric tides, the solar thermal tide is stronger than either the lunar or solar gravitational tides, and the lunar gravitational tide is stronger than the solar gravitational tide.⁶ The ionospheric dynamo is thus dominated by solar heating, with the next strongest influence being the lunar tide.

11.6.2 Boundary Current

The *boundary current*, a.k.a. *magnetopause current* or *Chapman-Ferraro current*, is a diamagnetic current (Sect. 11.5.5) formed by the interaction of the solar wind with the Earth's magnetosphere at the magnetopause. Figure 11.24 illustrates schematically the principles involved.

The right-hand rule (Sect. 11.5.5) shows that positive ions in the solar wind gyrate out of the page when they encounter the Earth's magnetic field, and electrons gyrate into the page. The resulting current direction is out of the page, or from dawn to dusk (see Fig. 11.32 for orientations). Individual particles in this current are simply performing an arc of gyration, rather than flowing in the manner of a conduction current.

From the right-hand rule, the induced magnetic field of the boundary current opposes the Earth's magnetic field on the sunward side and strengthens it on the side facing the Earth, in effect compressing the magnetic field on the noon side of the Earth. Above and below, field lines that would have closed on the sunward side are swept

⁶This is because the differential gravitational force is proportional to r^{-3} .

back to the magnetotail by the same process, with the solar wind particles creating a dusk to dawn diamagnetic current that provides closure for the dawn-to-dusk current.

A *neutral point*, or a point of zero magnetic field, marks where the field lines diverge above each polar cap. As Fig. 11.24 shows, the neutral points are sunward of the Earth. A *polar cusp*, a region of funnel-shaped magnetic field lines, surrounds each neutral point. The polar cusps can guide solar wind particles into the atmosphere. As these particles travel along the magnetic field lines, they are accelerated by field-aligned electric fields, and are energetic enough by the time they reach the atmosphere to generate dayside aurorae.

The acceleration is an important part of this process: Solar wind particles have energies of only tens of eV, whereas spacecraft passing through the cusp measure electron energies of hundreds of eV associated with diffuse red auroral glow and several keV associated with dayside auroral arcs (Knudsen, D. J. 2013, *private communication*). Thus, the magnetosphere has to provide field-aligned electric fields to accelerate them. How these electric fields arise is an area of active research.

An increase in the solar wind flux results in an increase in the boundary current. This in turn causes an increase in the magnetic field strength at the Earth's surface and marks the onset of a magnetic storm (Sect. 11.6.4).

11.6.3 Ring Current

11.6.3.1 Magnetic Mirrors

Figure 11.25 shows a positively charged particle following a helical path into a region of converging magnetic field lines. Using the guiding center concept, we may describe the particle at any given instant as moving at speed v_{\perp} in a gyrocircle of radius r_c , while the center of the gyrocircle follows the central field line to the right at speed v_{\parallel} . We now look at the subsequent motion of this particle.

If the field lines converge at angle θ relative to the central field line, then the Lorentz force, $\vec{F}_B = q\vec{v} \times \vec{B}$, on the particle is also at angle θ to the plane of the gyrocircle, as indicated in Fig. 11.25. The components of F_B perpendicular and parallel to the central field line are then

$$F_{\perp} = F_B \cos \theta \quad (11.90)$$

$$F_{\parallel} = F_B \sin \theta \quad (11.91)$$

F_{\perp} produces gyromotion, while F_{\parallel} acts to change v_{\parallel} . The speed of the guiding center thus increases or decreases, depending on the relative directions of F_{\parallel} and v_{\parallel} . (In Fig. 11.25, v_{\parallel} would decrease.)

F_{\parallel} depends only on q, B, v_{\perp} (through F_B), and θ and is independent of v_{\parallel} . Thus, in Fig. 11.25, if the guiding center is brought to rest, it will immediately start to move with increasing speed toward the left, i.e., the converging field lines form a magnetic mirror, reflecting incoming particles back toward the region of weaker field.

Fig. 11.25 A charged particle in a region of converging magnetic field lines

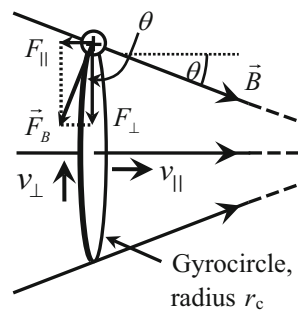
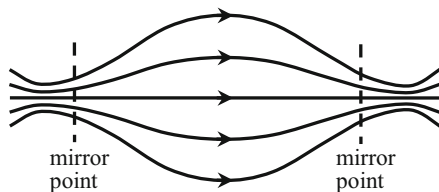


Fig. 11.26 Magnetic bottle



Two magnetic mirrors opposing each other form a magnetic bottle (Fig. 11.26), providing one of the methods proposed for containing the million-degree plasma in a fusion reactor.

11.6.3.2 Characteristics of the Motion

We now look for constants of the motion for the particle in Fig. 11.25. We take the case where:

- The magnetic field is constant in time as seen by an external observer (the particle, however, encounters a changing magnetic field as it moves through the converging field lines).
- The field lines are not necessarily straight, but they converge symmetrically about the central field line of the particle's motion, and the magnetic field strength is uniform over any given plane perpendicular to the central field line, although it changes from one plane to the next along the field line.
- The rate of convergence of the magnetic field lines is “slow;” i.e., the angle θ in Fig. 11.25 is small, so that $\cos \theta \approx 1$. Then, over any one gyrocircle, the change in the gyroradius is small compared to the gyroradius itself.

The particle then moves in a gyrocircle, the radius of which changes as the magnetic field strength changes, and the speed and direction of travel of which change because of $F_{||}$.

Gyromotion can be regarded as a current loop in which the current consists of one particle of charge q passing a given point on the gyrocircle f times per second. f is referred to as the *frequency of gyration*. The magnetic moment of a current loop is

$$\mu_B = IA \quad (11.92)$$

where I is the current and A is the area of the loop. The magnetic moment of the gyromotion can then be shown to be (see the problems in the Challenges section at the end of this chapter)

$$\mu_B = \frac{qr_c v_\perp}{2} \quad (11.93)$$

The angular momentum of a particle of mass m moving with speed v_\perp in a gyrocircle of gyroradius r_c is

$$L = mv_\perp r_c \quad (11.94)$$

From (11.93) and (11.94) we obtain

$$\mu_B = \frac{qL}{2m} \quad (11.95)$$

The torque on a particle equals the rate of change of its angular momentum:

$$\tau = \frac{dL}{dt} \quad (11.96)$$

However, the torque exerted on a charged particle by the magnetic force is zero; hence, from (11.96), the angular momentum of a particle undergoing gyromotion does not change with time and is a constant of the motion. It then follows from (11.95) that the magnetic moment, μ_B , is also a constant of the motion.

Because we are taking the case where B is uniform over the gyrocircle, the magnetic flux through the gyrocircle is

$$\Phi_B = BA \quad (11.97)$$

It then follows from previous results that

$$\Phi_B = \frac{2\pi m}{q^2} \mu_B \quad (11.98)$$

Hence, Φ_B is also a constant of the motion.

It can also be shown that the particle's kinetic energy, $K = 1/2mv^2$, is a constant of the motion, and hence, from Pythagoras' theorem,

$$\frac{1}{2}mv^2 = \frac{1}{2}mv_\perp^2 + \frac{1}{2}mv_\parallel^2 = \text{const} \quad (11.99)$$

The results above show that, for a particle undergoing gyromotion, Φ_B , L , and K are constants of the motion. As the magnetic field changes, r_c changes to conserve the magnetic flux through the gyrocircle. As r_c changes, v_\perp changes to conserve angular momentum; and as v_\perp changes, v_\parallel changes to conserve kinetic energy.

For the case where the particle is moving toward increasing B , as in Fig. 11.25, (11.99) shows that if v_\perp becomes equal to v then $v_\parallel = 0$ and further progress is impossible. F_\parallel , however, is non-zero and pushes the particle back toward weaker magnetic field. For a symmetrical magnetic bottle, as in Fig. 11.26, the particle will mirror back and forth inside the bottle without contacting any physical walls, making magnetic bottles very useful for fusion reactors operating at millions of degrees temperature.

11.6.3.3 Trapping and Precipitation

The inner magnetic field lines in Fig. 11.24 (i.e., those not extending off down the magnetic tail) form a curved analog of Fig. 11.26 and cause charged particles to mirror back and forth between the northern and southern hemispheres. In the Earth's magnetosphere, these regions of trapped charged particles are the *Van Allen radiation belts*, consisting of an inner belt of high-energy protons (10–100 MeV) at distances of $\sim 1\text{--}3R_E$ above the Earth's surface and an outer belt of high-energy electrons (0.1–10 MeV) and ions at $\sim 1\text{--}10R_E$ above the Earth's surface, peaking in electron density between 2.3 and $3R_E$ above the surface. The protons in the inner belt are produced by β -decay of neutrons created by cosmic ray collisions with nuclei in the upper atmosphere.

If one of these particles enters the atmosphere before mirroring then collisions in the atmosphere will prevent it from reflecting. This loss of particles from the trapping region is known as *precipitation*.

The three constants of the motion found in Sect. 11.6.3.2 allow the magnetic field strength, B_R , to be found at the mirror point (the subscript, R, signifies “reflection”) for any given pitch angle, α_0 , and magnetic field strength, B_0 , at the magnetic equator (the location where the magnetic field is weakest). Some relevant parameters are illustrated in Fig. 11.27. At the magnetic equator, for a particle of speed v , we can define

$$v_\parallel^0 = v \cos \alpha_0 \quad (11.100)$$

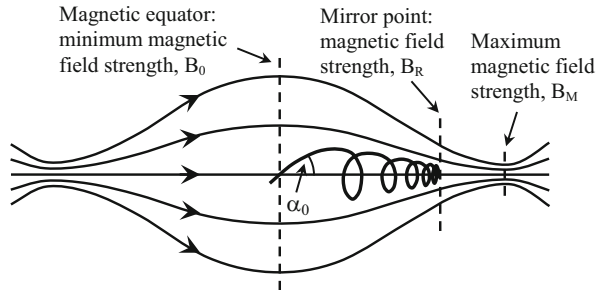
$$v_\perp^0 = v \sin \alpha_0 \quad (11.101)$$

At the mirror point,

$$v_\parallel^R = 0 \quad (11.102)$$

and therefore, from the constancy of the kinetic energy in (11.99),

Fig. 11.27 Parameters for a magnetic mirror. α_0 is the pitch angle at the magnetic equator



$$v_{\perp}^R = v \quad (11.103)$$

From (11.94), (11.103), and the constancy of the angular momentum, we obtain

$$v_{\perp}^0 r_c^0 = v_{\perp}^R r_c^R = v r_c^R \quad (11.104)$$

Then

$$\frac{r_c^0}{r_c^R} = \frac{v}{v_{\perp}^0} \quad (11.105)$$

Finally, from the remaining characteristic of the motion, the constancy of the magnetic flux within the gyrocircle, we have

$$B_0 \pi (r_c^0)^2 = B_R \pi (r_c^R)^2 \quad (11.106)$$

from which, with (11.101) and (11.105),

$$B_R = B_0 \left(\frac{r_c^0}{r_c^R} \right)^2 = B_0 \left(\frac{v}{v_{\perp}^0} \right)^2 = B_0 \left(\frac{v}{v \sin \alpha_0} \right)^2 \quad (11.107)$$

or

$$B_R = \frac{B_0}{\sin^2 \alpha_0} \quad (11.108)$$

Thus, the magnetic field strength at the mirror point depends only on B_0 and α_0 and is independent of the charge, mass, and kinetic energy of the particle. Equation (11.108) shows that, in a magnetic bottle such as that in Fig. 11.27, particles of smaller α_0 mirror at larger B_0 , i.e., closer to the point of maximum field strength, B_{\max} . If the field strength, B_R , required at the mirror point [from (11.108)] is greater than B_{\max} then the bottle is unable to constrain these particles, and they escape through the ends of the bottle. The *critical pitch angle* at the

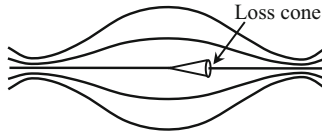


Fig. 11.28 The loss cone. All particles traveling within the loss cone (angular radius α_C) at the magnetic equator escape from the magnetic bottle

magnetic equator, α_C , so called because all particles of $\alpha_0 < \alpha_C$ escape, is obtained by setting $B_R = B_{\max}$ in (11.108), yielding

$$\alpha_C = \sin^{-1} \sqrt{\frac{B_0}{B_{\max}}} = \sin^{-1} \frac{1}{\sqrt{\mathfrak{R}}} \quad (11.109)$$

where the *mirror ratio*

$$\mathfrak{R} \equiv \frac{B_{\max}}{B_0} \quad (11.110)$$

is the ratio of the strongest to the weakest magnetic field strength. α_C defines the *loss cone*, as illustrated in Fig. 11.28. A similar loss cone exists for particles traveling toward the left.

In similar fashion, the loss cone in a planetary magnetosphere separates particles that are lost by precipitation into the atmosphere from those that mirror. B_M is then the magnetic field strength at the exobase, where collisions are frequent enough to remove the particles.

If a process injects particles into a planetary magnetosphere with an initially isotropic distribution of pitch angles at the magnetic equator, then the fraction, f , of these particles that are precipitated equals the fraction of half a sphere [2π steradians (sr)] taken up by the loss cone. (There are 4π sr in a complete sphere, but only half of the particles are traveling toward any given end of the magnetic bottle in Fig. 11.28.) To find the fraction precipitated we first need to find the solid angle, Ω , taken up by a cone of angular radius α_c , then take the ratio of this result to 2π sr.

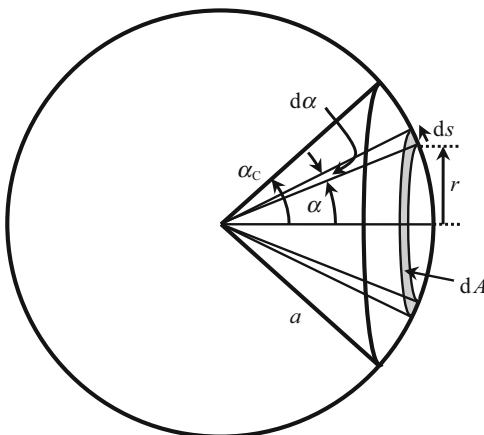
In Fig. 11.29, the area on the surface of the sphere intersected by the loss cone is

$$\begin{aligned} A &= \int_{\alpha=0}^{\alpha_C} dA = \int_{\alpha=0}^{\alpha_C} 2\pi r \, ds = \int_{\alpha=0}^{\alpha_C} 2\pi (a \sin \alpha) (a d\alpha) \\ &= 2\pi a^2 \int_{\alpha=0}^{\alpha_C} \sin \alpha d\alpha = 2\pi a^2 (1 - \cos \alpha|_{\alpha=0}^{\alpha_C}) \end{aligned}$$

or

$$A = 2\pi a^2 (1 - \cos \alpha_C) \quad (11.111)$$

Fig. 11.29 Quantities required to find the solid angle in steradians taken up by a loss cone of angular radius α_C



The fraction of particles that are precipitated is then

$$\begin{aligned} f &= \frac{\Omega}{2\pi} = \frac{1}{2\pi} \left(\frac{A}{a^2} \right) = \frac{1}{2\pi} \frac{2\pi a^2 (1 - \cos \alpha_C)}{a^2} = 1 - \cos \alpha_C \\ &= 1 - \sqrt{1 - \sin^2 \alpha_C} = 1 - \sqrt{1 - \frac{B_0}{B_M}} \end{aligned}$$

from (11.96) or

$$f = 1 - \sqrt{1 - \frac{1}{\mathfrak{R}}} \quad (11.112)$$

11.6.3.4 The Ring Current

Figure 11.30a illustrates schematically the path of a charged particle trapped in a planetary magnetosphere, mirroring back and forth between the northern and southern magnetic poles. Gradient and curvature drift (Sect. 11.5.9) cause positive charges to drift out of the page and negative charges to drift into the page in this region of the diagram, creating a current, the *ring current*, in the direction shown.

In the Earth's magnetosphere, the ring current is carried by the outer Van Allen radiation belt and is strongest in the region $\sim 2\text{--}4R_E$ above the Earth's surface. As illustrated in Fig. 11.30b, the induced magnetic field within the ring current opposes the intrinsic magnetic field in the region between the ring current and the Earth's surface and reduces the measured magnetic field at any point on the Earth's surface.

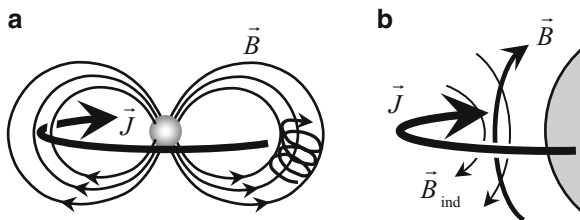


Fig. 11.30 The ring current. (a) The *helix* shows part of the path of a charged particle mirroring between the northern and southern hemispheres. The *heavy arrow* shows the direction of the gradient and curvature drift of a positively charged particle, and the resulting current direction. (b) Within the ring's radius, the induced magnetic field of the ring current opposes the intrinsic magnetic field of the Earth

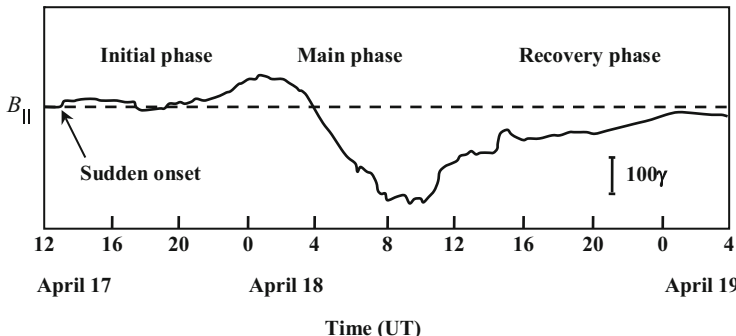


Fig. 11.31 Magnetic storm recorded at Guam. The horizontal component of the Earth's magnetic field is shown as a function of universal time (UT). The tracing has been redrawn and slightly smoothed. After Cahill 1968, Fig. 1, p. 264

11.6.4 Magnetic Storms

A *magnetic storm* (Fig. 11.31) is a worldwide disturbance in the horizontal component, B_{\parallel} , of the geomagnetic field at the Earth's surface. The initial phase typically begins with a sudden onset in which B increases by several to several tens of gammas ($1\gamma = 1\text{ nT}$) in a few minutes, and lasts from tens of minutes to several hours. The main phase, where B_{\parallel} decreases below its pre-storm value, typically lasts from several hours to about 2 days, and recovery can take from several days to a month, depending on the strength of the storm. For comparison, the Earth's magnetic field strength at the surface is about 30,000–60,000 nT.

The sudden onset and initial phase occur when an enhancement in the solar wind flux, e.g., from a solar flare, encounters the Earth's magnetosphere, increasing the boundary current and compressing the magnetosphere on the Earth's dayside (Sect. 11.6.2). After some delay, the main phase of the storm begins as processes in the magnetosphere inject charged particles into the outer van Allen belt,

increasing the ring current (Sect. 11.6.3). Precipitation through the loss cone produces diffuse (mostly subvisual) aurorae, whereas the bright auroral arcs are produced by particles from further out in the plasma sheet, at \sim 6 Earth radii, being accelerated along magnetic field lines into the auroral oval by field aligned electric fields (Knudsen, D. J. 2013, *private communication*). The recovery phase occurs as the ring current slowly dies back and the magnetosphere returns to its undisturbed state.

Magnetic storms fall into two broad categories, related to the particle source regions on the Sun. Strong magnetic storms occur individually and result from transient high-energy phenomena: solar flares and coronal mass ejections (CME). Weaker magnetic storms often recur with a 27-day period, equal to the synodic rotation period of the Sun, and result from relatively steady streams of particles from coronal holes in the Sun's polar regions sweeping past the Earth as the Sun rotates.

The decay of the ring current during the recovery phase requires particle loss outside the loss cone, which occurs at least in part by charge-exchange interactions of ring-current ions with exospheric neutral hydrogen (Sect. 10.4.1.4). The large pressure scale height of hydrogen results in a density of $\sim 10^9$ H atoms/m³ at the inner edge of the ring current and $\sim 10^8$ m⁻³ at geosynchronous orbit ($6.6R_E$). Fast ions capture an electron from a slow-moving H atom, resulting in a fast-moving neutral atom and a slow-moving proton. The spherical volume of neutral H surrounding the Earth is detectable by reflected UV light as the *geocorona*.

The decay processes operate continuously, so the existence of a steady ring current outside magnetic storms shows that, even in quiet times, the outer radiation belt is continuously replenished on timescales of a few days.

11.6.5 Magnetospheric Convection

The solar wind outside the magnetopause exerts a viscous drag on the plasma inside the magnetosphere, arising through waves and particle diffusion across the magnetopause. [Viscous drag occurs when two media (here, the solar wind and magnetospheric plasma) that are moving relative to each other interact as fluids.] This interaction creates a boundary layer just inside the magnetopause in which magnetospheric plasma flows antisunward at some fraction of the solar wind speed. Continuity then requires a return flow through the rest of the magnetosphere. These particles pass the Earth and rejoin the boundary particles to complete the circulation.

Currents created by the interaction of this flow with the Earth's magnetic field in turn modify the magnetic field in such a way that the magnetic field lines can be regarded as being carried with the particles as they move, stretching the magnetosphere into a long magnetotail in the antisunward direction. This continuous circulation of particles and magnetic field down and back up the magnetotail is known as *magnetospheric convection*.

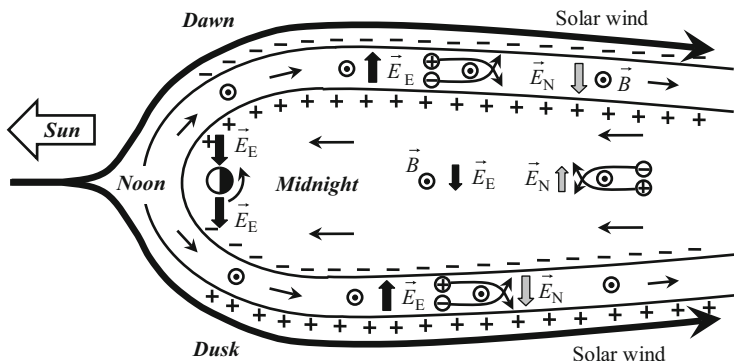


Fig. 11.32 Magnetospheric convection (Not to scale)

Figure 11.32 illustrates magnetospheric convection, looking down on the equatorial plane from above the North Pole of the Earth. The Earth rotates in the direction indicated. Directions in the magnetosphere are denoted by whether they are above the dawn, noon, dusk, or midnight point on the Earth's equator. Illustrative positive and negative charges are shown in each region, and circled dots denote magnetic field out of the page (south to north).

In the boundary layer, convection of charges past magnetic field lines creates a magnetic force in the dawn-to-dusk direction on positive charges and dusk-to-dawn on negative charges. These directions are reversed in the return flow. Magnetic forces can be modeled as arising from *non-electrostatic electric fields*, \vec{E}_N (grey arrows), by treating the magnetic force as if it were a non-electrostatic electric force arising from a non-electrostatic electric field, $\vec{F}_B = \vec{F}_N = q\vec{E}_N$. Then

$$q(\vec{v} \times \vec{B}) = q\vec{E}_N \\ \therefore \vec{E}_N = \vec{v} \times \vec{B} \quad (11.113)$$

Thus, \vec{E}_N is in the $\vec{v} \times \vec{B}$ direction, from dawn to dusk in the boundary layer, and dusk to dawn in the return flow (Fig. 11.32).

\vec{E}_N produces charge distributions at the interfaces between the boundary layer and the solar wind, and between the boundary layer and the return flow, as shown in Fig. 11.32. These charge distributions in turn produce *electrostatic fields*, \vec{E}_E (black arrows), in the dusk-to-dawn direction in the boundary layer and dawn-to-dusk in the return flow, as indicated.

Magnetospheric convection also creates electric fields, and therefore electric currents, in the ionosphere near each pole. This produces the *auroral oval*, the *eastward and westward electrojets* (part of the auroral oval), and other phenomena.

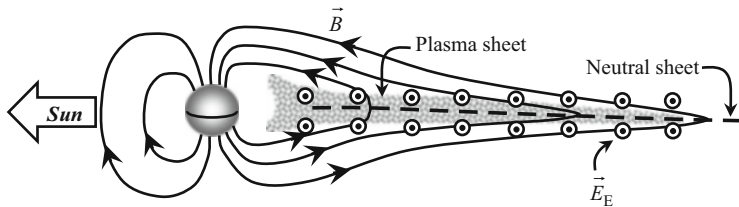
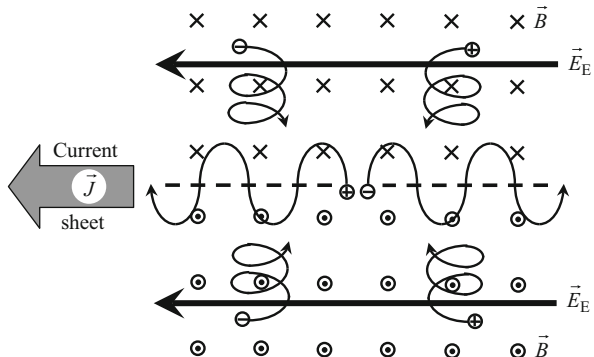


Fig. 11.33 The magnetotail neutral sheet and plasma sheet

Fig. 11.34 $\vec{E} \times \vec{B}$ drift and the magnetotail current sheet



11.6.6 The Magnetotail Current Sheet

Figure 11.33 illustrates schematically (not to scale) a vertical cross-section through the magnetosphere. The dashed line denotes the neutral sheet and the circled dots denote the electrostatic field in the magnetotail, directed from dawn to dusk (toward the viewer).

Figure 11.34 shows a view in the magnetotail, facing toward the Earth (i.e., looking toward the left from the right edge of Fig. 11.33). The dashed line again denotes the neutral sheet, with magnetic field away from the observer on the north side (above) and toward the observer on the south side (below).

In regions away from the neutral sheet, positive and negative charges undergo $\vec{E} \times \vec{B}$ drift toward the neutral sheet. Because they drift in the same direction, this motion does not give rise to a current. The resulting collection of electrons and ions near the neutral sheet is the *plasma sheet* (see Fig. 11.33). Positive and negative charges in the plasma sheet now drift in opposite directions as they oscillate across the neutral sheet, producing a dawn-to-dusk current density, variously called the *neutral sheet current*, *magnetotail current sheet*, or *cross-tail current*.

The return flow on the outside of the magnetotail in Fig. 11.9 is in the same direction as the return flow of the dayside boundary current (Sect. 11.6.2). These two flows merge near the Earth.

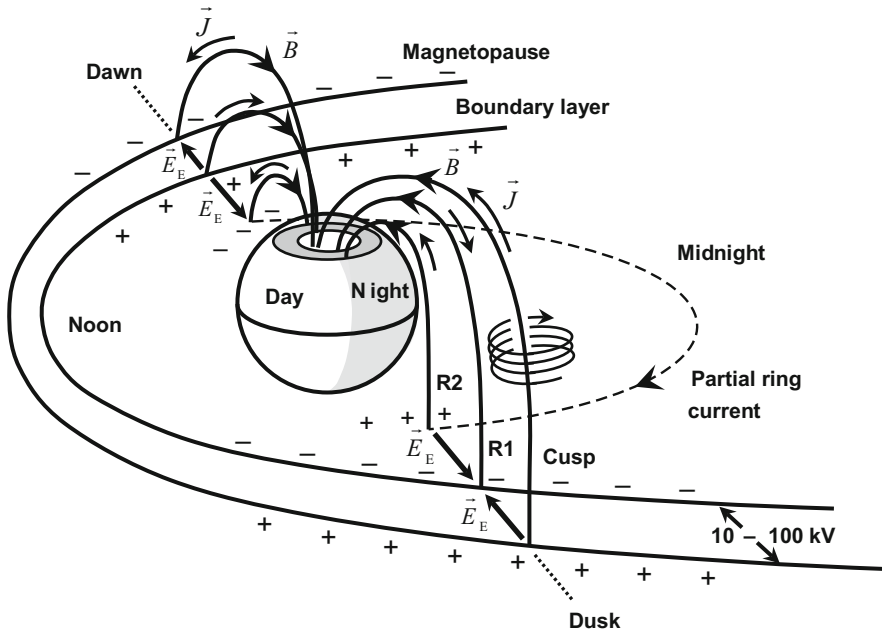


Fig. 11.35 Coupling of the low-latitude magnetosphere and boundary layer to the northern ionosphere (not to scale). The magnetic field lines act as electrical conduits connecting the convection emf in the boundary layer to the polar cap (white ellipse) and the convection emf in the magnetosphere to the auroral oval (grey ring). The cusp field-aligned current (FAC) connects the magnetopause to the polar cusp in the noon region of the polar cap. The region 1 (R1) FAC connects the inner edge of the boundary layer to the high-latitude edge of the auroral oval and the region 2 (R2) FAC connects the ring current to the low-latitude edge of the auroral oval. The R2 FAC is closed by an enhancement of the ring current (the *partial ring current*) on the midnight side of the Earth. The convection electric field between the ring current and the Earth is zero. See also Fig. 11.32

11.6.7 Coupling Between the Magnetosphere and the Ionosphere

Aurorae are caused by precipitation of energetic electrons into the ionosphere. The electrons collide with and excite atoms and molecules, notably O, N, and N₂, and visible light is emitted when these species decay back to the ground state.

Time-varying electric currents (the *solar disturbed*, or S_D, current system) associated with the aurora occur at altitudes between 100 and 150 km and cause significant Joule heating in the ionosphere. These currents are always present, and so are their attendant magnetic fields. As the ionospheric currents vary, their time-varying magnetic fields induce emfs in electric circuits on the ground and elsewhere. During particularly strong magnetic storms, these induced emfs can be powerful enough to disrupt power grids.

Here, we describe the S_D current system. Figure 11.35 is a perspective view of Fig. 11.32, showing the charge separation at the magnetopause boundary layer, the

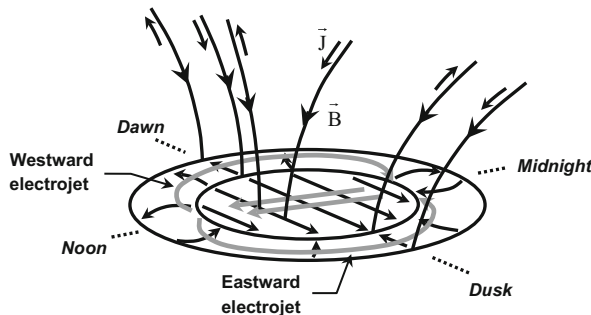


Fig. 11.36 Schematic diagram of ionospheric currents. The arrows beside the magnetic field lines are field-aligned (or Birkeland) currents; black arrows in the auroral oval and polar cap represent the directions of the electric field and the Pedersen current system; the gray arrows represent the Hall current system

resulting electrostatic fields, and some of the magnetic field lines coupling the magnetosphere to the northern ionosphere. These field lines also connect to the southern ionosphere (not shown in the diagram).

The boundary layer acts as a magnetohydrodynamic (MHD) generator: magnetospheric convection carries plasma antisunward through the Earth's magnetic field, creating a non-electrostatic field, \vec{E}_N that in turn produces a charge separation and a consequent electrostatic field, \vec{E}_E (cf. Sect. 11.6.5 and Fig. 11.32). The electromotive force (emf), ε , of this source may be calculated from

$$\varepsilon = \int \vec{E}_N \cdot d\vec{\ell} = \int (\vec{v} \times \vec{B}) \cdot d\vec{\ell} \quad (11.114)$$

and is typically 10–100 kV. The polarity of the source is as indicated in Figs. 11.32 and 11.35. The region just inside the boundary layer also acts as an MHD generator, with the opposite direction of magnetospheric convection and polarity of the emf.

Magnetospheric plasma is essentially collisionless, so the conductivity is very large parallel to \vec{B} and very small perpendicular to \vec{B} . The magnetic field lines thus act as electrical conduits connecting the magnetospheric sources of emf to the ionospheric load. *Field-aligned currents* (called *Birkeland currents* in the Earth's magnetosphere, after their discoverer) then flow into and out of the ionosphere in the directions dictated by the polarity of the sources, as shown in Fig. 11.35. The current direction inside the magnetopause and magnetosphere in Fig. 11.35 is opposite to the electrostatic field, as required in a source of emf.

Figure 11.36 shows the magnetic and electrostatic fields and consequent current systems in the polar cap and auroral oval. Inspection of Figs. 11.35 and 11.36 shows that the dusk-to-dawn electric field in the boundary layer maps into the ionosphere as a dawn-to-dusk electric field in the polar cap, and the dawn-to-dusk electric field in the magnetosphere maps into the ionosphere as a dusk-to-dawn electric field in the auroral oval.

The electric and magnetic fields in the ionosphere create the Pedersen current system parallel to the electric field and the Hall current system antiparallel to the $\vec{E} \times \vec{B}$ direction (Sect. 11.5.7). The Pedersen current system has divergence (currents begin, end, or flow in opposite directions at boundaries) and is closed by the Birkeland currents to and from the magnetosphere, whereas the Hall current system is without divergence.

The Hall currents are more limited in spatial extent and therefore more intense in the auroral oval than in the polar cap and are referred to as electrojets (Fig. 11.36). During a moderately sized aurora, the electrojets can carry currents of several million amperes.

The idealized current orientation shown in Fig. 11.36 must be modified because electron precipitation results in a greater density of free charge and therefore conductivity in the auroral oval than in the polar cap. Because the Hall current is dominated by electrons drifting opposite to the current direction and the mobility of electrons is higher in the auroral oval (i.e., there is an impedance mismatch between the auroral oval and the polar cap), negative charge occurs where the Hall current enters the polar cap and a corresponding positive charge where the Hall current leaves the polar cap. The electrostatic field of these charges adds vectorially to the one shown in Fig. 11.36 to create a resultant electrostatic field directed from a point between midnight and dawn toward a point between noon and dusk. The (final) Pedersen current is parallel to the total electric field and the Hall current is perpendicular to it, so the Pedersen and Hall current systems are rotated clockwise (in the dawn to midnight direction) from the orientation shown in Fig. 11.36.

Fig. 11.37 shows the S_D current system at 2400 GMT averaged over a 12-month period in 1932–1933. Noon is downward. Note that the S_D current system is fixed relative to the Sun, and the Earth rotates counterclockwise under it. The westward electrojet is much stronger than the eastward and gives a maximum current density in the hours after midnight, above latitudes between 60° N and 70° N.

11.6.8 Magnetospheric Substorms

Magnetic substorms appear to be different in character and cause from magnetic storms (Sect. 11.6.4): (1) they are detected primarily at high geomagnetic latitudes, rather than worldwide as for magnetic storms; (2) the initial increase in B_{\parallel} is lacking; (3) they tend to be stronger (i.e., deeper) but of much shorter duration than magnetic storms, typically 1–3 h; and (4) they often occur within a couple of hours after the vertical component of the IMF changes from northward to southward and stays that way. Point (2) shows that, unlike magnetic storms, enhancements of the solar wind are not involved, and (1) shows that the change in the ring current is much smaller than in magnetic storms.

Magnetic substorms can also occur during magnetic storms, but appear to differ from those described above, e.g., by injecting considerably more charged particles into the inner magnetosphere.

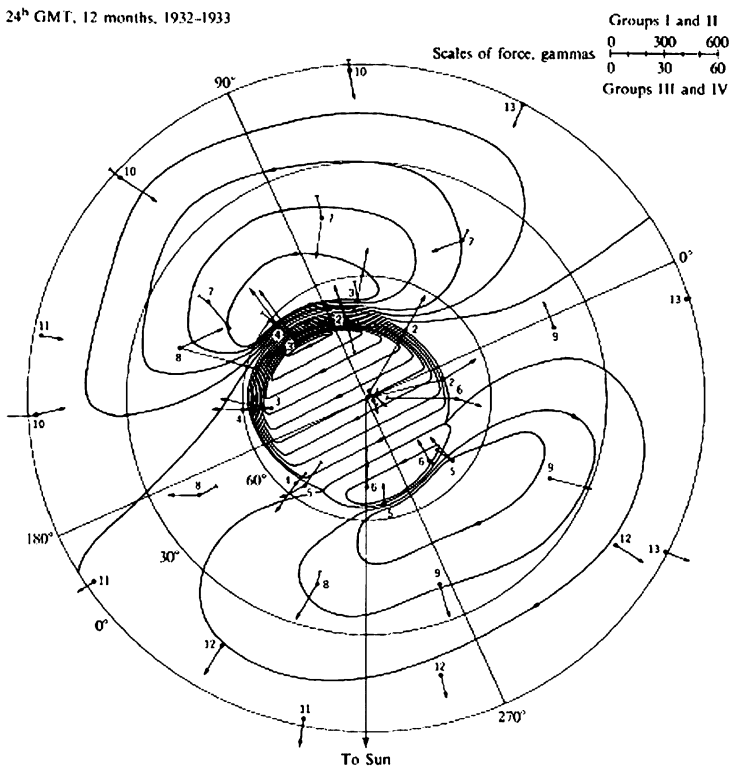


Fig. 11.37 The S_D ionospheric current systems. A current of 50,000 A flows between successive contours. Noon is towards the bottom. Current density is maximum shortly after local midnight. (From Silsbee and Vestine 1942, Fig. 8; and Parks 1991, Fig. 7.11, p. 281, with the latter's permission)

Figures 11.38 and 11.39 illustrate some aspects of the present picture of a magnetic substorm. When the IMF is southward, in the opposite direction to the planetary field, solar magnetic field lines can connect with those of the Earth near the dayside magnetic equator (Sergeev et al. 2012; Angelopoulos 2008; Milan et al. 2007). This process of *magnetic reconnection* converts closed, magnetospheric field lines into open field lines, which are then swept past the Earth and into the tail by the solar wind (Fig. 11.38). The loading of the tail with flux transported from the dayside magnetosphere increases the magnetic field strength in the tail by (typically) 10–30 %, and also increases the flaring of the tail (see Fig. 11.40b-d for an illustration of this phenomenon in Mercury's magnetotail). Because of the flaring, the solar wind ram pressure on the tail increases, compressing the plasma sheet; and when this becomes thin enough instabilities arise, causing:

- (i) disruption of the cross-tail current near the Earth and the creation of field-aligned currents between there and the ionosphere (Fig. 11.39). The two

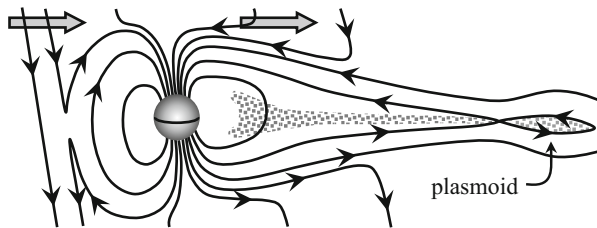


Fig. 11.38 Magnetic reconnection of southward IMF with the Earth's magnetic field at the dayside magnetospheric boundary. Magnetic reconnection also occurs in stretched magnetic field lines in the magnetotail, as described in the text

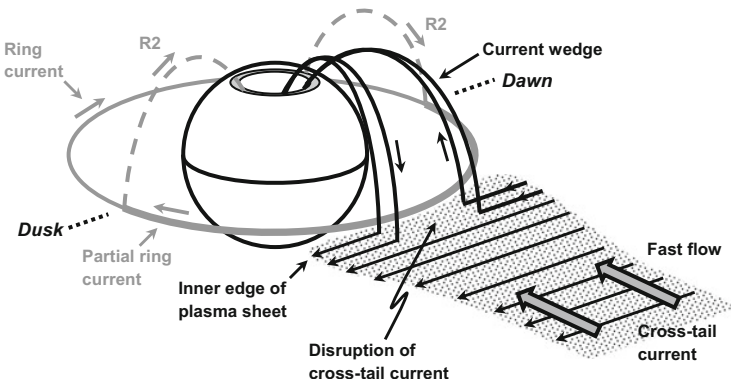


Fig. 11.39 Disruption of the cross-tail current at the inner edge of the plasma sheet and formation of the substorm current wedge to and from the ionosphere in the auroral oval (not to scale). Stippled region: plasma sheet; long, black arrows: cross-tail current; thick arrows: fast Earthward flow of plasma from the magnetotail. The region 2 (R2) currents joining the ring current to the auroral oval are also shown, in grey

field-aligned currents form a wedge-shaped structure when viewed from above the polar cap. This current wedge causes electrojet intensification and auroral breakup; i.e., a sudden expansion of the aurora with rapidly-moving curtains and other structures. The electrojet produces the magnetic signature of the substorm.

- (ii) fast transport of plasma earthward along the neutral sheet from further out in the tail; and
- (iii) magnetic reconnection of open magnetotail field lines across the neutral sheet (average distance $\sim 18 R_E$, where R_E is the radius of the Earth). The reconnection closes the field lines on the earthward side and creates detached regions of plasma and magnetic field called *plasmoids* on the tailward side (Fig. 11.38). The plasmoids convect tailward (away from the Earth) while the reconnected field line and associated plasma convect Earthward.

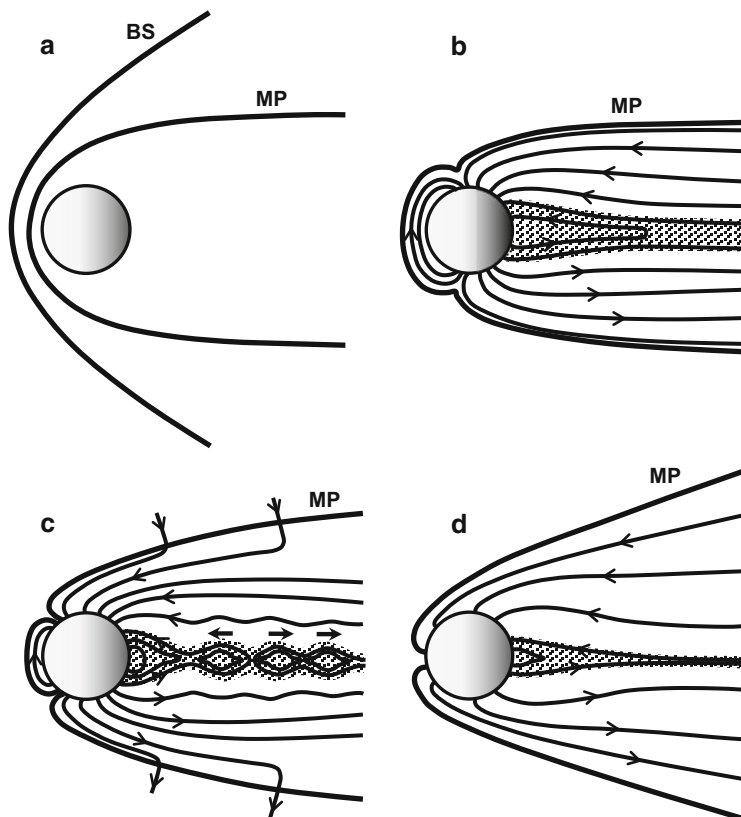


Fig. 11.40 The magnetosphere of Mercury. BS = bow shock; MP = magnetopause; stippled regions = magnetotail plasma sheet. North is upward and the Sun is to the left. (a) The mean configurations of the bow shock and magnetopause relative to the size of Mercury, approximately to scale. (b) Mercury's magnetopause, magnetosphere and plasma sheet under conditions of northward IMF. (c) Magnetopause and magnetosphere under conditions of southward IMF. (d) Magnetopause and magnetosphere under conditions of southward IMF and extreme loading by the solar wind. (a–c) Adapted from Slavin et al. 2012, Figs. 1 and 10, modified by permission of the American Geophysical Union; (d) Adapted from Slavin et al. 2010, Fig. 4, by permission of the authors and publisher

The order of points (i)–(iii), above, is still uncertain because they occur within ~ 1 min of each other (Angelopoulos 2008). It is possible that the current disruption occurs first, resulting in plasma flow and magnetic reconnection (an inside-out scenario), or reconnection may occur first, resulting in plasma flow and current disruption (an outside-in scenario).

This cycle in which open field lines are created by magnetic reconnection at the dayside magnetopause, swept into the magnetotail where they are reconnected, and swept back toward the Earth and into the dayside magnetosphere again is referred to as the *Dungey cycle*. The typical cycle time in the terrestrial magnetosphere is ~ 1 h.

It is also instructive to consider the Dungey cycle in terms of energy. Solar wind kinetic energy is converted to energy stored as magnetic flux in the magnetotail via dayside reconnection and transport of magnetic field lines into the magnetotail. The stored energy in the magnetotail is then converted into heat via magnetic reconnection, plasma transport and dissipation (heating) in the magnetotail, and dissipation in the electrojet. The magnetosphere therefore acts in part as a heat engine, converting solar wind kinetic energy into heat.

11.7 Magnetospheres of Mercury, Venus, and Mars

11.7.1 Mercury

Mercury's magnetosphere was probed by the *Mariner 10* spacecraft in its first and third flybys in 1974 and 1975 (the second flyby was at a distance of 48,000 km, too distant to obtain magnetospheric measurements), and by the *MESSENGER* spacecraft in three flybys in 2008 and 2009. *MESSENGER* entered orbit around Mercury on March 18, 2011 and began making more continuous observations of the magnetosphere (Sect. 9.1.3).

Mercury was found by *Mariner 10* to have a global magnetic field with characteristics best explained by an active core dynamo, and this picture has been confirmed by *MESSENGER*. Mercury is thus, at present, the only terrestrial planet besides the Earth found to have an internally-generated magnetic field. Characteristics of this field as measured by *MESSENGER* (Anderson et al. 2011) are:

- Magnetic field strength at Mercury's surface: $\sim 1\%$ of that at the Earth's surface.
- Polarity: Same as the Earth. Magnetic field lines are directed northward outside the planetary surface and southward along the rotation axis. Thus, the north-seeking pole of a compass on Mercury's surface would point north.
- Configuration: Primarily dipolar. The dipole term $g_{10} = -195 \pm 10$ nT, giving a dipole moment $\mu = lg_{10} R_M^3 = 2.83 \times 10^{12}$ T m³, where R_M is Mercury's radius (2,440 km); dividing this value of μ by the quantity $\mu_0/4\pi$ yields 2.83×10^{19} amp m², or $\sim 4 \times 10^{-4}$ of that of the Earth.
- Axial tilt: $< 3^\circ$ from the planetary rotation axis, or possibly not tilted at all. The Earth's magnetic dipole, by comparison, is tilted $\sim 11^\circ$ from the rotation axis.
- Dipole offset: Centered on the spin axis but displaced 484 ± 11 km north of the center of the planet. The corresponding quadrupole term is $g_{20} = -74 \pm 4$ nT, giving a ratio $g_{20}/g_{10} = 0.38$. (The larger this ratio, the more the center of the dipole is offset north or south of the planet center along the rotation axis.)

The only other planet with an axially-aligned dipole is Saturn, for which $g_{20}/g_{10} = 0.072$; i.e., the dipole offset is a factor of 5 greater for Mercury than for Saturn, relative to the planetary diameter. Thus, with its axially-aligned dipole and large dipole offset, Mercury's magnetic field is distinct from that of any other planet.

11.7.1.1 Magnetospheric Dynamics

Mean distances from planet center are $1.3 R_M$ to the magnetopause nose (the closest point of the magnetopause to Mercury's surface) and $1.7 R_M$ to the bow shock (Slavin et al. 2010). Figure 11.40a shows the mean configurations of the magnetopause and bow shock relative to the planet, approximately to scale. Because of Mercury's weak magnetic field, however, these boundaries vary significantly with the solar wind strength and IMF direction, as illustrated in Figs. 11.40b, c and d; e.g., the mean magnetopause position during northward IMF is $\sim 1.5 R_M$.

Figure 11.40b shows a typical magnetospheric configuration when the IMF has a northward component (toward the top of the page). In this case, the entire surface of Mercury is protected from the solar wind by the magnetosphere, the tail shows minimal flaring, and the plasma sheet has maximum thickness.

Figure 11.40c shows a typical magnetospheric configuration when the IMF has a southward component (toward the bottom of the page) (Slavin et al. 2010). As in the Earth's magnetosphere during southward IMF, magnetic reconnection takes place near the dayside magnetic equator and the solar wind sweeps the resulting open field lines past the planet and into the tail, loading the tail with magnetic flux and compressing the plasma sheet (Sect. 11.6.8 and Fig. 11.38). When this sheet becomes sufficiently thin it becomes unstable, giving rise to substorm-like behavior with magnetic reconnection in the tail, ejection of plasmoids, and plasma flow toward the planet.

Typical reconnection rates at Mercury's magnetopause are ~ 10 times those at the Earth (Slavin et al. 2012), probably because of the stronger IMF, and flux loading increases the magnetic field strength in the magnetotail lobes by as much as a factor of ~ 2 , compared to 10–30 % for the Earth. The Dungey cycle time is $\sim 1\text{--}2$ min, compared to ~ 1 h for the Earth, ~ 1 week for Saturn, and ~ 1 month for Jupiter.

With southward IMF, the dayside reconnection significantly reduces the altitude of the dayside magnetopause and displaces the cusps at the magnetic poles toward the equator (Fig. 11.40c). Under extreme conditions, 100 % of the planet's magnetic flux can be transferred to the tail (Slavin et al. 2010). In this case, the two cusps merge into a single, broad cusp at the equator (Fig. 11.40d). This extreme configuration is expected to be highly unstable, and substorm-like behavior will quickly transfer magnetic flux back to the dayside on the Dungey cycle timescale.

The strong resemblance of Mercury's magnetospheric processes to those of the Earth suggests that there could also be a similar set of field-aligned currents (FACs); and indeed a region 1-type FAC of $\sim 1.4 \times 10^6$ A has been observed at the magnetopause, along the boundary between the open field lines in the polar cusp and the closed field lines in the magnetosphere. However, there is a problem: On Mercury, in order to close the circuit (Lyatsky et al. 2010), a current of this magnitude requires a load whose conductance is ~ 35 S (1 S = 1 siemens = 1 mho, the SI unit of conductance, and the inverse of resistance). On the Earth, the ionosphere provides the load, but Mercury's extremely tenuous ionosphere (predominantly Na^+ and Mg^+ with a number density of only $\sim 10 \text{ cm}^{-3}$) can provide

a height-integrated Pedersen conductance of only $\sim 5 \times 10^{-6}$ S, far too small to sustain the current observed. Two other suggested possibilities also appear to be ruled out (Lyatsky et al. 2010 and references therein):

- Ion pick-up conductance due to ionization and subsequent $\vec{E} \times \vec{B}$ drift of atoms sputtered from Mercury's surface by the solar wind. However, the maximum pick-up conductance is expected to be ~ 0.2 S which, while much higher than the classical ionospheric conductance, is still two orders of magnitude too low.
- Surface conductivity. However, if Mercury's crust has a similar conductivity to that of the lunar crust, then the maximum surface conductance is likely to be ~ 0.1 S, which again is insufficient.

Lyatsky et al. (2010) show that Alfvén waves (transverse plasma oscillations in which the ions provide the inertia and the magnetic field provides the restoring force) may be capable of providing the required closure for the FACs.

11.7.1.2 Particle Trapping

The Earth's Van Allen radiation belts (Sect. 11.6.3.3) consist of high-energy (keV to MeV) protons and electrons gyrating around magnetic field lines and mirroring back and forth between the magnetic poles. Gradient and curvature drift in this population gives rise to the diamagnetic ring current parallel to the geomagnetic equator (Sect. 11.6.3.4). An equivalent trapping region around Mercury was not expected because, if we scale the Earth's magnetosphere to Mercury based on the respective magnetopause positions measured from planetary center, the trapping region would be located inside the planet ($r < 1R_M$).

Nevertheless, *MESSENGER* detected an increase in low-energy (1–10 keV) ions and electrons centered on Mercury's magnetic equator (Schriever et al. 2011) a short distance below the magnetopause (e.g., near $1.4 R_M$ for a magnetopause distance of $1.5 R_M$), accompanied by a decrease in magnetic field strength by 5–50 nT. The magnetic field decrease indicates the presence of a diamagnetic current, which suggests that the keV particles form a ring current as described above. Only about 10 % of the particles make a complete drift orbit around the planet; the rest are lost either by precipitation at the planetary surface (the loss cone angle is $\sim 30^\circ$) or by escaping through the magnetopause. For this reason, the particles are referred to as *quasi-trapped*. The distances to the surface and the magnetopause also limit their energies; e.g., protons of energy > 20 keV gyrating around magnetic field lines at $1.4 R_M$ at the magnetic equator ($B \sim 0.83$ nT) will escape through a dayside magnetopause at $1.5 R_M$. The mean lifetime of a quasi-trapped particle in Mercury's magnetosphere is a few minutes, compared to several days for even very-high-energy particles trapped in the Earth's magnetosphere.

To maintain a continuous population, the large loss rate must be balanced by a compensating rate of supply. The dominant source appears to be the planetward magnetospheric convection in the magnetotail plasma sheet.

11.7.1.3 Mercury's Weak Magnetic Field

Planetary dynamos are thought to operate on the principle of *magnetostrophic balance*, characterized by force balance between the Coriolis force, pressure gradient force, and Lorentz force (equation 11.53). The ratio of the Lorentz force to the Coriolis force (a quantity referred to as the *Elsasser number*, Λ) should therefore be of order 1. Dynamo models for Mercury that include magnetostrophic balance predict magnetic fields similar in strength to the Earth's field. In reality, however, Mercury's observed global magnetic field has a surface field strength $\sim 10^{-2}$ of that of the Earth and a dipole moment $\sim 10^{-4}$ of that of the Earth, and extrapolation of the observed external magnetic field to the dynamo region gives an Elsasser number $\Lambda \sim 10^{-4}$. Mercury's weak magnetic field, therefore, rather than being a simple consequence of a smaller, more slowly-rotating planet, has in fact proven quite difficult to model.

Two non-dynamo models that have been proposed (Wicht et al. 2007 and references therein) are,

1. Remanent crustal magnetism from a now-defunct early dynamo. Runcorn (1975) has shown that “for a shell of any thickness magnetized by a dipole at its centre, the latter field being subsequently removed . . . , the shell gives rise to zero dipole moment, because the polar regions . . . are exactly compensated by the greater volume of more weakly oppositely magnetized material in the equatorial regions,” and “all harmonics of the field external to the shell completely vanish.” E.g., Runcorn (1975) argues that the almost-zero dipole moment of the Moon requires a core dynamo at the time the crust formed.

Runcorn's theorem applies only if the magnetization is linearly proportional to the magnetic field vector, \vec{B} . This is the case if the material is weakly susceptible to magnetization, such as olivine, pyroxene and hematite, but if it is strongly susceptible, such as magnetite or iron, then the magnetization depends nonlinearly on the magnetizing field, and the remanent field outside the shell is not zero (Crary and Bagenal 1998). Lunar and Martian materials are weakly magnetizable so Runcorn's theorem applies, but the situation is less clear for a highly-differentiated planet like Mercury because it depends on how much iron remains in the mantle and crust, and in what form.

For remanent magnetism to be the source of Mercury's global field, therefore, either there would need to be substantial amounts of strongly-magnetizable material in layers outside the core that are below the Curie temperature, or conditions would need to be found to prevent large-scale uniformity in the magnetic response of the crust to the dynamo field, e.g., by eliminating either the polar or the equatorial contribution. It is difficult to see how the latter situation would arise, and the state of iron in Mercury's mantle and lower crust is difficult to evaluate at the present time.

2. Thermoelectric generator. In this model, topographic undulations at the core–mantle boundary give rise to temperature differences that in turn create a thermoelectric emf. Electric currents produced in the core and mantle by this

emf create a weak toroidal (i.e., zonal) magnetic field. If convection in the core is too slow to produce a classical self-sustaining dynamo, its passage through this toroidal field may nevertheless generate electric currents that in turn produce the observed weak, global field. The thermoelectric effects combined with slow convection thus create an electric generator rather than a self-sustaining dynamo.

It is also possible that a magnetostrophic dynamo does exist in the core, but conditions within the core prevent the full magnetic field from being expressed externally (Wicht et al. 2007 and references therein). Thermal conduction through Mercury’s stable lithosphere is expected to be small enough that the heat flow through the core-mantle boundary is subadiabatic. Convection in the outer core would then be from chemical buoyancy due to a chemical gradient (Sect. 9.1.4) rather than thermal buoyancy due to an adiabatic temperature gradient. In this case, most of the outer core could be convectively stable, with convection occurring in only a thin shell outside the inner core. If the dynamo in this shell varies with time, then the changes in the magnetic field will take time to diffuse through the conducting outer core. (See Sect. 8.5.3 for an example of diffusion of magnetic field through a conducting medium.) If the field in the dynamo region is dominated by multipole components, then the rapidly-varying higher-order components will be strongly attenuated in the external field and the external field will be dominated by the weaker, more slowly-varying dipole and quadrupole components, as observed.

Another possibility is that negative feedback from the diamagnetic boundary current, or Chapman-Ferraro current, at the dayside magnetopause (Sect. 11.6.2) limits the strength of the core dynamo (Heyner et al. 2011). Application of the right-hand rule to the Chapman-Ferraro current in Fig. 11.24 shows that the magnetic field of this current is from south to north inside the planet’s core, opposite to the dipole field of the core dynamo. Numerical simulations show that the negative feedback provided by this process can limit the global field of the dynamo to small values, but only if the dynamo is weak to begin with. Mercury is expected to have had a vigorously-convectiong core when it first formed, and therefore a strong primordial dynamo. It is likely that this convection and dynamo died out as Mercury cooled. Later, as cooling continued, the inner core began to form and convection restarted. If the dynamo increased gradually, then negative feedback could possibly prevent the dynamo and global magnetic field from growing past their present low values.

11.7.2 Venus

11.7.2.1 Internal Magnetic Field

No internally generated magnetic field has yet been detected around Venus. The upper limit on the magnetic dipole moment set by the *Magellan* orbiter is 1.5×10^{-5} that of the Earth.

Slow rotation (sidereal rotation period = 243 days, retrograde) has sometimes been cited as the reason why Venus has no observed intrinsic magnetic field, but in fact all of the terrestrial planets have more than enough rotation to create an electric dynamo if the structural and thermal conditions are met (Stevenson 2003 and references therein). However, because Venus is not rotationally distorted, its interior structure cannot be investigated by the evolution of spacecraft orbits. Consequently, the interior structure of Venus is poorly constrained by observations, and it is not known how much, if any, of the core is solid.

If the lack of an observed field arises from a lack of convection in the core, then the two most likely reasons are (1) the core is entirely molten or (2) there is a solid, inner core, but convection is suppressed. A completely molten core could occur if the impurity concentration is greater than in the Earth's core or may simply be a result of the lower central pressure compared to the Earth, because of the smaller planetary mass and radius (Stevenson et al. 1983).

Even if there is a solid, inner core, convection may be suppressed in the outer core (Nimmo 2002). The absence of plate tectonics, which is the dominant heat flow mechanism in the Earth's lithosphere, reduces the heat flow to space from Venus' interior (Sects. 9.2.7 and 9.2.8). This results in a hotter mantle and therefore a smaller temperature gradient in the outer core. If this temperature gradient is subadiabatic, then there will be no thermal convection.

If the catastrophic resurfacing model (Milone and Wilson 2014, Sect. 9.2.8) is correct, then low heat flow may alternate with periods of high heat flow. In this case, the absence of a global magnetic field may be a temporary, or possibly cyclic, property of Venus.

11.7.2.2 Induced Magnetosphere

Despite the absence of an internally driven magnetosphere, the interaction of the solar wind and IMF with Venus' ionosphere creates a magnetic obstacle that deflects the solar wind around the planet. Figure 11.41 illustrates some of the processes involved. The IMF can be regarded as frozen into the solar wind plasma and carried toward Venus at the solar wind velocity, \vec{v}_{SW} .

The motion of the IMF toward Venus at velocity \vec{v}_{SW} is equivalent to the motion of the Venus ionospheric conductor through the IMF at velocity $-\vec{v}_{\text{SW}}$: a motional electric field and current are induced in the ionosphere as shown in Fig. 11.41. The induced magnetic field, \vec{B}_{IND} , adds to \vec{B}_{IMF} on the sunward side of this current, increasing the magnetic field strength above the ionosphere, and opposes it on the side toward Venus. Thus, the magnetic field pressure

$$P_{\text{IMF}} = \frac{B_{\text{IMF}}^2}{8\pi}$$

increases in the region above the ionosphere, while the ionosphere is compressed by the incoming solar wind plasma and IMF. These processes are evident in passages

Fig. 11.41 The flow of IMF towards the ionospheric conductor induces a northwards current in the ionosphere for the IMF direction shown

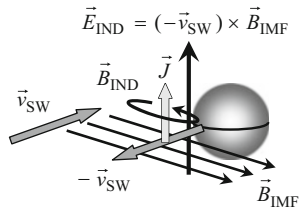
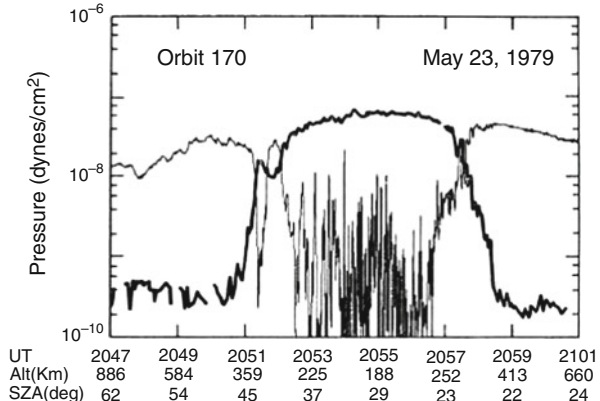


Fig. 11.42 Magnetic field pressure (light lines) and ionospheric plasma pressure (heavy lines) vs. altitude from one passage of *Pioneer Venus* through the midday ionosphere (Elphic et al. 1980, Fig. 6, p. 7683; copyright 1980, American Geophysical Union. Reproduced by permission of American Geophysical Union.)

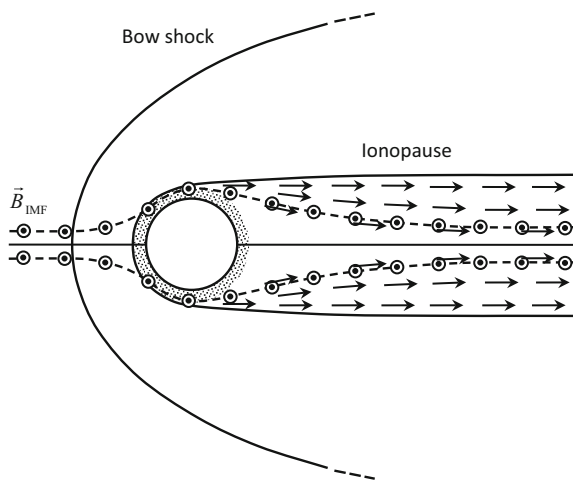


of *Pioneer Venus* through the midday ionosphere: with increasing altitude, the ionospheric electron density drops to near zero in the same region where the magnetic field strength increases from near zero to a value somewhat elevated above that far from Venus (see Fig. 12, p. 892, Russell and Vaisberg 1983). Balance is achieved when the inward force due to the magnetic pressure at the ionopause, the outer boundary of the ionosphere, equals the outward force due to the ionospheric plasma pressure. This is illustrated in Fig. 11.42, where magnetic field and ionospheric plasma pressure measured by *Pioneer Venus* are plotted against altitude above the surface of Venus.

If the ionosphere were superconducting, the IMF would be completely excluded, and the magnetic field would be zero below the ionopause. Instead, the spikes in Fig. 11.42 suggest that magnetic field enters the Venus atmosphere in localized “flux ropes.”

The altitude of the ionopause depends on the solar wind strength. When the solar wind strength is low, the ionopause is at high altitudes where individual ions follow their own trajectories. The result is a diamagnetic current similar in physical cause to the Earth’s boundary current, except that instead of solar wind ions moving toward the right into an internally generated magnetic field in Fig. 11.24, ionospheric ions in Fig. 11.41 move toward the left into the IMF (in the solar wind frame). Because the IMF is horizontal and eastward in the figure, the diamagnetic current is northward.

Fig. 11.43 IMF flow around Venus, viewed from the plane of the local IMF. The *circled dots* show magnetic field lines oriented toward the observer, and the arrows show the flow of low-energy ionospheric ions. Based on Russell and Vaisberg (1983), Fig. 18, p. 901



When the solar wind strength is high, the ionopause descends to lower altitudes and higher densities, where collisions occur. Whereas diamagnetic currents are dissipationless, collisions produce dissipation, and the current becomes an actual flow of charge in a resistive medium.

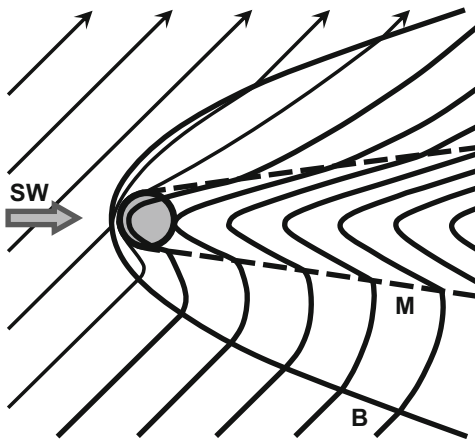
With the IMF effectively excluded from the ionosphere, the solar wind is deflected northward and southward past the planet, carrying the IMF with it (Figs. 11.42 and 11.43), forming a magnetocavity downwind from the planet where solar wind ions are excluded. The magnetic polarity in this cavity varies with the orientation of the IMF, unlike the magnetotails of planets with intrinsic magnetic fields. As with internally generated magnetospheres, a bow shock forms where the solar wind is slowed to subsonic speeds.

Solar rotation causes the outwardly-travelling IMF to form a spiral pattern around the Sun (referred to as the *Parker spiral*), in which the angle that the IMF makes with the radial direction from the Sun increases with distance from the Sun. This angle is 35° at Venus, 45° at the Earth, and 57° at Mars. This angle creates an asymmetry in Venus' magnetotail magnetic field, as shown in Fig. 11.43, with the field being stronger on one side of the tail than on the other.

In Fig. 11.43, the components of the magnetic field parallel to the magnetotail axis are oppositely-directed, and give rise to a cross-tail current and plasma sheet in a manner analogous to those in the Earth's magnetotail (Sect. 11.6.6). The induced electric field and current are directed out of the page (perpendicular to the magnetic field lines (Fig. 11.44)) for the magnetic field orientation shown in Fig. 11.43.

In an *induced magnetosphere*, such as that at Venus, the magnetic field direction is controlled by the direction of the IMF. Thus, processes that require the IMF to oppose the direction of the planetary field, including dayside reconnection, tailward flux transport, and magnetotail flux loading (Sect. 11.6.8), are absent in an induced magnetosphere. It was therefore somewhat surprising when *Venus Express* observed the magnetic and plasma-density signatures of plasmoids travelling

Fig. 11.44 IMF flow around Venus, viewed from above and perpendicular to the plane of the local IMF. SW solar wind direction; B bow shock; M magnetopause. Based on McComas et al. (1986), Fig. 1



toward the planet in Venus' magnetic tail (Zhang et al 2012), because in the case of the Earth and Mercury, plasmoids are created by magnetic reconnection in the magnetotail in response to flux loading. These plasmoids occur $\sim 1\text{--}3 R_V$ down the tail from the planetary surface (where R_V is the radius of Venus) as the interplanetary field lines slip past Venus, and appear to be fairly common. The processes causing the reconnection are not yet clear.

11.7.2.3 Atmospheric Loss Rates

Measurements by *Pioneer Venus Orbiter* near solar maximum and more recently by *Venus Express* near solar minimum have shown that atmospheric loss from Venus is dominated by nonthermal escape of H^+ and O^+ . The loss rates from *Venus Express* are $7.1 \times 10^{24} \text{ s}^{-1}$ for H^+ and $2.7 \times 10^{24} \text{ s}^{-1}$ for O^+ (Fedorov et al. 2011), with an estimated factor of 2 uncertainty in each value. The major ion acceleration processes are, (i) ion pick-up by the convecting magnetic field, (ii) magnetohydrodynamic plasma instabilities at the induced magnetosphere boundary, and (iii) polarization electric fields (i.e., electric fields caused by charge separations) oriented radially at low altitudes in the nightside ionosphere. The ions flow away from the planet primarily along the magnetotail plasma sheet and magnetotail boundary.

The hydrogen loss rate by Jeans escape of $2.5 \times 10^{19} \text{ s}^{-1}$ (Sect. 11.2.5.1) is negligible compared to the nonthermal rate above.

Neutral H and O also escape. Hot (i.e., energetic) H atoms are produced with sufficient energy to escape by (11.28)–(11.31), (11.34), (11.36) and other reactions. Hot O with sufficient energy to escape is produced by sputtering, as follows (Lammer et al. 2006). Planetary oxygen atoms on the dayside are ionized, picked up by the IMF and accelerated toward the planet. They then undergo charge exchange reactions and become hot, neutral O travelling toward the planet.

Subsequent collisions with cold O can create outward-moving O with enough energy to escape. Loss rates of neutral H and O are 50 % and 25 %, respectively, of the H and O ion loss rates (Barabash et al. 2007). Pickup ions from the hot H and O coronae also contribute to the atmospheric loss, but these rates are much smaller than those within the tail.

The loss of H and O from Venus' atmosphere is equivalent to a loss of water, so the ratio of the number of H atoms that escape per second to the number of O atoms would be expected to be 2:1. The observed numbers, above, give a ratio of $(1.5 \times 7.1 \times 10^{24} \text{ s}^{-1})/(1.25 \times 2.7 \times 10^{24} \text{ s}^{-1}) = 3.2 : 1$. Given the estimated factor of 2 uncertainties, this result is consistent with a 2:1 ratio.

The solar wind-ionosphere interaction on Venus has contributed significantly to atmospheric loss over the life of the planet. The dominant processes are (1) charge-exchange reactions and subsequent ion pick up by the IMF and (2) sputtering. In the former, solar wind ions and electrons ionize atomic H and O in the exosphere of Venus (e.g., $\text{O} + \text{e}^- \rightarrow \text{O}^+ + 2\text{e}^-$), and the resulting H^+ and O^+ are picked up by the IMF and carried off in the solar wind flow around the planet. In the latter, fast solar wind ions collide with neutral atoms in the exosphere or near the exobase. In the solar wind impact region, a cascade of collisions results in some atmospheric neutral atoms moving outward; in the solar wind flow around the planet, motion is tangential and a single collision can eject the atmospheric neutral.

11.7.3 Mars

11.7.3.1 Martian Magnetosphere

Of the many spacecraft to have visited Mars, the most accurate magnetic field measurements have been made by *Mars Global Surveyor (MGS)*. *MGS* used aerobraking to refine its initial, highly elliptical orbit to a final, circular orbit at 400 km altitude, and in this process dipped into the Martian atmosphere, to altitudes as low as 101 km, to slow its orbital speed. In so doing, it became the first spacecraft to carry magnetometers below the Martian ionosphere, where the magnetic fields associated with the Martian crust and interior are stronger and the magnetometers are shielded from the external magnetic fields of the solar wind-ionosphere interaction (Sect. 11.7.2.2). Because of a solar panel anomaly, NASA extended the aerobraking period to ~ 18 months to reduce the force on the solar panels, allowing magnetometer readings to be taken over ~ 20 % of the Martian surface to much greater accuracy and higher resolution than is possible from the final 400 km mapping altitude.

To the limit of observations, Mars has no global magnetic field. *MGS* established an upper limit of $2 \times 10^{17} \text{ A/m}^2$ for a global dipole moment, corresponding to a magnetic field strength at the Martian equator of 0.5 nT, about 10^{-6} that of the

Earth (Acuña et al. 2001); but the observations are in fact equally well represented by a dipole moment of zero. The interaction of the Martian atmosphere and ionosphere with the solar wind and IMF thus creates an induced magnetosphere, similar to that at Venus (Sect. 11.7.2.2).

A surprising and significant discovery by *MGS* is the existence of intense, localized remanent magnetism in the Martian crust (Connerney et al. 1999). Although some anomalies have been found in the younger, northern lowlands, by far the majority and the strongest occur in the ancient southern highlands. These anomalies appear in the *MGS* data as linear, approximately parallel, east–west-trending features up to 1,000–2,000 km in length and ~200 km in width, of alternating magnetic polarity. The 200 km width is imposed by the resolution of the *MGS* data, so in fact there could be finer lineations. Magnetic field strengths are up to ~1,500 nT at periapsis (≥ 100 km altitude) and ~200 nT at the final mapping altitude of 400 km. These fields dwarf their terrestrial counterparts: the strongest crustal magnetic anomalies on the Earth produce variations of ± 10 nT in the dipole field at 400 km altitude. The dipole moment of (any) one 2,000 km long anomaly 200 km wide is an order of magnitude greater than that of the Kursk magnetic anomaly in Russia, one of the largest on the Earth.

The intense magnetization is consistent with the fact that the iron content of the Martian crust is much higher than on the Earth (17 % in the soil at the Pathfinder landing site and 15–30 % in Martian meteorites, compared to 1 % on the Earth), but it also requires a relatively intense inducing field, similar to or greater than that of the present-day Earth. The most likely model for this field is a global magnetic dipole created by an electric dynamo in a molten core. The timescale of this dynamo can be estimated from the fact that, within the southern highlands, magnetization tends to be absent in the material covering the large impact basins such as Argyre and Hellas. These are believed to have formed within the first 300 My of the accretion of Mars, suggesting that the dynamo died out during the earliest epoch on Mars. The scarcity and weakness of anomalies in the northern lowlands also suggests that the dynamo died out before the formation of the main north-south dichotomy of Mars; but it then becomes difficult to account for the anomalies that do exist there.

The most straightforward explanation for the linearity and alternating polarity of the anomalies is that they formed during an early period of plate tectonics, in which crustal spreading was accompanied by reversals of the putative Martian magnetic dipole as the spreading crust cooled below the Curie point. Although alternative explanations have not been ruled out, this model has an advantage of self-consistency in that plate tectonics increases the heat flux through the crust and thus the probability of core convection and an electric dynamo (Sect. 11.7.2.1). One requirement of the crustal spreading model is a symmetry axis analogous to mid-ocean ridges where new crust is being created on the Earth. None have yet been discovered, but large areas of the highlands have been reworked by impacts, thermal events, and fracturing, and such features may not have survived.

Mars is thus unique in the solar system in having both an induced magnetosphere and intrinsic magnetic fields associated with the crust. These crustal fields are strong enough to create small, magnetosphere-like cavities extending beyond

400 km altitude (the orbit of *Mars Global Surveyor*), and have magnetopause-like boundaries that exclude the solar wind and IMF from the cavity. These cavities rotate with the planet every 24 h, dynamically altering the induced magnetospheric structure of Mars.

The magnetic anomalies give rise to aurorae bright enough to be visible to the naked eye for an observer on the Martian surface (Lundin et al. 2007). The anomalies create a multipole magnetic field with closed field lines over the anomalies and open, cusp-like field lines between them. The aurorae occur \sim 50–80 km above the surface on “semi-open” flux tubes along the boundaries between the closed and open field lines, as do aurorae on the Earth. Field-aligned currents have been observed in these flux tubes, consisting of downward-accelerated electrons and upward-accelerated ionospheric ions (O^+ , O_2^+ and CO_2^+). Precipitation of the electrons into the Martian atmosphere produces the aurorae.

Field-aligned currents require an acceleration mechanism in the magnetosphere to act as a source of emf. In the terrestrial magnetosphere, the acceleration is provided by magnetic reconnection across the plasma sheet in the magnetotail (Sect. 11.6.8), and Halekas et al. (2009) report 26 such events strong enough to have clear signatures in *MGS* magnetometer data. Given the complex interplay of solar wind, crustal, and draped magnetospheric field lines, it would not be surprising if magnetic reconnection occurs commonly at Mars and provides a source for the aurorae.

11.7.3.2 Atmospheric Loss Mechanisms

Atmospheric loss from Mars is dominated by loss of hydrogen and oxygen. Hydrogen loss in turn is dominated by Jeans escape, at a rate of $\sim 2.2 \times 10^{26} \text{ s}^{-1}$ (Sect. 11.2.5.1). For comparison, the next important hydrogen loss mechanism is ion pickup, with a rate of $1.2 \times 10^{25} \text{ s}^{-1}$ for each of H^+ and H_2^+ (Lammer et al. 2003).

The rate of loss of H is set by the rate of supply of H_2 to the exosphere from below, which in turn is set by chemical reactions involving the dissociation of water. The loss mechanisms for hydrogen and oxygen are in fact mutually self-limiting: two H escape for each O (Lammer et al. 2003, and references therein). In effect, water molecules are being lost to space.

The stoichiometric 2:1 ratio in the loss of H and O requires an oxygen loss rate of $\sim 1.1 \times 10^{26} \text{ s}^{-1}$. (*Stoichiometric ratio* refers to the component elements being present in the exact proportion indicated by the chemical formula for the compound, in this case, H_2O .) Lammer et al. (2003) calculate an O^+ ion pickup rate of $3 \times 10^{24} \text{ s}^{-1}$. Combined with dissociative recombination [via (11.21)] and sputtering rates from the literature of $5.0 \times 10^{24} \text{ s}^{-1}$ and $4.3 \times 10^{23} \text{ s}^{-1}$, respectively, they obtain a total oxygen loss rate of $8.4 \times 10^{24} \text{ s}^{-1}$. This is more than a factor of 20 lower than required by the stoichiometric ratio. Another sink is therefore required for oxygen, and the most likely candidate appears to be oxidation of the regolith. Meteoric gardening (excavation of fresh regolith and burial of older, oxidized regolith) is suspected to be sufficient to maintain an active sink.

With a loss rate of 1.1×10^{26} molecules s⁻¹ over the life of Mars ($\sim 4.6 \times 10^9$ y), a surface layer of water ~ 2.5 m deep would have been lost. Greater solar UV flux in the early solar system might increase this to ~ 20 m. In fact, various Martian surface features (cf. Sect. 9.3.3 of Milone and Wilson 2014) may indicate a layer of water as much as 500 m deep when Mars was young, so other loss mechanisms may also have been important in the past.

The present Martian atmosphere contains only $\sim 1/10,000$ as much water as there is in the Earth's atmosphere. This amount is enough to cover the surface of Mars with a uniform layer of water only 10 μm thick. This has not always been so: The amount of water in the north polar remnant ice cap is $\sim 10^5$ times greater.

Challenges

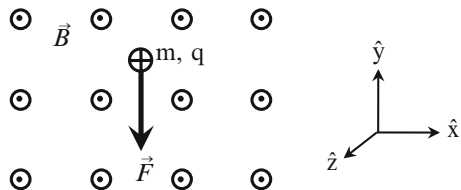
- [11.1] In (11.26), derive $\lambda_J = r_x/H_x$ and $\lambda_J = (v_{esc}/v_{th})^2$ from the expression $\lambda_J = GMm/(kT_x r_x)$.
- [11.2] Derive (11.93) from (11.92). [Hint: Electric current equals the amount of charge passing a given point per second; how is the current associated with a gyrating particle related to the charge of the particle and the period of the gyromotion?]
- [11.3] Derive (11.98) from (11.76) and other previous results.
- [11.4] Justify, using $\vec{F}_B = q\vec{v} \times \vec{B}$, the statement preceding (11.99) that the kinetic energy of the particle is constant. [A descriptive answer is acceptable, but the description should be physically precise.]
- [11.5] Spacecraft orbiting through the trapping region of a planetary magnetosphere, such as the Earth's Van Allen radiation belts, do not necessarily orbit in the plane of the magnetic equator; thus, they sample the magnetosphere at a range of magnetic latitudes. For uniformity of data, measured pitch angles are usually referred to the magnetic equator. If the spacecraft measures a pitch angle, α , for a particle at a location away from the magnetic equator where the magnetic field strength is B , and if *on the same field line* the magnetic field strength at the magnetic equator is B_0 , show that the pitch angle, α_0 , of the particle as it crosses the magnetic equator is given by

$$\sin^2 \alpha_0 = \frac{B_0}{B} \sin^2 \alpha$$

[Hint: μ_B and Φ_B are constants of the motion. Express the pitch angles in terms of v_\perp at B and v_\perp^0 at B_0 , and use (11.93) and (11.97).]

- [11.6] The loss cone is approximately 3° for particles on the geomagnetic equator at $6 R_E$ above the Earth's surface, i.e., particles of this pitch angle mirror at ionospheric heights:
 - What is the mirror ratio, i.e., the ratio of the magnetic field strength at the ionosphere to that at the geomagnetic equator, along this field line? [Hint: Refer to problem 11.4. What is the pitch angle at the mirror point?]

Fig. 11.45



- b. If particles are injected with an initially isotropic distribution of pitch angles at $6 R_E$ on the geomagnetic equator, what fraction of these particles are precipitated?
- [11.7] Equations (11.77) and (11.79) in Sect. 11.5.6 give, respectively, the $\vec{F} \times \vec{B}$ drift velocity, \vec{v}_D , and its more commonly used form, the $\vec{E} \times \vec{B}$ drift velocity. The purpose of this problem is to derive (11.77) and (11.79).

Figure 11.45 shows a uniform magnetic field, \vec{B} , out of the page. In addition to any magnetic forces, all charges in this region also feel a downward force, \vec{F} , of external origin (e.g., gravitational or electrical) of uniform magnitude regardless of position. (\vec{F} is unrelated to \vec{B} .)

- a. Suppose you take hold of the charge shown above and run with a constant (vector) velocity, \vec{v} , holding tightly onto the charge so it cannot execute gyromotion. In what *direction* would you have to run so that the total force (or net force) on the particle is zero? Draw a vector diagram showing and labelling \vec{B} , \vec{v} , and all forces. Then write down the vector equation relating \vec{F} , \vec{v} , and \vec{B} . (In this and the other parts, below, keep careful track of minus signs.)
- b. Evaluate the quantity $(\vec{v} \times \vec{B}) \times \vec{B}$ for this situation, using the unit vectors shown above. Express your answer in terms of a single unit vector, then rewrite your answer to express the quantity $(\vec{v} \times \vec{B}) \times \vec{B}$ in terms of \vec{v} .
- c. Obtain (11.77) from your answers to parts a and b.
- d. Now assume that the force, \vec{F} , is caused by an electric field vertically downward in the reference frame of the diagram (i.e., $\vec{F} = q\vec{E}$). In *your* reference frame, the force on a stationary particle is zero. It follows that, by running, you have placed yourself in a reference frame in which the electric field is zero: if you let go of the particle, it will remain at rest in your reference frame, so evidently there is no electric field.

If a particle is now released at rest in the original reference frame of the diagram, what initial velocity will *you* see for this particle? What subsequent motion do you expect to see for this particle? (Remember, in your reference frame there is only a magnetic field.) By extension, what subsequent motion would an observer see who is at rest in the reference frame of the diagram? What is the $\vec{E} \times \vec{B}$ drift velocity of the guiding center in the reference frame of the diagram? (Also check that the drift velocity *is* in the direction of $\vec{E} \times \vec{B}$.)

References

- Acuña, M.H., Connerney, J.E.P., Wasilewski, P., Lin, R.P., Mitchell, D., Anderson, K.A., Carlson, C.W., McFadden, J., Reme, H., Mazelle, C., Vignes, D., Bauer, S.J., Cloutier, P., Ness, N.F.: Magnetic field of Mars: summary of results from the aerobraking and mapping orbits. *J. Geophys. Res.* **106**(E10), 23403–23417 (2001)
- Anderson, B.J., Johnson, C.L., Korth, H., Purucker, M.E., Winslow, R.M., Slavin, J.A., Solomon, S.C., McNutt Jr., R.L., Raines, J.M., Zurbuchen, T.H.: The global magnetic field of Mercury from MESSENGER orbital observations. *Science* **333**, 1859–1862 (2011)
- André, M., Yau, A.: Theories and Observations of Ion Energization and outflow in the High latitude Magnetosphere. *Space Sci. Rev.* **80**, 27–48 (1997)
- Angelopoulos, V.: The THEMIS Mission. *Space Sci. Rev.* **141**, 5–34 (2008)
- Barabash, S., Fedorov, A., Sauvaud, J.-J., Lundin, R., Russell, C.T., Futaana, Y., Zhang, T.L., Andersson, H., Brinkfeldt, K., Grigoriev, A., Holmström, M., Yamauchi, M., Asamura, K., Baumjohann, W., Lammer, H., Coates, A.J., Kataria, D.O., Linder, D.R., Curtis, C.C., Hsieh, K.C., Sandel, B.R., Grande, M., Gunell, H., Koskinen, H.E.J., Kallio, E., Riihelä, P., Säles, T., Schmidt, W., Kozyra, J., Krupp, N., Fränz, M., Woch, J., Luhmann, J., McKenna-Lawlor, S., Mazelle, C., Thocaven, J.-J., Orsini, S., Cerulli-Irelli, R., Mura, M., Milillo, M., Maggi, M., Roelof, E., Brandt, P., Szego, K., Wintingham, J.D., Fahrm, R.A., Scherer, J., Sharber, J.R., Wurz, P., Bochsler, P.: The loss of ions from Venus through the plasma wake. *Nature* **450**, 650–653 (2007)
- Cahill Jr., L.J.: Inflation of the inner magnetosphere. In: Carovillano, R.L., McClay, J.F., Radoski, H.R. (eds.) *Physics of the Magnetosphere*, pp. 263–270. Reidel, Dordrecht (1968)
- Chen, R.H., Cravens, T.E., Nagy, A.F.: The Martian ionosphere in light of the Viking observations. *J. Geophys. Res.* **83**, 3871–3876 (1978)
- Chaufray, J.Y., Bertaux, J.L., Leblanc, F., Quémérais, E.: Observation of the hydrogen corona with SPICAM on Mars Express. *Icarus* **195**, 598–613 (2008)
- Connerney, J.E.P., Acuña, M.H., Wasilewski, P., Ness, N.F., Reme, H., Mazelle, C., Vignes, D., Lin, R.P., Mitchell, D., Cloutier, P.: Magnetic lineations in the ancient crust of Mars. *Science* **284**(5415), 794–798 (1999)
- Crary, F.J., Bagenal, F.: Remanent ferromagnetism and the interior structure of Ganymede. *J. Geophys. Res.* **103**, E11, 25,757–25,773 (1998)
- Elphic, R.C., Russell, C.T., Slavin, J.A., Brace, L.H.: Observations of the dayside ionopause and ionosphere of Venus. *J. Geophys. Res.* **85**, 7679–7696 (1980)
- Fedorov, A., Barabash, S., Sauvaud, J.-A., Futaana, Y., Zhang, T.L., Lundin, R., Ferrier, C.: Measurements of the ion escape rates from Venus for solar minimum. *J. Geophys. Res.* **116**, A07220 (2011). doi:[10.1029/2011JA016427 \(9 pages\)](https://doi.org/10.1029/2011JA016427)
- Griffiths, D.J.: *Introduction to Electrodynamics*, 3rd edn. Prentice-Hall, Upper Saddle River, NJ (1999)
- Halekas, J.S., Eastwood, J.P., Brain, D.A., Phan, T.D., Øieroset, M., Lin, R.P.: In situ observations of reconnection hall magnetic fields at Mars: evidence for ion diffusion region encounters. *J. Geophys. Res.* **114**, A11204 (2009). doi:[10.1029/2009JA014544 \(18 pages\)](https://doi.org/10.1029/2009JA014544)
- Heyner, D., Wicht, J., Gómez-Pérez, N., Schmitt, D., Auster, H.-U., Glassmeier, K.-H.: Evidence from numerical experiments for a feedback dynamo generating Mercury’s magnetic field. *Science* **334**, 1690–1693 (2011)
- Hunten, D.M.: Thermal and nonthermal escape mechanisms for terrestrial bodies. *Planet. Space Sci.* **30**(8), 773–783 (1982)
- Hunten, D.M., Pepin, R.O., Walker, J.C.G.: Mass fractionation in hydrodynamic escape. *Icarus* **69**, 532–549 (1987)
- Knudsen, D.J.: Private communication (2013)
- Korte, M., Constable, C.: Improving geomagnetic field reconstructions for 0–3 ka. *Phys. Earth Planet. In.* **188**, 247–259 (2011)
- Iribarne, J.V., Cho, H.-R.: *Atmospheric Physics*. Reidel, Dordrecht (1980)

- Lammer, H., Lichtenegger, H.I.M., Biernat, H.K., Erkaev, N.V., Arshukova, I.L., Kolk, C., Gunell, H., Lukyanov, A., Holmstrom, M., Barabash, S., Zhang, T.L., Baumjohann, W.: Loss of hydrogen from the upper atmosphere of Venus. *Planetary and Space Science* **54**, 1445–1456 (2006)
- Lammer, H., Lichtenegger, H.I.M., Kolb, C., Ribas, I., Guinan, E.F., Abart, R., Bauer, S.J.: Loss of water from Mars: implications for the oxidation of the soil. *Icarus* **165**, 9–25 (2003)
- Lundin, R., Winningham, D., Barabash, S., Frahm, R., Brain, D., Nilsson, H., Holmström, M., Yamauchi, M., Sharber, J.R., Sauvaud, J.-A., Fedorov, A., Asamura, K., Hayakawa, H., Coates, A.J., Soobiah, Y., Curtis, C., Hsieh, K.C., Grande, M., Koskinen, H., Kallio, E., Kozyra, J., Woch, J., Fraenz, M., Luhmann, J., McKenna-Lawler, S., Orsini, S., Brandt, P., Wurz, P.: Auroral plasma acceleration above Martian magnetic anomalies. *Space Sci. Rev.* **126**, 333–354 (2007)
- Lyatsky, W., Khazanov, G.V., Slavin, J.A.: Alfvén Wave Reflection model of field-aligned currents at Mercury. *Icarus* **209**, 40–45 (2010)
- McComas, D.J., Spence, H.E., Russell, C.T., Saunders, M.A.: The average magnetic field draping and consistent plasma properties of the Venus magnetotail. *J. Geophys. Res.* **91**(A7), 7939–7953 (1986)
- Milan, S.E., Provan, G., Hubert, B.: Magnetic flux transport in the Dungey Cycle: a survey of dayside and nightside reconnection rates. *J. Geophys. Res.* **112**, A01209 (2007). doi:[10.1029/2006JA011642](https://doi.org/10.1029/2006JA011642) (13 pages)
- Milone, E.F., Wilson, W.J.F.: Solar System Astrophysics: Planetary Atmospheres and the Outer Solar System, 2nd edn. Springer, New York (2014)
- Nair, H., Allen, M., Anbar, A.D., Yung, Y.L.: A photochemical model of the Martian atmosphere. *Icarus* **111**, 124–150 (1994)
- Nimmo, F.: Why does Venus lack a magnetic field? *Geology* **3**(11), 987–990 (2002)
- Olson, P., Deguen, R.: Eccentricity of the geomagnetic dipole caused by lopsided inner core growth. *Nature Geoscience* **5**, 565–569 (2012)
- Parks, G.K.: Physics of Space Plasmas, an Introduction. Addison-Wesley, Redwood City, CA (1991)
- Parks, G.K.: Physics of Space Plasmas, an Introduction. 2nd ed. Harper-Collins, Perseus Books, Reading, MA (2003)
- Runcorn, S.K.: An ancient lunar magnetic dipole field. *Nature* **253**, 701–703 (1975)
- Russell, C.T., Vaisberg, O.: The interaction of the solar wind with Venus. In: Hunten, D.M., Colin, L., Donahue, T.M., Moroz, V.I. (eds.) *Venus*, pp. 873–879. University of Arizona Press, Tucson, AZ (1983)
- Schrivner, D., Trávníček, P.M., Anderson, B.J., Ashour-Abdalla, M., Baker, D.N., Benna, M., Boardsen, S.A., Gold, R.E., Hellinger, P., Ho, G.C., Korth, H., Krimigis, S.M., McNutt Jr., R.L., Raines, J.M., Richard, R.L., Slavin, J.A., Solomon, S.C., Starr, R.D., Zurbuchen, T.H.: Quasi-trapped ion and electron populations at Mercury. *Geophys. Res. Lett.* **38**, L23103 (2011). doi:[10.1029/2011GL049629](https://doi.org/10.1029/2011GL049629) (6 pages)
- Sergeev, V.A., Angelopoulos, V., Nakamura, R.: Recent advances in understanding substorm dynamics. *Geophys. Res. Lett.* **39**, L05101 (2012). doi:[10.1029/2012GL050859](https://doi.org/10.1029/2012GL050859) (10 pages)
- Silsbee, H., Vestine, E.: Geomagnetic bays, their frequency and current systems. *Terr. Magn. Atmos. Electr.* **47**, 195–208 (1942)
- Slavin, J.A., Anderson, B.J., Baker, D.N., Benna, M., Boardsen, S.A., Gold, R.E., Ho, G.C., Imber, S.M., Korth, H., Krimigis, S.M., McNutt Jr., R.L., Raines, J.M., Sarantos, M., Schriver, D., Solomon, S.C., Trávníček, P., Zurbuchen, T.H.: MESSENGER and Mariner 10 Flyby observations of magnetotail structure and dynamics at Mercury. *J. Geophys. Res.* **117**, A01215 (2012). doi:[10.1029/2011JA016900](https://doi.org/10.1029/2011JA016900) (4 pages)
- Slavin, J.A., Anderson, B.J., Baker, D.N., Benna, M., Boardsen, S.A., Gloeckler, G., Gold, R.E., Ho, G.C., Korth, H., Krimigis, S.M., McNutt Jr., R.L., Nittler, L.R., Raines, J.M., Sarantos, M., Schriver, D., Solomon, S.C., Starr, R.D., Trávníček, P.M., Zurbuchen, T.H.: MESSENGER observations of extreme loading and unloading of Mercury’s magnetic tail. *Science* **329**, 665–668 (2010)

- Stevenson, D.J.: Planetary magnetic fields. *Earth Planet. Sci. Lett.* **208**, 1–11 (2003)
- Stevenson, D.J., Spohn, T., Schubert, G.: Magnetism and thermal evolution of the terrestrial planets. *Icarus* **54**, 466–489 (1983)
- Vasyliūnas, V.M., Song, P.: Meaning of ionospheric Joule heating. *J. Geophys. Res.* **110**, A02301 (2005). doi:[10.1029/2004JA010615 \(8 pages\)](https://doi.org/10.1029/2004JA010615)
- Wicht, J., Mandea, M., Takahashi, F., Christensen, U.R., Matsushima, M., Langlais, B.: The origin of Mercury's internal magnetic field. *Space Sci. Rev.* **132**, 261–290 (2007)
- Zhang, T.L., Lu, Q.M., Baumjohann, W., Russell, C.T., Fedorov, A., Barabash, S., Coates, A.J., Du, A.M., Cao, J.B., Nakamura, R., Teh, W.L., Wang, R.S., Dou, X.K., Wang, S., Glassmeier, K.H., Auster, H.U., Balikhin, M.: Magnetic reconnection in the near Venusian magnetotail. *Science* **336**, 567–570 (2012)

Chapter 12

The Giant Planets

The giant planets contain the bulk of the angular momentum of the solar system and the dominant mass among the planets. The magnetosphere of the Jovian system dwarfs the Sun in size. Jupiter, Saturn, and Neptune radiate considerably more energy than they receive from the Sun. The physical and orbital properties of the giant planets are summarized in Table 12.1 excerpted from Cox (2000), the 2012 Astronomical Almanac, Tholen et al. (2000), and other sources, including the NASA-Goddard Space Flight Center website links at <http://nssdc.gsfc.nasa.gov/planetary/factsheet/>.

It is not difficult to imagine a scenario in which a much more massive object than Jupiter, our solar system's largest planet, is a binary star companion to the Sun. In such a case, one would think that planets either would be ejected from the inner system entirely or perhaps find a niche at one of the stable Lagrangian points (Milone and Wilson 2014, Sect. 3.3). Jovian-type planets thus far detected in extra-solar planetary systems will be considered in Chap. 16; it turns out, though, that planets are being found in binary and multiple star systems.

The giant planets have been visited by eight spacecraft, with one more *en route*:

Pioneer 10. Jupiter flyby Dec 1973.

Pioneer 11. Flybys: Jupiter, Dec 1974; Saturn, Sep 1979.

Voyager 1. Flybys: Jupiter, Mar 1979; Saturn, Nov 1980.

Voyager 2. Flybys: Jupiter, Jul 1979; Saturn, Aug 1981; Uranus, Jan 1986; Neptune, Aug 1989.

Ulysses. Jupiter flybys Feb 1992 and 2003–2004.

Galileo. Jupiter orbit Dec 1995–Sep 2003. *Galileo* also released a probe which entered Jupiter's atmosphere on Dec 7, 1995.

Cassini. Jupiter flyby Dec 2000; Saturn orbit insertion Jul 2004. *Cassini* also released the *Huygens* probe which landed on the surface of Titan, Saturn's largest satellite, on Jan 14, 2005.

New Horizons. Jupiter flyby Feb 2007.

Juno. *En route*; Jupiter orbit insertion Aug 2016.

Table 12.1 Giant planets data

Property/planet	Jupiter	Saturn	Uranus	Neptune
<i>Mean orbital data^a</i>				
Mean distance (au)	5.203	9.537	19.191	30.069
Eccentricity	0.0484	0.0542	0.0472	0.0086
Inclination (to the ecliptic plane)	1°305	2°484	0°770	1°769
Sidereal period (J y)	11½856	29½424	83½747	163½723
<i>Physical data</i>				
Mass (kg) (in Earth masses)	1.8981(2) × 10 ²⁷	5.6831(6) × 10 ²⁶	8.6809(9) × 10 ²⁵	1.0241(2) × 10 ²⁶
Equatorial radius (km) (in Earth radii)	317.828 71,492(4)	95.161 60,258(4)	14.536 25.559(4)	17.148 24.764(15)
Oblateness (flattening) ^b	11.2089	9.4491	4.0073	3.8826
J_2^c	0.0644874	0.097962	0.022927	0.017081
J_3^c	0.014736(1)	0.016298(10)	0.003343	0.003411(10)
J_4^c	—	—	—	—
J_5^c	—	—	—	2.6(+12/-20) × 10 ⁻⁵
J_6^c	3.1(20) × 10 ⁻⁵	1.03(50) × 10 ⁻⁴	—	—
Mean density ^d (kg/m ³)	1,327	687.1	1,270	1,638
Equatorial surface gravity (m/s ²)	24.79	10.44	8.87	11.0
Equatorial escape velocity (km/s)	59.5	35.6	21.4	23.6
<i>Photometric data</i>				
$V_{\text{opposition}}$ (mean distances)	-2.70	+0.67	+5.52	+7.84
$(B - V)$	+0.83	+1.04	+0.56	+0.41
$(U - B)$	+0.48	+0.58	+0.28	+0.21

<i>Radiative energy data</i>				
Visual albedo	0.52	0.47	0.51	0.41
(geometric)				
Bolometric albedo	0.27 ± 0.01	0.24 ± 0.01	0.22 ± 0.05	0.22 ± 0.05
(geometric) ^e				
Bolometric albedo	0.343 ± 0.032	0.342 ± 0.030	0.300 ± 0.049	0.290 ± 0.067
(Bond) ^e				
Absorbed power	49.82 ± 2.43	10.18 ± 0.46	0.521 ± 0.037	0.203 ± 0.020
(10^{16} W)				
Observed power ^e	83.65 ± 0.84	19.77 ± 0.32	0.560 ± 0.011	0.534 ± 0.029
Derived internal power	33.8 ± 2.6	9.59 ± 0.47	0.039 ± 0.038	0.331 ± 0.035
(10^{16} W)				
T_{eq} (predicted effective	109.3 ± 1.3	80.5 ± 0.9	58.1 ± 1.0 ^f	46.6 ± 1.1
temp; K)				
T_{eff} (from observed	124.4 ± 0.3	95.0 ± 0.4	59.1 ± 0.3	59.3 ± 0.8
power; K) ^e				

The parentheses following planetary masses, radii, and potential coefficients contain the uncertainties in units of the last decimal place
a Orbital elements for the epoch J2000 and with respect to the mean ecliptic and equinox of J2000.0, a Julian year (Jy) is 365.25 days long

$$b_e = (R_{\text{eq}} - R_{\text{pol}})/R_{\text{eq}}$$

c Gravitational potential coefficients: see Milone and Wilson (2014, Ch. 5.3)

d Computed using volumetric radius [$(R_{\text{eq}}^2 R_{\text{pol}})^{1/3}$]

e Data from Pearl and Conrath (1991) and Pearl et al. (1990)

f “Fast rotator” case; for “slow rotator” case, $T = 69.1^\circ \text{ K}$

These encounters have provided important clues about the structures of the magnetospheres, atmospheres, meteorology, and even their interiors of these planets. The remarkable details revealed have been supplemented by changes in atmospheric structures revealed through extended HST observations.

The extensive satellite and ring systems of the giant planets as well as the moons of Mars and the Pluto-Charon double dwarf planet will be left to Chap. 13, which picks up from the end of our discussions later in this chapter of the contributions of Jupiter's Galilean moon Io to Jupiter's magnetospheric composition, and the interaction of Saturnian moons with that planet's magnetosphere.

First, we summarize the properties of the gaseous giant planets of our solar system in Table 12.1. Note that we have two types of these gaseous planets: the truly giant planets, Jupiter and Saturn, two orders of magnitude more massive than the Earth and around $10\times$ its diameter, and the two lesser giants, Uranus and Neptune, more massive than Earth by only an order of magnitude and just a few times its diameter.

12.1 Jupiter

Jupiter was the principal god of Rome and among the Greeks the cultural equivalent to Zeus, king of the gods in the pantheon of Mt Olympus. The planet's slow, stately movement in the heavens (12 years to complete a circuit, spending 1 year in each of the zodiacal signs) and its bright appearance convey the impression of majesty and power. It is an appropriate association, since Jupiter is the most massive ($\sim 318M_{\oplus}$) and the largest of all the planets ($\sim 11R_{\oplus}$).

12.1.1 Visible Phenomena

The classic source of details about Jupiter's observed features has been the popular book, *The Planet Jupiter* by Peek (1981). Other detailed sources have been Bronshten (1969) and Gehrels (1976). More recent summaries of Jupiter's properties are found in Rogers (1995), Beebe (1997), and, for all the giant planets, Irwin (2009).

An occultation of a star by Jupiter, observed by Baum and Code (1953), provided the first direct evidence of the bulk composition of Jupiter's atmosphere. With a derived effective scale height, $H = 8.3$ km, and an assumed $T = 86$ K, from Kuiper (1952), they derived a mean molecular weight of 3.3. Later, occultations of brighter stars, with a revised temperature at the observed level in Jupiter's atmosphere of 170 K (Hunten and Veverka 1976), gave a scale height of 27 km and a mean molecular weight of

$$\mu = kT/[Hgm_u] = 1.38 \times 10^{-23} \times 170 / [27,000 \times 24.8 \times 1.67 \times 10^{-27}] \approx 2.1$$

where $g = 24.8 \text{ m/s}^2$ is the gravitational acceleration at Jupiter's cloud tops. A molecular weight this small reveals hydrogen and helium to be major constituents of the atmosphere. The escape velocity is 59.5 km/s, so from (10.6), all gases are retained that have mean molecular weights greater than

$$\mu_{\text{crit}} = 8.980 \times 10^5 \times T/v_\infty^2 = 0.04$$

Thus, Jupiter has retained essentially all of its hydrogen over the age of the solar system, assuming no major changes in temperature.

The mean density of Jupiter ($1,327 \text{ kg/m}^3$) is slightly less than that of the Sun, but it (as well as the other giant planets) does not have solar composition. In particular, it is slightly deficient in helium compared to the Sun, as we note below. Jeans escape is not the relevant mechanism to explain the apparent deficiency, but rather a fractionation of the material in Jupiter's deep atmosphere and its strong gravitational field.

The measured rotation periods, P_{rot} , depend on latitude, ϕ , and there is another period, associated with a deeper source, perhaps in the solid body of the planet, determined from radio emissions. Three systems are recognized:

$$\begin{aligned} P_{\text{rot}}^I &= 9^{\text{h}}50^{\text{m}}30.0^{\text{s}} \quad (|\phi| < 10^{\circ}) \\ P_{\text{rot}}^{II} &= 9^{\text{h}}55^{\text{m}}40.6^{\text{s}} \quad (|\phi| > 10^{\circ}) \\ P_{\text{rot}}^{III} &= 9^{\text{h}}55^{\text{m}}29.704^{\text{s}} \quad (\text{System III; presumably solid body}) \end{aligned}$$

where we list the most recently-determined value for the System III period (Yu and Russell 2009). The planet's flattening is 0.0649, considerable when compared to the terrestrial planets, but it must be remembered that what is being viewed is the exterior of a largely fluid object that is rapidly rotating, and therefore necessarily spheroidal, not spherical.

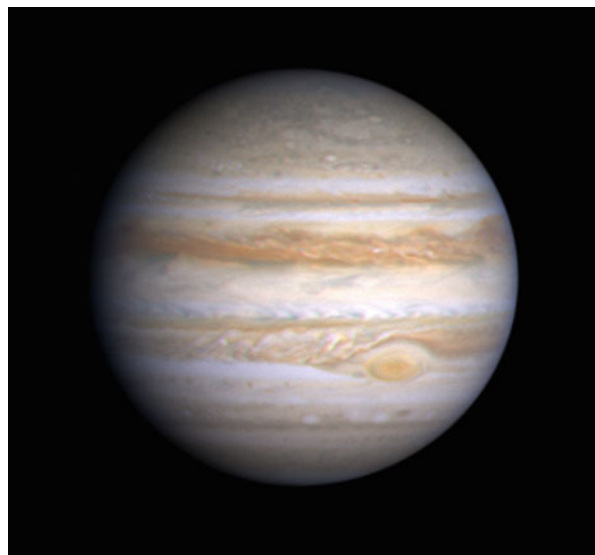
The circulation pattern in Jupiter's extensive gaseous atmosphere demonstrates strong geostrophic effects. The Rossby number (Sect. 10.5.1; Lewis 1997, p. 182), as it applies to giant planet circulation, is

$$Ro = [dv/dt]/[4\pi v \sin \phi/P] = v_x/(fL) \quad (12.1)$$

where $dv/dt = v^2/R$ is the inertial acceleration, ϕ is the latitude [λ in (10.74)], P is the rotation period, v_x is the eastward wind component, $f = 2\Omega \sin \phi$ is referred to as the *Coriolis parameter*, Ω is the angular rate of rotation, and L is a “characteristic length” for horizontal motions, the largest of which are up to about the planetary radius R . The Coriolis acceleration is generally important in the giant planets, especially for large-scale motions, except near the equator (where $\phi = 0$), so the Rossby number is small.

In steady-state situations, the Coriolis force is balanced by horizontal pressure gradient forces, creating geostrophic winds (Sect. 10.3.5). Near the equator and at latitudes $\pm 30^{\circ}$, the zonal wind speeds are in excess of 100 m/s, whereas the belt

Fig. 12.1 A composite image of Jupiter in three passbands, as viewed from the Cassini Orbiter on October 8, 2000, at a distance of 77.6 million km from Jupiter. Note the bright zones, dark belts, Great Red Spot, white ovals and brown barges. NASA/JPL/CICLOPS/University of Arizona image PIA02821



winds tend to show retrograde rotation relative to the planet (i.e., currents moving from E to W; on Earth, these would be called “easterlies;” Sect. 10.3.7). With $v_x = 100$ m/s and $fL = 12,600$, $Ro \approx 0.01$, indicating Coriolis effects to be highly important.

Jupiter presents a banded appearance (see Figs. 12.1 and 12.2), with dark bands (belts) interspersed among light bands (zones). Note that the strongest winds are in the equatorial zones and are “westerlies.” At first glance, this seems opposite to what is expected, because Fig. 10.31 indicates that the corresponding equatorial zone on Earth has easterly “trade winds.” The difference comes about because in the case of the Earth, we are looking at surface winds; at altitude, at the top of the Hadley cell, these winds are westerly. The winds on Jupiter, and on the other giant planets, are similarly seen at the tops of their circulation cells. The zones represent cooler, higher regions of the atmosphere and the belts warmer and lower regions. The white colors of the zones are due to ammonia (NH_3) crystals condensing in the troposphere from rising gas. The belts are dark, reddish-brown, and deep purple and indicate regions which are free of the overlying ammonia clouds. However, their visibilities vary greatly over time. UV photolysis of H_2S may explain the colors. For detailed discussions of low-resolution Jovian atmospheric phenomena, see Bronshten (1967). For a detailed account of Jupiter’s photochemistry, see Lewis (1997, pp. 185–202).

The arrows in Fig. 12.2 indicate wind speeds and directions relative to Jupiter’s underlying interior rotation. Relative to this interior rotation, Jupiter’s dominant circulation at cloud level consists of alternating easterly and westerly jetstreams. (When viewed from Earth, Jupiter’s rotation carries all of these jets eastward, with adjacent jets moving at different speeds.)

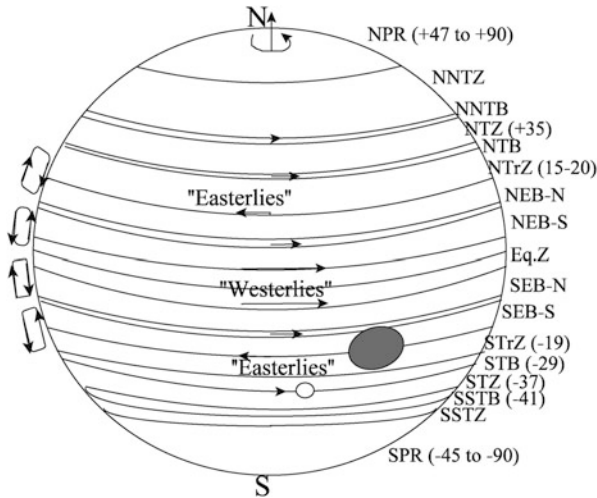


Fig. 12.2 The zones (Z) and belts (B) of Jupiter's atmosphere. Other abbreviations are E/Eq (equatorial), N (north), S (south), T (temperate), Tr (tropical); NPR and SPR are North and South Polar Regions, respectively. The *parenthetical numbers* are the approximate latitudes in degrees. The *arrows* indicate roughly the wind direction and relative speed, measured relative to the underlying interior rotation. The Jupiter that we see in visual light is dominated by high-altitude effects: We see the tops of the convective cells. The zones are *lighter bands*, marking ascending (high-pressure) columns of gas; the belts are *darker* and indicate descending (low-pressure) columns. The Great Red Spot and a white oval are also shown

The Great Red Spot (GRS), seen in Figs. 12.1 and 12.3, has been observed, arguably, since the seventeenth century, with occasional fading and with return to former dark red intensity, and considerable variation in longitude (about its own mean position), but little variation in latitude. It is located in the Southern Tropical Zone at $\sim 20^{\circ}\text{S}$. It is $\sim 50,000$ km across, has a CCW rotation, and its top is significantly cooler and hence higher than all other features of the surrounding atmosphere. Thus it represents a region with strongly upwelling material, the buoyancy of which has carried it to more than 8 km above the highest cloud deck. Long thought to be a consequence of a *Taylor instability*, an atmospheric disturbance produced by heavy winds crossing over a surface obstruction (Hide 1961), it is now viewed as an intense storm, albeit a long-lasting one. Ingersoll et al. (2004, Sects. 6.3 and 6.7) summarizes both observations and theories.

In addition to the GRS, there are *brown barges* (probably NH_4SH clouds), *white ovals* (NH_3 clouds), some of which can be seen in Figs. 12.1 and 12.4, *plumes* (high-altitude cirrus clouds of NH_3 , spread out by high-altitude winds), and *blue-grey regions*. The latter occur most often in the North Equatorial Belt and show the strongest infrared emission at 5 μm . They are thought to be the lowest regions of atmosphere that can be viewed from outside the planet.

The atmosphere is expected to behave as a perfect gas to a depth of ~ 400 km down from the cloud tops, with increasing deviation from the perfect gas law below this depth.

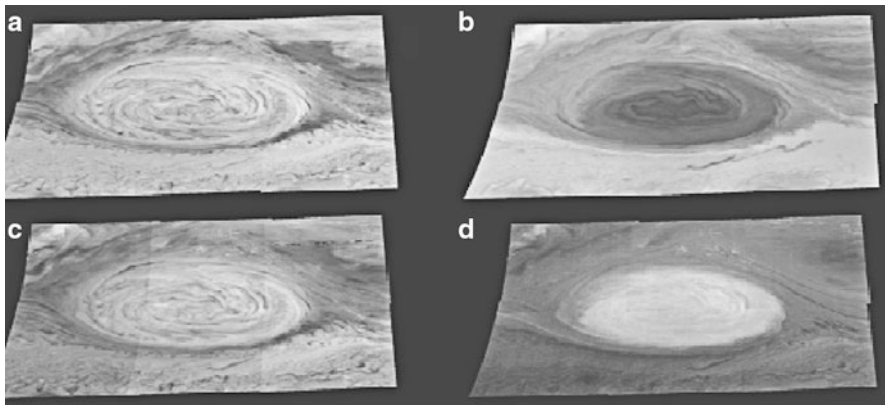


Fig. 12.3 Mosaics of six images of the Great Red Spot in each of four passbands centered on (a) 415 nm, (b) 757 nm, (c) 732 nm, and (d) 886 nm. From the *Galileo* mission Solid State Imaging System, obtained on June 26, 1996. Credits: NASA/JPL/California Institute of Technology. Image PIA00721



Fig. 12.4 Structure in the equatorial zone and belts of Jupiter, as viewed by the Cassini Orbiter near its closest approach. Note the blue-grey clouds. The picture is a modified composite of images in three passbands: 728, 752, and 889 nm, in bands of methane and the continuum. The Great Red Spot is seen at the lower right. Bright white points may be high-altitude lightning. NASA/JPL/CICLOPS/Univ. of Arizona image PIA02877

Jupiter was visited by *Pioneer 10* (1973), *Pioneer 11* (1974), *Voyager 1* and *2* (1979), *Ulysses* (1992 and 2003–2004), *Galileo* (1995–2003), *Cassini* (2000), and *New Horizons* (2007). Another spacecraft, the *Juno* orbiter, is *en route* with orbit insertion projected for Aug 2016. *Galileo* carried a probe which entered

the atmosphere of Jupiter and studied the properties of the outer atmosphere. The probe gave evidence of decidedly drier atmosphere than expected, but one which confirmed the interior-driven circulation model of the atmosphere, i.e., that the circulation does not depend at least primarily on solar heating: winds as high as 650 km/s extend down to 130 km below the cloud tops.

The presence of ammonia and methane in the upper atmosphere of Jupiter and of methane in the other giant planets has been known since the 1930s, but subsequent studies have revealed the presence of hydrogen sulfide (H_2S), phosphine (PH_3), germane (GeH_4), and CO in Jupiter. Aside from H_2S , which is thought to be in equilibrium, these molecules must be newly convected into the high atmosphere because in equilibrium other gases are expected which are not found (e.g., P_4O_6 by reaction of PH_3 with H_2O). In this way, vigorous convection is seen to be present in Jupiter, Saturn, and Neptune, but less so in Uranus. The presence of likely chromophores, as certain colorful compounds are known, such as sulfur, hydrogen sulfide (H_2S), ammonium hydrosulfide (NH_4SH), and their photochemical byproducts, such as hydrazine (N_2H_4), and possibly involving hydrocarbons, is needed to explain the redder colors.

As noted previously, the white clouds seen in Jupiter's zones are likely ammonia which condenses out at high altitudes in that planet's atmosphere. Because gases condense out when their equilibrium vapor pressures are equal to their partial pressures, the altitude at which this happens varies from planet to planet. Thus, ammonia condenses out below the visible cloud decks in Uranus and Neptune, and the dominant spectral signatures from those planets are of methane, the clouds of which are seen in those planets. Indeed, clouds are principal features in Figs. 12.1 through 12.11!

12.1.2 Jovian Atmospheric Structure

One model for the structure of Jupiter (from top down) is as follows:

1. Topmost layer: solid NH_3 particles; $P \approx 1$ bar ($\sim 10^5$ Pa); $T \approx 150$ K
2. More massive cloud: solid NH_4SH (ammonium hydrosulfide) particles; $P \approx 2\text{--}5$ bars; $T \approx 210$ K
3. Dense layer of H_2O ice crystals
4. Thin layer of dilute aqueous ammonia solution; $P \approx 7$ bars; $T \approx 280$ K
5. Gaseous hydrogen ($\text{H}_2 + \text{He}$)
6. Liquid molecular hydrogen (layers 5 + 6 : to $0.78\mathfrak{R}_J$)
7. Liquid metallic hydrogen, to $0.2\mathfrak{R}_J$
8. Solid core of ice, rock, Fe-S

Some of this structure was studied by the *Galileo* Probe (see Fig. 12.5).

A classic work on the interiors of the giant planets is Wildt (1961). Since then both observations and theoretical models have progressed, as has knowledge of the Earth's interior and the properties of the phases of hydrogen, helium, and of

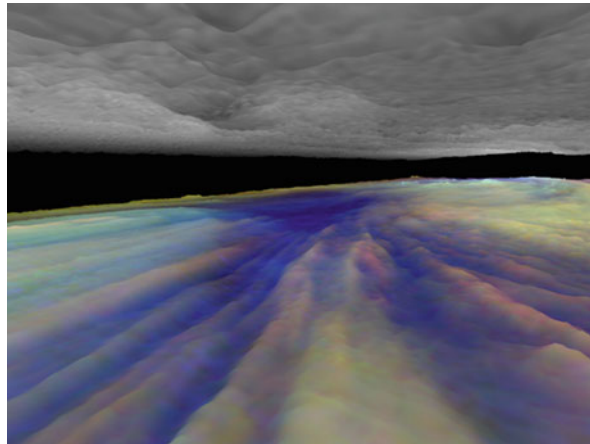


Fig. 12.5 3D visualization of the structure of the atmosphere of Jupiter near the equator, as revealed by the *Galileo* Probe. The empty layer is clear dry air; above it is haze and below are thick clouds. The *blue area* marks a region of dry, descending air, while the *whitish region to the right* is ascending, moist air. The *blue-green-red colors* indicate enhanced reflection/emission in the 889, 727, and 756 nm passbands, respectively. Image PIA01192, courtesy of NASA/JPL/CalTech

ices generally; but for its elegance, scientific approach, and clarity this work is still worth reading. Guillot et al. (2004) provide a good post-*Galileo* summary.

The fractional abundance of He relative to everything else, including H, in Jupiter's atmosphere, 0.234 ± 0.005 by mass, is only slightly less than that in the protosolar nebula, 0.275 ± 0.01 (von Zahn et al. 1998).¹ At the pressures that are thought to exist within Jupiter (>3 Mbar), hydrogen should become metallic. Helium has been thought to be immiscible in this material; if it is, helium drops can “rain” down toward the center of the planet but this hypothesis has been challenged, both as a source for the excess heat flux and on the basis that the diffusion coefficient is too low to permit this. For the other gas giants:

- On Saturn, the temperatures are lower, and He should separate more fully than on Jupiter; also, the smaller size of Saturn suggests that Saturn would have cooled more quickly and the separation would occur earlier than on Jupiter. Both arguments suggest that the helium abundance in Saturn's atmosphere

¹ The observed He abundance in the solar convection zone and photosphere is 0.24 ± 0.01 by mass, obtained from helioseismology (von Zahn et al. 1998; Proffitt 1988; see Milone and Wilson 2014, Sect. 4.10, for a discussion of helioseismology). Stellar evolution computations incorporating diffusion then give the initial He abundance of the Sun (and therefore of the protosolar nebula and the initial abundance for Jupiter) as 0.275 (Proffitt 1988). The present He abundance in Jupiter's outer layers is therefore very nearly equal to that in the Sun's outer layers, although this is a coincidence because the processes are very different: downward diffusion of helium gas over the life of the Sun compared to separation and descent of liquid helium over a time smaller than the age of Jupiter.

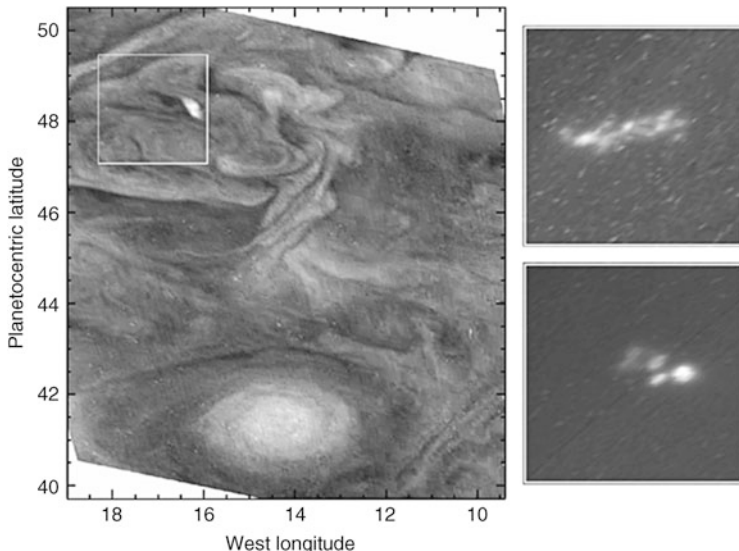


Fig. 12.6 Lightning near the Great Red Spot on Jupiter. The image on the *left* was taken during the Jovian day. The *box* indicates a bright ammonia cloud in an updraft region and to the *immediate left*, a clear downdraft region. The *insets* indicate extensive lightning in nightside images of the boxed area; they were taken 110 min after the dayside view and were taken with exposures of 167 s for the upper and 39 s with higher gain for the lower. The nightside images were taken only 218 s apart! The lightning strikes may appear fuzzy because they appear at the level of water vapor, ~75 km below the cloud decks, and ammonia clouds overlay them, acting as a diffusion screen. Credits: NASA/JPL/California Institute of Technology. Image PIA01638

should be lower than in Jupiter's. However, the helium abundance in a planetary atmosphere is difficult to determine remotely, because it is measured by the effect that helium has on other things; e.g., from the mean molecular mass obtained from the scale height; or from the effect that He has on the infrared spectrum of H₂ (collision-induced absorption lines of H₂ are influenced both by H₂–H₂ interactions and by H₂–He interactions). A re-analysis of *Voyager 2* data (Conrath and Gautier 2000) gave a value of 0.18–0.25 He by mass, and preliminary results from one experiment on *Cassini* gave a value of 0.13, while another gave a higher result more consistent with the *Voyager* result (Fouchet et al. 2009). In any case, all results suggest at least some helium depletion in Saturn's atmosphere. The model of Anderson and Schubert (2007) predicts a transition from H₂ to metallic H at about 0.5R_S for Saturn.

- The internal pressures on Uranus and Neptune are too low for the metallic hydrogen transition, so there is no separation and the He abundance is, as a consequence, close to the proto-solar nebula ratio of 0.275 by mass, but with considerable uncertainty (0.262 ± 0.048 for Uranus and 0.32 ± 0.05 for Neptune).

Both lightning (see Fig. 12.6) and aurorae have been seen in Jupiter's atmosphere from Earth (see Fig. 12.21) and by spacecraft.

Jupiter has an extensive magnetosphere, to be discussed separately below. The other giant planets also have extensive magnetospheres, although the sources of the magnetic fields in the lesser giants are not clear. The presumption is that in Jupiter it arises in the metallic hydrogen region.

12.2 Saturn

Saturn, the farthest and slowest moving planet known in antiquity, was the Roman god of agriculture and the father of the other gods. In Greece, the planet was called *Kronos*, noted for its slow motion among the stars. The Greek word for time, *chronos*, is found in such English words as *chronometer* and is, at least sometimes, identified with it (van der Waerden 1974, pp. 188–197). The planet's sidereal period of $29^{\circ}46'$ implies a mean motion of only $0.033^{\circ}/\text{d}$ or about a degree a month.

Known for its beautiful ring system, visible even in small telescopes, Saturn presents a yellow appearance in the sky. Its colors indicate Saturn to be the reddest of the giant planets with $(B - V) = 1.04$ and $(U - B) = 0.58$.

Saturn is the least dense of all the planets and the most flattened with an oblateness of nearly 10 %.

As on Jupiter, Saturn's dominant circulation pattern at cloud level consists of zonal jets of different speeds, visible as the banded structure in Fig. 12.7. Figure 12.8 provides a close-up view. On Saturn, adjacent mid-latitude jets differ

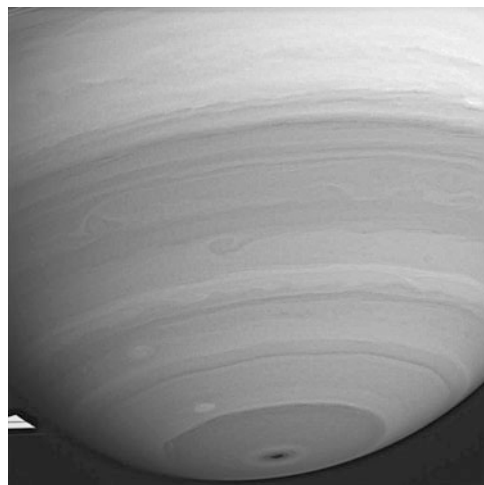
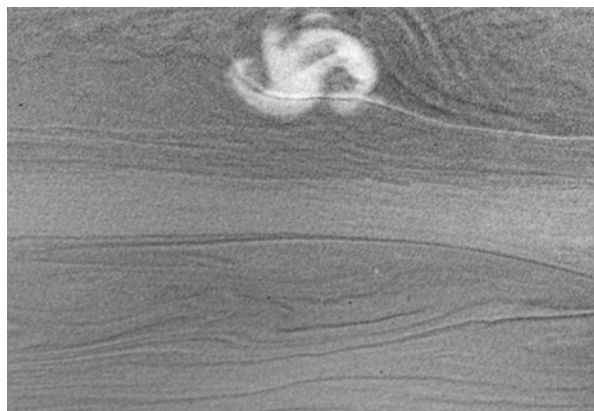


Fig. 12.7 An image of Saturn at 728 nm wavelength, as seen by the *Cassini* orbiter wide-angle camera on July 31, 2005, from a distance of 1.3 million km. The South Pole is seen at the bottom. Note the presence of white ovals and turbulent features, similar to those on Jupiter. NASA/JPL/Space Science Institute image PIA07585. A composite color image of the North Pole as imaged by Cassini cameras on October 10, 2013 can be found at: http://www.nasa.gov/mission_pages/cassini/multimedia/pia17474.html#.Uqy69-KQmZ1

Fig. 12.8 An intense storm visible even through the extensive upper haze layer to viewers on Earth. This image was captured on the nightside of Saturn by the Cassini Orbiter. The atmosphere is illuminated by sunlight reflecting off the rings. NASA/JPL/CICLOPS/Space Science Institute image PIA07789



in relative motion by \sim 100–200 m/s, and the equatorial jet is about 350 m/s faster than the fastest mid-latitude jets. One difference from Jupiter, however, that is immediately apparent in photographs of the two planets is that the features on Saturn are much more muted. This is because the zones and belts are 100 km deeper in the atmosphere than in Jupiter, and a high-altitude haze masks the colorful materials below. Consequently the features on Saturn suffer from poor contrast.

There are three regimes or “systems” of rotation assigned to the planet, although the rotational velocities vary in detail from zone to zone and belt to belt. Prior to the Cassini mission, the velocity regions were

$$\begin{aligned}P_{\text{rot}}^{\text{I}} &= 10^{\text{h}} 14^{\text{m}} \text{ (equator)} \\P_{\text{rot}}^{\text{II}} &= 10^{\text{h}} 38^{\text{m}} \text{ (temperate zones)} \\P_{\text{rot}}^{\text{III}} &= 10^{\text{h}} 39^{\text{m}} 22^{\text{s}} \text{ (System III, from radio data)}\end{aligned}$$

However, *Cassini’s* measures of the radio period have yielded a range from $10^{\text{h}} 47^{\text{m}} 06^{\text{s}}$ in 2004 to $10^{\text{h}} 32^{\text{m}} 35^{\text{s}}$ in 2007, implying that the $P_{\text{rot}}^{\text{III}}$ as observed is not that of Saturn’s interior (which should have a constant rotation rate) but of a magnetic field structure that may be modulated by Saturn’s plasma disk (Gurnett et al. 2007). Also, if the interior rotated with the System III period given above, the entire atmosphere at cloud level would be moving eastward at different speeds relative to the interior rotation, with the equatorial jet moving at \sim 470 m/s. This would make Saturn’s atmosphere surprisingly different from Jupiter’s.

Methods for determining the interior rotation rate that do not depend on the magnetic field have been developed by Anderson and Schubert (2007) and Read et al. (2009). The former find $10^{\text{h}} 32^{\text{m}} 35^{\text{s}} \pm 13^{\text{s}}$ for Saturn’s interior rotation period using occultation, Doppler, and gravity data. This value is consistent with a period they found from *Voyager 1* and 2 data: $10^{\text{h}} 32^{\text{m}} 55^{\text{s}} \pm 30^{\text{s}}$. Read et al. (2009) find $10^{\text{h}} 34^{\text{m}} 13^{\text{s}} \pm 20^{\text{s}}$ from meteorological dynamics models, by varying parameters to minimize instability in the shear between zonal jets of different speeds. Using a reference frame rotating at $10^{\text{h}} 34^{\text{m}} 13^{\text{s}}$, the circulation pattern is much more like Jupiter’s, with easterly and westerly jets alternating at mid-latitudes and a faster,



Fig. 12.9 Saturnian aurorae seen simultaneously at both poles, captured in UV light with the STIS instrument onboard the Hubble Space Telescope. Note the auroral oval, similar to that seen on Earth. Note also the similarity in alignment of both magnetic and rotational poles in Saturn. During the impacts of the components of the Comet Shoemaker-Levy 9, aurorae were triggered at both magnetic poles of Jupiter. Credits: HST/ESA/NASA/JPL/J.T. Trauger. Courtesy, John Trauger. Image PIA01269

westerly jet at the equator. Saturn's mid-latitude jet speeds in this case are \sim 50–100 m/s, and \sim 380 m/s for the equatorial jet.

The velocities of regions within about 15° of the equator are extremely high, \sim 400 km/s. Curiously, the speeds of corresponding latitudes in the N and S hemispheres do not match. In particular, winds near 70°N are \sim 100 km/s, but the same latitude in the south has slight negative (retrograde) speeds.

Saturn has been visited by *Pioneer 11*, *Voyager 1*, and *Voyager 2*, and the spacecraft *Cassini*, comparable to *Galileo* in many respects, has been in orbit around Saturn since 2004. The images of the planet itself have been overshadowed by the magnificent images of the rings and moons of the planets (see Chap. 13), but are spectacular, nonetheless, as evidenced by Figs. 12.7 and 12.8.

Saturn has visible aurorae (see Fig. 12.9), indicating the presence of a magnetosphere and thus a strong magnetic field, only $34\times$ weaker than Jupiter's (but still about 600 times that of Earth). The upper atmosphere also exhibits weak, collision-excited UV emission from H and H₂, termed *electroglow*. Proposed sources of the colliding particles include precipitated electrons from the magnetosphere and locally-produced ions and low-energy electrons in the ionosphere.

Spectra of Saturn show a helium depletion compared to Jupiter, a circumstance that may be coupled to Saturn's radiative emission, which exceeds that received from the Sun by more than a factor of 2. Further discussion of Saturn's properties can be found in Gehrels and Matthews (1984), but the Cassini mission has already resulted in much additional detail about Saturn's properties.

A mysterious aspect of Saturn is its very large obliquity (26.7°). The giant planets are believed to have formed in two steps: a solid core forms first by collisional accretion of rock-and-ice planetesimals; then, after this core reaches a mass of several Earth masses, it accretes gases from the solar nebula by gravitational attraction. As with the terrestrial planets, the random collisions of planetesimals may have left the core with a non-zero obliquity; but the subsequent attraction of ~ 300 Earth masses of gas onto Jupiter and $\sim 80\text{--}90$ Earth masses onto Saturn from material in a single plane (the solar nebula, essentially the same as their orbital planes) would have left Jupiter and Saturn with obliquities close to zero. Jupiter's obliquity is 3.1° . Another possible cause, a collision after Saturn formed, appears to be ruled out by Saturn's very large rotational angular momentum (its large mass and 10.7 h rotation period).

The resolution to the mystery may lie in a spin-orbit coupling of Saturn with Neptune (Ward and Hamilton 2004; Hamilton and Ward 2004). If Saturn were the only planet in the solar system, then its orbit would remain fixed and the Sun's gravitational pull would cause Saturn's spin angular momentum vector, \mathbf{s} , to precess around the total orbital angular momentum vector, \mathbf{k} , of the solar system (which for a one-planet system would also lie along Saturn's orbit normal, \mathbf{n}). (Actually, since Saturn has satellites, of which one (Titan) is massive, the Sun causes the satellite orbits to precess, and the satellites cause Saturn to precess to maintain its equator in the plane of the satellite orbits.) The gravitational pull of a second planet whose orbital plane is inclined to that of Saturn would cause Saturn's orbital plane to precess, such that both \mathbf{s} and \mathbf{n} precess about \mathbf{k} at the same uniform rate, with the vectors \mathbf{k} , \mathbf{n} and \mathbf{s} coplanar. This condition of uniform precession and coplanar \mathbf{k} , \mathbf{n} and \mathbf{s} is referred to as a *Cassini state*, and Saturn is currently in such a state. If there are other gravitating objects in the system (in Saturn's case, the dominant objects are Jupiter, Uranus, Neptune and the Edgeworth-Kuiper Belt), then all of these objects influence Saturn, as well as each other. What is interesting is that Neptune's orbital precession period is 1.87×10^6 y (known to a few tenths of a percent) and Saturn's spin axis precession period is 1.8×10^6 y (known only to within several percent), so the two are equal within current uncertainty. If this apparent equality is real and not just a coincidence, then Saturn must have entered a spin-orbit resonance with Neptune at some time in the past, probably early in the life of the solar system due to evolutionary effects such as the erosion of an early, more massive Edgeworth-Kuiper belt and/or slow orbital migration of Neptune. Once established, Saturn would adjust to maintain the resonance and the Cassini state provided changes to Neptune's orbit were slow-paced. Because of the Cassini state, changes in Saturn's orbital plane would be accompanied by changes in its obliquity. Numerical simulations by Hamilton and Ward (2004) indicate that, even if Saturn's initial obliquity were very small, this process is capable of pumping up the obliquity to values similar to the present one.

12.3 Uranus

Uranus was discovered by William Herschel (1738–1822) in 1781 with a 6½ in. telescope during a sky survey. Uranus appeared as a round, nebulous disc with a motion of 1"75 per hour, and Herschel assumed he had discovered a new comet. Later, he realized that it had a circular and therefore non-typical orbit for a comet, and its 84^y period indicated a mean distance of 19 au. He called it *Georgium Sidus*, “George’s Star” after his royal patron, George III. Jérôme Lalande (1732–1807), at the Collège de France in Paris, called it “Herschel,” but Bode’s suggestion, Uranus, after the sky god of the ancient Greeks, became generally accepted.

Bode subsequently discovered that Uranus had been charted by John Flamsteed (1649–1719), the first Astronomer Royal, on December 23, 1690, and labeled 34 Tauri; he also found that it had been cataloged as number 964 by Tobias Mayer (1723–1762) of Göttingen in 1756. The earlier observations were sufficient to compute an orbit. In addition, Pierre Charles Lemonnier (1715–1799) found in 1788 that he himself had made observations of Uranus in 1764 and 1769.

Later it was discovered that Flamsteed had observed it on other occasions also, and so had James Bradley (1693–1762) on December 3, 1753. More than a dozen other pre-discovery observations were detected over the next 30 years, allowing a very precise orbit to be computed.

See Grosser (1962) or Turner (1963) for more detailed accounts of the discovery of Uranus and its importance for the subsequent discovery of Neptune.

Uranus’s magnitude at opposition is $V = 5.52$, and thus detectable, in principle, to the naked eye. There is, however, no evidence of pre-telescopic observations of it. It has a maximum angular size of 3"9, so little detail has been discerned on its disk as observed with ground-based telescopes.

Uranus’s density is less than that of the Sun, and it is clearly a lesser giant, with a radius only $\sim 4R_{\oplus}$ and a mass of only $14.5M_{\oplus}$.

Telescopically, Uranus is somewhat green in appearance. Methane was identified in its atmosphere spectroscopically by Wildt (1931, 1932). Uranus is a very dark planet with little contrast among its features, and the contrast in the images returned by *Voyager 2* (which arrived at Uranus in 1986) needed to be stretched to show banded structure near the pole. E-W motion was seen in a sparse number of spots and streaks; some of these can be seen in Fig. 12.10. Observations of selected features in the atmosphere showed that the rotation rate varied with latitude, as on Jupiter and Saturn.

Uranus’ rotation axis is oriented 97°86 to its orbital axis so that the planet’s north pole,² when viewed “pole-on,” is rotating CW, or retrograde to its orbital motion. From *Voyager 2* radio data, its rotation period is given as $-0.71833\text{ d} = -17^{\text{h}}14^{\text{m}}24^{\text{s}}$.

The fact that Uranus’ rotation axis lies almost in its orbital plane creates bizarre “seasons” for Uranus. Over an 84-year interval, the Sun will illuminate successively

²i.e., the pole on the north side of the planet’s orbital plane, as per the terrestrial analog.

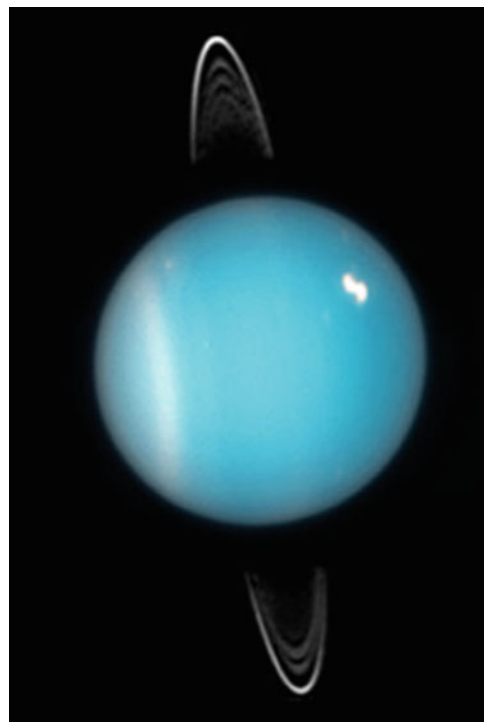


Fig. 12.10 Uranus as seen by the Hubble Space Telescope, showing backscattered rings, polar clouds, and a relatively high, bright cloud, probably of methane, the red absorption of which gives rise to the greenish blue hue of the planet's atmosphere. Image hs-2007-32-c. Credits: NASA, ESA, and M. Showalter (SETI Institute)

lower latitudes beginning at one of the rotation poles until the other pole is facing the Sun, and then increasing latitudes again until the original orientation is reached again. Nevertheless, when the south pole was pointed almost directly towards the Sun, *Voyager 2* found remarkably uniform temperatures throughout the atmosphere even at the winter side. This justifies to some extent the isothermal or rapid rotator assumption for the computation of the equilibrium temperature.

Uranus' atmosphere has abundant hydrogen and, from *Voyager 2* data, the helium abundance is essentially solar, $Y = 0.262 \pm 0.048$ by mass. Superheated water is expected to be present in its extensive gaseous atmosphere, perhaps in an ocean 10,000 km deep.

The planet has a magnetic field, and some evidence for lightning in the form of whistlers was detected by radio receivers on *Voyager*. The *Voyager* data also displayed a very strong UV emission (called the *electroglow*; see Sect. 12.2) from a region 1,500 km above the cloud tops on the sunlit side. Similar, though fainter, electroglows have been seen on Jupiter, Saturn, and Titan.

12.4 Neptune

Almost immediately, it became clear that something was wrong with the theory of Uranus' motion. By 1829, the theory of mutual perturbations developed by Pierre-Simon de Laplace (1749–1827) was applied to the orbit of Uranus but its positions could not be reproduced to better than $\sim 1/2'$. Moreover it was clear that the residuals were not due to observational error. Five hypotheses were put forward in explanation:

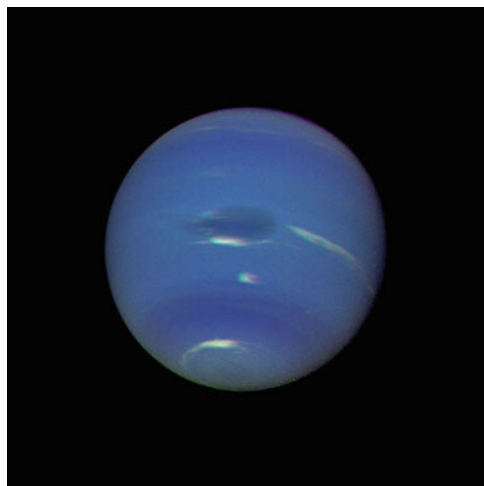
1. The (hypothetical) cosmic fluid of Descartes, causing a drag force; but there was no evidence for such a fluid, or for a mechanism by which it could produce the perturbations in Uranus but in nothing else.
2. Perturbations due to an unobserved massive satellite; but the time scale of such perturbations would be expected to be shorter than those seen in Uranus' motion.
3. A comet had struck Uranus close to the time of its discovery, changing its orbit; but perturbations continued; moreover, two elliptical orbits were still insufficient to recover the motion (that cometary masses were insufficient to cause such effects was not known at the time).
4. The law of gravity was either not effective or changed at the (great) distance of Uranus; but all previous challenges to the Newtonian law had been refuted. The hypothesis in this case was impossible to refute except empirically.
5. Finally, the existence of a trans-Uranian planet.

The Royal Academy of Sciences in Göttingen offered a prize for the resolution of the problem, with a deadline of November 1, 1846. The problem was independently taken up by John Couch Adams (1819–1892) and Urbain J. Leverrier (1811–1877). Adams communicated his prediction of a trans-Uranian planet to the Astronomer Royal in October, 1845, and Leverrier communicated his to the French Academy of Sciences on November 10. James Challis, Director of the Cambridge Observatory, based on Adams' prediction, started searching in July, 1846, but was unsuccessful. Johann Gottfried Galle (1812–1910) and d'Arrest compared Leverrier's predicted position to recent charts and found Neptune in September, 1846. The predictions, as Airy, the Astronomer Royal conceded, were similar, and Neptune was found within a degree of the prediction by Leverrier, and with about the predicted angular size.

According to Leverrier, the Bureau des Longitudes in Paris proposed the name *Neptune* (it now appears that they did no such thing; it was Leverrier's suggestion). A suggestion by Galle that it be called Janus was rejected because Leverrier said in a letter to Galle that "the name Janus, would imply that this is the last planet of the solar system, which we have no reason at all to believe" (cited in Grosser 1962, p. 123). See Grosser (1962) and Turner (1963) for more historical details.

There is an interesting continuation of this story on the other side of the Atlantic. Seventy years after the Revolution, the United States was still a young country, and two American astronomers, Benjamin Pierce and Sears Cook Walker, saw in the discovery of Neptune an opportunity to advance American science on the world

Fig. 12.11 A *Voyager 2* image of Neptune showing the main discernible features of its atmosphere: The Great Dark Spot (GDS) at disk center, bright streaks of cirrus, and Spot D2, below the GDS. As on the greater giants, belts and zones are present, if subdued due to overlaying haze. NASA/JPL image PIA02245



stage by making follow-up discoveries (Kent 2011). Both Adams and Leverrier had had to assume a distance for Neptune in order to predict its position, and had arbitrarily placed it at the distance predicted by the Titius-Bode law for a hypothetical eighth planet. This assumption resulted in a highly-elliptical orbit, very unlike that of the other planets. Walker searched through historical records and found that Lalande had recorded Neptune's position about 50 years earlier, in May of 1795, without recognizing it as a planet. Armed with this longer timeline, Walker was able to calculate and publish a precise orbit for Neptune, the first person to do so, finding that it was almost circular. Pierce re-examined all the data, verifying Walker's orbit, and caused a bit of a stir by announcing that the true orbit was so different from that calculated by Adams and Leverrier that Neptune's discovery "must be regarded as a happy accident."

Subsequently, it was found that Neptune had also been observed by Galileo in 1612–1613. Its mean motion is only 0.006° per day for a period of 165^y .

Neptune's size ($3.9R_\oplus$) and mass ($17M_\oplus$) make it a lesser giant and near twin of Uranus. Its density is the highest of the giant planets, $1,760\text{ kg/m}^3$, but it must still be composed mainly of H and He.

Neptune's maximum angular diameter is $2.^{\circ}3$, so little detail is discernible from Earth. What we know of the planet's cloud decks was obtained from the sole space probe flyby, that of *Voyager 2*, which arrived at Neptune in 1989.

Neptune, like Uranus, has abundant methane in its atmosphere. Its most characteristic feature in *Voyager 2* imagery is the Great Blue (or Dark) Spot, seen at disk center in Fig. 12.11, comparable in shape and scale to the GRS on Jupiter. It was located at 20°S and rotated CCW, indicating that it was a similar meteorological phenomenon. It had an associated high-altitude haze. In Hubble imagery 5 years later, however, it had vanished, and a new dark spot appeared in the northern hemisphere within the next year.

The *Voyager* imagery also shows additional dark spots at higher latitudes (55° S) and a highly variable, irregular feature, the “scooter” is seen at 42° S. Neptune also has higher altitude, white methane “cirrus” clouds amidst a more general methane haze. They are ~ 100 km or more long and cast shadows down on the cloud decks below a 50 km clear region.

Wind velocities in Neptune’s atmosphere vary from about 450 m/s retrograde at the equator to about 300 m/s prograde at 70° S latitude, giving Neptune the greatest range of planetary wind velocities in the solar system. Consequently, rotation periods derived from atmospheric features vary considerably with latitude. Tracking of cloud structures has revealed a rotational period of $\sim 17\text{--}18^{\text{h}}$ at $\sim 30^{\circ}$ N and S latitude and $16\text{--}17^{\text{h}}$ at $\sim 45^{\circ}$ S (Gibbard et al. 2002 and references therein).

Neptune also has a magnetic field and a magnetosphere. The rotation rate from radio emissions, determined by *Voyager 2*, is $16^{\text{h}}108 \pm 0.006$ (Lecacheux et al. 1993); it possibly represents the rotation of a deep atmospheric layer—an electrolytic sea below the Neptunian cloud decks—but if so, this is likely to have been modified by the drag of the magnetic field as suggested by Karkoschka (2011), and thus not a true interior rotation period. Indeed, Karkoschka found two features: a South Polar Wave and a South Polar Feature that seem to track the interior. With them he determined $P = 15^{\text{h}}9663 \pm 0.0002$.

Neptune, like Jupiter and Saturn, appears to have a higher temperature than thermal equilibrium predicts. It has been suggested that here the explanation may be a greenhouse effect, caused by absorption by methane, which traps infrared radiation below the CH₄ clouds. However, most sources suggest that an internal source of heat is responsible. See Sect. 12.6 and, for an alternative explanation, Lunine (1993).

12.5 Internal Pressures

The steady-state pressure is related to the radius of a planet through the equation of hydrostatic equilibrium (10.12):

$$\frac{dP}{dr} = -g\rho$$

and (through an equation of state) to (10.21):

$$\frac{dP}{P} = -(\mu m_u g / kT) dr$$

In order to find the exact pressure at the center of a planet, the density is needed as a function of depth. Unfortunately, unlike the Earth, where the Adams-Williamson equation can be used to integrate over all radii from center to the surface (Milone and Wilson (2014), Sect. 5.4.2), we do not have the acoustical wave speeds at various points in the interiors of the other planets, at present. Therefore the models are less well constrained than for the Earth.

Fig. 12.12 Density profiles from models of Jupiter and Saturn, after Marley (1999)

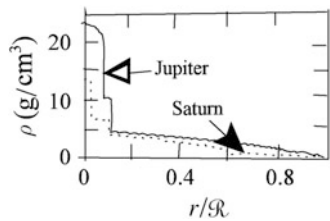
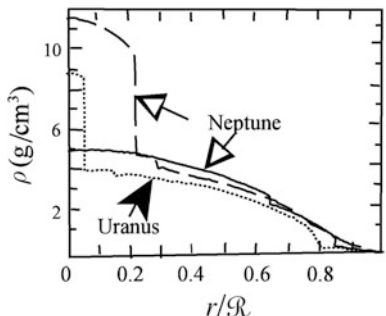


Fig. 12.13 Density profiles from two of several models of Neptune and a model for Uranus, after Marley (1999)



One may, however, make use of the mean density to estimate the central pressure. The simplest form that can be used is

$$P_0 - P_R = - \langle g\rho \rangle [0 - R] \quad (12.2)$$

where the subscripts indicate the values of r . Obtaining $\langle g\rho \rangle$ is perhaps easier said than done. One could take $(g/2)R\langle\rho\rangle$ as an approximation, but this leads to a computed central pressure of 1.7 Mbar for the Earth, and 10.9 Mbar for Jupiter, compared to 3.5 and 40 Mbar, respectively, from the models.

Another approximation is to substitute for g and then M in (10.17), to give

$$dP/dr = -GM r^{-2} \rho = -(4\pi G/3) r^{3-2} \rho^2 = -(4\pi G/3) r \rho^2 \quad (12.3)$$

with, perhaps, the approximations, $\langle\rho^2\rangle = \langle\rho\rangle^2$, and $P_R = 0$, giving

$$P_0 = -1/2(4\pi G/3) \langle\rho\rangle^2 [0 - R^2] = -(2\pi G/3) \langle\rho\rangle^2 R^2 \quad (12.4)$$

Calculation of the central pressure, P_0 , with this equation gives about the same result for the Earth, but a slight improvement for Jupiter (12.6 Mbar). Models of the interiors of the giant planets have been produced by, among others, Zharkov and Trubitsyn (1978) and Stevenson (1989). The latter computes central pressures of the order of 4×10^{12} Pa ($\sim 4 \times 10^7$ bars or 40 Mbar) for Jupiter, $\sim 10^{12}$ for Saturn, and less than 10^{12} for Uranus.

The march of density with radius in the interiors of the giant planets are shown in Figs. 12.12 and 12.13, taken from Marley (1999). See also Marley and Fortney (2007).

12.6 Excess Radiation

Table 12.1 indicates the energy received, the albedos, and the equilibrium and effective temperatures. The effective temperature for Uranus is that for a rapidly rotating planet. During the *Voyager* flyby, one pole faced the Sun. One would expect that the emission would come from only the one polar region, and the effective temperature should be larger by the factor $2^{1/4} = 1.19$, or $T_s = 69.1$ K. In fact, Uranus was seen to be nearly isothermal, and so to have a very efficient circulation system. Thus there is no strong evidence for radiation excess for Uranus, to one sigma or less.

As noted, one of the mysteries about some of the gas giants is an energy excess: three of the four giant planets appear to radiate more energy than they receive from the Sun, as seen in Table 12.1 (but Lunine 1993, has noted that the situation for Uranus and Neptune is more complex than the mere comparison of IR flux temperatures with expected equilibrium temperatures, indicating that there may be no excess from Neptune, either). In any case, there is no dispute about the excess radiation from Jupiter and Saturn. Of course, the source of the excess may not be the same in each planet in which it is seen. It also needs to be mentioned that the thermal emission in which the excess is seen is independent of the non-thermal radiation, which has its origin in the magnetospheres. The origin of the latter is relatively well understood.

Of the possible sources of a gas giant's internal heat flux, primordial heat is a possibility, but contraction (conversion of the potential energy of the planet's material into kinetic energy as it falls toward the center) is not favored at present because the giants have liquid mantles and liquids must resist compression.

Another suggested possibility involves selective “fall out” of some material—such as a “rain” of helium in the interior (see the review of Hubbard et al. 2002). This mechanism is thought to be important in Saturn, where the outer atmosphere may be more deficient in helium than is Jupiter, as noted in Sect. 12.1. Because Uranus does not have an observed deficiency of helium, this may explain its lack of excess infrared emission. Questions have arisen about the effectiveness of the diffusion of He in this mixture (one estimate giving a diffusion time scale that greatly exceeds the age of the solar system), and some calculations show that even if all of the He that appears to be missing in the upper atmosphere of Jupiter had settled onto the core, the energy released would still not account for the observed energy excess. We avoid questions about the efficiency of the settling process, both because of these uncertainties and because there are disagreements between the models of the interior and of the sound profiles deduced from measurements of Jupiter's global oscillations (one of the ways to reconcile the data is to have the H and He immiscible; notwithstanding work on equations of state and simulations of such mixtures [Levashov et al. (2006) and references therein]. See Guillot et al. (2004) for further discussion and recent models.

An alternate theory for the excess in Jupiter has been advanced by Ouyed et al. (1998): that high enough temperatures in the early core accretion stages of giant planet formation in the early solar system allowed deuteron-deuteron nuclear reactions to take place; for this to happen efficiently, 5–15 % of the total deuterium of the planet needs to have been stratified in a deep layer within its interior.

Ouyed et al. (1998) indicate that this could have been achieved in other planets (of Jupiter mass or greater), thereby explaining inflated “hot Jupiter” exoplanets (Ouyed private communication, 2013; see Sect. 16.4) but the theory does not seem to have found wide acceptance. At the time of writing, the matter is unsettled.

An unexpected discovery from the *Voyager* and *Cassini* missions is that the emitted power and effective temperature, T_{eff} , of Jupiter and Saturn vary with time (Li et al. 2010, 2012). Jupiter was emitting 3.8 % more power when *Cassini* flew past in 2000 than during the *Voyager* encounters in 1979. This is equivalent to an increase of 1.2 K in T_{eff} . From orbit, *Cassini* measured a decrease in Saturn’s emitted power and T_{eff} of 2 % and 0.5 K, respectively, between 2004 and 2009, but the 2009 values were nevertheless 6.4 % and 1.47 K higher (respectively) than when *Voyager 2* visited in 1980. The shorter-term variation on Saturn (2004–2009) appears to be caused by seasonal variations in cloud and haze structure, which affect both absorption and emission, and by variations in tropospheric temperatures. However, 1980 and 2009 are almost exactly one Saturn year apart, so there are evidently long-term trends that are not caused by seasonal variations. They may be related to long-term changes in vertical and horizontal cloud structure and/or energy transport by atmospheric waves.

The effect of these variations on the planetary heat budget will not be known until the corresponding variations in absorbed power have been determined.

Whatever the source of radiated energy from their interiors, the origins of the giant planets are also strongly debated. The leading theories, core accretion, and gravitational instability, both have impediments to full acceptance. The problems have to do mainly with the time scales for disk dissipation and formation and the mass of the protostellar disk in which they must have been formed. Because we have yet to discuss the important insights gained from the small bodies of the outer solar system and because there are now many planetary systems known, we will take up the discussion of formation in the last two chapters.

12.7 Ionospheres of the Giant Planets

In Chap. 11 on planetary ionospheres we discussed the cause, structure, and composition of the ionospheres of the inner planets. We now expand on the discussion in Sect. 11.4 about propagation of electromagnetic radiation through planetary ionospheres. Recall that the index of refraction in the ionosphere, n , decreases for greater ion density, N , because, from (11.55), (11.56), and (11.57),

$$n^2 = 1 - N e^2 / \left[(2\pi f)^2 m e_0 \right] = 1 - (f_0/f)^2 \quad (12.5)$$

where f is the frequency of the radio wave and f_0 is the plasma frequency. Thus, as a radio “ray” moves higher into the ionosphere from a point below, so that N increases, the ray is bent *away* from the normal, as in Fig. 11.6. From (11.63),

$$n^2 = 1 - \cos^2 \alpha_0 \quad (12.6)$$

so

$$f_0^2 = f^2 \cos^2 \alpha_0 \quad (12.7)$$

If f is the lowest frequency that can pass through the ionosphere for a given incident angle, α_0 , we can invert (12.7) to define the quantity

$$f_c^2 = f_0^2 \sec^2 \alpha_0 \quad (12.8)$$

where f_c is called the *critical frequency* for the particular angle of incidence, α_0 . This is equivalent to (11.64). The critical frequency is thus a cut-off frequency for rays entering with angle α_0 . Because the secant function can be no smaller than 1, the critical frequency must be greater than the plasma frequency. The result is a cone of visibility determined by the ionosphere.

Note that the detection of Jovian decametric radio noise depended on the fact that Jupiter's radiation was able to penetrate the Earth's ionosphere!

In the presence of magnetic fields, the situation is even more complicated, leading to birefringence, causing one of the planes of polarization of the wave to be removed. The index of refraction in this case becomes

$$n^2 = 1 - f_0^2 / [f(f \pm f_H)] \quad (12.9)$$

where

$$f_H = eB / (2\pi m) \quad (12.10)$$

the *cyclotron frequency*. The “+” case represents the *ordinary ray*, the “−” case, the *extraordinary ray*.

The presence of strong magnetic fields led the discoverers of Jovian decametric radiation (Burke and Franklin 1955) to conclude that the extraordinary ray was internally reflected within Jupiter's ionosphere, although subsequent observations cast doubt on this interpretation (Franklin and Burke 1958).

Later it was realized that the motion of the inner Galilean satellite, Io, can trigger Jovian decametric radiation through a dumping of high-energy particles into the Jovian ionosphere; this is described in Sect. 12.8.5.

12.8 The Jovian Magnetosphere

Some properties of the giant planet magnetospheres are summarized in Table 12.2 and illustrated in Fig. 12.14.

The most extraordinary of all the bizarre properties of the giant planets may be their extensive magnetospheres. Each one has a volume that dwarfs the Sun in scale, although this was unknown until the *Pioneer* and *Voyager* visits. In the case

Table 12.2 Properties of giant planet magnetospheres

Property/planet	Jupiter	Saturn	Uranus	Neptune
Dipole moment ($T\ m^3$)	1.584×10^{20}	4.633×10^{18} ^a	3.9×10^{17}	2.2×10^{17}
Dipole tilt from rotation axis	$\sim 10^\circ$ ^b	$< 1^\circ$	60° ^b	47°
Dipole offset	$0.11 R_J$ ^{c,d}	$0.036 R_S$ ^a	$0.31 R_U$ ^{c,e}	$0.55 R_N$ ^{c,f}
Surface field ($10^{-4}\ T$)	$4-13$ ^c	$0.2-0.8$ ^c	$0.1-0.9$ ^c	$0.1-0.8$ ^c
Interior rotation period	$9^h\ 55^m\ 26.^s704$	$9^h\ 34^m\ 13.^s$	$9^h\ 55^m\ 26.^s$	$16^h\ 6^m\ 36.^s$

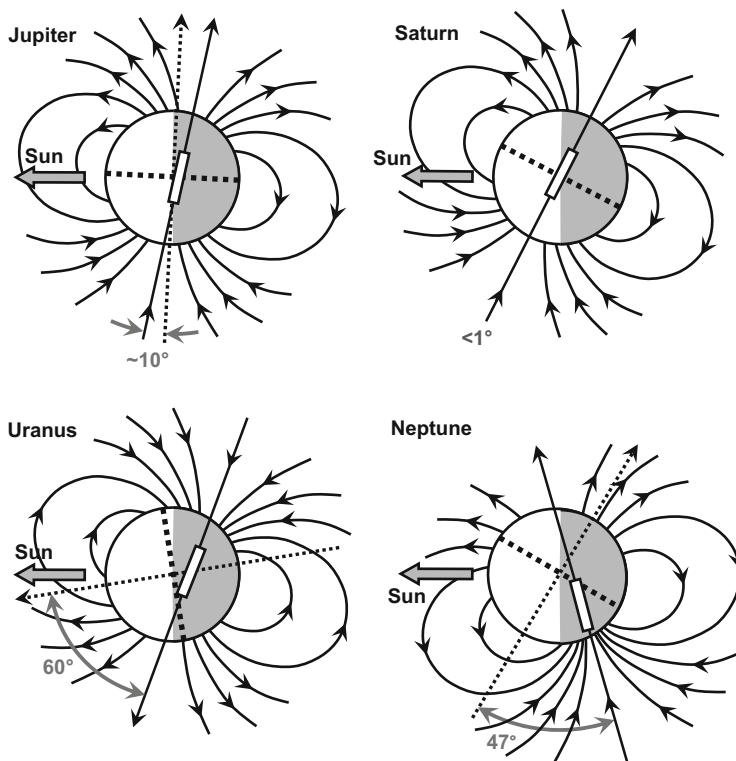
^aBurton et al. (2009) (Cassini data)^bRussell and Dougherty (2010)^cConnerney (1993) (Pioneer and Voyager data)^d $0.10 R_J$ parallel to equatorial plane and $0.01 R_J$ S of equatorial plane (Pioneer 11 data)^e $0.03 R_U$ parallel to equatorial plane and $0.31 R_U$ toward the pole that is north of the orbital plane^f $0.49 R_N$ parallel to equatorial plane and $0.24 R_N$ S of equatorial plane

Fig. 12.14 The inner magnetospheres of the giant planets. Dotted arrow: Rotation axis. Dotted diameter: Equator. Thick arrow: Direction to the Sun. Long, solid arrow: Magnetic axis. (For Saturn, the rotation and magnetic axes coincide to within 1° .) White rectangle: Dipole center and orientation. (The white rectangle does not represent the location where the field is generated, it is simply the center of the dipole geometry. The field is believed to be generated in a thick, conducting shell in the liquid mantle of each planet.) The rotation axis is in the plane of the page and each planet has been rotated to best show the magnetic axis. Nevertheless, the rotation and magnetic axes are not necessarily coplanar; e.g., Neptune's magnetic axis is tilted 22° to the plane of the page. Magnetic field lines leave the planet at the magnetic north pole and enter the planet at the magnetic south pole

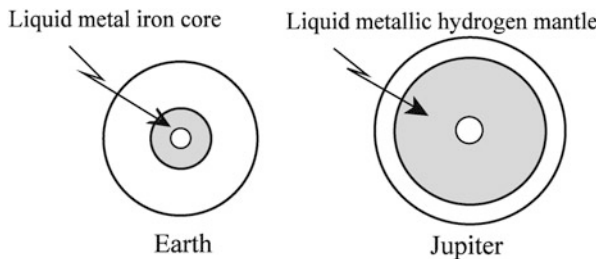


Fig. 12.15 The sources of global magnetic fields on Earth and Jupiter; figures not to scale

of Jupiter, the main phenomena, especially the decametric radio emissions, had been known from ground-based radio astronomy since the 1950s, so the spacecraft were equipped with extensive particle detectors and magnetometers; but the full extent and complexity of its magnetosphere were realized only with the spacecraft flybys. The magnetospheres of Saturn, Uranus and Neptune were completely unknown until the flybys.

Most of the Jovian magnetosphere corotates with Jupiter, in contrast to that of the Earth, with which only the innermost magnetosphere corotates.

Jupiter's magnetosphere is divided into three main regions according to the field geometry and the processes operating. The sizes of all three regions vary considerably according to solar wind conditions.

12.8.1 Inner Magnetosphere of Jupiter

Jupiter's inner magnetosphere is illustrated in Fig. 12.14. Its characteristics are

- Quasi-dipolar field produced by Jupiter's internal dynamo:
 - It is tilted $\sim 10^\circ$ to Jupiter's rotation axis.
 - It has opposite polarity to that of the Earth.

⇒ The N rotational pole is near the N magnetic pole.
- It has stronger quadrupole and octupole moments than Earth, suggesting that the dynamo is closer to the surface than is Earth's. This, in turn, suggests that it is produced (most likely) in the liquid metallic hydrogen mantle (Fig. 12.15).
- This region gives rise to *Decimetric* radiation (*DIM*), illustrated in Fig. 12.16, and as observed in Fig. 12.17. It is characterized by
 - Radio wavelength radiation at $\lambda \approx 0.1\text{ m}$
 - Synchrotron radiation from trapped relativistic electrons with energies $\sim 10\text{--}40\text{ MeV}$ mirroring back and forth near the magnetic equator

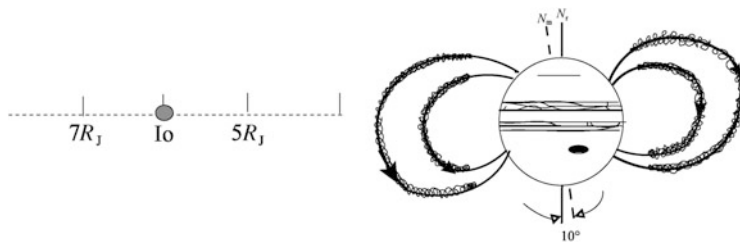


Fig. 12.16 The DIM source region, the radiation belts, and the locations of the orbit of the Galilean satellite Io

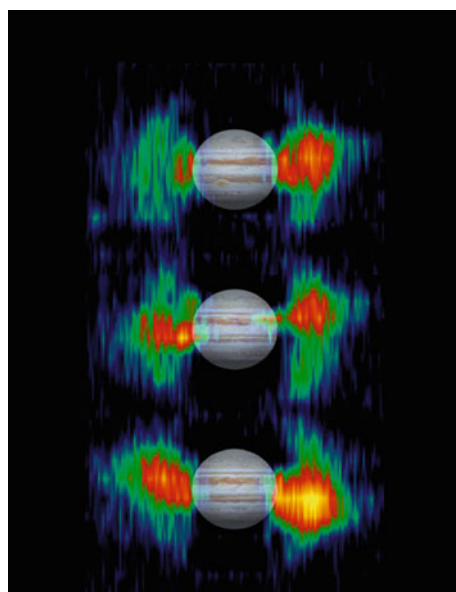


Fig. 12.17 The inner magnetosphere of Jupiter is revealed by the radiation belts at three moments in the 10 h rotation period of Jupiter. The particle density is coded so that *light colors* indicate higher density. They were observed by Cassini during its flyby of Jupiter en route to Saturn. NASA/JPL image PIA03478

- Two dominant source regions, one located close to the magnetic equator at $1.45\text{--}1.75 R_J$ and pitch angles near 90° , and the other crossing the magnetic equator at $2.27\text{--}2.50 R_J$ and mirroring over a large range of magnetic latitudes

12.8.2 Middle Magnetosphere of Jupiter

The field lines in this region are oriented approximately radially outward from Jupiter and roughly parallel to the equatorial plane. Parallel field lines require a

Fig. 12.18 The Jovian magnetodisk

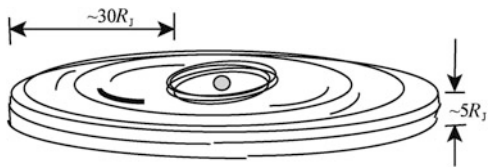
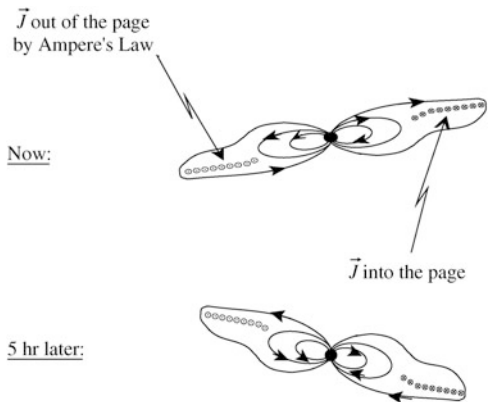


Fig. 12.19 The wobbling of the Jovian magnetodisk



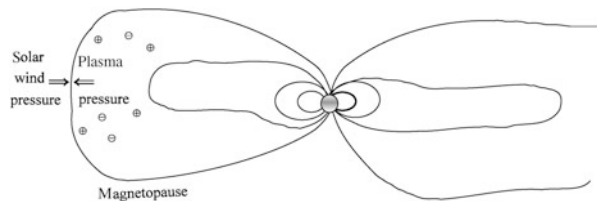
sheet of current: this implies the existence of a disk-like current sheet around Jupiter, the *magnetodisk*, illustrated in Fig. 12.18. The precise geometry is uncertain: close to Jupiter it appears to be parallel to the *magnetic* equator; further out, it appears to be parallel to Jupiter's *rotational* equator, so it wobbles as Jupiter rotates, as seen in Fig. 12.19.

12.8.3 Outer Magnetosphere of Jupiter

This is the region between the magnetodisk and the magnetopause. It includes a *magnetotail* a few au long, with cross-sectional radius $\sim 150\text{--}300R_J$, the upper and lower parts of which are separated by a current sheet that is a continuation of the magnetodisk, and is $\sim 5R_J$ thick. The configuration is sketched in Fig. 12.20.

The outer magnetosphere is highly variable, with inner edge $\sim 30\text{--}50R_J$, outer edge $\sim 45\text{--}100R_J$ (dayside). It is inflated by plasma pressure of energetic ions that have energies of 20–40 keV, similar to energies of particles in the Earth's ring current. The dominant ions are H, He, S, O. The number densities of the sulfur and oxygen ions are approximately that of hydrogen, $n_{S,O} \approx n_H$.

Fig. 12.20 The outer magnetosphere of Jupiter. This is the largest structure in the solar system, dwarfing the Sun in scale



The plasma pressure inflates the outer magnetosphere to about twice the size expected from the planetary dipole alone. This implies that the magnetosphere is soft, like a partially filled balloon, and that it is easily compressed by variations in the solar wind. In fact, the distances of the bow shock and the magnetopause from Jupiter can vary by about a factor of 2.

12.8.4 *Jovian Aurorae*

On the Earth, the energy source driving magnetospheric and auroral processes is the solar wind. In contrast, the dominant energy source for Jovian magnetospheric and auroral processes is Jupiter's rotation. Because the rotation is essentially constant, bright aurorae occur continuously at Jupiter's poles.

The auroral zone on Jupiter can be divided into four parts, as illustrated in Fig. 12.21: the main auroral oval, polar emissions poleward of the main oval, diffuse emission equatorward of the main oval and sometimes separated from it as a separate oval, and the magnetic footprints of the moons Io, Europa and Ganymede (Sect. 12.8.4). The electron flux for the main auroral oval is generated by processes in the middle magnetosphere at distances $\sim 20\text{--}30 R_J$ from Jupiter's center, associated with the breakdown of corotation. Io, Europa and Ganymede orbit at 5.9, 9.4 and 15 R_J , respectively, so magnetic field lines from them map to points outside the main oval (see Fig. 11.35 for a similar geometry).

The equatorward diffuse emissions map via magnetic field lines to radii in the equatorial plane $\sim 9\text{--}17 R_J$ from Jupiter's center, where wave activity ("whistler-mode waves") has been observed by *Galileo*. It is believed that these waves scatter electrons into the loss cone, resulting in electron precipitation in Jupiter's atmosphere.

12.8.5 *Interaction with Io*

It is appropriate to include a discussion of Io in this chapter, because satellites and rings are considered next, in Chap. 13, and because Io has a major influence on Jupiter's magnetosphere.

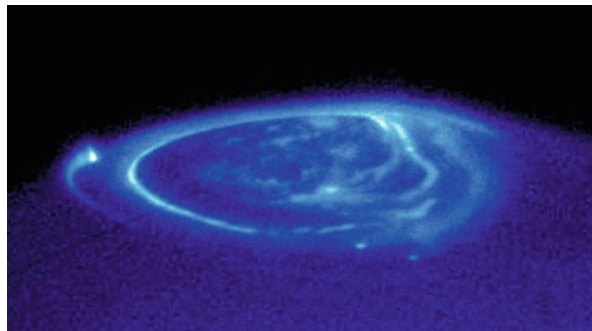


Fig. 12.21 Jupiter's northern aurora, photographed by the Hubble Space Telescope. The main auroral oval is visible (bright oval), as are polar emissions interior to the main oval, and diffuse emission just outside the main oval on the left and separated from it on the right. The magnetic footprints of the moons Io (bright spot and arc on the *left*), Ganymede (*left hand* of the two bright spots on the *lower right*, outside the main oval) and Europa (bright spot to the *right* and *below* Ganymede's footprint) are also visible. Image STSCI-PRC00-38. Credit: NASA and the Hubble Heritage Team (STScI/AURA). Acknowledgement: NASA/ESA, John Clarke (University of Michigan)

Several components of the interaction are illustrated in Fig. 12.22. Neutral atoms of S, O, Na, K and Cl escape from Io to form neutral clouds of these elements co-orbiting with Io around Jupiter. (Io orbits Jupiter in the plane of Jupiter's rotational equator.) These clouds are superimposed on each other, but have independent shapes. Although S and O make up >90 % (by mass or by number of atoms) of the elements leaving Io, Na scatters sunlight much more efficiently and is therefore the most visible neutral component.

Ions leaving the neutral clouds, as well as directly from Io, create a torus of plasma that corotates with the Jovian magnetic field and therefore might be expected to align with the Jovian magnetic equator, which is inclined $\sim 10^\circ$ from the rotational equator (Fig. 12.14). However, the centrifugal forces on the ions (as viewed in the rotating reference frame of the torus) act in the plane of the rotational equator and cause the torus to align in a plane inclined at 7° from the rotational equator. As viewed by an inertial observer outside the Io-Jupiter system, the magnetic equator and the torus wobble together as Jupiter rotates (cf. Fig. 12.19). The torus is dominated by O^+ , O^{++} , S^+ , S^{++} , and S^{+++} ions and electrons, with mean ion energies of ~ 100 eV and mean electron energies ~ 5 eV. Other aspects of Fig. 12.22 are discussed below.

Volcanism on Io (Sect. 13.1.2.1) is the ultimate source for all particles escaping from Io. The eruptions consist predominantly of silicate lavas and plumes of sulfur dioxide (SO_2), with smaller amounts of sulfur (S_2), SO, NaCl, K, and other molecules. The resulting tenuous atmosphere is composed primarily of SO_2 with $\sim 3\text{--}10\%$ SO by number and small amounts of other components. It is not yet clear whether this atmosphere is maintained directly by volcanic outgassing or if the

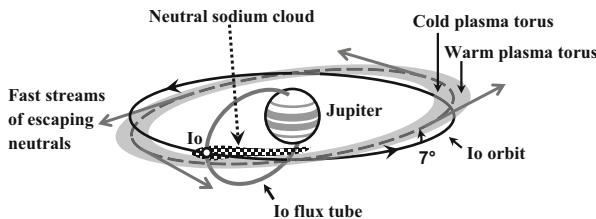


Fig. 12.22 The interaction between Io and the magnetosphere of Jupiter. Jupiter is shown to scale relative to Io's orbit, but Io is greatly enlarged for visibility. Io's orbit is in the plane of Jupiter's rotational equator. The plasma torus, consisting of cold plasma within Io's orbital distance (dashed line) and warm plasma outside, is inclined 7° from the rotational equator and corotates with Jupiter (57 km/s faster than Io). The torus is inclined 3° from the magnetic equator, and the two wobble together as Jupiter rotates. Neutral S, O, Na, K and Cl atoms from Io spread out into banana-shaped clouds ahead of and within, and behind and outside, Io's orbit (only the sodium cloud is shown). Streams of fast neutral atoms spread outward in a sheet from the plasma torus and eventually escape from the Jovian system. Note also the flux tube along which ions and electrons stream between the Jovian atmosphere and Io

gases condense on the surface and the atmosphere is maintained by sublimation. Although there are conflicting observations and major uncertainties, the surface pressure appears to be $\sim 6 \times 10^{-10}$ bar near the equator (see the review by Lellouch et al. 2007), decreasing gradually to about $\pm 45^\circ$ latitude and dropping precipitously at greater latitudes. In the upper atmosphere, there is a bound ionosphere with peak electron densities $10^4\text{--}10^5 \text{ cm}^{-3}$ extending to ~ 200 km altitude near the center of the upstream hemisphere (opposite to Io's orbital motion) and to ~ 400 km near the boundary of the upstream and downstream hemispheres, plus a plasma wake extending downstream (in the direction of Io's orbital motion) as far as $10 R_{\text{Io}}$.

The observed loss rate of SO_2 molecules from Io is $1.6 \times 10^{28} \text{ s}^{-1} = 1,700 \text{ kg/s}$ or 1.7 tonne/s (Saur et al. 2003), although it is not known what fraction of this mass is lost in molecular vs. atomic form (Schneider and Bagenal 2007). This is $\sim 5\%$ of the amount of SO_2 being outgassed by volcanoes, the rest condensing onto the surface. The measured mean column density of SO_2 (the number of molecules above a 1 m^2 surface area) is $\sim (1\text{--}5) \times 10^{20} \text{ m}^{-2}$ over 50–70 % of Io's surface, so a bit of algebra shows that if all volcanic activity suddenly ceased, the observed loss rate would eliminate Io's atmosphere in ~ 10 days. Io thus has a tenuous but very dynamic atmosphere with a short replenishment time.

Na atoms are lost at a rate of $\sim 10^{27} \text{ s}^{-1}$, or about 2 % of the SO_2 rate by mass, and the loss rates of K and Cl are similar, $\sim 1\text{--}3\%$. SO_2^+ and S_2^+ have also been seen in the plasma torus and must therefore have escaped Io in molecular form, and dust streams composed primarily of NaCl grains have been detected, correlating with Io's position. The dust composes $< 0.1\%$ of the mass lost by Io, which is too low to account for all of the Na and Cl observed in Jupiter's magnetosphere. Thus, additional loss mechanisms are required.

Based on several independent lines of reasoning, including observed UV emission by O and S atoms and ions near Io, available power for ionization, and a 3D model of Io's atmosphere and ionosphere interacting with the plasma torus, Saur et al. (2003) show that at most 20 % of the loss from Io is in the form of ions. The dominant transfer process from Io's atmosphere to the plasma torus is thus through the neutral clouds.

Maximum ejection speeds in the volcanic plumes are \sim 1 km/s, which is significantly smaller than Io's escape speed of 2.6 km/s, so escape is not by direct ejection from the volcanoes. The mean atmospheric temperature is governed by several factors including distances from the Sun and Jupiter and volcanic heating, and is very uncertain, but a value in the range 200–300 K appears not unreasonable. At 300 K, the mean thermal speed of an oxygen atom (the lightest dissociation product of SO₂) is \sim 0.5 km/s, or \sim 1/5 v_{esc} , so Jeans escape is also insignificant.

Some of the mechanisms controlling the interaction of Io with the Jovian magnetosphere are (see Schneider and Bagenal 2007, for a more complete description):

- Sputtering [Sect. 11.2.5.3(e)]:

The corotational speed at Io's orbit is 74 km/s and Io's orbital speed is 17 km/s, so the ions in the torus are passing Io and the neutral clouds at a relative speed of 57 km/s. (Random thermal motion actually creates a distribution of speeds about this value.) Each S⁺ and O⁺ thus has 540 and 270 eV, respectively, of kinetic energy, which is enough to sputter several atmospheric atoms or molecules upward. The mean speed of sputtered particles is significantly less than escape speed, so most go into Io's extended corona. Those that do escape, however, are the primary source for the neutral clouds, and therefore ultimately for the plasma torus. Sputtering from Io's surface is inhibited by the atmosphere, which appears to be collisionally thick over \sim 70 % of the surface, and is not considered a significant source.

- Pickup ions [Sects. 11.2.5.3(e), 11.2.5.3(f) and 11.5.6]:

About 1/3 of the atoms in the neutral cloud are ionized by electron impact and then picked up by Jupiter's corotating magnetic field. The accelerated ions form the plasma torus. This also happens in Io's corona, supplying a smaller number of ions. The plasma in the torus is therefore self-sustaining: Torus ions sputter atmospheric atoms into the corona and the neutral clouds, and these atoms are in turn ionized to supply the ions for the torus. The cycle can continue only if there is a particle source to balance particle losses from the torus (see below), and an energy source to balance energy losses from the torus (radiative losses and collisions with slower-moving particles). The particle source is Io's volcanism, and the energy source is Jupiter's rotation.

- Charge-exchange reactions [Sect. 11.2.5.3(a)]:

The other 2/3 of the atoms in the neutral cloud are ionized by charge-exchange reactions, in which a slow-moving atom in the neutral cloud becomes a slow-moving ion that is picked up by the corotating magnetic field and added to the torus, and a fast-moving ion in the torus becomes a fast-moving neutral atom that leaves the torus tangentially at the corotational speed of 74 km/s (Fig. 12.21).

The escape speed from Jupiter at Io's orbit is ~ 24 km/s, so these fast neutral atoms form a thick sheet of escaping atoms in the plane of the torus, expanding out through Jupiter's magnetosphere into interplanetary space.

Thus, all of the particles entering the neutral clouds from Io are eventually ionized and enter the torus. The mean lifetime of ions in the torus is ~ 100 rotations around Jupiter, so each rotation of the torus through the neutral clouds adds $\sim 1\%$ new ions to the plasma.

- Molecular ion dissociation:

NaCl and other Na molecules from Io are ionized and picked up by the corotating magnetic field. When they are subsequently dissociated by radiation or electron impact, one product atom retains the charge of the molecule and remains in the torus and the other is neutral and joins the expanding sheet described above.

- Plasma transport:

Plasma diffusion across magnetic field lines is inhibited, but does occur, as evidenced by the dominance of sulfur and oxygen ions throughout Jupiter's magnetosphere. These ions must have originated from Io. Diffusion from the ion torus is strongly influenced by centrifugal forces (when viewed in the rotating frame), so outward ion diffusion is considerably faster than inward diffusion. The part of the plasma torus beyond Io's orbit ($\sim 6\text{--}7 R_J$ from Jupiter) therefore consists of relatively fresh, hot plasma (~ 100 eV) diffusing outward on time-scales of tens of days. The part of the torus interior to Io's orbit is replenished only very slowly so the plasma has time to cool radiatively to <1 eV. In a narrow band along Io's orbit ($5.6\text{--}6 R_J$), residence times are intermediate and the plasma cools only to ~ 20 eV.

- Io-generated field-aligned currents [Sects. 11.5.6 and 11.6.7]:

Figure 12.23 shows Io orbiting within Jupiter's corotating magnetic field. As seen by an inertial observer, Io's orbital motion carries it out of the page at 17 km/s and the corotation carries the magnetic field lines out of the page at 74 km/s. As seen by a non-inertial observer corotating with Jupiter, therefore, the magnetic field lines are stationary and Io is moving into the page at $74 - 17 = 57$ km/s. This motion of Io relative to Jupiter's magnetic field creates a non-electrostatic electric field $\vec{E} = \vec{v}_{Io} \times \vec{B}$ between the magnetic field lines on either side of Io, directed radially outward from Jupiter. Thus, Io acts as a source of emf, driving field-aligned currents into Jupiter's ionosphere along the outer field line and back to Io along the inner field line. Pedersen currents in Jupiter's ionosphere close the circuits, and also create a Hall current system in Jupiter's ionosphere (see Sect. 11.5.7).

The current at Io is most likely carried by Io's ionosphere and ions created in its neutral corona, rather than by Io's surface materials or interior.

Precipitation of electrons from the Io flux tube into Jupiter's atmosphere produces a bright spot of auroral emission somewhat equatorward of the auroral oval in each hemisphere, referred to as the *Io footprint* (see Fig. 12.21). Fainter footprints are produced by flux tubes from Europa and Ganymede.

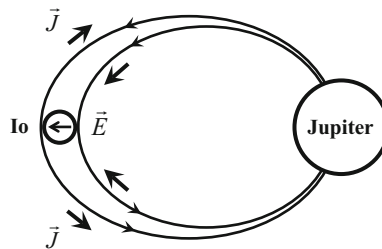


Fig. 12.23 The Io flux tube and field-aligned currents. Jupiter is shown to scale relative to Io's orbit, but Io is greatly enlarged for clarity. The arrow within Io indicates the non-electrostatic electric field, \vec{E} , created by Io's motion relative to the magnetic field lines. The arrowheads on the field lines indicate the magnetic field direction, and the *larger arrows* beside the field lines indicate the direction of the field-aligned currents, \vec{J} , driven by the non-electrostatic electric field. The circuits are closed by Pedersen currents in Jupiter's ionosphere

12.8.5.1 Decametric Radiation (DAM)

Decametric radiation (DAM) is the strongest radio emission from Jupiter, with $\sim 10^{10}$ W of emitted power and wavelengths generally in the tens of meters (deca is a prefix meaning 10). The frequency range is from a few MHz to nearly 40 MHz, or wavelengths from slightly over 7.5 m to several tens of meters. It is highly variable, with time scales of seconds to tens of seconds and structure down to milliseconds, and is produced by electrons in the tens of keV range (Burke and Franklin 1955).

Two types of DAM sources have been identified, those controlled by Io (referred to as Io-DAM) and those not controlled by Io (non-Io-DAM). A useful description can be found in Imai et al. (2008).

Io-DAM is seen when Io is at 90° phase at the eastern extremity of its orbit as seen from the Earth, and at 240° phase when Io is approaching the western extremity of its orbit. (0° phase occurs when Io is at superior geocentric conjunction with Jupiter, centrally behind Jupiter as seen from the Earth.)

Non-Io-DAM is closely tied to Jupiter's System III central meridian longitude (CML). The central meridian in this case is a longitude line on Jupiter passing through a hypothetical fixed point that rotates with Jupiter's interior as given by the System III period (Sect. 12.1.1), and the CML measures the angle that this central meridian makes with the direction to the Earth. Three such regions have been identified: C is found at CML $\sim 330^\circ$; A and B are found at CML $\sim 250^\circ$ and $\sim 160^\circ$, respectively, when observed at 16 MHz, but they gradually merge into a single source at $\sim 205^\circ$ as the frequency is lowered to 9 MHz.

Both Io-DAM and non-Io-DAM are almost completely elliptically or circularly polarized, which suggests that the radiation is produced by gyromotion.

The non-Io-DAM sources A and B are polarized in the right-hand sense, whereas source C can be polarized in either the right- or the left-hand sense. Sources A and B

are thought to be located in the northern auroral zone and source C in the southern auroral zone, on field lines that pass through the magnetic equator at Io's orbit, 5.9 R_J from Jupiter's center. The lack of correlation with Io's phase then suggests that they are associated with the Io torus rather than with Io itself.

The Io-DAM sources are believed to lie in or above the auroral zone on Jovian magnetic field lines that pass through the magnetic equator at Io's orbit, in flux tubes that were previously energized by Io but are now at a relatively-large angle ahead of (downstream from) Io.

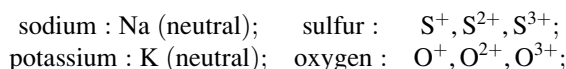
The high intensity of emission suggests that the emission mechanism involves collective phenomena, not just individual electrons executing gyromotion. Specifically, it is believed to involve the electron cyclotron maser instability, in which the relativistic mass increase causes electrons executing gyromotion about a magnetic field line to bunch up rather than being spread out uniformly around the magnetic field line (see Mauk 1982, for a description of this process). This emission is circularly to elliptically polarized, with the radiation beamed into a forward-pointing, thin-walled, hollow cone. The half-angle of the cone increases with increasing frequency. For a single, extended source region in which all cone axes point along magnetic field lines, this model produces two apparent source regions (like a rainbow being visible at only two points around the horizon), with the apparent source regions approaching each other as the frequency is decreased.

12.8.5.2 Neutral and Ionized Population of the Jovian Magnetosphere

The species observed in the magnetosphere are



The species concentrated in the Io plasma torus and neutral clouds:



Abundance ratios and sources

$$\frac{\text{C}}{\text{He}} \sim \text{solar}$$

∴ The source of C and He is the solar wind;

$$\frac{\text{H}}{\text{He}} > \text{solar}$$

∴ The major source of the hydrogen is the Jovian ionosphere; (Jupiter has approximate solar abundances of H and He (Sect. 12.1.2), but H has a larger scale height than He; consequently, there is a preferential escape of H relative to He from the ionosphere into the magnetosphere).

Jupiter's ionosphere is also the most likely source for the H₂ and H₃.

$\frac{S}{He} >>$ solar, and increases toward Jupiter
 and Io ∴ the source of S is Io.

- A. $\frac{O}{He} >>$ solar, in the region close to Jupiter and Io
 ∴ the source of O is Io.
- B. $\frac{O}{He}$ is nearer to solar in the outer magnetosphere
 ∴ the solar wind may be an important source also.

Io is the source for at least half the number of particles and 98 % of the mass in the Jovian magnetosphere.

12.8.5.3 Jovian Magnetodisk and the Vasyliūnas Cycle

In a terrestrial magnetosphere, such as at the Earth and Mercury, gradient and curvature drift by the ions and electrons in the trapping region produce a ring current (Sect. 11.6.3.4). In a rotationally-dominated magnetosphere such as at Jupiter and Saturn, the ring current is produced by inertial effects. As viewed in the rotating reference frame, the ions and electrons in the Io plasma torus and elsewhere exert a centrifugal force outward against the magnetic field. The situation is somewhat analogous to a plasma (e.g., the solar wind) striking a region of magnetic field and producing a boundary current. In the case of Jupiter and Saturn, the magnetic field is southward in the equatorial plane and the outward push by the plasma produces a ring of current directed eastward, in the direction of planetary rotation. However, the mass of ions provided by Io and the rotational speed of Jupiter are both much greater than is the case for the Earth, and the inward pressure on the plasma provided by the magnetic field cannot balance the outward pressure created by the centrifugal force on the ions. Consequently, the ions move outward, dragging the magnetic field lines with them until the magnetic pressure from the stretched field lines balances the outward pressure from the plasma. The ring current therefore expands radially outward to form a magnetodisk enclosed above and below by the stretched magnetic field lines (Figs. 12.19 and 12.20).

The supply of ions to the magnetosphere is referred to as *mass loading*. If the mass load becomes too great then the field lines will be stretched to the point that they reconnect across the current sheet, creating a plasmoid that can travel freely down the magnetotail and out of the Jovian system. The magnetic flux interior to the reconnected field line is now empty of plasma and returns inward until mass loading stretches it outward again. This cycle in which closed field lines are reconnected in a rotationally-dominated magnetosphere is referred to as the *Vasyliūnas cycle*, and differs from the Dungey cycle (Sects. 11.6.8 and 11.7.1.1) in the solar-wind-dominated magnetospheres of the Earth and Mercury, in which open magnetotail field lines are reconnected.

If the angular momentum of the outwardly-diffusing ions were conserved, then their speed around Jupiter would decrease with increasing radial distance from

Jupiter. However, the corotational speed of the magnetic field lines increases with increasing distance, with the result that the ions tend to drift backward relative to the magnetic field. Newly-created ions formed from slow-moving neutral atoms by electron impact or charge exchange also find themselves in a situation of being immersed in a magnetic field that is moving faster than they are. In both cases, the backward force (opposite to the direction of rotation) by the ions on the magnetic field creates a current, referred to as a *corotational enforcement current*, directed radially outward. From the right-hand rule, the $\vec{j} \times \vec{B}$ force on this current is in the direction of corotation, accelerating the ions toward the corotational speed. The corotational enforcement current is closed by field-aligned currents to and from Jupiter's ionosphere.

The magnetic field lines of the ring current are directed radially outward above the magnetodisk and radially inward below it, while the corotational enforcement current creates a weaker azimuthal field directed backward above the magnetodisk and forward below it. The vector sum of these radial and azimuthal field components results in a magnetic field above and below the magnetodisk that bends somewhat backward, trailing the rotation.

12.9 Saturn's Magnetosphere

Saturn's magnetosphere was first investigated during the *Pioneer 11*, *Voyager 1* and *Voyager 2* flybys, and has since been studied by *Cassini* since its arrival in 2004. With *Cassini*, we have been able to measure its properties over most of the equatorial magnetosphere and their variations over an extended time. A detailed review of Saturn's magnetosphere may be found in Arridge et al. (2011) and a less extensive review by Krupp et al. (2009), and the reader is referred to these works for references.

Saturn's magnetosphere is in some ways intermediate between those of Jupiter and the Earth, and in other ways it is more complex and uniquely Saturnian. For example, its rotational period is very similar to that of Jupiter, but its dipole moment is more than 30 times weaker (Table 12.2). Because Saturn's radius is ten times larger than that of the Earth, its magnetic field strength at the cloud tops is similar to that at the Earth's surface, $\sim 0.2\text{--}0.5 \times 10^{-4}$ T, and the magnetic field strength in the magnetosphere is much weaker than that of Jupiter. The average distance from the center of Saturn to the subsolar magnetopause is $25 R_S$, with observed excursions to ~ 17 and $\sim 29 R_S$. For comparison, the subsolar magnetopause distance at Jupiter varies between $\sim 50 R_J$ and $>100 R_J$, and between 6 and 15 Earth radii for the Earth. Saturn's magnetosphere is dominated by rotation, but being weaker, dayside reconnection and the sweeping of open field lines into the tail lobes also plays a role. It is also much more strongly mass-loaded than the Earth's; compared to Jupiter, however, the amount of mass-loading is significantly smaller, but with the lower magnetospheric field strength, the mass-loading can actually have a stronger effect. Thus, whereas the Earth's magnetosphere is specifically dominated

by the solar wind and Jupiter's by rotation, Saturn's magnetosphere shows characteristics of both.

The inner, dipolar region of the magnetosphere (Fig. 12.14) extends from Saturn's surface to $\sim 6 R_S$, close to the orbit of Dione. This region very closely corotates with Saturn, and also encloses the main rings, the three inner satellites, Mimas, Enceladus and Tethys, and the dominant sources of mass-loading for the magnetosphere. Beyond $6 R_S$, mass-loading causes the magnetospheric plasma to lag behind corotation, resulting in a quasi-dipolar region and ring current, and beyond that a thin magnetodisk (Section 12.9.2). Under strong solar wind conditions, the dayside magnetopause can be compressed to $\sim 23 R_S$ and the quasi-dipolar region extends to the magnetopause, so that the magnetodisk is excluded from the dayside. Under weaker solar wind conditions the magnetosphere expands, the quasi-dipolar region recedes to only $\sim 16 R_S$, and the hinged magnetodisc extends around the dayside, producing a more symmetric magnetosphere beyond $16 R_S$; see Arridge et al. (2011) for more details, especially their Figs. 9–11.

12.9.1 Neutral and Ionic Content

Saturn differs from Jupiter in the neutral and ionic species that dominate its magnetosphere: on Saturn, these are derived primarily from water, whereas on Jupiter they are derived from SO_2 from volcanism on Io. The dominant neutral species in Saturn's magnetosphere are H_2O , OH , O , H , H_2 and O_2 , which are ionized to form primarily O^+ , O_2^+ , OH^+ , H_2O^+ , H_3O^+ , H^+ , and H_2^+ .

The most important source of water is the satellite Enceladus. As discovered with the *Cassini* orbiter, watery plumes, or “geysers,” erupt from an area of “tiger stripes” on the southern hemisphere of Enceladus (Sect. 13.1.3), apparently originating in a liquid ocean below the icy crust. The plumes are composed of >90 % water vapor, with one to a few percent each of N_2 , CO_2 and CH_4 . Trace amounts of other organic molecules are also present, along with NH_3 , and Na . The ejection rate of water in the plumes has been estimated at $\sim 1\text{--}5 \times 10^{27} \text{ H}_2\text{O s}^{-1}$, or $150\text{--}300 \text{ kg s}^{-1}$, but is suspected to vary by as much as an order of magnitude. The ejection speed appears to be 2–3 times Enceladus’ escape speed of 0.25 km/s , but much less than its orbital speed of $\sim 12.5 \text{ km s}^{-1}$; so most of the plume material escapes, but remains close to Enceladus’ orbit. The lifetime of the molecules is $\sim 1,000 \text{ h}$, or 20–50 orbital revolutions around Saturn, and the material has time to spread, forming a nearly uniform neutral torus centred on Enceladus’ orbit ($r = 4 R_S$). The neutral molecules are also ionized to form a plasma torus that corotates with Saturn.

Ice grains are also ejected by the plumes at a rate of $\sim 5 \text{ s}^{-1}$, of which $\sim 10 \%$ escape and form the E ring.

The main rings of Saturn are composed of dust-sized and larger objects made up primarily of ice, and are a source of H_2 and O_2 in quantities comparable to those from Enceladus. Possible mechanisms include photo-desorption of water

molecules, sputtering by energetic magnetospheric particles, and meteoroid impacts. However, the rings absorb ions and electrons efficiently, so the particle flux over the rings is very low, and the UV flux appears to be too low to eject molecules in the required quantities. Therefore, meteoroid impacts are thought to be the dominant mechanism. The production rate of oxygen, either as O or O₂, is estimated to be $\sim 1 \times 10^{26} \text{ O s}^{-1}$, of which about half are scattered out of the ring environment. Of the latter, computations indicate that most follow large orbits that eventually re-impact the ring particles, ~14 % are lost into Saturn's atmosphere, and 0.4 % escape.

Those that remain in the ring environment continue to orbit Saturn with the rings and reach thermal equilibrium with the ring particle surfaces without being re-absorbed. Thus, the rings can be said to have an atmosphere. The scale height is of the order of 1,500 km for O₂ and 6,000 km for H₂, although the scale heights are slightly different on the two sides because of the different surface temperatures of the illuminated and dark sides of the rings. Production of O₂ and H₂ is balanced primarily by photodissociation to atomic O and H. The reaction releases energy, so much of the O and H escapes from Saturn. The rest is ionized and picked up by the magnetosphere or collides with and sticks to the ring particles. Being lighter, H is lost at a faster rate than O.

The rings not only have an atmosphere, they also have an ionosphere: *Cassini* has detected O₂⁺, O⁺ and H⁺ with an O₂⁺ density at $\sim 2.2 \text{ R}_S$ of $\sim 10^5\text{--}10^6 \text{ m}^{-3}$, compared to a rough upper limit of 10^{11} m^{-3} for the neutrals.

Sputtering from the icy surfaces of the inner satellites, including Enceladus, also contributes to the neutrals in the inner magnetosphere, although at lower rates than the two processes described above. Saturn's polar wind is believed to add a few kg/s of H⁺, H₂⁺ and H₃⁺ in the magnetosphere, a much smaller amount than from other sources. Titan also produces significant H₂ by thermal escape, producing its own H₂ torus and, by ionization, an H⁺ torus. The latter is a major source for H⁺ ions in the outer magnetosphere.

With Titan's dense, nitrogen-rich atmosphere, it was thought that it would also be a major source of neutral and ionized nitrogen through atmospheric sputtering. However, nitrogen has not been detected from Titan, and Enceladus contributes all or most of that seen. The reason may be related to the complexity and high variability of the magnetosphere near Titan's orbit, in part because the solar wind is occasionally strong enough to push the magnetopause inward past Titan's orbit, allowing ions to escape the Saturnian system. If the plasma sheet is bowl-shaped as discussed below, then Titan would also spend part of its time outside the flow of heavy ions that cause atmospheric sputtering.

12.9.2 Magnetospheric Currents

Because of Saturn's fast rotation and strong mass-loading, its ring current is in the form of a magnetodisk similar to that of Jupiter. On the dayside, the magnetodisk is variable in extent depending on the solar wind pressure (Sect. 12.9.1), but typically

extends to within a few R_S of the magnetopause; on the nightside it merges continuously with the cross-tail current sheet. During Saturn's southern summer, the magnetotail is north of the ring plane, and the magnetodisk on the nightside is warped from parallel to the magnetic (and rotational) equator closer to the planet to parallel to the solar wind direction further from the planet. Somewhat surprisingly, several sets of data from *Cassini* indicate that the magnetodisk on the dayside at this time also shows a warp away from the magnetic equator in the same sense as on the nightside, giving the disk a bowl-shaped appearance. Some other data, however, did not show this effect, so it may vary with solar wind strength. Presumably, the warps would be toward the south during northern summer and absent at the equinoxes when the magnetotail is in the equatorial plane.

Because of Saturn's weaker magnetic field (compared to Jupiter), the magnetodisk is strongly influenced by variations in solar wind pressure. When the solar wind is weaker, the magnetic field of the magnetodisk current dominates the internal dipole field and the magnetodisk is almost symmetric, but when the solar wind is stronger, compressing the dayside magnetosphere, the ring current weakens on the dayside, the dayside magnetic field becomes more dipolar, and the magnetodisk becomes highly asymmetric.

Also with Saturn's weaker intrinsic magnetic field, the corotational enforcement current produces a more strongly swept-back configuration in the field lines above and below the magnetodisk than occurs at Jupiter (Sect. 12.8.5.3). The outwardly-directed (from Saturn) field-aligned currents appear to map to $\sim 3\text{--}4 R_S$ in the equatorial plane, which identifies the inner boundary of the corotational enforcement current system.

12.9.3 Radiation Belts

Absorption of energetic particles by the main rings prevents radiation belts from forming between 1.2 and $2.3 R_S$, but a permanent radiation belt consisting of $\sim \text{keV}$ to several tens of MeV protons has been found between $2.3 R_S$ and the orbit of Tethys at $4.9 R_S$; temporary belts have been observed to form and decay between the orbit of Tethys and $\sim 8 R_S$ (a region encompassing the orbit of Dione at $6.3 R_S$), and another belt has been discovered to exist between Saturn and the rings (Roussos et al. 2008, 2011; Krupp et al. 2009). The radiation belts beyond the rings have been investigated *in situ* with *Cassini*'s particle detectors, but the innermost belt has so far been detected only by energetic neutral atoms reaching *Cassini* from charge-exchange reactions in the belt.

The transient belts form as a result of solar wind disturbances that compress Saturn's magnetosphere. It is not clear if solar wind particles leak into the magnetosphere and are transported to the belt region and accelerated to $>$ MeV energies, or if the compression creates processes that accelerate magnetospheric particles and inject them into the belt. After a belt forms, the particle paths gradually migrate

inward, and the belt decays over a time of several weeks as particles are removed by hitting the surfaces of Dione and Tethys.

The main belt between the rings and Tethys is very stable, and no solar wind effect has been detected. This means that Tethys must be very efficient at removing the inwardly-migrating particles each time an outer, transient belt is formed, leaving the inner belt isolated from solar wind disturbances. The particle source for the inner belt must therefore also be independent of the Sun and the solar wind. The source is believed to be galactic cosmic rays of GeV energies striking particles in Saturn's atmosphere and the rings, ejecting high-energy neutrons. About 0.1 % of these neutrons decay within Saturn's magnetosphere, producing >10 Mev protons and high-energy electrons which can become trapped in the radiation belt. The process is referred to as *cosmic ray albedo neutron decay*, or CRAND. The belt also contains a lower-energy population of ions with a flux similarly independent of solar wind conditions. Their origin is unknown, but may be related in some way to galactic cosmic rays or to interactions involving the higher-energy population.

The innermost belt, between the rings and Saturn, is believed to be caused by double charge exchange between the main belt and Saturn's exosphere: Charge exchange between slow-moving neutrals and energetic ions in the main belt creates energetic neutrals, some of which travel into Saturn's exosphere inside the rings and exchange charge with slow-moving ions. The result is a fast-moving ion that is picked up by the magnetic field interior to the rings.

12.9.4 *Saturn Kilometric Radiation (SKR)*

Saturn emits strongly at frequencies of \sim 20–1,200 kHz (wavelengths \sim 250 m to 15 km), referred to as the *Saturn kilometric radiation*, or SKR. The frequencies are below the critical frequency for the terrestrial ionosphere (Sect. 11.4.2), and so are difficult to detect from Earth. Studies therefore need to be done from spacecraft.

The characteristics of the emission suggest very strongly that, like the Jovian decametric radiation, it is caused by the Cyclotron Maser Instability (Sect. 12.8.5.1). The source region appears to be localized on magnetic field lines with upward currents (downward-moving electrons) that map to the ionosphere in Saturn's permanent auroral oval (Lamy et al. 2010).

A mysterious aspect of the SKR emissions is that they show a strong modulation at the rotational period of Saturn's magnetic field structure (Sect. 12.2). This is surprising because Saturn's dipole axis essentially coincides with its rotation axis, so there is no obvious asymmetry to create the modulation. Some suggested causes include periodic plasmoid ejection, the position of Titan in its orbit (possibly by influencing plasmoid ejection), and instabilities at the rotation period that propagate to other regions of the magnetosphere. For example, the plasma sheet has been observed to rock up and down at the SKR frequency.

We now move on to a more general exposition of the moons and rings of the solar system.

Challenges

- [12.1] Derive an expression for the central pressure and density of a planet, and use it to calculate the central pressure of each of the giant planets.
- [12.2] Work out an expression for and compute the central temperature of each of the giant planets.
- [12.3] The 21 fragments of Comet Shoemaker-Levy 9 impacted Jupiter in 1994 at speeds of ~ 60 km/s. Compute the explosive energy in each of the impacts of the ~ 1 km diameter chunks of cometary material. Assume densities of 250 kg/m^3 for the comet.
- [12.4]
 - (a) Verify the values for the absorbed power and their uncertainties in Table 12.1, using the Bond albedos³ and the solar luminosity ($3.845 \times 10^{26} \text{ W} \pm 8.000 \times 10^{23} \text{ W}$). The uncertainties may be found from the square root of the sum of the squares of the individual relative uncertainties.
 - (b) Verify the predicted and observed temperatures and their uncertainties in Table 12.1, using the absorbed and observed powers.
 - (c) Compute the “energy budget” (power emitted/power absorbed) and its uncertainty for each planet in Table 12.1. Discuss the numerical significance of the individual values, given their uncertainties. The energy budget of Saturn is greater than that of Jupiter. Is this difference significant? What about Neptune?

References

- Anderson, J.D., Schubert, G.: Saturn’s gravitational field, internal rotation, and interior structure. *Science* **317**, 1384–1387 (2007)
- Arridge, C.S., André, N., McAndrews, H.J., Bunce, E.J., Burger, M.H., Hansen, K.C., Hsu, H.-W., Johnson, R.E., Jones, G.H., Kempf, S., Khurana, K.K., Krupp, N., Kurth, W.S., Leisner, J.S., Paranicas, C., Roussos, E., Russell, C.T., Schippers, P., Sittler, E.C., Smith, H.T., Thomsen, M. F., Dougherty, M.K.: Mapping magnetospheric equatorial regions at Saturn from Cassini Prime Mission observations. *Space Sci. Rev.* **164**, 1–83 (2011)
- Baum, W.A., Code, A.D.: Photometric observations of the occultation of σ Arietis by Jupiter. *Astron. J.* **58**, 108–112 (1953)
- Beebe, R.: Jupiter the Giant Planet. 2nd ed., Smithsonian Institution, Wash., D.C. (1997)
- Bronshcen, V. A. (ed.): The Planet Jupiter (Tr. by A. Moscana). Israel Program for Scientific Translations (1969). Orig. Publ. in Russian, USSR Academy of Sciences, Moscow (1967)
- Burke, B.F., Franklin, K.L.: Observations of a variable radio source associated with the planet Jupiter. *J. Geophys. Res.* **60**, 213–217 (1955)

³The Bond albedo is formally defined, for example, by Lewis (1997, VI, p. 235) for a reflecting astronomical body over a passband (characterized by $\lambda = \lambda_{\text{eff}}$), such that: $A_B = [\int F_{\lambda,\text{reflected}} d\lambda / \int F_{\lambda,\text{incident}} d\lambda]$. Note: This is a *bolometric* Bond albedo only if the integration is taken over all wavelengths. See also the introduction to Chap. 9 of Milone and Wilson (2014).

- Burton, M.E., Dougherty, M.K., Russell, C.T.: Model of Saturn's internal planetary magnetic field based on Cassini observations. *Planet. Space Sci.* **57**, 1706–1713 (2009)
- Connerney, J.E.P.: Magnetic fields of the outer planets. *J. Geophys. Res.* **98**(E10), 18,659–18,679 (1993)
- Conrath, B.J., Gautier, D.: Saturn helium abundances: a reanalysis of Voyager measurements. *Icarus* **144**, 123–134 (2000)
- Cox, A.N. (ed.): *Allen's Astrophysical Quantities*, 4th edn. Springer-Verlag, New York (2000)
- Fouchet, T., Moses, J., Conrath, B.J.: Saturn from Cassini-Huygens. In: Dougherty M.K., Esposito, L.W., Krimigis, S.M. (eds.) Springer Praxis Books (2009). ISBN: 978-1-4020-9216-9 (Print) 978-1-4020-9217-6 (Online)
- Franklin, K.L., Burke, B.F.: Radio observations of the planet Jupiter. *J. Geophys. Res.* **63**, 807–824 (1958)
- Gehrels, T. (ed.): *Jupiter*. University of Arizona Press, Tucson, AZ (1976)
- Gehrels, T., Matthews, M.S.: *Saturn*. University of Arizona Press, Tucson, AZ (1984)
- Gibbard, S.G., Roe, H., de Pater, I., Macintosh, B., Gavel, D., Max, C.E., Bains, K.H., Ghez, A.: High-resolution infrared imaging of Neptune from the Keck telescope. *Icarus* **156**, 1–15 (2002)
- Grosser, M.: *The Discovery of Neptune*. Harvard University Press, Cambridge (1962)
- Guillot, T., Stevenson, D.J., Hubbard, W.B., Saumon, D.: The interior of Jupiter. In: Bagenal, F., Dowling, T.E., McKinnon, W.B. (eds.) *Jupiter: The Planet, Satellites and Magnetosphere*, pp. 35–57. Cambridge University Press, Cambridge (2004)
- Gurnett, D.A., Persoon, A.M., Kurth, W.S., Groene, J.B., Averkamp, T.F., Dougherty, M.K., Southwood, D.J.: The variable rotation period of the inner region of Saturn's plasma disk. *Science* **316**, 442–445 (2007)
- Hamilton, D.P., Ward, W.R.: Tilting Saturn. II. Numerical model. *Astron. J.* **128**, 2510–2517 (2004)
- Hide, R.: Origin of Jupiter's Great Red Spot. *Nature* **190**, 895–896 (1961)
- Hubbard, W.B., Burrows, A., Lunine, J.I.: Theory of giant planets. *Annu. Rev. Astron. Astrophys.* **40**, 103–136 (2002)
- Hunten, D.M., Veverka, J.: Stellar and spacecraft occultations by Jupiter: a critical review of derived temperature profiles. In: Gehrels, T. (ed.) *Jupiter*, p. 247. University of Arizona Press, Tucson (1976)
- Imai, M., Imai, K., Higgins, C.A., Theiman, J.R.: Angular beaming model of Jupiter's decametric radio emissions on Cassini RPWS data analysis. *Geoph. Res. Letters* **35**, L17103, doi: 10.1029/2008GL034987 (2008)
- Ingersoll, A.P., Dowling, T.E., Giersch, P.J., Orton, G.S., Read, P.L., Sanchez-Lavega, A., Showman, A.P., Simon-Miller, A.A., Vasavada, A.R.: Dynamics of Jupiter's atmosphere. In: Bagenal, F., Dowling, T.E., McKinnon, W.B. (eds.) *Jupiter: The Planet, Satellites and Magnetosphere*, pp. 105–128. Cambridge University Press, Cambridge (2004)
- Irwin, P.G.J.: *Giant Planets of our Solar System. Atmospheres, Composition, and Structure*. Springer, Heidelberg, and Praxis, New York (2009)
- Karkoschka, E.: Neptune's rotational period suggested by the extraordinary stability of two features. *Icarus* **215**, 439–448 (2011)
- Kent, D.: The curious aftermath of Neptune's discovery. *Phys. Today* **64**(12), 46–51 (2011)
- Krupp, N., Roussos, E., Lagg, A., Woch, J., Müller, A.L., Krimigis, S.M., Mitchell, D.G., Roelof, E.C., Paranicas, C., Carberry, J., Jones, G.H., Hamilton, D.C., Livi, S., Armstrong, T.P., Dougherty, M.K., Sergis, N.: Energetic particles in Saturn's magnetosphere during the Cassini nominal mission (July 2004–July 2008). *Planet. Space Sci.* **57**, 1754–1768 (2009)
- Kuiper, G.P.: Planetary atmospheres and their origin. In: Kuiper, G.P. (ed.) *The Atmospheres of the Earth and Planets*, pp. 306–405. University of Chicago Press, Chicago (1952)
- Lamy, L., Schippers, P., Zarka, P., Cecconi, B., Arridge, C.S., Dougherty, M.K., Louarn, P., André, N., Kurth, W.S., Mutel, R.L., Gurnett, D.A., Coates, A.J.: Properties of Saturn kilometric radiation measured within its source region. *Geophys. Res. Lett.* **37**, L12104 (2010). doi:[10.1029/2010GL043415](https://doi.org/10.1029/2010GL043415) (6 pages)

- Lecacheux, A., Zarka, P., Desch, M.D., Evans, D.R.: The sidereal rotation period of Neptune. *Geophys. Res. Lett.* **20**, 2711–2714 (1993)
- Lellouch, E., McGrath, M.A., Jessup, K.L.: Io's atmosphere. In: Lopes, R.M.C., Spencer, J.R. (eds.) *Io After Galileo: A New View of Jupiter's Volcanic Moon*, pp. 231–264. Springer Praxis Books, New York (2007)
- Levashov, P.R., Filinov, V.S., Bonitz, M., Fortov, V.E.: Path integral Monte Carlo calculations of helium and hydrogen-helium plasma thermodynamics and the deuterium shock Hugoniot. *J. Phys. A Math. Gen.* **39**, 4447–4452 (2006)
- Lewis, J.S.: *Physics and Chemistry of the Solar System*. Academic, San Diego, CA (1997). Revised edition
- Li, L., Baines, K.H., Smith, M.A., West, M.A., Pérez-Hoyos, S., Trammell, H.J., Simon-Miller, A.A., Conrath, B.J., Gierasch, P.J., Orton, G.S., Nixon, C.A., Filacchione, G., Fry, P.M., Momary, T.W.: Saturn's emitted power. *J. Geophys. Res.* **115**, E11002 (2012). doi:[10.1029/2010JE003631](https://doi.org/10.1029/2010JE003631) (16 pages)
- Li, L., Conrath, B.J., Gierasch, P.J., Achterberg, R.K., Nixon, C.A., Simon-Miller, A.A., Flasar, F.M., Banfield, D., Baines, K.H., West, R.A., Ingersoll, A.P., Vasavada, A.R., Del Genio, A.D., Porco, C.C., Mamoutkine, A.A., Segura, M.E., Bajoraker, G.L., Orton, G.S., Fletcher, L.N., Irwin, P.G.J., Read, P.L.: Emitted power of Jupiter based on Cassini CIRS and VIMS observations. *J. Geophys. Res.* **117**, E11002 (2010). doi:[10.1029/2012JE004191](https://doi.org/10.1029/2012JE004191) (17 pages)
- Lunine, J.I.: The atmospheres of Uranus and Neptune. *Annu. Rev. Astron. Astrophys.* **31**, 217–263 (1993)
- Marley, M.S.: Interiors of the giant planets. In: Weissman, P.R., McFadden, L.-A., Johnson, T.V. (eds.) *Encyclopedia of the Solar System*, pp. 339–355. Academic, San Diego, CA (1999)
- Mauk, B.H.: Electromagnetic wave energization of heavy ions by the electric “Phase Bunching” process. *Geophys. Res. Lett.* **9**(10), 1163–1166 (1982)
- Milone, E.F., Wilson, W.J.F.: *Solar System Astrophysics: Background Science and the Inner Solar System*, 2nd edn. Springer, New York (2014)
- Ouyed, R., Fundamenski, W.R., Cripps, G.R., Sutherland, P.G.: D-D fusion in the interior of Jupiter. *Astrophys. J.* **501**, 367–374 (1998)
- Pearl, J.C., Conrath, B.J.: The Albedo, effective temperature, and energy balance of Neptune, as determined from Voyager data. *J. Geophys. Res.* **96** (Supplement), 18921–18930 (1991)
- Pearl, J.C., Conrath, B.J., Hanel, R.A., Pirraglia, J.A., Coustenis, A.: The Albedo, effective temperature, and energy balance of Uranus, as determined from Voyage IRIS data. *Icarus* **84**, 12–28 (1990)
- Peek, B.M.: *The Planet Jupiter: The Observer's Handbook*, 2nd edn. Faber and Faber, London (1981)
- Proffitt, C.R.: Effects of heavy-element settling on solar neutrino fluxes and interior structure. *Astrophys. J.* **425**, 849–855 (1988)
- Read, P.L., Dowling, T.E., Schubert, G.: Saturn's rotation period from its atmospheric planetary-wave configuration. *Nature* **460**, 608–610 (2009)
- Rogers, J.H.: *The Giant Planet Jupiter*. Cambridge University Press, Cambridge (1995)
- Roussos, E., Krupp, N., Armstrong, T.P., Paranicas, C., Mitchell, D.G., Krimigis, S.M., Jones, G.H., Dialynas, K., Sergis, N., Hamilton, D.C.: Discovery of a transient radiation belt at Saturn. *Geophys. Res. Lett.* **35**, L22106 (2008). doi:[10.1029/2008GL035767](https://doi.org/10.1029/2008GL035767) (5 pages)
- Roussos, E., Krupp, N., Paranicas, C.P., Kollmann, P., Mitchell, D.G., Krimigis, S.M., Armstrong, T.P., Went, D.R., Dougherty, M.K., Jones, G.H.: Long- and short-term variability of Saturn's ionic radiation belts. *J. Geophys. Res.* **116**, A02217 (2011). doi:[10.1029/2010JA015954](https://doi.org/10.1029/2010JA015954) (20 pages)
- Russell, C.T., Dougherty, M.K.: Magnetic fields of the outer planets. *Space Sci. Rev.* **152**, 251–269 (2010)
- Saur, J., Strobel, D.F., Neubauer, F.M., Summers, M.E.: The ion mass loading rate at Io. *Icarus* **163**, 456–468 (2003)

- Schneider, N.M., Bagenal, F.: Io's neutral clouds, plasma torus, and magnetospheric interaction. In: Dr. Lopes R. M. C., Dr. Spencer, J.R. (eds.) *Io After Galileo*. Springer Praxis Books, New York (2007). ISBN 978-3-540-34681-4 (Print) 978-3-540-48841-5 (Online), 22 pages
- Stevenson, D.J.: Implications of the giant planets for the formation and evolution of Planetary Systems. In: Weaver, H.A., Danly, L. (eds.) *The Formation and Evolution of Planetary Systems*, pp. 75–90. Cambridge University Press, Cambridge (1989)
- Tholen, D.J., Tejful, V.G., Cox, A.N.: Planets and satellites. In: Cox, A.N. (ed.) *Allen's Astrophysical Quantities*, p. 12.2. AIP Press, Springer, New York (2000)
- Turner, H.H.: *Astronomical Discovery*. University of California Press, Berkeley (1963)
- von Zahn, U., Hunten, D.M., Lehmacher, G.: Helium in Jupiter's atmosphere: results from the Galileo probe helium interferometer experiment. *J. Geophys. Res.* **103**, 22,815–22,829 (1998)
- van der Waerden, B.L.: *Science Awakening II. The Birth of Astronomy*. Noordhoff, Leyden (1974)
- Ward, W.R., Hamilton, D.P.: Tilting Saturn. I. Analytic model. *Astron. J.* **128**, 2501–2509 (2004)
- Wildt, R.: Ultrarote Absorptionsbande in den Spektren der Grossen Planeten. *Naturwissenschaften* **19**, 109–110 (1931)
- Wildt, R.: Methan in den Atmosphären der Grossen Planeten. *Naturwissenschaften* **20**(47), 851 (1932)
- Wildt, R.: Ch. 5: Planetary interiors. In: Kuiper, G.P., Middlehurst, B.M. (eds.) *Planets and Satellite*, pp. 159–212. University of Chicago Press, Chicago, IL (1961)
- Yu, Z.J., Russell, C.T.: Rotation period of Jupiter from the observation of its magnetic field. *Geophys. Res. Lett.* **36**, L20202 (2009). doi:[10.1029/2009GL040094](https://doi.org/10.1029/2009GL040094) (4 pages)
- Zharkov, V.N., Trubitsyn, V.P.: *Physics of Planetary Interiors*. Pachart Publishing House, Tucson, AZ (1978) (Tr. W. B. Hubbard)

Chapter 13

Satellite and Ring Systems

13.1 Satellites

Satellites have been discussed for decades, for example, in a number of large books on planetary satellites published at the University of Arizona (such as, Burns 1977 or Burns and Matthews 1986), and spectacular images from the Voyager missions appear in multiple cached collections. The Galileo and Cassini missions have revealed even more detail and have probed the structure, composition, and environs of the Jovian and Saturnian moons even more thoroughly.

The radii of the satellites of the giant planets vary tremendously, with the largest moons (Ganymede and Titan) exceeding Mercury in size. The Galilean moons, Earth's moon, Titan, and Triton are the largest satellites and constitute a class of giant moons. Most of these moons (and even some slighter ones) possess atmospheres; Titan's is so extensive that it is optically thick to visible radiation. Study of its surface has been mainly through radar, but the photometric passbands of the instruments aboard the Cassini Orbiter have revealed some of the surface features and the Huygens probe that it released revealed a surprisingly familiar-looking world as it approached the surface.

Each satellite has its own particular properties and its own thermal history. The satellites demonstrate a variety of color, as evidenced by their photometric color indices. This information, along with reflectance spectroscopy, provide useful clues about the surface structure and composition of the satellites.

A number of lesser moons, from tens to hundreds of kilometers in radius, make up the bulk of the Saturnian and Uranian systems. These moons too are diverse: the very dark moon known as Umbriel in the Uranian system contrasts with the bright, icy moons Ariel, Oberon, and Titania.

The moons of the giant planets show a surprising amount of activity; several display bright, whitish smears across reworked landscapes, sharply contrasting with ancient cratered terrains. The smallest moon which shows these properties, Miranda, displays amazing landforms: at least three large, ovoidal or trapezoidal coronae made up of an outer belt of approximately parallel ridges and troughs

around an inner, smoother region; tilt-block style normal faults with cliffs up to 3 km high; and fault canyons up to 20 km deep. Such an amazing disparity of surface features could have been produced by the recent reconsolidation of a shattered moon after a major impact, in which the coronae formed as heavier material sank after reconsolidation. Such violent events must have been numerous since the origin of the solar system. Alternatively, the outwardly-facing tilt blocks and other features suggest an extensional origin in which the crust was forced apart by plumes of material rising from the interior (Pappalardo et al. 1997 and references therein). Tidal heating during a short-lived orbital resonance with another Uranian satellite could have provided the internal heat to drive the plumes. In the Saturnian system, the tiny moon Enceladus displays water geysers, demonstrating vigorous present-day tidal heating.

The major moons, and some of the planets and dwarf planets—e.g., Ganymede, Mercury, Ceres, and Pluto—may be the last of a larger population of intermediate-sized objects which were abundant in the early solar system. Most of them were either ejected from the inner solar system or had a violent end, such as a hypothetical Mars-sized body that has been proposed to have impacted the Earth to form the Moon. As we will demonstrate in Chaps. 14 and 15, many solar-orbiting smaller bodies appear binary or multiple, possible evidence of wide-spread collisions.

Fragments of larger moons may make up many of the rest of the current satellite population; and many of the outliers seem to be captured asteroids. The two Martian moons, Phobos and Deimos, are likely in this category.

The outer moons of the solar system tend to be icy bodies, but there are some bodies that appear to have densities less than 1 g/cm^3 ! Of course some of the densities are ill-determined, but the trend of lower density with distance outward from the sun is certainly striking.

In the Jovian system, the Galilean satellites show a similar trend of decreasing densities with distance from Jupiter. There is some suggestion that this is because Jupiter was much hotter earlier in its history, but the inner ones could have lost much of their volatiles through tidal heating subsequent to their formation.

The relative resurfacing ages of the satellites can be determined by the cratering densities, if correct assumptions are made about impact frequency with time across the solar system. The various ages of the surfaces on the Galilean moons can be seen in Johnson (1990, p.176, Fig. 7) where the numbers of craters are plotted against crater diameter for the Galilean satellites, Earth, Mars, and the Moon. The absence of cratering implies a youthful, that is, reworked surface. For example, the cratering densities for Io and Europa are artificially low because of the very active surfaces of these bodies. Both have two heat sources:

1. Radioactivity
2. Tidal action

The latter is much stronger than the former in Io, with its abundant volcanism and limited size. On Europa, on the other hand, tidal action is weaker because it depends on r^{-3} , so that radioactivity may play a more important role in maintaining its watery mantle (or lower crust).

Magnetometer data gathered by the *Galileo* orbiter, show evidence for a deep, salty ocean below the thick, icy crust of Callisto. Tidal heating is negligible, so radioactivity must be the dominant source of its heat.

Although Jupiter's main satellites very likely accreted from ices as well as rock, another important source of icy materials has been cometary bombardment, a process that is continuing today, as Comet Levy-Shoemaker 9 illustrated in 1994 when its fragments collided with Jupiter.

If we count as “major moons” those with a radius exceeding 1,000 km, there are seven: the Moon; the Galilean satellites Io, Europa, Ganymede, and Callisto; Titan; and Triton. Relaxing the definition to moons that exceed 1,000 km in diameter we can add four moons of Saturn (Tethys, Dione, Rhea, and Iapetus), four moons of Uranus (Ariel, Umbriel, Titania, and Oberon), and, significantly, Charon. Finally, if we relax the definition somewhat more to include objects with smaller diameters, say roughly 500 km, we may add Enceladus in the Saturnian system and Miranda (470 km) in the Uranian system. Mimas is just under 400 km diameter; Nereid is only 340 km in diameter and the dark moon Proteus, also in the Neptunian system, is an irregular object with dimensions 436 × 416 × 402 km.

Table 13.1 lists the orbital characteristics of the major moons of the planets. Table 13.2 does the same for the physical characteristics. In both tables, one or more colons after an entry indicate levels of uncertainty. The sources for both are the Astronomical Almanac for 2013 and online: <http://asa.usno.navy.mil>, and mainly for unnamed satellites, the IMCCE-SAI, the Natural Satellites Service online files; additional data are from links from NASA's Solar System Exploration site: <http://solarsystem.nasa.gov/planets/profile.cfm?Display=Moons> and the University of Hawaii's Institute for Astronomy website, <http://www.ifa.hawaii.edu/research/research.htm> and from the current literature. The sources for the data in the online tables are available in links to those tables. The satellite numbers in Column 1 are usually expressed in Roman numerals. The unnamed satellites (and some of the more recently named ones) are identified in terms of the discovery notation: *S/YYYY PN*, where the initial *S* = “Satellite”; *Y* denotes discovery year; *P* is the planet initial; and *N* is the sequence number of discovery within the year. Information on the discoveries and naming of moons by the International Astronomical Union can be found in Blunck (2009). Relatively newly named satellites have their discovery designations noted in the alternative final column under “Comment.” Values of orbital elements are usually mean quantities, and the inclinations are with respect to the planet's equator, unless noted otherwise (note the variation in some cases). The many unfilled columns, especially of masses and photometric characteristics, demonstrate how much work still needs to be done to study these objects. Note the similarities among some of the satellites, strongly suggesting a common origin for groups of them. Identified Jovian satellite “families” include the Himalia family of directly orbiting moons and the Pasiphae family of retrograde revolving moons; within the retrograde “family” one can identify groups such as Ananke and Carme, again named for prototypes. The NASA site identifies Saturn satellite groups as “Inuit” (prograde) and “Norse” (retrograde). In late 2012, there were 67 known satellites of Jupiter, 62 of Saturn, 27 of Uranus, and 13 of Neptune. It is also known that two of the “dwarf planets” have

Table 13.1 Orbital elements of solar system natural satellites

No. Name	P (d)	a (10^3 km)	e	i ($^\circ$)	$d\Omega/dt$ ($^\circ$ /y) [or $d\varpi/dt$]/comment
<i>Earth</i>					
1. Moon	27.321661	384.400	0.0549	18.28–28.58	19.34 ^a
<i>Mars</i>					
1. Phobos	0.31891011	9.376	0.0151	1.075	158.8
2. Deimos	1.2624408	23.458	0.0002	1.788	6.260
<i>Jupiter</i>					
1. Io	1.769137761	421.80	0.004	0.036	48.6
2. Europa	3.551181055	671.10	0.009	0.466	12.0
3. Ganymede	7.15455325	1,070.40	0.001	0.177	2.63
4. Callisto	16.6890170	1,882.70	0.007	0.192	0.643
5. Amalthea	0.49817908	181.40	0.003	0.380	914.6
6. Himalia	250.56	11,461	0.162	27.496	524.4
7. Elara	259.64	11,741	0.217	26.627	506.1
8. Pasiphae	743.63	23,624	0.409	151.431	185.6
9. Sinope	758.90	23,939	0.250	158.109	181.4
10. Lysithea	259.20	11,717	0.112	28.302	506.9
11. Carme	734.17	23,404	0.253	164.907	187.1
12. Ananke	629.77	21,276	0.244	148.889	215.2
13. Leda	240.92	11,165	0.164	27.457	545.4
14. Thebe	0.6745	221.9	0.018	1.080	—
15. Adrastea	0.298	129.0	0.002	0.054	—
16. Metis	0.295	128.0	0.001	0.019	—
17. Callirhoe	736	24,596	0.206	143 ^a	— = S/1999 J1
18. Themisto	130	7,450	0.20	46	— = S/2000 J1 ^b
19. Megalite	734.1	23,439	0.528	151.7	— = S/2000 J8
20. Taygete	650.1	21,672	0.246	163.5	— = S/2000 J9
21. Chaldene	591.7	20,299	0.155	165.6	— = S/2000 J10
22. Harpalyke	617.3	20,918	0.200	149.3	— = S/2000 J5
23. Kalyke	767	24,136	0.318	165.8	— = S/2000 J2
24. Iocaste	606.3	20,643	0.269	149.9	— = S/2000 J3
25. Erinome	661.1	21,868	0.347	160.9	— = S/2000 J4
26. Isonoe	704.9	22,805	0.281	165.0	— = S/2000 J6
27. Praxidike	624.6	21,098	0.146	146.4	— = S/2000 J7
28. Autonoe	778.0	24,413	0.459	152.1	— = S/2001 J1
29. Thyone	610.0	20,770	0.283	148.3	— = S/2001 J2
30. Hermippe	624.6	21,048	0.248	149.8	— = S/2001 J3
31. Aitne	679.3	22,274	0.311	164.3	— = S/2001 J11
32. Eurydome	752.4	23,831	0.326	150.4	— = S/2001 J4
33. Euanthe	620.9	20,983	0.143	146.0	— = S/2001 J7
34. Euporie	555.2	19,509	0.101	146.4	— = S/2001 J10
35. Orthosie	613.6	20,850	0.286	140.9	— = S/2001 J9
36. Sponde	690.3	22,548	0.519	155.2	— = S/2001 J5
37. Kale	679.4	22,301	0.325	164.8	— = S/2001 J8
38. Pasithee	748.8	23,780	0.280	165.6	— = S/2001 J6

(continued)

Table 13.1 (continued)

No. Name	<i>P</i> (d)	<i>a</i> (10^3 km)	<i>e</i>	<i>i</i> ($^\circ$)	$d\Omega/dt(^{\circ}/y)$ [or $d\varpi/dt$]/comment
39. Hegemone	715	23,006	0.249	152.3	– = S/2003 J8
40. Mneme	599.7	20,500	0.208	148.0	– = S/2003 J21
41. Aoede	747	23,744	0.405	159.4	– = S2003 J7
42. Thelxinoe	635.8	21,317	0.238	151.0	– = S2003 J22
43. Arche	748.7	23,765	0.224	163.3	– = S/2002 J1
44. Kallichore	681.9	22,335	0.223	163.9	– = S/2003 J11
45. Heliike	601.4	20,540	0.138	154.6	– = S/2003 J6
46. Carpo	455.1	17,056	0.295	55.1	– = S/2003 J20
47. Eukelade	735.3	23,485	0.283	164.0	– = S/2003 J1
48. Cyllene	737.8	23,545	0.412	141.0	– = S/2003 J13
49. Kore	807.2	24,974	0.222	140.9	– = S/2003 J14
50. Herse	715.4	23,097	0.200	164.2	– = S/2003 J17
<i>Unnamed satellites of Jupiter (at present writing)</i>					
S/2000 J11	288.5	12,623	0.215	28.55	– = S/1975 J1 ^c
S/2003 J2	983	28,494	0.380	151.8	–
S/2003 J3	505	18,291	0.241	143.7	–
S/2003 J4	722	23,196	0.204	144.9	–
S/2003 J5	761	24,020	0.2095	165.0	–
S/2003 J9	684.0	22,382	0.269	164.5	–
S/2003 J10	768.4	24,185	0.214	164.1	–
S/2003 J12	533.0	18,952	0.376	145.8	–
S/2003 J15	667.2	22,012	0.113	140.8	–
S/2003 J16	596.8	20,434	0.269	148.6	–
S/2003 J18	607.7	20,683	0.138	146.5	–
S/2003 J19	700.8	22,746	0.334	162.9 ^a	–
S/2003 J23	759.2	23,991	0.309	149.2 ^a	–
S/2010 J1	724.3	23,237	0.320	163.2	–
S/2010 J2	588.4	20,229	0.308	150.3	–
S/2011 J1	582.2	20,102	0.296	162.8	–
S/2011 J2	725.1	23,267	0.387	151.9	–
<i>Saturn</i>					
1. Mimas	0.942421952	185.54	0.020	1.574	365.0
2. Enceladus	1.370218092	238.07	0.0047	0.009	156.2 ^d
3. Tethys	1.887802533	294.67	0.0001	1.091	72.25
4. Dione	2.736915569	377.42	0.0022	0.028	30.85 ^d
5. Rhea	4.51750271	527.07	0.0010	0.333	10.16
6. Titan	15.9454484	1,221.87	0.0288	0.312	0.5213 ^d
7. Hyperion	21.2766581	1,500.93	0.0232	0.615	–
8. Iapetus	79.331115	3,560.9	0.0293	8.313	–
9. Phoebe	546.414	12,893	0.1756	173.7 ^a	–
10. Janus	0.6945	151.46	0.007	0.163	– = S/1980 S1
11. Epimetheus	0.6942	151.41	0.010	0.351	– = S/1980 S3
12. Helene	2.7369	377.40	0.000	0.212	– = S/1980 S12
13. Telesto	1.8878	294.66	0.001	1.158	– = S/1980 S13

(continued)

Table 13.1 (continued)

No. Name	<i>P</i> (d)	<i>a</i> (10^3 km)	<i>e</i>	<i>i</i> ($^\circ$)	$d\Omega/dt(^{\circ}/y)$ [or $d\varpi/dt$]/comment
14. Calypso	1.8878	294.66	0.001	1.473	– = S/1980 S14
15. Atlas	0.6019	137.67	0.001	0.003	– = S/1980 S28
16. Prometheus	0.6130	139.38	0.002	0.008	– = S/1980 S27
17. Pandora	0.6285	141.72	0.004	0.050	– = S/1980 S26
18. Pan	0.5750	133.58	0.002	0.007	– = S/1981 S13
19. Ymir	1,315	23,130	0.33	173	– = S/2000 S1
20. Paaliaq	687	15,198	0.36	45	– = S/2000 S2
21. Tarvos	926	18,239	0.54	33	– = S/2000 S4
22. Ijiraq	451	11,442	0.32	47	– = S/2000 S6
23. Suttungr	1,017	19,465	0.11	176	– = S/2000 S12
24. Kiviuq	449	11,365	0.33	46	– = S/2000 S5
25. Mundilfari	952	18,722	0.21	167	– = S/2000 S9
26. Albiorix	783	16,394	0.48	34	– = S/2000 S11
27. Skathi	728	15,641	0.27	153	– = S/2003 S1
28. Erriapus	871	17,604	0.47	34	– = S/2003 S1
29. Siarnaq	896	17,531	0.30	46	– = S/2000 S3
30. Thrymr	1,092	20,219	0.49	176	– = S/2003 S1
31. Narvi	956	18,719	0.35	135	– = S/2003 S1
32. Methone	1.010	194.44	0.0001	0.007	– = S/2004 S1
33. Pallene	1.154	212.28	0.004	0.181	– = S/2004 S2
34. Polydeuces	2.737	377.20	0.019	0.177	– = S/2004 S5
35. Daphnis	0.594	136.50	0.000	0.000	– = S/2005 S1
36. Aegir	1,026	19,614	0.241	167.0	– = S/2004 S10
37. Bebhionn	835	17,119	0.47	35	– = S/2004 S11
38. Bergelmir	1,007	19,372	0.15	158	– = S/2004 S15
39. Bestla	1,053	19,959	0.77	148	– = S/2004 S18
40. Farbauti	1,079	20,291	0.21	158	– = S/2004 S9
41. Fenrir	1,269	22,611	0.13	163	– = S/2004 S16
42. Fornjot	1,354	23,609	0.19	168	– = S/2004 S8
43. Hati	1,080	20,304	0.29	163	– = S/2004 S14
44. Hyrrokkin	932	18,437	0.33	152	– = S/2004 S19
45. Kari	1,231	22,089	0.48	156	– = S/2006 S2
46. Loge	1,311	23,058	0.19	168	– = S/2006 S5
47. Skoll	878	17,665	0.46	161	– = S/2006 S8
48. Surtur	1,297	22,704	0.45	178	– = S/2006 S7
49. Anthe	1.0365	197.7	0.001	0.1	– = S/2007 S4
50. Jarnsaxa	965	18,811	0.22	163	– = S/2006 S6
51. Greip	921	18,206	0.33	180	– = S/2006 S4
52. Tarqeq	888	18,009	0.16	46	– = S/2007 S1
53. Aegaeon	0.808	167.5	0.0002	0.001	– = S/2008 S1
<i>Unnamed satellites of Saturn (as of present writing)</i>					
S/2004 S7	1,103	19,800	0.180	165.1	–
S/2004 S12	1,048	19,650	0.401	164.0	–
S/2004 S13	906	18,450	0.273	167.4	–

(continued)

Table 13.1 (continued)

No. Name	P (d)	a (10^3 km)	e	i ($^\circ$)	$d\Omega/dt$ ($^\circ$ /y) [or $d\varpi/dt$]/comment
S/2004 S17	913	18,600	0.259	166.6	–
S/2006 S1	972	18,981	0.130	154.2	–
S/2006 S3	1,142	21,132	0.471	150.8	–
S/2007 S2	800	16,560	0.218	176.7	–
S/2007 S3	1,100	20,578	0.130	177.2	–
S/2009 S1	0.473	117	0.0	0.0	–
<i>Uranus</i>					
1. Ariel	2.520379052	190.9	0.0012	0.041	6.8
2. Umbriel	4.14417646	266.0	0.0039	0.128	3.6
3. Titania	8.70586693	436.3	0.0011	0.079	2.0
4. Oberon	13.4632342	583.5	0.0014	0.068	1.4
5. Miranda	1.413479408	129.9	0.0013	4.338	19.8
6. Cordelia	0.335033842	49.75	0.0003	0.085	548.5
7. Ophelia	0.376400393	53.8	0.0099	0.104	417.9
8. Bianca	0.434578986	59.2	0.0009	0.193	298.7
9. Cressida	0.463569601	61.8	0.0004	0.006	256.9
10. Desdemona	0.473649597	62.7	0.0001	0.113	244.3
11. Juliet	0.493065489	64.4	0.0007	0.065	222.5
12. Portia	0.513195920	66.1	0.0001	0.059	202.6
13. Rosalind	0.558459529	69.9	0.0001	0.279	166.4
14. Belinda	0.623527470	75.3	0.0001	0.031	128.8
15. Puck	0.761832871	86.0	0.0001	0.319	80.91
16. Caliban	579.73	7,231.0	0.018	141.53 ^a	– = S/1997 U1
17. Sycorax	1,288.38	12,179	0.52	159.42 ^a	– = S/1997 U2
18. Prospero	1,978.37	16,277	0.44	151.83 ^a	– = S/1999 U3
19. Setebos	2,225.08	17,420	0.59	158.24 ^a	– = S/1999 U1
20. Stephano	677.47	8,007	0.22	143.82 ^a	– = S/1999 U2
21. Trinculo	749.40	8,505	0.22	166.97 ^a	– = S/2001 U1
22. Francisco	267.09	4,283	0.13	147.25	– = S/2001 U3
23. Margaret	1,661.00	14,147	0.68	57.37	– = S/2003 U3
24. Ferdinand	2,790.03	20,430	0.40	169.79	– = S/2001 U2
25. Perdita	0.638	76.417	0.003	0.068	– = S/1986 U10
26. Mab	0.923	97.736	0.003	0.134	– = S/2003 U1
27. Cupid	0.613	74.392	0.001	0.099	– = S/2003 U2
<i>Neptune</i>					
1. Triton	5.87685407 ^a	354.759	0.000016	156.865	0.5232
2. Nereid	360.134	5,513.818	0.7507	7.090	0.039
3. Naiad	0.29440	48.227	0.00033	4.74	620.2
4. Thalassa	0.31148	50.075	0.00016	0.21	551.1
5. Despina	0.33466	52.526	0.00014	0.07	466.0
6. Galatea	0.42875	61.953	0.00012	0.05	261.3
7. Larissa	0.55465	73.548	0.00139	0.20	143.5
8. Proteus	1.122	117.646	0.0005	0.075	28.80
9. Halimede	1,881.04	15,728	0.571	134.1	– = S/2002 N1

(continued)

Table 13.1 (continued)

No. Name	P (d)	a (10^3 km)	e	i ($^\circ$)	$d\Omega/dt$ ($^\circ$ /y) [or $d\varpi/dt$]/comment
10. Psamathe	9,116.64	46,695	0.450	137.4	– = S/2003 N1
11. Sao	2,914.695	22,422	0.293	48.5	– = S/2002 N2
12. Laomedea	3,166.718	23,571	0.424	138	– = S/2002 N3
13. Neso	9,737.565	48,387	0.495	132.6	– = S/2002 N4
<i>Unnamed satellite of Neptune (at present writing)</i>					
S/2004 N1	0.93618	105.28	–	–	–
<i>(134340) Pluto^e</i>					
1. Charon	6.38723	19.571	0.0000	96.145	– = S/1978 P1
2. Nix	24.8562	48.675	0.0023	96.18	– = S/2005 P2
3. Hydra	38.2065	64.780	0.0052	96.36	– = S/2005 P1
4. Kerberos	32.1	59:	–	–	– = S/2011 P1
5. Styx	20.2	47:	–	–	– = S/2012 P1
<i>(136199) Eris^f</i>					
1. Dysnomia	15.774	37.35	0.0	61 or 142	– = S/2005 Eris 1

^aRelative to ecliptic^bAlso J18 = S/1975 J1^cLost after 2000, but recovered by Scott Sheppard in 2012, according to<http://nssdc.gsfc.nasa.gov/planetary/factsheet/joviansatfact.html>^dVariation in periapse (not node) longitude^eData from Buie et al. (2006) for epoch 1,452,600.5, and Tholen et al. (2008). $M_{\text{Pluto}} = 2.3041 \times 10^{22}$ kg^fData from Brown et al. (2006); Brown and Schaller (2007)

moons. Eris has one: Dysnomia (Brown et al. 2006), and Pluto has five moons: Charon, Nix, Hydra (Weaver et al. 2006), Kerberos, and Styx. More solar system satellite discoveries can be expected.

We next discuss the properties of the major moons of the solar system, in the context of satellite populations of the giant planets and Pluto. No permanent natural satellites have been found around Mercury and Venus, and the Earth’s moon was discussed in Chap. 8. We note that recent simulations suggest at least 1 km-sized natural satellite likely to be present in a highly complex orbit around Earth. Until it is actually discovered, however, we begin this exposition with the moons of Mars.

13.1.1 The Moons of Mars

The moons were first described in some detail, not in any scientific publication, but in a work of satirical fiction: *Gulliver’s Travels*, by Jonathan Swift (1667–1745), published in 1726. Cited by Abell (1969), among many authors, the text describing the discovery of the astronomers in the enlightened land of Laputa, reads:

Table 13.2 Physical properties of solar system natural satellites

No.	Name	M/M_{Pl}	R (km)	$P_{\text{rot}}(d)/S^a$	A_V	V_0	B-V	U-B
<i>Earth</i>								
1.	Moon	0.0123000371	1,737.4	S	0.11	-12.74	0.92	0.46
<i>Mars</i>								
1.	Phobos	1.672×10^{-8}	13.4, 11.2, 9.2	S	0.07	11.9	0.6	-
2.	Deimos	2.43×10^{-9}	7.5, 6.1, 5.2	S	0.07	13.0	0.65	0.18
<i>Jupiter</i>								
1.	Io	4.704×10^{-5}	$< 1,821.3 >^b$	S	0.62	5.02	1.17	1.30
2.	Europa	2.528×10^{-5}	$< 1,562.0 >^b$	S	0.68	5.29	0.87	0.52
3.	Ganymede	7.805×10^{-5}	2,632.3	S	0.44	4.61	0.83	0.50
4.	Callisto	5.667×10^{-5}	2,409.3	S	0.19	5.65	0.86	0.55
5.	Amalthea	1.10×10^{-9}	125, 73, 64	S	0.09	14.1	1.50	-
6.	Himalia	2.2×10^{-9}	75, 60, 60	0.40	0.03	14.6	0.67	0.30
7.	Elara	4.58×10^{-10}	40	-	0.03	16.3	0.69	0.28
8.	Pasiphae	1.58×10^{-10}	18:	-	0.04:	17.02	0.74	0.34
9.	Sinope	3.95×10^{-11}	14:	0.548	0.04:	18.1	0.84	-
10.	Lysithea	3.31×10^{-11}	12:	0.533	0.04:	18.3	0.72	-
11.	Carme	6.94×10^{-11}	15:	0.433	0.04:	17.6	0.76	-
12.	Ananke	1.58×10^{-11}	10:	0.35	0.04:	18.8	0.90	-
13.	Leda	5.76×10^{-12}	5:	-	0.04:	19.0	0.7	-
14.	Thebe	7.89×10^{-10}	58, 49, 42	S	0.05	16.0	1.3	-
15.	Adrastea	3.95×10^{-12}	10, 8, 7	S	0.01:	18.7	-	-
16.	Metis	6.31×10^{-11}	30, 20, 17	S	0.06	17.5	-	-
17.	Callirhoe	5×10^{-13}	3.5:	-	0.06:	20.7	0.72	-
18.	Themisto	4×10^{-13}	2:	-	0.06:	20.3	0.83	-
19.	Megaclite	-	2:	-	0.06:	22.1	0.94	-
20.	Taygete	-	2:	-	0.06:	22.9	0.56	-
21.	Chaldene	-	1.5:	-	0.06:	22.5	-	-
22.	Harpalyke	-	1.5:	-	0.06:	22.2	-	-
23.	Kalyke	-	2:	-	0.06:	21.8	0.94	-
24.	Iocaste	-	2:	-	0.06:	22.5	0.63	-
25.	Erinome	-	1.5:	-	0.06:	22.8	-	-
26.	Isonoe	-	1.5:	-	0.06:	22.5	-	-
27.	Praxidike	-	2.5:	-	0.06:	22.5	0.77	-
28.	Autonoe	-	1.5:	-	0.06:	22.0	-	-
29.	Thyone	-	1.5:	-	0.06:	22.3	-	-
30.	Hermippe	-	2:	-	0.06:	22.1	-	-
31.	Aitne	-	1.5:	-	-	22.7	-	-
32.	Eurydome	-	1.5:	-	-	22.7	-	-
33.	Euanthe	-	1.5:	-	0.06:	22.8	-	-
34.	Euporie	-	1:	-	0.06:	23.1	-	-
35.	Orthosie	-	1:	-	0.06:	23.1	-	-
36.	Sponde	-	1:	-	0.06:	23.0	-	-
37.	Kale	-	1:	-	0.06:	23.0	-	-
38.	Pasithee	-	1:	-	0.06:	23.2	-	-
39.	Hegemone	-	1.5:	-	0.04:	22.8	-	-

(continued)

Table 13.2 (continued)

No.	Name	M/M_{J1}	R (km)	$P_{\text{rot}}(d)/S^a$	A_V	V_0	B-V	U-B
40.	Mneme	—	1:	—	0.04:	23.3	—	—
41.	Aoede	—	2:	—	0.04:	22.5	—	—
42.	Thelxinoe	—	1:	—	0.04:	23.4	—	—
43.	Arche	—	1.5:	—	0.04:	22.8	—	—
44.	Kallichore	—	1:	—	0.04:	23.7	—	—
45.	Helike	—	2:	—	0.04:	22.6	—	—
46.	Carpo	—	1.5:	—	0.04:	23.0	—	—
47.	Eukelade	—	2:	—	0.04:	22.6	—	—
48.	Cyllene	—	1:	—	0.04:	23.2	—	—
49.	Kore	—	1:	—	0.04:	23.6	—	—
50.	Herse	—	1:	—	—	23.4	—	—
<i>Unnamed satellites of Jupiter (at present writing)</i>								
S/2000 J11	—	2.0	—	—	22.4	—	—	—
S/2003 J2	—	1.0	—	—	23.2	—	—	—
S/2003 J3	—	0.5	—	—	23.6	—	—	—
S/2003 J4	—	1.0	—	—	22.7	—	—	—
S/2003 J5	—	1.75	—	—	22.0	—	—	—
S/2003 J9	—	0.65	—	—	23.6	—	—	—
S/2003 J10	—	0.9	—	—	23.6	—	—	—
S/2003 J12	—	0.65	—	—	23.8	—	—	—
S/2003 J15	—	0.7	—	—	23.3	—	—	—
S/2003 J16	—	0.75	—	—	23.0	—	—	—
S/2003 J18	—	1.0	—	—	23.0	—	—	—
S/2003 J19	—	0.75	—	—	23.5	—	—	—
S/2003 J23	—	1.0	—	—	23.5	—	—	—
S/2010 J1	—	1:	—	—	23.7	—	—	—
S/2010 J2	—	0.65:	—	—	24.2	—	—	—
S/2011 J1	—	0.9:	—	—	23.5	—	—	—
S/2011 J2	—	1:	—	—	23.7	—	—	—
<i>Saturn</i>								
1.	Mimas	6.61×10^{-8}	208, 197, 191	S	0.6	12.8	—	—
2.	Enceladus	1.90×10^{-7}	257, 251, 248	S	1.0	11.8	0.70	0.28
3.	Tethys	1.09×10^{-6}	538, 528, 526	S	0.8	10.3	0.73	0.30
4.	Dione	1.93×10^{-6}	563, 561, 560	S	0.6	10.4	0.71	0.31
5.	Rhea	4.06×10^{-6}	765, 763, 762	S	0.6	9.7	0.78	0.38
6.	Titan	2.366×10^{-4}	2,574.73	S	0.22	8.28	1.28	0.75
7.	Hyperion	1.00×10^{-8}	180, 133, 103	C	0.25	14.4	0.78	0.33
8.	Iapetus	3.18×10^{-6}	746, 746, 712	S	0.05 ^c	11.0	0.72	0.30
9.	Phoebe	1.45×10^{-8}	109, 109, 102	0.4	0.08	16.7	0.63	0.34
10.	Janus	3.34×10^{-9}	102, 93, 76	S	0.6	14.4	—	—
11.	Epimetheus	9.26×10^{-10}	65, 57, 53	S	0.5	15.6	—	—
12.	Helene	4.48×10^{-11}	22, 19, 13	—	0.6	18.4	—	—
13.	Telesto	1.27×10^{-11}	16, 12, 10	—	1.0	18.5	—	—
14.	Calypso	6.33×10^{-12}	15, 12, 7	—	0.7	18.7	—	—
15.	Atlas	1.16×10^{-11}	20, 18, 9	—	0.4	19.0	—	—

(continued)

Table 13.2 (continued)

No.	Name	M/M_{pl}	R (km)	$P_{\text{rot}}(d)/S^a$	A_V	V_0	B-V	U-B
16.	Prometheus	2.81×10^{-10}	68, 40, 30	S	0.6	15.8	—	—
17.	Pandora	2.41×10^{-10}	52, 41, 32	S	0.5	16.4	—	—
18.	Pan	8.71×10^{-12}	17, 16, 10	—	0.5:	19.4	—	—
19.	Ymir	—	10:	—	0.08:	21.9	0.80	—
20.	Paaliaq	—	13:	—	0.08:	21.2	0.86	—
21.	Tarvos	—	7:	—	0.08:	23.0	0.78	—
22.	Ijiraq	—	6:	—	0.08:	22.6	1.05	—
23.	Suttungr	—	4:	—	0.08:	23.9	0.47	—
24.	Kiviuq	—	8:	—	0.08:	22.6	0.92	—
25.	Mundilfari	—	3:	—	0.08:	23.8	0.58	—
26.	Albiorax	—	16:	—	0.08:	20.5	0.80	—
27.	Skathi	—	4:	—	0.08:	23.6	0.72	—
28.	Errapius	—	5:	—	0.08:	23.3	0.71	—
29.	Siarnaq	—	21:	—	0.08:	20.1	0.87	—
30.	Thrymr	—	4:	—	0.08:	23.9	0.41	—
31.	Narvi	—	2.5:	—	0.06:	23.8	—	—
32.	Methone	—	1.6	—	—	25.1	—	—
33.	Pallene	—	3, 3, 2	—	—	24.5	—	—
34.	Polydeuces	—	1.5, 1.2, 1.0	—	—	24.8	—	—
35.	Daphnis	1.48×10^{-13}	4, 4, 3	—	—	23.4	—	—
36.	Aegir	—	3:	—	0.06:	24.4	—	—
37.	Bebhionn	—	3:	—	0.06:	24.1	—	—
38.	Bergelmir	—	3:	—	0.06:	24.2	—	—
39.	Bestla	—	3.5:	—	0.06:	23.8	—	—
40.	Farbauti	—	2.5:	—	0.06:	24.7	—	—
41.	Fenrir	—	2.0:	—	0.06:	25.0	—	—
42.	Fornjot	—	3:	—	0.06:	24.6	—	—
43.	Hati	—	3:	—	0.06:	24.4	—	—
44.	Hyrrokkin	—	4:	—	0.06:	23.5	—	—
45.	Kari	—	3.5:	—	0.06:	23.9	—	—
46.	Loge	—	3:	—	0.06:	24.6	—	—
47.	Skoll	—	3:	—	0.06:	24.5	—	—
48.	Surtur	—	2.5:	—	0.06:	24.8	—	—
49.	Anthe	—	1:	—	0.06:	26.	—	—
50.	Jarnsaxa	—	2.5:	—	0.06:	24.7	—	—
51.	Greip	—	3:	—	0.06:	24.4	—	—
52.	Tarqiq	—	3.5:	—	0.06:	23.9	—	—
53.	Aegaeon	—	0.25:	—	0.06:	26.5	—	—
<i>Unnamed satellites of Saturn (at present writing)</i>								
S/2004 S7	—	3:	—	—	24.5	—	—	—
S/2004 S12	—	2.5:	—	—	24.8	—	—	—
S/2004 S13	—	3:	—	—	24.5	—	—	—
S/2004 S17	—	2:	—	—	25.2	—	—	—
S/2006 S1	—	3:	—	—	24.6	—	—	—
S/2006 S3	—	3:	—	0.06:	24.6	—	—	—

(continued)

Table 13.2 (continued)

No.	Name	M/M_{Pl}	R (km)	$P_{\text{rot}}(d)/S^a$	A_V	V_0	B-V	U-B
S/2007 S2	–	3:	–	–	24.4	–	–	–
S/2007 S3	–	2.5:	–	–	24.9	–	–	–
S/2009 S1	–	0.15:	–	–	26.8	–	–	–
<i>Uranus</i>								
1. Ariel		1.56×10^{-5}	$< 578.9 >^b$	S	0.39	13.2	0.65	–
2. Umbriel		1.35×10^{-5}	584.7	S	0.21	14.0	0.68	–
3. Titania		4.06×10^{-5}	788.9	S	0.27	13.0	0.70	0.28
4. Oberon		3.47×10^{-5}	761.4	S	0.23	13.2	0.68	0.20
5. Miranda		0.08×10^{-5}	240, 234, 233	S	0.32	15.3	–	–
6. Cordelia		5.18×10^{-10}	13	–	0.07:	23.1	–	–
7. Ophelia		6.21×10^{-10}	15	–	0.07:	22.8	–	–
8. Bianca		1.07×10^{-9}	23:	–	0.07:	22.0	–	–
9. Cressida		3.95×10^{-9}	33:	–	0.07:	21.1	–	–
10. Desdemona		2.05×10^{-9}	30:	–	0.07:	21.5	–	–
11. Juliet		6.42×10^{-9}	43:	–	0.07:	20.6	–	–
12. Portia		1.92×10^{-8}	55:	–	0.07:	19.9	–	–
13. Rosalind		2.93×10^{-9}	30:	–	0.07:	21.3	–	–
14. Belinda		4.11×10^{-9}	34:	–	0.07:	21.0	–	–
15. Puck		3.33×10^{-8}	78:	–	0.07:	19.2	–	–
16. Caliban		8.45×10^{-9}	30:	–	0.07:	22.4	–	–
17. Sycorax		6.19×10^{-8}	60:	–	0.07:	20.8	–	–
18. Prospero		–	15:	–	0.07:	23.2	–	–
19. Setebos		–	18:	–	0.07:	23.3	–	–
20. Stephano		–	10:	–	0.07:	24.1	–	–
21. Trinculo		–	7:	–	0.06:	25.4	–	–
22. Francisco		–	7:	–	0.06:	25.0	–	–
23. Margaret		–	8:	–	0.06:	25.2	–	–
24. Ferdinand		–	8:	–	0.06:	25.1	–	–
25. Perdita		–	13	–	–	24.0	–	–
26. Mab		–	12:	–	0.07:	25.4	–	–
27. Cupid		–	9	–	–	25.9	–	–
<i>Neptune</i>								
1. Triton		2.089×10^{-4}	1,353	S	0.756	13.47	0.72	0.29
2. Nereid		3.01×10^{-7}	170	–	0.155	19.7	0.65	–
3. Naiad		1.90×10^{-9}	29	–	0.072	23.9	–	–
4. Thalassa		3.66×10^{-9}	41	–	0.091	23.3	–	–
5. Despina		2.05×10^{-8}	74	–	0.090	22.0	–	–
6. Galatea		3.66×10^{-8}	79	–	0.079	21.9	–	–
7. Larissa		4.83×10^{-8}	96	–	0.091	21.5	–	–
8. Proteus		4.914×10^{-7}	218, 208, 201	S	0.096	19.8	–	–
9. Halimede		–	25:	–	0.06:	24.5	–	–
10. Psamathe		–	18:	–	0.06:	25.6	–	–
11. Sao		–	14:	–	0.06:	25.4	–	–
12. Laomedeia		–	17:	–	0.06:	25.4	–	–
13. Neso		–	22:	–	0.06:	24.6	–	–

(continued)

Table 13.2 (continued)

No.	Name	M/M_{Pl}	R (km)	$P_{\text{rot}}(d)/S^a$	A_V	V_0	B-V	U-B
<i>Unnamed satellite of Neptune (at present writing)</i>								
S/2004 N1	—	9:	—	—	—	—	—	—
<i>Pluto^d</i>	1.3041×10^{22}	1,180	—	0.3	15.12	0.80	0.31	—
1. Charon	0.1165	604 ± 1^d	S	0.372	18.0	0.71	—	—
2. Nix	4.481×10^{-5}	44	—	0.08	24.6	0.64	—	—
3. Hydra	2.413×10^{-5}	36	—	0.18	24.4	0.91	—	—
4. Kerberos	—	7.5:	—	—	25.8	—	—	—
5. Styx	—	5:	—	—	—	—	—	—
<i>Eris^e</i>	—	—	—	—	—	—	—	—
1. Dysnomia	—	175 ± 75	—	—	—	—	—	—

^aS ≡ synchronous case: $P_{\text{orbit}} = P_{\text{rot}}$; C ≡ chaotic

^bGeometric mean of 1,829, 1,819, 1,816 km for Io (J1); of 1,564, 1,561, 1,561 km for Europa (J2); of 581, 578, 578 km for Ariel (U1) for sub-planet, polar, and equatorial (normal to line of centers) radii, respectively. The geometric mean represents a volumetric radius, with which one can calculate mean density

^cA for the leading side of Iapetus; bright, trailing side value: 0.5

^dWeighted mean of occultation results from Gulbis et al. (2006) and Sicardy et al. (2006); data from Buie et al. (2006); Buie et al. (2010); Zalucha et al. (2011); Pluto's mass is in kg

^eData from Brown et al. (2006) and: <http://www.gps.caltech.edu/~mbrown/planetlila/>

...satellites, which revolve about Mars, whereof the innermost is distant from the centre of the primary planet exactly three of the diameters, and the outermost, five; the former revolves in the space of ten hours, and the latter in twenty one and a half, so that the squares of their periodical times are very near the same proportion with the cubes of their distance from the centre of Mars, which evidently shows them to be governed by the same law of gravitation that influences the other heavenly bodies.

The similarity to Phobos and Deimos would be remarkable (the actual distances are 2.76 and 6.9 \mathfrak{R}_\odot and periods are 7^h65 and 30^h3, for Phobos and Deimos, respectively) unless it were the case that Swift attended the same parish church as the Astronomer Royal (B. Marsden, ~1962, *private communication to EFM*). When that could have happened is unclear, as Swift spent much of his time in Ireland, but if it were the case, perhaps Britain's weather prevented the requisite follow-ups that a publication by an eminent astronomer would require. At least one other astronomer suspected the existence of two satellites for Mars: Johannes Kepler (1571–1630), much earlier, although Kepler's conjecture was not based on observation. The moons' discovery is formally credited to Asaph Hall (1829–1907), an astronomer with the US Naval Observatory, in 1877.

The moons are non-spherical, and they are heavily cratered; they are blanketed in regolith, especially Deimos, as Figs. 13.1 and 13.2 demonstrate. Phobos orbits Mars in so short a period that it is seen to move from west to east in the Martian sky. The densities of these bodies are low, 1.9 g/cm³ for Phobos and 1.8 for Deimos. The overall impression is that they are captured asteroids of C or D class, with reflection spectra similar to carbonaceous chondrites (refer to Chap. 15),



Fig. 13.1 Phobos, the inner natural satellite of Mars. Its reflection spectra suggest it to be similar to asteroids types C or D (see Chap. 15). The large crater on the *right* is Stickney, 9.6 km in total width. The orbit is within the synchronous orbital radius of Mars and is subject to decay due to tidal interaction (see Milone and Wilson 2014, Sect. 3.7, and Sect. 13.2). Phobos is expected to collide with Mars within 10^8 years if it does not break up first and form a ring. The quasi-parallel grooves are unrelated to Stickney, and are believed to be secondary crater chains from impacts on Mars (Murray et al. 2006). From the High Resolution Imaging Science Experiment (HiRISE) camera on NASA's Mars Reconnaissance Orbiter. Image PIA10367, courtesy of NASA/JPL-Caltech/University of Arizona

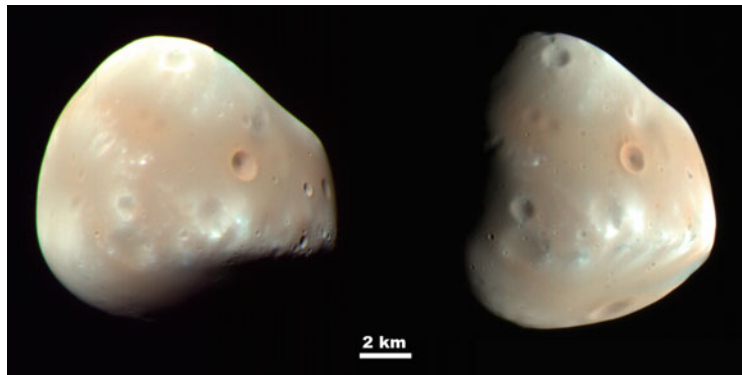


Fig. 13.2 Two images of the smaller Martian moon Deimos taken on Feb. 21, 2009 by the High Resolution Imaging Science Experiment (HiRISE) camera on NASA's Mars Reconnaissance Orbiter. The images are $5^h\ 35^m$ apart, but the Sun has shifted, illuminating the similar views differently. The colors are enhanced in these near IR, red, and blue-green combined images. Smoother areas seem to be heavily space-weathered and dusty. Note the extent to which its craters are filled with regolith. HiRISE images ESP_012065_9000 and ESP_012068_9000 combined in NASA image PIA 11826. Courtesy of NASA/JPL-Caltech/University of Arizona

but the mechanism for capture of these objects is unclear. Such asteroids are found in the outer asteroid belt, so they must have been captured. Phobos has a nearly circular orbit today. The capture mechanism for Phobos could have been orbital braking and circularization in a short-lived but extensive proto-Mars atmosphere; but Deimos would have had to arrive after this to avoid a collision with Phobos in that moon's initial highly eccentric orbit. Therefore Deimos' capture is the more problematic. Another mystery is why, if it survived from the early solar system, Phobos' orbit is now decaying rapidly: in a relatively short span of time ($<10^8$ years), it will have either crashed on Mars or disintegrated due to tidal stress. The Russian Phobos mission provided some clues to their origins, but the total picture has yet to be assembled.

13.1.2 *The Moons of Jupiter*

The satellites of the outer planets are in two main categories according to their orbits: direct and indirect. The direct satellites revolve in the same direction as their planet rotates. The indirect satellites have retrograde revolutions ($i > 90^\circ$) and usually high inclinations. The innermost satellites are connected with the rings of the planet, to be discussed later in this chapter. The outer satellites are almost certainly all captured objects, and the high inclinations and retrograde motions strongly suggest cometary origin.

The Galilean moons constitute a separate group, the major moons of the largest satellite system in the solar system. Discovered by Galileo, these four moons (which he called the Medicean satellites) were apparently not known in antiquity, even though in recent times individuals with exceptional acuity have demonstrated that they can see these fifth magnitude objects, and (traditional) knowledge of them has been attributed to certain cultures. As for the physical nature of these moons, the bulk of our data have come from the two Voyager missions, the extended Galileo mission, and the brief more recent visit by Cassini on its way to Saturn. Because their orbital properties have been mentioned before, we briefly describe only their physical properties. We describe them in the usual order, according to proximity to Jupiter, but Fig. 13.3 shows them in arranged order of size.

13.1.2.1 **Io**

The properties, origin, and escape of Io's atmosphere and Io's interaction with Jupiter's magnetosphere are described in Sect. 12.8.5. Here, we discuss Io's surface and interior.

Io rotates synchronously with its revolution around Jupiter, so that it always turns the same face to Jupiter. However, Io is also trapped in a 2:1 orbital resonance with Europa, so that Io always feels the strongest gravitational pull from Europa at the same point in its orbit (every second orbit of Io). This resonant

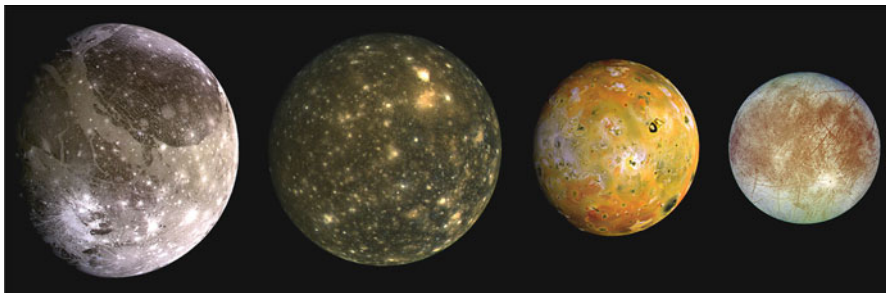


Fig. 13.3 A composite of Voyager and Galileo images of the Galilean moons of Jupiter in order of decreasing size: Ganymede (the largest moon in the solar system), Callisto, Io, and Europa, from *left to right*, respectively. North is up for each image, and scaled to 10 km/pixel. NASA/JPL/DLR/USGS image PIA00601

interaction produces a forced eccentricity of Io's orbit, causing Io to *librate*, or oscillate, about the Io-Jupiter line once each orbit. (A person on Jupiter would see Io appear to rock back and forth slightly, once each orbit.) The resulting tidal flexing of Io generates so much heat that Io is the most volcanic object in the solar system. The resurfacing rate from volcanic materials, amounting to ~1 cm depth per year, is so great that no impact craters have yet been found, even in the highest-resolution images (Williams et al. 2011). As a result of this heating, Io must have lost all of its icy volatiles long ago. The remaining volatiles—sulfur and sodium, for instance—constitute major components of the volcanic ejecta and of the surface terrain. This is the most active volcanic body discovered in the solar system, with perhaps a score of volcanoes active at any one time. Pools of lava with ‘islands’ have been imaged, and lava streams extend for many kilometers across the surface.

Volcanic plumes, analogous to Earth's geysers, may reach as high as 300 km above the surface and their conical sheets may be more than 1,000 km across. A direct link between the plumes and active volcanoes has been observed, as, for example, in Fig. 13.4.

In addition to these features, there are also lakes of lava and volcanic flows, as Fig. 13.5 shows. Galileo thermal imagers and ground-based infrared detectors indicate that although most of the thermal anomalies (events where the surface is not at the thermal equilibrium temperature expected from solar heating) are low-temperature events, there are lava temperatures even higher than the 1,400 K measured for lava on Earth. By itself, at 1 mbar pressure, sulfur boils at 450 K. Therefore, the hotter lava cannot be composed of molten sulfur alone, although impurities can raise the boiling point. The consensus seems to be that molten rock is present, at least in the high-temperature flows (Matson and Blaney 1999).

The internal heat escaping from Io has been measured at 1.05×10^{14} W, corresponding to a mean heat flux at Io's surface of 2.5 W/m^2 (Veeder et al. 2012).

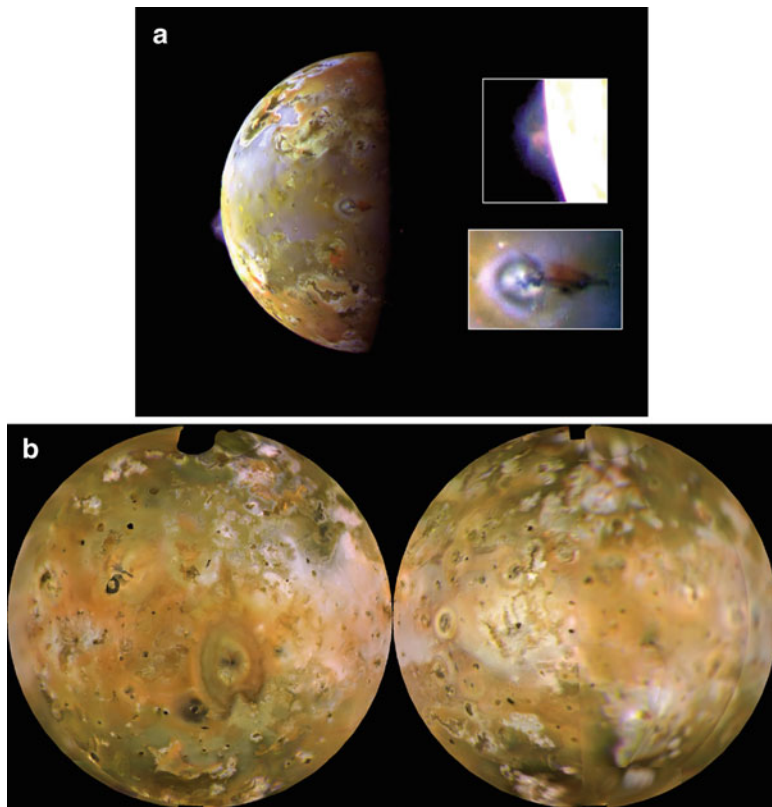


Fig. 13.4 (a) Io in eruption as seen by Galileo Orbiter. The volcanic plume on the limb originates from Pillan Patera while that at disk center is from Prometheus. Both illustrate the plume and conical sheet of the ejecta. NASA image PIA00703. (b) Annotated US Geological Survey maps of Io, based on Voyager I data. In natural color and done in equal area projection. At the *left center of the left figure* is the cloven-hoofed ejecta sheet of Pele. Pre-eruption Pillan is to its *upper right*. Original NASA/JPL/USGS image PIA00318

About half comes from hotspots covering 1.2 % of Io's surface, and much of the rest may come from small areas such as covered lava flows and subsurface dikes that are still warm but not bright enough to be detected by *Galileo*. The largest single contribution, 9.1 % of the total or 9.6×10^{12} W, is emitted by Loki Patera, a volcanic depression with a lava lake ~200 km across.

The atmosphere is primarily plume-fed SO₂, as described in Sect. 12.8.5. Sulfur, as a dissociation product of escaping SO₂, has blanketed Jupiter V (Amalthea), giving it an intense red color (see Table 13.2).

In addition to the volcanic structures, there are also lineated mountains (i.e., with well-defined ridges and grooves) ranging from 1 to 18 km in height. They are believed to have formed by tectonic processes: volcanic materials accumulate and compress the crust, and this eventually leads to fracturing, faulting, and uplift

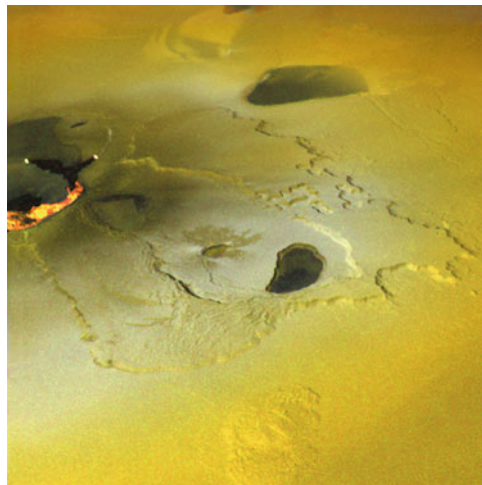
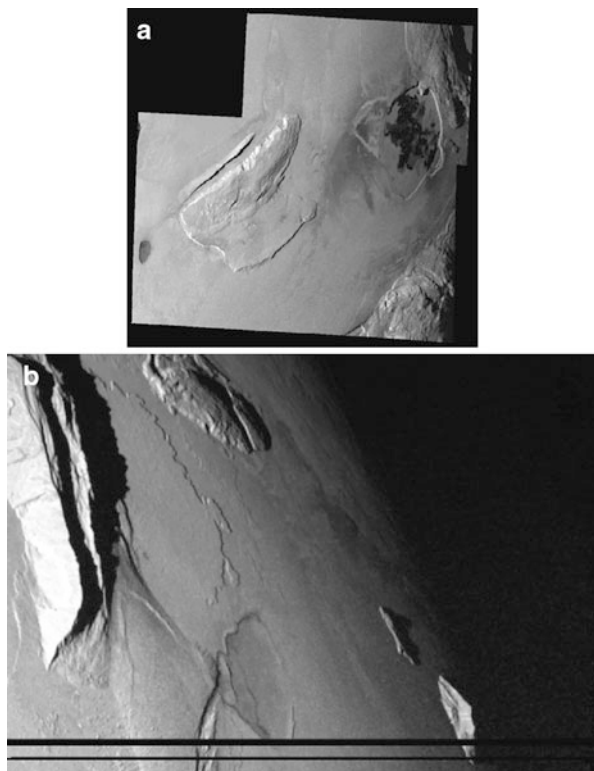


Fig. 13.5 From *Galileo*: a five-color mosaic of the Tvashtar Catena, a chain of calderas on Io. The white spots at left are places where hot lava is emerging from the toes of the flow; the bright white, yellow and reddish patches are false color representations from IR imagery that mark a 60 km long lava stream, now beginning to cool. The diffuse dark region around the main caldera marks deposits from a recent plume eruption. NASA/JPL/University of Arizona image PIA02550

(Williams et al. 2011). See Milone and Wilson (2014), Sect. 9.3 for descriptions of the known types of faults. Figure 13.6 illustrates some of these mountains.

Io has one of the higher densities among the major moons, $\sim 3,527 \text{ kg/m}^3$, attributed to the long-ago depletion of the most volatile ices. Measurements of Io's gravitational quadrupole moments by the *Galileo* spacecraft give an axial moment of inertia coefficient $K = 0.37685 \pm 0.00035$ (Anderson et al. 2001). Interior models compatible with these values of the mean density and moment of inertia indicate either an Fe-S core of 550–900 km radius or an Fe core of 350–650 km radius. The core is surrounded by a rocky mantle of density $3,250\text{--}3,700 \text{ kg m}^{-3}$, with forsterite (Mg_2SiO_4) the most likely mineral, and a lower-density, rigid crust (Khurana et al. 2011 and references therein). Lava temperatures at the surface indicate upper-mantle temperatures of $1,250\text{--}1,450^\circ\text{C}$, which suggests a partially or fully molten asthenosphere between the crust and the mantle. From magnetic induction studies as Io orbits within Jupiter's strong magnetic field, Khurana et al. (2011) find that the asthenosphere is at least 50 km thick, and molten enough (>20 % melt fraction) to provide a globally-continuous electrically conducting layer. The core has to be hotter than the mantle, and the melting point of iron is $\sim 1,400\text{--}1,500^\circ\text{C}$, so the high mantle temperature suggests that the core is completely molten. The complete lack of a detectable internal magnetic field also supports a fully-molten core.

Fig. 13.6 Mountains on Io, seen by Galileo Orbiter. (a) To the left of center is Shamsu Mons, through which a 10-km wide canyon can be seen. NASA/JPL/University of Arizona mosaic image PIA02555. (b) A view of 7-km high Mongibello Mons on the upper left; other mountains are seen even closer to the terminator. NASA/JPL/University of Arizona/ASU image PIA03886



13.1.2.2 Europa

This icy moon shows evidence of cracks and crustal movement, indirect evidence of fresh deposition on the surface, and a paucity (but not absence) of impact craters that indicate a recent, highly renewed surface. The presence of chaotic terrain, in which the patterning suggests rotation of ice “rafts,” extensive (wrinkle) ridges, dark spots (interpretable as upwelling material), and the near absence of craters provide strong indirect evidence of a water layer or, alternatively, of a slushy mantle. Yet there has been no direct visual evidence of a water layer beneath the visible icy crust: no geysers.

Besides the surface features, evidence for a subsurface ocean has been provided by gravity and magnetometer data from *Galileo*. Europa’s mean density is $2,989 \text{ kg m}^{-3}$, and from gravity measurements by *Galileo*, its axial moment of inertia coefficient $K = 0.346$ (Anderson et al. 1998). The latter value shows that Europa is differentiated, and models by Anderson et al. (1998) indicate a metallic core of radius $\sim 400\text{--}800 \text{ km}$ for an Fe-FeS eutectic composition (see Sect. 5.4.4.5) or $\sim 250\text{--}600 \text{ km}$ for pure Fe (from their Fig. 1, assuming a maximum mantle density of $3,700 \text{ kg m}^{-3}$). The core is overlain by a rocky mantle and a

low-density crust (assumed water ice) 100–200 km thick. Europa has no intrinsic magnetic field, but magnetic fields induced by Europa's passage through Jupiter's magnetic field (which varies with time as seen by Europa) show that the crust contains a strongly electrically-conducting layer <100 km thick (Schilling et al. 2007). The simplest explanation is a liquid water ocean below the solid, icy crust. The solid ice in turn is believed to consist of a rigid layer underlain by a warmer, ductile layer, with estimates of the combined thickness ranging between 5 and 60 km.

The existence of a melt layer must be due to a combination of tidal effects and radioactive heating of the interior, because neither alone should be sufficient to explain the heated layer. Although there are relatively few craters, compared to those on the outer Galilean moons, there are ringed plains, indicating modification and resolidification following impacts.

Features on Europa include:

Linea: relatively smooth linear features, sometimes with linear ridges and grooves within them. The latter are called double ridges, and they may be flanked by parallel cracks, 1–2 km on either side (e.g., Androgeos Linea). Some have been interpreted as strike-slip faults, e.g., Astypalaea Linea, 290 km in length; however, other explanations are: volcanism, tidal squeezing, diapirism, compression, shear heating, and heating by magmatic sills. These and other models are reviewed by Dombard et al. (2013), who prefer the magmatic sill model which accounts for the parallel grooves and yet does not require a globally thin lithosphere. The latter requires a higher than observed thermal flux (1 W/m^2 vs. $\sim 10 \text{ mW}$). In addition to these linea, there are also arcuate grooves.

Lenticulae: spotted features, darker than surroundings

Chaotic terrain: regions of fractured, rotated blocks of material

Figure 13.7 illustrates these features.

Europa also has a tenuous atmosphere and ionosphere produced by energetic particles in Jupiter's magnetosphere striking Europa's icy surface. These particles eject H₂O by sputtering and produce H₂ and O₂ by *radiolysis*¹ (Plainiki et al. 2012). The radiolysis creates a reservoir of H₂ and O₂ molecules locked in the ice, from which individual molecules are ejected by sputtering. The atmospheric H₂O is then broken down by photolysis, producing H, O, OH and other water-group species. The hydrogen undergoes thermal (Jeans) escape, so Europa's atmosphere is predominantly O₂. The total release rate of H₂O over Europa's surface is $\sim 10^{27} \text{ s}^{-1}$, producing an average number density of $\sim 1.5 \times 10^{12} \text{ H}_2\text{O m}^{-3}$ at low altitudes ($< 0.1 R_E$). The average O₂ number density is $\sim 6 \times 10^{13} \text{ H}_2\text{O m}^{-3}$ at low altitudes. With their lower mass and larger scale heights, H₂ and H₂O become the dominant species at higher altitudes ($> 0.1 R_E$). Electron impact ionization creates an ionosphere extending throughout the atmosphere, with maximum ion densities $\sim 10^8 \text{ electrons m}^{-3}$ near the surface.

¹ The term *radiolysis* refers to the chemistry that follows the impact of ionizing radiation.

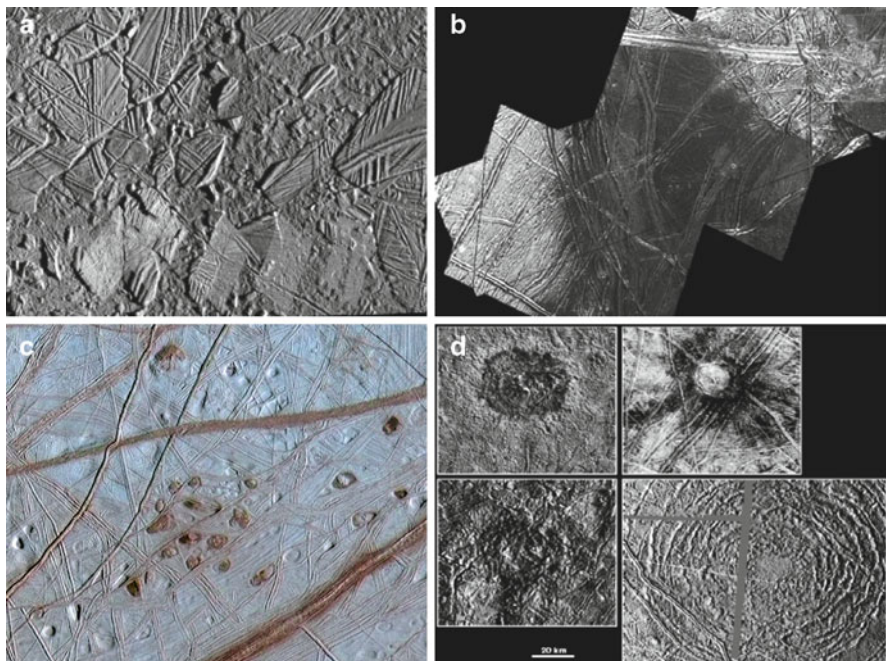


Fig. 13.7 Europan terrain. (a) Conamara Chaos, where blocks of icy crustal material have been disrupted and refrozen into new consolidations. Long linear ridges and faults as well as arcuate features are characteristic of Europa's surface. Credit: NASA/JPL/Arizona State University. NASA image PIA01403, from Galileo Orbiter's solid-state camera. (b) A mosaic of images of a dark, low area region near the equator. Although few, a cluster of small impact craters suggests that they are secondary craters from a major impact. NASA/JPL image PIA01405 produced by Deutsche Zentrum für Luft und Raumfahrt (DLR). All these images are from the Solid State Camera aboard Galileo. (c) A composite image of a lenticular region on Europa from the Galileo mission. The spots, typically ~10 km in diameter, may mark regions of upwelling material, melting and staining the ice above it, and due to the very low surface temperature of Europa, refreezing. NASA/JPL/University of Arizona/University of Colorado image PIA03878. (d) Craters on Europa. CW from the *upper right*: Cilix, Tyre, Mannann'an, and Pwyll. Tyre is analogous to the ringed plains of the Moon, Mercury, and Callisto. It may represent a major impact that broke through the hard icy crust into a slushier interior. The part of the structure shown here is 40 km diameter. NASA/JPL image PIA01661, produced by DLR

Europa's protected ocean makes it a candidate for biotic studies, in company with a number of other venues in the solar system where water exists in abundance, including the interiors of the giant planets, Ganymede, Titan, and on the small Saturnian moon, Enceladus.

Finally, water vapor detected in HST spectroscopy carried out in Dec., 2012, strongly suggests that these molecules arose from surface plumes. As on Enceladus, such activity appears to be strongest when furthest away from its planet, and may be centered on *linnae* regions. See: <http://www.nasa.gov/content/goddard/hubble-europa-water-vapor/#.Uq0kIeKQmZ0> for more details

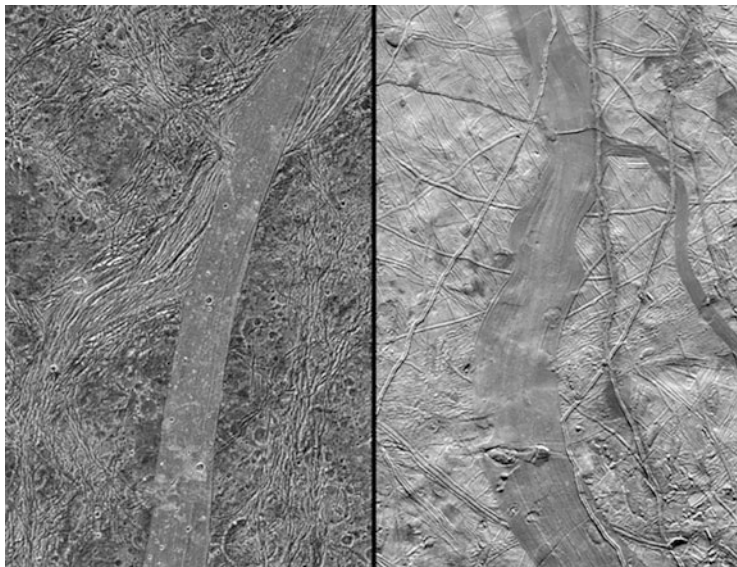


Fig. 13.8 Arbela Sulcus on Ganymede, *left*, and a similar feature on Europa, *right*, matched to the same resolution, 133 m/pixel. Tectonic effects are thought to be responsible for both: crustal spreading on Europa and strike-slip faulting on Ganymede. Note, however, the absence of craters on the Europa sulcus indicating a much younger surface. NASA/JPL image PIA02575, produced by Brown University

13.1.2.3 Ganymede

The largest moon of the solar system has a thick, icy crust, with a mixture of mainly two types of terrains: great grooved areas vs. heavily cratered plains. The dark, cratered plains are ancient (3.7–4.0 Gy), as indicated by the high frequency of craters. The grooved terrain is lighter, and more recent (3.1–3.7 Gy). The grooves are 5–10 km wide, and may represent fault-separated blocks of crust. This terrain may represent water ice which penetrated from depth and filled surface cracks and rifts, much like magma on the terrestrial planets. The Galileo Regio is an example of a dark furrowed region, and it, too, is ancient, but not as ancient, judging from crater frequencies, as the ancient cratered plains. New craters are bright, indicating fresh ice exposure. The general appearance of Ganymede is dark. Craters are numerous, their age being indicated, as on the Moon, by rim sharpness and by brightness, with darkness associated with older craters. Principle features (illustrated in Figs. 13.8 and 13.9) are:

Sulci: (singular: *sulcus*) similar to the *linea* of Europa

Palimpsests: bright and circular areas, probably sites of impacts

Penepalimpsests (dome craters): perhaps an intermediate form between craters and palimpsests, suggesting evolutionary connections

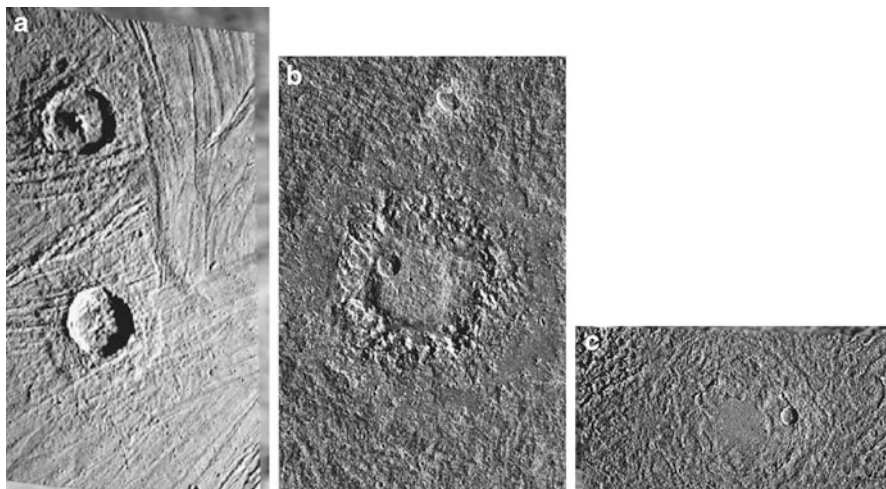


Fig. 13.9 Craters and crater remnants on Ganymede. (a) Craters Gula (*top*) and Achelous. The latter is ~35 km diameter and its sharpness, brightness, and relatively undisturbed debris apron, suggest that it is also the younger of the two. (b) Neith, a “dome crater” or “penepalimpsest” with a dome of 45 km diameter, surrounded by concentric roughlands and plain. See Fig. 13.11 for a similar feature on Callisto. (c) An image from the Marius Regio of Buto Facula, a palimpsest, ~45 km in diameter with a smooth center and rings of concentric arcs surrounding it. The morphologies of these features may depend on the energy of the impactor and other circumstances and may not represent a temporal evolutionary sequence, but the penepalimpsest and palimpsest features appear to be far older than the craters in (a). NASA/JPL images PIA01660, PIA01658, and PIA01659, respectively, produced by Deutsche Zentrum für Luft und Raumfahrt (DLR)

Ganymede’s axial moment of inertia coefficient, $K = 0.3105$, is indicative of interior diversity and its mean density, $1,936 \text{ kg/m}^3$, suggests water ice as well as rock. Several polymorphs of ice, Ice I, Ice III, Ice V and VI (Fig. 13.12), are thought to exist in the deep interior of Ganymede. The latter form of ice, for instance, has a density of $1,310 \text{ kg/m}^3$ and can only be found at pressures between 620 MPa and 2.2 GPa and within a temperature range of 130 to ~350 K. Ganymede has a tenuous atmosphere.

Galileo detected an intrinsic magnetic field around Ganymede consistent with a centered dipole tilted 4° from the rotation axis (Kivelson et al. 2002). The dipole is directed southward (north magnetic pole in the southern hemisphere) like that of the Earth and opposite to Jupiter’s, with a dipole moment of $1.32 \times 10^{13} \text{ Tm}^3$ and a surface magnetic field at the equator of 719 nT or ~1/40 of that at the Earth’s surface, and ~1,200 nT at the poles. The field is strong enough to create a small magnetosphere around Ganymede with closed field lines shielding the surface from Jupiter’s magnetospheric particle radiation within $\sim 50^\circ$ of the equator, and field lines open to Jupiter’s magnetosphere north and south of this zone. The boundary between the closed and open field line regions can be easily seen in color photographs of Ganymede, where bombardment by Jupiter’s particle

radiation travelling on open field lines has lightened the surface in the polar regions (Khurana et al. 2007).

The equatorial magnetopause is at ~ 2 Ganymede radii, and there is a region of trapped electrons in the region of closed field lines. Thus far, Ganymede is the only planetary moon found to have an intrinsic magnetic field.

The source of the field has been vigorously debated, with each proposed model having both attractions and unresolved difficulties or uncertainties. Proposed models include (see Bland et al. 2008 and references therein):

1. Core dynamo at the present day: This is the most-favoured model. Three versions are described below,
 - (a) Thermal convection after secular cooling for 4.5 Gy: However, thermal convection might be expected to have ceased after ~ 1 Gy.
 - (b) Chemical convection after secular cooling for 4.5 Gy: This is possible, but is thought to require rather special conditions; e.g., core sulfur content unusually low or unusually high.
 - (c) Slow, cool accretion: If Ganymede accreted slowly, then it would have been cooler initially and may have heated up (e.g., by radioactive decay) enough to differentiate only within the last 1 Gy. In this case, thermal convection could still be operating. Ganymede's grooved terrain is believed to have an age of 1–2 Gy and could represent a higher heat flow stage resulting from increased heat transport from the putative newly-convectiong core. It is difficult to judge this model without further data.
2. Dynamo in an electrically-conducting ocean below the icy crust: This appears to require unrealistically high fluid velocities (1 m s^{-1}) to sustain a dynamo.
3. Remanent magnetism: The attraction of this model is that there are difficulties in accounting for the existence of a core dynamo today, but one may have operated early in the life of Ganymede. Layers outside the core could have remanent magnetism if they cooled below the Curie point while the dynamo was active. As shown in Sect. 11.7.1.3, this requires that the material be strongly susceptible to magnetization (e.g., magnetite or pure iron). This might be possible, because Ganymede has a greater iron content than the Moon and Mars, but it is not clear how much of the iron remained outside the core when Ganymede differentiated, and in what form.

In any case, all of the models above except the second require an iron-rich core, whether or not it contains an active dynamo.

From gravity data, the icy crust is ~ 800 km thick, overlying a rocky mantle. Although the intrinsic magnetic field dominates any induced magnetic field that may be present, the multiple flybys by *Galileo* with different orbital geometries allowed Kivelson et al. (2002) to resolve the quadrupole moments in the overall field. Assuming that these are from an induced field they find a liquid water layer somewhere below the surface. Thermal modeling (temperature profile vs. melting temperature of the different ice phases) then suggests a liquid, electrically-conducting layer perhaps 100 km thick centered ~ 170 km below the surface.

However, they also note that the quadrupole moments could be part of the intrinsic field, in which case the existence of a liquid water layer becomes much more speculative.

Like Europa and Callisto, Ganymede has a tenuous, predominantly O₂ atmosphere with an extended exosphere of predominantly H atoms. The atmosphere is created by radiolysis and sputtering in the open field line regions around Ganymede's poles (see Sects. 11.2.5.3, 13.1.2.2 and 13.1.2.4 for discussion of these and other atmospheric processes); but the surface temperature near the subsolar point (150 K) is high enough that sublimation of H₂O may produce a predominantly H₂O atmosphere within approximately $\pm 45^\circ$ latitude, with O₂ dominating poleward of there (Marconi 2007).

13.1.2.4 Callisto

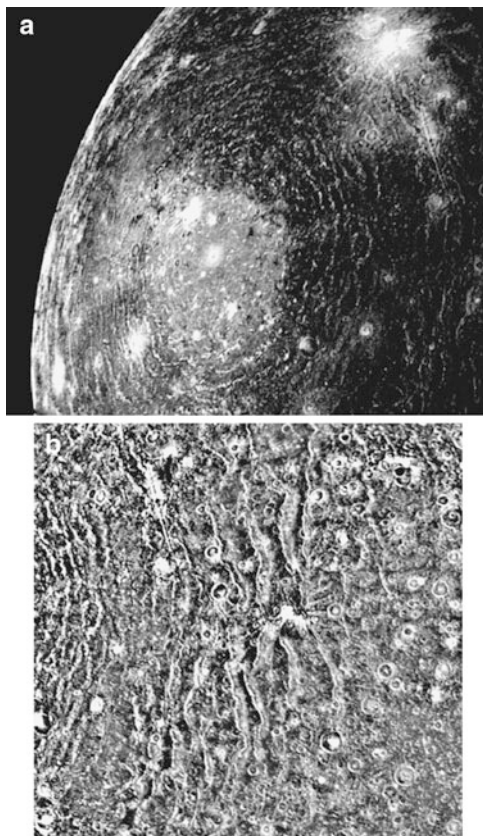
This darker icy moon is the most heavily cratered of the giant Jovian moons, an indication of a relatively unmodified surface. Its mean density is just slightly less than that of Ganymede. Craters are the dominant feature of Callisto, with age characteristics as on Ganymede. Here, however, cratered plains are not interrupted by extensive grooved and lineated features. The well-known ringed plain, Valhalla, a large ringed basin (Fig. 13.10), appears similar to such features as the Caloris Basin on Mercury and Mare Orientale on the Moon. It apparently marks the site of a major impact. Resurfacing is done through impacts, solar wind, and cosmic rays, as on the Moon; younger craters are identified by bright icy surfaces. Figure 13.11 reveals the presence of dome craters on Callisto, indicating a parallel if possibly non-coeval process of crater evolution to that happening on Ganymede.

Callisto's axial moment of inertia coefficient is $K = 0.3549 \pm 0.0042$ (Anderson et al. 2001). If it were completely undifferentiated, then transitions to denser ice phases at different depths would yield $K = 0.38$ (McKinnon 1997); but if it were completely differentiated, a value $K \sim 0.31$ similar to Ganymede might be expected. Callisto therefore appears to have undergone significant although incomplete differentiation into a rock-metal core and a rock-ice mantle—see Milone and Wilson (2014, Fig. 5.18).

Galileo detected an induced magnetic field around Callisto that is best explained by a liquid, electrically-conducting layer (e.g., a salty ocean) of at least 10 km thickness within the top 300 km of the surface (Zimmer et al. 2000). A model for Callisto that is consistent with the gravity data and geochemical and thermal constraints (Kuskov and Kronrod 2005) gives a rock-iron core of radius 500–700 km overlain by a rock-ice mantle not less than 1,400 km thick and an outer water-ice shell up to ~ 300 km thick. Where the Ice III phase would be located in the outer shell, the ice is above the Ice III melting point, giving an liquid water layer 120–180 km thick beneath an outermost layer of Ice I 135–150 km thick.

In three of the four Galilean moons, water ice is the dominant characteristic, but what is meant by the term “ice” depends on where it is in the phase diagram, a plot

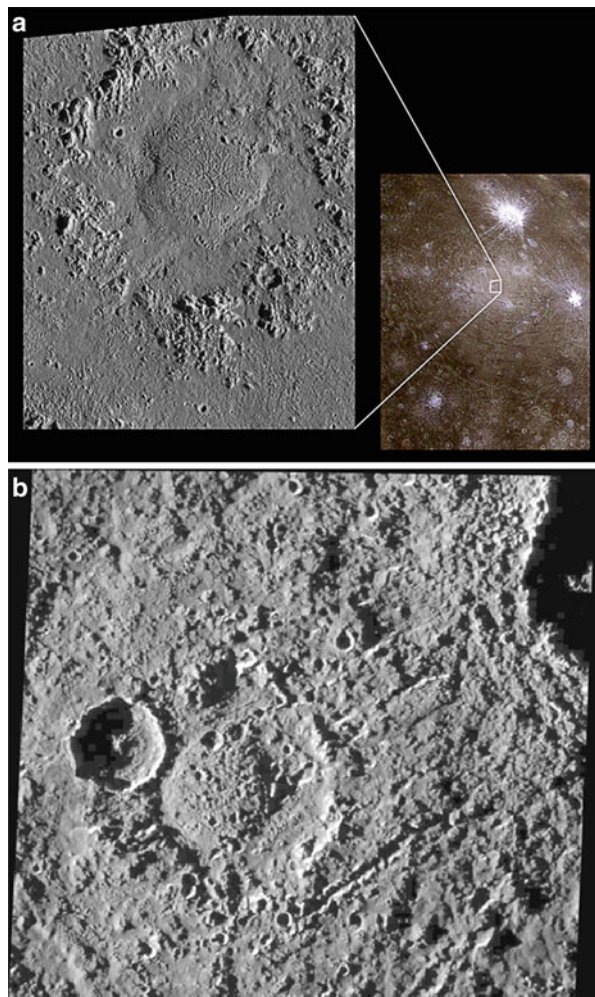
Fig. 13.10 (a) Valhalla, a great multi-ringed plain on Callisto as seen by Voyager 1. It marks a major impact event, the antiquity of which is indicated by the many smaller craters superimposed upon it. NASA image PIA02277, produced by JPL. (b) The plastic deformations of the concentric rings and craters of various ages are seen in this Voyager 1 detail of Valhalla. NASA/JPL image PIA00484



of the pressure against the temperature. Figure 13.12, after Taylor (1992, Fig. 6.8.1) is the phase diagram of water ice. The density of ice varies with phase, and it is possible for lower density ice to move through overlying material of higher density. On Earth, when salt is the lower density material, and it pushes through overburden, a *diapir* may result in a salt dome. Rathbun, Musser, and Squyres (1998) have described the properties that such diapirs must have if they are present on Europa. In particular, the diapirs must be no deeper than the base of the ice layer, whether this be underlain by rock or by liquid, and lay within a few tens of kilometers below the surface. Perhaps the spots in Fig. 13.7c are due to such features.

A study by Chuang and Greeley (2000) of material that fell away from impact crater walls indicates that the movement of rock and ice on the surface of Callisto appears to be similar to that of rock glaciers on Earth, but the ice is not as ductile and undergoes brittle deformation. The deposits, individual blocks of which may be several tens of meters high, and up to 1 km across, are seen also at the bases of scarps and cliffs; they have yield strengths similar to dry-rock avalanches on Earth. Nearby impacts appear to trigger some of the slides, but these authors suggest that

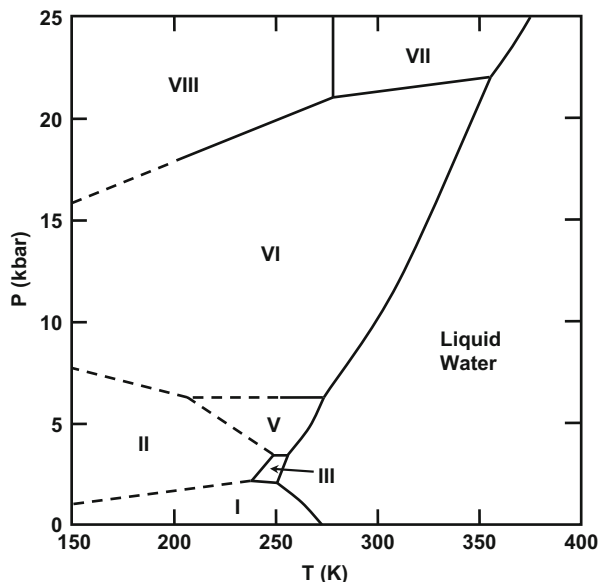
Fig. 13.11 (a) (left) From the Solid State Camera on Galileo, Doh, a dome crater on Callisto, located within the Asgard multi-ring basin visible in the wider image. Note its similarity to the Neith crater on Ganymede (in Fig. 13.9). NASA/JPL image PIA01648, produced by Arizona State University. **(b)** From the same instrument, another dome crater, Har, on which are superimposed a much newer crater of 20 km diameter on the *left*, many smaller craters, and the secondary craters caused by the ejecta of the larger crater to the *upper right*, Tindr. NASA/JPL image PIA01054, produced by Arizona State University



ice sublimation undermines a near-surface layer and that seismic events generated by impacts trigger them.

Callisto has a tenuous atmosphere produced by sputtering of H₂O, O₂ (from radiolysis) and CO₂ from the surface ice by high-energy particles from the Jovian magnetosphere, with O₂ being the most abundant atmospheric species. Modeling of the atmosphere (Liang et al. 2005) indicates that the exobase is at ~200 km altitude, so in the lower atmosphere the H₂O reaches equilibrium with the surface at a vapor pressure of $\sim 4 \times 10^{-5}$ μbar . Number densities near the surface are, O₂: $\sim 7 \times 10^{15} \text{ m}^{-3}$; CO₂: $\sim 4 \times 10^{14} \text{ m}^{-3}$ (partial pressure $\sim 7.5 \times 10^{-6} \mu\text{bar}$); H₂O: $\sim 2 \times 10^{15} \text{ m}^{-3}$. Photolysis and dissociative recombination then produce H, H₂, O, OH, and CO, and photoionization produces an ionosphere that includes O₂⁺, O⁺, H₂O⁺, CO₂⁺, and CO⁺. Radio occultation observations of *Galileo* passing behind

Fig. 13.12 The phase diagram for water ice. Dashed lines indicate estimations/extrapolations. After Hobbs (1974, Table 1.10, Fig. 1.18) and Taylor (1992 Fig. 6.8.1, p. 256). Triple points from Hobbs (Table 1.10). Taylor notes that as Ice VIII changes to Ice I, the ice will undergo an expansion of volume because Ice VIII has a density of $\sim 1,670 \text{ kg/m}^3$. This adaptation reprinted with the permission of Cambridge University Press



Callisto's atmosphere give electron densities of $1.53 \times 10^{10} \text{ m}^{-3}$ at 27.2 km altitude and $1.74 \times 10^{10} \text{ m}^{-3}$ at 47.6 km.

Atmospheric loss of H and H₂ is by Jeans escape from the exobase. ~10 % of the O atoms are produced by dissociative recombination of H₂O⁺ + e⁻ with speeds > v_{esc}, but primarily at altitudes of ~50 km, well below the exobase; so Jeans escape is insignificant and loss is by atmospheric sputtering by high-energy magnetospheric ions. H₂O is lost by photodissociation and escape of the products.

13.1.3 The Moons of Saturn

Saturn has one giant-class moon and a host of intermediate and small satellites. As in the Jovian system, some of these satellites are associated with the rings; some may provide parent material for them (as Fig. 13.13 suggests about Pan). The discovery of propeller-shaped moonlets of ~5 km length and 300 m width, embedded within a small and relatively undisturbed area of the A-ring (Fig. 13.14), implies that they are fragmented remains of much larger moons that were the source material for the rings. By extrapolation to the entire ring system, there may be millions of such embedded moonlets.

In Milone and Wilson (2014), Sect. 3.3, we discussed the restricted three-body problem and mentioned Trojan asteroids, located at the L4 and L5 points of Jupiter and the Sun. In the Saturn system, Polyduces and Helene are Trojan moons of Dione and Saturn; and Telesto and Calypso are Trojan moons of Tethys and Saturn.

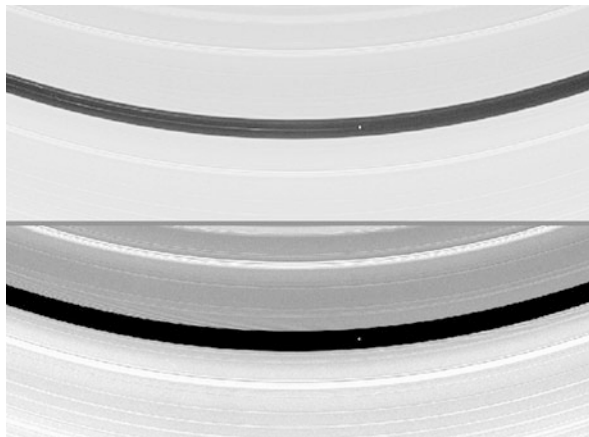


Fig. 13.13 A Cassini Orbiter view of the tiny satellite Pan orbiting in the Encke gap in the Saturnian ring system processed in two ways. Note the trail of ringlet material sharing Pan's orbit in the *top panel*, and the uneven edges of the adjacent rings in the *lower panel*. The co-orbital material undergoes horseshoe-shaped orbits relative to Pan, according to Murray (2007), and its source may be impacts on the ring moon by interplanetary material. The uneven ring edges preceding and following Pan are created by Pan's shepherding. NASA/JPL/ESA/Italian Space Agency(ASI), image PIA07528, produced by the Cassini Imaging Team

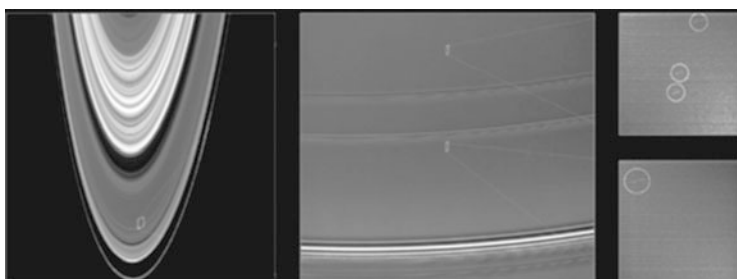


Fig. 13.14 Viewed from the Cassini orbiter, propeller-shaped moons within the A-ring may be fragments of larger moon(s). The moonlets' long axes are tilted by $\sim 20^\circ$ offset. NASA/JPL/Space Science Institute, Boulder, image PIA07792

As also for Jupiter, many satellites have retrograde orbits, most with high inclinations. The orbits of many of these, and some of the moons with direct orbits, are in fact irregular, with major excursions of their orbital elements motions, including eccentricity and inclination.

The intermediate-sized satellites have presented puzzles ever since the Voyager missions revealed fresh ice resurfacing on the faces of several moons (Rhea, Tethys, Dione). Finally, a smoking gun was discovered on Enceladus: geysers were seen (Figs. 13.15 and 13.16) and strong evidence for Europa plumes (see

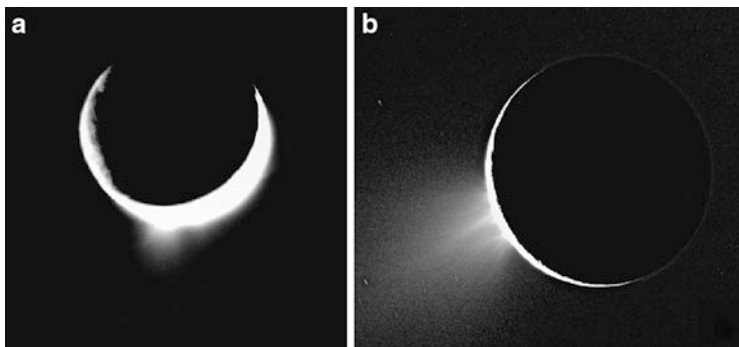


Fig. 13.15 Evidence for plumes of material erupting from the south polar surface of Enceladus, near the features referred to as “tiger stripes” (see Fig. 13.16), as caught by Cassini on different dates near “new moon” phase in 2005. (a) From image PIA07798, 2005 Feb. 17, at phase angle 153.3° , South Pole down; (b) from image PIA07758, 2005 Nov. 27, at phase angle 161.4° , S. Pole to lower left. The images are reminiscent of the plumes seen on Io, but here, due to water ejected from geysers. Carbon dioxide and methane have also been detected in the plumes. NASA/JPL/Space Science Institute images

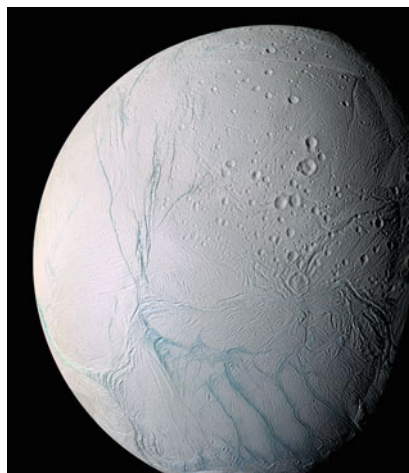


Fig. 13.16 The Cassini Orbiter view of Enceladus. Note the varieties of terrain on this icy moon. It undergoes substantial tidal forces from Saturn and Titan and from closer moons. The “tiger stripes” region near the South Pole, the site of newly discovered water plumes, can be seen at the bottom of the image. The moon’s icy blue color can be seen in this color image. See Porco et al. (2006) for a full discussion. NASA/JPL/Space Science Institute, Boulder, image PIA07800

above) has appeared as we go to press. As on Europa and Io, tidal interactions coupled with internal heat sources are thought to be responsible.

Mysteries, however, abound, e.g., the side of the small moon Iapetus (Fig. 13.17a) that faces forward in its orbit has an albedo a factor of ten greater than the trailing side.

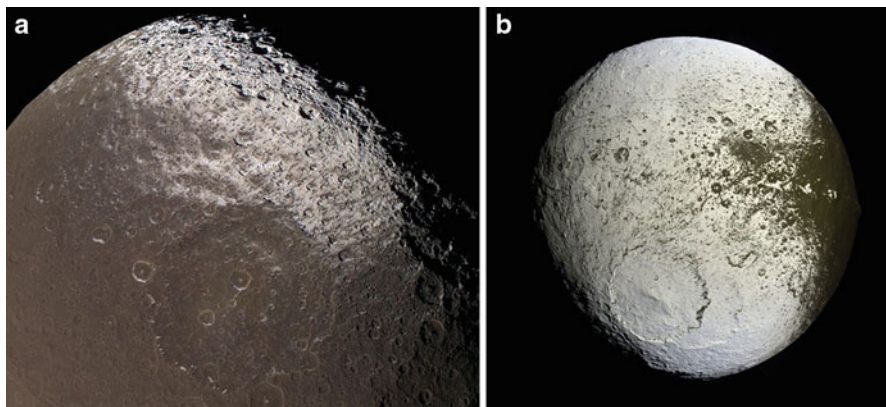


Fig. 13.17 (a) Cassini reveals the faces of Iapetus: dark terrain on most of the sunlit side and bright terrain at the top (and into the night side). This NASA/ESA/ASI image, taken on December 31, 2004 from a distance of 172,900 km, is a composite of three-passband observations at 338, 568, and 930 nm. NASA/JPL/Space Science Institute, Boulder, image PIA06167 (b). A mosaic of 60 images of Iapetus from the Cassini Orbiter on Sept. 10, 2007 taken at a distance of 73,000 km. Note the heavy frost on this trailing side of Iapetus, and the two huge superposed impact craters. Credits: NASA/JPL/Space Science Institute, Boulder, image PIA 08384

Figure 13.17b, from *Cassini*, shows why: bright, heavily frosted areas contrast to dark areas where the frost has sublimated. The source of the dark material appears to be a faint but very large dust ring around Saturn, discovered by Verbiscer et al. (2009) using the infrared *Spitzer Space Telescope*. The ring extends at least from 128 to 207 R_S , and probably farther ($R_S = 60,330$ km is Saturn's radius), and is $40 R_S$ thick. It is also very faint, similar in brightness to Jupiter's gossamer rings, and is probably composed of dust and small debris ejected from the satellite Phoebe (retrograde orbit of radius $215 R_S$) by impacts. Hence, it has been named the Phoebe ring. Computations show that ring particles of cm size and smaller will gradually migrate inward, and because they are very likely in retrograde orbits, many will collide head-on into the leading face of Iapetus. Phoebe had already been thought to be the origin of Iapetus' dark material because *Cassini* spectra showed similar composition, but a mystery still remains in that the material on Iapetus is reddish, whereas Phoebe is gray. One resolution that has been suggested is that the material is initially reddish, but slowly darkens and becomes grayer with exposure to radiation. Thus, the old surface of Phoebe would be gray, but the material on Iapetus would be mostly reddish material freshly excavated from Phoebe by impacts. (A 10 μm -sized grain takes a few tens of millions of years to reach Iapetus from Phoebe.) The moon Hyperion also appears to have a coating of this material, but over its entire surface because of its chaotic rotation (see below).

Iapetus has also been seen to have a large equatorial ridge, ~15 km high; Levison et al. (2011) suggest this to have been caused by a ring of material from a glancing collision, with tidal de-spinning of Iapetus carried out by a coalesced moon and by Saturn.

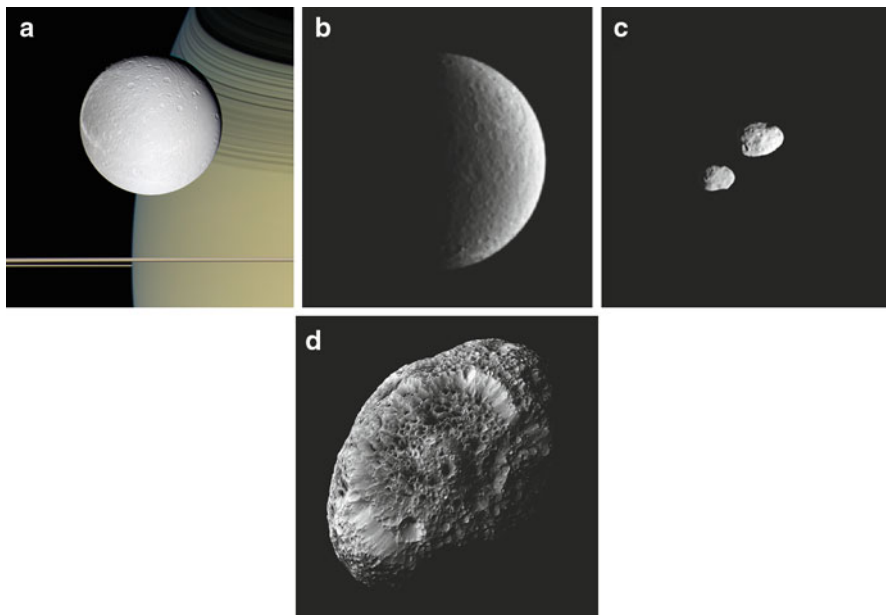


Fig. 13.18 Intermediate-sized moons as seen by Cassini Orbiter. (a) Dione and the rings of Saturn; (b) Rhea seen at phase angle 90° , on Mar. 15, 2005; (c) The coorbital moons Epimetheus (left) and Janus (right), on Mar. 20, 2006; Janus was in the lower orbit at the time.; and (d) the bizarre surface of Hyperion with high crater frequency in and slumping on the rims of a huge sunken crater. Cassini Orbiter NASA/JPL/Space Science Institute, Boulder images PIA07744, PIA06641, PIA08170, and PIA07740, respectively

The intermediate-sized moons display surface modifications in the form of bright streaks, as Fig. 13.18(a) demonstrates. Occultation data show that Enceladus has a tenuous (and strongly localized) atmosphere (Hansen et al. 2006). Many of these moons show irregular orbits, undergoing variations in eccentricity and inclination, leading to tidal force variation. Wisdom et al. (1984) pointed out long ago that Hyperion's principal moments of inertia, A, B, C, give a value $(B - A)/C \sim 0.26$, when stability requires $(B - A)/C \ll 1$, rendering it susceptible to chaotic tumbling; i.e., without a stable spin axis or rate. This chaotic rotation has been confirmed by light curve analyses (Klavetter 1989a, b). Hyperion is seen to have such an irregular surface that it more closely resembles a sponge than a moon.

Cassini has also discovered Rhea to have an atmosphere. Molecular oxygen (O_2) is created by radiolysis and sputtering (Sect. 13.1.2.2) and makes up $\sim 70\%$ of the atmosphere; the other $\sim 30\%$ is CO_2 (Teolis et al. 2010). The origin of the CO_2 has not yet been identified, but three possibilities have been suggested: (1) sputtering of primordial CO_2 present in the ice; (2) sputtering of CO_2 created in the ice by radiolysis involving H_2O , radiolytic O_2 , and carbonaceous minerals or organic molecules either present in the ice or deposited by micrometeoroid impacts; and (3) outgassing of primordial CO_2 or CO_2 produced by aqueous chemistry in Rhea's interior. Because the corotational speed of Saturn's magnetosphere at Rhea's orbit

is greater than Rhea's orbital speed, the sputtering occurs preferentially on Rhea's trailing hemisphere; but the O₂ is believed to form a bulge on the dayside because of the higher temperature and therefore greater scale height there.

The total number of O₂ molecules in the atmosphere is estimated to be $(2.5 \pm 0.5) \times 10^{29}$, approximately equal to the number of molecules in a cube 22 m on a side at STP in the Earth's atmosphere. The O₂ is lost at a rate of $\sim 2.2 \times 10^{24} \text{ s}^{-1}$ (2.7 % of these by Jeans escape and the rest by ionization and pickup by Saturn's corotating magnetic field), so the mean lifetime of O₂ in the atmosphere is $\sim 10^5$ s or ~ 1 day.

Although Dione and Tethys are less able to retain an atmosphere than Rhea because of their smaller mass, similar processes should nevertheless be taking place. Indeed the presence of an O₂ atmosphere around Dione has been detected indirectly by observation of O₂⁺ pickup ions streaming from the satellite along its plasma wake (Tokar et al. 2012). The measured ion densities suggests an O₂-dominated atmosphere with an O₂ density near the surface of $\sim 0.6\text{--}5 \times 10^{10} \text{ m}^{-3}$, similar to that derived for Rhea by Teolis et al. (2010). Another indirect detection by *Cassini* magnetometer observations of disturbed magnetic field lines upstream from Dione, caused by the interaction of atmospheric ions with Saturn's corotating magnetic field, suggested an O₂ density about two orders of magnitude greater. These measurements were made during a different passage of *Cassini* past Dione when the transient radiation belt (Sect. 12.9.3) was particularly intense, so it is possible that the sputtering rate at Dione depends strongly on the intensity of this belt. A similar attempt to detect an atmosphere around Tethys did not show any magnetic field perturbation attributable to an atmosphere or ionosphere.

13.1.3.1 Titan

Discovered by Christiaan Huygens (1629–1695) in 1655, Titan is the largest and brightest of the moons of Saturn; indeed its physical size nearly matches Ganymede, the largest moon of the solar system. It has a nearly circular orbit with a period of 15°95, and an inclination to Saturn's equator of 0°35. It rotates in the same period as it revolves about Saturn, and so is locked in a 1:1 spin-orbit resonance.

Spectacular images were obtained from the Huygens probe that was released from the Cassini Orbiter to descend onto Titan's surface. The Huygens probe revealed ground terrain similar to coastal areas on Earth, but shaped not by water but by methane, possibly in solution with ethane. After the heated probe landed, it detected sublimed methane gas. The presence of drainage channels, replete with dendritic tributaries and apparent shore lines, lends a decidedly terrestrial appearance to the surface (Figs. 13.19 and 13.20). The details on the surface near the probe can be seen in Fig. 13.20.

Titan's mean density is 1,881 kg m⁻³, which is very similar to Ganymede (1,936 kg m⁻³) and Callisto (1,834 kg m⁻³) and indicates a similar ratio of rock and ice. Two independent determinations of its moment of inertia coefficient, K = 0.3431 ± 0.0004 and 0.3438 ± 0.0005 (Iess et al. 2012), agree with each other, placing Titan closer to Callisto (K = 0.355) than Ganymede (K = 0.311) in

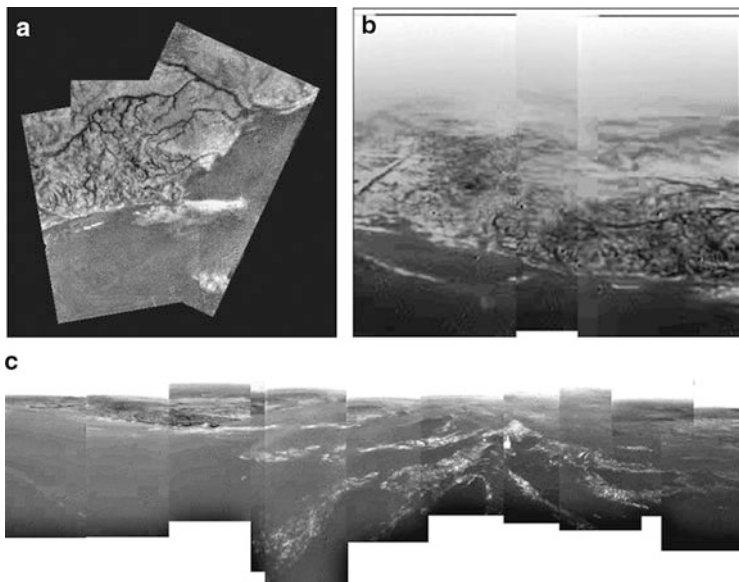


Fig. 13.19 (a, b) Views of the surface of Titan by the Huygens probe, as it descended into the atmosphere. With conditions near the triple point of methane, the rivers, shoreline, and methane (and/or ethane) clouds visible in these images make sense. (c) A mosaic providing a 360° panoramic view of Titan as seen from Huygens as it descended toward its landing site. The area over which the probe drifted in image (b) is visible in the *upper left* part of image (c). NASA/JPL/ESA/Univ. of Arizona images PIA07236, PIA07231, and PIA07230, respectively

Fig. 13.20 The surface of Titan, as revealed by the Huygens probe. The area resembles a mud flat—with rocks. The bright elongated rock just below the left center of the image is 15 cm across and is 85 cm from the camera. The roundedness of the rocks indicates weathering as an important process. Credits: NASA/JPL/ESA/University of Arizona image PIA07232



its degree of internal differentiation: it is somewhat more centrally-condensed than Callisto, but does not appear to have separated into a dense, metallic core with a rocky mantle as has Ganymede. A possible model that is consistent with its mean density and moment of inertia would be a core made up of a uniform mixture of rock and ice of radius 2,050–2,100 km and density 2,550–2,600 kg m⁻³, with an outer layer of water ice 475–525 km thick (Iess et al. 2010). The different phases of ice in this layer would have different densities. Three-layer models are also possible, with a smaller core of pure rock surrounded by a rock-ice mantle and an icy outer layer.

An interesting question is whether Titan has a subsurface ocean similar to those believed to exist in Ganymede and Callisto. This can be determined from Titan's elastic response to tidal distortion by Saturn. One measure of this elasticity is the k_2 potential Love number, for which a typical value for a body with a subsurface ocean is ~ 0.4 (Sect. 5.3). The measured value for Titan is $0.63 \pm \sim 0.1$ (Iess et al. 2012), which could be satisfied by a very low viscosity layer (an ocean) near the surface, or a low-viscosity deep interior. The latter appears to be ruled out by the rock-ice core, which should be solid for an object the size of Titan, so the measured value is strongly suggestive of a subsurface ocean.

Titan has a very interesting atmosphere. First, it is the only moon in the solar system to have a substantial atmosphere, with a pressure at the surface of 1.4 times the pressure at sea level on the Earth and a mean surface temperature of 94 K. The dominant atmospheric component near the surface is nitrogen (N₂), with $\sim 5\%$ methane (CH₄) by number and trace amounts of other gases, including ethane (C₂H₆).

Second, Titan is the only object in the solar system besides the Earth to have open, stable bodies of liquid on its surface: liquid methane and ethane on Titan and liquid water on the Earth. The stability of the lakes on Titan also means that Titan is the only solar system body except the Earth to have a hydrological cycle.

Third, Titan resembles Venus and the Earth in having a hard surface and a substantial atmosphere (like a terrestrial planet made of ice), but because of its 16-Earth-day rotational period and 27° obliquity, it gives us a new perspective on atmospheric circulation: the Earth is a fast rotator with seasons, Venus is a slow rotator without seasons, and Titan is a slow rotator with seasons.

Titan lacks significant quantities of ozone (O₃), so like Venus and Mars it lacks a temperature maximum between the stratosphere and mesosphere. The atmospheric temperature decreases from 94 K at the surface to a broad minimum of ~ 70 K at ~ 50 km altitude, marking the tropopause, then increases again through the strato-mesosphere and into the thermosphere where temperatures exceed 160 K.

The Huygens descent probe measured westerly winds with speeds of 90–105 m s⁻¹ at 120–140 km altitude, ~ 10 times Titan's rotation speed. Thus, like Venus, Titan's upper atmosphere superrotates in the direction of planetary rotation (retrograde, or easterly, for Venus, and prograde, or westerly, for Titan) and is in cyclostrophic balance. (Refer to Chap. 10 for meteorology definitions and discussions.) Superimposed on the zonal superrotation is a meridional circulation in the upper atmosphere consisting of a single pole-to-pole Hadley cell with air rising in the summer hemisphere and descending in the winter hemisphere. The descending branch provides the mechanism for carrying the

hydrocarbon products of methane photolysis from the upper atmosphere down to the troposphere, and the upper-level air converging on the pole produces a polar vortex in the winter hemisphere. The Hadley cell weakens and then reverses near each equinox.

Below ~20 km altitude in the troposphere, numerical models predict relatively low speeds and a geostrophic balance like the Earth, a result that is consistent with wind speeds measured by the Huygens probe. The dominant meridional circulation pattern consists of a northern and a southern Hadley cell with air rising near the subsolar latitude and descending at ~60° N and S. (On Titan, the subsolar latitude varies between $\pm 27^\circ$.) The pattern shifts north and south with the seasons as on Earth, with the winter-hemisphere cell extending across the equator and the summer-hemisphere cell becoming much weaker.

Numerical models predict sporadic (non-permanent) methane clouds in the troposphere at ~15–18 km altitude between $\pm 60^\circ$ latitude, and below ~30 km altitude in each polar region; and permanent ethane clouds or mist mostly above the tropopause. When Cassini arrived in mid-2004, it was late summer in Saturn's southern hemisphere (late winter in the northern), and lower-altitude clouds were found mostly in the south polar region. The extent of these clouds decreased toward Saturn's equinox in 2009, and by 2010, equatorial cloud systems were being observed. Stratospheric clouds of hydrocarbon ice crystals were seen in both the polar and equatorial regions.

Surface features on Titan are hidden below an atmospheric haze that is optically thick at visual wavelengths, but transparent to infrared and radar. As of 2012, ~50 % of Titan's surface had been mapped to ~350 m resolution, and ~2 % in stereo. Surface features revealed by *Cassini* and from Earth include,

- Lakes and seas composed of a solution of methane, ethane and nitrogen, of which methane is the dominant component. The total volume of liquid is estimated to be 9,000 km³. They are confined, at least at the present epoch on Titan, to latitudes within 30° of the north and south poles. There is a great range in sizes from small to large: Ontario Lacus, a large lake near Titan's south pole, is 15,000 km² in area, about 20 % smaller than Lake Ontario, one of the Earth's Great Lakes; and Kraken Mare in the northern hemisphere (Fig. 13.21), Titan's largest sea, is similar in size to the Earth's Caspian Sea. Ligeia Mare (Fig. 13.21), Titan's second-largest sea, reaches a depth of 170 m. Observed variations in radar reflectivity may be due to ice alternately floating or sinking (Hofgartner & Lunine 2013).
- River valleys and dendritic channels. In the polar regions these valleys are occupied by liquid methane and ethane flowing into the lakes and seas, but they are found also at lower or equatorial latitudes, where they are apparently dry. In 2012, ESA announced the discovery of a river 400 km long, named Vid Flumina, flowing into Ligeia Mare in the northern hemisphere, Titan's second-largest sea (Fig. 13.2).
- Mountainous regions. Much of Titan's surface is within a few hundred meters of the mean elevation, but a number of areas are up to 2 km higher than nearby plains. These areas have the form of parallel ridges and grooves suggesting

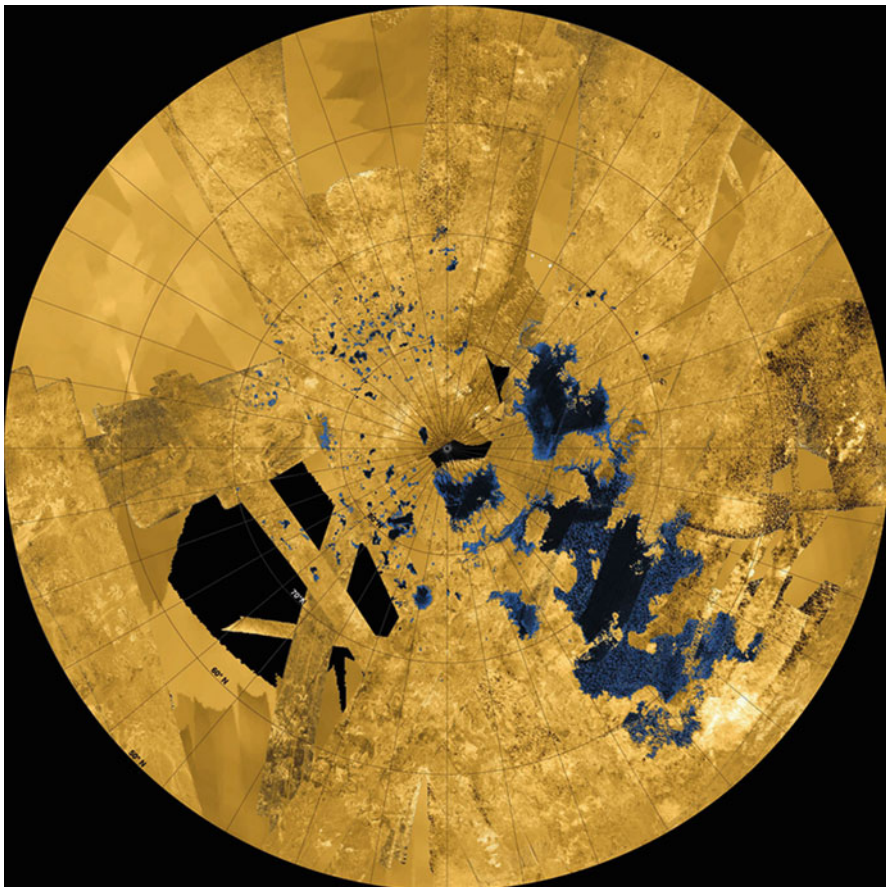


Fig. 13.21 A colorized mosaic from NASA's Cassini mission centered on Titan's north pole, extending to $\sim 50^{\circ}$ N. 0° W longitude is at the bottom and 90° W at the left. Kraken Mare, Titan's largest sea, lies between 60° and 80° latitude in the lower-right quadrant. Ligeia Mare, Titan's second-largest sea ($\sim 125,000\text{ km}^2$ in area), is above and to the right of the north pole, and Punga Mare is just below the north pole. The river Vid Flumina flows from the south-east into the inlet at longitude 245° , latitude 65° at the top of the lower-right bay of Ligeia Mare. NASA Image PIA17655, Credits: NASA/JPL-Caltech/ASI/USGS

formation by tectonic processes, and are believed to result from lateral compression. This could arise through gradual solidification of a subsurface ocean if it is deep enough to form a higher phase of ice as it froze; e.g., Ice III and Ice V have densities of $1,160\text{ kg m}^{-3}$ and $1,240\text{ kg m}^{-3}$, respectively, at 350 MPa, compared to $1,130\text{ kg m}^{-3}$ for water at the same pressure. The ice occupies a smaller volume than the water, so the layers above it have to settle inward, compressing the surface laterally.

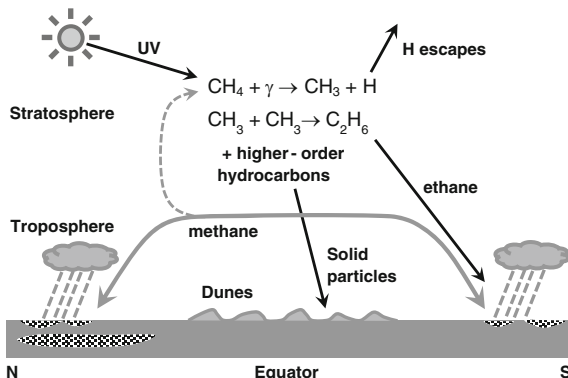
- Volcanic regions. Stereo radar mapping by *Cassini* has revealed a number of features very reminiscent of volcanoes. One, Sotra Facula (*facula* is a Latin word meaning “torch”), is a roughly circular feature located 15° S of Titan’s equator that includes two peaks with summits ~1 km above the surrounding topography, and a depression ~1.6 km in depth that may be a volcanic patera (Kirk et al. 2010). Lobate flows extend ~180 km northward. Although other interpretations have been proposed, the feature is strongly suggestive of a cold volcano (a *cryovolcano*), in which case the lobate flows would have formed by solidification of water, or a mixture of water, ammonia and methane, vented from the depression at some time in the past. The ammonia and methane lower the melting temperature of water, allowing it to flow at lower temperatures, because of the properties of eutectics; see Sect. 5.4.4.5.
- Sand dunes. Dune fields are fairly common at low latitudes on Titan. There appear to be two categories (Radebaugh et al. 2007): *Cat scratch dunes* and *sand sea dunes*. Cat scratch dunes form very dark arcuate lines, that have been likened to cat scratches (perhaps multiple times on a favorite spot on a scratching post!), and clump together in patches, whereas sand sea dunes occur on the extensive radar-dark areas called *sand seas*. Sand sea dunes are relatively straight, up to 100–150 m in height, 1–2 km wide and 1–2 km apart, and 10 to >100 km in length, very similar in morphology and size to the linear dunes found in the Namib, Sahara and Arabian deserts on the Earth. (The Belet sand sea extends for nearly 2,000 km across Titan.) These dunes grade into cat scratch dunes at the margins of the sand seas, so the difference between the two appears to relate to the available supply of sand. Dune fields cover ~20 % of Titan’s surface, but in contrast to the polar lakes and seas, they are found almost entirely within $\pm 30^\circ$ of the equator (Lunine and Lorenz 2009). Sand seas are limited to $\pm 10^\circ$ of the equator.

Abundant dunes require extensive reservoirs of sand, as well as winds that are both strong enough to transport sand grains and reasonably constant in direction. The sand grains are probably composed of organics that have precipitated onto Titan’s surface from the atmospheric haze. On the Earth and Titan, the threshold wind speed is 0.5–1 m s⁻¹ (winds of this strength were observed by the Huygens probe as it descended to Titan’s surface), and on Titan the dune morphology indicates winds primarily westerly (i.e., toward the east). This is actually a problem for modeling, because Hadley circulation should produce easterly surface winds in the tropics, but the resolution to this problem has yet to be found.

- Impact craters. As of 2012, ~60 circular features had been found on Titan, of which about half have diameters >20 km. One, Menrva Crater, is 425 km in diameter and has the form of a multi-ringed basin. Filling in of the craters by wind-blown sand provides evidence of long-term surface modification on Titan.

The existence of methane-rich lakes (Fig. 13.21) and abundant methane (~5 % by number) in the atmosphere suggests the presence of a methane hydrological

Fig. 13.22 The methane hydrological cycle on Titan. Stippled areas represent methane-ethane lakes, seas, and subsurface reservoirs. Based on Fig. 9 of Lunine and Lorenz (2009), with permission of the authors and publisher



cycle on Titan, by analogy to the hydrologic cycle for water on the Earth; see Lunine and Lorenz (2009) and Lunine and Atreya (2008) for more details. The basic cycle is illustrated in Fig. 13.22.

Methane in the atmosphere is maintained in equilibrium with the methane in the lakes by evaporation and precipitation. Methane gas is transported seasonally between the polar regions (solid, grey arrow). It is also transported into the stratosphere (dashed, grey arrow), where it is dissociated into hydrogen and the very reactive methyl radical, CH_3 , by photolysis and impacts by charged particles (the latter not shown in Fig. 13.22). Further reactions produce predominantly ethane (C_2H_6), but also higher-order hydrocarbons such as acetylene and propane, and nitriles such as hydrogen cyanide and cyanoacetylene. The stratospheric reactions provide a net loss for methane because they are irreversible: the hydrogen is lost from the atmosphere by Jeans escape, and the higher-order hydrocarbons polymerize, condense into aerosols (hence Titan's atmospheric haze), and fall to the surface.

The ethane condenses to some extent at the 70 K temperature minimum at the tropopause (perhaps only at the poles) and descends to the surface, where at 94 K it forms a liquid that is fully miscible with the methane (also a liquid at 94 K). The methane and ethane form the lakes, along with dissolved atmospheric nitrogen. Methane has a relatively high vapor pressure and freezes at 91 K. Ethane has a much lower vapor pressure, and freezes at 90 K. The lakes are likely not pure methane because, with its higher vapor pressure, evaporative cooling of a pure methane lake at 94 K would cause it to freeze. A 50 % component of ethane in the lake, however, would reduce the vapor pressure and evaporative cooling enough that the lake could remain liquid (Lunine and Atreya 2008).

A difficulty with the cycle as described above is that methane is continuously lost, with a timescale of only tens of millions of years, and ethane continuously accumulates. At the present age of the solar system, Titan's surface should be covered with a global ocean of ethane hundreds of meters thick (Lunine and Atreya 2008).

A source equivalent to a global methane layer a kilometer deep would be required to maintain the atmosphere at its present level of methane over geologic time. It is

Table 13.3 Titan's atmosphere

Constituent		Amount
N ₂	(Nitrogen)	80–98 %
CH ₄	(Methane)	0.1–20 % [2.2 % at 850 km]
Ar	(Argon)	<1 %
CO	(Carbon monoxide)	29–52 ppm
H ₂	(Hydrogen)	[20 ppm]
C ₂ H ₆	(Ethane)	1–15 ppm
C ₂ H ₄	(Ethylene)	0.01–15 ppm
C ₂ H ₂	(Acetylene)	2–5 ppm
C ₃ H ₈	(Propane)	0.04–0.7 ppm
CH ₃ C ₂ H	(Methylacetylene)	0.004–0.5 ppm
HCN	(Hydrogen cyanide)	0.05–0.5 ppm
HC ₃ N	(Cyanoacetylene)	≤0.002–0.03 ppm
CO ₂	(Carbon dioxide)	0.001–0.04 ppm
C ₂ N ₂	(Cyanogen)	≤0.002–0.006 ppm
H ₂ O	Water	4 ppb

unlikely that the lakes can accomplish this, because they would need to be tens of kilometers deep; and a subsurface aquifer (or, more correctly, “alkanifer”) system densely packed over the upper tens of kilometers of icy crust is considered equally unlikely (Lunine and Atreya 2008). A more plausible source might be that methane is trapped in the icy crust as a methane *clathrate hydrate*, which methane forms with H₂O at high pressures. It could be a primordial component of Titan, or it could have been produced by water-rock reactions involving CO₂ and ammonia (NH₃). Outgassing or cryovolcanism could then supply this methane to the atmosphere.

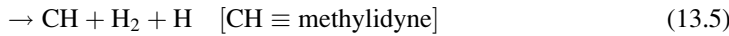
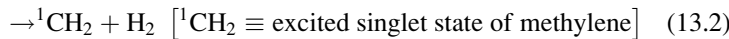
Ammonia may be decomposed by photolysis, resulting in the overwhelming presence of nitrogen in the atmosphere, and the loss of hydrogen to space. By implication, therefore, ammonia may indeed have been an important primordial component of Titan.

Another difficulty is that equatorial regions, including the Huygens landing site, show dendritic features, but these regions appear to be too dry for precipitation at the present time. One solution might be that methane gradually increases in the atmosphere by evaporation from the lakes until rainstorms occur; then these wet the tropics but also deplete the atmospheric methane, and the process repeats on a cyclic timescale of 10–100 years (Lunine and Atreya 2008).

The atmospheric composition as deduced through Voyager UVS and IRIS observations is highly altitude dependent, as summarized by Wilson and Atreya (2004). At 1,400 km, for example, the abundance of CH₄ has been measured as $20 \pm 2\%$ (Strobel et al. 1992). The atmospheric abundance ranges for CH₄ at $h > 700$ km, those deduced for N₂ and Ar, and those from 100 to 300 km levels for the other constituents, are given in Table 13.3. The water observation is from ISO (Coudren et al. 1998).

Diacetylene (C_4H_2 , 0.001–0.04 ppm), acetonitrile (CH_3CN , 0.001–0.04 ppm), and helium were also detected.

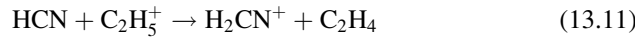
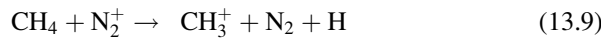
The presence of so many hydrocarbons in Titan's atmosphere can be understood given the apparent abundance of methane. The expected pathways have been discussed by Wilson and Atreya (2004). Some of the methane photolysis pathways are given below, beginning with the five possible ways for the photodissociation of methane high in Titan's atmosphere. There is no consensus on the “branching ratios,” i.e., on what fraction of the CH_4 molecules undergoing dissociation follow which pathway that results in other products, but the first of the pathways represented by (13.1) through (13.5) seems the most important, especially when photons other than Lyman α photons are considered. Comments are square-bracketed.



Ethylene is produced through:



It can be produced also through a chain involving N_2 in an ion exchange reaction:



concluding with a de-excitation process:



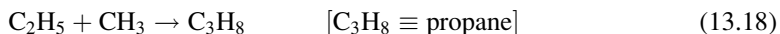
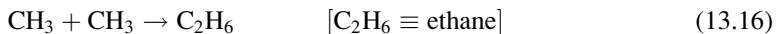
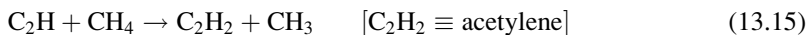
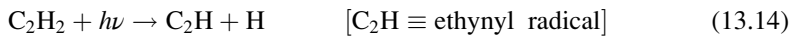
Equations (13.8) through (13.12) can be summed up in the equation:



N^+ and N_2^+ ions are produced through photons with $\lambda < 79.6$ nm and by collisional excitation by electrons.

The comprehensive model produced by Wilson and Atreya (2004), from which this atmospheric chemistry discussion derives, predicts the latter pathway (13.13) of ethylene production to be most important at $h = 1,060$ km, but the peak production of C_2H_4 , according to that model, occurs with (13.6) and (13.7), at $h = 800$ km, with branching ratios of 56 % and 42 %, respectively.

The ethylene is a major source of acetylene. Through other pathways, the methyl and ethyl radicals combine to produce propane in the lower atmosphere. CH radicals help to produce methylacetylene ($\text{CH}_3\text{C}_2\text{H}$) and propylene (C_3H_6). Acetylene helps to produce benzene (C_6H_6), which may have been detected in the atmosphere (Costenis et al. 2003). Other potential pathways can produce the other species. For example (from Strobel 1982):



Some alternate pathways are:

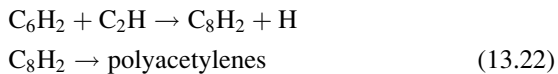
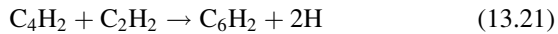
Alternative to (13.15):



followed by:



Alternative to (13.20):



where C_6H_2 is triacetylene and C_8H_2 is tetraacetylene. The C_2H_2 and C_2H_4 , among other species, can condense, causing mist and rain in the lower atmosphere, as was

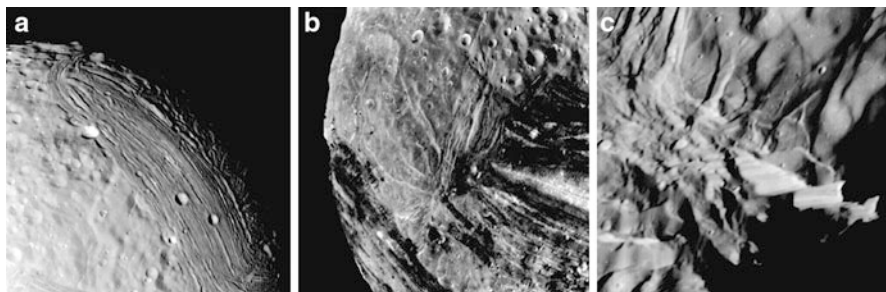
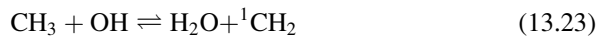


Fig. 13.23 Images of the surface of the Uranian moon Miranda as seen by Voyager 2. (a) The “racetrack,” resembling the sulci of Ganymede and Europa. (b) Arcuate features punctuated by large and small craters and highly contrasting terrain. (c) A huge scissor fault, with a progressive scarp, reaching ~15 km above the surface, seen here on the terminator. From the Voyager 2 flyby of Uranus in January, 1986. NASA/JPL images PIA00141, PIA00140, and PIA00044, respectively

seen by the Huygens probe. H and H₂ can then escape from the thermosphere of Titan. Lyman α observations of a wide hydrogen torus about Titan’s orbit were made by Voyager; CH₄ atoms, the other hydrocarbons, and nitrides are likely sources. At Titan’s temperature, 95 K, water on the surface may not sublime, and so probably has been retained by the planet, and it can be produced high in the atmosphere through the reaction:



This concludes our discussion of Titan.

13.1.4 Uranian Moons

The satellites of Uranus are intermediate-sized or small bodies. The first five were named for characters in the Shakespearean comedy, “A Midsummer Night’s Dream.” The five largest moons were discovered with modest groundbased telescopes. Since then, many more have been added from both space mission imagery and from large ground-based searches. The resurfacing that was seen on the intermediate moons of Saturn is also seen on those of Uranus. The characteristic description of most of the moons is “dark,” although resurfacing of some of the icy moons is apparent. The detail of Miranda as revealed by Voyager demonstrated extraordinarily large relief. The “race course” is reminiscent of the sulci of the Galilean moons Europa and Ganymede, but the huge *scissor fault* has no precedent elsewhere (Fig. 13.23).

Some of the intermediate-sized Uranian moons, like those of Saturn, appear to have reworked surfaces, probably from the same cause. The moons have slightly

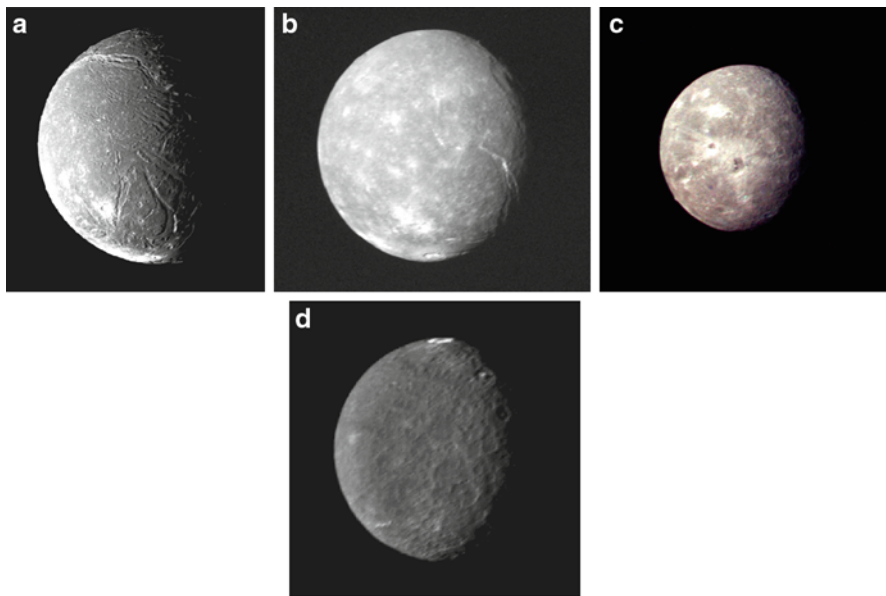


Fig. 13.24 Voyager 2 images of (a) Ariel, (b) Titania, (c) Oberon, and (d) Umbriel. Ariel, Titania, and Oberon have lengthy arcuate valleys and scarps, and bright areas where impacts have excavated fresh ice. Umbriel has limited areas displaying these features, and the overall impression is of an older surface, covered by a very dark regolith. All are heavily cratered. NASA/JPL images PIA01534, PIA01979, PIA00034, and PIA00040, respectively

different albedos (and on some, these vary across the surface), but all are dark, as Table 13.2 indicates. Several of the larger of these Uranian moons are seen in Fig. 13.24.

Titania is the largest and most massive. Ariel is the brightest, with a visual albedo, $A_V = 0.35$ (compare to Umbriel, for which $A_V = 0.19$). The darkest of the five largest moons, Umbriel, nevertheless has bright regions, perhaps the sites of more recent impacts which excavated fresh ice. According to de Pater et al. (2006), the small moon Mab shows H_2O ice absorption features at 2 μm similar to those of the larger moons, and unlike the smaller moons interior to its orbit.

13.1.5 Neptunian Moons

Little is known of the Neptunian system, but its principal moon, Triton was observed in some detail by Voyager 2. Nereid was discovered in 1949 by Gerard Peter Kuiper (1905–1973); its orbit has a high eccentricity (0.75) and an inclination of 28° . It displays light albedo regions and it has been compared to Phoebe in its physical properties (see Fig. 13.25).

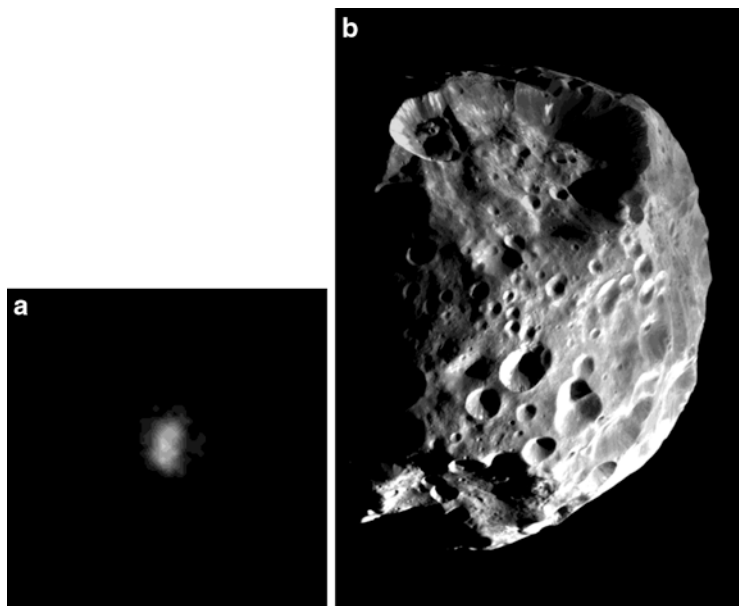


Fig. 13.25 Two small, resurfaced satellites: (a) A Voyager 2 view of Nereid in the Neptune system. NASA/JPL image PIA00054; (b) An image mosaic of Saturn's moon Phoebe as seen by Cassini on June 11, 2004 from a distance of 32,500 km. The scale is 190 m/pixel. NASA image PIA06064. Credits: NASA/JPL/Space Science Institute

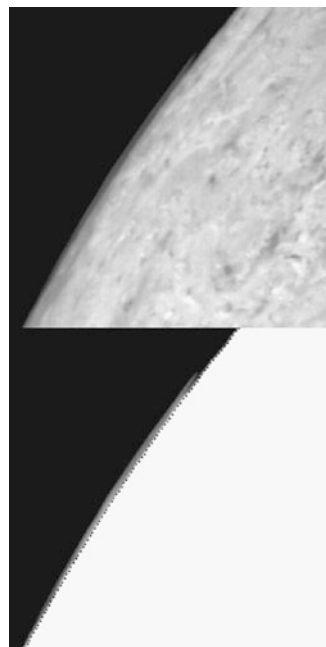
13.1.5.1 Triton

Discovered by Lassell in 1846, Triton is the only one of the major moons (under any of the three definitions above) that is moving in a retrograde (CW) orbit around its planet. Yet, its orbital eccentricity is small. Its blue color, high albedo, and visual appearance indicate that it is an icy world, with a measured temperature of 38 ± 4 K.

Triton's orbital plane is tilted 157° to Neptune's rotation axis, which is in turn inclined 23° to Neptune's orbit. Because Triton's orbit precesses about Neptune's rotation axis once every ~ 4 Neptunian years, the angle that Triton's equator makes with Neptune's orbital plane varies. At the present time, this angle is $\sim 50^\circ$, giving Triton extreme, somewhat Uranus-like seasons.

From ground-based reflection spectroscopy, Brown and Cruikshank (1997) have identified features of N_2 , CH_4 , CO_2 , and CO in Triton's surface ices, with N_2 being by far the dominant component. The atmosphere is primarily N_2 in equilibrium by sublimation with N_2 in the ice, with an atmospheric pressure determined by *Voyager* in 1989 of $14 \mu\text{bar} = 1.4 \text{ Pa}$. This pressure had doubled by 1999 (Lellouch et al. 2010 and references therein), indicating seasonal variation in the atmospheric pressure as Triton approached southern summer solstice in 2000. In addition to N_2 , ground-based infrared spectroscopy in 2009 detected CH_4 and CO in Triton's atmosphere at partial pressures of $10 \text{ nbar} = 10^{-8} \text{ bar}$ and 24 nbar , respectively. With an assumed

Fig. 13.26 Evidence for clouds in the atmosphere of Triton over its south polar cap provided by Voyager 2. The lower image is of higher contrast to emphasize the extent and height of this layer. NASA/JPL image PIA02203



atmospheric pressure (due almost entirely to N₂) of \sim 40 μ bar by linear extrapolation from 1989 and 1999, these are 2.5×10^{-4} and 6×10^{-4} that of N₂, respectively (Lellouch et al. 2010).

It is interesting that in the phase diagram of nitrogen, the triple point, where it can exist as solid, liquid, or gas, is 0.123 bar and 63.15 K. These conditions may be found in Triton's interior. The thermal profile of the atmosphere is such that the temperature decreases up to \sim 50 km, and thereafter rises in the thermosphere to \sim 100 K above 300 km. Despite its extremely tenuous atmosphere, there are clouds: evidence for, and the extent of, a polar cap layer 4–8 km high can be seen in Fig. 13.26.

Features on the satellite include a “cantaloupe” region of dimpled and striated areas (see Fig. 13.27). There are nitrogen geysers, the plumes of which reach heights of 8 km, and apparently cryovolcanoes, involving melted ice rather than rock. The evidence and possible mechanisms are discussed by McKinnon and Kirk (1999). The surface relief is \sim 1 km and this requires a fairly rigid crust. The mean density of Triton is $2,075 \pm 19$ kg/m³. These data imply an important role for volatile ices, which, in the outer solar system, serve the same role as water ice does on Earth, and possibly also for water ice, which may serve the same role here as silicate rock does on Earth.

During the Voyager 2 flyby of Triton, the region between -40 and -60° latitudes (where the plumes were observed) was sub-solar.

There has been substantial resurfacing. The largest impact crater is Mazomba, 27 km across, and impact craters on Triton are generally sparse. Internal heating must have accompanied Triton's capture from an original parabolic orbit as well as any collisions it may have had before settling into its present-day retrograde but

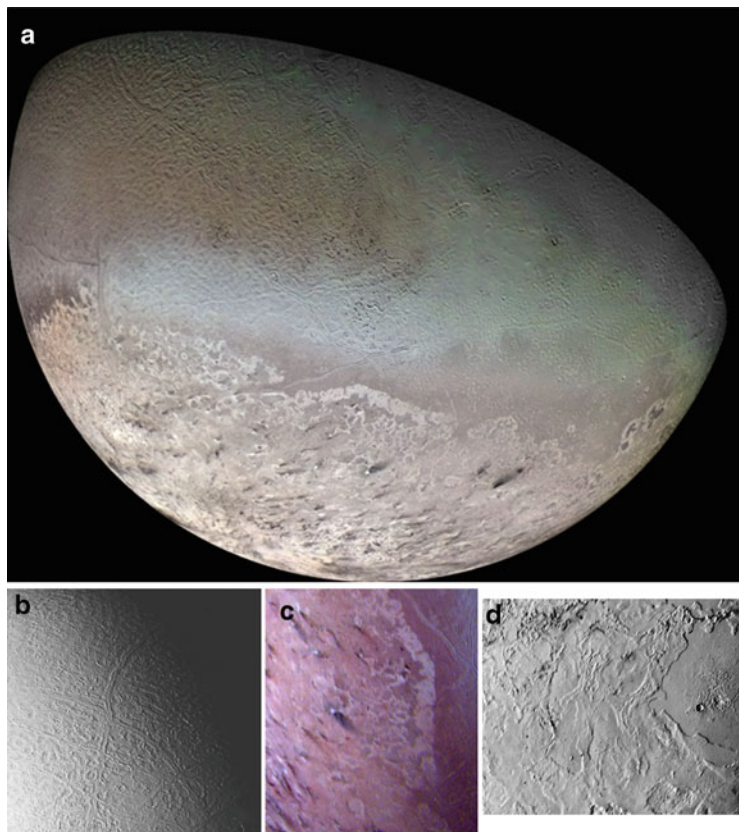


Fig. 13.27 (a) A color mosaic of Triton, the giant moon of Neptune, based on three-passband images recorded by Voyager 2 in its 1989 flyby of Neptune. Notice the blue-green “cantaloupe” terrain at the top, the bright and somewhat pink regions of frost condensation, probably of methane, in a broad area around the South Pole, and the demarcation region between them, in which craters can be seen. In the polar region, dark plumes, likely geysers of nitrogen, are visible. In between are dark spots with bright rims of unknown origin. Produced by the USGS, NASA/JPL image PIA00317. (b) “Cantaloupe” terrain. (c) Plumes from geysers may extend up to 150 km from their vents. (d) Ruach Planitia, a possible caldera of a cryovolcano. From *left to right*, (b)–(d) are NASA/JPL images PIA01537, PIA02214, and PIA02208, respectively

nearly circular orbit. Moreover, tidal dissipation would have heated the moon: today Triton is rotating synchronously.

13.1.6 Pluto-Charon

We discuss Pluto as well as Charon among the moons because the ratio of radii of Pluto to Charon is smaller than that for any major planet to its major moon, making this a kind of binary system, and because in scale Pluto belongs to the population of the major moons—objects that long ago collided with planets, and were either

captured by them or expelled from the inner solar system through interactions with the giant planets. It is also an icy denizen of the outer solar system. Its orbital inclination (17.2) and eccentricity (0.25) are larger than those of any of the major planets, and its perihelion lies within the orbit of Neptune. The two objects cannot collide because Pluto is locked into a 3:2 (orbit:orbit) period resonance with Neptune, a circumstance that makes it a *plutino*; it is the largest known member of this group. Its physical properties suggest Pluto to be a likely member of the Edgeworth-Kuiper Belt of remote, icy bodies, heavily laced with hydrocarbons (refer to Chaps. 14 and 15 for more details). It is one of the largest members of this class known to date, but may not be the largest.

Historically, Pluto was the last “planet” to be discovered (in 1930 by Clyde Tombaugh (1906–1997), a Lowell Observatory employee engaged in a search for a trans-Neptunian planet undertaken and directed by Percival Lowell (1853–1916)), and it now has joined a number of asteroids (Ceres and Vesta among others) that were once considered “planets”. The IAU has designated Pluto a *dwarf planet*, no longer in the same category as the eight planets. Indeed, at least one other such dwarf object (Eris) is now known to be similar in size.

Pluto’s largest, moon, Charon was discovered in 1978 by US Naval Observatory staff members Christy and Harrington while they were carrying out astrometric work on the position of Pluto. The discovery provided the first opportunity to obtain a precise mass for Pluto: $1.304(6) \times 10^{22}$ kg. This result confirmed what its very small influence on the positions of Uranus and Neptune had already suggested: not much mass! Moreover, its extreme faintness (~15th magnitude) had strongly suggested a small diameter; the most recent determination, based on several observed stellar occultations, is 2,360 (+20 to –10) km. From its mass and diameter, Pluto’s density is 1,895 (+97 to –49) kg/m³, similar to that of Triton (2,060 kg/m³). One model for Pluto’s interior that is consistent with this density is a combination of 70 % rock and 30 % ice.

Charon was observed to occult a star in 2005, and this provided a precise radius (Table 13.2). Charon’s diameter is 1,208 km, or 51 % that of Pluto. This is the largest ratio of secondary to primary body diameters in the solar system. Pluto and Charon are locked into a 1:1 spin:orbit resonance; their revolution and rotations have the same period.

Pluto’s equator is tilted about 120° from its orbital plane, giving it extreme seasons like Uranus and Triton; but, unlike the almost-circular orbits of Uranus and Neptune, Pluto’s orbital eccentricity of 0.24 means that it is 60 % further from the Sun at aphelion than at perihelion. Pluto passes spring equinox very close to the time of perihelion (Young 2013) and, because orbital speed is greatest at perihelion, summer solstice occurs only 42 years later. It then takes another $(248^{\circ}/2) - 42^{\circ} = 82^{\circ}$ to reach autumnal equinox. Pluto passed perihelion in 1989, and will reach summer solstice in 2031.

Near perihelion, Pluto was seen to have an N₂ atmosphere that, as on Triton, is in equilibrium with the N₂ surface ice through sublimation. CH₄ and CO (but not CO₂, in contrast to Triton) have also been detected in the N₂ ice and in the atmosphere (Lellouch et al. 2011). The surface pressure is ~100 µbar, or ~1/100 that on Mars. This value can vary significantly over time, however, as the seasons progress and Pluto’s distance from the Sun varies. Despite the increasing illumination in the

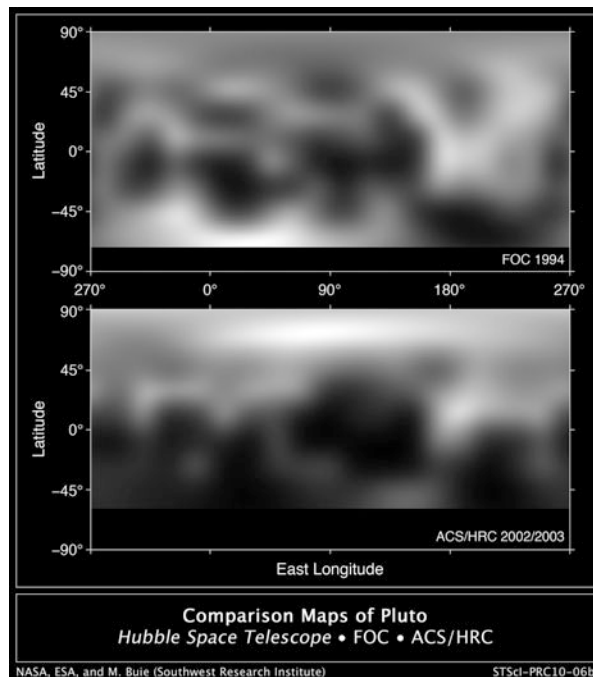


Fig. 13.28 Seasonal changes on Pluto over ~8 years, imaged by the Hubble Space Telescope. The *top picture* was taken in 1994 by the European Space Agency's Faint Object Camera. The *bottom image* was taken in 2002–2003 by the Advanced Camera for Surveys. Pluto's north pole was tilted somewhat toward the Earth in each view. The *dark band at the bottom* of each map is the region around the south pole that was hidden from view at the time the data were taken. Credit: NASA, ESA, and M. Buie (Southwest Research Institute) Photo No. STScI-PR10-06b

northern hemisphere, it is possible that the increasing distance from the Sun will result in the atmosphere condensing almost entirely onto the surface before summer solstice occurs.

Charon appears to have a water ice coating, but no volatile ices. A determination of the temperatures of Pluto and Charon has revealed that Pluto's measured temperature is 10 K cooler than its equilibrium temperature (i.e., 43 K as opposed to 53 K), whereas Charon's observed temperature is 53 K. This is attributed to the evaporation of methane from Pluto's frosty surface under sunlight, as feeble as it may be, thus cooling the surface.

Light and dark albedo markings on Pluto have been imaged by the Hubble Space Telescope (Fig. 13.28). These markings changed dramatically between the 1994 and the 2002–2003 observations, with the north polar region becoming brighter and southern latitudes becoming darker. The measured atmospheric pressure approximately doubled over this time, so the albedo changes may be a result of seasonal interactions between the surface and the atmosphere as Pluto moves away from perihelion and the northern hemisphere becomes more strongly sunlit.

Dynamically, the Pluto-Charon system is also interesting. The inclination of the rotation and Charon orbital planes are retrograde, with an inclination relative to the ecliptic of 99°. Pluto's orbital properties, its possible relation to Triton and other objects in the outer solar system, and its status as a planet are discussed further in Sect. 13.4.2.

New Horizons, a mission to Pluto and the Kuiper Belt, was launched on January 19, 2006 and is enroute to a flyby of Pluto and Charon, at present writing. By means of gravity-assist orbital planning, it is expected not to take more than a century, as it would with a purely Hohmann orbital transfer, but to arrive at the Pluto-Charon system by July 14, 2015, if the mission proceeds as planned. The mission is equipped with a CCD for visual imaging, a near-infrared imaging spectrometer, an ultraviolet imaging spectrometer, and other instruments to analyze particle emissions and dust, and to conduct radio experiments.

13.2 Origins of Ring Systems

Ring systems may be the debris of either tidally destroyed moons or of “failed” moons—i.e., material that began to be created through collisions but was unable to accrete into cohesive moon bodies because of tidal disruption. In some cases, rings may be created by on-going processes: micrometeoroid impacts (Saturn’s Phoebe ring) or ejection of particles from a moon by geophysical processes (Saturn’s E ring).

Tidal instability may be calculated and a critical distance from the planet, the Roche limit, obtained for any satellite of total mass $2m$ and orbital radius r . The tidal force is a differential gravitational force. The magnitude of the acceleration or force per unit mass of this tide-raising force may be expressed as:

$$a_{\Delta g} = \partial/\partial r (-GM/r^2) \cdot \Delta r = 2GM/r^3 \cdot \Delta r \quad (13.24)$$

(Milone and Wilson 2014, Sect. 3.7) where M is the mass of the primary, the planet in this case. Considering that the satellite is being pulled apart, we make the assumption that two halves of equal mass are involved; the separation of their centers is then equal to Δr .

To the differential gravitational force we must add the differential centripetal force (or, in the rotating frame, the differential centrifugal force) due to the differential motion of this extended object around the planet.

The centripetal acceleration may be expressed in terms of the angular velocity, $\boldsymbol{\omega} = (v/r) \hat{\boldsymbol{\omega}}$:

$$\mathbf{a}_c = \boldsymbol{\omega} \times (\boldsymbol{\omega} \times \mathbf{r}) \quad (13.25)$$

the magnitude of which, in a circular orbit, becomes:

$$a_c = v^2/r = \omega^2 \cdot r = a_{\text{gravity}} \equiv GM/r^2 \quad (13.26)$$

so that

$$\omega^2 \cdot \Delta r = GM/r^3 \cdot \Delta r \quad (13.27)$$

The magnitude of the differential centripetal force per unit mass is therefore:

$$a_{\Delta c} = |\partial/\partial r(\omega \times \omega \times r)| \cdot \Delta r = \omega^2 \cdot \Delta r = GM/r^3 \cdot \Delta r \quad (13.28)$$

Combining both, we get the magnitude of the total disruptive differential force per unit mass:

$$a_{\Delta f} = a_{\Delta g} + a_{\Delta c} = 3GM/r^3 \cdot \Delta r \quad (13.29)$$

For *stability*, self-gravity must exceed the disruptive force, so, recalling that the satellite mass is $2m$, the force inequality condition becomes:

$$Gm^2/(\Delta r)^2 > 3GM(2m)/r^3 \cdot \Delta r \quad (13.30)$$

or

$$Gm^2/(\Delta r)^3 > 6GMm/r^3$$

so that

$$r^3 > 6(M/m) \cdot (\Delta r)^3 \quad (13.31)$$

With densities $\rho_s = 2m/[(4/3)\pi(\Delta r)^3]$, $\rho_p = M/[(4/3)\pi R_p^3]$, for the satellite and planet, respectively, (13.31) becomes:

$$r^3 > 6(M/m) \cdot (\Delta r)^3 = 12[\rho_p/\rho_s] \cdot R_p^3 \quad (13.32)$$

The *critical distance* within which a body cohering exclusively through gravitational attraction will be torn apart by tidal effects is therefore:

$$r_{\text{critical}} > \left\{ 12[\rho_p/\rho_s] \cdot R_p^3 \right\}^{1/3} = 2.29R_p \cdot [\rho_p/\rho_s]^{1/3} \quad (13.33)$$

Such a critical distance is usually called a *Roche limit*, after a mid-nineteenth century celestial mechanician named Édouard Roche (1820–1883). With a somewhat more rigorous treatment for a satellite held together purely by gravitational forces, Roche obtained a numerical factor of 2.45.

One may also calculate the critical density of a satellite, ρ_s , for stability at a given distance from the planet. From (13.32),

$$(\rho_s)_{\text{critical}} > 12 \left[R_p^3/r^3 \right] \rho_p \quad (13.34)$$

This can be used, for example, to study the makeup of the object that gave rise to a particular ring. The demise of the object through tidal disruption can be predicted if

1. It is massive enough to raise a significant tide on its parent planet
2. It is within the synchronous orbit distance

The latter condition arises because in this case, the period of the satellite is smaller than the rotation period of the planet (the synchronous orbital period), so the satellite orbits faster on average than a point on the surface rotates. Tidal friction then produces a bulge on the planet behind the moon, and this bulge retards the moon and causes orbital decay, until the Roche limit (for its density) is reached.

One may use the principle of differential gravitational attraction to study the stability of a satellite orbit around a planet with respect to disruption, by, say, the star of the planetary system. It is also applicable to such cases as the tidal effect on a globular cluster at its pericenter distance to the galactic center, or on one galaxy in proximity to another. Within ring systems, the perturbations by a moon on a ringlet (a name given to a single ring strand in a ring system) can cause the ring to expand outward or to fall back toward the planet, if the moon is revolving faster or slower than the ringlet, respectively. A pair of moons straddling a ring can then “shepherd” the ring, with the inner moon constraining the ring particles from moving into lower orbits and the outer moon constraining particles from moving to higher orbits, as we illustrate below.

13.3 Ring Structures

13.3.1 Jovian Rings

There are basically three ring structures, all discovered in the Voyager 1 flyby. For scale, the radius of Jupiter, $R_J = 71,400 \text{ km}$.

- Halo ring: $R_{\text{inner}} \cong 92,000 \text{ km}$ from Jupiter’s center and width of 30,500 km, with thickness $\sim 20,000 \text{ km}$ (there is a substantial drop in brightness interior to 100,000 km)
- Main ring: $R_{\text{inner}} = 122,500$; $\Delta R = 6,400 \text{ km}$; thickness less than 30 km

Associated satellites:

Metis (J16) with $a = 128,100 \text{ km}$
 Adrastea (J15), with $a = 128,900 \text{ km}$

- Inner Gossamer ring: 128,900–181,000 km

Associated satellite:

Amalthea (J5), with $a = 181,400 \text{ km}$

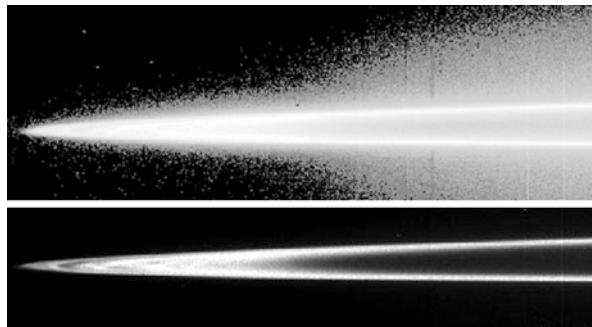


Fig. 13.29 Composite views of Jupiter's rings assembled from Galileo Orbiter images. A brightness enhancement in the upper image permits the cloud of particles constituting the halo ring to be visible. In the *lower image*, structure in the main ring can be seen. NASA/JPL/Cornell image PIA01622

- Outer Gossamer ring: 128,900–225,000 km

Associated satellite:

Thebe (J14), with $a = 221,900$ km

Tiny dust grains forward-scatter light (i.e., scatter the light in approximately the same direction it was originally going) much more efficiently than do larger objects. Consequently, if a ring looks bright when backlit then it must be dusty, and if it looks faint when backlit then it must lack dust and be composed of larger objects. Views seen by the Galileo Orbiter while in Jupiter's shadow (so the rings are backlit) are reproduced in Fig. 13.29. The reflection properties of these rings ($A_V \approx 0.05$ for all four) suggest $\sim 3\text{ }\mu\text{m}$ -size dust particles.

The thickness of the main ring is only 30 km. The greater thickness of the gossamer rings is explained mainly by the inclinations of the source moons of these rings. Figure 13.30 reproduces NASA graphics showing the orbital locations of the larger ring moons amid the rings.

Dust in a ring has a limited orbital lifetime because of radiation pressure, interactions with the planetary magnetic field (dust grains become charged by charge exchange with the magnetospheric plasma and the photoelectric effect: absorption of a solar UV photon followed by ejection of an electron), and perturbations by orbiting satellites. Therefore, the dust in the rings must be continuously replenished. One source for the dust in the main and gossamer rings is micrometeoroid impacts on their accompanying satellites, Metis, Adrastea, Amalthea and Thebe; but *New Horizons* also detected clumps of material in the main ring, which is between the orbits of Metis and Adrastea (Showalter et al. 2007). The clumps were seen only in reflected light and not in forward-scattered light, indicating that these clumps are composed of larger objects. Micrometeoroid impacts on these objects may be the dominant source of dust for the main ring. (Data from *New Horizons*, as it passed closely by the Jovian system in Feb 2007 on its way to Pluto, ruled out any embedded satellites >0.5 km in radius.)

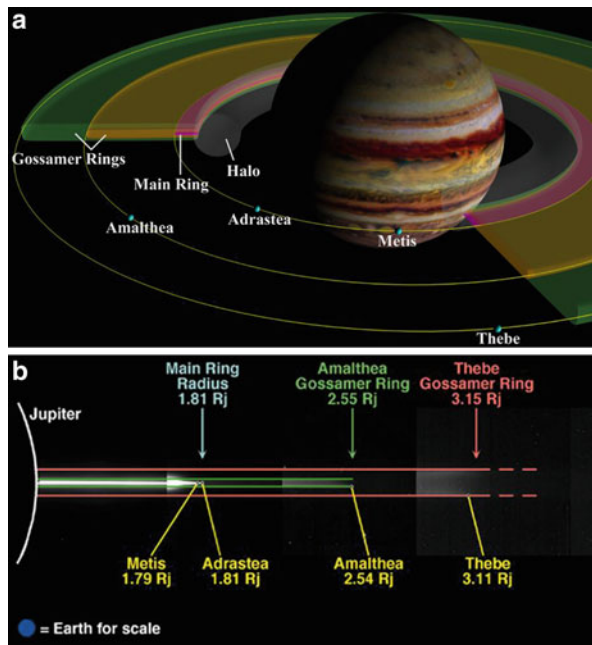


Fig. 13.30 Graphics of the Jovian rings, based on Galileo Orbiter Solid-State Imager data showing the locations of the orbits of small moons associated with the rings (see Table 13.2). The thickness and bluntness of the *Gossamer rings* are due to the orbital inclinations of their sources, the moons Adrastea and Thebe. NASA/JPL images produced by Cornell University: (a) PIA01627 and (b) part of PIA01623, where successive *left to right panels* have increasing sensitivity, in order to display the faint outer rings

The halo ring is composed of main ring particles on decaying orbits, gradually spiraling into Jupiter's atmosphere. The shape of the ring is believed to be caused by the particles passing through *Lorentz resonances*. A Lorentz resonance is similar to a gravitational resonance (e.g., the 3:2 orbital resonance between Neptune and Pluto) except that the perturbation is caused by the planetary magnetic field rather than by the gravitational force from a planet or satellite. The strongest Lorentz resonances are generally those for which $T/T' = (n + 1)/n$, where T and T' are the orbital period of the particle and the period of variation of the magnetic disturbance (equal to the rotational period of the planet for a corotating magnetic field), respectively, and n is an integer (Burns et al. 2001). The outer edge of the halo ring, located at the inner edge of the main ring, is very close to the 3:2 resonance position, and the inner edge is very close to the 2:1 resonance position. As dust particle orbits decay, their inclinations are pumped up as they pass through the 3:2 Lorentz resonance, producing a markedly widened ring as their orbits continue to decay. It is not clear what happens at the 2:1 resonance at the inner edge. The orbital inclinations may be pumped up further, reducing the ring density to invisibility, or the eccentricities may be pumped up, sending the particles plummeting into Jupiter's atmosphere, or perhaps by that time sputtering has eroded the dust particle sizes to essentially zero.

Because of the decay of particle orbits, each gossamer ring is bounded at its outer edge by the orbit of its source satellite and extends inward to the outer edge of the main ring. The two rings therefore overlap within Amalthea's orbit, but because the Thebe ring is wider than the Amalthea ring, it appears as an extension of the ring plane above and below the Amalthea ring (Showalter et al. 2008).

There is a faint extension of the Thebe ring considerably beyond Thebe's orbit, visible to at least 280,000 km from Jupiter's center (this is shown well in Fig. 2c of Showalter et al. 2008). Because particle orbits decay with time, an explanation is required for the extension. Dust grains that were ejected from Thebe in an outward direction from Jupiter will follow orbits just outside that of Thebe (Hamilton and Kruger 2008). These grains pass through Thebe's shadow periodically, losing charge because of the disappearance of solar UV photoionization. The resulting periodically-varying interaction with Jupiter's corotating magnetic field excites periodic oscillations in the grains' orbital eccentricities and semimajor axes, creating the outward extension of the ring. A similar extension of the Amalthea ring may exist, but is embedded within the Thebe ring and is too faint to distinguish.

13.3.2 Saturnian Rings

These were discovered by Galileo in 1610 but identified only as *ansae*, “handles” (as on urns). Their “disappearance” was noted in 1612. Huygens proposed the idea of an equatorial disk in 1655. In 1675, Jean-Dominique Cassini (1748–1845) detected a discontinuity within the rings—now known as *Cassini's Division*, separating Rings A and B. Broad disk instability was demonstrated by Simon de Laplace, who also showed in 1785 that only narrow ringlets were stable because of shearing effects. That the rings were indeed not solid but had to be made of particles was shown by James Clerk Maxwell (1831–1879) in 1857. The measurement of Doppler shift variation across the rings by J. E. Keeler (1857–1900) and W. W. Campbell (1862–1938) in 1895 confirmed Keplerian velocities.

There are four ring systems visible from ground-based telescopes on Earth: A, B, C, D. These are shown in Fig. 13.31. The F, G and E rings are less visible and were discovered by spacecraft. The F and G rings are seen in Fig. 13.32. The E ring is so wide that the orbits of Enceladus, Tethys, Dione, and other moons are embedded in it. The inner to outer ring structure (location, width, and vertical thickness if determined), is as follows ($R_S = 60,268$ km):

- Ring D: $1.11\text{--}1.24R_S$ (66,900–74,510 km);
- Ring C: $1.24\text{--}1.53R_S$ (74,568–92,000 km);
- “Titan ringlet” at $1.29R_S$ (77,871 km);
Maxwell Gap at $1.45R_S$ (87,491 km), 270 km wide;
- Ring B: $1.53\text{--}1.95R_S$ (92,000–117,580 km; and thickness 0.1–1 km);
Cassini Division (B to A, 117,500 km) contains ~20 ringlets;

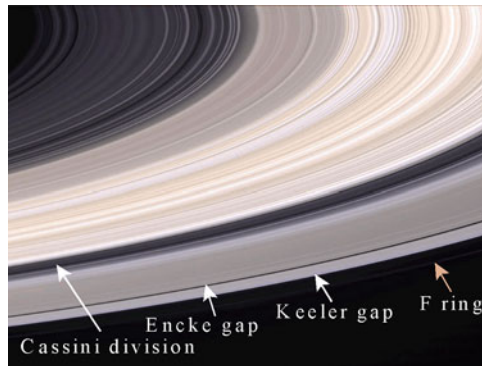


Fig. 13.31 A Cassini view of the rings of Saturn. From the *left*: the faint D-ring complex of ringlets; the C ring with its narrow Maxwell gap; the very bright B ring, terminated by the Cassini's Division (with faint ringlets); the A ring with the Encke gap and very narrow Keeler gap near its outer edge; and the F ring just beyond the A-ring edge. NASA/JPL/Space Science Institute, Boulder image PIA05421; annotation by E. F. Milone

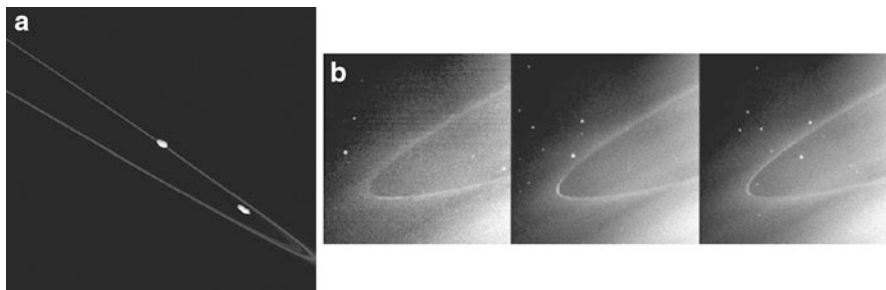
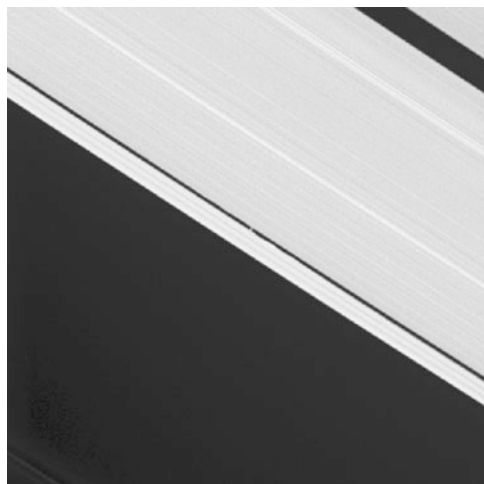


Fig. 13.32 (a) The F ring of Saturn and the shepherding moons Prometheus (102 km length, 483,500 km distance) on the *left* and Pandora (84 km long, 459,000 km distance) on the *right*, as seen by Cassini Orbiter. NASA/JPL/Space Science Institute, Boulder image PIA07653. (b) Cassini's views of the G ring separated by intervals of 45 min, with bright, sharp arcs in an otherwise diffuse ring. The movement of the spacecraft is reflected in the positional shifts in the background stars. NASA/JPL/Space Science Institute, Boulder image PIA07718

- Ring A: $2.03\text{--}2.27R_S$ ($122,170\text{--}136,775$ km; thickness $0.1\text{--}1$ km);
 - Encke gap at $2.22R_S$ ($133,589$ km; 325 km wide);
 - Keeler gap at $2.27R_S$ ($136,530$ km, 35 km wide);
 - Associated satellites:
 - Pan (S18), $a = 133,580$ km;
 - Atlas (S15), $a = 137,670$ km;
 - Daphnis (S35), $a = 136,530$ km;

Fig. 13.33 Cassini discovered Daphnis (~7 km across) within the Keeler gap, visible here in the center of the image. The Encke gap is visible at the *upper right corner* and the faint F ring at the *lower left corner*. This image was obtained on August 1, 2005 when Cassini was 835,000 km from Saturn. A NASA/JPL/Space Science Institute, Boulder image, PIA07584



- Ring F center: $2.33R_S$ (140,180 km);
Associated (shepherding) satellites:
Prometheus (S16), $a = 139,353$ km;
Pandora (S17), $a = 141,700$ km;
- Ring G: $2.75\text{--}2.89R_S$ (166,000–174,000 km; and thickness 100–1,000 km);
Associated satellite:
Aegaeon (S53), $a = 167,500$ km;
- Ring E: 3.00 to $\sim 8.0R_S$ (181,000 to $\geq 483,000$ km; and thickness $\sim 1,000$ km); see text for associated satellites.

The visual albedo (A_V) values for Rings A, B, and C are 0.60, 0.65, and 0.25, respectively; the suggested composition is water ice, at least for the brighter values. Beyond the G ring, the E ring is even more diffuse.

Images from the Cassini Orbiter have spotlighted the actions of the small moons in clumping as well as shepherding the ring particles. Janus (S10) and Epimetheus (S11) are co-orbital at $a = 151,472$ km; they share the same orbital region, but alternately slow down and speed up each other so that they exchange levels and orbital speeds before they can actually collide. Prometheus and Pandora shepherd the F ring, the outer moon retarding and the lower moon accelerating ring particles so that they stay more or less confined to a narrow, if irregular, ring (Fig. 13.32a). Like Pan in the Encke gap, Daphnis (S35) = S2005/S1 plays a similar role in the Keeler gap (Fig. 13.33).

Among the larger moons, Enceladus orbits in the E-ring's brightest part and contributes to it. It is perhaps no coincidence that the intermediate moons Dione, Tethys, and possibly Rhea, with evidence of ice flows on their surfaces, are also within the E ring; they too may be contributing to it.

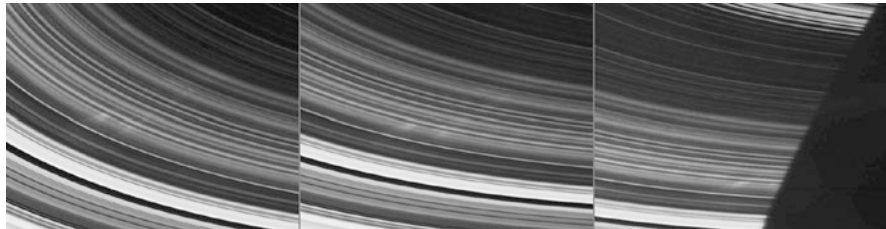


Fig. 13.34 Bright spokes seen in outer B ring by the Cassini Orbiter. They are viewed at a phase angle $\Phi \approx 145^\circ$, while those seen by the Voyagers were viewed at low-phase angles. The spokes are $\sim 3,500$ km long and ~ 100 km wide. NASA/JPL/Space Science Institute, Boulder images PIA07731

A much more distant ring of material, called the Phoebe ring, was discovered in 2009, evidently created by material ejected from the satellite, Phoebe. It is in the plane of Saturn's ecliptic, and therefore inclined at 27° to the plane of the inner rings. More information on the Phoebe ring is provided in Sect. 13.1.3.

A possible ring of material around Rhea was announced by the *Cassini* team (Jones et al. 2008). The ring was not seen directly, but was deduced from an observed depletion of energetic electrons within a distance of 8 Rhea radii of Rhea's center as the spacecraft passed ~ 200 km south of the satellite's equatorial plane. The best explanation appeared to be a low-optical-depth disk of material or a set of rings or arcs containing objects up to ~ 1 m in size. However, a subsequent thorough search in both forward- and back-scattered light failed to find any evidence for such a disk or rings (Tiscareno et al. 2010), and they are now believed not to exist. The cause of the decrease in electron detections has not been determined.

Finally, we note the presence of “spokes” among Saturn's rings (Fig. 13.34). These are transient, quasi-radial features whose origin has been much debated. We discuss the nature and possible origin of these spokes in Sect. 13.3.5; in addition, the ring temperatures shown in Fig. 13.35 suggest that thermal effects may also play a role.

13.3.3 Uranian Rings

Nine rings around Uranus were discovered through the occultation of a star on March 19, 1977 by airborne (Elliot et al. 1977) and ground-based (Millis et al. 1977) teams. The discovery was confirmed by Voyager 2, which found two more rings. They are all extremely dark ($A \approx 0.03$). The widths vary between 1 and 100 km; there is one broad ring (ϵ) and one diffuse one, 1986 U2R.

There are several groups of Uranian rings: 6, 5, 4; α , β , η , γ , δ , ϵ ; and rings 1986 U2R and 1986 U1R (see Figs. 13.36 and 13.37). Associated moons are Cordelia (U6), at $a = 1.947R_U$, and Ophelia (U7), at $a = 2.105R_U$. The individual ring

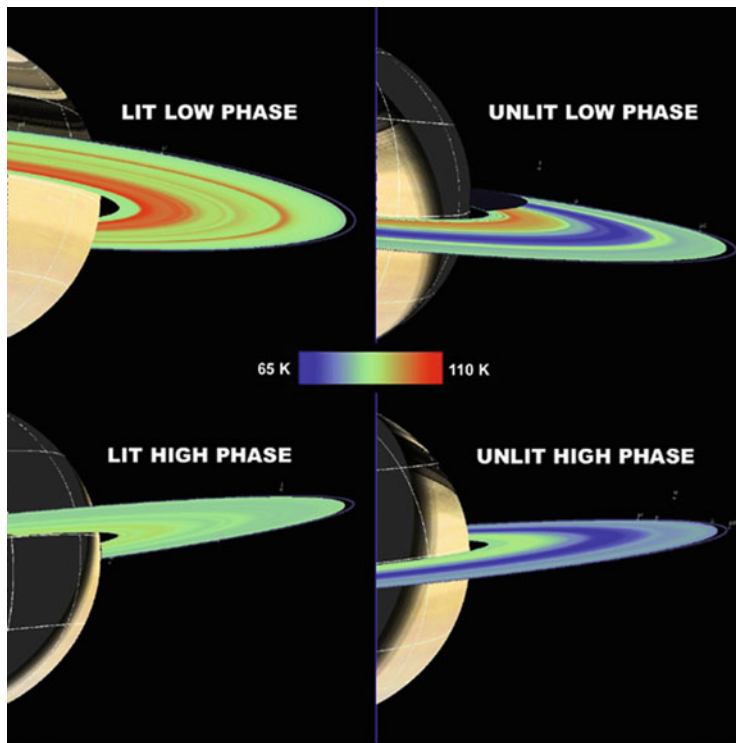


Fig. 13.35 Sun-lit and unlit ring temperatures, measured from low and high-phase angles from Cassini Orbiter. The relative coolness of the B-ring particles is attributable to their high albedo; the darker rings absorb more sunlight. Note the strong thermal emission from the C ring, and the Cassini gap where the ringlets have lower albedo. A NASA/JPL/GSFC graphic, PIA03561, produced by Goddard Space Flight Center

semi-major axes (in units of the radius of Uranus, $R_U = 25,559$ km) and eccentricities are as follows:

- Ring ζ (R/1986 U2) $1.45\text{--}1.5R_U$;
- Ring 6: $1.638R_U$, $e = 0.0014$;
- Ring 5: $1.654R_U$, $e = 0.0018$;
- Ring 4: $1.667R_U$, $e = 0.0012$;
- Ring α : $1.751R_U$, $e = 0.0007$;
- Ring β : $1.788R_U$, $e = 0.0005$;
- Ring η : $1.847R_U$;
- Ring γ : $1.865R_U$;
- Ring δ : $1.891R_U$, $e = 0.0005$;
- Ring λ (R/1986 U1): $1.96R_U$;
- Ring ϵ : $2.002R_U$, $e = 0.0079$; associated shepherding satellites: Cordelia, Ophelia.

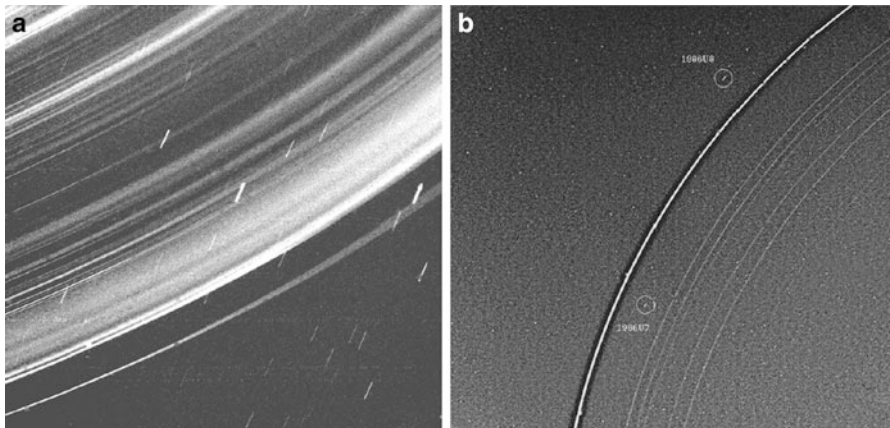


Fig. 13.36 The Uranian ring system as seen by Voyager 2. (a) A 96-s exposure of the rings. The star images, as well as the blurring of the ringlets on the *upper right*, reflect the motion of the spacecraft. (b) An annotated high-resolution image showing shepherding satellites. NASA/JPL image PIA00142 and PIA01976, respectively

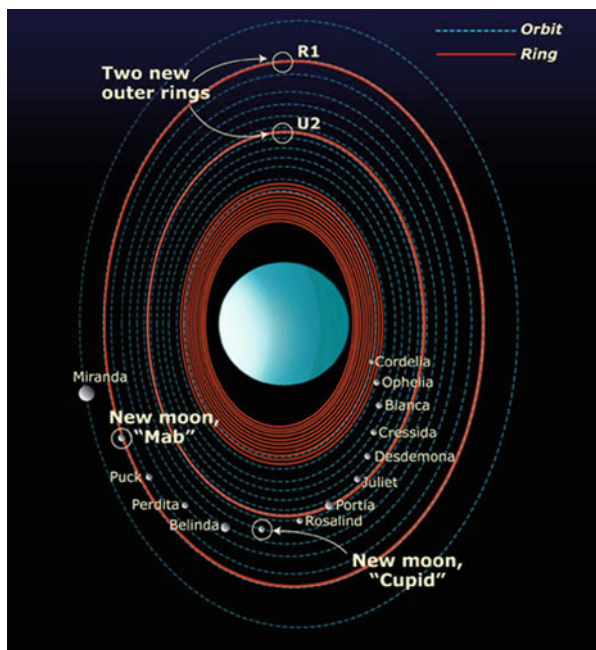


Fig. 13.37 A graphic showing the relationship between the rings and the orbits of associated moons in the Uranian system. Some of the newer (HST) discoveries are indicated. Note the orbit of the satellite Mab, centered on R/2003 U1, here abbreviated to “U1”; the moons Portia and Rosalind flank R/2003 U2, labeled “U2”. A NASA graphic, slightly altered by E.F. Milone. Credits: NASA/ESA/A. Feild (STScI)

- R/2003 U2: $2.59\text{--}2.74R_U$; associated satellites: Portia and Rosalind
- R/2003 U1: $3.37\text{--}4.03R_U$; associated satellite: Puck and Mab

The epsilon ring is less than 150 m thick, and the thickness of most of the other rings is typically ~ 100 m. From observations of the ζ ring, de Pater et al. (2011) describe it as “puffy” and state a full thickness of ~ 850 km, but without specifying an uncertainty. All have visual albedos ~ 0.03 . Two outer rings were discovered more recently (Showalter and Lissauer 2006; de Pater et al. 2006). The ring system is apparently unstable. Individual rings varied in position between the Voyager mission and recent HST and Keck observations; and ring brightnesses changed because of changes in the distribution of dust in the ring plane, and because the Uranian equinox occurred in 2007, producing ring plane crossings and views of the dark side of the rings as seen from the Earth (de Pater et al. 2007). Optically-thin rings brighten as the opening angle decreases to zero (edge-on view) because more particles are visible along each line of sight, whereas optically-thick rings fade because particles are both shaded and obscured by other particles. For this reason, the ϵ ring, dominant to 2006, appeared to be absent in 2007.

The variable nature of the rings brings to the fore observations recorded by William Herschel (1798) to the effect that he suspected one or more rings to be present while he measured the positions of moons of the “Georgian planet.” His careful descriptions are matched by equally careful descriptions of the state of the speculum mirror and optical setup that could contribute to an appearance of such a phenomenon. He concludes (on p. 70) that “... the observation of 26th [Feb., 1792] seems to be very decisive against the existence of a ring.” He considered that a ring could be so oriented so as to be almost invisible, but that in the course of ten years, changed projections would have allowed it to be seen clearly (“we must by this time have had a pretty good view of the ring itself”). He concludes: “I venture to affirm, that it has no ring in the least resembling ... those, of Saturn.”

13.3.4 Neptunian Rings

Stellar occultations provided evidence of partial rings (“ring arcs”); variable thickness rings were confirmed by Voyager 2. There are five known rings; of these, two are wide and one is quite clumpy. Figure 13.38 shows the extent and clumpiness of the rings and the presence of shepherds. It has been estimated that the amount of material in the Neptunian rings is only $\sim 1\%$ of that in the Uranian ring system. The Neptunian ring structure (in units of $R_N = 24,800$ km) is as follows:

-
- Galle = 1989N3R: $1.5R_N$ [inner extent of 1989N3R];
1.69 (1,700 km width); and
 $2.0R_N$ [outer extent of 1989N3R].
 - Associated satellites: Naiad (N3), $a = 1.945R_N$;
Thalassa (N4), $a = 2.019R_N$.
-

(continued)

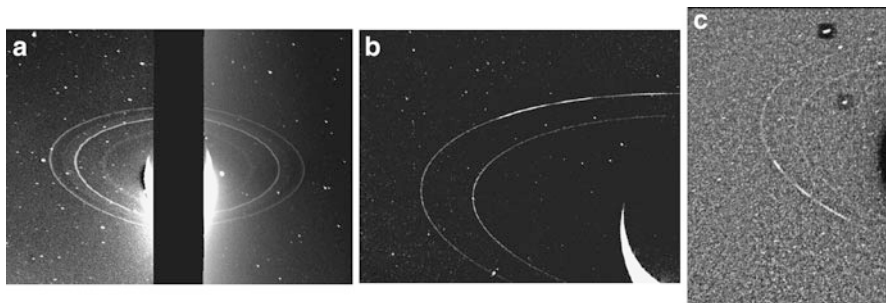


Fig. 13.38 Neptune's rings as seen by Voyager 2. (a) Composite long-exposure images of the rings on either side of Neptune; (b) short exposures showing clumpiness; and (c) the presence of a shepherding satellite outside a faint ring. NASA/JPL images PAI01997, PIA01493, and PIA00053

-
- Leverrier = 1989N2R: $2.15R_N$ (narrow and unresolved by Voyager 2);
Associated satellite: Despina (N5), $a = 2.118R_N$.
 - Lassell = 1989N4R: 2.14 to $\sim 2.31R_N$ ($\sim 4,000$ km width).
 - Arago = 1989N5R: $2.31R_N$ (~ 100 km width).
 - Adams = 1989N1R: $2.54R_N$ (16 km width); (clumpy: three bright arcs, 4° , 4° , and 10°);
Associated satellite: Galatea (N6), $a = 2.498R_N$.
-

13.3.5 Nature and Possible Origins of the Ring Structures

The detailed views returned by the Pioneer, Voyager, Galileo, New Horizons and Cassini missions to the giant planets demonstrated very complex structure in the rings. The presence of gaps among the rings, of large numbers of thin individual rings, kinked and eccentric rings, and co-orbital and shepherding satellites were largely unexpected!

The gaps can be generally understood as analogous to the Kirkwood gaps created in the asteroid belt by Jupiter, with particular moons taking the role of Jupiter. In one case, the Encke gap in Saturn's A ring is apparently due to the moon *Pan* moving within it. *Atlas* seems to moderate the outer A-ring dynamics.

The extremely thin ringlets can be understood as a consequence of small moons located on either side (the *shepherding moons*), whose accelerations act mutually to confine the material of the ring to a narrow torus between them. Saturn's narrow F ring is such a structure with shepherds *Prometheus* and *Pandora*.

The kinked nature of some of the rings, such as the F ring of Saturn, may be due to a shepherding moon in an eccentric orbit, or involvement of more moons (such as Pan in Fig. 13.13) so that shepherding action is performed in a non-uniform way. Perhaps eccentric rings have an explanation in moon eccentricities, but the dynamics of the individual ring particles, through perturbation-induced collisions, certainly add to the non-uniformities. Indeed the propagation of the effects persists around the ring following the passage of the moon.

To the class of unexpected phenomena can be added Neptune's outer ring, which is very clumpy (Earth-based occultation data suggested that the rings were only arcs; *Voyager 2* images showed highly variable ring brightness but not the absence of material in any parts of the ring). The explanation for the bright arcs is not yet known, although dust is suspected. Jupiter's rings are composed mostly of dust. The dust in the two gossamer rings is believed to come from micrometeoroid impacts on their attendant satellites, but the dust in the main and halo rings is believed to come from micrometeoroid impacts on larger objects that form clumps in the main ring. The nature and origin of these objects is as yet unknown.

The origin of Saturn's broad, bright rings is also unknown at present, but a recent model may shed light on the problem (Canup 2010). Planet formation models suggest that the giant planets grew to their present size by pulling material around themselves from the solar nebula. From numerical and analytical modeling, Canup (2010) finds that several satellites the size of Titan were likely to have formed within this smaller nebula around Saturn. As each one formed, it would have gradually lost energy by interacting gravitationally with the nebula and spiraled into Saturn. Titan was the last large satellite to form, and the only one to still be outside Saturn when the nebula dispersed (four remained around Jupiter, the Galilean satellites). The model predicts that the second-to-last would probably have fully differentiated from tidal heating as it approached Saturn, creating a pure ice outer layer that would be disrupted when it spiraled within Saturn's Roche radius. The dense core would survive intact to plunge into Saturn, leaving the icy debris to form a disk of about 100 times the mass of the present rings. The decay timescale of the disk from drag by the gas in the nebula is about ten times longer than the lifetime of the nebula, so the disk remains while collisions in the disk cause the disk to expand outward, with the ice that migrates beyond the Roche radius re-accreting to form small satellites. This could account for the small, inner, icy satellites out to and including Tethys.

The makeup of the rings varies from planet to planet, and from one ring to another. The bluer outer rings of Saturn and Uranus suggest material of different composition.

Saturn's bright rings show strong water (ice) absorption bands, and observations suggest that most of the mass in Saturn's main rings consists of debris in the range 1 cm to 10 m diameter. In contrast, those of the other giants are extremely dark, preventing their early visual detection from Earth. Uranus' rings are dominated by 10-cm to 10-m sized particles (French et al. 1991), although there are dusty rings as well. Dust is nearly ubiquitous in ring systems (with important exceptions, such as the *e* ring of Uranus).

Voyager images showed transient "spokes" on Saturn's B ring, with maximum extents typically \sim 10,000 km radially and \sim 2,000 km in width. Follow-up observations have been made with the Hubble Space Telescope (HST) since 1995 and from the *Cassini* Orbiter since 2004; see Mitchell et al. (2013) for discussion of the *Cassini* observations and a review of earlier results and references.

The spokes generally appear dark in backscattered light (sun behind the viewer) and bright in forward-scattered light, indicating particle sizes similar to the wavelengths of light; the average particle size in one spoke whose IR spectrum was

observed with the *Cassini* Orbiter was 3.5 μm . Individual spokes are optically thin: $\tau \sim 0.01$ when viewed normally.

Typical spoke lifetimes are about half an orbital period, and the spokes are most common, and also most radial, near the morning ansa (astronomical east side of the rings). Keplerian rotation (slower orbital speeds with increasing distance from Saturn) then stretches them as they continue around the planet. These characteristics suggest that they form preferentially in the midnight-to-morning sector of the rings. New spokes tend to form on one side or the other of the synchronous orbital radius (112,200 km from Saturn's center), where the orbital period of a particle equals the rotation period of Saturn's magnetic field. They then expand both inward and outward at initial speeds of $\sim 0.5 - 1$ km/s, but slowing as they grow toward maximum extent. Observed deviations from purely Keplerian changes in the spoke edges show that the particles are negatively charged.

Spoke activity level as indicated by the integrated optical depth (a measure of the number and size of particles in the spoke) varies with a period equal to that of the northern source of Saturn's kilometric radiation (SKR; see Sect. 12.9.4) on both the northern and southern faces of the rings, with the southern-side spokes showing a weaker correlation also with the southern SKR. There is also a seasonal effect: HST data showed the spokes to gradually disappear as the tilt angle between the Sun and the rings approached and exceeded 15° , and not to re-appear until this angle had decreased again, more than a year after *Cassini*'s arrival at Saturn.

No completely satisfactory model has yet been proposed for the creation of the spokes. It is clear, however, that the spokes are influenced not only by Saturn's gravitational field (e.g., Keplerian stretching) but also by Saturn's magnetosphere (e.g., non-Keplerian motions and correlation with SKR, itself originating in or near the auroral ovals and therefore connected to the magnetosphere). Also, the spoke particles are much too massive for magnetic effects to move them at the observed speeds of radial growth of the spokes. One model that has been well developed (Goertz and Morfill 1983) is as follows. Meteoroid impacts on the B ring produce neutral atoms that are ionized by solar UV. This plasma charges the ring particles negatively, and dust-sized particles of ice are ejected from their surfaces and levitated above and below the rings by electrostatic repulsion. The plasma is picked up by Saturn's corotating magnetic field and drops back if within (pulls ahead if outside) the synchronous orbital radius because of the difference between Keplerian and corotational motion; and because the plasma has been left with a net positive charge, this creates a charge separation and azimuthal electrostatic field eastward (westward) between the plasma and the dust. Saturn's magnetic field is directed southward through the rings (see Fig. 12.14), so the plasma $\vec{E} \times \vec{B}$ drifts radially inward (outward), interacting with the ring particles and raising fresh dust as it does so. ($\vec{E} \times \vec{B}$ drift is discussed in Sect. 11.5.) The charged dust particles are, by comparison, massive and continue to be influenced primarily by Saturn's gravitational field, so the spokes become stretched by their (primarily) Keplerian motions. This model, however, produces radial growth of the spoke only away from the synchronous orbital radius, whereas spokes are observed to grow at both ends, away

from and toward this radius. Also, spoke edges are sometimes observed to show non-Keplerian deviations in the opposite sense to that predicted by this model (Mitchell et al. 2013).

The intensity of the sunlight, I , at any wavelength, λ , scattered by a small, spherical dust particle depends on the intensity it sees, I_0 , its radius, R , the index of refraction of the material of which it is composed, m , and the distance from the observer (in this case, the spacecraft), r . It also depends on the scattering function appropriate for the particle, F . The dependencies can be folded into the equation (after Greenberg 1968, Sect. 8.5, esp. p. 347):

$$I_r(\theta, \lambda) = (\lambda/2\pi)^2 I_0(\lambda) F(\theta, \lambda, R, m) r^{-2} \quad (13.35)$$

In the case of photometric observations, the expression must be integrated over the passband in which the observation is made. The function F is defined by Van de Hulst such that

$$F(\theta, \lambda, R, m) = \frac{1}{2} [i_{\parallel}(\theta) + i_{\perp}(\theta)] \quad (13.36)$$

where i_{\parallel} and i_{\perp} refer to the scattering functions for polarized radiation along and perpendicular to the scattering plane, respectively. In practice, there is a distribution of sizes of dust grains, $n(R)$, which must be known, in order for the scattering to be computed. This is a difficult problem in the rings, because the radio and radar observations have revealed meter-sized objects in some of the rings, and, as we have seen, the rings tend to be collections of closely spaced ringlets, perturbed and shepherded by moons, and the shapes of the particles may need to be better known.

The propagation of waves due to dynamical interactions has been discussed by Shu (1984), Franklin et al. (1984) and by Dermott (1984), among others. Fridman and Gorkavyi (1997, especially Sect. 2.1) make a convincing case that the ringlet structure in the Saturnian rings is largely due to resonance effects produced by the moons: linear wave in Cassini's Division due to Iapetus; extended spiral wave in the B ring due to Janus; a 3:5 damped wave resonance in the A ring due to Mimas; bending waves in the C ring due to resonances with Titan. Moreover, they indicate that one mode of the resonances may also involve vertical oscillations.

The source of dust seen among the ring systems may in part be collisions involving close satellites, and impacts on them by interplanetary material. Fragments chipped off these moons could be accompanied by the ejection of micron or sub-micron-sized particles. The discovery of apparently-fragmented moonlets embedded in a placid region of the Saturnian rings (Fig. 13.14) supports the idea as does the existence of ringlets accompanying some satellites, such as the material sharing Pan's orbit in the Encke gap (see Fig. 13.13).

Charged particles may arise from ionization or from electron impact. The magnetic fields of the gas giants sweep through the ring systems, and charged particles will be accelerated as a consequence, leading to periodic phenomena such as spokes.

The dynamics and the history of study of the rings and their phenomena, and their interactions with the moons, can be found in the comprehensive treatment by Fridman and Gorkavyi (1997). However, ring mysteries remain; for example the D

and F rings of Saturn, the arcs of the Adams ring of Neptune, and, most dramatically, the rings of Uranus all have exhibited major changes on timescales of years.

13.4 Orbital Stability of the Moons

13.4.1 Satellite Stability

The severe tidal stress that satellites undergo if they are within the Roche limit of their planet would seem to make it less likely that the Moon originated in a rapidly rotating Earth and was sheared off through rotational instability, as was suggested by George H. Darwin (1845–1912). The orbital evolution of the Moon in any case depends on the tidal bulge of the Earth. Since the Earth is rotating more rapidly, the tidal bulge is ahead of the Moon on the Moon-facing side, and is accelerating it so that a_{Moon} is increasing by a few centimeters per year. In future, the Earth will be slowed by tidal friction so that the length of the day will increase to the length of the month; i.e., the Moon will be in a geosynchronous orbit. It has been conjectured that, at that point, braking by solar tides will cause a_{Moon} to decrease slightly, resulting in the Moon orbiting faster than the Earth is rotating. The Earth's tidal bulge then lags behind the Moon, and the Moon will spiral inward, eventually entering the Roche limit to be tidally disrupted. If this is correct, Earth is destined to become a ringed planet.

In addition to the stability with respect to the Roche limit or the synchronous orbit radius, satellites are also subject to the gravitational attraction of the Sun. The possibility that some of the satellites were captured from solar orbits rather than born in situ has been examined through orbital analysis.

Victor Szebehely (1979) used a parameter of the restricted three-body problem to study the stability of satellite orbits that were known at the time. The analysis is based on a theorem of G. W. Hill (1878) that a satellite orbit around the smaller mass of a restricted three-body problem is stable if it is located inside a zero-velocity curve surrounding only this smaller mass (the planet). This approximately-spherical volume is often referred to as the Hill sphere, and its radius as the Hill radius. The Hill stability criterion is as follows. Consider (13.37), an expression for the differential tide raising force by a large mass, such as the Sun, on a planet-moon system. For orbital stability, we want this force to be exceeded by the gravitational force between the moon and the planet. With m , M_p , M_s as the mass of the moon, the planet, and the Sun, respectively, r_{ps} the distance of the planet-moon system from the Sun, and $\Delta r = r_{mp}$ the distance of the moon from the planet, we may write:

$$\left(GM_s m / r_{ps}^3 \right) \Delta r < GM_p m / r_{mp}^2 \quad (13.37)$$

Table 13.4 Critical satellite orbital radii^a

Planet	r_{\max} (km)	$r_{\text{moon}}^{\text{b}}$ (km)
Mercury	74×10^3	—
Venus	338×10^3	—
Earth	501×10^3	384×10^3 (Moon)
Mars	362×10^3	—
Jupiter	177×10^5	188×10^4 (Callisto)
Saturn	217×10^5	130×10^5 (Phoebe)
Uranus	233×10^5	584×10^3 (Oberon)
Neptune	388×10^5	551×10^5 (Nereid)
Pluto	192×10^5	196×10^2 (Charon)

^aFrom Szebehely (1979, Table 1, pp. 177, 179)^b r_{moon} is the orbital radius of the large moon farthest from the planet

We may now define the Hill radius, r_H , for the planet as the value of r_{mp} for which these two forces are equal:

$$r_H = [(1/3)M_p/M_s]^{1/3} r_{\text{ps}} \quad (13.38)$$

If the actual orbital radius of the moon is equal to or exceeds the Hill radius, the orbit may be considered unstable. In the case of the Moon's orbit, $r_H = 1.496 \times 10^6$ km, or ~ 4 times the mean Earth-Moon distance.

Hill concluded that the Moon's orbit is stable. Szebehely applied a variation of this definition with a tighter stability criterion to all the planets of the solar system and found critical distances from each of the planets within which satellites would be in "stable" orbits. Several of the outer satellites of Jupiter (J8, J9, J11, and J12) are outside the stable zone, while J7, Phoebe (S9, in a retrograde orbit), and the Moon, are just inside the stability line (Table 13.4).

This suggests that capture origins are therefore possible for these bodies also. Indeed, the currently favored theory for the origin of the Moon is through a collision of the Earth with a larger, perhaps Mars-sized, object, with only crust and mantle materials being ejected as debris from which the Moon subsequently formed.

If Szebehely is correct, most of the major satellites originated in the orbital planes in which we find them today (Triton, with its retrograde orbit, is an obvious exception). Presumably the coplanar planetary satellite systems formed through condensation and accretion in similar fashion to the solar system itself. That these systems are in the rotational plane of the planet implies that the obliquities were determined before the satellites were formed, within disks around the planets.

13.4.2 Conjectures about Pluto

Prior to the discovery of large numbers of icy objects in the outer solar system, climaxing in the discovery of such an object possibly larger than Pluto that resulted ultimately in its reclassification, Pluto presented an interesting and apparently

unique case among the outer planets. It had been argued that Pluto in its present orbit was a product of a catastrophic interaction between a large intruder and an earlier Neptunian satellite system that disrupted that initial system and resulted in the ejection of Pluto. It is not impossible that this scenario did indeed occur, because the origins of the moons (Sect. 13.5) are themselves far from well established, but current thought tends toward a different (Kuiper Belt) origin for Pluto and its moons. In favor of the Neptune collision theory were the circumstances that:

1. Pluto's orbit is so eccentric that perihelion falls within the solar distance of the orbit of Neptune.
2. Pluto's size made it the smallest "planet" (in the pre-2006 usage of this term), smaller than Triton, Neptune's major moon.
3. The orbits of the known moons of the Neptune system are unusual: Triton's orbit is retrograde ($i = 157^\circ$); Nereid has an inclination of 27.6° and an eccentricity $e = 0.751$; the second largest moon is triaxial in shape and the fourth largest is also non-spherical.
4. Triton and Pluto have similar sizes and densities and they both have surfaces of nitrogen ice (Charon, on the other hand, has water ice on its surface).

Against were:

1. The Neptune–Pluto resonance: at present Neptune and Pluto are orbit-orbit coupled. The ratio of sidereal periods is 3:2, making interaction impossible, at present, anyway. Orbital integrations over millions of years suggest that while Pluto's orbit is chaotic, this basic resonance does not change. Over gigayears, however, the integrations cannot be performed with sufficiently high accuracy to cast further light on the issue.
2. A major interaction within a satellite system is intrinsically unlikely.
3. Pluto was known to have a satellite (at present writing it is known to have five, actually), making it resemble a planet more closely than some type of minor planet. The Pluto–Charon system is even more of a "double-planet" than is the Earth–Moon system. The satellite/planet mass ratio was the largest in the solar system (when, that is, Pluto was considered a planet).

Among the arguments against, however, numbers 2 and 3 have become less and less convincing with time. Unlikely events have happened in the solar system's history; the Moon is thought to have had its origin in a major collision with a Mars-sized body and an early Earth (see Chap. 8). Regarding argument 3, even before Pluto's demotion from planetary status, the reality of asteroid companions was accepted, thanks to the evidence of occultations and of radar and optical imaging from spacecraft (such as Galileo's imaging of Ida and Dactyl). Even more to the point, three of the four brightest icy objects of the outer solar system that were investigated by Brown et al. (2006) were shown to have companions. So, satellites by themselves are not sufficient for either a planetary definition or a collisional origin. Finally, Venus and Mercury show that it is not a necessary one either.

A preferred current theory is that Pluto is a member of the Kuiper Belt. *Centaurs* are asteroids that cross the orbit of Saturn and they are thought to be escaped former denizens of the Kuiper Belt, itself the supposed source of short-period comets. The comet-like asteroid (2060) Chiron = 95P/Chiron (more recent discoveries have shown such an object to be not uncommon) is also thought to have originated there. Prior to the discovery of Eris (Brown et al. 2005), Pluto could have been considered the largest known trans-Neptunian object, and the largest known asteroid. This theory would not help to explain the strange condition of the Neptunian system, but there is no necessary reason why it should. A number of icy, trans-Neptunian objects have been discovered to have the 3:2 orbital resonance with Neptune. Indeed, it appears that Pluto is merely the largest object in this class; appropriately, the members of this class are referred to as *plutinos*.

2003 UB313 (Eris) occulted a star on 06 Nov 2010 as seen from two sites in Chile, with a near miss at a third site, allowing a precise determination of its diameter: $2,326 \pm 12$ km (Sicardy et al 2011). Its known size, distance and apparent brightness as seen from the Earth now give it an albedo of 0.96, while its infrared flux gives it a surface temperature of 23 K. Eris' mass was already known from the orbital radius and period of its satellite, Dysnomia, so its density could be calculated: $2,520 \pm 50$ kg m⁻³, making it denser than Pluto. Pluto's diameter is less precisely known, but lies between 2,300 and 2,400 km, so within 75 km or so, Pluto and Eris are twins in size. Although Eris' diameter was less well known in 2006 (in fact, at that time it was thought to be slightly larger than Pluto), their close resemblance required the IAU to define what a planet is and is not, which it attempted to do at the General Assembly meeting in Prague in 2006. Originally, a committee created to deal with this issue recommended an expansion of the definition to include both Pluto, Eris and a number of other objects; but this was rejected by the General Assembly, and, instead a less inclusive definition was adopted that named eight planets (Mercury through Neptune) and designated smaller but still round objects (that could pull themselves together through self-gravity) such as Ceres, Pluto, and Eris as "dwarf planets."

Regarding its origin, the Pluto system is long thought to have begun in a collision. Scenarios of a proto-Triton interaction with a proto-Pluto were created by Dormand and Woolfson (1989), Farinella et al. (1979), and Harrington and Van Flandern (1979). A review of these works is provided by Woolfson (1999). Recent scenarios involve formation within the Kuiper Belt by a collision of an object with the proto-Pluto.

The discovery of two more moons about Pluto in 2003 (Weaver et al. 2005) and another two in 2011 and 2012 has added complication but not decreased the likelihood of an impact origin for Charon. Stern et al. (2006) note that the specific angular momentum of Charon is so high that the Pluto-Charon pair was likely created in a collision. The proximity of the other four moons, in coplanar orbits, argues for their creation at the same time. A grazing impact to account for the origin of Charon, with debris coalescing to form the outer moons Nix and Hydra, has been proposed by Canup (2011), updating her earlier (Canup 2005) work with giant impact simulations to form the Pluto-Charon system.

13.5 Origins of the Moons

One may conclude that the present moons of the solar system represent two very different populations (with possible examples given in parenthesis):

1. Small bodies (asteroids; Phobos and Deimos; the outer moons of the giant planets), including, for present purposes, the icy bodies of the outer solar system, and cometary objects
2. Primordial/reconstituted moons (the major moons of the solar system)

Primordial large moons that are primarily rocky no longer exist as isolated bodies in the inner solar system except, arguably, for Mercury and maybe Mars. During the early stages of the solar system they careened about and collided with each other or with the larger planets or were ejected; today most of the remaining bodies of this population are preserved in the potential wells of the major planets, like the sabre-toothed tigers in the tar pits beneath Los Angeles.

Some, perhaps most, of the larger moons revolve in the equatorial planes of their primaries. Although evidential, this is not really convincing evidence that they originated in disks about the planets because the tendency is for (close) orbits to become coplanar and circular with time. Thus, cases where there are departures from this scenario, as for Triton, or our Moon, become very interesting.

Next we will discuss another class of small bodies, the comets. In Chap. 15, we discuss their cousins, the myriad asteroids of the solar system, including the icy denizens of the outer solar system, to which Pluto and some of the icy moons of the outer planets may be closely related.

Challenges

- [13.1] Plot the densities of the major moons (say of size 100 km and up) against their distances from the planet for each of the giant planets. Place on the plot the synchronous orbit limit for each planet. From the results of this plot, what can you deduce about the origins of the moons of the outer planets? The synchronous radius has importance for accelerating satellites into higher and lower orbits. Illustrate how this happens. Make a copy of your plot for Q. [13.2]. [Hint: spreadsheets are very useful for this type of work.]
- [13.2] Calculate the Roche limits for density values in the range $1,000\text{--}3,000 \text{ kg/m}^3$ and place these along with the observed limits for the ring systems on a copy of your plot for Q. [13.1]. Now what can you deduce about the origin of the *ring* systems?
- [13.3] The Galilean satellites have been shown to have orbital resonances among them (see Wilson and Milone 2014, Sect. 3.7.3). Examine closely the periods of the other giant planet moons for similar effects.

- [13.4] Organize the satellites of the outer planets in groups as suggested (a) by orbital characteristics and (b) by physical characteristics. Comment on the differences and similarities between the two groups and what this suggests for the origins of the moons in each group.
- [13.5] Consider the situation and conclusions of Sect. 13.2 for the case of a retrograde satellite.
- [13.6] The heights of the eruptive plumes on Io vary from 60 to 400 km. Given the mass and radius of Io from Table 13.2, compute the ejection velocities required to reach these heights, and compare them to the escape velocity.
- [13.7] Compute the escape velocity from Titan, and the molecular weight of a molecule that can be retained over billions of years, assuming no major or prolonged temperature increases. Discuss the retention of NH₃ and CH₄ on Titan, and of volatile gases generally from the objects in the outer solar system.

References

- Abell, G.: Exploration of the Universe, 2nd edn. Holt, Rinehart and Winston, New York (1969) (1st edn. 1964)
- Anderson, J.D., Schubert, G., Jacobson, R.A., Lau, E.L., Moore, W.B., Sjogren, W.L.: Distribution of rock, metals, and ices in Callisto. *Science* **280**, 1573–1576 (1998)
- Anderson, J.D., Jacobson, R.A., Lau, E.L.: Io's gravity field and internal structure. *J. Geophys. Res.* **106**(E12), 32,963–32,969 (2001)
- Bland, M.T., Showman, A.P., Tobie, G.: The production of Ganymede's magnetic field. *Icarus* **198**, 384–399 (2008)
- Blunck, J.: Solar System Moons: Discovery and Mythology. Springer, New York (2009)
- Brown, R.H., Cruikshank, D.P.: Determination of the composition and state of icy surfaces in the outer solar system. *Annu. Rev. Earth Planet. Sci.* **25**, 243–277 (1997)
- Brown, M.E., Schaller, E.L.: The mass of the dwarf planet Eris. *Science* **316**, 1585 (2007)
- Brown, M.E., Trujillo, C.A., Rabinowitz, D.L.: Discovery of a planetary-sized object in the scattered Kuiper Belt. *The Astrophysical Journal* **635**, L97–L100 (2005)
- Brown, M.E., van Dam, M.A., Bouchez, A.H., Le Mignant, D., Campbell, R.D., Chin, J.C.Y., Conrad, A., Hartman, S.K., Johansson, E.M., Lafon, R.E., Rabinowitz, D.L., Stomski Jr., P.J., Summers, D.M., Trujillo, C.A., Wizinowich, P.L.: Satellites of the largest Kuiper Belt objects. *Astrophys. J.* **639**, L43–L46 (2006)
- Buie, M.W., Grundy, W., Young, E.F., Young, L.A., Stern, S.A.: Orbits and photometry of Pluto's satellites: Charon, S/2005 P1 and S/2005 P2. *Astron. J.* **132**, 290–298 (2006)
- Buie, M.W., Grundy, W.M., Young, E.F., Young, L.A., Stern, S.A.: Pluto and Charon with the Hubble Space Telescope. II. Resolving changes on Pluto's surface and a map for Charon. *Astron. J.* **139**, 1128–1143 (2010)
- Burns, J.A. (ed.): Planetary Satellites. University of Arizona Press, Tucson, AZ (1977)
- Burns, J.A., Matthews, M.S. (eds.): Satellites. University of Arizona Press. (1986)
- Burns, J.A., Hamilton, D.P., Showalter, M.R.: Dusty rings and circumplanetary dust: observations and simple physics. In: Grun, E., Gustafson, B.Å.S., Dermott, S., Fechtig, H. (eds.) *Interplanetary Dust*, pp. 641–726. Springer, New York (2001)
- Canup, R.M.: A giant impact origin of Pluto-Charon. *Science* **307**, 546–550 (2005)
- Canup, R.M.: Origin of Saturn's rings and inner moons by mass removal from a lost Titan-sized satellite. *Nature* **468**, 943–946 (2010)

- Canup, R.M.: On a giant impact origin of Charon, Nix, and Hydra. *Astron. J.* **141**, 35–43 (2011)
- Chuang, F.C., Greeley, R.: Large mass movements on Callisto. *J. Geophys. Res.* **105**, 20,227–20,244 (2000)
- Coustenis, A., Salama, A., Lellouch, E., Encrenaz, T., Bajoraker, G.L., Samuelson, R.E., De Graauw, T., Feuchtgruber, H., Kessler, M.F.: Evidence for water vapor in Titan's atmosphere from ISO/SWS data. *Astron. Astrophys.* **336**, L85 (1998)
- Coustenis, A., Salama, A., Schulz, B., Ott, S., Lellouch, E., Encrenaz, T., Gautier, D., Feuchtgruber, H.: Titan's atmosphere from ISO mid-infrared spectroscopy. *Icarus* **161**, 383–403 (2003)
- Cuzzi, J.N., Lissauer, J.J., Esposito, L.W., Holberg, J.B., Marouf, E.A., Tyler, G.L., Boischot, A.: Saturn's rings: properties and processes. In: Greenberg, R., Brahic, A. (eds.) *Planetary Rings*, pp. 73–199. University of Arizona Press, Tucson, AZ (1984)
- de Pater, I., Hammel, H.B., Gibbard, S.G., Showalter, M.R.: New dust belts of Uranus: one ring, two ring, red ring, blue ring. *Science* **312**, 92–94 (2006)
- de Pater, I., Hammel, H.B., Showalter, M.R., van Dam, M.A.: The dark side of the rings of Uranus. *Science* **317**, 1888–1890 (2007)
- de Pater, I., Dunn, D.E., Hammel, H.B., Showalter, M.R., Gibbard, S., Matthews, K., van Dam, M., Sromovsky, L., Fry, P., Hartung, M., Nicholson, P.: Keck and VLT AO observations and models of the Uranian rings during the 2007 Ring Plane Crossings. *Eur. Planetary Sci. Conf. Abstracts Vol. 6, EPSC-DPS2011-268-2* (2011)
- Dermott, S.F.: Dynamics of narrow rings. In: Greenberg, R., Brahic, A. (eds.) *Planetary Rings*, pp. 589–637. University of Arizona Press, Tucson, AZ (1984)
- Dombard, A.J., Patterson, G.W., Lederer, A.P., Prokter, L.M.: Flanking fractures and the formation of double ridges of Europa. *Icarus* **223**, 74–81 (2013)
- Dormand, J.R., Woolfson, M.M.: *The Origin of the Solar System: The Capture Theory*. Ellis Horwood, Chichester (1989)
- Elliot, J.L., Dunham, E.W., Mink, D.J.: The rings of Uranus. *Nature* **267**, 328–330 (1977)
- Farinella, P., Milani, A., Nobili, A.M., Valsacchi, G.B.: Tidal evolution and the Pluto-Charon system. *Moon Planets* **20**, 415–421 (1979)
- Franklin, F., Lecar, M., Wiesel, W.: Ring particle dynamics in resonances. In: Greenberg, R., Brahic, A. (eds.) *Planetary Rings*, pp. 562–588. University of Arizona Press, Tucson, AZ (1984)
- French, R.G., Nicholson, P.D., Porco, C.C., Marouf, E.A.: Dynamics and structure of the Uranian rings. In: Bergstrahl, J.T., Miner, E.D., Matthews, M.S. (eds.), *Uranus*, pp. 327–409. University of Arizona Press, Tucson, AZ (1991)
- Fridman, A.M., Gorkavyi, N.N.: *Physics of Planetary Rings: Celestial Mechanics of Continuous Media*. Springer-Verlag, Berlin (1997) (tr. D. ter Haar)
- Greenberg, J.M.: Interstellar Grains, chapter 9. In: Middlehurst, B.M., Aller, L.H. (eds.) *Nebulae and Interstellar Matter*. University of Chicago Press, Chicago, IL (1968)
- Grün, E., Morfill, G.E., Mendis, D.A.: Dust-magnetosphere interactions. In: Greenberg, R., Brahic, A. (eds.) *Planetary Rings*, pp. 275–366. University of Arizona Press, Tucson, AZ (1984)
- Gulbis, A.A.S., Elliot, J.L., Person, M.J., Adams, E.R., Babcock, B.A., Emilio, M., Gangestad, J. W., Kern, S.D., Kramer, E.A., Osip, D.J., Pasachoff, J.M., Souza, S.P., Tuvikene, T.: Charon's radius and atmospheric constraints from observations of a stellar occultation. *Nature* **439**, 48–51 (2006)
- Hamilton, D.P., Kruger, H.: The sculpting of Jupiter's gossamer rings by its shadow. *Nature* **453**, 72–75 (2008)
- Hansen, C.J., Esposito, L., Stewart, A.I.F., Colwell, J., Hendrix, A., Pryor, W., Shemansky, D., West, R.: Enceladus' water plume. *Science* **311**, 1422–1425 (2006)
- Harrington, R.S., Van Flandern, T.C.: The satellites of Neptune and the origin of Pluto. *Icarus* **39**, 131–136 (1979)

- Herschel, W.: "Observations and Reports tending to the Discovery of one or more Rings of the Georgian Planet, and the flattening of its polar Regions," In "On the Discovery of four additional Satellites of the Georgium Sidus. The retrograde Motion of its old Satellites announced; and the Cause of their Disappearance at certain Distances from the Planet explained." *Phil. Trans. Roy. Soc. London* **88**, 47–79 (esp., pp. 67–70) (1798)
- Hill, G.W.: Researches in the lunar theory. *Am. J. Math.* **1**, 5–26, 129–147, and 245–260 (1878)
- Hobbs, P.V.: *Ice Physics*. Clarendon, Oxford (1974)
- Hofgartner, J.D., Lunine, J.I.: Does ice float in Titan's lakes and seas?" *Icarus* **223**, 628–631 (2013)
- Iess, L., Rappaport, N.J., Jacobson, R.A., Racioppa, P., Stevenson, D.J., Tortora, P., Armstrong, J.W., Asmar, S.W.: Gravity field, shape, and moment of inertia of Titan. *Science* **327**, 1367–1369 (2010)
- Iess, L., Jacobson, R.A., Ducci, M., Stevenson, D.J., Lunine, J.I., Armstrong, J.W., Asmar, S.W., Racioppa, P., Rappaport, N.J., Tortora, P.: The Tides of Titan. *Science* **337**, 457–459 (2012)
- Johnson, T.V.: The Galilean satellites. In: Beatty, J.K., Chaikin, A. (eds.) *The New Solar System*, 3rd edn, pp. 171–188. University Press, Cambridge (1990)
- Jones, G.H., Roussos, E., Krupp, N., Beckmann, U., Coates, A.J., Crary, F., Dandouras, I., Dikarev, V., Dougherty, M.K., Garnier, P., Hansen, C.J., Hendrix, A.R., Hospodarsky, G.B., Johnson, R.E., Kempf, S., Khurana, K.K., Krimigis, S.M., Krüger, H., Kurth, W.S., Lagg, A., McAndrews, H.J., Mitchell, D.G., Paranicas, C., Postberg, F., Russell, C.T., Saur, J., Seiß, M., Spahn, F., Srama, R., Strobel, D.F., Tokar, R., Wahlund, J.-E., Wilson, R.J., Woch, J., Young, D.: The dust halo of Saturn's largest icy moon, Rhea. *Science* **319**, 1380–1384 (2008)
- Khurana, K.K., Pappalardo, R.T., Murphy, N., Denk, T.: The origin of Ganymede's polar caps. *Icarus* **191**, 193–202 (2007)
- Khurana, K.K., Jia, X., Kivelson, M.G., Nimmo, F., Schubert, G., Russell, C.T.: Evidence of a global magma ocean in Io's interior. *Science* **332**, 1186–1189 (2011)
- Kirk, R.L., Howington-Kraus, E., Barnes, J.W., Hayes, A.G., Lopes, R.M., Lorenz, R.D., Lunine, J.I., Mitchell, K.L., Stofan, E.R., Wall, S.D.: La Sotra y las otras: topographic evidence for (and against) cryovolcanism on Titan. Abstract #P22A-03 presented at 2010 Fall Meeting, AGU, San Francisco, CA, 13–17 Dec (2010)
- Kivelson, M.G., Khurana, K.K., Volwerk, M.: The permanent and inductive magnetic moments of Ganymede. *Icarus* **157**, 507–522 (2002)
- Klavetter, J.J.: Rotation of Hyperion. I—observations. *Astron. J.* **97**, 570–579 (1989a)
- Klavetter, J.J.: Rotation of Hyperion. II—dynamics. *Astron. J.* **98**, 1855–1874 (1989b)
- Kuskov, O.L., Kronrod, V.A.: Internal structure of Europa and Callisto. *Icarus* **177**, 550–569 (2005)
- Lellouch, E., de Bergh, C., Sicardy, B., Ferron, S., Käufl, H.-U.: Detection of CO in Triton's atmosphere and the nature of surface-atmosphere interactions. *Astron. Astrophys.* **512**, L8 (2010)
- Lellouch, E., de Bergh, C., Sicardy, B., Käufl, H.U., Smette, A.: High resolution spectroscopy of Pluto's atmosphere: detection of the 2.3 μm CH₄ bands and evidence for carbon monoxide. *Astron. Astrophys.* **530**, L4 (2011)
- Levison, H.F., Walsh, K.J., Barr, A.C., Dones, L.: Ridge formation and de-spinning of Iapetus via an impact-generated satellite. *Icarus* **214**, 773–778 (2011)
- Liang, M.-C., Lane, B.F., Pappalardo, R.T., Allen, M., Yung, Y.L.: Atmosphere of Callisto. *J. Geophys. Res.* **110**, E02003 (2005). doi:[10.1029/2004JE002322](https://doi.org/10.1029/2004JE002322) (9 pages)
- Lunine, J.I., Atreya, S.K.: The methane cycle on Titan. *Nat. Geosci.* **1**, 159–164 (2008)
- Lunine, J.I., Lorenz, R.D.: Rivers, lakes, dunes, and rain: Crustal processes in Titan's methane cycle. *Annu. Rev. Earth Planet. Sci.* **37**, 299–320 (2009)
- Marconi, M.L.: A kinetic model of Ganymede's atmosphere. *Icarus* **190**, 155–174 (2007)
- Matson, D.L., Blaney, D.L.: Io. In: Weissman, P.R., McFadden, L.A., Johnson, T.V. (eds.) *Encyclopedia of the Solar System*, pp. 357–376. Academic, San Diego, CA (1999)
- McKinnon, W.B.: Mystery of Callisto: is it undifferentiated? *Icarus* **130**, 540–543 (1997)

- McKinnon, W.B., Kirk, R.L.: Triton. In: Weissman, P.R., McFadden, L.-A., Johnson, T.V. (eds.) *Encyclopedia of the Solar System*, pp. 405–434. Academic, San Diego, CA (1999)
- Mignard, F.: Effects of radiation forces on dust particles in planetary rings. In: Greenberg, R., Brahic, A. (eds.) *Planetary Rings*, pp. 333–366. University of Arizona Press, Tucson, AZ (1984)
- Millis, R.L., Wasserman, L.H., Birch, P.V.: Detection of rings around Uranus. *Nature* **267**, 330–331 (1977)
- Milone, E.F., Wilson, W.J.F.: *Solar System Astrophysics: Background Science and the Inner Solar System*, 2nd edn. Springer, New York (2014)
- Murray, C.D.: Saturn's dynamical rings. *Phys. Today* **60**(8), 74–75 (2007)
- Murray, J. B., Iliffe, J. C., Muller, J.-P. A. L., Neukum, G., Werner, S., Balme, M., and the HRSC Co-Investigator Team: New evidence on the origin of Phobos' parallel grooves from HRSC Mars. *Lunar and Planetary Science Conference XXXVII*, abstract 2195 (2006)
- Pappalardo, R.T., Reynolds, S.J., Greeley, R.: Extensional tilt blocks on Miranda: evidence for an upwelling origin of Arden Corona. *J. Geophys. Res.* **102**(E6), 13,369–13,379 (1997)
- Plainiki, C., Milillo, A., Mura, A., Orsini, S., Massetti, S., Cassidy, T.: The role of sputtering and radiolysis in the generation of Europa exosphere. *Icarus* **218**, 956–966 (2012)
- Porco, C.C., et al.: Cassini observes the active south pole of Enceladus. *Science* **311**, 1393–1400 (2006)
- Radebaugh, J., Lorenz, R., Lunine, J., Wall, S., Boubin, G., Reffet, E., Kirk, R., Lopes, R., Stofan, E., Soderblom, L., Allison, M., Callahan, P., and the Cassini Radar Team: Dunes on Titan from Cassini radar. Abstract #1412 presented at the Lunar and Planetary Science XXXVIII Conference, March 12–16, 2007, League City, Texas (2007)
- Rathbun, J.A., Musser Jr., G.S., Squyres, S.W.: Ice Diapirs on Europa: implications for liquid water. *Geophys. Res. Lett.* **25**(22), 4157–4160 (1998)
- Schilling, N., Neubauer, F.M., Saur, J.: Time-varying interaction of Europa with the Jovian magnetosphere: constraints on the conductivity of Europa's subsurface ocean. *Icarus* **192**, 41–55 (2007)
- Showalter, M.R., Lissauer, J.J.: The second ring-moon system of Uranus: discovery and dynamics. *Science* **311**, 973–977 (2006)
- Showalter, M.R., Cheng, A.F., Weaver, H.A., Stern, S.A., Spencer, J.R., Throop, H.B., Birath, E. M., Rose, D., Moore, J.M.: Clump detections and limits on moons in Jupiter's ring system. *Science* **318**, 232–234 (2007)
- Showalter, M.R., de Pater, I., Verbanac, G., Hamilton, D.P., Burns, J.A.: Properties and dynamics of Jupiter's gossamer rings from Galileo, Voyager, Hubble and Keck images. *Icarus* **195**, 361–377 (2008)
- Shu, F.: Waves in planetary rings. In: Greenberg, R., Brahic, A. (eds.) *Planetary Rings*, pp. 513–561. University of Arizona Press, Tucson, AZ (1984)
- Sicardy, B., et al.: Charon's size and an upper limit on its atmosphere from a stellar occultation. *Nature* **439**, 52–54 (2006)
- Sicardy, B., Ortiz, J.L., Assafin, M., Jehin, E., Maury, A., Lellouch, E., Gil-Hutton, R., Braga-Ribas, F., Colas, F., Hestroffer, D., Lecacheux, J., Roques, F., Santos-Sanz, P., Widemann, T., Morales, N., Duffard, R., Thirouin, A., Castro-Tirado, A.J., Jelínek, M., Kubánek, P., Sota, A., Sánchez-Ramírez, R., Andrei, A.H., Camargo, J.I.B., da Silva Neto, D.N., Ramos Gomes Jr, A., Vieira Martins, R., Gillon, M., Manfroid, J., Tozzi, G.P., Harlingten, C., Saravia, S., Behrend, R., Mottola, S., García Melendo, E., Peris, V., Fabregat, J., Madiedo, J.M., Cuesta, L., Eibe, M.T., Ullán, A., Organero, F., Pastor, S., de los Reyes, J.A., Pedraz, S., Castro, A., de la Cueva, I., Muler, G., Steele, I.A., Cebrián, M., Montañés-Rodríguez, P., Oscoz, A., Weaver, D., Jacques, C., Corradi, W.J.B., Santos, F.P., Reis, W., Milone, A., Emilio, M., Gutiérrez, L., Vázquez, R., Hernández-Toledo, H.: A Pluto-like radius and a high albedo for the dwarf planet Eris from an occultation. *Nature* **478**, 493–496 (2011)
- Stern, S.A., Mutchler, M.J., Weaver, H.A., Steffl, A.J.: A giant impact origin for Pluto's small moons and satellite multiplicity in the Kuiper Belt. *Nature* **439**, 946–948 (2006)

- Strobel, D.F.: Chemistry and evolution of Titan's atmosphere. *Planet. Space Sci.* **30**(8), 839–848 (1982)
- Strobel, D.F., Summers, M.E., Zhu, X.: Titan's upper atmosphere: structure and ultraviolet emissions. *Icarus* **100**, 512–526 (1992)
- Szebehely, V.: A general study of satellite stability. In: Nacozy, P., Ferraz-Mello, S. (eds.) *Natural and Artificial Satellite Motion*, pp. 175–180. University of Texas Press, Austin, TX (1979)
- Taylor, S.R.: *Solar System Evolution: A New Perspective*. Cambridge University Press, Cambridge (1992)
- Teolis, B.D., Jones, G.H., Miles, P.F., Tokar, R.L., Magee, B.A., Waite, J.H., Roussos, E., Young, D.T., Crary, F.J., Coates, A.J., Johnson, R.E., Tseng, W.-L., Baragiola, R.A.: Cassini finds an oxygen–carbon dioxide atmosphere at Saturn's icy moon Rhea. *Science* **330**, 1813–1815 (2010)
- Tholen, D.J., Buie, M.W., Grundy, W.M., Elliott, G.T.: Masses of Nix and Hydra. *Astron. J.* **135**, 777–784 (2008)
- Tiscareno, M.S., Burns, J.A., Cuzzi, J.N., Hedman, M.M.: Cassini imaging search rules out rings around Rhea. *Geophys. Res. Lett.* **37**, L14205 (2010). doi:[10.1029/2010GL043663](https://doi.org/10.1029/2010GL043663) (5 pages)
- Tokar, R.L., Johnson, R.E., Thomsen, M.F., Sittler, E.C., Coates, A.J., Wilson, R.J., Crary, F.J., Young, D.T., Jones, G.H.: Detection of exospheric O₂⁺ at Saturn's moon Dione. *Geophys. Res. Lett.* **39**, L03105 (2012). doi:[10.1029/2011GL050452](https://doi.org/10.1029/2011GL050452)
- Veeder, G.J., Davies, A.G., Matson, D.L., Johnson, T.V., Williams, D.A., Radebaugh, J.: Io: volcanic thermal sources and global heat flow. *Icarus* **219**, 701–722 (2012)
- Verbiscer, A.J., Skrutskie, M.F., Hamilton, D.P.: Saturn's largest ring. *Nature* **461**, 1098–100 (2009). doi:[10.1038/nature08515](https://doi.org/10.1038/nature08515) (3 pages)
- Weaver, H.A., Stern, S.A., Mutchler, M.J., Steffl, A.J., Buie, M.W., Merline, W.J., Spencer, J.R., Young, E.F., Young, L.A.: Discovery of two new satellites of Pluto. *Nature* **439**, 943–945 (2006)
- Weaver, H. A., et al.: IAU circular 8625, 1 (2005)
- Williams, D.A., Keszthelyi, L.P., Crown, D.A., Yff, J.A., Jaeger, W.L., Schenk, P.M., Geissler, P. E., Becker, T.L.: Volcanism on Io: new insights from global geologic mapping. *Icarus* **214**, 91–112 (2011)
- Wilson, E.H., Atreya, S.K.: Current state of modeling the photochemistry of Titan's mutually dependent atmosphere and ionosphere. *J. Geophys. Res.* **109**(1–39), E06002 (2004). doi:[10.1029/2003JE002181](https://doi.org/10.1029/2003JE002181)
- Wisdom, J., Peale, S.J., Mignard, F.: The Chaotic rotation of Hyperion. *Icarus* **58**, 137–152 (1984)
- Woolfson, M.M.: The Neptune-Triton-Pluto system. *Mon. Not. Roy. Astron. Soc.* **304**, 195–198 (1999)
- Young, L.A.: Pluto's seasons: new predictions for New Horizons. *Astrophys. J. Lett.* **766**, L22 (2013). doi:[10.1088/2041-8205/766/2/L22](https://doi.org/10.1088/2041-8205/766/2/L22). 6 pages
- Zalucha, A.M., Gulbis, A.A.S., Zhu, X., Strobel, D.F., Elliot, J.L.: An analysis of Pluto occultation light curves using an atmospheric radiative-conductive model. *Icarus* **211**, 804–818 (2011)
- Zimmer, C., Khurana, K.K., Kivelson, M.G.: Subsurface oceans on Europa and Callisto: constraints from Galileo magnetometer observations. *Icarus* **147**, 329–347 (2000)

Chapter 14

Comets and Meteors

14.1 Comets in History

Because of the effects comets have had on our intellectual history, and on the development of astronomy, in this chapter we delve a bit more into past perceptions than we have done in most of the earlier chapters.

14.1.1 Early History

Comets, a name derived from “hairy stars” (in the Greek, *αστηρ κομήτης*, aster’ come’tes), have been studied, feared, and admired throughout history, partly because they commanded attention. To many they represented a sign or a message, and given human history such as it has been, comets often did precede some momentous event. The early Christian theologian Origen (~184–254), in his discussion of the Star of Bethlehem (*Contra Celsus*, Book 1, Chap. LIX, Crombie, trsl. 1994; excerpted in Kelley and Milone 2011, p. 134), comments,

It has been observed that, on the occurrence of great events, and of mighty changes in terrestrial things, such stars are wont to appear, indicating either the removal of dynasties or the breaking out of wars, or the happening of such circumstances as may cause commotions upon the earth. But we have read in the Treatise on Comets by Chaeremon the Stoic [Alexandria, first century], that on some occasions also, when good was to happen, [comets] made their appearance; and he gives an account of such instances. [Brackets added by present authors.]

Records of probable comet observations go back to at least the seventh c. BC; here, we provide only the briefest summary of other historical commentaries on comets:

- The records of the “Wên Hsien Thung Khao” or “Historical Investigation of Public Affairs” by Ma Tuan-Lin and a supplement list 372 comets observed in the period 613 BC–1621 AD. The list includes several observations of Halley’s comet, for the dates: 240 BC, 87 BC, 11 BC, 66 AD, and all subsequent returns to the end of the chronicle; records of 467 and 163 BC also may refer to this comet.

- The Pythagoreans in the 6th c. BC considered comets to be planets which appeared infrequently.
- Anaxagoras of Clazomenae (5th c. BC) and Democritus of Abdera (5th–4th c. BC) thought comets were conjunctions of planets.
- Ephorus of Cyme (4th c. BC) observed the comet of 371 BC to split into two stars.
- Apollonius of Myndus (4th c. BC) commented that comets were distinct heavenly bodies with orbits.
- Aristotle (4th c. BC) stated that comets were:
 - Outside the ecliptic, therefore they were *not* planets
 - Also, therefore, they could not be conjunctions of planets
 - They were *not* coalescences of stars; but were
 - Atmospheric phenomena (possibly omens of droughts or high winds).
- Posidonius (1st–2nd c. BC) also thought they were atmospheric phenomena. He saw one during a solar eclipse and argued that sometimes comets were invisible because they were lost in the Sun's glare.
- Seneca (1st c. AD) reviewed previous writings.
- Pliny the Elder (1st c. AD, who died studying the eruption of Vesuvius that buried Pompeii) cataloged comets.

Other writings on comets were contributed by:

- The Venerable Bede (672–735)
- Thomas Aquinas (1225–1274)
- Roger Bacon (1214–1294)

In a scientifically more active era, the fifteenth century, the pace began to pick up:

- Paolo Toscanelli (1397–1482), later adviser to Columbus, made positional measurements of several comets relative to stars.
- Georg von Purbach (1423–1461) attempted to measure the distance to a comet.
- Johann Müller, also known as Johannes de Monte Regio or Regiomontanus (1436–1476), student of Purbach, observed and studied the structure of comets.

These activities marked advances; on the other hand, a contemporary figure, Matthew of Avila, expounded that comets caused evil, because “their hot, putrid vapours contaminated the air.”

Fortunately, progress seems to have continued. In ~1550 the mathematician Jerome Cardan (Girolamo Cardano, 1501–1576) described a comet as “a globe in the sky illuminated by the Sun, the rays of which, shining through the comet, give the appearance of a beard or tail.” More science was to come.

14.1.2 Tycho Brahe and the Comet of 1577

Tycho Brahe (1546–1601) had determined the “nova” of 1572 (SN 1572) to be located somewhere beyond the Moon, and thus not to be a comet or meteor (which

were thought to be formed below the orbit of the Moon). The discovery of a truly “new” star clearly outside the terrestrial regions damaged the credibility of the Aristotelian immutability of the heavens. In 1577, Brahe turned his attention to the great comet of that year (C/1577 V1) and determined its parallax to be within his observational error, set mainly by his measuring device. His instrument was a cross-staff which produced a mean measurement error of ~ 4 arc-min. This established an upper limit to the parallax, and therefore a lower limit to the comet’s distance:

$$R = R_{\oplus} / \sin p \geq R_{\oplus} / 0.0011636 = 859R_{\oplus} = 5.48 \times 10^6 \text{ km}$$

This minimal distance is $\sim 14 \times$ the Moon’s distance (384,400 km or $60R_{\oplus}$). This result demonstrated that Aristotle’s theory of comets is incorrect, because comets, or least the Comet of 1577, could not be in the Earth’s atmosphere without producing a large, measurable parallax.

The imperial court physician and astronomer Thaddeus Hagecius (1525–1600) at Prague is also said to have attempted a measurement of the parallax. The separation between the two sites was 600 km, and the differential parallax was found to be $\lesssim 2'$ implying a distance of at least 1.03×10^6 km, again, further than the Moon.

Brahe concluded that at the time of observation the comet lay between the Moon and Venus. He suggested further that the orbit was “oval”, possibly the first informed argument that non-circular motion occurred in the heavens.

The parallax observations were confirmed by, among others, Michael Maestlin (or Mästlin, 1550–1631), who found that the comet’s distance varied between 155 and $1495R_{\oplus}$. The latter result meant that part of the comet’s orbit was within the celestial sphere associated with Venus. The ancient view was that the planets traveled on celestial spheres, and various later proponents in the European and Islamic worlds held this view also. The observations of the comet of 1577 indicated that the crystalline sphere of Venus had been penetrated.

Tycho’s instruments improved greatly in the years following and by 1585, when another comet appeared, the achievable precision of his measurements was ~ 1 arc-min. This comet, too, was demonstrated to be more distant than the Moon. This was a further refutation of ancient ideas, and this was made public, for the first time, apparently, by Christoph Rothmann (1560–1600) in a book published in 1585, regarding the comet observed in that year. Thus the credibility of the celestial spheres had been shattered forever by the end of the sixteenth century. See Gingerich and Westman (1988) for a delightful account of the personalities of that era, the discoveries, and the reception of those discoveries.

Returning to the Comet of 1577, we note that the linear dimensions of the comet measured $8'$ for the head and 22° and $2^\circ 5'$ for the length and width of the tail, respectively. Brahe concluded that the comet was huge and porous, permitting sunlight to filter through it. Attacks were made on these interpretations by, among others, Galileo Galilei (1564–1642). In a curious kind of defense of Aristotle,

Galileo argued that comets could be “optical illusions;” he suggested that vapors arising from the Earth’s atmosphere could reflect sunlight in such a way that they would be visible once outside the Earth’s shadow. This may seem odd in retrospect, but Copernicus, too, had thought that comets were a terrestrial phenomenon. The attacks were countered by Kepler (in *Tychonis Brahei Dani Hyperaspistes*), who defended the accuracy of Brahe’s observational results.

14.1.3 Later Historical Studies

Johannes Kepler (1571–1630) studied the comets of 1607 and 1618 and published the results in *de Cometis*, in 1619. He thought comets moved along straight lines but with irregular speed. The description is comprehensible when one considers that the paths of comets traveling in highly eccentric ellipses or parabolas when seen on edge could resemble straight lines.

In the seventeenth century a number of others carried out comet studies as well; for example:

- Johannes Hevel (1611–1689) made the first comprehensive survey in 1654 and suggested that comets originated in the atmospheres of Jupiter and Saturn
- Giovanni Borelli (1608–1679) thought that cometary orbits were parabolic, as did
- Georg S. Dörffel (1643–1688), who argued that the orbit of the comet of 1680, that was observed to make a rapid turn near the Sun and move back in the same direction it had come, was a narrow parabola with a very short perihelion distance
- Edmond Halley (1656–1742) was the first to determine that comets could be periodic and the first to successfully predict a return date, 1758
- Isaac Newton (1642–1727) discussed the elliptical nature of cometary orbits (as determined by Halley) and noted the high eccentricities of comets. In the *Principia*, III, 1686 (Cajori rev. of Motte tr., 1962, pp. 497, 498), he stated that

“I am out in my judgement, if they are not a sort of planets revolving in orbits returning into themselves with a continual motion; . . .”

and proposed that

“. . . their orbits will be so near to parabolas that parabolas can be used for them without sensible error.”

Some of Newton’s other points were that:

- comets shine by reflected sunlight
- tails arise from comets’ atmospheres (following Kepler)
- the mutual gravitational effects of the large numbers of comets will perturb their orbits, so that elements will change from one apparition to the next
- a “new star” could be produced by the infall of a comet into an “old star.” (Newton cites Tycho’s supernova of 1572 as an example; cf., Cajori tr., 1962, pp. 540–542)

- Alexis-Claude Clairaut (1713–1765) performed the first perturbation calculations and predicted a return date of Halley’s comet perihelion passage of April 15, 1759
- Johann Franz Encke (1791–1865) was the second to predict the return of a comet—and to determine the periodicity of the shortest-period comet, that of: January, 1786; November, 1795; October, 1805; and of November, 1818. He also noted that the period was decreasing: $\Delta P/\Delta t < 0$. This implies that the semi-major axis is decreasing, so the comet is essentially spiraling into the Sun. From Kepler’s third law,

$$P^2 = (M_{\odot} + m) a^3 = Ma^3 \quad (14.1)$$

where P is the sidereal period in years, M the total mass, m the comet’s mass, and a the semi-major axis in astronomical units. Differencing and then dividing through by (14.1), one finds:

$$2\Delta P/P = \Delta m/M + 3\Delta a/a \quad (14.2)$$

Although a comet loses mass continually and hemorrhages material as it rounds perihelion, the first term on the right-hand side is still negligible due to the solar mass in the denominator; hence,

$$\Delta a/a = (2/3) \Delta P/P \quad (14.3)$$

Encke attributed the period decrease he determined for the comet that bears his name to a resisting medium or to a belt of meteoritic particles. Other deviations in the orbit he attributed to the heating effects of sunlight on the comet. The effect on the orbit is determined by the direction as well as the speed of the comet’s rotation.

- John Herschel (1792–1871) observed that Biela’s Comet of 1772 split into two in 1846 and that a luminous bridge joined the two parts, each of which subsequently developed tails. The twin comets returned in 1852, but have not been seen since.

The idea that non-gravitational forces act on comets was probably first advanced by Friedrich Wilhelm Bessel (1784–1846), but, as noted above, Encke, and, much later, Brian Marsden, applied it so that the effects could be quantified.

For more comprehensive treatments of the development of ideas about comets, see Brandt and Chapman (1981), Bailey et al. (1990), or Yeomans (1991).

14.2 Comet Designations

In ancient Mesopotamia, the name for a comet was *sallamu*. According to Ronan and Needham (1981, p. 208), ancient Chinese names for comets were “brush-stars,” “long stars,” and “candle-flame stars.” Several of the objects referred to in the Chinese annals as “sweeping stars” are comets; and it is possible that the large sizes,

Fig. 14.1 Halley's Comet (1P/Halley), seen from Cancun, Mexico during the January 1986 apparition, a relatively unfavorable one for visibility in the northern hemisphere. Photo by E. F. Milone



and blue colors attributed to some, refer to appearances of comets or at least to some phenomenon other than novae. Objects reported for 76 BC (“candle star”), 48 BC (“blue-white”, “star as big as a melon”) and 5 BC (“sweeping star”) fall into this category. Some are reported as being as “big” as the Sun, or some other object. Presumably, in a phrase such as “as big as the Sun,” angular size is intended. However, the context of comments about size in the Chinese annals usually makes it clear that brightness and not a true angular size is being described; for example, the *Sung-shih* and *T'ung-k'ao* annals report that from July 28 to August 6, 1203, a star with a blue-white color, “no flame or tail,” as “big” as Saturn, stayed at *Wei* (Scorpius).

In modern usage, a comet is always named for its discoverer(s), but additional designations are given to it to indicate the order of appearance or detection and the nature of the comet. Thus, for example, the designation 1P refers to the first comet discovered for which an accurate orbit was computed (Comet Halley), and the fact that it is a periodic comet (see below for letter designations).

Formerly comets had two types of year designations. One indicated the year of discovery with a lower case letter indicating the order of discovery in that year; another usage gave the year of perihelion passage followed by a Roman numeral indicating the sequence within the year. A year-type designation is still used for the discovery or recovery date, but now it contains a code for every half month (A = Jan 1–15; B = Jan 16–31, etc.) followed by a sequence number in Arabic numerals. Thus, for example, 1P/1982 U1 or 2P/1822 L1.

The naked eye appearance or *apparition* of Halley's Comet in 1985–1986 (Fig. 14.1) was preceded by its detection as a very faint object in 1982; its former year designations were 1982i and 1986 III; its current provisional designation records its last apparition: 1982 U1. This indicates when it was recovered.

A third modern designation indicates if the comet is periodic (*P*), i.e., has appeared at two (or more) perihelia, or not (*C*), if it is defunct (*D*), i.e., has failed to return or is known no longer to exist, is later found to be an asteroid (*A*), or, if it

is not possible to compute an orbit either because the data are inadequate or because the comet is one for which a meaningful orbit cannot be computed, for whatever reason (X). Thus, for example, *D/1993 F2-K*, designates one of the now defunct components (“*K*”) of the disintegrated comet also known as Shoemaker-Levy 9. The distinction between the asteroids and comets is likely to be increasingly blurred as the icy bodies of the outer solar system are investigated in detail; the objects in the Edgeworth–Kuiper Belt (see below and Chap. 15) are, in fact, thought to be an ultimate source of short-period comets. The term “short-period” has traditionally been applied to comets with periods of 200 years or less.

The current preferred designation for Halley’s Comet is *IP/Halley* or *IP (Halley)*, thus independent of apparition.

A description that applies to a particular appearance would be, for example, *Comet IP/1982 U1*, or *Comet IP/-239 K1*; and, as we note, the designation for the comet per se, would be comet *IP/Halley*. A number of short-period comets can be observed around the orbit, and thus no longer receive an appearance or recovery designation; for example, comet *2P/1822 L1* was a provisional designation for comet *2P/Encke*, and it has been observable continually since discovery.

14.3 Cometary Orbits

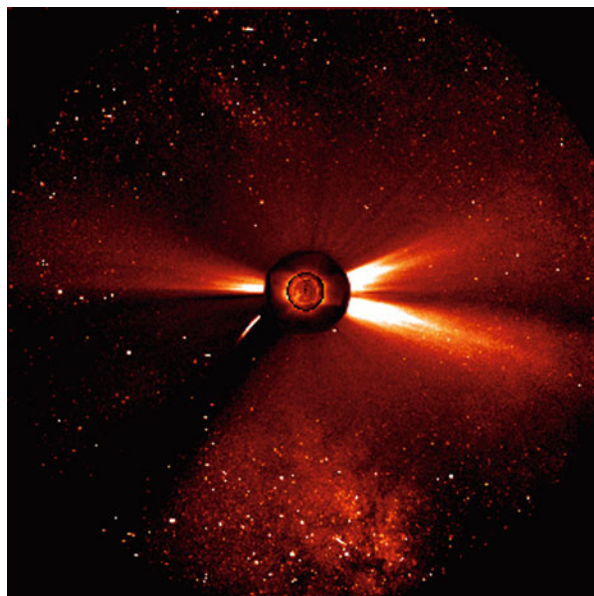
There are two types of comets distinguished by their orbits:

- Periodic comets (i.e., $P \lesssim 200^y$)
- Parabolic comets or nearly parabolic, sometimes called long-period comets

There were 2221 comets in the Marsden and Williams (2005) catalog of cometary orbits. Of these, 341 comets had periods of less than 200 year; of the 341 comets, 203 had been seen at least twice, 138 were (to that date) single-apparition comets. Seven short-period comets had become “defunct” in the sense that they had not been detected at recent predicted returns. Since then, however, the discovery of comets has burgeoned. On Dec. 28, 2010 it was announced that the ESA/NASA SOHO satellite had discovered its 2000th comet. Although a coronal observatory, the SOHO cameras have contributed greatly to cometary knowledge. In addition, the STEREO SECCHI satellites are also producing many comet discoveries and recoveries.

In describing typical cases, Marsden and Williams (1997) state that the average short-period comet has the properties: $P = 7$ year; $q = 1.5$ au; $i = 13^\circ$. They note further that there are twice as many short-period comets with longitudes of perihelion in the semi-circle centered on Jupiter’s perihelion than in the opposite semi-circle. Jupiter not only dominates the short-period comets, it sometimes captures them into its own satellite family. A recent example was Comet Shoemaker-Levy 9 (D/1993 F2), that collided with Jupiter in 1994. Some have argued that most

Fig. 14.2 A SOHO image of SOHO-6 (C/1996 Y1), a sun-grazing comet (the streak to the lower left of the Sun). Courtesy of SOHO/LASCO-EIT-UVCS/consortium. SOHO is a project of international cooperation between ESA and NASA



comets with periods up to 20 years, should be designated “Jupiter-family” comets. In fact, however, there are families of comets connected to each of the giant planets, but dynamical modeling has shown these comets as capable of migrating inward, past the outer giants.

Several families of comets approach the Sun very closely, each family possibly being the fragments of a single comet. The *Kreutz sungrazing group*, with perihelia less than 0.02 au (a few solar radii), is by far the largest: the discovery of the 1000th member, C/2006 P7 (SOHO), was announced by ESA already on August 10, 2006. Although the family was first recognized by Heinrich Carl Friedrich Kreutz (1854–1907) in the nineteenth century (Kreutz 1888), most have been discovered in SOHO, Solar and Heliospheric Observatory (Domingo et al. 1995), coronographs, especially those on the Naval Research Laboratory’s LASCO, Large Angle and Spectrometric Coronagraph (Brueckner et al. 1995). A Kreutz-group, sun-grazing comet, SOHO-6 (C/1996 Y1), can be seen in Fig. 14.2, along with coronal streamers.

Three other sungrazing families, named for their discoverers, have been recognized in SOHO images: the *Meyer group* (named for Maik Meyer) with perihelia 0.03–0.04 au, the *Marsden group* (for Brian Marsden) with perihelia near 0.05 au, and the *Kracht group* (for Rainer Kracht), believed to be related to the Marsden group, with perihelia only slightly smaller than those of the Marsden group. The 2005 General Catalogue listed 59, 23, and 24 members, respectively, in these three groups, but all have grown greatly since then. At current writing, Meyer’s website, <http://www.comethunter.de/groups.html> lists 108, 34, 37, and 4 for the Meyer, Marsden, Kracht, and Kracht2 groups (the latter a possible new group), respectively. Altogether, to 2010, more than 2000 sun grazers had been detected.

Of the parabolic or near parabolic orbit comets in the General Catalogue (2005), about 200 had eccentricities greater than one, but only two of these had eccentricities greater than 1.01:

Comet Spacewatch (C/1997 P2), with $e = 1.028407$

Comet Bowell (C/1980 E1) with $e = 1.057322$

Both are in direct orbits with relatively small inclinations ($14^\circ 5$ and $1^\circ 7$), and with arguments of perihelia, $\omega = 25^\circ 4$ and $135^\circ 1$, respectively.

Plots of the cometary distribution against eccentricity and against inclination show the rarity of hyperbolic speeds. Therefore, these objects are bound to the solar system, i.e., they share the common motion of the Sun orbiting the galactic center. There are no comets known with $e \gg 1$, although some speculate that such highly eccentric comets may arise at a frequency as high as 1/century.

It is not difficult to see how a comet may acquire a parabolic or even mildly hyperbolic orbit, however: at great distances from the major planets, the net gravitational field felt by a comet is produced by the entire planetary system; as it approaches, it may be accelerated by local encounters, the effects of which may accumulate until the orbital speed equals or even slightly exceeds the solar escape velocity while in the inner solar system. This is a natural form of the slingshot-assists designed by space probe engineers. Most likely it will not escape from the solar system into the galaxy, but it is certainly possible. This possibility for our solar system suggests the possibility of (very rare) intrusions by extrasolar comets. Similarly, a comet may lose energy through encounters, and wind up in a tighter orbit, or enthrallled to a gas giant. We reconsider the origin of comets again in Sect. 14.7.

The techniques for computing cometary orbits are given by Danby (1988), Moulton (1914), Murray and Dermott (1999), among others. A particular concern for calculating orbits or ephemerides for many comets is the large eccentricity, which limits the methods that can be employed.

Comets have small masses, so their effects on planets are relatively minor, while the effects of the planets on comets are considerable. One may apply the equations of a restricted three-body system (defined in Milone and Wilson 2013, Sects. 3.3 and 3.6), in which a body of negligible mass (the comet) moves in the combined gravitational field of two massive bodies (Sun and planet) that follow circular orbits about each other, to explore this. Consider Fig. 14.3, after Danby (1988, Fig. 8.1), where $\mu = m_2$ and $1 - \mu = m_1$, in a new unit of mass such that $m_1 + m_2 = 1$, and with $m_1 > m_2$ so that $\mu < 0.5$.

Let the unit of distance be $x_2 - x_1$. The orbital motion of m_2 is equivalent to the rotation of this coordinate system's x -axis about the origin, O. The angular velocity of rotation, Ω , may be written (Danby 1988, p. 253; see also (3.7) and (3.10) of Milone and Wilson 2013, noting that, for a central force and circular orbits, there is no θ component and $r = \text{constant}$),

$$\Omega = \kappa \left\{ [(1 - \mu) + \mu]/[x_2 - x_1]^3 \right\}^{1/2} \quad (14.4)$$

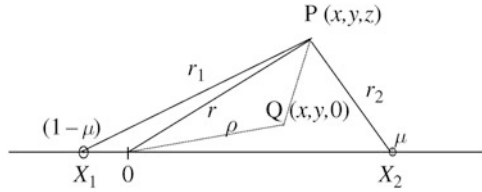


Fig. 14.3 A coordinate system rotating about O, the origin placed at the center of mass of two massive bodies, $\mu = m_2$ and $1 - \mu = m_1$. The y-axis is positive upward from the origin and in the plane of the page, the z-axis is positive out of the page; it is the rotation axis. In the restricted three-body system, m_1 and m_2 are massive bodies in circular orbits and the object at P has so negligible a mass, m , that it has no effect on the other two objects. Q is the projection of P onto the (x,y) plane, a distance ρ from the origin. Illustration adapted from Danby (1988, Fig. 8.1) with permission

where the constant $\kappa = \sqrt{G}$ includes units of time. Changing the time unit such that $\kappa = 1$ (and therefore $G = 1$) yields the result that $\Omega = 1$ (see Danby (1962, pp. 138–141; 1988, pp. 146–149).

The distance of m at P from the two finite masses is given by

$$r_1^2 = (x - x_1)^2 + (y - 0)^2 + (z - 0)^2$$

and

$$r_2^2 = (x - x_2)^2 + (y - 0)^2 + (z - 0)^2 \quad (14.5)$$

In this rotating system, the square of the speed, v' , of m at P is given by

$$v'^2 = \dot{x}^2 + \dot{y}^2 + \dot{z}^2 \quad (14.6)$$

Recall from (10.58) and (10.59), that the acceleration of the object at point Q in a rotating frame is

$$\mathbf{a} = \mathbf{a}' + \boldsymbol{\Omega} \times \mathbf{v}' + \boldsymbol{\Omega} \times (\mathbf{v}' + \boldsymbol{\Omega} \times \mathbf{r}) = \mathbf{a}' + 2\boldsymbol{\Omega} \times \mathbf{v}' + \boldsymbol{\Omega} \times (\boldsymbol{\Omega} \times \mathbf{r}) \quad (14.7)$$

where \mathbf{a} is acceleration and \mathbf{v} , velocity, and the primed and non-primed quantities relate to motion as seen in and outside the rotating frame, respectively. Also, from the exposition of the two-body solution in Milone and Wilson 2013, Sect. 3.1, the dot product of the velocity and the acceleration is

$$\mathbf{v} \cdot \mathbf{a} = -\mathbf{v} \cdot \mathbf{r}/r^3 = v_r/r^2 \quad (14.8)$$

where we have substituted \mathbf{v} for $d\mathbf{r}/dt$, \mathbf{a} for $d^2\mathbf{r}/dt^2$, and v_r for the radial component of velocity, dr/dt . Recall also that $m_1 + m_2 = 1$ and $G = 1$. In a rotating coordinate system (see Sect. 10.3.1), this becomes,

$$\mathbf{v} \cdot \mathbf{a} = \mathbf{v} \cdot [\mathbf{a}' + 2\boldsymbol{\Omega} \hat{\mathbf{z}} \times \mathbf{v}' - \boldsymbol{\Omega}^2 \mathbf{r}] = v_r/r^2 \quad (14.9)$$

From (3.16) of Milone and Wilson (2013), the two-body energy equation is

$$v^2 = (2/r) - h^2/r^2 + 2E \quad (14.10)$$

where E is the total energy, the sum of the kinetic and potential energy. This energy integral is modified in the rotating frame of the restricted three-body case to *Jacobi's integral* (Danby 1988, p. 254), namely,

$$v'^2 = x^2 + y^2 + 2(1 - \mu)/r_1 + 2\mu/r_2 - C \quad (14.11)$$

Note that $\Omega = \Omega \hat{\mathbf{z}} = \hat{\mathbf{z}}$ because $\Omega = 1$ here, so that the motion of m in the rotating reference frame is:

$$\mathbf{v}' \equiv d\mathbf{r}'/dt = (\mathbf{v} \equiv d\mathbf{r}/dt) - \hat{\mathbf{z}} \times \mathbf{r} \quad (14.12)$$

In Sect. 10.3.1, we assumed for exposition purposes that the point under consideration was in the plane of rotation. In fact, this is not essential, because $\mathbf{r} = \boldsymbol{\rho} + z\hat{\mathbf{z}}$ so that $\hat{\mathbf{z}} \times \mathbf{r} = \hat{\mathbf{z}} \times \boldsymbol{\rho}$. We find, after substituting this in (14.12), taking the self-product, and rearranging,

$$\begin{aligned} v'^2 &= v^2 - 2\mathbf{v} \cdot (\hat{\mathbf{z}} \times \boldsymbol{\rho}) + \rho^2 \\ &= v^2 - 2\mathbf{v} \cdot (\hat{\mathbf{z}} \times \mathbf{r}) + \rho^2 \\ &= v^2 - 2\hat{\mathbf{z}} \cdot (\mathbf{r} \times \mathbf{v}) + x^2 + y^2 \end{aligned} \quad (14.13)$$

With the last equation of (14.13), Jacobi's integral, (14.11), becomes:

$$v^2 - 2\hat{\mathbf{z}} \cdot (\mathbf{r} \times \mathbf{v}) = 2(1 - \mu)/r_1 + 2\mu/r_2 - C \quad (14.14)$$

after subtracting $x^2 + y^2$ from both sides. Suppose now that a comet is the object at P, the Sun is at x_1 , and a giant planet is at x_2 in Fig. 14.3. Jupiter is the most massive gas giant, so from Table 12.1, $\mu \lesssim 10^{-3}$. Given the position and velocity of the comet at any instant, some of the elements are readily determinable. From the vis-viva equation [Milone and Wilson 2013, (3.37)], we obtain the semi-major axis, a :

$$v^2 = 2/r - 1/a \quad (14.15)$$

From the dot product of the $\hat{\mathbf{z}}$ vector and the angular momentum, \mathbf{h} [see Milone and Wilson 2013, (3.11a)], actually the *specific angular momentum*—the angular momentum per unit mass, and from [Milone and Wilson 2013, (3.24)], we have:

$$\hat{\mathbf{z}} \cdot (\mathbf{r} \times \mathbf{v}) = \hat{\mathbf{z}} \cdot \mathbf{h} = [a(1 - e^2)]^{1/2} \cos i \quad (14.16)$$

where e and ι are the eccentricity and the inclination, respectively. These relationships may be useful in determining whether an observed comet has been observed in a previous apparition. Substitution of (14.15) and (14.16) into (14.14) yields the relation,

$$(1/a) + 2[a(1 - e^2)]^{1/2} \cos \iota = 2/r - 2(1 - \mu)/r_1 + 2\mu/r_2 + C \quad (14.17)$$

What is interesting about (14.17) is that even though the comet's orbital elements may have changed due to the perturbation of a giant planet, C is a constant. If we assume that $r = r_1$ and judge that μ is small enough to be ignorable, we may make the further simplification,

$$a^{-1} + 2[a(1 - e^2)]^{1/2} \cos \iota \approx C \quad (14.18)$$

Having computed C for a previous comet, we can test if a comet seen at another apparition is the same, by computing its C as well and comparing them. The criterion for identifying the similitude of the two comets, namely, the validity of the equality

$$a_1^{-1} + 2[a_1(1 - e_1^2)]^{1/2} \cos \iota_1 = a_2^{-1} + 2[a_2(1 - e_2^2)]^{1/2} \cos \iota_2 \quad (14.19)$$

is known as *Tisserand's criterion*, after the French celestial mechanician, François Félix Tisserand (1845–1896). Equation (14.18) or an equivalent expression, has been referred to as the *Tisserand invariant* or *Tisserand parameter*. More recently, additional uses have been found for this remarkable relation. It has been used to study the scattering of dust grains in various parts of the solar system (Gor'kavi et al. 1997), as well as to speed up the planning of space probe trajectories (Strange and Longuski 2002). The criterion has also been used to distinguish different groups of short-period comets (see Sect. 14.7).

From time to time, comets approaching a major planet are perturbed so badly that their orbital elements are greatly changed. Marsden (1963) investigated a number of these “lost” comets, and by integrating the orbits over time and taking into account the perturbations to which they were subjected during close approaches, was able to predict future apparitions. In this way, Comet 9P/Tempel 1 was recovered in 1972, and, on reexamination, was found as a very faint image on a plate taken by E. Roemer in June, 1967, as Marsden had predicted. It had librated about a 2:1 resonance with Jupiter after the major perturbations by Jupiter in 1941 and 1953.

Thanks to its recovery, 9P/Tempel 1 was the successfully targeted site of the “Deep Impact” mission in 2005; as a consequence it has become the best imaged comet, at least at high resolution, and one of the best studied to date (A'Hearn et al. 2005; Sunshine, et al. 2005).

14.4 Typical and Historically Important Comets

In addition to Halley's Comet and the historic comet of 1577 noted in Table 14.1, some others of historic interest are indicated below.

The shortest-period periodic comets with more than one appearance are:

- Comet 2P/Encke ($P = 3\text{y}3$), seen every revolution since 1822
- Comet 107P/Wilson–Harrington ($P = 4\text{y}30$), seen six times up to 1997
- Comet 26P/Grigg–Skjellerup ($P = 5\text{y}11$), seen 18 times up to 1997;
- Comet 79P/du Toit–Hartley ($P = 5\text{y}21$), seen three times up to 1997.

Other examples of short-period comets are:

- Comet 29P/Schwassmann–Wachmann 1 ($P = 14\text{y}9$), seen six times up to 1997
- Comet 55P/Temple–Tuttle ($P = 33\text{y}2$), seen five times since 1366
- Comet 95P/Chiron (=1977 UB) ($P = 50\text{y}7$), once classified as an asteroid (now classified a Centaur)—one that grew a tail!
- Comet 13P/Olbers ($P = 69\text{y}6$), seen in 1815, 1887, and 1956
- Comet 109P/Swift–Tuttle ($P = 135\text{y}$), seen five times since 69 BC (See Fig. 14.4)
- Comet 9P/Tempel 1 ($P = 5\text{y}50$), seen twice before it was lost in 1879, and continually since its 1967 recovery.

The orbital parameters of selected comets can be found in Table 14.1, excerpted from Marsden and Williams (2005).

The date of the last perihelion (to present writing) is indicated along with the other elements, presented here for representative purposes only. The earliest provisional designation is given when there are other names. The epoch for the elements (in the format: E:YYMMDD), also enclosed in parentheses but given only for some cases, is typically close to the time of perihelion passage, but usually not exactly on it. Subject to perturbations, small-mass bodies such as comets may undergo large changes in orbital elements, therefore for calculation purposes, the epoch to which the elements refer is an important datum. Other tabulated quantities are: the period, P , perihelion distance in astronomical units, q , argument of perihelion, ω , longitude of the ascending node, Ω , and the inclination, i . An inclination greater than 90° implies retrograde orbital motion (CW motion as view from above the North ecliptic pole). The elements are “osculating,” in the sense that they agree closely with (literally, “kiss”) the orbit near the epoch, but depart from the true elements with time due to the perturbations to which the comet is subjected. These perturbations may be non-gravitational as well as gravitational; we discuss them further in later sections.

A fuller discussion of cometary orbits and designations as well as references to data sources can be found in the latest edition of the Catalogue of Cometary Orbits (at current writing: Marsden and Williams, 17th edition, 2008; the Minor Planet Center, Smithsonian Astrophysical Observatory, Cambridge, MA.).

Aspects of some of the more recent developments in cometary dynamics can be found in Fernández (1999).

Table 14.1 Selected comets

Comet name (or other designation)	T_{per}	P_{sid} (y)	q (au)	e	i (deg)	Ω (deg)	ω (deg)
C/1577V1	1577.83	$>10^3$	0.178	1.0	104.8	31	256
3D/Biela ^a (1772 E1, 1832S1)	1832.62	6.65	0.879	0.751	13.2	251	222
6P/d'Arrest (1678 R1; E:02/02/15)	2002.60	6.53	1.353	0.613	19.5	140	177
2P/Encke ^b (1786 B1; E:03/12/27)	2004.00	3.30	0.338	0.847	11.8	335	186
21P/Giacobini–Zinner (1900 Y1; E:05/07/09)	2005.50	6.62	1.038	0.706	31.8	195	173
1P/Halley ^c (-239K1, E:86/02/19)	1986.11	76.0	0.587	0.967	162.2	59	112
C/Ikeya–Seki ^d (1965S1-A, -B)	1965.80	880.	0.008	1.000	141.9	347	69
C/1973 E1 ^e (Kohoutek; E:73/12/24)	1973.99	...	0.142	1.000	14.3	258	38
13P/Olbers (1815 E1, 1956 A1)	1956.46	69.6	1.179	0.930	44.6	86	65
12P/Pons–Brooks (1812 O1)	1954.39	70.9	0.774	0.955	74.2	256	199
29P/1902 E1	2004.52	14.7	5.724	0.044	9.4	312	49
(Schwassmann–Wachmann-1, 1927V1; E:41/07/04)							
D/Shoemaker–Levy ^f (1993F2-O)	1994.24	17.7	5.380	0.207	5.8	221	355
109P/Swift–Tuttle ^g (-68 Q1, 1992S2)	1992.95	135.	0.964	0.960	113.4	139	153
55P/Tempel–Tuttle (1366 U1, 1965 IV)	1998.16	33.2	0.977	0.906	162.4	235	172
C/Hale–Bopp (1995 O1) ^h	1997.25	$\geq 10^3$	0.914	0.995	89.4	282	131

^aDiscovered by M. Biela in 1826; later identified with comets of 1772 and 1806, it was seen again in 1832. John Herschel (1792–1871) saw it split in two in 1846; both parts returned in 1852 but not thereafter. A meteor stream occupies the orbit

^bMéchain made the first recorded observation in January, 1786. The comet was observed by Caroline Herschel in October, 1805. The first computed elements and prediction of return were by Johann Encke (1791–1865) for 1822. To 2003, there were 59 recorded appearances, the largest number of known appearances of any comet. It is not visible to the naked eye

^cThis is the oldest known extant periodic comet. There have been 30 recorded appearances: 240, 164, 87, and 12 BC, and AD 66, 141, 218, 295, 374, 451, 530, 607, 684, 760, 837, 912, 989, 1066, 1145, 1222, 1301, 1378, 1456, 1531, 1607, 1682, 1759, 1835, 1910, and 1986. This is probably the comet depicted in the Bayeaux tapestry and is the most likely model for the comet in Giotto's *Adoration of the Magi*

^dA long “short-period” comet. The eccentricity is slightly smaller than 1.000, but is rounded off

^eAn alleged “virgin comet,” its early brightness far from the Sun led some to predict that it would be one of the brightest comets ever seen. Its subsequent dimness suggests that its likely origin was in the Kuiper Belt, not in the Oort Cloud, as initially supposed, so that its material had been reprocessed to some degree. C/1973 E1 was studied from SkyLab. Its eccentricity was computed to be 1.000008

^fThis comet was independently discovered by three groups on photographic images in 1993; it was captured by Jupiter after tidal interaction probably in July 1992 into a satellite orbit; the interaction broke up the comet into 21 major fragments which collided with Jupiter in July, 1994. This comet was not visible to the naked eye, but is historically important as an example of the explosive effects of such collisions. The elements of Marsden (1993) are given for nucleus 7 = segment Q

^gThere have been five recorded appearances: 69 BC, and AD 188, 1737, 1862, and 1992 (see Fig. 14.4)

^hSee Fig. 14.5

Fig. 14.4 Comet 109P/Swift–Tuttle as imaged by John Mirtle, November 14, 1992. This was only the fifth apparition at which this comet has been observed in recorded history



Fig. 14.5 C/1995 O1 (Hale–Bopp) as it appeared on April 1, 1997. Note the two types of tails: a thick amorphous dust tail and a blue (in Ektachrome photography) ion tail. Image by John Mirtle

1P/Halley is the best-known and one of the best-studied comets. At its last apparition, there were 7469 astrometric observations alone made of it. It is one of two extant, bright, short-period comets (the other being Comet 109P/Swift–Tuttle), and its apparitions have had impacts on human history. Mark Twain said that he came in with it and would go out with it; he did. The earliest firm date we have for a perihelion passage is 239 BC; the 30 known returns with their apparition designations are listed in Table 14.2.

Table 14.2 Comet 1P/Halley perihelion passages

Date		Designation	Associated event
240 BC	Mar. 25	1P/-239K1	
164	Nov. 13	1P/-163 U1	
87	Aug. 06	1P/-86 Q1	
12	Oct. 11	1P/-11 Q1	Candidate for Star of Bethlehem
66 AD	Jan. 26	1P/66 B1	
141	Mar. 22	1P/141F1	
218	May 18	1P/218H1	
295	Apr. 20	1P/295J1	
374	Feb. 16	1P/374 E1	
451	Jun. 28	1P/451L1	
530	Sep. 27	1P/530 Q1	
607	Mar. 15	1P/607H1	
684	Oct. 03	1P/684 R1	Depicted in Nuremberg Chronicles
760	May 21	1P/760K1	
837	Feb. 28	1P/837F1	
912	Jul. 19	1P/912J1	
989	Sep. 06	1P/989N1	
1066	Mar. 21	1P/1066G1	Woven into the Bayeux Tapestry
1145	Apr. 19	1P/1145G1	
1222	Sep. 29	1P/1222 R1	
1301	Oct. 26	1P/1301 R1	Possibly depicted by Giotto in the <i>Adoration of the Magi</i>
1378	Nov. 11	1P/1378S1	
1456	Jun. 10	1P/1456K1	Size measured by Toscanelli; distance sought by Purbach
1531	Aug. 26	1P/1531 P1	Depiction by Apian
1607	Oct. 28	1P/1607S1	Studied by Kepler
1682	Sep. 15	1P/1682 Q1	
1759	Mar. 13	1P/1758 Y1	Predicted by Halley
1835	Nov. 16	1P/1835 P1	Birth of Mark Twain (Samuel Clemens)
1910	Apr. 20	1P/1909 R1	Mark Twain's death
1986	Feb. 09	1P/1982 U1	

14.5 Cometary Structure

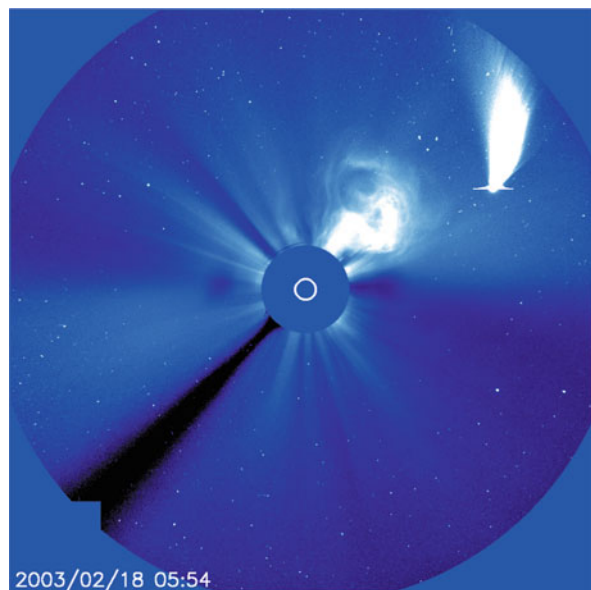
Far from the Sun, the comet shines by light reflected from the comet surface, later (when the comet is closer to the Sun) to be known as the *nucleus*. The observed brightness thus depends both on solar and terrestrial distances:

$$\ell \propto \left(\frac{1}{r_{\oplus}^2}\right) \left(\frac{1}{r_{\odot}^2}\right) \quad (14.20)$$

As it gets closer to the Sun, however, the equation changes to:

$$\ell \propto \left(\frac{1}{r_{\oplus}^2}\right) \left(\frac{1}{r_{\odot}^n}\right) \quad (14.21)$$

Fig. 14.6 Comet NEAT (C/2002 V1), a long-period (37,000 year) comet with $q = 0.10$ au (near the upper right). A large coronal mass ejection is also visible, traveling outward from the Sun toward the comet. It missed! Credit: SOHO/LASCO (ESA & NASA)



where $n \approx 4.2 \pm 1.5$, and is variable both from comet to comet and over time for the same comet.

As it approaches the Sun, the nucleus is warmed by the Sun. Local, sub-solar heating warms the ices and causes sublimation. The gases may explosively escape from warm pockets, bringing out dust with them.

The dust is acted upon by sunlight and may be driven away by radiation pressure. A repulsive force $2\text{--}3\times$ gravity will drive out the dust; a broad, curved tail will result from the net accelerations on each dust particle as it travels away from the moving nucleus.

The solar UV and x-ray photons ionize the liberated gas molecules and the solar wind then drives the ions away at higher speeds than the photons drive away the dust. A repulsive force $20\text{--}30\times$ gravity causes a fast ejection and a straight tail.

Consequently, the basic components of comets near perihelion are:

- *Nucleus* of dust and ices, $\sim 0.2\text{--}100\text{: km}$ (where the colons imply uncertainty) in diameter. The nucleus of Comet 19P/Tempel 1 was found to have a mean radius of 3.0 ± 0.1 km. The largest comet observed to have entered the inner solar system, Comet Hale-Bopp (C/1995 O1), had a mean radius of 37 ± 3 km (Szabó et al. 2012).
- *Coma* of evaporated gases and dust, typically $\sim 10^4\text{--}10^5$ km diameter
- *Hydrogen envelope*, typically $\sim 10^7$ km across
- *Dust and ion tails*, typically 10^8 km in length near perihelion

Figure 14.6 from the LASCO instrument aboard SOHO illustrates the appearance of a comet at perihelion.

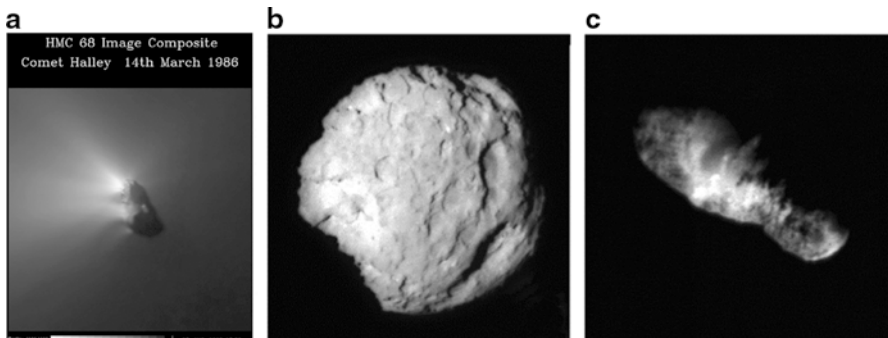


Fig. 14.7 Images of comets. (a) 1P/Halley from the *Giotto* Mission. Its size is $\sim 15 \times 7 \times 7$ km. Credit: ESA/MPS; (b) 81P/Wild 2, ~ 5 km across, imaged by the *Stardust* Mission spacecraft Navigation Camera on January 2, 2004. Image PIA06285, courtesy of NASA/JPL-Caltech; (c) 19P/Borrelly, 8-km-long, imaged at a distance of 3417 km, during the *Deep Space 1* mission. Image PIA03500, courtesy of NASA/JPL. See also Fig. 14.12

The maximum size of a comet nucleus is unknown at present. If the icy bodies beyond the orbit of Neptune and those that have migrated inward turn out to have the same composition and structure (see below), the limit may be of order 10^3 km. The *coma* is a parabolic envelope of dust particles; in fact a series of overlapping comae (or comas) are expected for particles of different sizes, the smallest being closest to the nucleus; closest of all is the icy halo of ~ 10 km separation from the nucleus, and the most extensive dust halo reaching to 10^4 km or more (Brandt and Chapman 1981, pp. 137–143).

The hydrogen envelope or corona contains the shock front (magnetopause) separating the solar wind and the cometary magnetosphere, typically at $\sim 10^6$ km from the nucleus. The presence of such a cloud was predicted by Biermann (1968).

Far from the Sun, the comet presents a heavily cratered, non-spherical surface with ice and dust. We discuss cometary composition in the next section, but thanks to the imagery provided by space missions, we have a good idea of the appearance of a few comets. Figure 14.7 shows several of them.

14.6 Cometary Composition

Comets have been observed since the 1910 perihelion passage of Halley to exhibit spectral emission of hydrocarbons and their radicals, especially CN and C₂. The classic model for a cometary nucleus was suggested by Fred L. Whipple: the “dirty iceball.” The model explains several properties of comets:

- Asteroidal appearance at large solar distances
- Extensive gas production near the Sun
- Dust tail development with approach to the Sun

Photochemistry of the subliming gases can occur immediately or in transit as the molecules and dust separate from the nucleus and enter first the coma and then the tail. The density appears high enough near the nucleus to involve chemical reactions.

Seven different comets have now been visited by a total of eight spacecraft:

1P/Halley	Suisei; Giotto; Vega 1; Vega 2 (all in 1986)
9P/Tempel 1	Deep Impact (2005); Stardust NExT (2011)
19P/Borelly	Deep Space 1 (2001)
21P/Giacobini-Zinner	ICE (1985)
26P/Grigg-Skjellerup	Giotto (1992)
81P/Wild 2	Stardust (2004)
103P/Hartley	EPOXI (Deep Impact extended mission) (2010)

ESA's *Rosetta* mission, launched in 2004, is currently *en route* to 67P/Churyumov-Gerasimenko, with arrival planned for mid-2014 while the comet is far enough from the Sun to not yet be active. It will then spend about a year accompanying the comet through perihelion and back out toward Jupiter. Part way through the encounter, it will send a lander, *Philae*, to the comet's surface.

All of the above comets except Halley are Jupiter family comets and are believed to have originated in the Edgeworth-Kuiper Belt (cf Sect. 15.7.2); Halley is the prototype for the Halley group of comets, which are believed to originate from the Oort cloud (see Sect. 14.7 for a discussion of comet families and groups).

Stardust dropped off samples of cometary dust from 81P/Wild 2 (pronounced "Vilt-Two") as it passed the Earth in 2006, and then continued on to comet 9P/Tempel 1. The *Deep Impact* spacecraft released a 370-kg copper projectile that collided with 9P/Tempel 1, creating a plume of ejecta that was studied by the spacecraft and from Earth.

The masses and mean densities of comets are very difficult to determine because no comet has yet been found to have a satellite, and the gravitational acceleration felt by passing spacecraft has been too minute to measure. The best available method to find the mass, other than sending a spacecraft, is to estimate the non-gravitational force (Newton's 3rd law reaction force) on the comet by the jets of escaping material, integrated over the period of activity each time the comet approaches and recedes from the Sun, and to measure the resulting acceleration of the nucleus from the changes in the comet's orbit, such as the change in perihelion date. If the volume can also be measured then the density can be calculated.

The mean densities obtained for eight comets are in the range of 100 kg m^{-3} (2P/Encke) to 700 kg m^{-3} (1P/Halley) (Table 1 of A'Hearn 2011). However, see Peale (1989) for a discussion of the potentially large uncertainties inherent in this method. Taken at face value, these densities indicate a high degree of porosity; indeed, from the characteristics of the ejecta plume when the Deep Impact projectile struck 9P/Tempel 1, the surface materials of the comet appear to have

Table 14.3 Comets' hydrocarbons composition relative to water ice^a

Comet	CO	CH ₃ OH	CH ₄	C ₂ H ₆	C ₂ H ₂	HCN
C/Hyakutake ^b	14.9 ± 1.9	1.7–2.0	0.70 ± 0.08	0.62 ± 0.07	0.16 ± 0.08	0.18 ± 0.04
Hale-Bopp ^b	12.4 ± 0.4	2.1	1.45 ± 0.16	0.56 ± 0.07	0.16 ± 0.08	0.18 ± 0.04
Ikeya-Zhang ^b	4.7 ± 0.8	2.5 ± 0.5	0.51 ± 0.06	0.62 ± 0.13	0.18 ± 0.05	0.18 ± 0.05
1P/Halley ^b	3.5	1.7 ± 0.4	<1	0.4	0.3	0.2
Lee ^b	1.8 ± 0.2	2.1 ± 0.5	1.45 ± 0.18	0.67 ± 0.07	0.27 ± 0.03	0.29 ± 0.02
C/1999 S4	0.9 ± 0.3	<0.15	0.18 ± 0.06	0.11 ± 0.02	<0.12	0.10 ± 0.03
Tempel 1 ^{b,c}	...	1.3 ± 0.2	...	0.19 ± 0.04	...	0.18 ± 0.06
Tempel 1 ^{b,d}	4.3 ± 1.2	1.0 ± 0.2	0.54 ± 0.30	0.19 ± 0.04	0.13 ± 0.04	0.21 ± 0.03

^aWater ice abundance = 100^bSee Figs. 14.8, 14.5, 14.10, 14.1 and 14.7, 14.9, and 14.12, resp., for images of these comets^cPre-impact values only; comet showed slight activity level prior to impact^dPost-impact values only; rapid fall-off in intensity of lines implies no ongoing jet**Fig. 14.8** C/1996 B2 (Hyakutake). Note the disconnects in the ion tail, indicative of the effects of the solar wind plasma on the ionized particles created by photolysis in sunlight. Photo by John Mirtle, March 24, 1996

a density and strength similar to dry, lightly-packed mountain snow (Richardson and Melosh 2013). The resulting bulk density of 9P/Tempel 1 is 400^{+600}_{-200} kg m⁻³ (Richardson et al 2007).

More than 20 primary molecules (i.e., molecular species present as ices in the comet) have been identified in spectra of the coma, both from spacecraft and from ground-based and Earth-orbiting observatories. The most abundant of these molecules is H₂O. The relative abundances of the others, measured relative to water, vary from one comet to another. Those reaching abundances of 1 % or higher relative to water, with their observed ranges, are, from Fig. 4 of Mumma and Charnley (2011),



Fig. 14.9 Comet C/1999H1 (Lee). Note the sharp “beak,” or spiky sunward ion tail. This particular “antitail” is probably not an optical illusion, produced solely by geometric projection, but is seen sometimes in first-time (sometimes referred to as “virgin”) comets, that alone may have the icy volatiles in sufficient amount and location necessary to produce sizable and rapid ejection responses to sunlight. Perhaps a slow rotation aids the effect. Such a prominent antitail was seen also in C/1956 R1 (Arend–Roland) in 1957. Image obtained by John Mirtle, August 11, 1999



Fig. 14.10 Comet 153P/Ikeya–Zhang. Note the tight region of streamers feeding the ion tail, but contained within the broad dust tail. This would seem to present difficulties for the theory that the solar wind sweeps around the head of the comet to produce the ion tail and constrain the streamers. Photo by John Mirtle. See also the photo of Comet 23P/Brorsen–Metcalf, Figure 14.11, where the streamers extend out to a considerable distance from the nucleus



Fig. 14.11 Comet 23P/Brorsen–Metcalfe. Note the clean features of the ion tail, indicating smooth flow from the solar wind during the time interval of propagation of the ion tail components. Photography by John Mirtle

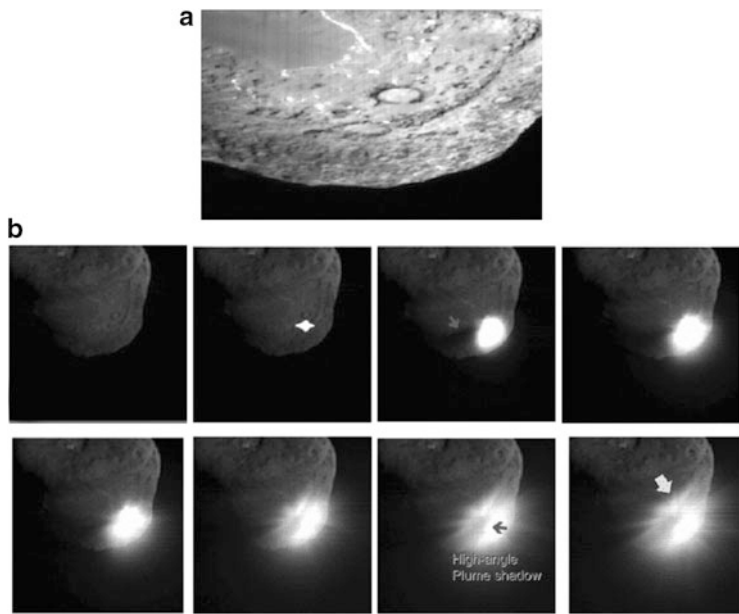


Fig. 14.12 9P/Tempel 1, from the *Deep Impact* mission. (a) Pre-impact image showing not only heavily cratered areas but also smooth areas and scarps, as bright icy areas gleam in sunlight. NASA/JPL-CalTech/Univ. of Maryland image PIA02135 (b) The impact, rays, spreading fireball, shadows. Credits: NASA/JPL-CalTech/U of Md., M. F. A'Hearn et al. (2005)

H ₂ O	100 %
CO ₂	3–30 %
CO	0.4–20 %
CH ₄	0.2–2 %
C ₂ H ₆	0.1–2 %
CH ₃ OH	0.2–6 %
H ₂ CO	0.1–1 %
NH ₃	0.2–1 %
H ₂ S	0.1–1 %

These are the abundances measured in the coma and can include both primary and product molecules (those produced by chemical reactions in the inner coma); CO and H₂CO are particularly notable in this respect. Other primary molecules with maximum abundances $\geq 0.1\%$ are C₂H₂, HOCH₂CH₂OH, HCOOH, HCN, HNCO, OCS, SO₂ and S₂; and with maximum abundances $\geq 0.01\%$, HCOOCH₃, CH₃CHO, NH₂CHO, HNC (predominantly a product species), CH₃CN, HC₃N and H₂S.

The measured abundances of hydrocarbons in Halley and other recent comets are shown in Table 14.3, taken from Mumma et al. (2005). Relative abundances for carbon monoxide (CO), methanol (CH₃OH), methane (CH₄), ethane (C₂H₆), acetylene (C₂H₂), and hydrogen cyanide (HCN) are shown. Some data are rounded off. The authors note that for 9P/Tempel 1, the number of molecules of water increased after the impact by about a factor of 2 (Fig. 14.12b).

Chemical processing occurs in the coma. Daughter species found there include: CO, CN, C₂, C₃, CH, NH, NH₂, OH, O, C, and CS.

The most abundant ionized primary molecule in the inner coma is H₂O⁺, but this reacts quickly with H₂O to produce H₃O⁺, so H₃O⁺ is the most abundant ion in the inner corona out to $\sim 3 \times 10^4$ km from the nucleus. Beyond this distance, the most abundant molecule is O⁺. The ion tail shows features of: H₂O⁺, CO⁺, N₂⁺, CH⁺, CO₂⁺, and OH⁺.

The relative mix of these gases differs from that in the interstellar medium, indicating that some processing has occurred.

The element composition in 1P/Halley, as given in Taylor (1992, Table 3.10.2), shows that, compared to the Sun, Halley is strongly depleted in H; slightly enriched in C, O, Na, Si, S, Ti, and Co; slightly deficient in Al, K, Cr, Mn, Fe, and Ni; and about the same in N, Mg, and Ca.

In 1P/Halley, it was observed that different vents showed different rates of NH₃ and H₂CO relative to H₂O venting. Similar effects have been seen in other comets. This implies a heterogeneous structure.

Although volatiles had been observed previously, the actual detection of water ice *on the surface* through reflectance spectroscopy of a comet was first achieved by the Deep Impact mission on 9P/Tempel 1 (Sunshine et al. 2005).

Various processes which can affect the nucleus are:

- Impacts, which heat, cause “farming”, ejection of matter and secondary cratering
- Micrometeorites, which add to the regolith
- Irradiation of the crust by cosmic rays
- Solar heating, usually ineffective at aphelia, where most of the time is spent

These processes can lead to several conditions on the nucleus:

- Refractory veneer on the crust
- Hydration reactions
- Loss of volatiles through “volcanoes”
- Formation of organic compounds
- Shock effects

During its flyby of 1P/Halley, the Vega spacecraft measured the dust properties: No calcium-aluminum-rich inclusions (CAI), the presence of which is characteristic of carbonaceous chondrites (a type of undifferentiated meteorites—see Sect. 15.2.2), were seen. The dust had three main components (Grün and Jessberger 1990):

1. CHON particles (for the elements that dominate)
2. Silicate particles
3. mixtures of the two, similar to carbonaceous chondrites but enriched in CHON elements

The net results indicate a resemblance to Brownlee particles, captured by high-altitude aircraft.

The overall composition resembles CI-type meteorites (Flynn 2002); the ices in particular could be primordial, but the Fe/Si and Mg/Si ratios are the lowest in the solar system. If CO is a true parent molecule in 1P/Halley, as it has now been seen to be in other comets, then the nucleus must have a temperature ~ 25 K when unheated. For 1P/Halley and other comets, the carbon isotopes ratio, $^{12}\text{C}/^{13}\text{C} \approx 90$ (Wyckoff et al. 2000), although individual grains vary from 1 to 5000! This compares to ~ 89 for the solar system and 72–94 for the interstellar medium at 10 kpc from the galactic center (Milam et al. 2006).

The impact of the Deep Impact mission’s 370 kg space probe on the nucleus of Comet Tempel 1 (A’Hearn et al. 2005) caused a clear increase in the brightness of the comet that was noted by ground-based observers. The resulting dust cloud was observed at the Frederick C. Gillette (Gemini North) Telescope by Harker et al. (2005). In infrared spectra between 8 and 13 μm they observed in the ejecta a broad silicate emission feature which they attributed to amorphous pyroxene, amorphous olivine, and magnesium-rich crystalline olivine. They also saw features of amorphous carbon grains. The addition of orthopyroxene to their model did not improve their fitting. Modeling the rate of cooling and flux dispersal, they estimated that 10^4 – 10^5 kg of dust had been ejected; none had been observed prior to impact. Sugita et al. (2005) came to a similar conclusion about silicate grains from data taken with the Subaru telescope. Figure 14.12 shows the comet and the fireball created by the impact.

Silicates were the most abundant component of the dust in the Deep Impact ejecta plume, based on the IR spectrum obtained by the Spitzer Space Telescope. Minerals identified by numerical modeling of the spectrum include (Lisse et al. 2007; see Milone and Wilson 2013 Chap. 7 for a discussion of the mineralogy of olivines and pyroxenes):

- Olivine $[(\text{Mg},\text{Fe})_2\text{SiO}_4]$: This was the most abundant silicate. The dominant form of olivine in the dust was Mg-rich forsterite, which crystallizes from

amorphous olivine (also present, with about half the abundance of forsterite by mole) at \sim 1,100 K. Fe-rich fayalite, which crystallizes from amorphous olivine at \sim 1,400 K, is also present, with about $\frac{1}{4}$ of the abundance of forsterite by mole. \sim 72 % of the olivine is crystalline. Temperatures this high require formation in the inner solar system.

- Pyroxene $[(\text{Mg},\text{Fe})\text{SiO}_3]$: \sim 2/3 of the abundance of olivine by mole. The majority of the pyroxene is Fe-rich ferrosilite, with >90 % of the pyroxene crystalline. This large a crystal fraction is consistent with the lower temperature (800–900 K) required for pyroxene to crystallize, compared to olivine.
- Clays: \sim 3 % of the silicates by mole were phyllosilicates in the form of the iron-rich, sodium-bearing smectite,¹ nontronite $[\text{Na}_{0.33}\text{Fe}_2(\text{Si},\text{Al})_4\text{O}_{10}(\text{OH})_2 \cdot 3 \text{H}_2\text{O}]$. Nontronite is interesting because its formation normally requires abundant liquid water in the region of the solar nebula where it formed or in the parent body of the comet. It is also the only major source found for the sodium in the comet's tail. The Na atoms would be released from the nontronite by dehydration and UV processing.
- Carbonates: Similar in abundance to the nontronite, and probably composed of magnesite (magnesium carbonate, MgCO_3) and siderite (iron carbonate, FeCO_3). Liquid water had been thought to be required for carbonates also, but recent work suggests that it can form from water vapor in the presence of CO_2 gas and silicates.

Small quantities of polycyclic aromatic hydrocarbons (PAHs) were also detected. PAHs consist of a repeating hexagon structure of C and H atoms; e.g., $\text{C}_{14}\text{H}_{10}$ (anthracene). At least one sulfide may be present, but was unconfirmed in 2006.

The ratio of gas to dust varies from comet to comet, with some comets having very little dust (see, for example, Fig. 14.13). However, IR measurements seem to suggest greater uniformity than do those made in the visible part of the spectrum. The $\text{CO}/\text{H}_2\text{O}$ ratio varies as well, so that the prominent CO^+ ion tail seen in comets C/1961 R1 (Humason) and C/1908 R1 (Morehouse) is weak in other comets.

In most comets, the emission features of C_2 and C_3 are 20–50 % stronger than those of CN but in some comets they are deficient by up to a factor 20. Finally, oxides tend to be more abundant in comets other than those in the short-period comet group. The greater oxide composition is closer to interstellar values and suggests that the comets in a disk near the ecliptic plane were formed in a more chemically reducing environment. As we discuss in the next section, kinematic evidence, too, points to a different place of origin for the longer period comets compared to the short-period variety. Once near the Sun, photolytic reactions can produce the observed species. The chemical reactions in comets are reviewed by Colangeli et al. (2004).

Extreme UV emissions from sun-grazing comets are now routinely observable thanks to the AIA, *Atmosphere Imaging Assembly*, on the *Solar Dynamics Observatory* (Bryans and Pesnell 2012). The sequence and duration of stages of ionization of oxygen (at least from stages III through VI) can be studied.

¹ Phyllosilicates are silicate minerals characterized by sheets of silicate tetrahedra and/or octahedra. Smectite is a family of phyllosilicate clay minerals characterized by repeating layers in which a single octahedral sheet is sandwiched between two tetrahedral sheets.

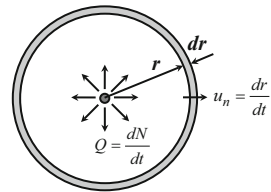
Fig. 14.13 C/2004 Q2 (Machholz), with sharply defined streamers but very faint dust tail at 5 o'clock, obscured by twilight. The Pleiades star cluster is in the upper left. Photo by John Mirtle



14.7 Induced Magnetospheres of Comets

The primary molecules are ejected from the nucleus by sublimation at a speed of $\approx 1 \text{ km/s}$, and the escape speed from a typical comet nucleus is only ~ 1 to a few m/s, so both the neutral primary molecules and their neutral chemical products stream freely outward through the coma at $\approx 1 \text{ km/s}$. If the number of such particles produced by the nucleus over a time, t , is N , then we can write the production rate as $Q = dN/dt$. If we consider an arbitrary spherical shell of thickness dr and volume $dV = 4\pi r^2 dr$ centered on the nucleus (Fig. 14.14), then in the absence of ionization all of these neutrals would pass through this shell in a time dt with speed $u_n = dr/dt$. Again in the absence of ionization, given a spherically-symmetric, steady-state flow, the number density, $n(r)$, of neutrals in the shell as a function of distance, r , from the nucleus would be

Fig. 14.14 Neutral atoms and molecules streaming outward at speed u_n from a comet nucleus (small circle at center) at a rate, Q (atoms or molecules per second). These particles pass through shells of thickness dr at distances, r , from the nucleus



$$n_n(r) = \frac{dN}{dV} = \frac{Qdt}{4\pi r^2 dr} = \frac{Q}{4\pi u_n} \frac{1}{r^2} \quad (14.22)$$

Ionization, however, decreases the number of neutrals at a constant fraction per unit time as seen by an observer moving with the flow. This behavior is mathematically similar to radioactive decay, so ionization (by itself) produces an exponential decrease of n_n with time and therefore with distance from the nucleus. This introduces a factor $\exp(-t/\tau_n) = \exp(-r/[u_n \tau_n]) = \exp(-r/\lambda_n)$ into (14.22), where we have used $t = r/u_n$. Here, τ_n is the mean lifetime against ionization and λ_n is a characteristic distance equal to the e-folding distance in n_n for parallel flow (i.e., in the absence of inverse-square decrease). Then for a spherically-symmetric, steady-state outflow with ionization,

$$n_n = \frac{Q}{4\pi u_n} \frac{1}{r^2} \exp(-r/\lambda_n) \quad (14.23)$$

$\tau_n \approx 10^6$ s when the comet is 1 au from the Sun, so the mean distance that a neutral particle moves from the comet before being ionized is $\lambda_n = u_n \tau_n \approx 10^6$ km (Cravens and Gombosi 2004). As a result, the neutral gas coma extends to large distances from the nucleus.

The primary ionization mechanism for cometary neutrals is photoionization by solar radiation. By the list in Sect. 14.6, this produces large numbers of heavy ions. In addition, although charge transfer collisions of solar wind protons with cometary neutrals are of much lesser importance and do not increase the number of ions, they do increase the number of heavy ions. All of these ions are picked up by the interplanetary magnetic field (IMF), which is being carried outwards from the Sun by the solar wind at speeds of ~ 400 km/s. The IMF upstream (sunward) from the nucleus is slowed by this mass-loading and also by the pressure of the thermalized ions, creating a bow shock measured by spacecraft flybys at 4×10^5 km subsolar distance from Halley's nucleus, and $\sim 10^4$ km for less active comets such as Giacobini-Zinner or Grigg-Skjellerup. Halley's bow shock was clearly-defined, with $\Delta r/r \sim 10^{-2}$, where Δr is the shock width and r is its distance from the nucleus. In the case of less active comets such as Giacobini-Zinner and Grigg-Skjellerup, $\Delta r/r \sim 1$, making the interaction more equivalent to a bow wave than a bow shock.

The interplanetary field lines continue to slow past the bow shock and pile up on the sunward side of the nucleus, while their sideward extensions continue past and drape around the nucleus, creating an induced magnetosphere and magnetotail. Ions being carried down the magnetotail by the IMF streaming past the nucleus are visible from the Earth as the ion tail, or plasma tail, of the comet. These tails sometimes stretch for great distances: the *Ulysses* spacecraft passed through the tail of the long-period comet Hyakutake at a distance of 3.8 au from the nucleus, and detected heavy cometary ions and parallel magnetic field lines directed away from the comet, as expected of a comet tail.

The ion tail is occasionally seen to disconnect from the comet and stream off in the anti-sunward direction, while a new tail soon forms. The most popular model for these disconnection events is magnetic reconnection across the magnetotail, with the open field line carrying the plasma down the tail while magnetic tension causes the newly-closed field line to snap back toward the comet.

At the bow shock the IMF is still dominated by solar wind ions, but closer to the nucleus the cometary pick-up ions outnumber the solar wind ions. The point where the two contributions are equal is referred to as the *cometopause*; thus, the cometopause is a compositional boundary, inside which the IMF is dominated by cometary ions. In the case of Halley, the *Giotto* spacecraft found the cometopause at $1\text{--}2 \times 10^5$ km (subsolunar distance) from the nucleus (Fig. 5 of Cravens and Gombosi 2004).

Giotto also found a diamagnetic (field-free) cavity surrounding the nucleus, with the boundary on the sunward side \sim 5,000 km from the nucleus. This boundary is created by friction resulting from momentum-transfer collisions between the outwardly-moving neutrals and the inwardly-moving ions (Cravens and Gombosi 2004). Outside this cavity, the inwardly-transported ions stagnate before slipping past the comet outside the cavity boundary. The diamagnetic cavity is expected to be smaller for less active comets, but no spacecraft has passed close enough to any comet except Halley to detect it. The structure of the stagnation region and diamagnetic cavity for these comets is thus as yet unknown.

The induced magnetospheres of comets resemble that of Venus (Sect. 11.7.2) in many ways, but also differ in fundamental ways. Taking Halley's comet as an example, its bow shock during the 1986 flybys was at a subsolar distance $\sim 4 \times 10^5$ km, or $\sim 10^5$ times the radius of the nucleus, compared to only $\sim 9,000$ km ($1.5 R_{\text{Venus}}$) from the centre of Venus. The reason for this immense difference in size is Venus' much greater escape speed. Venus retains its neutrals as an atmosphere, so the ionization occurs close to the planet, whereas Halley's neutrals stream freely away from the nucleus and the mass-loading occurs at many times 10^5 km distance. The cometopause also forms by a different mechanism from an ionopause: the cometopause is formed by inwardly-streaming cometary ions being brought to rest (in the radial sense) by momentum transfer from outwardly-streaming neutrals, whereas Venus' ionopause is formed where the magnetic pressure of the IMF, carried by inwardly-streaming solar wind ions, equals the thermal pressure of planetary ions already present in Venus' ionosphere.

14.8 Origins of Comets

14.8.1 Formation of the Nucleus

The high porosity of comets, the ease with which they can be disrupted by internal gas pressure and tidal effects from planets, the indications noted above of heterogeneous composition, and the large size range of nuclei from a few km to \sim 160 km (95P/Chiron) suggest that the formation of comets began with the accretion of dust grains to form *cometesimals* which then collided to form the parent bodies of today's comets. Different models for the formation process have been developed (see, e.g., Skorov and Blum 2012). The basic ideas are as follows.

The dust grains in comets formed at temperatures as high as 1,400 K in the inner solar nebula, as noted above. Ice grains, however, must have formed beyond the *snow line* (aka *frost line* or *ice line*, \sim 5 au) where temperatures are low enough (less than \sim 150 K) that water, ammonia, and methane can condense as ices. The grains in each of these two regions collided and stuck together to form aggregates over timescales of the order of 10^3 – 10^4 years, with the refractory dust aggregates being transported beyond the snow line. The size of an aggregate is limited first by bouncing, where, after aggregates reach a certain size they bounce off each other rather than sticking, and then (at larger sizes) by collisional fragmentation. The resulting sizes are believed to have been from \sim 0.1 mm to \sim 1 m. Gravitational attraction between the silicate and ice aggregates in regions as far out as 30 au and beyond then led to the formation of cometesimals and, through collisions of cometesimals, the parent bodies of comet nuclei.

14.8.2 Origin of the Present Distribution of Comets

If comets were truly interstellar in origin, at very large distances they would have positive velocities relative to the Sun, and as a consequence, would appear to have strongly hyperbolic paths. This not being the case, an overwhelming majority appear to be bona fide members of the solar system.

The number of comets in the direction of the apex of the Sun's motion² is approximately the same as from other directions; therefore, there is little evidence that any significant number of these comets has come from outside the solar system. The perturbations on comets by the giant planets, and especially Neptune, suffice to increase the speeds at which some comets approach the inner solar system so that they appear to have just slightly more energy than 0.

² Sometimes called the *solar apex*, the direction in space toward which the Sun is moving with respect to the motions of nearby stars; it is roughly at $\alpha = 18^\text{h}$ and $\delta = 30^\circ$; see Milone and Wilson 2013, Sect. 4.2.

The distribution of the inclinations of the comets with parabolic and nearly parabolic orbits shows them to be roughly isotropically distributed. Thus, they probably originate in a spherical or spheroidal region around the Sun. This region is called the *Oort cloud*, after the astronomer who first suggested it, Jan Oort (1900–1992). If there were a cloud of comets at $\sim 10^5$ au from the Sun, to satisfy the observed frequency of comets in the inner solar system, $\sim 10/\text{y}$, from the ratio of the order of the angular size of the solar system to that of the entire sphere (4π), the probability of a comet moving toward the inner solar system is

$$\Omega/(4\pi) \approx 10/N \quad (14.24)$$

where Ω is the solid angle taken up by the planetary orbits, say a region 10 au across, and N is the total number of comets in the cloud. For a comet coming from high-ecliptic latitudes, then, the chance is

$$\Omega/(4\pi) \approx (10/10^5)^2 = 10^{-8}$$

so that, if all comets had the same probability, the population of the Oort cloud would be $N \approx 10^9$. However, the probability depends also on the ecliptic latitude, so that in the ecliptic plane, the inner solar system presents a very narrow target region and the probability is much less, perhaps $\leq 10^{-9}$.

Estimates of comet numbers in the Oort cloud have been as high as $\sim 10^{12}$, and its radius is estimated at $\sim 40,000$ au.

Stagg and Bailey (1989) argued for the existence of the original, large-scale Oort cloud alone for cometary origin, albeit one with some central concentration; Bailey and Stagg (1990), and other work, suggested three sources of comets:

1. The outer Oort cloud, $2-5 \times 10^4$ au, spherical, $1-2 \times 10^{12}$ comets
2. The inner Oort cloud, $2-20 \times 10^3$ au, flattened, $2 \times 10^{12}-10^{13}$ comets
3. The Edgeworth-Kuiper Belt (or Cloud), 30–50 au, highly flattened, with mostly low-eccentricity, low-inclination orbits

The orbital properties of the short-period comets suggest, in fact, two groups of these comets: those with periods less than 20 year and with prograde orbits that lie as close to the ecliptic plane as the asteroids, and a smaller group with higher inclinations and often retrograde orbits, and periods that may be less than 20 years, but as great as 200 years. Most of the former have been referred to as *Jupiter-family* comets. The latter, sometimes called the *Halley group*, have been thought to be from the Oort cloud but the Jupiter family originating from the *Edgeworth–Kuiper Belt* (referred to also as the *Kuiper–Edgeworth*, or simply the *Kuiper Belt*), or possibly from an inner Oort cloud, if it exists. Recent work suggests that the direct source of the Jupiter-family comets and maybe a significant fraction of the Halley group also is the *scattered disk*, a population of higher-eccentricity, higher-inclination objects, fed by migrants from both the classical Edgeworth–Kuiper Belt and from the Uranus–Neptune region. The dwarf planet Eris is thought to be a member of this scattered population of icy objects.

Fernández (1999, pp. 550–551) shows that the *Tisserand invariant*, T , [written as one side of (14.17), but with a substitution involving the perihelion distance $q = a(1 - e)$] can be used to distinguish the Jupiter-family (with $\sim 2 < T < 3.0$) comets from the one-pass comets (sometimes called “non-periodic” or “long-period” comets) and Halley group comets ($T < 2$). This, Fernández argues, makes the Oort cloud a less likely site of origin for the short-period comets. Note, though, that the Tisserand criterion and “invariant,” as useful as they are, can only be approximate. The solar system, after all, is an n -body system, and the restricted three-body condition (Sun–Jupiter–comet) is approximate only.

A body of what were formerly considered to be asteroids, the *Centaurs*, has been found at distances of ≥ 10 au. It has been conjectured that they are “escaped” members of the Edgeworth–Kuiper Belt, a collection of objects with semi-major axes extending over a range of several tens of aus. Although these objects will be discussed in more detail in Chap. 15, we note here that there are a few hundred of these objects known thus far.

Identified as an “asteroid–comet transition object,” and by some as a Centaur despite its small q value, 944 *Hidalgo* has a reflectance spectrum described as that of a “dead comet” (Beatty and Chaikin 1990, p. 196). It has a mean distance, $a = 5.85$ au, eccentricity, $e = 0.655$, and inclination to the ecliptic plane, $i = 42^\circ 36'$, and thus moves between the orbits of Mars and Saturn. It appears to be an object that has migrated inward.

The first Centaur recognized as such is (2060) *Chiron*, designated 95P/1977 UB following the detection of a persistent coma and sometimes tail from this object by Meech and Belton (1990). Chiron has orbital elements: $a \approx 13.6$ au, $e = 0.38$, and $i = 6^\circ 95'$. This orbit ranges from within that of Saturn to nearly the orbit of Uranus, and is subject to chaotic variation. From the duration of an occultation of a star, this object appears to have a diameter ~ 160 km or more. The most recent determination, 216 ± 10 km with a Bond albedo of $16 \pm 3\%$, is based on Spitzer Space Telescope and Herschel Space Observatory data (Fornasier et al. 2012). The Centaur (10199) Chariklo was determined to be even larger ($\sim 240 \pm 7$ km) and darker ($\sim 3.5 \pm 1\%$) by the same group. Compared with recent work on the nucleus of the “giant” comet C/1995 O1 (Hale-Bopp): diameter 74 ± 6 km, $A = 8 \pm 1$ km (Szabo et al. 2012) or 94 ± 15 km, $A = 5.5 \pm 2\%$ (Kidger et al. 2012), these Centaurs, at least, are the largest comet-like or “active icy” objects studied to date.

Cruikshank et al. (1998) obtained reflectance spectra between 0.4 and 2.4 μm of the Centaur (5145) *Pholus* that revealed a surface much more characteristic of comets than of asteroids, with water vapor absorption bands (1.5 and 2.1 μm), and possibly one due to methanol, CH_3OH ; the spectrum was modeled with two types of terrain: amorphous carbon (carbon black) covering $\sim 62 \pm 5\%$ of the surface; and a second type (over 38 % of the surface) made up of 55 % olivine, 15 % water ice, 15 % methanol, and 15 % organic solids (tholins). They did not achieve better fitting with NH_3 included. The investigators suggest that the active components in the model are principal constituents of a comet nucleus and that Pholus is basically a comet that has never been active.

Such research provides the critical clues needed to understand the outer solar system. It reveals clearly that comets are icy bodies with insufficient gravity to retain their volatiles as the latter sublime when in close proximity to the Sun. Therefore, the dividing line between a comet and some similarly constructed icy object may be decided by its escape velocity and its perihelion distance.

We have traced the origin of comets to the Oort cloud and to the Edgeworth–Kuiper Belt, but we have not discussed how comets get to the planets’ orbital region, other than through random motion.

Perturbations by passing stars or by tidal effects of the galaxy or of interactions with massive gas/dust clouds have been suggested as triggers for comets in the Oort cloud itself. The probability discussion about how often a perturbed comet will enter the realm of the major planets still holds. The existence of a spherical region has itself been argued to have developed as a result of randomizing perturbations by passing stars (Fernández 1999, p. 555), or gas/dust clouds.

For objects in the Edgeworth–Kuiper Belt, simulations suggest that if they come closer than \sim 40 au, they will be perturbed into chaotic behavior and will eventually migrate through the zones of the major planets into that of Jupiter, thus accounting for the Jupiter family of short-period comets. The origin of the scattered population we will take up in Chap. 15.

Finally, “Main Belt Comets” have been discovered among the asteroids between Mars and Jupiter (Sect. 15.7.3). P/2013 P5 produced six dust tails, possibly spun off from the equator by the object’s high rotational speed, aided by its low gravitational attraction (Jewitt et al. 2013).

14.9 Cometary Demise

Comets are indeed delicate. The Minor Planet Center in a recent posting lists 23 that were observed to have split and 21 that have faded out or disintegrated completely since 1975 alone. Boehnhardt (2004) provides a list and suggests that multiple splittings may evolve into families of comets, citing the Kreutz sun-grazing comets as examples, although most such fragments have short lives. His Fig. 2 suggests that very few survive more than 1,000 days.

The mechanism of splitting is likely tidal action. D/Shoemaker–Levy 9 disintegrated following a close approach to Jupiter, was perturbed into a Jovian orbit, and eventually all 21 fragments collided with Jupiter. 73P/Schwassmann–Wachmann 3 started to break up 16 days before its 1995 perihelion passage, accompanied by strong OH emission, increased dust ejecta, and a brightness increase of four magnitudes (Sekanina 2005). On the same pass, it fragmented further. An infrared mosaic (Fig. 14.15) from the Spitzer Space Telescope obtained during the 2006 apparition shows 45 of the 65 or more fragments and a long dust trail connecting them. In July 2012, LASCO–SOHO observers reported two potential comet fragments close to Comet Machholz (Fig. 14.13) according to K. Battam of NRL (http://sungrazer.nrl.navy.mil/index.php?p=news/machholz_babies).

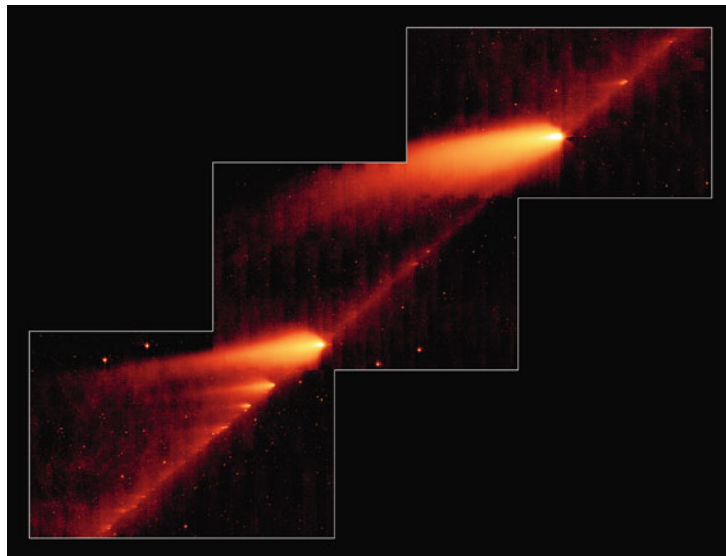


Fig. 14.15 An infrared false-color mosaic of 44 fragments (of at least 65 components known at that time) and sun-warmed IR-emitting dust of P73/Schwassmann–Wachmann 3 on May 4–6, near its 2006 perihelion passage, as viewed from the Spitzer Space Telescope. Altogether, 45 fragments are visible in this image. Credits: W. T. Reach/Caltech/JPL/NASA. Image PIA08452. Courtesy, William T. Reach

A comet loses mass every time it rounds perihelion, hence it has a finite lifetime when near the Sun. The attrition rate depends critically on the perihelion distance and on the period. A typical comet with perihelion distance, $q \gtrsim 0.6$ au has sufficient material for $\sim 10^3$ perihelion passes. In the case of Halley's Comet, for example, the ESA spacecraft *Giotto* measured emission indicating a gas loss rate of ~ 20 t/s and a dust loss rate of 3–10 t/s. Therefore, in 100 days centered on perihelion, 1.8×10^8 t of gas and $\sim 4 \times 10^7$ t of dust are lost. The mass of the comet from perturbations on the spacecraft was determined as 10^{11} t. Thus, we see that

$$\tau \approx 10^{11} / 2 \times 10^8 = 500 \text{ passes},$$

reasonably close to prediction.

The dust material becomes entrapped in planetary gravitational fields or orbits the Sun until it is either driven out into the solar system or spirals into the Sun. Large clouds of very fine dust were seen in the vicinity of Halley during its 1986 perihelion passage. This dust moves in associated orbits with the comet and spreads out along the orbit with time. The ascending and descending nodes of the comet thus become the intersections of the Earth with the cometary debris.

We next discuss the dust and occasionally clumps of material entering the atmosphere, in the form of cometary debris, viz., meteor showers; then we discuss meteors generally, and, finally, micrometeorites in the upper atmosphere of Earth.

14.10 Meteor Showers

Although at least one of what we currently call “meteor showers” had been known for centuries if not for millennia, the scientific establishment was slow to appreciate them. “The tears of St. Lawrence,” who was martyred in Rome on Aug. 10, 258, were not recognized to be meteors falling on his name day, until after the Perseids were rediscovered in the mid-19th century. A delightful account of modern astronomy’s rediscoveries of meteor showers can be found in Littmann (2005), at <http://www.skyandtelescope.com/observing/objects/meteors/3304116.html?page=1&c=y>.

Meteor showers today are named for a star or region of the sky from which they appear to radiate: the *radiant*. The radiant arises because, as the particles approach the Earth, they are traveling in roughly parallel paths similar to that of the comet from which they originated. Just as two rails on a long, straight section of railroad track appear to converge on (or radiate from) a single point on the horizon, the meteors appear to radiate from a single point on the sky. Figure 14.16 illustrates the effect.

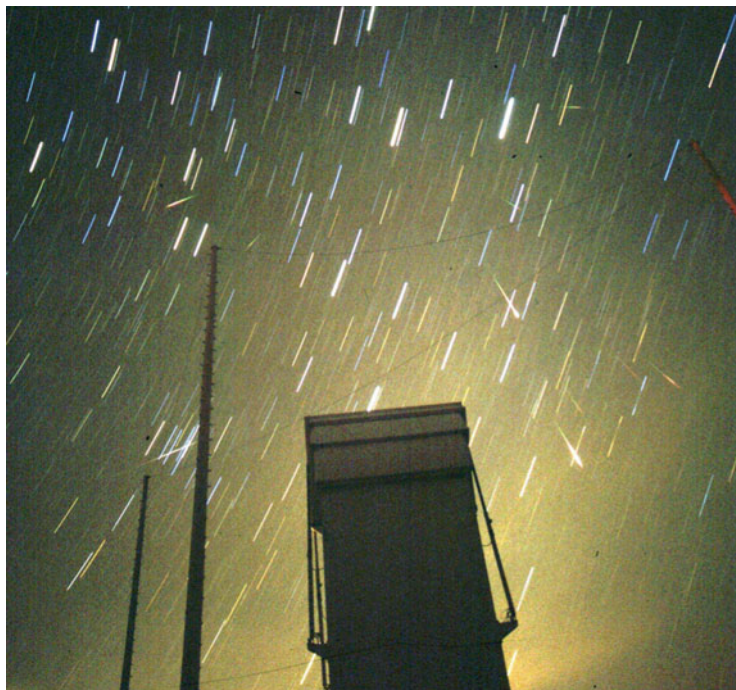


Fig. 14.16 Leonid meteors can be seen in this untracked photograph of the northern sky taken by Dr. W. Livingstone on November 18, 2001. The arcs are concave toward the north celestial pole and the ratio of their length to that of the full minor circles is the fraction of the sidereal day of the exposure. Finally the radiant of the shower can be traced. Courtesy, Dr. William Livingstone, Tucson, Arizona

Table 14.4 Selected meteor showers

Name	UT date	Δt	Radiant (2000)	Associated comet or asteroid
Quadrantids ^a	Jan. 4.0	1 ^d	15 ^h 30 ^m	+51°
Lyrids ^b	Apr. 23.7	3	18 16	+35
η Aquarids ^c	May. 5.4	10	22 27	+00
S δ Aquarids	Jul. 29.2	12	22 36	-17
N δ Aquarids	Aug. 12	5	21 24	-05
Perseids ^d	Aug. 12.9	20	03 04	+58
Draconids	Oct. 10	1	17 40	+54
Orionids ^e	Oct. 22.5	7	06 20	+15
S Taurids	Nov. 3.5	30	03 32	+14
N Taurids	Nov. 13.5	30	03 55	+23
Leonids ^f	Nov. 18.0	6	10 08	+22
Andromedids ^g	Nov. 20	21	00 52	+55
Geminids ^h	Dec. 14.8	8	07 32	+32
Ursids	Dec. 23.0	5	14 28	+76
				8P/Tuttle

^aFrom an old constellation named *Quadrans muralis*; the radiant is in Bootes. Typical modern rate: ~80/h

^bThe last major shower was in 1803; Chinese records list showers on March 23, 687 BC (“stars flew”) and March 26 15 BC (“stars fell like a shower”); a Korean record lists an April 3, 1136 shower. Typical modern rate: 15/h

^cThe earliest of five possible showers in Chinese records occurred on April 8, 401. Typical modern rate: 60/h

^dMany records of Perseids are found in Asian sources. The earliest firm identification is that of a shower on July 17, 36 AD (“more than 100 small stars flew”). Typical modern rate: 95/h. A Perseid candidate can be seen in Fig. 14.17

^eWidely variable in rates from year to year (~4×). Chinese records indicate major displays on September 23, 585 AD (“many stars chased each other”), September 25, 930, and several dates in the fifteenth, and one in the seventeenth century. Typical modern rate: 30/h

^fThe period of comet 1866 I = Tempel-Tuttle was 33^y176. Every 33y, with some disappointments, e.g., in 1933, Leonids have been impressive, as in 1966. Chinese, Korean, and Japanese annals record many such displays starting on October 15/16, 931 AD. Several orbit clumpings allow for showers in adjacent years also. The Leonids can be seen in Fig. 14.16

^gAlso called the *Bielids*. *Meteor storms* were seen in 1872 and 1885 with rates ~75,000 m/h. Little activity has been seen since, but the nodes of the orbit undergo rapid regression

^h3200 Phaethon is, at least at present, considered an asteroid. Typical modern rate for the Geminids: ~90/h.

In addition to these well-known showers, others include: the γ Delphinids, α Hydrids, Coma Berenicids, κ Serpentids, α Centaurids, γ Normids, π Puppids, Piscis Austrinids, α Capricornids, and the Puppid/Velids. Many more meteor showers have been found in recent years; see Jenniskens (2012) who discusses these new showers, the techniques used to discover them, and maps. See Jenniskens (2008) for a comprehensive treatment of the entire topic

A list of prominent meteor showers can be found in Table 14.4, mostly taken from Table 5.8 of Kelley and Milone (2011). For the most part, these showers represent the interaction between cometary dust tails and the Earth. Occasionally, larger fragments, resulting in *bolides* (bright, often exploding, meteors—see Sect. 14.11) are visible. For more observational detail, consult Kronk (1988).



Fig. 14.17 A possible sporadic meteor or outlying Perseid meteor (*upper right*) is captured in this image of the northern Milky Way on August 9, 2013, 11:11 pm, MDT taken by Dr. T. A. Clark from Eastend, Saskatchewan, looking NE, approximately centered upon the border region of Cassiopeia and Cepheus. The “W” asterism in Cassiopeia is visible just below the image center. Courtesy, Dr. T. A. Clark

14.11 Individual Meteors

14.11.1 Basic Meteor Phenomena and Circumstances

The term *meteor* derives from the Greek, *μετέορος*, *meteoron*, “thing of the air.” It is a luminous phenomenon, an incandescence caused primarily by ram-pressure heating of an object as it traverses the upper atmosphere. Ram pressure is the pressure exerted on a fast-moving object by the air it compresses in front of it. In the case of a meteor, the extremely rapid compression heats the air, and part of this heat is transferred to the object itself. Prior to entry, i.e., in space, the object is called a *meteoroid*.

The estimated frequency of meteors is $\sim 8 \times 10^9$ /day of which 25×10^6 are bright enough to be seen. The conditions for visibility are:

- A distance from the observer of less than ~ 200 km
- Altitude 80–95 km (only the brightest last long enough to be seen at elevations lower than 80 km)

The very brightest are called *bolides* or *fireballs*, which occur at a rate of 10^4 – 10^5 /day. These meteors sometimes explode in the air and can be heard.

One estimate of the total meteoric mass accumulated by the Earth in one day is 10^3 t (Dubin 1955).

There are two types of meteors:

1. *Sporadic meteors*—meteors from objects on individual orbits
2. *Shower meteors*—meteors from swarms of objects, mostly comet debris, appearing from distinct *radians* in the sky.

Spectra indicate that 99 % of the light is from gases glowing at temperatures $\sim 10^3$ K. The species seen are: Ca II, Fe II, Al, N, Na, Mg, Mn, Si, and H.

14.11.2 Meteor Heating and Incandescence

The visibility of the meteor as it moves through the atmosphere indicates that its kinetic energy is partly converted into radiant energy. The underlying principles and some of the data can be found in Hawkins (1964) and in the papers presented by Kaiser (1955). More recent treatments of the ablation process are given by Caplecha et al. (2000) for large meteoroids, Campbell-Brown and Koschny (2004) for small, and Schaefer and Fegley Jr. (2004) for application of an equilibrium vaporization model to the ablation of the chemical components of stony meteorites. Here, we develop some of the principles from basic physics.

The meteoroid is modeled as a sphere of mass m , radius R , and cross-section $A = \pi R^2$, traveling at speed v through air of density ρ_{air} . In time Δt it travels a distance $\Delta l = v\Delta t$, and encounters air of volume $V_{\text{air}} = A\Delta l$ and mass $m_{\text{air}} = \rho_{\text{air}} V_{\text{air}}$. In the upper part of the trail most of the air flows freely around the meteoroid and is pushed sideways to roughly speed v by the passage of the meteoroid. Lower in the trail, where the air is denser, most of the air in volume V_{air} is swept up and compressed into a cap, a *bow shock*, traveling at the same speed as the meteoroid. The process reaches a quasi-steady state where the rate of new air being swept up equals the rate of old air streaming off the side (quasi-steady because the air density increases with time as the meteoroid descends through the atmosphere).

We now derive equations for the drag force on the meteoroid, its acceleration, and its rate of mass loss by ablation. The work-kinetic energy theorem states that the work, W , done on any object by all forces acting on it equals the change in its kinetic energy, K . Then, treating the air as the system and the meteoroid as an external agent doing work on the system, we have

$$\frac{W_{\text{air}}}{\Delta t} = \frac{\Delta K_{\text{air}}}{\Delta t} \quad \text{or} \quad \frac{dW_{\text{air}}}{dt} = \frac{dK_{\text{air}}}{dt} \quad (14.25)$$

where the first of equations (14.25) equates the average rate at which work, W_{air} , is done on the air by the meteoroid over any time interval Δt to the average rate of change of kinetic energy of the air over the same time interval, and the second equates the instantaneous rate at which the meteoroid does work on the air at time t to the derivative of the kinetic energy at that instant. W_{air} and dW_{air} are macroscopic and microscopic *amounts* of work done, whereas ΔK_{air} and dK_{air} are macroscopic and microscopic *changes* in kinetic energy.

Because the process is quasi-steady state, $\Delta K_{\text{air}}/\Delta t$ and dK_{air}/dt are essentially equal. Then if the meteoroid accelerates all of the air in volume V_{air} from $v_0 = 0$ to $v_f = v$ in time Δt , the rate of change of the kinetic energy of the air is

$$\frac{dK_{\text{air}}}{dt} = \frac{\Delta K_{\text{air}}}{\Delta t} = \frac{\frac{1}{2} m_{\text{air}} v^2 - 0}{\Delta t} = \frac{\frac{1}{2} \rho_{\text{air}} A \Delta \ell v^2}{\Delta t} = \frac{1}{2} \pi R^2 \rho_{\text{air}} v^3 \quad (14.26)$$

where A and $\Delta \ell$ are defined above.

The meteoroid does work W_{air} on the air and, conversely, the air does work W_m on the meteoroid. We can postulate that these quantities may be equal, or they may not be equal (a postulate that seems unassailable!). Then the two quantities are related by

$$\frac{dW_m}{dt} = \Gamma \frac{dW_{\text{air}}}{dt} \quad (14.27)$$

where at this point Γ is simply the appropriate ratio of one to the other.

The work done on the meteoroid by the air may be regarded as being caused by a *drag force*, F_d , exerted on the meteoroid by the air. Then the rate at which the air does work on the meteoroid equals the power, P_d , delivered to the meteoroid by the drag force. Power is force times velocity, so

$$\frac{dW_m}{dt} = P_d = F_d v. \quad (14.28)$$

Substituting (14.28), (14.25), and (14.26) into (14.27), we obtain the drag force equation,

$$F_d = \frac{1}{2} \Gamma \pi R^2 \rho_{\text{air}} v^2. \quad (14.29)$$

Thus, Γ is the *drag coefficient*, not be confused with the lapse rate of Sects. 10.2.2 and 10.4.1.1. From (14.27) and Newton's third law, one might expect that in many circumstances $\Gamma = 1$. This is the case where the air flows freely around the meteoroid in the upper part of its trail. The *Knudsen number*, K , defined as the ratio of the mean free path of the meteoroid to its radius, R , is >10 in this *free molecular flow* regime. Lower in the atmosphere, following a transition region where $0.01 < K < 10$, a cap of air (*shock*) forms over the oncoming face of the meteoroid, Γ decreases to 0.5, and $K < 0.01$. This is the *continuous flow* regime. Peak brightness occurs at intermediate values of Γ .

We may obtain the *drag equation* giving the acceleration of a meteoroid of mass m from (14.29) by applying Newton's second law, $F_d = m dv/dt$, and replacing m by $(4/3)\pi r^3 \rho_m$, where ρ_m is the meteoroid's density:

$$\frac{dv}{dt} = \frac{3\Gamma \rho_{\text{air}} v^2}{8R\rho_m} \quad (14.30)$$

Some fraction, Λ , of the work that the air does on the meteoroid enters the meteoroid as heat, Q , and causes ablation through melting and vaporization. Then, from (14.27),

$$\frac{dQ}{dt} = \Lambda \frac{dW_m}{dt} = \Lambda \Gamma \frac{dW_{\text{air}}}{dt} \quad (14.31)$$

Define $L = \text{heat of ablation}$, the amount of heat required to ablate a unit mass of meteoroid, measured from the undisturbed (interplanetary) state of the material. For silicate rock $L = 8 \times 10^{10} \text{ erg/g} = 8 \times 10^6 \text{ J/kg}$. Then

$$\frac{dQ}{dt} = L \frac{dm}{dt} \quad (14.32)$$

Using (14.25), (14.26), and (14.32) in (14.31), we obtain the *ablation equation*,

$$L \frac{dm}{dt} = \frac{1}{2} \Lambda \Gamma \pi R^2 \rho_{\text{air}} v^3. \quad (14.33)$$

The meteor emits light as a result of ablation, excitation and ionization of its atoms by collisions with air molecules, as suggested by Levin (1955),

$$I = \frac{1}{2} (dm/dt) v^2 \tau \quad (14.34)$$

where I is the luminous energy radiated per second, and the *luminous efficiency*, the fraction of energy of the vapor trail atoms that goes into radiation is

$$\tau \approx 2.0 \times 10^{-10} v \quad (14.35)$$

where v is expressed in cm/s or $2.0 \times 10^{-5} v$ when v is in km/s. Speeds of meteors vary from ~ 12 km/s for “slow” meteors to ~ 72 km/s for “fast” ones. Consequently, $\tau \approx 2.4 \times 10^{-4}$ for $v \approx 12$ km/s, and $\tau \approx 1.4 \times 10^{-3}$ for $v \approx 72$ km/s. Brown et al. (2002) cite values of $\sim 3\%$ for photographic measurements of fireballs but note that this is expected to vary not only with v but also with mass, path entry angle, shape, composition, and porosity, thus differing from bolide to bolide. The ablation rate is

$$dm/dt = (4/9) (m/H) v \cos z \quad (14.36)$$

where the scale height $H = kT/(\mu g)$ is assumed to be $6.5 \times 10^5 \text{ cm} = 6.5 \text{ km}$ [see (10.25)], μ is the mass of an air molecule—see (10.4), g is the gravitational acceleration, and z is the path angle from vertical. This value for H is consistent with $\mu = 28.8$, $g = 9.55 \text{ m}^2/\text{s}$, and $T \approx 215 \text{ K}$, at an altitude of 85–90 km.

Hawkins (1964, p. 7) related the intensity to the visual magnitude through the expression:

$$V \approx 24.3 - 2.5 \log I \quad (14.37)$$

where the constant presumably includes a correction from bolometric (i.e., across all wavelengths) to visual brightness and I is in units of erg/s. A distance of 100 km from the observer is assumed.

The meteor may be detected by radar. Its visibility at radio wavelengths depends on the number of ions produced. Suppose the evaporation rate of the meteoric atoms can be written as

$$\langle m \rangle^{-1} dm/dt \quad (14.38)$$

where $m = \sum \mu m_u$, is the sum of the masses of all atoms of various atomic weights in the meteor, so that $\langle m \rangle$ is the mean mass of the atoms of the meteor. Then the rate of ionizations (the number of ions produced per second) is, very approximately,:

$$N_i = (\beta / \langle m \rangle) dm/dt \quad (14.39)$$

where β is the probability of ionization, which, in turn, depends on the velocity:

$$\beta \approx 2.0 \times 10^{-26} v^{3.4} \quad (14.40)$$

where again v is expressed in cm/s. For “slow” meteors, $\beta \approx 10^{-5}$ and for “fast” meteors, $\beta \approx 4 \times 10^{-3}$.

The number of electrons produced per unit length is then approximated by:

$$N_q = (1/v) N_i \quad (14.41)$$

The relative energy that goes into ionization, light, and heat has been estimated to be 1:10:10⁵ for “slow” meteors, and 5:10²:10⁵ for “fast” meteors, respectively Hawkins (1964, p. 19).

The brightness, I , varies with time, producing the meteor’s light curve. For bright meteors, I depends very much on the air density. If $\rho_{I_{\max}}$ is the atmospheric density at which the meteor achieves maximum brightness, and with an assumed exponential decrease of ρ with height (Hawkins, p. 20), then the brightness at any other air density is:

$$I = (9/4) I_{\max} (\rho / \rho_{I_{\max}}) \left\{ 1 - [\rho / (3\rho_{I_{\max}})]^2 \right\} \quad (14.42)$$

However, faint meteors do not follow this prescription as closely. Flare-ups are seen in the light curves. Disintegration into fragments may be responsible. Break-up pressure is about 2×10^4 dynes/cm² = 2,000 N/m².

Given n fragments of a total mass of m and radius R , each fragment will have average mass m/n and radius $r \approx R/n^{1/3}$. In this case, the drag equation (14.30) becomes

$$\frac{dv}{dt} = \frac{3\Gamma \rho_{\text{air}} v^2 n^{1/3}}{8R\rho_m} \quad (14.43)$$

For the fragmented case, the vaporization rate, (14.33), becomes, for each fragment:

$$L \left(\frac{dm}{dt} \right)_i = \frac{1}{2} \Lambda \Gamma \pi \rho_{\text{air}} r_i^2 v_i^3 \quad (14.44)$$

and for all n fragments:

$$L \frac{dm}{dt} = \frac{1}{2} \Lambda \Gamma \pi \rho_{\text{air}} R^2 v^3 n^{1/3} \quad (14.45)$$

where we have simplified the term $nR^2 n^{-2/3}$.

This means that a fragmented meteor decelerates more quickly and evaporates faster than an unfragmented meteor, resulting in an initial burst of light, followed by fading, higher in the atmosphere.

The brightness of a meteor also depends on the angle, z , at which it descends. Substitution of (14.34)–(14.36) into (14.37) shows the explicit dependence. The V magnitude then becomes

$$V = 24.3 - 2.5 \log(6.8 \times 10^{-17} m v^4 \cos z) \quad (14.46)$$

With $m = 1$ g, speed $v = 30$ km/s = 3×10^6 cm/s, and with $z = 45^\circ$, $V = +0.3$. At $v = 72$ km/s, the brightness increases to -3.5 , brighter than all the objects in the sky but the Sun, Moon, and sometimes Venus.

The length and duration of a meteor depend on its speed. Hawkins estimated the height range (we will call it Δh) over which a meteor can stay visible (brighter than $V = +5$, say) as 35 km; hence the path length will be given by

$$\Delta \ell = \Delta h / \cos z = 35 \sec z \text{ km} \quad (14.47)$$

The duration of visibility, Δt , then becomes,

$$\Delta t = \Delta \ell / v = 35 \sec z / v \quad (14.48)$$

Therefore, a meteor with $v = 30$ km/s, $z = 45^\circ$, and peak magnitude $V \approx 0$ will remain visible ($V \lesssim 5$) over a path range of $\Delta \ell = 49$ km, and will be seen for $\Delta t \approx 1.6$ s.

Shower meteors greatly increase in number for an interval of time when the Earth intersects the orbit of the debris; sporadic meteors show a more gradual variation, involving time of day and year, and location on the Earth. The number of meteors brighter than ~ 0 magnitude decreases with increasing brightness. Hawkins (1964, p. 10) cited data from the American Meteor Society of the average influx rates of very bright meteors. See Fig. 14.18 for the daily rate of *bolides* aka *fireballs*, meteors at least as bright as the brightest planet, so brighter than $V \approx -5$, visible at nearly any time of day.

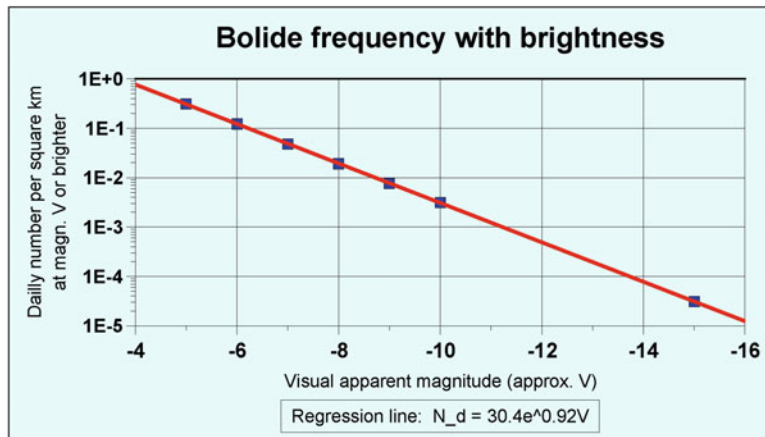


Fig. 14.18 Bolide frequency. The daily number of bolides per square kilometer at visual magnitude (effectively) V , or brighter. Data from the American Meteor Society cited by Hawkins (1964), and transformed and plotted by E.F. Milone

N_d is the number per day, per square kilometer of meteors brighter than or equal to magnitude V . A meteor of -15 magnitude would be $10 \times$ brighter than the full moon, but a meteor this bright or brighter over a square kilometer occurs only once per 32,000 days, or once in ~ 88 years, effectively once in a lifetime. However, the number of people consciously aware of such events has been increasing, so the older frequencies may be underestimates. (See, e.g., <http://www.amsmeteors.org/wp-content/uploads/2013/03/AMS-Fireball-Stats.pdf>)

Hawkins also gave the distribution of all meteors with photographic and visual magnitudes brighter than m_p and m_v , respectively [where $m_p \approx B - 0.11$, $m_v \approx V$ (Allen 1973, p203)]. The compilation is for meteors that are at or brighter than the naked eye limit, $\sim +5$. He summarized the data in the following relations, where N_h is expressed in numbers per km^2 per hour:

$$\begin{aligned}\log N_h &= 0.538m_p - 4.34 \\ \log N_h &= 0.538m_v - 5.17\end{aligned}\quad (14.49)$$

Brown et al. (2002) have made use of much more data to find the frequency of impactors per unit of total and optical energy estimates, the latter based on optical data, assumed temperature of 6000 K, and a luminous efficiency of 10 %.

For bolides, we may use the precise expressions of Brown et al. (2002), given in terms of energies and meteoroid diameters:

$$\begin{aligned}\log N_E &= a - b \log E \\ \log N_D &= c - d \log D\end{aligned}\quad (14.50)$$

where N_E is the annual cumulated total of objects with energy $\geq E$, N_D is that for objects of diameter $\geq D$, and for energies expressed in kilotons ($1 \text{ kt} = 4.185 \times 10^{12} \text{ J}$) and D

is meters, $a = 0.568(15)$, $b = 0.90(3)$, $c = 1.57(3)$, and $d = 2.70(8)$ where the uncertainties are in units of the last decimal place.

Although the basic approach has proven very useful, the physics is still not fully understood. A comparison by Campbell-Brown et al. (2013) of observed meteors with predictions of two current ablation models shows similarly satisfactory fittings for wide-field camera light curves, but, they note, fail to fit the meteor wakes' brightness profiles observed in the narrow-field camera light curves.

14.12 Micrometeorites

These are mainly spheroidal particles with diameters between 25 and 500 μm (Rietmeijer 2002). From data obtained from the Long Duration Exposure Facility satellite, an estimated $4 \pm 2 \times 10^4$ metric tons of micrometeoroids are encountered by the Earth each year (Hutchison 2004, p. 3). The rates of accretion are:

$$\begin{aligned} 1 \text{ m}^{-2}\text{d}^{-1} &\text{ for } 10 \text{ }\mu\text{m-sized particles} \\ 1 \text{ m}^{-2}\text{year}^{-1} &\text{ for } 100 \text{ }\mu\text{m-sized particles} \end{aligned}$$

Brownlee particles are scooped up by stratospheric collectors aboard aircraft or high-altitude balloons. They are of two types:

1. CP (for chondritic porous). These have:

- Mixed composition
- Resemblance to chondrules of chondrite meteorites (possibly a chondrule precursor)
- Mainly pyroxene composition
- Metal deficiency

2. CS (for chondritic smooth). These have:

- Resemblance to CI meteorite matrix
- Clusters of $0.3 \mu\text{m}$ spheres
- Hydrated silicates
- Probable origin in CI, CM-type meteorites (see Sect. 15.2.2).

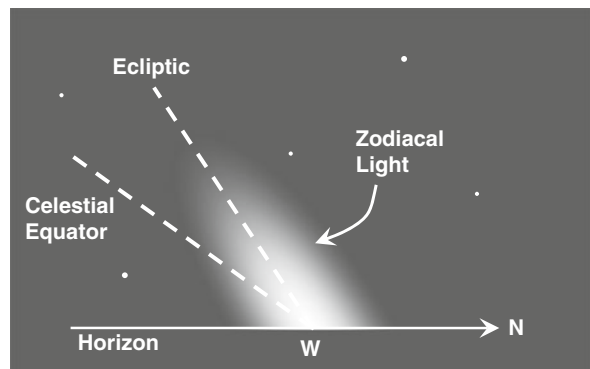
Both types show strong enhancement of deuterium (similar to giant molecular clouds).

Particles of size $> 100 \mu\text{m}$ form spherules and contain magnetite.

The origin of the dust is thus the debris of comets and asteroids, the latter component produced by the “asteroid mill.” The dust is a distant component of the solar corona (the *F-corona*). Near Earth, the density is $\sim 10^{-10}/\text{m}^3$.

The dust is seen phenomenologically in the *zodiacal light*, a conical distribution of material aligned along the ecliptic, before sunrise in the eastern sky or after sunset in the western sky. This is best visible in Spring at dusk, and in Fall at dawn, in the Northern hemisphere, when the ecliptic achieves its highest angle in the sky relative to the celestial equator (see Fig. 14.19).

Fig. 14.19 Zodiacal light can be seen optimally in evening twilight in the Northern hemisphere spring, and in other places and times when the ecliptic makes a large angle with respect to the horizon



It can also be seen, but only in exceptionally dark and high-altitude sites, in the *Gegenschein*, or “counterglow” opposite the Sun in the sky.

Rietmeijer (2002), citing studies of micrometeorites from a wide range of locations (from ocean sediments to the stratosphere) concludes that although cometary dust is more abundant in the zodiacal cloud, the ratio of asteroidal to cometary dust on Earth is ~4:1, due to the smaller tensile strength of the latter.

Some sources suggest that there is an interstellar component as well.

The Stardust mission returned grain material from the Jupiter-family comet 81P/Wild 2; many grains appeared similar to chondrules and calcium-aluminum inclusions (CAI), and only a small fraction were judged to be pre-solar in origin, suggesting wide dispersal of material from the asteroid belt region (Brownlee et al. 2012; Nakashima et al. 2012).

Next we discuss the fate of this dust.

14.13 Dust Destinies

Basically, there are three possible fates for these little particles:

- To be swept up by a planet or other body
- To be blown away from the Sun by radiation pressure or by the solar wind
- To spiral into the Sun via the *Poynting–Robertson effect*

14.13.1 Radiation Pressure

The pressure due to the momentum of solar photons can be written:

$$P = \mathfrak{I}_\odot/c \quad [J/m^3] \quad (14.51)$$

where c is the speed of light and $\mathfrak{I}_\odot = \mathfrak{I}(r)$ is the radiative flux from the Sun at distance r , and is expressed in units of W/m^2 . As per [Milone and Wilson 2013, (6.15)], (14.51) may be rewritten:

$$P = \mathcal{L}_\odot / (4\pi cr^2) \quad (14.52)$$

where \mathcal{L}_\odot is the solar luminosity (expressed in W), so that the force on the dust particle due to radiation pressure is:

$$F_{RP} = PA = [\mathcal{L}_\odot / (4\pi cr^2)] [\pi R^2] \quad (14.53)$$

where $A = \pi R^2$ is the cross-sectional area and R is the radius of the dust particle. This can be compared to the gravitational force:

$$F_G = \frac{GM_\odot m}{r^2} = \left(\frac{GM_\odot}{r^2} \right) \rho \left(\frac{4\pi}{3} \right) R^3 \quad (14.54)$$

where the density, ρ , of the particle has been substituted. The ratio of these two forces will indicate which way the particle moves:

$$\begin{aligned} F_{RP}/F_G &= [\mathcal{L}_\odot / (4\pi GM_\odot)][(4c/3)\rho R]^{-1} \\ &= [(3\mathcal{L}_\odot) / (16\pi c GM_\odot)](\rho R)^{-1} \end{aligned} \quad (14.55)$$

$$= 5.8 \times 10^{-4} (\rho R)^{-1} \quad (14.56)$$

when the SI values $\mathcal{L}_\odot = 3.9 \times 10^{26}$ W, $M_\odot = 2.0 \times 10^{30}$ kg, $c = 3.0 \times 10^8$ m/s are substituted.

The forces balance when this ratio is unity, or when the product, $\rho R = 5.8 \times 10^{-4}$. When this product is smaller, the radiation pressure dominates.

Thus, for $\rho = 1,000 \text{ kg/m}^3$, $R_{\text{crit}} = 6 \times 10^{-7} \text{ m} = 0.6 \mu\text{m}$, so that smaller particles of this density are pushed away from the Sun.

For much denser particles, say $\rho = 6,000 \text{ kg/m}^3$, the critical size is smaller: $R_{\text{crit}} = 1 \times 10^{-7} \text{ m} = 0.1 \mu\text{m}$.

When gravity dominates, the particle will spiral in. This is why: (14.53) and (14.54) are radial forces, and if these were the only forces acting on the particle then circular orbits would be stable at a reduced speed (compared to orbital speed without radiation pressure) of $v = \sqrt{\{[GM_\odot - 3\mathcal{L}_\odot / (16\pi c R \rho)]/r\}}$. However, even if the transverse motion is at circular velocity initially, aberration will result in a component of the radiation pressure opposing this velocity. The very small acceleration causes the speed to drop below the circular value, causing the dust to spiral into the Sun.

The timescale is given by:

$$\tau = 7 \times 10^5 \rho R r^2 \text{ years} \quad (14.57)$$

where ρ is in kg/m^3 , R is in m, and (in this expression only), r is in au. Thus, for $R = 1 \mu\text{m}$, $\rho = 1,000 \text{ kg/m}^3$,

$$\begin{aligned} r = 1.0 \text{ au}, & \quad t = 700 \text{ y} \\ 2.8 \text{ au}, & \quad t = 5500 \text{ y} \\ 10 \text{ au}, & \quad t = 70,000 \text{ y} \end{aligned}$$

and, for $R = 1 \mu\text{m}$, $\rho = 3,000 \text{ kg/m}^3$,

$$r = 1 \text{ au}, \quad t = 2100 \text{ y}$$

and the other times scale up by a factor of 3 also, with the density.

For still denser and/or larger particles, the lifetime increases in proportion. Thus, asteroid dust tends to stay around the original orbit longer (and therefore accumulate to a higher concentration) than lighter cometary material.

An improvement to the approximation for the force due to radiation pressure represented by (14.53) can be obtained if diffraction is included for very small particles (this has the effect of making the effective cross-section of the particle greater than its geometrical area). In addition, the absorptivity ($=1-A$, where A is the bolometric albedo), the fraction of photons that encounter the particle that are absorbed, should be taken into account. These two effects tend to work against each other, but the former effect is important only for very small particles. Folding the two effects into a quantity Q for radiation pressure coefficient, if gravity is ignorable, the net force is then given by

$$\mathbf{F}_{RP} = [\mathcal{L}_\odot / (4\pi c r^2)] (Q\pi R^2) \left[(1 - 2v_r/c)\hat{\mathbf{r}} - (v_\theta/c)\hat{\boldsymbol{\theta}} \right] \quad (14.58)$$

where the velocity terms in the right square bracket represent the “Poynting–Robertson drag.” What we now call the *Poynting–Robertson effect* was first suggested by Poynting (1903) and applied to the solar system quantitatively by Robertson (1937). Lengthy and critical discussions of the Poynting–Robertson effect can be found in Klačka et al. (2012) and in citations therein. Detailed discussions of the state of knowledge about and the fate of the dust can be found in Williams (2002), in Murad and Williams (2002), and in Duncan and Lissauer (1999).

Great progress in understanding comets has occurred, but much is yet to be learned, especially if recent reports of detections of main asteroid belt comets (e.g., Hsieh et al. 2004) are verified.

This concludes our discussion of cometary phenomena. Next we shall examine the denizens of the Edgeworth–Kuiper Belt and their generally rockier cousins, the main-belt asteroids. First we turn our attention to the study of meteorites, then to the asteroids, and finally to the likely origin for the solar system in light of what we know both about our planetary system and those of other stars.

Challenges

- [14.1] Organize the historical theories of the nature of comets. Is there more evidence for smooth historical progression or for abrupt paradigm shifts?
- [14.2] On the basis of information in this chapter and from the orbital and physical data of Tables 13.1 and 13.2, which, if any, of the present day moons of the planets are likely to have been comets or Centaurs originally?
- [14.3] Discuss the limitations of Tisserand's criterion and the precision with which the left and right sides of the equality need to agree.
- [14.4] (a) Compute the expected brightness of a slow (12 km/s), 10 g meteor of silicate composition; assume a vertical path. Make any other necessary assumptions, describing what they are.
(b) How many meteors of this or greater brightness are potentially visible during the year all over the entire Earth?
- [14.5] Suppose the particle of Q. [14.4] were a fast (72 km/s) meteor with a mass of 10^{-2} g; (a) how bright would it get and (b) how long could it be seen?
- [14.6] If the particle of Q. [14.5] avoided the Earth, what other destiny/ destinies might await it, and on what time scale?
- [14.7] C/1973 E1 (Kohoutek) was widely expected to provide a brilliant display when it reached perihelion; it was anticipated to be the “comet of the century.” Comet C/2012 S1 (Ison) was similarly anticipated to be a “comet of the century” but had faded even before its disintegration during perihelion passage on Nov. 27, 2013. Investigate why they were expected to be brilliant, why they were not, and why such apparitions nevertheless are valuable for cometary astronomy.

References

- A'Hearn, M.F., et al.: Deep impact: excavating comet tempel 1. *Science* **310**, 258–264 (2005)
- A'Hearn, M.F.: Comets as building blocks. *Ann. Rev. Astron. Astrophys.* **49**, 281–299 (2011)
- Allen, C.W.: *Astrophysical Quantities*. 3rd ed. The Athlone Press, London (1973)
- Bailey, M.E., Stagg, C.R.: The origin of short-period comets. *Icarus* **86**, 2–8 (1990)
- Bailey, M.E., Clube, S.V.M., Napier, W.M.: *The Origin of Comets*. Pergamon Press, Oxford (1990)
- Beatty, J.K., Chaikin, A.: *The New Solar System*, 3rd edn. Sky Publishing Corp, Cambridge (1990)
- Biermann, L.: On the emission of atomic hydrogen in comets. Joint Institute for Laboratory Astrophysics, Boulder (1968). JILA Report No. 93
- Boehnhardt, H.: Split comets. In: Festou, M.C., Keller, H.U., Weaver, H.A. (eds.) *Comets II*, pp. 301–316. University of Arizona Press, Tucson (2004)
- Brandt, J.C., Chapman, R.D.: *Introduction to Comets*. University Press, Cambridge (1981)
- Brown, P., Spalding, R.E., ReVelle, D.O., Tagliaferri, E., Worden, S.P.: The flux of small near-Earth objects colliding with the Earth. *Nature* **420**, 294–296 (2002)
- Brownlee, D., Joswiak, D., Matrajt, G.: Overview of the rocky component of Wild 2 comet samples: Insight into the early solar system, relationship with meteoritic materials and the differences between comets and asteroids. *Meteoritics & Planetary Science* **47**(4), 453–470 (2012)

- Bryans, P., Pesnell, W.D. The Extreme-Ultraviolet from Sun-Grazing Comets. *Astrophys J.* **760**, (18), 8pp (2012). doi: 10.1088/0004-637X/760/1/18
- Brueckner, G.E., Howard, R.A., Koomen, M.J., Korendyke, C.M., Michels, D.J., Moses, J.D., Socker, D.G., Dere, K.P., Lamy, P.L., Llebaria, A., Bout, M.V., Schwenn, R., Simnett, G.M., Bedford, D.K., Eyles, C.J.: The large angle spectroscopic coronagraph (LASCO). *Solar Phys.* **162**, 357–402 (1995)
- Cajori, F., tr., Sir Isaac Newton's Mathematical Principles of Natural Philosophy and his System of the World, revision of A. Motte's 1729 translation. Reprinting, 1962 (Berkeley, CA: University of California Press)
- Campbell-Brown, M.D., Koschny, D.: Model of the ablation of faint meteors. *Astron. Astrophys.* **418**, 751–758 (2004)
- Campbell-Brown, M.D., Borovička, J., Brown, P.G., Stokan, E.: High-resolution modelling of meteoroid ablation. *Astron. Astrophys.* **557**, A41 (13pp) (2013)
- Capecha, Z., Borovicka, J., Spurný, P.: The solar system – dynamical behavior of meteoroids in the atmosphere derived from very precise photographic records. *Astron. Astrophys.* **357**, 1115–1122 (2000)
- Colangeli, L., Brucato, J.R., Bar-Nun, A., Hudson, R.L., Moore, M.H.: Laboratory experiments on cometary materials. In: Festou, M.C., Keller, H.U., Weaver, H.A. (eds.) *Comets II*, pp. 695–717. University of Arizona Press, Tucson (2004)
- Cravens, T.E., Gombosi, T.I.: Cometary magnetospheres: a tutorial. *Adv. Space Res.* **33**, 1968–1976 (2004)
- Cruikshank, D., et al.: The composition of centaur 5145 pholus. *Icarus* **5**, 389–407 (1998)
- Danby, J.M.A.: *Fundamentals of Celestial Mechanics*, 1st edn. The Macmillan Company, New York (1962)
- Danby, J.M.A.: *Fundamentals of Celestial Mechanics*, 2nd edn. Willmann-Bell, Richmond (1988)
- Domingo, V., Fleck, B., Poland, A.I.: The SOHO Mission: an overview. *Solar. Phys.* **162**, 1–37 (1995)
- Dubin, M.: Meteor Ionization in the E-region. In: Kaiser, T.R. (ed.) *Meteors*, pp. 111–118. Pergamon Press, London (1955)
- Duncan, M.J., Lissauer, J.J.: Solar System Dynamics. In: Wessman, P.R., McFadden, L.-A., Johnson, T.V. (eds.) *Encyclopedia of the Solar System*, pp. 809–824. Academic Press, San Diego (1999)
- Fernández, J.A.: Cometary dynamics. In: Wessman, P.R., McFadden, L.-A., Johnson, T.V. (eds.) *Encyclopedia of the Solar System*, pp. 537–556. Academic Press, San Diego (1999)
- Flynn, G.J.: Extraterrestrial dust in the near-earth environment. In: Murad, E., Williams, I.P. (eds.) *Meteors in the Earth's atmosphere*. Cambridge University Press, Cambridge (2002)
- Fornasier, S., Lellouch, E., Müller, T., Santos-Sanz, P., Panuzzo, P., Kiss, C., Lim, T., Mommer, M., Bockelée-Morvan, D., Vilenius, E., Stansberry, J., Tozzi, G. P., Mottola, S., Delsanti, A., Crovisier, J., Duffard, R., Henry, F., Lacerda, P., Barucci, A., & Gicquel A. 2013. TNOs are Cool: A survey of the trans-Neptunian region. Results from the PACS and SPIRE observations with the Herschel Space Observatory. *Geophysical Research Abstracts*, 14, EGU2012-2878 (2012)
- Gingerich, O., Westman, R.S. The Wittich Connection: Conflict and Priority in Late Sixteenth-Century Cosmology. *T Am Philos Soc* **78**, Part 7, (1988)
- Gor'kavi, N.N., Ozernoy, L.M., Mather, J.C.: A New approach to dynamical evolution of interplanetary dust. *Astrophys. J.* **474**, 496–502 (1997)
- Grün, E., Jessberger, E.K.: Dust. In: Huebner, W.F. (ed.) *Physics and Chemistry of Comets*, pp. 113–176. Springer-Verlag, Berlin (1990)
- Harker, D.E., Woodward, C.E., Wooden, D.H.: The dust grains from 9P/tempel 1 before and after encounter with deep impact. *Science* **310**, 278–280 (2005)
- Hawkins, G.S.: *Meteors, Comets, and Meteorites*. McGraw Hill, New York (1964)
- Hsieh, H.H., Jewett, D.C., Fernandez, Y.R.: The strange case of 133P/Elst-Pizarro: a comet among the asteroids. *Astron. J.* **127**, 2997–3017 (2004)

- Hutchison, R.: *Meteorites*. Cambridge University Press, Cambridge (2004)
- Jenniskens, P.M.: *Meteor Showers and their Parent Comets*. Cambridge University Press, Cambridge (2008)
- Jenniskens, P.M.: New meteor showers discovered. *Sky Telesc.* **124**, 20–25 (2012)
- Jewitt, D., Agarwal, J., Weaver, H., Mutchler, M., Larson, S.: The extraordinary multi-tailed Main-Belt Comet P/2013 P5. *Astrophys. J. Lett.* **778**: L21 (4pp) (2013)
- Kaiser, T.R. (ed.): *Meteors*. Special Supplement (Vol. II) to the Journal of Atmospheric and Terrestrial Physics. Pergamon Press, London (1955)
- Kelley, D.H., Milone, E.F.: *Exploring Ancient Skies*, 2nd edn. Springer, New York (2011)
- Kidger, M.R., Müller, T., Altieri, B., Abreu, A., Bockelee-Morvan, D., Coia, D., Crovisier, J., González, B., Llorente, A., Lorente, R., Lucas, L., Riedinger, J., Rodríguez, F., Sierra, M. M. 2012. “Far infrared observation of comet C/1995 O1 (Hale-Bopp) with the Herschel Space Observatory at $r = 29.95\text{AU}$,” *Asteroids, Comets, Meteors 2012*, Niigata, Japan. Lunar Planetary Institute Contribution No. 1667, #6321.
- Klačka, J., Petržala, J., Pástor, P., and Kómar, L. The Poynting–Robertson effect: A critical perspective. *Icarus* (2012, in press)
- Kreutz, H.C.F. Untersuchungen über das System der Cometen 1843I, 1880I and 1882II, I. Theil,” *Publ. Sternwarte Kiel*, No. 3 (1888).
- Kronk, G.W.: *Meteor Showers: A Descriptive Catalog*. Enslow Publishers, Inc, Hillside (1988)
- Levin, B.J.: Physical theory of meteors and the study of the structure of the complex of meteor bodies. In: Kaiser, T.R. (ed.) *Meteors*, pp. 131–143. Pergamon Press, London (1955)
- Lisse, C.M., Kraemer, K.E., Nuth III, J.A., Li, A., Joswiak, D.: Comparison of the composition of the Tempel 1 ejecta to the dust in Comet C/Hale–Bopp 1995 O1 and YSO HD 100546. *Icarus* **187**, 69–86 (2007)
- Marsden, B.G.: On the orbits of some long lost comets. *Astron. J.* **68**, 795–801 (1963)
- Marsden, B.G. Periodic Comet Shoemaker-Levy 9 (1993e). IAU Circular No. 5906, (1993)
- Marsden, B.G., Williams, G.V.: *Catalogue of Cometary Orbits 1997*, 12th edn. Minor Planet Center, Cambridge (1997)
- Marsden, B.G., Williams, G.V.: *Catalogue of Cometary Orbits 2005*, 16th edn. Minor Planet Center, Cambridge (2005)
- Meech, K.J., Belton, M.J.S.: The atmosphere of 2060 Chiron. *Astron. J.* **100**, 1323–1338 (1990)
- Milam, S.N., Savage, C., Brewster, M.A., Ziurys, L.M., Wyckoff, S.: The $^{12}\text{C}/^{13}\text{C}$ isotope gradient derived from the millimeter transitions of CN: the case for galactic chemical evolution. *Astrophys. J.* **634**, 1126–1132 (2006)
- Milone, E.F., Wilson, W.J.F.: *Solar System Astrophysics: Background Science and the Inner Solar System*, 2nd edn. Springer, New York (2014)
- Moulton, F.R.: An introduction to celestial mechanics. MacMillan, New York (1914). 10th printing, 1951
- Mumma, M.J., DiSanti, M.A., Magee-Sauer, K., Bonev, B.P., Villanueva, G.L., Kawakita, H., Dello Russo, N., Gibb, E.L., Blake, G.A., Lyke, J.E., Campbell, R.D., Aycock, J., Conrad, A., Hill, G.M.: Parent volatiles in comet 9P/Tempel 1: before and after impact. *Science* **310**, 270–274 (2005)
- Mumma, M.J., Charnley, S.B.: The chemical composition of comets—emerging taxonomies and natal heritage. *Ann. Rev. Astron. Astrophys.* **49**, 471–524 (2011)
- Murad, E., Williams, I.P. (eds.): *Meteors in the Earth’s Atmosphere. Meteoroids and Cosmic Dust and their Interactions with the Earth’s Upper Atmosphere*. Cambridge University Press, Cambridge (2002)
- Murray, C.D., Dermott, S.F.: *Solar System Dynamics*. University Press, Cambridge (1999). 2nd printing, 2001
- Nakashima, D., Ushikubo, T., Joswiak, D.J., Brownlee, D.E., Matrajt, G., Weisberg, M.K., Zolensky, M.E., Kita, N.T.: Oxygen isotopes in crystalline silicates of comet Wild 2: A comparison of oxygen isotope systematics between Wild 2 particles and chondritic materials. *Earth and Planet. Sci. Letts.* 357–358, 355–365 (2012)

- Newton, I. *Philosophiae Naturalis Principia Mathematica*. See Cajori, 1934 (1686)
Origen of Alexandria. 3rd c. *Contra Celsus*, tr. Crombie, in Roberts and Donaldson/Coxe, repr.
1994, pp. 422–423; excerpt appears in Kelley and Milone 2011, p. 134.
- Peale, S.J.: On the density of Halley's comet. *Icarus* **82**, 36–49 (1989)
- Poynting, J.H.: Radiation in the solar system: its effect on temperature and its pressure on small
bodies. *Proc. Royal Soc. Lond.* **72**, 265–267 (1903)
- Richardson, J.E., Melosh, H.J., Lisse, C.M., Carcich, B.: A ballistics analysis of the Deep Impact
ejecta plume: determining Comet Tempel 1's gravity, mass, and density. *Icarus* **190**, 357–390
(2007)
- Richardson, J.E., Melosh, H.J. An examination of the deep impact collision site on Comet Tempel
1 via Stardust-NExT: placing further constraints on cometary surface properties. *Icarus* **222**,
492–501 (2013)
- Rietmeijer, F.J.M.: Collected extraterrestrial materials: interplanetary dust particles, micromete-
orites, meteorites, and meteoric dust. In: Murad, E., Williams, I.P. (eds.) *Meteors in the Earth's
Atmosphere*, pp. 215–245. Cambridge University Press, Cambridge (2002)
- Robertson, H.P.: Dynamical effects of radiation in the solar system. *Mon. Not. R. Astron. Soc.* **97**,
423–438 (1937)
- Ronan, C.A., Needham, J.: *The Shorter Science and Civilisation in China: an Abridgement of
Joseph Needham's Original Text*. University Press, Cambridge (1981)
- Schaefer, L., Fegley Jr., B.: Application of an equilibrium vaporization model to the ablation of
chondritic and achondritic meteoroids. *Earth, Moon, and Planets* **95**, 413–423 (2004)
- Sekanina, Z.: Comet 73P/Schwassmann-Wachmann nucleus fragmentation, its light-curve signa-
ture, and close approach to earth in 2006. *Int. Comet Quart.* **27**, 225–240 (2005)
- Skorov, Y., Blum, J.: Dust release and tensile strength of the non-volatile layer of cometary nuclei.
Icarus **221**, 1–11 (2012)
- Stagg, C.R., Bailey, M.E.: Stochastic capture of short-period comets. *Mon. Not. R. Astron. Soc.*
241, 507–541 (1989)
- Strange, H.L., Longuski, J.M.: Graphical method for gravity-assist trajectory design. *J. Spacecraft.
Rock.* **39**, 9–16 (2002)
- Sugita, S., et al.: Subaru telescope observations of deep impact. *Science* **310**, 274–278 (2005)
- Sunshine, M., et al.: Exposed water ice deposits on the surface of Comet 9P/Tempel 1. *Science*
311, 1453–1455 (2005)
- Szabó, G.M., Kiss, L.L., Pál, A., Kiss, C., Sárneczky, K., Juhász, A., Hogerheijde, M.R.: Evidence
for fresh frost layer on the bare nucleus of Comet Hale-Bopp at 32 au distance. *Astrophys J*
761(8), 7pp (2012). doi:[10.1088/0004-637X/761/1/8](https://doi.org/10.1088/0004-637X/761/1/8)
- Taylor, S.R.: *Solar System Evolution: A New Perspective*. University Press, Cambridge (1992)
- Williams, I.P.: The evolution of meteoroid streams. In: Murad, E., Williams, I.P. (eds.) *Meteors in
the Earth's Atmosphere*, pp. 13–32. University Press, Cambridge (2002)
- Wyckoff, S., Kleine, M., Peterson, B.A., Wehinger, P.A., Ziurys, L.M.: Carbon isotope abun-
dances in comets. *Astrophys J* **535**, 991–999 (2000)
- Yeomans, D.K.: *Comets: a Chronological History of Observation, Science, Myth, and Folklore*.
Wiley, New York (1991)

Chapter 15

Meteorites, Asteroids and the Age and Origin of the Solar System

In the previous chapter, we discussed sporadic meteors and meteor showers and indicated that some of the former and most of the latter likely originate from comets. Here we discuss the source of the other meteors, especially those that survive their fiery passage through the atmosphere and impact the Earth. These *meteorites* have become a primary source of knowledge about the age and origin of the solar system. Another important source is the increasing number of small bodies being detected in both the inner and the outer solar system, so we will also describe what has been learned about these objects in recent years. Finally we consider the birth of the solar system in the context of what we know about proto-stellar disks.

15.1 Stones from Heaven

“It is easier to believe that two Yankee professors would lie than that stones would fall from heaven.” So Thomas Jefferson was reputed to have said, when he heard of a meteorite that was observed to fall on December 14, 1807 in Weston, Connecticut. Wasson (1985, p. 4), however, finds no evidence that Jefferson ever said it. Instead, in keeping with Jefferson’s reputation as a careful student of the natural sciences, he cites a letter by Jefferson to Daniel Salmon, written in February, 1808 about the meteorite that he described.

“its descent from the atmosphere presents so much difficulty as to require careful examination,” but, he added, “We are certainly not to deny whatever we cannot account for.” . . . “The actual fact however is the thing to be established.” He hoped this would be done by those qualified and familiar with the circumstances.

Scientists at the end of the eighteenth century were living in an age of rationalism; they usually dismissed claims of such phenomena as incredible “folk tales.” Nevertheless, Ernst Florenz Friedrich Chladni (1756–1827) argued that the evidence was very strong that meteors (bolides in particular) did produce meteorites sometimes, and argued that prehistoric meteorites might be present in the form of large iron masses. Subsequent carefully documented falls in the early nineteenth

century, such as that in Wethersfield, helped turn the tide of opinion. In retrospect, we know of meteorites in the remote past that were carefully cached away because they were indeed perceived to fall from heaven. Hence, in the New Testament book of Acts (19:35), Paul’s preaching of Christianity in the Asia Minor city of Ephesus infuriated its merchants and artisans, whose businesses were tied in with the worship of Artemis. Ephesus was described as the “temple Keeper,” and the city of “the great stone that fell from the sky.” Artemis was often depicted as a multibreasted goddess, a possible reference to the bossed and dimpled appearance of an iron meteorite [see Wood (1968) and Wasson (1985) for similar views]. Chinese records of meteorite observations date back to the seventh century BC; these and other historical data are reviewed in Kelley and Milone (2011, Section 5.6). For a thorough description of prominent meteorite craters on Earth, see Hodge (1994), and for a brief review of how they were produced, see Milone and Wilson 2014, Ch. 5.5.1.

15.1.1 Categories and Nomenclature of Meteorites

What were *meteoroids* in space, survived their passage through the atmosphere as *meteors* to land on Earth as *meteorites*. The term “meteor” is from the Greek word *μετεօρον* (plural: *μετεօρα*, “things in the air”). We discussed meteors in Sect. 14.10. Meteoroids will be discussed in Sect. 15.7, in the course of identifying the parent source bodies for the meteorites.

15.1.1.1 Broad Categories

Older astronomy textbooks usually referred to only three types of meteorites:

- *Aerolites* (more commonly known as *stony* meteorites or *stones*)
- *Siderites* (irons)
- *Siderolites* (stony-irons)

Although this categorization is still somewhat useful in describing broadly what type of meteorite one may find, today the classes are more numerous, and many subclasses of meteorites are recognized.

Classification identifies the nature of the meteorite, but another important aspect is the circumstance under which it is found: has it been lying around on the Earth’s surface for a lengthy and often unknowable amount of time where it was subjected to terrestrial contamination or was it recovered and carefully protected just after it fell? The answers to these questions may help to establish the reliability of compositional abundances in the meteorite. A “weathering grade” has been devised for Antarctic meteorites (Wlotzka 1993), for example, and, the degree to which the rock has been shocked also has been quantized, as “shock stages”.

15.1.1.2 Another Distinction: *Falls* and *Finds*

If meteorites are detected as meteors and are subsequently collected, they are called *falls*. They are overwhelmingly *stony*. The *Catalogue of Meteorites*¹ (Grady 2000) indicates that of the 22,507 meteorites known as of December 1999, 1,005 were falls. Of these, 940 are stones, 48 are irons, and 12 are stony-irons; 5 are unknown.

Meteorites which were *not* seen as meteors but which were discovered in the ground are known as *finds*. Formerly, the finds included irons in large numbers (42 %), but there were still more numerous stones (52 %) and some stony-irons (5 %) found. The number of stony meteorites among the finds was classically underestimated because they look much like terrestrial rocks, and so may go unnoticed, especially after the thin fusion crust (acquired from atmospheric heating during entry—cf. Sect. 14.10) has worn away. These meteorites also erode more easily than other types. Discoveries of huge numbers of meteorites on the ice sheets of Antarctica (17,808 as of December, 1999: 79 % of the total!) have helped to redress the balance and have produced some interesting surprises, too. With the discoveries in Antarctica, the *finds*' statistics have greatly improved: 95.59 % are stony; 3.84 % are irons, and 0.52 % are stony irons. Finally, meteorites have also been found in the hot deserts of Earth, on the Moon [Wood (1990, p. 244), states that up to 4 % by weight of lunar soils are meteoritic], and even on Mars, thanks to the exploration by the Spirit and Opportunity Rovers.

15.1.1.3 Nomenclature

Historical development has dictated the familiar names of individual meteorites, which are traditionally called by the geographic region in which the discovery was made. Thus, the *Millarville* meteorite was found on April 28, 1977, on a farm near Millarville, Alberta. In the 1970s, the Meteoritical Society established rules for the naming of meteorites, and its Committee on Meteorite Nomenclature makes decisions regarding assignment of and changes to meteorite names. Its decisions are published in the *Meteoritical Bulletin*. For the numerous finds in Antarctica and in desert areas of the world, a new naming convention provides the year of recovery followed by a sequence number of discovery, hence, *ALH 84001*, the first specimen collected during the 1984–(1985) (summer) field season in the Alan Hills region of Antarctica.

¹ The on-line catalogue of London's Natural History Museum, provides updated numbers for specific groups of meteorites. At the time of writing, the updates were to 2002. Hereafter, we refer to this source as NHM (2002): <http://www.nhm.ac.uk/research-curation/research/projects/metcat/search/metsPerGroup.dsml>

15.1.2 Petrographic Categories

Basically, *petrography* (sometimes called petrology) is the description and classification of rocks; *petrology* is, strictly, the study of rocks, and therefore a discipline within geology. The old categories of meteorites mentioned in Sect. 15.1 have not proven adequate to reveal the full range of information that they contain. Generally, classification techniques make extensive use of chemical composition and petrographic properties such as:

- Texture
- Water content
- Igneous glass state
- The presence of metallic minerals
- The structure and homogeneity of certain mineral compositions

More recent scholarship also suggests that the material of which meteorites are composed can take different forms depending on the physical conditions under which the rock was formed. Consequently, Urey and Craig (1953) began a systematic study of chondrite compositional differences; this was extended by John Wasson, who carried out similar work on the iron meteorites. On this basis, three main kinds of meteorites are recognized:

1. Non-differentiated meteorites
2. Differentiated silicate-rich meteorites (DSRs)
3. Iron meteorites

The latter two types require material to be *differentiated* or separated out, usually in a high temperature and pressure environment.

Meteorites may be classified by *group*, roughly analogous to spectral classification in stars, distinguished by mineral and chemical or isotopic composition. For example, there are 13 groups of iron meteorites.

A group may be further distinguished by *type*, or *class*, roughly analogous to the subclasses of stellar spectral types.²

Groups of meteorites may also be broadly linked in various ways; these linkages are termed *clans*. Table 15.1 (adapted from Wasson 1985, Appendix A), indicates the principal clans, groups, and types. A more recent summary of the classification of meteorites is given by Hutchison (2004).

²The analogy is limited because the spectral subclasses are refinements to the main classification criteria that are primarily dependent on the temperature of the photosphere. Here, the numbers represent different groups of properties, not completely dependent on the chemical composition.

Table 15.1 Classifications of meteorites^a

Clan	Group	Other names	% Falls ^b	Examples
<i>Chondrites</i>				
Refractory-rich	CV	Carbonaceous, C3	1.1	Allende
Minichondrule	CO	" C3	0.9	Ornans
"	CM	" C2	2.0	Murchison
Volatile-rich	CI	" C1	0.7	Orgueil
Ordinary	LL	Amphoterite	7.2	St. Mesmin
"	L	Hypersthene	39.3	Bruderheim
"	H	Bronzite	32.3	Ochansk
IAB inclusion	IAB chondrite		...	Copiapó
Enstatite	EL	Enstatite	0.9	Indarch
"	EH	"	0.7	Khairpur
...	Other chondrites	CH, CR, R	0.30	Kakangari
			...	Acfer 182; Renazzo; Rumuruti
<i>Differentiated meteorites (non-irons)</i>				
Enstatite	Aubrites	Enstatite achondrites	1.1	Norton County, Aubres
Igneous	Eucrites	Basaltic, Ca-rich, Pyroxene-Plagioclase achondrite	2.8	Juvinas, Pasamonte, Piplia Kalan, Sioux County
"	Howardites	{same as Eucrites}	2.5	Kapoeta
"	Diogenites	Hypersthene achondrites	1.1	Johnstown, Roda, Shalka
"	Mesosiderites	Stony-irons	0.9	Estherville
"	Pallasites	Stony-irons	0.3	Krasnoyarsk
...	Ureilites	Olivine-pigeonite achondrite	0.4	Novo Urei
...	Other differentiated silicate-rich meteorites	Angrites; SNC; lunar; ...	1.0	Angra dos Reis; Shergotty, Nakhla, Chassigny, ALH 84001; ALH 81005
<i>Differentiated meteorites (irons)</i>				
...	IAB irons	...	0.9	Canyon Diablo
...	IC irons	...	0.1	Bendegó
...	IIAB irons	...	0.5	Coahuila
...	IIC irons	...	0.1	Ballino
...	IID irons	...	0.1	Needles
...	IIE irons	...	0.1	Weekeroo
...	IIF irons	...	0.1	Monahans
...	IIIAB irons	...	1.5	Henbury
...	IIICD irons	...	0.1	Tazewell
...	IIIE irons	...	0.1	Rhine Villa
...	IIIF irons	...	0.1	Nelson County
...	IVA irons	...	0.4	Gibeon
...	IVB irons	...	0.1	Hoba
...	Other irons	...	0.6	Mbosi

^aMainly from Wasson (1985, Table A-1), among other sources^bExtrapolated from a limited sample; see Wasson (1985) for details

15.1.3 Meteorite Groupings and Subgroupings

15.1.3.1 Undifferentiated Meteorites

The principal (and under more recent classification schemes, *all*) undifferentiated meteorites are called *chondrites*, which can be defined as “microbreccias”, composed of matrices of material, each with its own “genetic” background history onto which varying amounts of molten drops (*chondrules*) of material were splashed. The detailed composition distinctions will be treated in Sect. 15.2.

The chondrite groups are indicated in Table 15.2, taken from Sears and Dodd (1988, p. 15), Taylor (1992, p. 108), and updated with material from Hutchison (2004, p. 30). The petrologic (or petrographic) classes of chondrites are given in number sequence in Table 15.3 [adapted from tables by Taylor (1992), Wasson (1985), Hutchison (2004, p. 41), and other sources]. The petrologic class is often given with the chondrite designation, e.g., CV3 for the Allende meteorite.

15.1.3.2 Differentiated Meteorites

The *differentiated silicate-rich* (DSR) and *iron* meteorites are *differentiated*: when the parent body was molten, contents were able to separate, depending on density, in a gravitational field. The silicates and metals were immiscible and thus separated quickly, with the denser molten metal ($\leq 7.9 \text{ g/cm}^3$) sinking to the centers of the parent bodies, and the silicates, much less dense, floating to the top.

Further differentiation in the silicate material, where densities range from 2.6 to 3.6 g/cm^3 , led to crustal and mantle silicate compositions and densities. We will discuss this process further in Sect. 15.3.

DSRs include all those groups which are neither chondrites nor irons.

The groups of differentiated silicate-rich meteorites are given in Table 15.4, taken mainly from Wasson (1985, Table II-3, p. 33). The extent to which differentiation occurred varied greatly. These meteorites are roughly of two kinds:

1. Those with high metal content, usually referred to as *stony-irons*.
2. Those with low metal content and igneous origin, often referred to as *achondrites*. The stony-irons include the groups: *pallasites* and *mesosiderites*.

The achondrites include the groups: *ureilites*, *aubrites*, *eucrites*, *diogenites*, and *howardites*.

Three groupings of DSR meteorites have known or strongly-suspected parent bodies, and one other meteorite shows an intriguing resemblance to a possible fourth parent body:

1. A small, but very important DSR achondrite group known as the *SNC* (pronounced “snick”) meteorites - [*S* for *shergottites* (after the prototype *Shergotty* meteorite), *N* for *nakhlites* (after the *Nakhla* meteorite), and *C* for *chassignite* (after the *Chassigny* meteorite)] - all named for the sites in which they were found. There are now several others, including the Alan Hills

Table 15.2 Chondrite groups^a

Group	Mg/Si	Ca/Si (%)	Fe/Si	Fayalite (%) ^b	Si (%)	Fe(met/tot) ^c	$\delta^{18}\text{O}$	$\delta^{17}\text{O}$
CI	1.07	0.062	0.87	...	10.5	0.0	~16.4	~8.8
CM	1.04	0.069	0.82	...	12.9	0.0	~12.2	~4.0
CO	1.05	0.07	0.78	...	15.9	0–0.2	~-1.0	~-5.1
CV	1.07	0.085	0.76	...	15.6	0–0.3	~0	~-4.0
CK	1.13	0.08	0.79	...	15.1	0.0		
CR	1.05	0.063	0.79	...	15.3	0.4		
CH	1.06	0.06	1.52	...	13.3	0.9		
H	0.95	0.052	0.82	16–20	16.9	0.58	4.1	2.9
L	0.93	0.05	0.58	23–26	18.5	0.29	4.6	3.5
LL	0.93	0.048	0.49	27–32	18.9	0.11	4.9	3.9
EH	0.73	0.036	0.87	...	16.7	0.76	5.6	3
EL	0.87	0.038	0.59	...	18.6	0.83	5.3	2.7
R	0.93	0.053	0.77	...	15.8	0.0		

^aData taken mainly from Taylor (1992, Table 3.6.1, p. 108), Sears and Dodd (1988, Table 1.1.3, p. 15), and Hutchison (2004, Table 2.1 and 2.2, pp. 29–30)

^bFayalite (Fe_2SiO_4) proportion of the total olivine

^cFraction of metallic iron to total iron

meteorite (Antarctica meteorite ALH84001). These meteorites have much younger radiogenic ages than most meteorites, indicating substantial remodification in a major body. In fact they appear to have Martian composition. The atmospheric samples encapsulated in glass globules embedded in the meteorites have isotope ratios of the Martian atmosphere. This is interesting in itself—because it indicates that over the time since the meteorites were blasted off the surface of Mars, the atmosphere has not changed greatly. Of course, if it had changed, and the composition were different from present day Mars, some other venue of origin might have been sought for them.

2. A small achondrite group, discovered in Antarctica, that has lunar composition.
3. The *HED* meteorites, named for the first letters of the three groups of which it is composed: the *howardites*, *eucrites* and *diogenites*. HED meteorites are fairly common, making up ~6 % of all meteorite falls on the Earth (Russell et al. 2012). (The distinction between falls and finds is discussed in Sect. 15.1.1.2) Since the 1970s, it has been recognized that these meteorites share many spectral characteristics with the asteroid (4) Vesta, suggesting that Vesta is the source of many or most of the HEDs. This point is discussed further in Sect. 15.7.5.
4. Yet another DSR meteorite, found in Morocco, is suspected of having an origin on Mercury.

Finally, the irons have large iron and nickel content. They consist of two main groups, distinguished by crystal structure: the *octahedrites* and the *hexahedrites*. There are, however, many possible groupings based on the relative abundances of such elements as nickel, germanium, gallium, and iridium. Table 15.5, adapted from Wasson (1985, Fig. II-4, p. 43) lists some of the properties of 13 groups of iron meteorites, and of the mesosiderite and the pallasite stony-iron groups. The irons are described further in Sect. 15.4.

Table 15.3 Petrologic classes of chondrites^a

Property	1	2	3	4	5	6
Olivine and pyroxene variation (%) Pyroxene ≥ 5 Olivine ≥ 3	0 < Pyroxene < 5 Uniform.....
Low-Ca pyroxene Mostly monoclinic..... Fe–Mg minerals.....
Structural state	Much Monoclinic
Secondary feldspar (grain size level.) Absent Orthorhombic.....
Igneous glass Clear and isotropic..... variable abundance.....
Metallic minerals (max. Nickel content) Taenite absent or minimal ($< 20\%$) Kamacite and taenite present. ($> 20\%$)
Sulfide minerals ($< \text{Nickel} >$ content)	None
Chondrules (overall texture)	None Very well-defined	Well-defined	Delineated	Poorly defined
Matrix texture	Fine-grained; opaque	Much opaque	Opaque	Transparent microcrystalline Recrystallized..... coarsening.....
Bulk carbon content (%)	3–5
Bulk water content (%)	~20

^aBased on Taylor (1992, Table 3.6.2, p. 108), van Schmus and Wood (1967, Table 2, p. 757), Sears and Dodd (1988, 1.1.4, pp. 23–24), Wasson (1985, Table II-2, p. 31), and Hutchison (2004, Table 2.4, p.41)

Table 15.4 Selected groups of differentiated silicate-rich meteorites^{a, b}

Group	Mineral	Concentration as silicates frac.	FeO/[FeO + MgO]%	Fe–Ni%	$(\delta^{18}\text{O})\text{‰}$	$(\delta^{17}\text{O})\text{‰}$	$(\Delta^{17}\text{O})\text{‰}$	Breccia type
Eucrites	Pigeonite	400–800	45–70	<1.0	3.61(5)	1.63(4)	-0.24(2)	Monomict
Howardites	Orthopyroxene	400–800	25–40	~1.0	3.25(11)	1.43(7)	-0.27(3)	Polymict
Diogenites	Orthopyroxene	~950	25–27	<1.0	3.41(4)	1.46(3)	-0.27(2)	Monomict
Mesosiderites	Orthopyroxene	400–800	23–27	30–55	3.41(6)	1.53(5)	-0.25(3)	Polymict
Pallasites	Olivine	~980	11–14	28–88	2.92(3) ^c	1.23(2) ^c	-0.28(1) ^c	Monomict
Aubrites	Clinopyroxene (low calcium)	~970	0.01–0.03	~1.0	5.26(5)	2.75(3)	+0.02(1)	Polymict
Ureilites	Olivine	~850	10–25	1–6.	6.93(14)	2.41(15)	-1.20(8)	Polymict

^aFrom Wasson (1985, Table II-3, p. 33)

^bdel values are means calculated from data of Clayton and Mayeda (1996, Table 1), who define $\Delta^{17}\text{O} = \delta^{17}\text{O} - 0.526 \times \delta^{18}\text{O}$. This quantity indicates the departure from the Terrestrial Fractionation Line in Fig. 15.7, and so indicates different places of origin or formation process. Parentheses contain the standard deviations of the means, in units of the last decimal place

^cMain group pallasites, Clayton and Mayeda list two other pairs of Pallasites with very different del values: (-2.80, -6.15, -4.68 for one pair and +2.26, 0.41, and -0.76 for the other, respectively)

Table 15.5 Iron Meteorite Groups^a and the Stony-Iron Mesosiderite and Pallasite Groups^b

Group	Bandwidth (mm)	Structure	Ni 10 ⁻⁶	Ga 10 ⁻⁶	Ge 10 ⁻⁶	Ir	Ge-Ni	Frequency correlation (%)	<Δ ¹⁷ O> (‰)
IA	1.0-3	Om-Ogg ^c	6-9	55-100	190-520	0.6-5.5	Negative	17.0	{ -0.48(2)
IB	0.01-1.0	Dom	9-25	11-55	25-190	0.3-2.0	Negative	1.7	{ }
IC	<3	Anomalous, Og	6-7	49-55	212-247	0.07-2.1	Negative	2.1	...
IIA	>50	Hexahedrite	5-6	57-62	170-185	2-60	Positive?	8.1	...
IBB	5-15	Ogg	~6	46-59	107-183	0.01-0.9	Negative	2.7	...
IC	0.06-0.07	O plessitic	9-12	37-39	88-114	4-11	Positive	1.4	...
ID	0.4-0.8	Of-Om	10-11	70-83	82-98	3.5-18	Positive	2.7	...
IE	0.7-2	Anomalous	8-10	21-28	62-75	1-8	Absent	2.5	+0.59(2)
IIF	0.05-0.21	Ataxite-Of	11-14	9-12	99-193	0.8-23	Positive	1.0	...
Mes. ^b	~1	Anomalous	6-10	9-16	37-56	2.2-6.2	Absent	...	-0.25(3)
Pal. ^b	~0.9	Om	8-13	14-27	29-71	0.01-2	Negative?	...	-0.28(1)
IIIA	0.9-1.3	Om	7-9	17-23	32-47	0.15-20	Positive	24.8	{ -0.21(2)
IIIB	0.6-1.3	Om	8-11	16-21	27-46	0.01-0.15	Negative	7.5	{ -0.43(6)
IIIC	0.2-3	Off-Ogg	6-13	11-92	8-380	0.07-2.1	Negative	1.4	...
IID	0.01-0.05	Ataxite-Off	16-23	1.5-5.2	1.4-4.0	0.02-0.07	Negative	1.0	...
IIIE	1.3-1.6	Og	8-9	17-19	34-37	0.05-6	Absent	1.7	...
IIIF	0.5-1.5	Om-Og	7-9	6.3-7.2	0.7-1.1	0.006-7.9	Negative	1.0	...
IVA	0.25-0.45	Of	7-9	1.6-2.4	0.09-0.14	0.4-4	Positive	8.3	+1.17(5)
IVB	0.006-0.03	Ataxite	16-18	0.17-0.27	0.03-0.07	13-38	Positive	2.3	

¹Mainly from Wasson (1985, Table II-5). Del values are averages from data of Clayton and Mayeda (1996, Table 1) for Iron Groups IAB, HE, for Mesosiderites, Pallastites, and for iron groups IIAB, IIICD, and IVA. Consult this source for which meteorites are included in the averages. The parentheses

contain the standard deviation of the means in units of the last decimal place

Mesosiderites and Pallasites

15.2 Undifferentiated Meteorites: The Chondrites

15.2.1 Defining the Chondrites

Chondrites make up the bulk of both the finds (66.8 %) and the falls (81.7 %), and thus are the most common meteorites. Grady (2000) listed 15,190 chondrites, of which 821 are falls.

These meteorites have three distinctive components:

1. Chondrules (not always present)
2. A matrix of material
3. Calcium-aluminum-rich inclusions (*CAIs*)

Although it has been broadened to include all undifferentiated meteorites, the term “chondrite” was originally applied only to meteorites containing small spherical objects called *chondrules* (from the Greek word for grain) which were once molten droplets. The degree to which they are present, their appearance, and their composition are important classifying parameters. They vary in size, composition, and texture.

The variety suggests that the chondrules made their appearance under varied conditions and places in the solar system.

Chondrules range in size from 0.5 to 2.5 mm, vary in texture and composition, and are often grouped into at least two types with less (type I) and more (type II) FeO content, other minerals, and differing oxidation states. See Hewins (1997); and Hutchison (2004) for details.

The space between chondrules is filled with a matrix, thought to be fine-grained material from the original solar nebula which somehow avoided the heating undergone by the chondrules. Mixed in with this material are broken chondrule and coarse-grained, high-temperature material. The matrix is rich in FeO and is composed of fine-grained (~1 μm) dark, opaque material.

The main compositional ingredients of chondrules of carbonaceous H3 and L3 chondrites (see below for the explanation of these types of meteorites) are:

- SiO_2 (45–50 % by weight)
- MgO (28–36 %)
- FeO (9–16 %)
- Al_2O_3 (3–5 %)
- CaO (2–3 %)

with oxides of Na, K, Cr, Ti, and Mn taking smaller shares.

Most chondrules are depleted in the non-exclusive categories of:

- *Siderophilic* elements (having affinity for iron and nickel) [These include: Pd, Au, Rh, Pt, Ir, Ru, Re, and Os; and to a lesser degree: Mo, Ge, As, Sb, Ni, Ag, Co, W, P, Ga, Cr, V, and Mn]; and in

- *Chalcophilic* elements (preferring the company of sulfur-bearing minerals) [These include: Ag, Bi, Cd, Cu, Hg, In, Pb, Sn, Te, Tl, and Zn]; but they are *not* depleted in:
- *Lithophilic* elements (having affinity for minerals rich in oxygen) [These include: Al, Ba, Ca, Ce, Cr, Cs, K, La, Mg, Na, Rb, Se, Sr, Th, U, and Yb].

In the Earth's crust, lithophilic elements dominate, chalcophilic elements are found concentrated in ore deposits, and the siderophilic elements are largely missing. In chondritic meteorites generally, the three major groups of elements are found much more mixed than on Earth's surface, with the matrix being much richer in iron content than are the chondrules. However, different kinds of chondrules may be found in one and the same meteorite, and the composition can vary among the kinds of chondrules. These results strongly suggest the presence of a very non-uniform medium in the early solar system, and the presence of short-lived radioactive nuclides such as ^{26}Al which decays to ^{26}Mg with a half-life of 0.72 My [See Gounelle and Meibom (2008) about the origin of the ^{26}Al].

The chondrules' textures suggest rapid heating and cooling, and there is a large enough population of fused chondrules to suggest that during formation their number density was relatively high. Experiments suggest that chondrule textures can be reproduced by temperatures of $\sim 1,550\text{ K}$ for $\sim 15\text{ min}$ followed by cooling at rates $\sim 500\text{ K/h}$. However, some appear to have been heated to temperatures as high as 1,700 K.

For the most part, chondrites have solar composition, but some chondrites differ in having fewer volatile elements.

A *volatile* substance is relatively fast to melt and then evaporate with increasing temperature whereas *refractory* material is relatively slow to melt and then evaporate. Conversely, on cooling, refractory materials condense out and solidify before volatiles. Another way to put it is that the refractory elements will condense out at relatively high temperatures, whereas the volatiles will remain gaseous until the temperature decreases further.

The *abundance* (formally defined as the ratio of the number of atoms of an element relative to those of another element) of volatile elements is one of the chief discriminators among groups of meteorites, and this includes chondrites.

The CAIs, which contain refractory elements (such as Ca, Al, Re) are further subdivided in their rare-earth-element composition. In general, the CAIs have refractory minerals (see Chapters 7 and 8 in Milone and Wilson (2014)], such as:

• Perovskite	(CaTiO_3)
• Melilite	$[\text{Ca}(\text{Al}, \text{Mg})(\text{Si}, \text{Al})_2\text{O}_7]$
• Spinel	$(\text{MgAl}_2\text{O}_4)$
• Hibonite	$[\text{Ca}(\text{Al}, \text{Mg}, \text{Ti})_{12}\text{O}_{19}]$

These minerals follow a *condensation sequence*, in the sense that they condense from vapor at successively lower temperatures in the order listed above, but the overall composition suggests episodes of condensation and melting in a complex early solar system environment. (For a general discussion of minerals, see Chapter 7, Milone and Wilson 2014).

15.2.2 Carbonaceous Chondrites

Grady (2000) listed 561, of which 36 are falls. Some of the groups are labeled CI, CV, CM, CO. The “C” in the groups *CI*, *CM*, *CO*, and *CV* means *carbonaceous*, i.e., containing carbon in great abundance. The second letter indicates the prototype: “I” of “CI” stands for *Ivuna*; the “V” of “CV”, for *Vigrano*; the “M” of “CM” for *Migei*; and the “O” of “CO” for *Ornans*. Additional groups are CH (“H” for High-Fe), CK (“K” for *Karroonda*), and CR (“R” for *Renazzo*). Numbers may be added after “C” to indicate petrologic class. Hybrid classifications, such as C2M and CM2, are also used.

The NHM (2002) update for the Grady catalogue listed the following numbers of discoveries for these groups: CI, 5; CM, 193; CO, 103; CV, 60; CH, 14; CK, 93; CR, 86. Although they have increased since then, the numbers provide relative frequency information.

The CO and CV types contain metallic iron; the CI and CM types do not; but the CI have more iron than most other chondrites, in a form such as FeO. The CI also contain more volatiles than most others [in Wasson’s (1985) classification, this is the *volatile-rich clan*]; for example, the water content may reach 10 % (Taylor 1992, p. 109). The CV group (half of the *C3* grouping) is the most refractory-rich (Wasson’s *refractory-rich clan*), followed by the CO and CM groups (Wasson’s *minichondrule clan*, and the other half of the *C3* and the *C2* groupings, respectively) which are about equal in refractory element composition. All contain iron in relatively large amounts compared to non-carbonaceous chondrites.

One of the most well-known of the carbonaceous meteorites is the *Allende*, observed to fall in 1969 from a bright bolide depositing an estimated tonne (1,000 kg) of material over a *strewn field* ellipse of $\sim 50 \times 10$ km size near the Mexican village Pueblito de Allende. The fall occurred while preparations were under way to study the rocks to be returned from the Moon, and the Allende furnished a large sample of extraterrestrial test material, essentially uncontaminated by terrestrial weathering and chemical processes. Petrologically, Allende (CV3) belongs to perhaps the most primitive class³ (3), and thus can, in principle, give the best evidence for conditions in the early solar system.

Calcium-aluminum-rich inclusions (CAIs) in a matrix interspersed with chondrules provide a rich mixture of information about the nature and origin of the source of the Allende material.

The abundance ratio $^{87}\text{Sr}/^{86}\text{Sr}$ is significantly lower than the value for achondrites and because this ratio increases with time, the carbonaceous chondrites may represent the oldest datable material in the solar system.

Figure 15.1 show the two faces of a slice of the Allende meteorite as photographed under slightly different lighting conditions. Notice the CAI and chondrules as well as the appearance of the fusion crust.

³ Classes (1) and (2) seem to have been subject to aqueous alteration, and (4) and (6) to alteration by heating.



Fig. 15.1 A small slice of the Allende meteorite, viewed from both sides, with each side photographed under slightly different lighting conditions. Note the fusion crust, the round chondrules, the surrounding matrix, and the white calcium–aluminum-rich inclusions (CAI). Photographs by E. F. Milone

15.2.3 Ordinary Chondrites

The *ordinary chondrites* are the most common among both the chondrites and all meteorites. Grady (2000) listed 14,265 ordinary chondrites, of which 739 are falls. They are further divided according to iron content, (parentheses gives the percentage of this type among the ordinary chondrites):

- “H” for high (48.8 %)
- “L” for low (43.6 %)
- “LL” for low iron and low metal (7.3 %)

The chondrule compositions in these meteorites are more or less uniform across subgroups. This means that the matrix and inclusions are the main sources of the differences. Ordinary chondrites are further separable from the carbonaceous chondrites and other meteorites on the bases of oxygen isotope and carbon content.

15.2.4 Enstatites

The *enstatite chondrites* contain an abundance of enstatite, MgSiO_3 . “EH” and “EL” indicate high and low iron content, respectively. These two subgroups have similar oxygen isotope ratios and solar volatile composition, but have different bulk properties, suggesting different parent bodies, though probably from the same general region of the solar nebula. Grady (2000) listed 201 enstatite meteorites of which 15 are falls. NHM (2002) lists the following: E, 47 (including 0 falls); EH, 128 (including 8 falls); and EL, 42 (including 7 falls).

15.2.5 *The R Group*

Finally, the *R* or *Rumurutiite* group is named after the *Rumuruti*, which fell in Kenya in 1934; it is the only fall in the group of 19, listed by Grady (2000). NHM (2002) shows 31 and no further falls. They are similar in bulk chemical composition to H chondrites, but with twice as much sulfur and roughly half the carbon content. They are also distinguished by isotope composition.

15.2.6 *Former Members, from the IAB Clan*

Finally, among Wasson's clans was one that included a slightly differentiated group of chondrites (currently classified, according to Hutchison (2004, p. 25) as a group of "primitive achondrites") and silicate inclusions of similar isotopic composition in a group of iron meteorites (IAB/IICD).

15.2.7 *Origins of the Chondrites*

The state of the iron is a further clue to the origins of these meteorites. The ratio of reduced iron (in the form of metallic iron or bound in FeS) to oxidized forms (in silicates and Fe_3O_4), and the abundance ratio $\text{FeO}/(\text{FeO} + \text{MgO})$ indicate the relative abundance of iron oxides.

As we have indicated for the carbonaceous chondrites, within each group there are six or sometimes seven stepped petrologic classes of each of ten bulk properties (see Table 15.3). On this basis, the Allende meteorite is classified as *CV3* (or, more precisely, *CV3.2*), the Bruderheim meteorite as *L3*, and the Abee chondrite as *EH4*.

The degree of *equilibration* (equilibration means that grains of the same material, such as olivine or orthopyroxene, have the same composition) may indicate (in an inverse manner) how closely a particular chondrite resembles the original solar nebula. Wasson suggests that the least equilibrated, Type 3 chondrites of the *CO*, *CV*, *H*, *L*, *LL*, and *EH* groups, most closely approximate those conditions, and therefore may represent the earliest primordial solar system material.

What distinguishes these types of meteorites is that they do not seem to have formed in a body larger than ~100 km in diameter, because their parent body did not melt, permitting the materials in it to *fractionate* or *differentiate* (separate out).

It has been estimated that the heat of accretion and radioactive isotopes combined could produce the fully melted condition—if the accretion body were large enough. Recall, however, from Chaps. 8 and 13 that the Earth's moon and several other moons, both large and small, have provided many surprises; it is quite possible, therefore, that there is a piece of the chondrite puzzle that has not yet been found. Nevertheless, as we have noted, the radioisotope studies suggest the

chondrites to be truly ancient, and this is reinforced by the ratio of the number of atoms of deuterium to those of hydrogen (D/H). In chondrites, D/H varies, from $\lesssim 10^{-5}$ (for some CM2 chondrites) to above terrestrial (for, e.g., some CV3 and LL chondrites). Compare these to the ratio for the interstellar medium (ISM), $\sim 1.5 \times 10^{-5}$, or that of terrestrial hydrogen (1.6×10^{-4}). Although an ISM composition is expected of the early solar nebula that eventually became the solar system, fractionation clearly occurred. The separation of isotopes depends on the reaction rates, and these depend on the rms speeds and thus on temperature and the atomic weights of the atoms within the compounds. Thus, D/H was higher in the inner solar nebula and decreased with distance from the Sun as the solar wind blew away more H than D atoms. But the D/H ratio of water that condensed during accretion beyond ~ 5 au (the “snow line”) increased with increasing distance. See Bertotti et al. (2003, pp. 229ff) for a fuller discussion.

The chondrules, and the CAIs, however, are relatively depleted in volatiles, therefore they must have been formed when the sun had already begun to disperse the volatile gases of the early solar system.

A number of theories for the origin of chondrules have been put forward:

1. Impacts on surfaces of planets
2. Impacts on chondrite parent bodies
3. Collisions between molten proto-planets
4. Volcanism on planetary surfaces
5. Solar nebula origin

The fifth is the least objectionable on the basis of available evidence and isotopic data. In this model, grains in the disk melted through one or more mechanisms to create the chondrules. Such mechanisms could be flares in the T Tauri stage of the Sun’s development, electrical discharges, and radioactive heating due to short-lived radioisotopes. Subsequent accretion with grains to form a matrix, the CAIs, along with metals, sulfides, minerals, and perhaps ices, formed the chondritic parent bodies. The accretion process is the primary process. Subsequent pressure and temperature variations produced different degrees of metamorphism, the secondary processes. Finally, shock events and weathering constituted tertiary processes. The earlier classification methods, emphasizing physical color and texture, tended to result in classification based on the shock and weathering events more than the origins and metamorphoses.

Now we begin an examination of the differentiated meteorites.

15.3 Differentiated Silicate-Rich Meteorites

The hypothesis mentioned in Sect. 15.1 that the suggested sources of differentiated silicate-rich (DSR) meteorites are the crusts and mantles of molten parent bodies has not been proven. It is, however, a logical and widely accepted hypothesis. In addition to accounting for the existence of irons, stony-irons, and that group of stony meteorites known as *achondrites*, there is still more evidence, which we present below. We discuss the achondrites and the stony-irons first, and then the irons.

DSR meteorites are usually found brecciated, i.e., they formed from rock that had become fragmented or crushed. If the breccias are of the same rock type, they are said to be *monomict*; if from different rock types, *polymict*. Additionally Hutchison (2004, p. 48) describes two other types of brecciated rock, *genomic* and *regolith* breccias. The former contains more than one petrologic class but only one chemical group. The latter are polymict breccias that formed on the surfaces of small bodies (no atmosphere), irradiated by solar wind, and consolidated by micro-meteorites and impact products.

15.3.1 The Igneous Clan

Grady (2000) listed 610 achondrites (including the *aubrites*, which we describe separately, later), of which 78 are falls.

Wasson links the five types: *howardites*, *eucrites*, *diogenites*, *mesosiderites*, and *pallasites* in the *igneous* clan. Their oxygen isotope ratios are similar. The compositions are consistent with origin in a common parent body. Hutchison, however, combines the first three into a petrogenetic association called *HED*. His other associations include the *main group pallasites*, the *mesosiderites*, the *IIIAB iron association*, and the Martian *SNC* meteorites. Other achondrite groups are the *acapulcoites*, *angrites*, *brachinites*, *lodranites*, and *winonaites*.

The characteristics of the HED meteorites are:

- **Eucrites.** Meteorites with typically ~3:7 mixture of anorthitic plagioclase and low-Ca pyroxene. Eucrites are often subdivided into basaltic and cumulate eucrites, the former having solidified from surface or near-surface lavas and the latter from more deeply-buried cumulates. Most basaltic eucrites are either monomict or polymict breccias, but the structure of unbrecciated examples in fact often resembles vesicular (i.e., frothy) terrestrial basaltic lava.
- **Diogenites.** Orthopyroxene- and/or olivine-rich meteorites, almost all either monomict or polymict breccias. The vast majority are rich in orthopyroxene (85–100 vol%), with the remaining components being 0 to a few vol% olivine (<1/3 of diogenites contain olivine), 0 to a few vol% plagioclase (primarily anorthitic), and other minerals (Beck and McSween 2010). The olivine, when present, is found as brecciated fragments. Some diogenites, however, have a strongly ultramafic composition, containing up to 68 vol% olivine; a few (“dunitic diogenites”) are >90 vol% olivine. Both composition and crystal size (up to 5 cm diameter) are consistent with solidification and fractional crystallization in the lower crust of a differentiated, terrestrial body.
- **Howardites.** Polymict breccias that have the same dominant rock type as the eucrites and diogenites.

Among the “stony-iron” meteorites, the major types are the *mesosiderites* and the *pallasites*. According to NHM (2002), the number of these two types of stony-irons is 120, with only 12 falls. Of these, mesosiderites number 68, of which seven are falls, and pallasites, 52, of which five are falls.

However they are classified, the *mesosiderites* and the *howardites* appear to be regolith breccias—and the *mesosiderites* may have originated on the impacted stony surfaces of bodies which were impacted by an iron meteorite (or vice versa).

The *pallasites* have equal parts of metal and olivine (the predominant mineral in the Earth's mantle) and thus may represent material at the interface of a mantle and core. A few pallasites of unusual composition may have resulted from large impact events on the surfaces of previously undifferentiated bodies. See Table 15.4.

15.3.2 Other DSR Meteorites

15.3.2.1 Aubrites

The *aubrites* consist almost entirely of the pyroxene mineral *enstatite* (MgSiO_3). In *aubrites*, the oxygen isotope ratios, among other properties, are similar to those in *EH* and *EL* chondrites, suggesting a link among these groups. NHM (2002), the updated, on-line version of Grady (2000), gives 47 of these, of which 9 are falls.

15.3.2.2 Ureilites

Ureilites are mixtures of ultramafic silicates and carbon-rich material. The carbon material contains diamonds, created through very high shockwave-driven pressure. The *ureilites* have oxygen isotope ratios similar to those of *CM* chondrites. There are 92 of these known, 5 of which are falls, according to NHM (2002).

15.3.2.3 SNC (Martian Meteorites)

Another group of DSRs includes the *Shergotty-Nakhla-Chassigny* (SNC) clan. NHM (2002) listed 37 SNC meteorites, of which 4 were falls: Shergotty (India, 1865); Zagami (Nigeria, 1962); Nakhla (Egypt, 1911), and Chassigny (France, 1815). The characteristics of these groups are as follows.

1. Shergottites have the minerals *pigeonite* [$\text{Ca}_x(\text{Mg}, \text{Fe})_{(1-x)}\text{SiO}_3$, with $x \leq 0.1$], *augite* (pyroxenes with some alumina), *maskelynite* (a type of plagioclase glass), and *magnetite*. The four earliest known specimens are:

The *Shergotty* meteorite, itself

Zagami (the largest, at 23 kg) with very similar composition (see Fig. 15.2)

ALH A77005 (collected by expedition “A” in the Alan Hills, Antarctica)

EET A79001 (collected by expedition “A” in the Elephant Moraine region, Antarctica)

2. Nakhellites are composed of *augite* (~79 % by weight!), *olivine*, *feldspars*, and *magnetite*. There are three known specimens:



Fig. 15.2 Fragments of the Zagami DSR achondrite Shergottite fall near Zagami, Nigeria, October 3, 1962. Noble gas analysis suggests a Martian source. Photograph by E. F. Milone

Nakhla (the most massive: 40 kg)

Lafayette (Indiana)

Governador Valadares (Brazil)

3. One known chassignite, *Chassigny*, a fall, of 4 kg weight, is primarily *olivine* (88.5 %), with small amounts of *augite*, *plagioclase* $[(\text{NaSi})_x(\text{CaAl})_{(1-x)}\text{AlSi}_2\text{O}_6$, with $0.1 \leq x \leq 0.9$], and *orthopyroxene* $[\text{Ca}_x(\text{Mg}, \text{Fe})_{(1-x)}\text{SiO}_3$, with $x \leq 0.5$]
4. One of the SNC meteorites is *ALH 84001*. Grady (2000) listed it as a separate subgroup, *orthopyroxenite*, and summarized the work done on this meteorite in this excerpt (we indicate omissions with ellipses):

“...collected ... 1984–85 ... originally classified as a diogenite. It was not recognised as an unusual additional member of the SNC group until 1993. It differs from the other martian meteorites in age, composition, texture and shock history, but has an oxygen isotope composition characteristic of the SNCs. ... Almost every aspect of the mineralogy, petrography, mineral chemistry, chronology and origin of ALH 84001 has been the subject of heated debate, fuelled in 1996 by an announcement that structures identified within the carbonate assemblages had been identified as a possible fossilised martian biota. ... As of December 1999, the biological, or otherwise, origin of the features had not been conclusively established to the satisfaction of the entire scientific community ... ALH 84001 is a fascinating meteorite in other ways. It has a much older crystallisation age [4.50–4.56 Ga] ... than the other SNC meteorites, and has a complex chronology and shock history ... multiple shock events.”

ALH 84001 is classified now as an *SNC orthopyroxenite* (the bulk is *orthopyroxene*, $(\text{Mg}, \text{Fe})\text{SiO}_3$). Elemental and isotopic composition of volatiles in its embedded glasses indicates a Martian origin. It is among the oldest known rocks on Earth. After its ejection from Mars in an impact event, it orbited the Sun for ~ 16 My before falling as a meteorite, $\sim 13,000$ y BP. It has 3.6–4.0 Gy old carbonate globules and associated magnetite crystals in fissures, some of which are purported to be biogenic in origin (by magnetotactic bacteria), and it has PAHs (for Polycyclic Aromatic Hydrocarbons—multiple aromatic carbon rings) also of possible Martian biogenic origin.

As noted, SNC meteorites include volatile abundances and, for most, isotope ratios consistent with an igneous origin on Mars. Figure 15.2 shows tiny fragments



Fig. 15.3 Lunar meteorite MET 01210. A basaltic regolith breccia, it was collected in 2001 in the Meteorite Hills, Antarctica, and described in the Antarctic Meteorite Newsletter, 27, No. 1, February 2004. It is composed mainly of very-low-titanium crust, which can be seen at the right. It is basically a collection of stone and mineral clasts or fragments in a glassy matrix (Righter and Gruener 2012). NASA photo, cf. http://curator.jsc.nasa.gov/antmet/lmc/M7_MET01210.pdf

(the scale is labeled in cm) of the Zagami fall, as authenticated by the Bethany Sciences Company. An ejection age of 2.81 million years was obtained by Eugster et al. (1997). Drake et al. (1994) and Bogard and Garrison (1998) found evidence of Martian composition. The degree of oxidation suggests possible oxidation of upwelling (mantle) magma through water-bearing material in the crust; exposure to an aqueous environment has also been suggested for ALH 84001. The case for Martian origin of the SNC meteorites has been made by Treiman et al. (2000).

15.3.2.4 Lunar Meteorites

Taylor (1992, Table 3.12.3, p. 132) provides a list of 11 lunar meteorites. Seven are classified as anorthositic breccia, two as basaltic breccia, and two as Mare gabbro. NHM (2002) listed 31 lunar meteorites, all of them finds. Finally, The Lunar Meteorite Compendium (Righter and Gruener 2012) as of late 2012 listed and illustrated 60 lunar meteorites, grouping 14 as basalts, 34 as feldspathic regolith breccia, and 18 as “mingled.” MET 01210, a lunar meteorite discovered in 2001 in the Meteorite Hills region of Antarctica, is made up primarily of very-low-titanium (VLT) basalt material (Zeigler et al. 2005; Joy et al. (2006)). It is shown in Fig. 15.3.

15.3.2.5 Candidate for a Mercury Meteorite

A possible meteorite from Mercury, NWA (Northwest Africa) 7325, was found in Morocco in 2012, although its origin is uncertain at present writing (Irving et al. 2013). It has a medium-grained plutonic igneous texture with a high

abundance of magnesian mafic silicates and calcic plagioclase, indicating crystallization at depth as a plagioclase-rich cumulate from a mafic magma. Its composition is different from other known meteorites, but its very low iron content is consistent with surface rocks on Mercury (which are known from remote sensing), as are the Al/Si and Mg/Si ratios. The Ca/Si ratio is much too high compared to Mercurian surface rocks, but this could be a result of solidifying at depth.

Regardless of the origin of NWA 7325, meteorites from Mercury should be found on the Earth (Gladman and Coffey 2009). Impact speeds on Mercury's surface are the highest in the solar system: 20–70 km/s (sometimes >80 km/s for comets), or 5–20 times Mercury's escape speed. These speeds are a result of Mercury's large orbital speed (~48 km/s) and the very high speeds with which objects perturbed from the asteroid belt cross Mercury's orbit. For comparison, the corresponding values for the Earth are 15–30 km/s, or 1.5–3 v_{esc} . Most ejecta that escape Mercury's gravitational field (which effectively means reaching distances >100 planetary radii) follow Mercury-like orbits around the Sun and eventually re-accrete onto Mercury. However, a small fraction is ejected directly into Earth-crossing orbits and another small fraction is gravitationally accelerated into Earth-crossing orbits by close encounters with Mercury and Venus.

15.3.2.6 Tektites

Lastly, we mention the *tektites*; these have terrestrial composition (except for a few that are “spiced” by meteoritic composition) and are almost certainly the crystallized droplets of impact melts which were strewn away from a terrestrial crater site. In at least one case (the *moldavite tektites* found in Bohemia), the associated crater is known (the Ries Crater in SE Germany).

15.4 Iron Meteorites

Irons are distinguished basically by their metallic crystalline structure:

- *Hexahedrites* consist entirely of single crystals of *kamacite* $[Fe_x-Ni_{(1-x)}$, with $0.96 \leq x \leq 0.93]$, in cubic structures. The nickel content of hexahedrites is always in the narrow range 53–58 mg/g.
- Most irons are *octahedrites*. *Kamacite* crystals grow in lamellae along four sets of crystalline planes of *taenite* $[Fe_x-Ni_{(1-x)}$, with $0.5 \leq x \leq 0.8]$. Exposed on a planar surface, the sections of kamacite lamellae appear as “kamacite bands.” The widths of these bands (“bandwidths” in Table 15.5) form a sequence from <0.1 to >3.3 mm. Etching with a dilute solution of nitric acid in ethyl alcohol of a polished plane section reveals the discontinuities in the octahedral structure; the structure is called the *Widmanstätten figures* or *patterns*. The longer the cooling time, and the lower the nickel content, the thicker the lamellae.

Fig. 15.4 A fragment of the Henbury iron meteorite find from the Northern Territory, Australia, 1931, according to the Bethany Sciences Company. It is classified as a medium octahedrite (IIAB), with bandwidth 0.9 mm. Photograph by E. F. Milone



- FeS and carbon inclusions are sometimes found in some groups (for example, IAB and IIICD irons).
- *Plessites* are mixtures of fine kamacite and taenite which have nickel concentrations exceeding ~12 %, and the iron meteorites which have plessite as well as a few fine kamacite spindles are called *plessitic octahedrites*. If they consist entirely of plessite, they are called *ataxites*, meaning “structureless.” This is a misnomer, based on poor-resolution microscopy; viewed with adequate resolution, small “sparklets” of kamacite can be seen in such rocks.

A principal classification tool for the irons is the relative abundance of certain trace elements, especially gallium, germanium, and iridium. The presence of iridium (Ir) in the Cretaceous-Tertiary interface (the geologic periods terminating and beginning the Mesozoic and Cenozoic Eras, respectively) suggested to Luis Alvarez (1980) that a large meteoritic impact was responsible for the demise of the dominant planetary life forms of the era.

Whereas the Ga and Ge concentrations usually occupy a narrow range for a particular find, the Ir concentration varies widely, but the correlation with Ni shows a slope which can help in further identification.

The results of the different iron groups suggest that different groups originated in different parent bodies, which were located at different distances from the Sun. Typical cooling rates for the iron meteorites are ~1 K/My, which suggests parent bodies of the order of 300 km radii. Reheating may have occurred in some cases; and the cooling age is relative only to the most recent time of heating, when presumably all other clocks were set/reset.

A fragment of the Henbury iron (IIAB) medium octahedrite, a 1931 find from the Northern Territory, Australia, as authenticated by Bethany Sciences, can be seen in Fig. 15.4.

Figure 15.5 displays two faces of a fragment of the Sikhote-Alin (eastern Siberia) fall of February 12, 1947, authenticated by the Bethany Sciences



Fig. 15.5 A fragment of the Sikhote-Alin meteorite fall in eastern Siberia, February 12, 1947. It is classified a Type IIAB iron, coarsest octahedrite, with bandwidth of 9 mm. The circumstances of this spectacular meteoritic fall are described by Fessenkov (1955). Photograph by E. F. Milone

Company. This iron meteorite is classified as Type IIAB, coarsest octahedrite, with bandwidth 9 mm. Fessenkov (1955) describes the “meteorite shower” of this impressive fireball fall.

15.5 Ages and Origins of Meteorites

The age of a meteorite may be reckoned in a number of ways. The meaning of “age” depends, in a sense, on the technique used to determine it. Fundamentally the age refers to the time elapsed since the material came together in a common, closed system. However, time elapsed since a certain major alteration took place can also qualify as an “age,” hence, there are radiometric or radiogenic, gas-retention, cosmic-ray exposure, and terrestrial “ages.”

15.5.1 Radiometric Ages

The most important ages are *radiometric*, i.e., determined from the decay of radioactive isotopes. The idea is this:

If N_D is the number of daughter atoms at some instant of time t , N is the number of radioactive nuclei producing the daughter atoms at time t , and if N_{D0} is the number of daughter atoms at some initial moment of time t_0 , then

$$N_D = N_{D0} + \alpha N \left(e^{\lambda(t-t_0)} - 1 \right) \quad (15.1)$$

where α represents the fraction of parent radioisotope atoms that will decay into this particular (“radiogenic”) daughter and λ is the decay constant. In the case of $^{87}\text{Rb} \rightarrow ^{87}\text{Sr}$, $\alpha = 1$; using the element name to represent numbers of atoms, and

Table 15.6 Radionuclides for age determinations^a

Parent	Daughter	Decay constant	Half-life
⁴⁰ K	⁴⁰ Ar, ⁴⁰ Ca	$5.55 \times 10^{-10} \text{ y}^{-1}$	1.25Gy
⁸⁷ Rb	⁸⁷ Sr	1.42×10^{-11}	48.8
¹⁴⁷ Sm	¹⁴³ Nd	6.54×10^{-12}	106.
¹⁷⁶ Lu	¹⁷⁶ Hf	1.94×10^{-11}	35.7
¹⁸⁷ Re	¹⁸⁷ Os	1.52×10^{-11}	45.6
²³² Th	²⁰⁸ Pb, ⁴ He	4.95×10^{-11}	14.0
²³⁵ U	²⁰⁷ Pb, ⁴ He	9.85×10^{-10}	0.704
²³⁸ U	²⁰⁶ Pb, ⁴ He	1.55×10^{-10}	4.47

^aData from Wasson (1985, Table E-1), Kirsten (1978), and Hutchison (2004, Table 6.1, p. 157)

normalizing to the numbers of atoms of the stable (“non-radiogenic”) isotope ⁸⁶Sr, we have:

$$\frac{{}^{87}\text{Sr}}{{}^{86}\text{Sr}} = \left(\frac{{}^{87}\text{Sr}}{{}^{86}\text{Sr}}\right)_0 + \left(\frac{{}^{87}\text{Rb}}{{}^{86}\text{Sr}}\right) \left(e^{\lambda(t-t_0)} - 1\right) \quad (15.2)$$

If the parent melt is uniformly-mixed, then at the time of solidification the initial ratio $({}^{87}\text{Sr}/{}^{86}\text{Sr})_0$ will be the same for all minerals condensing from the melt. However, different minerals may contain different initial amounts of ⁸⁷Rb, so over time the ⁸⁷Sr/⁸⁶Sr ratio increases at different rates for different minerals. At any given instant of time, (15.2) is a linear equation in the isotope abundances, so a plot of the abundance ratio $({}^{87}\text{Sr}/{}^{86}\text{Sr})$ vs. $({}^{87}\text{Rb}/{}^{86}\text{Sr})$ for different minerals in the meteorite then yields two important results:

1. The zero point, $({}^{87}\text{Rb}/{}^{86}\text{Sr}) = 0$, gives the initial ratio
2. The slope yields a constant dependent on the time and the decay constant (or *half-life*, to which it is related⁴)

The decay constant of ${}^{87}\text{Rb} = 1.42 \times 10^{-11} \text{ y}^{-1}$, corresponds to a half-life, $\tau_{\frac{1}{2}} = 48.8 \text{ Gy}$. Other radionuclides and their daughters are given in Table 15.6.

The mean age of the samples of different falls yields $t \approx 4.5 \times 10^9 \text{ years}$. The radiometric ages of some ${}^{87}\text{Rb} \rightarrow {}^{87}\text{Sr}$ determinations are given in Table 15.7, from Wasson (1985).

⁴The half-life is the time interval $(t - t_0)$ at the end of which $N/N_0 = \frac{1}{2}$, where N and N_0 are the numbers of radioactive nuclides at instants t and t_0 , respectively. It is related to the decay constant λ , as follows: the decay equation is

$$\frac{dN}{N} = -\lambda dt \quad (15.3)$$

the integration of which yields $N = N_0 e^{-\lambda(t-t_0)}$ so that $\ln(N/N_0) = -\lambda(t - t_0)$ and so when $N/N_0 = 1/2$, $\lambda(t - t_0)_{\frac{1}{2}} = \ln 2$. Then $(t - t_0)_{\frac{1}{2}} = 0.693/\lambda$, or $\lambda = 0.693/(t - t_0)_{\frac{1}{2}}$ and we obtain,

$$N = N_0 \exp \left[-0.693(t - t_0)/(t - t_0)_{\frac{1}{2}} \right] \quad (15.4)$$

Table 15.7 Selected meteoritic age determinations^a

Method	Meteorite	Class	Age (gy)	Ratio = (⁸⁷ Sr/ ⁸⁶ Sr)
⁸⁷ Rb– ⁸⁷ Sr	Indarch	EH4	4.39 ± 0.04	0.7005 ± 0.0009
"	Tieschitz	H3/L3.6	4.53 ± 0.06	0.69880 ± 0.00010
"	Soko-Banja	LL4	4.45 ± 0.02	0.69959 ± 0.00024
"	Allende ^b	CV3	4.5	0.69877 ± 0.00002
"	Norton County	Aub	4.39 ± 0.04	0.7005 ± 0.0004
"	Juvinas	Euc	4.50 ± 0.07	0.69898 ± 0.00005
"	Kapoeta ^c	How	4.44 ± 0.12	0.69885
"	Colomera	IIE	4.51 ± 0.04	0.69940 ± 0.00004
"	Kodaikanal	IIE	3.7 ± 0.1	0.713 ± 0.020
"	Nakhla	SNC	1.34 ± 0.02	0.70232 ± 0.00006

^aMainly from Wasson (1985, Table III-1, pp. 52–53) and Hutchison (2004, p. 73)

^bIsochrone is not well defined in Rb-Sr analysis; age from Pb-Pb analysis is 4.553 ± 0.004 Gy (Tatsumoto et al. 1976)

^cDifferent parts of the breccia yield different values, presumably metamorphic ages, in the range 3.5–3.8 Gy

The effect of age on the ratios of (15.2) is illustrated in Fig. 15.6, with data drawn from a variety of meteorites of different origins in the solar system; these include an iron meteorite, several chondrites, and two achondrites (a mesosiderite and a nakhlite). Note that in a very few cases the ages are below the ages of the solar system by significant amounts. It is not known exactly how the cosmic “clocks” were restarted in these cases. In the case of Nakhla and the shergottites (where a “whole-rock,” Sm-Nd isochron indicates that $(t - t_0) \equiv \Delta t = 1.3$ Gy, while Rb-Sr, referred to (Taylor 1992, p. 132) as “internal isochrons,” gives ~180 My, the very low age attributed to shocks) it is reasonable to suppose that these have something to do with the impact event that caused its ejection from Mars.⁵ This is supported by

⁵The question about the origin of the SNC meteorites aroused considerable controversy in past decades. Wasson (1985, p. 79) states that the escape velocity (in m/s) from planetary bodies with the density of ordinary chondrites, ~3,500 kg/m³, is:

$$v_{esc} \approx 1.4R \quad (15.5)$$

where R is the planetary radius in meters. In general, this quantity is:

$$v_{esc} = v_{parabolic} = [2GM/R]^{\frac{1}{2}} = [(8\pi G/3)\rho R^2]^{\frac{1}{2}} \quad (15.6)$$

which indeed yields ~1.40 for the constant in Wasson’s equation, with his assumptions. Actually, the density of Mars is ~3,900 kg/m³, so the appropriate coefficient for Mars is ~1.48. He asserts that if an object impacts a planetary body at several times the escape velocity, the mass of the ejecta will exceed the mass of the object. Mars’ escape velocity is 5.01 km/s and it has a mean orbital velocity of about 24 km/s (26.5 at perihelion), so that an object approaching at a high enough velocity to result in ejection of Martian material would need a velocity within ~15 km/s of this orbital speed. Such a difference is certainly plausible. In any case, the chemical evidence for Martian origin is fairly persuasive, and taken together the arguments support a Martian origin for the SNC meteorites.

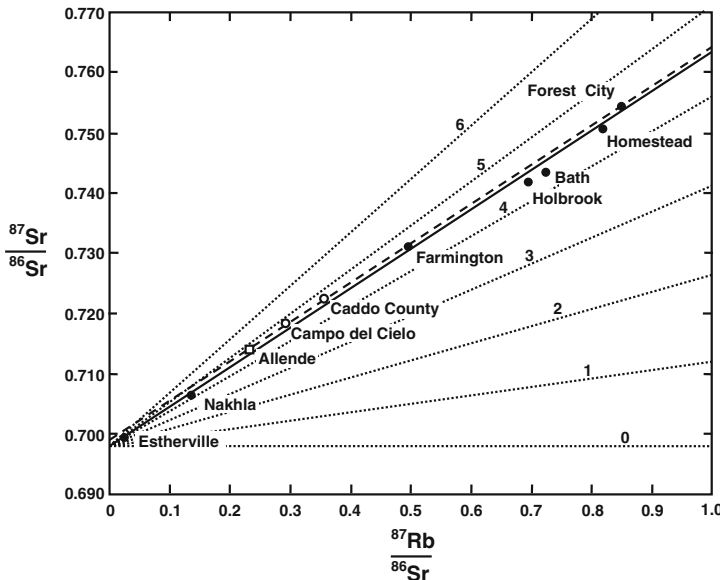


Fig. 15.6 Measured values of $^{87}\text{Sr}/^{86}\text{Sr}$ vs. $^{87}\text{Rb}/^{86}\text{Sr}$ for seven stony meteorites (solid dots, Pinson et al. 1965, Tables 1 and 2), a whole-rock sample from the Allende CV3 carbonaceous chondrite (open square, Shimoda et al. 2005), and a mineral sample from each of two iron meteorites (open circles, Liu et al. 2003). The dotted lines are isochrons labeled with ages in units of 10^9 years measured from when the material in the meteorites solidified from the solar nebula and was fully-mixed with $(^{87}\text{Sr}/^{86}\text{Sr})_0 = 0.698$, the value derived from the stony meteorites (Pinson et al. 1965). The solid dots lie close to a mean isochron of age $\sim 4.5 \times 10^9$ year (solid line). The dashed line shows the 4.5×10^9 year isochron for $(^{87}\text{Sr}/^{86}\text{Sr})_0 = 0.699$, the value derived from Allende and the iron meteorites (Shimoda et al. 2005, Liu et al. 2003), and provides a better fit to these meteorites. Figure inspired by Wood 1968, Fig. 4–1, p. 58

an analysis of the shergottite NWA 5298 (Moser et al. 2013) that targeted the mineral baddeleyite (ZrO_2), and yielded three critical dates: crystallization at 4 Gy BP, a probable volcanic eruption at -187 ± 33 My, and a shock-producing oblique impact and ejection, 22 ± 2 My ago.

15.5.2 Gas Retention Ages

When a gas is the daughter atom, the analyses yield *gas retention ages*. In Table 15.6, the processes are:

- $^{40}\text{K} \rightarrow ^{40}\text{Ar}$
- $^{232}\text{Th} \rightarrow ^4\text{He}$
- $^{235,238}\text{U} \rightarrow ^4\text{He}$

Sometimes the ages are the same as for the less volatile daughters, often they are younger, but none have been found to be older.

According to Wood (1968, p. 61), at temperatures above about 250 K, ^{40}Ar is able to diffuse out of mineral lattices and escape, but at lower temperatures it remains trapped.

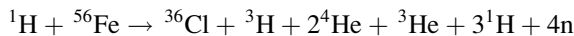
For helium, the temperature of escape must be much lower, perhaps 100 K or less.

Thus gas retention ages indicate the interval since the last instant that the meteoroid was subjected to temperatures above these limits. Passage through the atmosphere is not such a time, because the penetration depth for the ablation temperatures is a few centimeters at most for iron, and millimeters for chondritic meteorites.

15.5.3 Cosmic Ray Exposure Ages

Another type of dating is revealed by *cosmic ray exposure* ages. Cosmic rays (CR) bombard all exposed surfaces (and the Earth, where, however, they usually collide with atmospheric particles creating cascading cosmic ray showers of decreasing energies as they approach the surface of Earth).

On fully exposed surfaces, high energy particles may collide with nuclei of atoms, creating spallation products. For example, a high energy cosmic ray proton may collide with an iron nucleus to produce:



where n refers to neutrons. The resulting nuclides are called *cosmogenic nuclei*.

Cosmic rays may penetrate to a meter or so of rocky material, creating *spallation* products which are radioactive. These decay over time, but more are created through subsequent CR collisions. Wood (1968, p. 65) suggests that the best dates are obtained from comparison between two cosmogenic nuclei, one of which is radioactive, the other stable. The abundance of the stable isotope will increase with time, the other will approach a steady-state after a few half-lives, where the decrease due to decay is matched by the increase due to continuing exposure. Such a pair is ^{38}Ar , which is stable, and ^{39}Ar , which is radioactive with a half-life of only 325 years. The CR exposure ages tend to be much shorter than $^{87}\text{Rb} \rightarrow ^{87}\text{Sr}$ radiogenic and even gas-retention ages. This supports the idea that meteoroids are the results of repeated collisions and subsequent fragmentations, so that material once protected from cosmic rays by overburden subsequently becomes exposed to cosmic radiation.

15.5.4 Case Study: The Zagami SNC Basaltic Shergottite

This meteorite was a fall (October 3, 1962), so its *terrestrial age* (present year – fall year) is known exactly. The recovered mass of this meteorite is 18.1 kg, of which 13.74 % is iron (in all forms). A microscopic cross-section shows dark gray

pyroxene grains and light plagioclase glass in the form of maskelynite (Hutchison 2004, Fig. 9.8, where cross-sections of other SNC meteorites are also shown). Zagami contains amphibole (a group of hydrated silicate minerals; see Milone & Wilson 2014, Sect. 7.3), indicating formation in an aqueous environment, possibly a Martian “hydrosphere” (Karlsson et al. 1992), but an environment with 10 % of the water content of Earth. Studies of shock-melted pockets and veins of impact glass in Zagami indicate that the noble gas, and nitrogen and argon, isotope ratios resemble those of the Martian atmosphere; Zagami is enriched in ^{15}N and ^{40}Ar relative to ^{14}N and ^{36}Ar (Marti et al. 1995). The glasses were formed under a pressure of $\sim 31 \pm 2$ GPa and a temperature of ~ 220 °C. The isotope ^{17}O is enhanced relative to Earth rocks, and this, too, is the case for Mars. The oxides have yielded the amount of free oxygen (the *fugacity*) in the environment in which the basalt originated, presumably magma from the Martian mantle. From the noble gases, an ejection age (from Mars) of 2.81 My has been derived (Eugster et al. 1997). Similar ejection ages have been found for two other basaltic shergottites: Shergotty and QUE 94201, suggesting a common ejection event for all three. Bogard and Garrison (1999) obtained an Ar–Ar age of 242 My. Finally studies of the U–Pb, Rb–Sr, and Sm–Nd isotopes (Borg et al. 2005) have yielded two ages: a formation age of $4,550 \pm 10$ My and a *differentiation age* (the interval between Mars’ formation and the differentiation in a molten environment of the meteorite source material) of 163 ± 4 My, consistent with a *crystallization age* (the interval between source formation and the partial melting event that produced the rock in the crust of Mars).

15.6 Other Sources of Evidence for Meteoritic Origins

The evidence briefly summarized here strongly implies that meteorites of different composition originated in different places in the solar system, and that the differentiated meteorites have undergone further modification.

Isotope evidence further supports their disparate origins. The quantity $\delta^{17}\text{O}$ (‰) is defined as

$$\delta^{17}\text{O} (\text{\textperthousand}) \equiv 1000 \left[\left(\frac{{}^{17}\text{O}}{{}^{16}\text{O}} \right)_{\text{sample}} - \left(\frac{{}^{17}\text{O}}{{}^{16}\text{O}} \right)_{\text{standard}} \right] / \left[\left(\frac{{}^{17}\text{O}}{{}^{16}\text{O}} \right)_{\text{standard}} \right] \quad (15.7)$$

and similarly for the $\delta^{18}\text{O}$ (‰) quantity. These quantities (called “del” values) are usually normalized to SMOW (*standard mean ocean water*). The $\delta^{17}\text{O}$ (‰) vs. $\delta^{18}\text{O}$ (‰) plot provides a discriminant for various groups of carbonaceous chondrites, and for DSRs. This suggests that different conditions prevailed at different places in the original solar nebula to allow different degrees of fractionation. The del values that are given for the principal groups of DSRs in Table 15.4, for some irons in Table 15.5, and plotted in Fig. 15.7 [based on data from Clayton and Mayeda (1984, 1996) and Clayton et al. (1991)], illustrates this well.

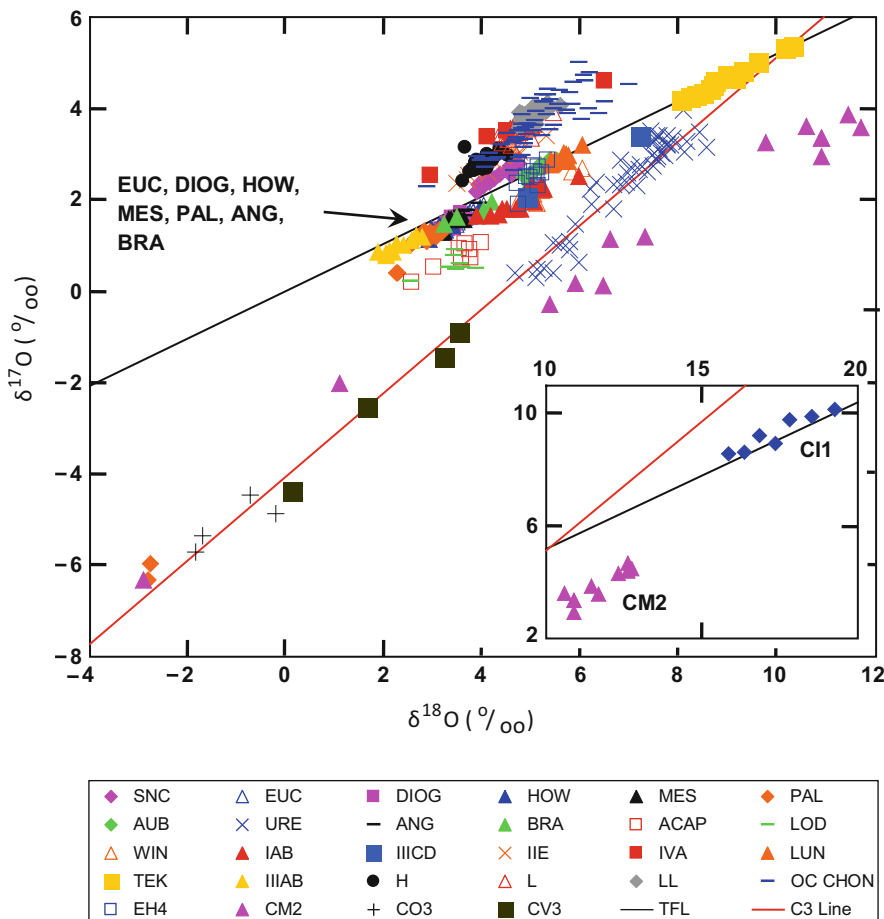


Fig. 15.7 Fractional oxygen isotopes of various meteorites, the Earth–Moon, and two lines: one approximating the theoretical mixing line for anhydrous minerals and the other the terrestrial fractionation line TFL. This sort of evidence points to heterogeneous origins in the early solar nebula and proto-planetary disk. The ratios of oxygen isotopes plotted are from analyses by Clayton and Mayeda (1984, 1996), and Clayton et al. (1991). The terrestrial fractionation line has a slope 0.52; the “C3 line” is a linear fit to the combined CO3 and CV3 data with slope 0.918 and zero point −4.036; similarly, the carbonaceous chondrite chondrules lay along a line with a slope ~1. These lines typify the distributions of the meteorites, and suggest that exchanges between at least two reservoirs (Clayton 1993; Wasson (1985, esp. pp. 68–74, 215–217), involving gas and dust components of the solar nebula, had occurred. The heating source is not yet agreed on. **Legend:** Achondrites: ACAP = Acapulcoites; ANG = Angrites; AUB = Aubrites; BRA = Brachinites; DIOG = Diogenites; EUC = Eucrites; HOW = Howardites; LOD = Lodranites; LUN = Lunar; SNC = Martian (Shergottites, Nakhltites Chassigny, Orthopyroxene); URE = Ureilites; WIN = Winonaites. Stony-irons: MES = Mesosiderites; PAL = Palasites Chondrites; OC CHON = Ordinary chondrite chondrules. TEK = tektites (Earth). For more chondrite group identifications see Table 15.2 (recall that numbers indicate petrologic classes), and for the irons’, see Table 15.5

When the values for the Allende CAIs are examined in this way, they fall along a line, and this line has a different slope from the fractionation line of terrestrial materials. Some of the Allende chondrules fall along the same line, others do not. Relations that involve del values of isotopes of other elements, for example $\delta^{48}\text{Ca}$ vs. $\delta^{50}\text{Ti}$ or $\delta^{30}\text{Si}$ vs. $\delta^{18}\text{O}$, similarly provide discriminants of this sort. For further details, see Taylor (1992, p. 101) and Wasson (1985).

Deuterium/hydrogen abundance is another indicator of origin, but its main value is in demonstrating the fractionation of hydrogen in the early solar nebula. Jupiter and Saturn have D/H ratios that most resemble the interstellar medium ($\sim 10^{-5}$). Those of Titan, Comet Halley, and Earth are all $\sim 2 \times 10^{-4}$; those of Uranus and Neptune lie somewhere in between.

15.7 Parent Bodies and the Asteroids

The pre-terrestrial encounter orbits of meteoroids that were sufficiently well observed as meteors (including some that were recovered as meteorite falls) demonstrate that these objects originate in the asteroid belt. They can be assumed to be, therefore, products of the “asteroid mill” which fragments larger bodies into smaller ones through multiple collisions over long periods of time. Chemical, mineralogical, textural, and isotopic studies of meteorites suggest that those we have found on the Earth come from $\sim 100\text{--}150$ different parent bodies (Burbine et al. 2002). In very few cases, however, can individual meteorites be linked to specific parent bodies with reasonable certainty.

15.7.1 *The Discovery of Ceres*

The initial detection of the asteroid (1) Ceres was made by Giuseppe Piazzi (1746–1826) on the first night of the nineteenth century (January 1 1801). The discovery was later realized to fit perfectly in the scheme of Johann Daniel Titius von Wittenberg (1729–1796) and published by him in his 1766 translation of a book on astronomy by Charles Bonnet. The relation went relatively unnoticed, however, until it was mentioned in a book by Johann Elert Bode (1747–1826) in 1772. Up to the discovery of Uranus, little was made of the progression, at least outside of Germany, as Bode himself complained. In retrospect, astronomers realized that Uranus fit the law well and, on this basis, Baron Francis X. von Zach (1754–1832), court astronomer at Gotha, began a campaign to look for the missing planet at 2.8 au, as predicted by the Titius-Bode law (see Milone and Wilson 2014, Chapter 1). In 1800 he had organized the sky into 24 zones, had organized a network of astronomers to search each one, and had just sent out the maps to the searchers, when announcement came of Piazzi’s discovery.

Thus, the “law” appeared to be verified, and indeed it was used in the theoretical calculations of the location of the trans-Uranian planet later to be called Neptune.

Note, however, that two of these three discoveries were purely serendipitous; the “predictions” were irrelevant. The third, that of Neptune, was basically accidental because the Titius-Bode relation predicted an incorrect distance for Neptune (cf. Sect. 12.4 for a justification for this statement).

Titius himself had suggested that there might be undiscovered *satellites* of Mars in the gap between Mars and Jupiter (“satellites” presumably on the grounds that a major planet would have been known from antiquity). Kepler had expressed a similar idea with respect to the location of undiscovered planets in this and other spaces.

The orbit was not determined when first observed because Piazzi was not able to observe it over a sufficiently large arc, as required with the methods of the day, before it came into conjunction with the Sun.

However, Karl Friedrich Gauss (1777–1855) invented a method by which an orbit could be computed from just three observations of position and velocity. Moreover, he invented a new computational scheme—the method of least squares—with which calculations could be expedited and parameters determined optimally (Gauss, 1809).

With this method Gauss produced an ephemeris for Ceres; armed with this, von Zach and Heinrich Wilhelm Matthäus (or Matthias) Olbers (1758–1840) relocated Ceres, and thus confirmed the discovery. Ceres was seen to have a semi-major axis of 2.767 au.

The mystery of the fourth “planet” was solved, but another mystery was encountered! Other new “planets” in this region began to be discovered: Pallas was discovered by Olbers on March 28, 1802; Juno in 1807, by Karl Ludwig Harding (1765–1834); and Vesta by Olbers in 1807. The law had predicted a planet, but due to some cataclysm, there were only fragments of the original planet left—according to a theory put forward by Olbers.

It was nearly 40 years, however, before more of the planetary “fragments” would be discovered—a very puzzling time in astronomy. More were indeed found, though, and the number of discoveries has been increasing ever since.

15.7.2 Nomenclature

In 1802, William Herschel, the discoverer of Uranus, had suggested that Ceres and Pallas presented such distinctly stellar appearances at the telescope, even under high magnification, that they would be best designated as “asteroids,” from the Greek *ἀστεροειδῆς*, “star-like.” This suggestion was not accepted at the time, but with more and more faint object discoveries, the term gradually came into vogue for these planetary “fragments.” Other names which have been used are, “minor planets,” “planetoids” and “small bodies.” In current usage, given the huge range of sizes and brightnesses, “asteroids” tends to be more frequently used than “minor

planets,” and “planetoids” has become rare. All three designations tend to be applied only to small bodies in the asteroid belt and the inner solar system. Thus, only the term “small bodies” is applied to all such objects everywhere in the solar system. Frequently, comets are included among them, as in the JPL Small-Object Database Browser (<http://ssd.jpl.nasa.gov/sbdb.cgi>).

Before a name for a “small body” is assigned (by the IAU), a provisional designation is given: year followed by a half-month code, and by another letter indicating the order of discovery in that half-month, similar to the (current) provisional naming of comets. When the discovery is confirmed, a sequence number and (possibly) a name are assigned. Thus (1) Ceres, (2) Pallas, etc., for established asteroids but the provisional designation 1999 CB (second to be discovered in the interval February 1–15 of the year 1999), for a more recently discovered object.

The main asteroid belt is a region between the orbits of Mars and Jupiter, roughly centered at 2.8 au from the Sun. As of July 2013, nearly 581,000 Main Belt asteroids had been discovered. There are many groupings of asteroids in this region; we describe the principal families in Sect. 15.7.3. Several gaps in the distribution of asteroids with semi-major axis (the *Kirkwood gaps*), as well as peaks, demonstrate the existence of commensurabilities with the planets, especially Jupiter. As a consequence, the main belt asteroids are separated by resonances into groupings as follows:

Grouping	Range (au)	Resonances
● Main Belt I	(2.06 < a < 2.50)	4:1 Jupiter, 3:5 Mars
● Main Belt II	(2.50 < a < 2.82)	3:1 Jupiter
● Main Belt III	(2.82 < a < 3.27)	5:2 Jupiter, 2:5 Mars
● Main Belt IV	(3.27 < a < 3.65)	2:1 Jupiter

In addition, there are somewhat less prominent gaps at 2.700, 2.955, 3.025 au, corresponding to period resonances with Jupiter (J) and Mars (M) of 8:3 (J) and 3:7 (M); 7:3 (J) and 3:8 (M); and 9:4 (J) and 1:3 (M), respectively. A host of other, still less-cleared gaps implies the existence of many more, if weaker, resonances. Of course the Kirkwood gaps do not translate into large empty spaces in the belt because all of these bodies are moving on eccentric orbits and are continuously perturbed into different Keplerian orbits; they represent only local minima in the frequency distribution of the asteroids’ mean distances.

The population of small bodies in the inner and outer solar system as of June 11, 2013 can be seen in Figs. 15.8 and 15.9, respectively. The innermost population is seen in Fig. 1.2 of Milone & Wilson (2014). Asteroids are continually being discovered, in both near and distant parts of the solar system.

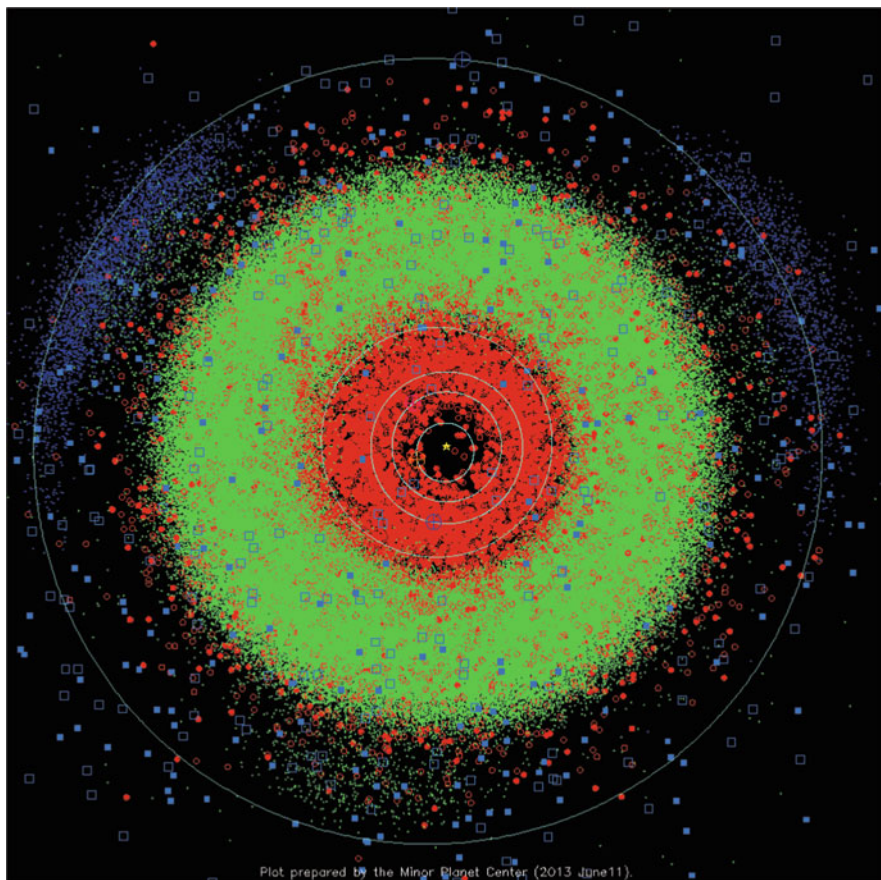


Fig. 15.8 The inner solar system with its small bodies, as it appeared on June 11, 2013. Mercury, Venus, Earth, Mars and Jupiter are indicated by *large open symbols* on their orbits. Numbered and well-observed objects are shown as *solid circles*; others are *open circles*; Main Belt Minor Planets (*green*) are seen between the orbits of Mars and Jupiter. Minor planets with perihelia $q < 1.3$ au are in *red*. Jupiter's Trojan asteroids (*dark blue*) cluster along Jupiter's orbit (*the outer circle*), centered on stations preceding and following Jupiter by 60° . The Hilda group of asteroids (Sect. 15.7.3) lies between the Trojans and the main belt asteroids, and opposite Jupiter as well as along the lines joining these three places. Courtesy Gareth Williams (Minor Planet Center, SAO, Cambridge, MA)

Large numbers of objects have been detected in the outer solar system since the 1990s, and the realization that the Pluto–Charon system has more in common with them and the large icy moons of some of the giant planets has thrown the nomenclature into some confusion. The meaning of the term “planet,” in particular, has required considerable discussion and although the IAU has resolved the issue for the moment, increasing numbers of substellar objects are being discovered both

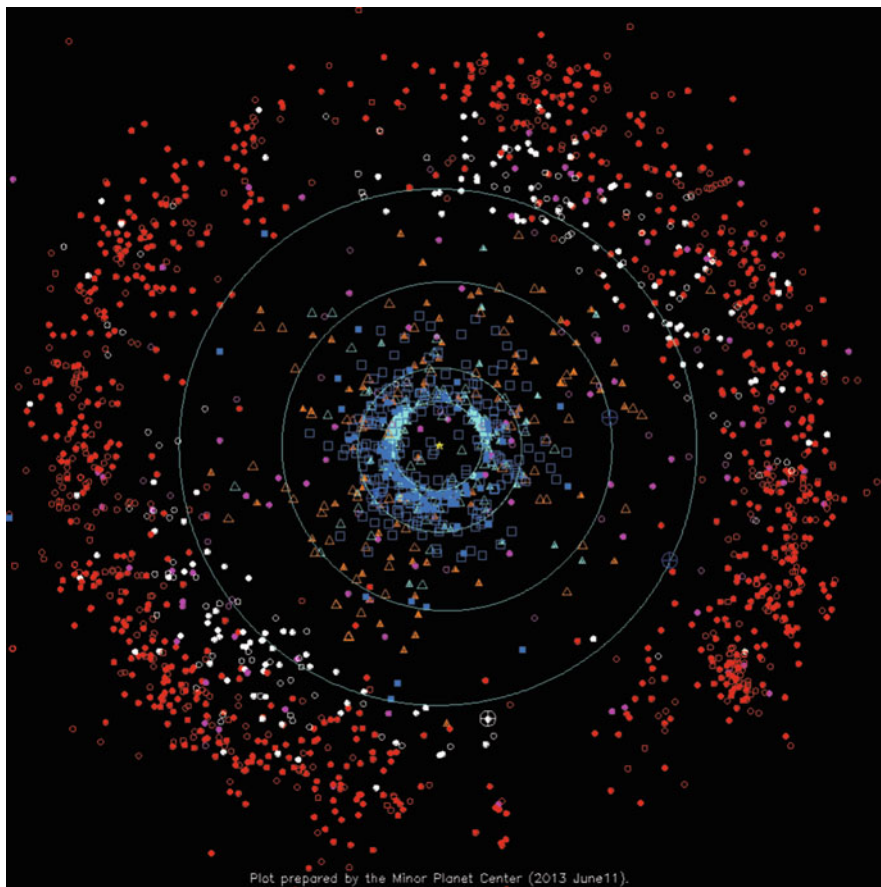


Fig. 15.9 The outer solar system as it appeared on June 11, 2013. Jupiter, Saturn, Uranus, and Neptune are represented as *dark open circles* on their orbits; Pluto (*white open symbol*) is seen to the right of the 6 o'clock position, just outside Neptune's orbit. Objects observed over more than one revolution are shown by *solid symbols*, otherwise by *open symbols*. Among the objects depicted are: Centaurs (*orange triangles*); Plutooids/Plutinos (*white circles*); “Classical” objects (*red circles*); numbered periodic comets (*filled light blue squares*) and other comets (*unfilled*); and unusual high-eccentricity objects (*cyan triangles*). The vernal equinox is to the *right*, and direct orbital motion is *counterclockwise*. Courtesy Gareth Williams (Minor Planet Center, SAO, Cambridge, MA)

within and outside the solar system. As they become better studied, these objects may well inspire further refinement of what we mean by the word “planet.”

Between Jupiter and Neptune, we find “*Centaurs*,” thought to have escaped from the *Kuiper Belt* [or the *Edgeworth-Kuiper Belt*, to honor not only Gerard Peter Kuiper (1950–1973), but also the Scottish astronomer Kenneth Edgeworth (1880–1972) who independently suggested versions of it], located between ~30 and ~50 au from the Sun. Bodies more distant than Neptune are called,

unsurprisingly, “*Trans-Neptunian Objects*.” The best known object of this group is the dwarf planet Pluto. Pluto is also trapped in a 3:2 resonance⁶ with Neptune; any object sharing this trait is a “*Plutino*.” The term “*Cubewano*” has been applied to an object in the main Edgeworth-Kuiper Belt, not trapped in a planetary resonance and with a typical distance of ~41 au.

15.7.3 Groups of Asteroids and Families of Orbits

Asteroids exhibit a wide variety of orbital elements and physical properties but many share similarities of various kinds, in addition to their direct orbits around the Sun. The term *family*, or *Hirayama family*, refers to asteroids whose orbital characteristics match so closely that they are, following work initially carried out by Kiyotsugu Hirayama (1918a, b), believed to share a common origin: from either an impact on or a complete disruption of a single parent body (Bendjoya and Zappalà 2002). The word *group* is a more general term referring to asteroids that share some characteristic or characteristics, such as orbital characteristics or spectral characteristics or both, but membership in a group does not signify a common origin. For example, the Hilda *group* (Fig. 15.8) is made up of all asteroids that are in a 3:2 resonance with Jupiter, regardless of origin. Within the Hilda group, two collisionally-born dynamical families have been identified (Brož and Vokrouhlický 2008): the Hilda *family*, associated dynamically with (153) Hilda, and the Schubart family, associated dynamically with (1911) Schubart. Hirayama identified only five families: *Koronis* (Fig. 15.11), *Eos*, *Themis*, *Flora* (Fig. 15.10), and *Maria*; Brouwer (1951) further divided Flora into five.

For the most part, asteroids are found in the region between Mars and Jupiter. These are the *main belt asteroids*, which can be seen as a thick torus in Fig. 15.8 and in Fig. 1.2 in Milone and Wilson 2014.

Among the orbital groups, somewhat arbitrarily separated primarily on the basis of semi-major axis and/or range of distance from the Sun, are the *Hilda group* (Fig. 15.8), the *Trojan* asteroids, associated with Jupiter (see below and Fig. 15.8), and the inner solar system asteroids that are grouped according to their orbital dispositions with respect to the Earth’s orbit. The inner groups (with number of members as of July, 2013) are:

- *Amors*, “Mars-crossers” (4,165 asteroids) which approach the Earth’s orbit but do not cross it, i.e., they have perihelia outside the Earth’s aphelion distance. Examples include the asteroids (1221) Amor, (1943) Anteros, (2061) Anza, (433) Eros (see Fig. 15.12), (1915) Quetzalcoatl, (2608) Seneca, and (2004) VB61

⁶This is the ratio of the sidereal orbital periods: $3P_{\text{Neptune}} = 2P_{\text{Plutinos}}$.

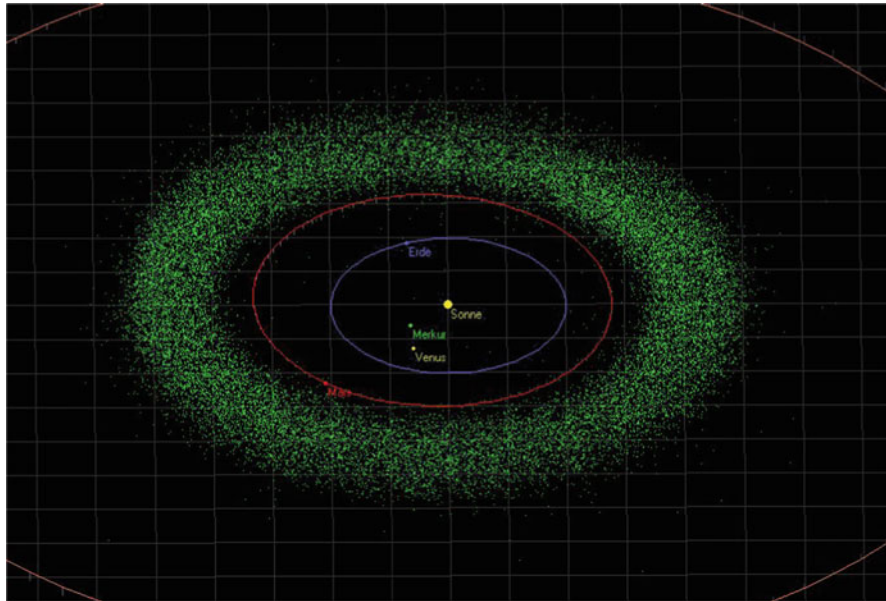


Fig. 15.10 The large Flora family of asteroids, one of the original Hirayama families, cropped from an *Easy-Sky* demo image, based on data from the MPC; courtesy Matthias Busch

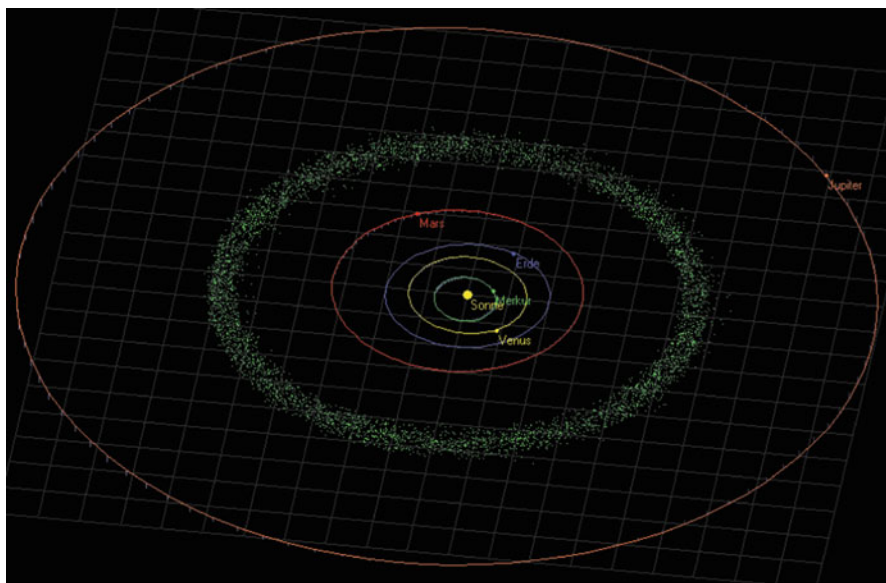


Fig. 15.11 The distribution of the Koronis family of asteroids, from an *Easy-Sky* demo image, based on data from the MPC; courtesy Matthias Busch

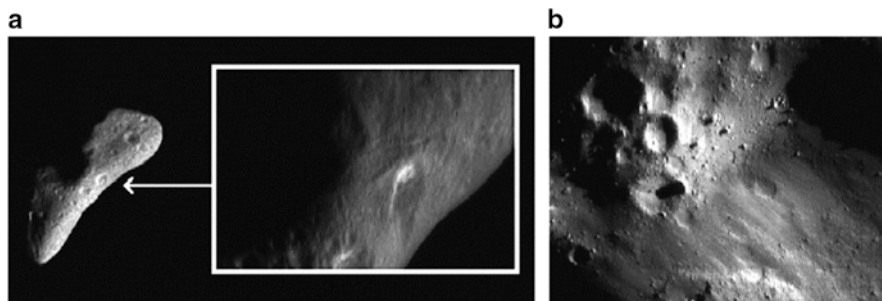


Fig. 15.12 Asteroid (433) Eros, as viewed from the NEAR Shoemaker spacecraft. (a) A view from February 12, 2000 at a distance of 1,748 km and higher resolution view (*inset*) from February 29, 2000 at a distance of 283 km. NASA/JPL image PIA02492. (b) A swath of Eros, only 1.4 km across as seen from an altitude of 35 km, imaged on January 7, 2001. NASA/JPL image PIA03132. Credit: NASA/JPL/JHUAPL (Applied Physics Laboratory of John Hopkins University)

- *Apollo* group (4,948 asteroids) which are “Earth-crossers,” with $a > 1.00$ au and $a(1-e) < 1$ au. Examples are: (2101) Adonis, (1862) Apollo, (1865) Cerberus, (1864) Daedalus, (2212) Hephastos, (3200) Phaethon, (1566) Icarus, and (2004) WS2
- *Atens* (766 asteroids), which have $a < 1.00$ au, and most, though not all, have their aphelia, $a(1+e)$, greater than 1 au. Examples: (2062) Aten, (2340) Hathor, (3554) Amun, (5381) Sekhmet, and (2004) WC1.

In addition to these groups, asteroids in the inner solar system can be placed into a general group known as “Near-Earth Asteroids” (or NEAs) and a somewhat more specific group known as *Potentially Hazardous Asteroids* (PHAs). The latter either cross Earth’s orbit or approach within 0.05 au, and have a minimum brightness, given in terms of the *absolute magnitude*, H , of 22. In this planetary science context, H is defined as the V magnitude the object would have if seen at opposition and at a distance of 1 au from the Earth. This H has also been expressed for passbands other than V and is so indicated with a subscript, e.g., H_B , for the B passband. N.B.: this “ H ” is *not* the Johnson photometric passband centered around 1.64 μm in the near infrared part of the spectrum. This planetary “absolute magnitude” should also not be confused with stellar *absolute magnitude*, the magnitude of a star at a 10 pc (for *parsecs*, each equal to about 3.26 light years) distance.

The MPC linked page <http://www.minorplanetcenter.net/iau/lists/Sizes.html> gives the corresponding sizes of asteroids for representative values of H for three albedos: $A = 0.50$, 0.25, and 0.05. If it is an icy body ($A = 0.50$), an object with $H = 22$ implies a 75 m diameter; if rocky ($A = 0.05$ or 0.25), $H = 22$ implies a diameter of 240 or 110 m, respectively.

The families include the following (with defining orbital elements; the semi-major axes are given in au):

● Nysa	($a \approx 2.43, e \approx 0.17, i \approx 3^\circ$)
● Koronis	($a \approx 2.85, e \approx 0.05, i \approx 2^\circ$)
● Eos	($a \approx 3.01, e \approx 0.07, i \approx 10^\circ$)
● Themis	($a \approx 3.13, e \approx 0.15, i \approx 1^\circ$)
● Flora	($a \approx 2.25, e \approx 0.15, i \approx 4.7^\circ$)

One of the Flora family “asteroids,” P/2013 P5, has been found to have grown multiple dust tails, and is considered to be a member of a small group called the *Main Belt Comets*. The tails are thought to be caused by rotational ejection due to low gravity and high spin (Jewitt et al. 2013). The Flora family are associated with LL (ordinary) chondrites (see Sect. 15.2.3).

Thanks to the use of clustering algorithms, such as the Hierarchical Clustering Method (HCM, Zappala et al. 1990), the Wavelet Analysis Method (WAM, Bendjoya et al. 1991), or the D criterion (Lindblad and Southwork, 1971), dozens of additional families have been identified, including: Eunomia, Vesta, Hygiea, Dora, Adeona, Lydia, and Massalia. The Vesta family (Sect. 15.7.5) is an obvious addition, because of unique composition as well as orbital similarities. Its mean elements are: $a \approx 2.37, e \approx 0.10, i \approx 6.7^\circ$. However, not all authorities are in agreement with what generally constitutes a real family. Classification by reflectance spectroscopy does not necessarily solve disagreements involving composition differences among alleged family members because fragments of the same parent body or bodies may present considerably different properties (if, for example, they were differentiated through some fractionation process). Nevertheless, the existence of families suggests a limited number of parent bodies.

Examples of more heterogeneous groups of asteroid are these:

● Hungaria	($1.2 < a < 2.00$)
● Phocaea	($a \approx 2.4, e \approx 0.25, i \approx 23^\circ$)
● Hilda	($a \approx 4, e \approx 0.15, i \approx 8^\circ$)
● Trojans (Jovian)	($a \approx 5.2, e \lesssim 0.1, i \lesssim 20^\circ$)

The Trojan asteroids are trapped at the stable Lagrangian points, L_4 and L_5 , $\sim 60^\circ$ from Jupiter’s location, and in a 1:1 resonance with Jupiter. At present writing, the MPC lists 3,891 asteroids that are trapped at L_4 and 1,994 at L_5 . We note also that Trojans have been detected around Mars [(5261) Eureka, (101429) 1998 VF31, (311999) = 207 NS2, and 2001 DH47 at L_5 ; and (121514) = 1999 UJ7 = 2002 AC180 at L_4]. (At this writing three of the Mars Trojans had sequence numbers but no formal names yet and one had not yet been assigned a number.) One has been discovered around Earth [an Apollo asteroid, 2010 TK7, at L_4]. Neptune has been found to have six at L_4 and three at L_5 . Finally, 2011 QF99 has been discovered to oscillate around Uranus’s L4 point (Alexandersen et al. 2013). Their simulations suggest that in ~ 1 My, this object will escape its co-orbital status and become a Centaur (Sect. 14.7; Fig. 15.9).

The number of known outer solar system objects is increasing rapidly. The asteroidal objects referred to as (2060) Chiron and (944) Hidalgo lay well beyond the main belt. Chiron has been identified as a Centaur, from its location, and as a

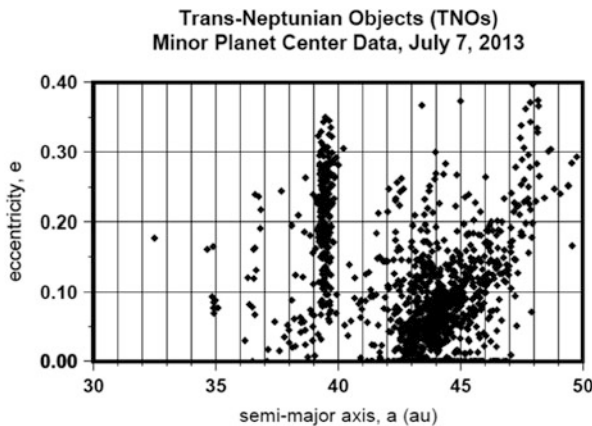


Fig. 15.13 The plot of eccentricities vs. semi-major axes for the Trans-Neptunian Objects of the solar system according to the list on the Minor Planet Center’s website in July, 2013. Note the large range of eccentricities for the objects between 39 and 40 au, characteristic of the “Plutinos.” The higher eccentricity objects beyond this distance are members of the “scattered” population

cometary body (P95/Chiron) on the basis of its coma observed during perihelion passage. In addition, observations of the Centaur (5145) *Pholus* indicate that it has a cometary surface; it is not impossible that all Centaurs are in fact cometary bodies and that they are related to the short-period comets. What is clear is that they are icy bodies.

We have already mentioned in Sect. 13.4.2 the “trans-Neptunian objects” (TNOs), a group of which (the *Plutinos*) are locked into a 3:2 orbital resonance with Neptune. As of 2002, there were 400 TNOs known and by 2007, 1,000; at present writing, 1,259 TNOs have been identified by the MPC. More discoveries are likely. Jewitt and Luu (2000) estimated that the number of such objects with diameters $\gtrsim 100$ km is of order $\sim 10^4$. They are seen in Fig. 15.9. Figure 15.13 where the TNO eccentricities are plotted against their semi-major axes, identifies the Plutinos at 39–40 au. The “Kuiper Belt objects” (KBOs), as they are commonly called, but for consistency should be renamed Edgeworth-Kuiper Belt Objects, or EKBOs, have been further identified as “classical” or “cold” and “scattered” or “excited” or “hot” KBOs. The classical variety is characterized by the upper limits, $i < 32^\circ$ inclination and $e < 0.2$, whereas the “excited” objects may have these values pumped up through interactions with the outer gas giants. Centaurs and scattered disk objects together number 364 at present. See Morbidelli and Brown (2004) for further discussion of current theories of the KBOs origin and evolution.

A collisional family of TNOs has now been recognized: the Haumea family ($a \approx 43.0$, $e \approx 0.13$, $i \approx 27^\circ$), thought to be the result of a collision which also produced Haumea’s moons. At present writing, the family has six members.

15.7.4 Dimensions and Masses of Asteroids

15.7.4.1 Asteroid Dimensions and Albedo

The diameters of asteroids can be determined from ground-based observatories in any of four ways, depending on distances from the Earth and from the Sun. All of them require knowledge of the distance. These methods are:

- *Micrometer measurement* of the angular diameter
- *Stellar occultation*
- *Radiometric determination*
- *Doppler radar observations*
- Because asteroids are neither particularly large nor close to us, there are few reliable *micrometer measures* of them. The relevant relation, is:

$$\theta = D/r \quad (15.8)$$

where θ is the angular diameter, D is the asteroid diameter, and r its distance.

The largest asteroid is Ceres, with a diameter of ~950 km and a mean opposition distance from Earth of ~1.8 au; therefore, the angular diameter of Ceres is only $206,265 \times 950 / (1.8 \times 1.5 \times 10^8) = 0.73$ arc-sec. The angular resolution of any telescope is $1.22 \lambda/d$, where λ is the wavelength (0.55 μm for green light) and d is the diameter of the telescope mirror or objective lens, in the same unit. Thus, in order to obtain a resolving power of 0.1 of this value or ~ 0.07 arc-sec, a telescope of only ~1.9 m is needed, but this is a theoretical value. Atmospheric seeing at even the best sites is limited to ~0.2 arc-sec; consequently, even this relatively easy asteroid observation is less precise than ~25 % for a single ground-based observation. To be sure, N observations can beat down the noise by the factor \sqrt{N} , and the use of adaptive and, even more usefully, active optics can greatly improve the precision of such measurements. But the usefulness of this technique is clearly limited. From space, however, the theoretical limit is approached more easily.

- *Stellar occultations* are a more promising technique, but here the observer cannot choose the targets and is at the mercy of the motions of the asteroid and the direction of the asteroid's shadow. Each occultation also provides a single cross-section of the asteroid, so determination of the shape of a non-spherical asteroid requires observation of several occultations. Nevertheless, David W. and Joan Bixby Dunham and colleagues have encouraged worldwide participation in occultation observations, with improved astrometry of asteroid and star positions as an important byproduct, since these must be improved for each event so that observers in various parts of the world can be alerted. Up to 1998, 170 ground-based occultations had been studied. By 2001, more than 280 had been observed thanks in part to the HIPPARCOS astrometric satellite mission, and, by 2007, this number had reached ~1,000 (Dunham, private commun., 2007). A spectacular example of the success of the technique

was the high precision determination of the size and shape of (2) Pallas by Dunham et al. (1990).

The positions and thus the orbits of asteroids are becoming better and better known thanks to the operations of the Minor Planet Center, in Cambridge, MA. The MPC encourages worldwide participation of asteroid observations and position reduction of CCD observations. The immense distance of a star means that the light rays are essentially parallel, and the length of the shadow of the asteroid is, very closely, the size of the asteroid; so a measurement of the duration of the event and the orbital speed of the asteroid at the time of the occultation and its distances to the Sun and Earth suffice.

- The *radiometric method* requires optical and infrared photometry so that both the radius and the bolometric albedo can be determined. The method is approximate, but one can pick one's targets—sufficient light gathering power, and thus size, for the available telescope being the only requirement. The relevant relations are as follows. The light reflected by the asteroid at all wavelengths is:

$$\ell_{\text{refl (bol)}} = [\mathcal{L}_\odot / (4\pi r_\odot^2)] a A \quad (15.9)$$

where \mathcal{L}_\odot is the solar luminosity, r_\odot is the asteroid's distance from the Sun, a is the cross-sectional area, and A is the bolometric albedo. Observations made from the Earth are diluted by the inverse square law, and they are made in discrete passbands of effective wavelength λ . Setting $a = \pi R^2$, where R is an effective radius, the reflected flux observed at the Earth is:

$$\mathfrak{I}_{\text{refl}(\lambda)} = [\ell_{\text{refl}(\lambda)} / (2\pi r_\oplus^2)] = [\mathcal{L}_{\odot,\lambda} / (8\pi r_\oplus^2 r_\odot^2)] R^2 A_\lambda \quad (15.10)$$

where $\mathcal{L}_{\odot,\lambda}$, and $\ell_{\text{refl}(\lambda)}$ are the solar luminosity and the reflected power in the passband,⁷ and r_\oplus is the asteroid's distance from the Earth. Note that the factor 2π in the denominator of the left-hand side of (15.10) is not strictly correct because the phase may not be exactly 0; however this factor is more accurate than 4π because the reflection is not isotropic. Now the solar luminosity at each wavelength is known, $\mathfrak{I}_{\text{refl}(\lambda)}$ is observed, and the distances known, so the quantity $R^2 A_\lambda$ is found. An integration of the flux of (15.10) over all wavelengths gives:

$$\mathfrak{I}_{\text{refl (bol)}} = \int \frac{\ell_{\text{refl}(\lambda)}}{(2\pi r_\oplus^2)} d\lambda = \int \frac{\mathcal{L}_{\odot,\lambda}}{8\pi r_\oplus^2 r_\odot^2} R^2 A_\lambda d\lambda = \text{const } AR^2 \quad (15.11)$$

If the integration can be carried out adequately, the product of A and R^2 can be found.

⁷These quantities made may be thought of as incremental amounts per wavelength interval, thus: $I_\lambda = \Delta I / \Delta \lambda$.

The factors can be separated with the help of infrared observations. The radiation which is not reflected is absorbed. The absorbed power must be reradiated, as noted earlier. The emitted light at the asteroid is:

$$\ell_{\text{em (bol)}} = f\pi R^2 \sigma T^4 = [\mathcal{L}_\odot / (4\pi r_\odot^2)] a(1 - A) \quad (15.12)$$

where f is a factor that takes the rotation of the object into account (for example, the factors 4 or 2 in the rapid vs. slow rotator models and somewhere in between for intermediate cases.), and T is the effective equilibrium temperature of the asteroid.

We observe passband fluxes in the infrared also (despite the use of the term “bolometer” for detectors in the thermal infrared), because careful corrections for terrestrial atmospheric absorption and emission must be made, and these are best done when the wavelength range over which the observations are made is stipulated. Then (for rapidly spinning asteroids) the emitted flux observed at the Earth is:

$$\mathfrak{I}_{\text{em } (\lambda)} = [\ell_{\text{em}(\lambda)} / (4\pi r_\oplus^2)] = [\mathcal{L}_{\odot, \lambda} / (16\pi r_\oplus^2 r_\odot^2)] R^2 (1 - A_\lambda) \quad (15.13)$$

where we have used $a = nR^2$. Integrating,

$$\begin{aligned} \mathfrak{I}_{\text{em (bol)}} &= \int \frac{\ell_{\text{em}(\lambda)}}{(4\pi r_\oplus^2)} d\lambda = \int \frac{\mathcal{L}_{\odot, \lambda}}{16\pi r_\oplus^2 r_\odot^2} R^2 (1 - A_\lambda) d\lambda \\ &= \text{const}' (1 - A) R^2 \end{aligned} \quad (15.14)$$

Define quantities χ_1 and χ_2 , such that

$$AR^2 = \chi_1 \quad (15.15)$$

and

$$(1 - A)R^2 = \chi_2 \quad (15.16)$$

Then,

$$(1 - A)/A = \chi_2/\chi_1 \quad (15.17)$$

whence:

$$A = \chi_1 / (\chi_1 + \chi_2) \quad (15.18)$$

and R is found from either (15.15) or (15.16).

Thus, in principle, the radii and the albedos are determinable. In practice, phase and asteroid shape effects complicate the observations and thus the analyses.

- *Radar observations* have been successfully applied to asteroids that approach Earth closely enough to be able to reflect sufficient power back to Earth for Doppler ranging analyses. The small asteroid (4769) Castalia was found to be double in this way.

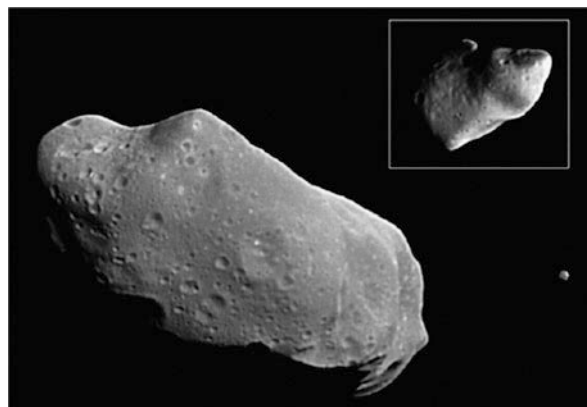


Fig. 15.14 Main panel: (243) Ida, an S-class asteroid and member of the Koronis family, and its small companion, 1993 (243)1 Dactyl, as seen on August 28, 1993 by the Galileo spacecraft. Ida: $58 \times 23 \times 15$ km; Dactyl: $1.2 \times 1.4 \times 1.6$ km. Inset: (951) Gaspra, $18 \times 10 \times 9$ km, visited by Galileo on Oct. 29, 1991. NASA/JPL image PIA00333

15.7.4.2 Asteroid Masses and Densities

The first asteroid discovered to be binary was (243) Ida (a member of the Koronis family of Fig. 15.11), whose satellite, Dactyl, was observed by the *Galileo* spacecraft in 1993 (see Fig. 15.14). The duration of the flyby was too short to allow a determination of Dactyl's orbit, but with an assumption that the orbit is stable, the first mass determination for a binary asteroid was made. The first determination of an asteroid's mass from a measured satellite orbit was for (45) Eugenia in 1999, from ground-based adaptive optics observations.

The asteroid (624) Hektor (Hector) seems to be a contact binary asteroid (in analogy with a class of eclipsing binary stars where two stars are in varying degrees of contact, and are known as “overcontact” binaries), in which two lobes of material appear joined by a narrow neck. Direct imaging of Edgeworth-Kuiper or “scattered” objects have shown several with companions (Brown et al. 2006).

Prior to the discovery of binary asteroids, masses were found by astrometry, in which measured asteroid positions on the sky as functions of time are used to find the orbital perturbations that asteroids exert on each other and (in the case of the more massive asteroids) on the planet Mars. Perturbations to the orbit of Mars are measurable because landers and orbiters allow the distance between the Earth and Mars to be determined to within ~ 5 m (Russell et al. 2012). The first mass determination of any asteroid was in 1966 for (4) Vesta from its perturbation of (197) Ariete. The two asteroids encounter each other every 18 years, so the perturbation increases with each encounter, allowing Vesta's mass to be determined. The asteroids (1) Ceres and (2) Pallas also have close orbits and undergo

mutual interactions; consequently, their masses have been determined. In two cases, we have placed our own satellites in orbits around asteroids: the Amor asteroid Eros was visited by the NEAR Shoemaker spacecraft (which landed on it!), and the *Dawn* spacecraft spent 14 months orbiting Vesta (Sect. 15.7.5). However, the number of such determinations is small.

Ground-based radar and Very Large Telescope observations have revealed an increasing number of asteroidal companions, and surveys for near-Earth objects are producing many new, very accurate positions for main-belt asteroids, so the number of asteroids with measured masses and densities is growing rapidly. According to the knowledgeable website, <http://www.johnstonsarchive.net/astro/asteroidmoons.html>, as of mid-2012, there were over 200 known or strongly suspected asteroids with companions, including 9 triple systems. Of these, 42 were NEOs, 14 Amors, 79 Main Belt asteroids, 4 Jupiter Trojans, 79 TNOs, including the dwarf planets (134340) Pluto (5 companions), (136199) Eris, and (136108) Haumea.

In addition, masses of some planetary moons thought to be captured asteroids, such as Phobos and Deimos, have been determined by mutual interaction and through spacecraft observations.

Table 15.8 lists the masses, densities and diameters of five asteroids. The first three masses were determined astrometrically and the last two from spacecraft orbits. Diameters A, B, and C are the axes of the three-axis ellipsoid that best fits the asteroid's size and shape. The astrometric method is less precise for (3) Juno than for Ceres and Pallas because Juno's more strongly inclined orbit results in fewer and weaker interactions with other asteroids.

Until a large number of independently determined masses are made, densities are in the same situation as the masses. So, at present we do not have really good estimates of the true densities of most asteroids.

15.7.5 Case Study: (4) Vesta

The *Dawn* spacecraft entered orbit around Vesta on July 16, 2011, and spent almost 14 months studying the asteroid from orbits as low as 210 km above the surface. On September 5, 2012, it left for Ceres, where it is expected to arrive in 2015. The purpose of the mission is to learn more about the early history of the solar system, and Vesta and Ceres were chosen as targets because they are large, intact survivors of two different populations of protoplanets. (Ceres and Vesta hold 33 % and 9 % of the total mass in the main asteroid belt, respectively.) Vesta's mean density ($3,456 \text{ kg m}^{-3}$) and basaltic surface identify it as having formed in the inner solar system (<5 au). Ceres' mean density of $2,090 \text{ kg m}^{-3}$ indicates a composition of about half rock and half ice, similar to the large, outer-planet moons Ganymede, Callisto, Titan and Triton. Ceres, therefore, formed in the outer solar system and later migrated into the main asteroid belt.

Table 15.8 Asteroid masses, densities and diameters

Name	Mass (kg)	Density (kg m^{-3})	A (km)	B (km)	C (km)
(1) Ceres ^a	$(9.462 \pm 0.001) \times 10^{20}$	$2,090 \pm 50$	975 ± 3.6	975 ± 3.6	909 ± 3.2
(2) Pallas ^a	$(2.01 \pm 0.13) \times 10^{20}$	$2,570 \pm 190$	574 ± 10^b	526 ± 3^b	501 ± 2^b
(3) Juno ^a	$(2.86 \pm 0.46) \times 10^{19}$	$3,200 \pm 560$	320 ± 5	267 ± 5	200 ± 5
(4) Vesta ^c	$(2.59076 \pm 0.00001) \times 10^{20}$	$3,456 \pm 35$	572.6 ± 0.2	557.2 ± 0.2	446.4 ± 0.2
(433) Eros ^d	$(6.687 \pm 0.003) \times 10^{15}$	$2,670 \pm 30$	34.4 ± 0.1	11.2 ± 0.1	11.2 ± 0.1

^aFrom Table 3 of Baer et al. (2011) and references cited therein. Mass from astrometric method^bDunham et al. (1990)^cFrom Table 1 of Russell et al. (2012). Mass from spacecraft orbit^dFrom Table 3 of Baer et al. (2011) and references cited therein. Mass from spacecraft orbit



Fig. 15.15 The asteroid (4) Vesta photographed by NASA’s *Dawn* spacecraft. The ion-powered spacecraft is illustrated artistically on the right. The 500-km diameter Rheasilvia impact basin near Vesta’s south pole is visible at the bottom of the image, with its large central mound projecting on the bottom left. Divalia Fossae, an approximately parallel set of troughs encircling Vesta near its equator, were probably created by the Rheasilvia impact. The prominent crater below right of center is Pinaria. Credit: NASA/JPL-Caltech

Figures 15.15 and 15.16 show global views of Vesta’s heavily-cratered surface. North is at the top. Two large impact basins dominate the region around the south pole:

- Rheasilvia (centered at 75° S): 500 km in diameter, 19 km deep, with an age from crater counts of 1.0 ± 0.2 Gy. Half of Rheasilvia is visible at the bottom of each figure, with its central mound visible at the bottom of each image. With a diameter of 180 km and a height above the basin floor of 21 km, the mound is about the same diameter and twice the height of the Hawaiian Islands, measured from the ocean floor.
- Veneneia (centered at 52° S), 400 km in diameter, 12 km deep, with an age from crater counts of 2.1 ± 0.2 Gy. Veneneia covers the lower-left quarter of Vesta in Fig. 15.16. Rheasilvia overlies about half of Veneneia.

Also visible in Fig. 15.15 is a set of approximately-parallel troughs, Divalia Fossae, that extend 2/3 of the way around Vesta, roughly following the equator but more closely following a great circle with its axis passing through the center of Rheasilvia at 75° S (Jaumann et al. 2012). Individual troughs are from 19 to 380 km in length and up to 15 km wide. The troughs have the form of graben, with flat floors between steep scarps. Less pronounced troughs, grooves, and chains of pit craters complete the circle. A second set of troughs, Saturnalia Fossae (Fig. 15.16), extends part way along a great circle with its axis passing through the center of Veneneia. The most prominent of these is 390 km long and 38 km wide. This set is evidently older than the

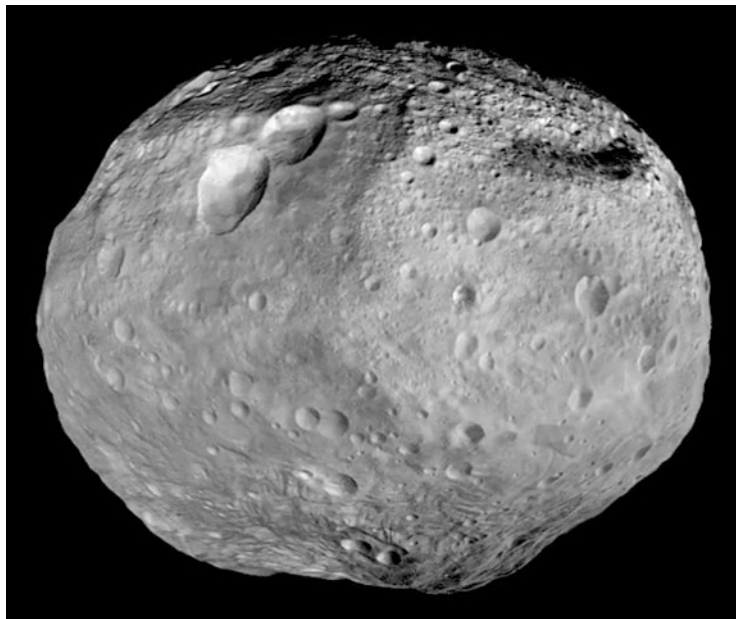


Fig. 15.16 The other side of Vesta from Fig. 15.15, a mosaic of images from NASA’s *Dawn* spacecraft. The “Snowman” is visible in the *upper left*, composed of the craters *Marcia* (*lower body*), *Calpurnia* (*upper body*) and *Minucia* (*head*). The central mound of *Rheasilvia* is at *bottom right*. The flat area covering the *lower-left quarter* of the image is the *Veneneia* impact basin. The *Saturnalia Fossae*, probably created during the *Veneneia* impact, are at the *top right*. NASA/JPL-Caltech/UCLA/MPS/DLR/IDA image PIA15678

first, having gentler slopes, rounded edges, more infilling, and heavy cratering. The orientation of the two sets of troughs relative to the two southern basins suggests that they were created by the intense seismic activity resulting from the impacts.

The second-order gravity coefficient, measured by tracking the *Dawn* spacecraft, is the quadrupole moment, $J_2 = 0.0317799 \pm 0.0000002$ (Asmar et al. 2012). (See Milone and Wilson (2014), Sections 5.3 and 5.4.3, for the definition and determination of J_2 and Table 9.1 for its values in the terrestrial planets.) This value and the observed basaltic surface indicate that Vesta is completely differentiated into a crust, mantle and metallic core. A model consistent with J_2 and the mean density (Table 15.8), assuming a core density equal to the mean density of iron meteorites ($7,400 \text{ kg m}^{-3}$) and a crustal thickness of 22.5 km, is (Asmar et al. 2012),

- Iron-nickel core: radius 105–120 km, ~18 % of Vesta’s mass;
- Olivine-rich mantle: density $3,170 \text{ kg m}^{-3}$;
- Crust (assumed 22.5 km thick): density $2,900 \text{ kg m}^{-3}$.

Although not all main belt asteroids have been found yet, let alone studied, Vesta’s spectral characteristics have long suggested that it is a (or, perhaps, the)

source of the howardite-eucrite-diogenite (HED) group of achondrites (Sect. 15.1.3.2). This identification has been confirmed by the spatially-resolved surface mineralogy observed by *Dawn*.

The completely differentiated nature of Vesta and the petrology of HEDs together suggest that Vesta completely melted from radioactive heating by the short-lived isotopes ^{26}Al and ^{60}Fe (De Sanctis et al. 2012). Fractionation during solidification of this magma ocean would produce the iron-nickel core, olivine-rich mantle, orthopyroxene-rich lower crust and pyroxene- and plagioclase-rich upper crust. In this scenario, the Rheasilvia and possibly Veneneia impacts are seen as the primary source for HED meteorites, with the howardites coming from the impact-gardened regolith, the eucrites from the upper crust and the diogenites from the lower crust. This complete differentiation requires that Vesta be fully-formed while ^{26}Al and ^{60}Fe were still abundant enough to melt it; i.e., within two million years of the first condensation of solids in the solar nebula.

Although the lower crust exposed in Rheasilvia is dominated by pyroxene-rich, diogenetic material in agreement with the broad outline given above, the walls and ejecta of smaller craters (shallower layers are ejected farther) show a more complex stratigraphy in the upper crust, with the composition varying over vertical scales of as little as a few hundred meters. Some HED meteorites also suggest a more complex history. It is therefore premature to distinguish between, for example, a broadly-layered crust with eucritic composition above and diogenitic composition below vs. a complex eucritic crust with intruded diogenitic plutons (De Sanctis et al. 2012).

It is possible that Vesta initially had an intrinsic magnetic field from a core dynamo. There would not be one today, because with Vesta's small size its core is expected to have solidified early in the asteroid's history, and any core dynamo should have died out in <100 My. Remanent magnetism could shed light on the presence or absence of an early dynamo, but *Dawn* lacks a magnetometer, and laboratory analyses of HEDs have shown that most have a low-coercivity⁸ composition that does not retain magnetism well. However, the eucrite ALH 81001, found in the Allan Hills in Antarctica in 1981, has a high coercivity because of its kamacite (Fe-Ni alloy) and FeS content, and paleomagnetic and isotopic analyses have shown that it cooled through the 780 °C Curie point of kamacite only 3.69 billion years ago in the presence of an ambient magnetic field of at least 2 μT, and possibly 12 μT or greater (Fu et al. 2012). Any magnetic field of the solar nebula should have dissipated in the first 6 My, as should an initially-strong solar magnetic field (the present interplanetary magnetic field strength is 10^{-3} μT at 1 au), so the most likely explanation is that this ambient field was due to remanent magnetism in Vesta's crust and/or mantle from an earlier core dynamo.

Assuming that Vesta is the (or at least a) source for HEDs, there is the question of how they get from Vesta to the Earth. Their cosmic ray exposure times range

⁸Coercivity measures the resistance that a ferromagnetic material offers to being demagnetized; e.g., permanent magnets are made from high-coercivity material (strongly resistant to being demagnetized).

from ~ 3 to 80 My, with clusters at ~ 12 , 22 and 36 My (Eugster et al. 2006). These ages are too long for them to have been ejected directly into Earth-crossing orbits by impacts on Vesta or another asteroid, and yet short enough to require continual replenishment rather than being perturbed out of a billion-year-old reservoir by collisions and near-misses. Some clues are provided by two (strongly-overlapping) groups of asteroids, all < 10 km diameter: the Vesta dynamical family; and the *Vestoid* group defined by spectral characteristics similar to Vesta (and thus also the HEDs) (Buratti et al. 2013). Vesta family members have eccentricities and inclinations similar to Vesta, and semi-major axes in the approximate range 2.26–2.47 au (Vesta’s semi-major axis is 2.36 au). 13,800 Vesta family members are known as of 2010 (Delisle and Laskar 2012 and references therein). The number of known Vestoids is much smaller because spectra take more time to obtain and analyze than do orbits, but the majority of known Vestoids are also Vesta family members. Some Vestoids are Earth-crossing asteroids and therefore not Vesta family members by definition, but they are believed to be former members whose orbits were perturbed as described below. The total Vesta family mass is consistent with an origin in the Rheasilvia impact.

Orbits within the asteroid belt are relatively stable (barring the occasional collision or near miss) except at certain resonance locations. The two resonances that concern the Vesta family are the 3:1 resonance with Jupiter at 2.5 au (the 3:1 Kirkwood gap) and the ν_6 (“nu-6”) secular resonance that defines the inner edge of the main asteroid belt. The ν_6 resonance occurs when the precession frequency of an asteroid’s longitude of perihelion is equal to that of Saturn (Froeschle et al. 1995). The ν_6 resonance occurs at 2.05 au for an asteroid of 0° inclination, but increases with increasing inclination; for Vesta’s inclination ($\sim 7^\circ$), it is at ~ 2.2 au (Morbidelli et al. 2002). Both of these resonances cause rapid evolution in orbital eccentricity: the median time for an asteroid to evolve from a quasicircular orbit to an Earth-crossing orbit is ~ 0.5 My in the ν_6 resonance and ~ 1 My in the 3:1 resonance.

There is also the problem of getting objects from Vesta to the location where these resonances apply. Computational models give maximum ejection speeds from impacts on Vesta of 0.6 km/s, whereas maximum speeds of 1 km/s would be required to produce the observed spread of Vesta family orbits directly from an impact (Binzel et al. 1999), and larger speeds still to put them into either resonance (let alone into an Earth-crossing orbit!). Instead, some mechanism of orbital evolution is required. For small asteroids like those in the Vesta family, this is accomplished by the Yarkovsky effect (Sect. 15.7.6): by (15.20), the semi-major axis of a kilometer-sized asteroid with a basaltic surface increases or decreases by $\sim 10^{-4}$ au/My (Morbidelli et al. 2002). Given the spread in orbits and asteroid diameters that would result from the initial impact, this mechanism can provide a continuous supply of Vesta family asteroids to the resonances (~ 0.1 – 0.2 au from Vesta) 1 Gy after the Rheasilvia impact, and collisions with and between these asteroids can supply the HED meteorites. Alternatively, the three strong peaks in ages of HEDs may suggest impacts directly on Vesta at these times.

HED meteorites show that Vesta’s crust has a very low volatile content. Nevertheless, pitted terrain can be seen in *Dawn* images that is similar in morphology and

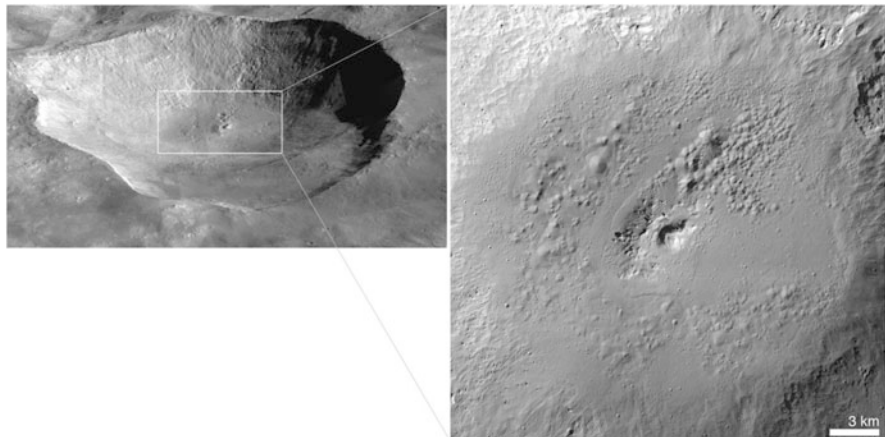


Fig. 15.17 Marcia crater (also shown in Fig. 15.16), estimated age of ~70 million years, a mosaic of images from by NASA’s *Dawn* spacecraft, shown with five times vertical exaggeration. The Sun is shining from the *right*. Raised debris is visible at the *center* of the close-up image on the *right*, surrounded by pitted terrain created by loss of volatiles that were originally delivered to Vesta by carbonaceous chondrites. The *white bar* in the enlarged image indicates a distance of 3 km. *NASA/JPL-Caltech/UCLA/MPS/DLR/IDA/JHUAPL* image PIA16182

location to pits on Mars that are known to result from slumping of the surface due to loss of buried volatiles (H_2O) (Denevi et al. 2012). The features consist of irregular, rimless depressions with diameters ~30 m to 1 km (30 m is only ~2 pixels wide in photographs from *Dawn*’s lowest orbit, so smaller pits may just not have been recognized) and depths from <50 m for the smaller pits to ~200 m for the largest complex of overlapping pits. They are found on otherwise smooth deposits on the floors of some young craters (Fig. 15.17), also atop terraces where the crater wall has slumped, and in the ejecta blanket surrounding the crater. The volatiles on Vesta are believed to have been delivered by carbonaceous chondrite meteorites, clasts of which are found in howardites. These clasts contain an average of ~9 wt% of mineralogically-bound water, and dark deposits on Vesta suggest that carbonaceous material can occupy up to 60 % of the regolith, giving a $0.6 \times 9 = \sim 5$ wt% exogenic water content in the regolith.

15.7.6 Asteroids and Meteorites

As the previous discussions of Vesta and of the HED meteorites suggests, and many previous sections illustrate, there is a close connection between asteroids and meteoroids. The meteoroid orbits determined from observed trajectories of meteors strongly suggest origins in the asteroid belt. Reflectance spectra support the association as well. On the basis of the reflectance spectra, which reveal band structures attributed to various minerals, and photometric albedos, asteroids have been

assigned classes. These are shown in Table 15.9, based, in part, on Chapman (1990, Table 1, p. 238) and Wetherill and Chapman [1988, esp., Table 2.1.3, p. 54, Tholen (1989), and Bus and Binzel (2002)].

Work carried out by Binzel, Bus, and Burbine (1998) indicates that ordinary chondrites are derived from the S-class main belt asteroids, and previous disagreement between asteroid and meteorite spectral features is likely due to size effects: larger asteroids have greater variation in surface characteristics as a result of collisional processing, amount of retained regolith, and time-dependent evolution, reducing the spectral match with the meteorites. The lack of D and P analogs is very likely due to the fragility of those icy bodies. The density of Halley's comet was determined to be $\sim 700 \text{ kg/m}^3$. Such material is easily destroyed by the pressures encountered in entry into a planetary atmosphere (of course a large amount of it can still trigger a great catastrophe!).

Asteroids have clearly undergone substantial modification. Evidence now suggests that many asteroids have some degree of aqueous modification as well. This could have taken place early in the solar system during the T Tauri stage of the Sun's evolution when, it is thought, the hydrated carbonaceous chondrites may have been exposed to short-lived sporadic heating and were subject to a variety of temperatures, thus resulting in the variety of petrologic types of Table 15.3.

Asteroids undergo dynamical or orbital evolution also, especially those in near resonances with Jupiter, i.e., near the Kirkwood gaps, which are subject to chaotic variation. Recent work has shown that objects moving in these orbits may do so for 10^5 years or more, but may suddenly be perturbed into very different orbits. It is conjectured that just such processes have led to the creation of the Earth- and Mars-crossing asteroids (Sect. 15.7.5).

In addition to the perturbations exerted by other objects, the radiation pressure of the Sun and the impact of the solar wind have non-gravitational effects which could be observable (such effects have certainly been seen in comets).

Finally, the Sun heats a rotating asteroid during its daytime, giving maximum surface temperatures near the dayside evening terminator, with corresponding minimum temperatures near the morning terminator after the surface has cooled at night. The greatest rate of momentum transfer to photons (thermal emission) is thus near the evening terminator and least near the morning terminator. This nonisotropic thermal emission creates a small net force on the asteroid directed radially outward from near the morning terminator. The small but systematic dynamical effect that this force produces on the motion of the asteroid is referred to as the *Yarkovsky effect*. The object is coolest on the night side of the sunrise terminator by an amount ΔT , and so will have a temperature $T - \Delta T$; on the sunlit side of the sunset terminator, on the other hand, the temperature will be $T + \Delta T$. The resulting force on the object from this effect will be

$$F_Y = (8/3) (\pi R^2 \sigma T^4 / c) (\Delta T / T) \cos \psi \quad (15.19)$$

Table 15.9 Asteroids and meteorites^a

Asteroid type (class)	Location	Range	Spectral data	A	Associated meteorites group/clan/type	Examples
	Peak (au)					
Q (primitive)	1	?	Similar to S; deeper absorption	moderate	Ordinary chondrites	(1862) Apollo
E (igneous)	1.9	1.9–3.1	Flat; slightly red	0.3–0.6	Aubrites (enstatite chondrites)	(44) Nyssa (434) Hungaria
S (igneous)	2.4	1.9–3.5	Red in visible; nine subtypes; abs. near 1 μm	0.1–0.2	Ordinary chondrites; may be pallasites	(433) Eros
V(igneous)	2.55	...	~S with pyroxene abs.	High	Basaltic achondrites	(5) Astraea
T (metamorphic)	2.7	2.5–3	Red in visible	0.04–0.1	Altered carbon. Chondrites?	(4) Vesta
A (igneous)	2.8	2.7–3.2	UV absorption; olivine absorption	0.1–0.4	Pallasites? Chassignites Olivine-rich achondrites	(114) Kassandra (496) Aeternitas
R (igneous)	2.9	...	Pyroxene, olivine similar to V type	~0.4	Olivine-rich achondrites	(349) Dembowska
C (primitive)	3.0	2.3–4.0	Red in visible; flat, dark; 3.07 μm absorption band (ices)	0.03–0.07	Carbonaceous chondrites (CM/CI)	(176) Iduna
K (primitive)	3.1	...	Weak 1 μm, no 2 μm abs.	Low	CV/CO Chondrites	(221) Eos
M (igneous)	3.0	2.3–3.5	Some what red	0.1–0.2	Irons	(16) Psyche; (21) Lutetia
B (metamorphic)	~3	2.3–4	Like C but slightly brighter; weaker UV abs.	0.04–0.08	Modified carbonaceous chondrites	(2) Pallas; 1999RQ36
G (metamorphic)	~3	2.3–4	Like C but strong UV absorption	0.05–0.09	"	(1) Ceres
F (metamorphic)	~3	2.3–4	Like C, flat; no UV	0.03–0.06	"	(302) Clarissa
P (primitive)	4.0	3.0–5.2	Similar to M but darker	0.02–0.06	None known	(87) Sylvia; (153) Hilda

D (primitive)	>5	3 – > 5	Redder than P	0.02–0.05	None known
L (primitive)	~2.4	2–3	‘Featureless S’; redder than K <0.75 μm, flat >0.75 μm	High and low	Jupiter Trojans; (944) Hidalgo (387) Aquitania

^aBased in part on Chapman (1990, Table 1, p. 236), Wetherill and Chapman (1988, esp. Table 2.1.3 on p. 54), Tholen (1989), and Bus and Binzel (2002). General information on locations of super classes:

Igneous (<2.7 a.u.); Metamorphic (~3.2 a.u.); Primitive (>3.4 a.u.)
Tholen’s (1989) broader categories include the C-group (types B,F,G, and C), the S group, and the X-group (types M,E, and P), as well as a “small-class” group (A,D,T,Q,R, and V types), based mainly on photometric photometry with the ECAS suite of filters. The Bus & Binzel scheme is based on higher spectral resolution and provides for 24 types arranged into C-, S-, and X-groups, with types that vary somewhat from Tholen’s, and the separate types T,D,L,d,O, and V. The K and L types are new from the Bus and Binzel (2002) scheme, but we have not tried to list all of the new types. In addition, there are at least two other types by which asteroids have been classified mineralogically. One of these is U, the third of an original 3-type (C, S, and U) classification scheme to include those objects which did not fit into either the “S” (for “siliceous” and presumably “stoney” objects) or the “C” (for “carbonaceous”) categories (see Chapman et al. 1975). “Carbonaceous” morphs into “primitive”/C-group and “siliceous” into S-group categories in later schemes. The other is X, a category that includes objects with mainly metallic features, which correlate more or less with iron or some of the stoney-iron meteorites

sometimes called the *Yarkovsky force*, where R is the particle's radius and ψ is its "obliquity," the angle between its orbital plane and its equator. When $0^\circ \leq \psi < 90^\circ$, the rotation is prograde (CCW as seen from the north ecliptic pole of the solar system), and when $90^\circ < \psi < 180^\circ$ it is retrograde. When prograde, the net force will be in the forward orbital direction, and both eccentricity and semi-major axis will be increased. When retrograde, the net result will be a decrease of the semi-major axis, and the object will spiral inward, toward the Sun. (The Yarkovsky effect becomes negligible for objects smaller than ~ 1 mm diameter because thermal conduction across the object evens out the temperature distribution on the surface. Smaller objects, such as dust grains, slowly spiral inward toward the Sun due to the *Poynting-Robertson effect*: in the reference frame of the grain, the solar photons approach from slightly in front, creating a component of momentum transfer from the radiation to the grain opposite to the grain's orbital direction; cf. Sect. 14.13.1.)

The occurrence of ΔT in the numerator means that, for a given rotation period and distance from the Sun, the force depends on the asteroid's albedo: low-albedo surfaces (e.g., basalt) heat up more quickly than high-albedo surfaces (e.g., iron). If $\Delta T \ll T$, the effect will be small, and the time scale will be very long. For a basalt surface, the rate of change of semi-major axis is

$$\frac{da}{dt} = 2.5 \times 10^{-4} \left(\frac{1 \text{ km}}{D} \right) \cos \psi \text{ au/My} \quad (15.20)$$

(Delisle and Laskar 2012). For 1-km diameter asteroid with obliquity near 0° or 180° , a increases or decreases, respectively, by 2.5×10^{-4} au per million years.

The D/H isotope ratios have shown that different meteorites originated in different places in the solar system, and indicate that the Moon was born very close to the Earth. The picture confirms the view that volatiles were driven out of the inner solar system at an early date, resulting in the availability of ices to form a profusion of bodies in the outer solar system.

The short-period comets, with direct orbits and moderate eccentricities, may be derived from icy bodies that may have been perturbed through collisional encounters in the Edgeworth-Kuiper Belt. This belt may, in turn, be the evolved remnant of the planetary disk of the early solar system. The existing TNO population show both a "classical" and a dynamically perturbed component, in which eccentricities and inclinations are more varied.

Dynamical studies have shown that long-period comets originate in very far orbits in the solar system (the *Oort Cloud*, after Jan Oort) and are perturbed, perhaps by a star traveling in the same direction but providing a slight negative acceleration resulting in an inward falling direction for the comet [see Sect. 14.7, and for a discussion of current views of the origin and changes to the Oort Cloud, see Dones et al. (2004)].

Consequently, we have no unambiguous evidence at present that anything seen on Earth has come from outside the material present in the original solar nebula except for interstellar dust grains entering the Earth's atmosphere (Taylor et al. 1996), photons, and cosmic rays.

15.8 Implications for the Origin of the Solar System

The current picture of the origin of the solar system is of a rotating solar nebula of gas and dust, which developed a disk in conservation of angular momentum as it gravitationally collapsed. Bipolar outflows may have accompanied the development of a thick disk. High temperatures would have characterized the inner nebula, at the core of which a star would be born, and the temperature gradient through the disk would have insured different rates of condensation with distance from the core. In the middle part of the disk, strong magnetic and electrostatic fields would have produced electric currents and electrical discharges that would have melted the aggregating dust particles and caused them to rain down on other components, giving rise to the undifferentiated bodies that became the chondrites. Fractionation processes would cause distributions of isotopes of various chemical species.

As aggregation proceeded and as the solar wind and radiation pressure of the young star drove away the dust and gas of the inner solar system, aggregates massive enough to differentiate did so. Subsequent major collisions disrupted many of these, giving rise to the iron and silicate-rich differentiated bodies, which were further impacted in most cases. The major planets themselves had disks and developed satellite systems and rings, some of which may be still present today.

In an initially hot environment, there is an expected sequence of condensations as the more refractory materials condense out of vapor first, and the more volatile materials later, when the temperature has decreased further. In this way, minerals appeared in a *condensation sequence*, the order in which the minerals condensed out of the solar nebula.

The outer sub-giant planets migrated into their present positions, possibly by absorbing orbital energy from encountered bodies, but mainly through gravitational interactions with the gas giants and with the outer disk. Most of the rocky and icy planetesimals were ejected or wound up in the Kuiper Belt. The remnants of the solar nebula are to be found still today in the Oort Cloud, some of the denizens of which were flung out there by interactions with the major planets early in the history of the solar system.

15.9 The Solar Nebula

Stars typically have their origins in the midst of a molecular cloud, which collapses to an association of stars. The association is usually born with an excess of dynamical energy, so the stellar system eventually dissipates. The Sun may have had its beginning in just such an environment.

Here we concentrate on the collapse leading to a single star, of solar mass, starting with a condensation from a molecular cloud, in order to see how the size

and mass of this condensing cloud depend on its temperature and the density. For a cloud of material that is gravitationally bound, it may be shown⁹ that

$$2 \langle K \rangle = - \langle U \rangle \quad (15.21)$$

where $\langle K \rangle$ is the mean kinetic energy and $\langle U \rangle$ is the mean potential energy. Equation (15.21) is a form of the *Virial Theorem*, an expression widely used in astrophysics, especially to determine the mass of an ensemble of objects, ranging from particles to galaxies. Because the total energy, E , is merely the sum of the kinetic and potential energies, we then have:

$$\langle E \rangle = \langle K \rangle + \langle U \rangle = - \langle K \rangle < 0 \quad (15.22)$$

Thus, the total energy of a bound ensemble is negative. In an ensemble of gaseous molecules, the kinetic energy may be expressed as

$$(3/2) kT = \frac{1}{2} m \langle v^2 \rangle \quad (15.23)$$

where $k = 1.38 \times 10^{-23}$ J/K is the Boltzmann constant and T is the temperature. The kinetic energy of the total ensemble of N molecules is then

$$K_{\text{ens}} = \sum K_i = (1/2) N m \langle v^2 \rangle = (3/2) N kT \quad (15.24)$$

If we use the approximation that the cloud is pure molecular hydrogen, so that

$$N = M / (2m_H) \quad (15.25)$$

where M is the total mass and m_H is the mass of the hydrogen atom, (15.24) becomes

$$K_{\text{ens}} = (3/2) kT M / (2m_H) \quad (15.26)$$

Applying the Virial Theorem to (15.26), and writing out the potential energy explicitly for the ensemble of mass $M = N(2m_H)$ (Milone and Wilson 2014, Chapter 5.3), we obtain from (15.21)

$$2(3/2)kTM / (2m_H) = GM^2 / \mathfrak{R} \quad (15.27)$$

where \mathfrak{R} is the radius of the cloud. This simplifies to

$$(3/2)kT / m_H = GM / \mathfrak{R} \quad (15.28)$$

and, substituting for the mass,

⁹For example, by Karttunen et al. (2003, pp. 146–148) or Zeilik and Gregory (1998, p. P12).

$$M = (4/3)\pi \mathfrak{R}^3 \rho \quad (15.29)$$

we obtain

$$kT/m_{\text{H}} = (8/9)\pi G \mathfrak{R}^2 \rho \quad (15.30)$$

so that the radius, expressed in terms of the temperature and density of the cloud, becomes

$$\mathfrak{R} = \{kT/[(8/9)\pi G \rho m_{\text{H}}]\}^{1/2} \quad (15.31)$$

In SI units,

$$\mathfrak{R} = 6.65 \times 10^6 (T/\rho)^{1/2} \quad (15.32)$$

With typical values $T = 10$ K, and $\rho = 10^{-15}$ kg/m³, the radius is about $\mathfrak{R} \approx 7 \times 10^{14}$ m = 4,700 au = 0.023 pc. Finally, from (15.29), the mass of such a cloud would be $M \approx 1.4 \times 10^{30}$ kg, or of the order of a solar mass.

The collapse of the cloud may not have been purely gravitational, however. In the presence of magnetic fields, expected because they are in fact present in the interstellar medium, ambipolar diffusion (cf. Sect. 11.1.1.5) can levitate ions while neutral atoms, molecules, and grains more readily fall into a gravitational well.

A shock-wave triggered collapse from a supernova explosion was suggested by Cameron and Truran (1977) to account for the presence of ²⁶Al, so useful as an alternative source for the melts required for the creation of chondrules, and for primordial planetary heat sources. According to Boss (1995), a speed for the shock of ~25 km/s would suffice to trigger a collapse. Another source, however, could be a red giant wind. In a recent study, Gounelle and Meibom (2008) argue that the radionuclides arose from the proto-Sun environment itself.

In the protostellar environment, the presence of even a slight amount of rotation in the initial cloud would result in sufficient rotation in the collapsed nebula to flatten it into a disk. A strong bipolar outflow is observed in some young pre-stellar objects, presumably emanating perpendicular to the disk; i.e., from the directions of the rotational poles. The mechanism for this bipolar outflow may be a strong wind emanating from the proto-Sun, the equatorial wind component of which is obscured by the disk. A discussion of other mechanisms, and a thorough review of the subject, can be found in Boss (2004).

As the disk rotates, shearing must take place, as suggested originally by Laplace, leading to Keplerian orbits for the condensation products.

We next consider the disks themselves.

15.10 The Proto-Planetary Disk

The planets of the solar system and planetary systems of other stars had their beginnings in a thick disk around the proto-star. The discovery of a disk around the bright star β Pictoris (Smith and Terrile 1984) called attention to this phenomenon as a general stage of all stars. *Remnant or debris disks* were then found around Vega (viewed pole-on), Fomalhaut, and ϵ Eridani. Since then the number of stars found to have disks has burgeoned.

In young associations, such as in Orion, in a rich star-forming region of the Milky Way, *proplyds* (for *proto-planetary disks*) may appear as elongated nebulae (Figs. 15.18 and 15.19) often with tail-like structures, subject to erosion by the intense UV and x-ray radiation and stellar winds from hot, new stars in the vicinity. That the objects contain stars, and are young, is generally accepted. O'Dell and Wen (1994) argue that proplyds are flattened envelopes or circumstellar disks, supporting an argument made earlier by Meaburn (1988), and demonstrate this with a rectangular profile for a dark, silhouetted object designated (on the basis of position) 183–405. It is clearly optically thick and was measured to have dimensions 1.2×0.9 arc-sec, corresponding to 550×410 au if at a distance of 460 pc. A rough calculation can provide a lower limit on the mass of this object. Following, O'Dell and Wen, the optical depth along a line of sight is given by

$$\tau = N_d \pi R^2 Q(2\pi R/\lambda) \quad (15.33)$$

where N_d is the number of particles in a column of radius R , and $Q(2\pi R/\lambda)$ is the extinction efficiency. The mass of material in this column is,



Fig. 15.18 Possible proplyds in Orion, as imaged with the HST wide field and planetary camera 2 on December 29, 1993 (O'Dell and Wen 1994, Figure 3c on plate 7). 183–405 is the dark object on the right, seen in silhouette. Courtesy, C. R. O'Dell, Vanderbilt University, NASA, and ESA. Reproduced by permission of the AAS

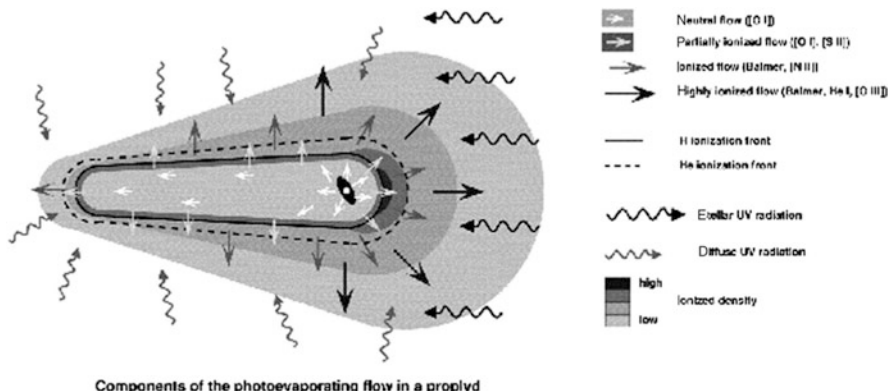


Fig. 15.19 A model for a proplyd, from Henney and O'Dell (1999, Figure 5, p. 2359), showing the effect of ionizing radiation from nearby hot stars. Note the circumstellar disk, a possible example of which O'Dell and Wen suggested was seen in silhouette in Fig. 15.18. Courtesy, C. R., O'Dell, Vanderbilt University, NASA, and ESA. Reproduced by permission of the AAS

$$m = N_d 4\pi R^3 \rho / 3 \quad (15.34)$$

where ρ is the density of the material, in kg m^{-3} . Substitution then yields,

$$m = 4R\rho\tau / [3Q(2\pi R/\lambda)] \quad (15.35)$$

With values of $\rho/[Q(2\pi R/A)] = 1,000 \text{ kg/m}^3$ and $R = 200 \text{ nm}$, summing over all columns in the line of sight to the object and using an average value of τ calculated over the entire rectangle, O'Dell and Wen obtained a minimum mass of about $4 \times 10^{23} \text{ kg}$, or as much as $100 \times$ larger allowing for underestimated gas content and conservative assumptions. This compares to $\sim 6 \times 10^{24} \text{ kg}$ for the Earth. Clearly this object can not be an equivalent of the solar system.

The Sun is relatively massive and luminous in its neighborhood, but as we have seen in the previous section, solar mass objects can be expected to form from molecular clouds.

A good recent summary of current knowledge of disks can be found in Williams and Cieza (2011). They make use of recent infrared and submillimeter observations to characterize the evolution of disks from the initial collapse phase through the dissipation of the gas through photoevaporation and condensation onto the central disk plane, to the remnant debris disk composed solely of large grains, planetesimals, and planet systems with the retinue of rings and moons.

The current view of planetary formation is that material within the disk will accrete through numerous collisions, and that objects in dense zones will grow to form protoplanets. The exact process is still a matter of some discussion as the number of extra-solar examples increases; we discuss this at the end of the next chapter. In any case, the formation of planetary embryos will create gaps in the

disks; gaps indeed have been observed in stellar remnant disks. The presence of gas, dust, and orbiting debris of various sorts will create a drag, however, and planets will tend to migrate inward at rates that depend on the viscosity of the disk as well as the mass of the planet, and, eventually, to fall into the star. Matsumura et al. (2007) have determined that the presence of a “dead zone,” a region of low viscosity, between the star and the proto-planet, can slow and even halt the migration of the planet. They have simulated the fates of both terrestrial and Jovian mass planets, showing that the presence of dead zones interior to their orbits allows planets time to create a gap within the disk, as accretion proceeds. Returning to our solar system, specifically, the debris disk and the protoplanets interacted with each other to an astounding extent, and these interactions continued well past the cessation of the growth of the planets. The presence of large amounts of debris far from the planetary orbits means that perturbations will be felt by the planets over time. An interesting series of simulations by Tsiganis et al. (2005) explores the evolution of the outer solar system at this stage forward. They assume a far-flung collection of Edgeworth-Kuiper Objects totaling $30\text{--}50 M_E$. By varying the initial orbits of the outer planets, they are able to determine the most likely sequence of migration events that created the present configuration. Key to the changes was the approach by Saturn to a 2:1 mean motion resonance with Jupiter. This circumstance, for reasons discussed in Chap. 16, led to large changes in the inclinations and eccentricities of the outer ice giants, Neptune and Uranus, causing them to move outward and cross orbits, scattering the outer belt objects as they did so. This action resulted in the Great Bombardment that befell the rest of the solar system, including the inner planets and the Moon. The Tsiganis et al. (2005) simulations also showed that the main satellites of the giant planets would have survived these events, but the irregular satellites would not have; therefore they are likely to have been acquired during or following the migrations. This depiction is called the “Nice Model,” after the city in France where these ideas were discussed extensively.

We now proceed to discuss the increasing numbers of extra-solar planetary systems, many of which appear to involve planets that are even more extreme in their physical and orbital properties than our own. In that context, we will reconsider the origin of planetary systems.

Challenges

- [15.1] Discuss how points along the plot of the ratios $^{87}\text{Sr}/^{86}\text{Sr}$ vs. $^{87}\text{Rb}/^{86}\text{Sr}$ change with time. What do we mean by “time” here anyway? (See Fig. 15.6)
- [15.2] Examine the validity of equations (15.5) and (15.6), defining all quantities, and evaluate the dynamic evidence that SNC meteorites come from Mars. Assume the correctness of Wasson’s assertion that an impactor with substantially greater speed than v_∞ may result in planetary mass loss.
- [15.3] Summarize the different types of ages that a meteorite can have and associate each with a stage of a meteorite’s history.

- [15.4] Examine the list of the principal types of asteroids and their associated meteorites. What can you conclude about the origin of those meteorites.
- [15.5] Discuss what meteorites could be expected from cometary impact on Earth and on meteoroids or their parent bodies. Do we have any evidence that such impacts occur in any known meteorite specimens?
- [15.6] Describe the time-line of the development stages of the material in the Zagami meteorite from the original aggregation of elements to the fall and recovery.

References

- Alexandersen, M., Gladman, B., Greenstreet, S., Kavelaars, J.J., Petit, J.-M., and Gwyn, S.: A Uranian Trojan and the frequency of temporary giant-planet co-orbitals. *Science* **341** (6149) 994–997 (2013)
- Alvarez, L.: Extraterrestrial cause for the Cretaceous-Tertiary extinction. *Science* **208**, 1095–1108 (1980)
- Asmar, S.W., Konopliv, A.S., Park, R.S., Raymond, C.A., Bills, B., Gaskell, R.W., Russell, C. T., Smith, D.E., Toplis, M., Zuber, M.T.: The gravity field of Vesta from Dawn. European Planetary Science Conference, Abstract EPSC 2012-814-1 (2012)
- Baer, J., Chesley, S.R., Matson, R.D.: Astrometric masses of 26 asteroids and observations on asteroid porosity. *Astronom. J* **141** (2011). doi: [10.1088/0004-6256/141/5/143](https://doi.org/10.1088/0004-6256/141/5/143) (12 pages)
- Beck, A.W., McSween Jr., H.Y.: Diogenites as polymict breccias composed of orthopyroxenite and harzburgite. *Meteor. Planet. Sci.* **45**(Nr 5), 850–872 (2010)
- Bendjoya, P., Zappalà, V.: Asteroid family identification. In: Bottke Jr., W.F., Cellino, A., Paolicchi, P., Binzel, R.P. (eds.) *Asteroids III*, pp. 613–618. University of Arizona Press, Arizona (2002)
- Bendjoya, P., Slezak, E., and Foreschle, C.: The wavelet transform: a new tool for asteroid family determination. *Astron. & Astrophys* **251**, 312–330 (1991)
- Bertotti, B., Farinella, P., Vokrouhlický, D.: *Physics of the Solar System*. Kluwer, Dordrecht (2003)
- Binzel, R.P., Bus, S.J., Burbine, T.H.: The orbital distribution of Vesta-like asteroids. 30th Lunar and Planetary Science Conference, Houston, Texas, Abstract 1216 (1999)
- Binzel, R.P., Bus, S.J., Burbine, T.H.: Relating S-asteroids and ordinary chondrite meteorites: the new big picture. *BAAS* **30**, 1041 (1998)
- Bogard, D.D., Garrison, D.H.: Relative abundances of Ar, Kr, and Xe in the Martian atmosphere as measured by Martian meteorites. *Geochim. Cosmochim. Acta* **62**, 1829–1835 (1998)
- Bogard, D.D., Garrison, D.H.: Argon 39–Argon 40 ‘ages’ and trapped Argon in Martian Shergottites, Chassigny, and Allen Hills 84001. *Meteorit. Planet. Sci.* **34**, 451–473 (1999)
- Borg, L.E., Edmunds, J.E., Asmerom, Y.: Constraints on the U–Pb isotopic systematics of Mars inferred from a combined U–Pb, Rb–Sr, and Sm–Nd isotopic study of the Martian meteorite Zagami. *Geochim. Cosmochim. Acta* **69**, 5819–5830 (2005)
- Boss, A.P.: Collapse and fragmentation of molecular cloud. II. Collapse induced by stellar shock waves. *Astrophys. J.* **439**, 224–236 (1995)
- Boss, A.P.: From molecular clouds to circumstellar disks. In: Festou, M.C., Keller, H.U., Weaver, H.A. (eds.) *Comets II*, pp. 67–80. University of Arizona Press, Tucson, AZ (2004)
- Brouwer, D.: Secular variations of the orbital elements of the minor planets. *Astronom. J.* **56**, 9–32 (1951)
- Brown, M.E., van Dam, M.A., Bouchez, A.H., Le Mignant, D., Campbell, R.D., Chin, J.C.Y., Conrad, A., Hartman, S.K., Johansson, E.M., Lafon, R.E., Rabinowitz, D.L., Stomski Jr., P.J.,

- Summer, D.M., Trujillo, C.A., Wizinowich, P.L.: Satellites of the largest Kuiper Belt objects. *Astrophys. J.* **639**, L43–L46 (2006)
- Brož, M., Vokrouhlický, D.: Asteroid families in the first-order resonances with Jupiter. *Month. Notice. R. Astronom. Soc.* **390**, 715–732 (2008)
- Buratti, B.J., Dalba, P.A., Hicks, M.D., Reddy, V., Sykes, M.V., McCord, T.B., O'Brien, D.P., Pieters, C.M., Prettyman, T.H., McFadden, L.A., Nathues, A., Le Corre, L., Marchi, S., Raymond, C., Russell, C.T.: Vesta, Vestaoids, and HEDs: *Dawn*, ground-based, and RELAB observations. 44th Lunar and Planetary Science Conference, Abstract 1845 (2013)
- Burbine, T.H., McCoy, T.J., Meibom, A., Gladman, B., Keil, K.: Meteoritic parent bodies: their number and identification. In: Bottke Jr., W.F., Cellino, A., Paolicchi, P., Binzel, R.P. (eds.) *Asteroids III*, pp. 653–667. University of Arizona Press, Tucson, AZ (2002)
- Bus, S.J., Binzel, R.P.: Phase II of the small main-belt asteroid spectroscopy survey: a feature-based taxonomy. *Icarus* **158**, 146–177 (2002)
- Cameron, A.G.W., Truran, J.W.: The supernova trigger for formation of the solar system. *Icarus* **30**, 447–461 (1977)
- Chapman, C.R.: Asteroids. In: Beatty J.K., Chaikin A. (eds) *The New Solar System*, 3rd ed, pp. 231–240. Sky, Cambridge, MA; Press Syndicate of University of Cambridge, Cambridge, UK (1990)
- Chapman, C.R., Morrison, D., Zellner, B.: Surface properties of asteroids: a synthesis of polarimetry, radiometry, and spectrophotometry. *Icarus* **25**, 104–130 (1975)
- Clayton, R.N.: Oxygen isotopes in meteorites. *Annu. Rev. Earth Planet. Sci.* **21**, 115–149 (1993)
- Clayton, R.N., Mayeda, T.K.: The oxygen isotope record in Murchison and other carbonaceous chondrites. *Earth Planet. Sci. Lett.* **67**, 151–161 (1984)
- Clayton, R.N., Mayeda, T.K.: Oxygen isotope studies of achondrites. *Geochim. Cosmochim. Acta* **60**(11), 1999–2017 (1996)
- Clayton, R.N., Mayeda, T.K., Goswami, J.N., Olsen, E.J.: Oxygen isotope studies of ordinary chondrites. *Geochim. Cosmochim. Acta* **55**, 2317–2337 (1991)
- De Sanctis, M.C., Ammannito, E., Capria, M.T., Tosi, F., Capaccioni, F., Zambon, F., Carraro, F., Fonte, S., Frigeri, A., Jaumann, R., Magni, G., Marchi, S., McCord, T.B., McFadden, L.A., McSween, H.Y., Mittlefehldt, D.W., Nathues, A., Palomba, E., Pieters, C.M., Raymond, C.A., Russell, C.T., Toplis, M.J., Turrini, D.: Spectroscopic characterization of mineralogy and its diversity across Vesta. *Science* **336**, 697–700 (2012)
- Delisle, J.-B., Laskar, J.: Chaotic diffusion of the Vesta family induced by close encounters with massive asteroids. *Astronom. Astrophys.* **540**, A118 (2012). doi:[10.1051/0004-6361/201118339](https://doi.org/10.1051/0004-6361/201118339) (8 pages)
- Denevi, B.W., Blewett, D.T., Buczkowski, D.L., Capaccioni, F., Capria, M.T., De Sanctis, M.C., Garry, W.B., Gaskell, R.W., Le Corre, L., Li, J.-Y., Marchi, S., McCoy, T.J., Nathues, A., O'Brien, D.P., Petro, N.E., Pieters, C.M., Preusker, F., Raymond, C.A., Reddy, V., Russell, C.T., Schenck, P., Scully, J.E.C., Sunshine, J.M., Tosi, F., Williams, D.A., Wyrick, D.: Pitted terrain on Vesta and implications for the presence of volatiles. *Science* **338**, 246–249 (2012)
- Dones, L., Weissman, P.R., Levison, H.F., Duncan, M.J.: Oort cloud formation and dynamics. In: Festou, M.C., Keller, H.U., Weaver, H.A. (eds.) *Comets II*, pp. 153–174. University of Arizona Press, Tucson, AZ (2004)
- Drake, M.J., Swindle, T.D., Owen, T., Musselwhite, D.S.: Fractionated Martian atmosphere in the nakhlites? *Meteoritics* **29**, 854–859 (1994)
- Dunham, D.W., Bixby Dunham, J., et al.: The size and shape of (2) Pallas from the 1983 occultation of 1 Vulpeculae. *Astronom. J.* **99**, 1636–1662 (1990)
- Eugster, O., Weigel, A., Polnau, E.: Ejection times of Martian meteorites. *Geochim. Cosmochim. Acta* **61**, 2749–2757 (1997)
- Eugster, O., Herzog, G.F., Marti, K., Caffee, M.W.: Irradiation records, cosmic-ray exposure ages, and transfer times of meteorites. In: Lauretta, D.S., McSween Jr., H.Y. (eds.) *Meteorites and the Early Solar System II*, pp. 829–851. University of Arizona Press, Tucson, AZ (2006)

- Fessenkov, V.G.: Sikhoté-Aline meteorite. In: Kaiser, T.R. (ed.) *Meteors*, pp. 179–183. Pergamon, New York (1955)
- Froeschle, C., Hahn, G., Gonczi, R., Morbidelli, A., Farinella, P.: Secular resonances and the dynamics of Mars-crossing and near-Earth asteroids. *Icarus* **117**, 45–61 (1995)
- Fu, R.R., Weiss, B.P., Shuster, D.L., Gattacceca, J., Grove, T.L., Suavet, C., Lima, E.A., Li, L., Kuan, A.T.: An ancient core dynamo in asteroid Vesta. *Science* **338**, 238–241 (2012)
- Gauss, K.F.: *Theoria motus corporum coelestium in sectionibus conicis solem ambientum* (Hamburg: Perthes und Besser) tr., Davis, C. H. 1857. *Theory of the motion of the heavenly bodies moving about the sun in conic sections* (Boston: Little, Brown & Company). Original reprinting, 1981. In *Werke*, Bd. 7. 1–280. Georg Olms Verlag, Hildesheim/New York (1809)
- Gladman, B., Coffey, J.: Mercurian impact ejecta: meteorites and mantle. *Meteorit. Planet. Sci.* **44**, 285–291 (2009)
- Gounelle, M., Meibom, A.: The origin of short-lived radionuclides and the astrophysical environment of solar system formation. *Astrophys. J.* **680**, 781–792 (2008)
- Grady, M.M.: Catalogue of Meteorites, 5th edn. The Natural History Museum, London (2000). Updates available at: <http://www.nhm.ac.uk/research-curation/research/projects/metcat/>
- Henney, W.J., O'Dell, C.R.: A Keck high-resolution spectroscopic study of the Orion Nebula proplyds. *Astronom. J.* **118**, 2350–2368 (1999)
- Hewins, R.H.: Chondrules. *Annu. Rev. Earth Planet. Sci.* **25**, 61–83 (1997)
- Hirayama, K.: Groups of asteroids probably of common origin. *Proc. Phys. Math. Soc. Japan Ser. 2* (9), 354–361 (1918a)
- Hirayama, K.: Groups of asteroids probably of common origin. *Astronom. J.* **31**, 185–188 (1918b)
- Hodge, P.: Meteorite Craters and Impact Structures of the Earth. The University Press, Cambridge (1994)
- Hutchison, R.: Meteorites. University Press, Cambridge, UK (2004)
- Irving, A.J., Kuehner, S.M., Bunch, T.E., Ziegler, K., Chen, G., Herd, C.D.K., Conrey, R.M., Ralew, S.: Ungrouped mafic achondrite Northwest Africa 7325: a reduced, iron-poor cumulate Olivine Gabbro from a differentiated planetary body. 44th Lunar and Planetary Science Conference, The Woodlands, Texas. Abstract 2164 (2013)
- Jaumann, R., Williams, D.A., Buczkowski, D.L., Yingst, R.A., Preusker, F., Hiesinger, H., Schmedemann, N., Kneissl, T., Vincent, J.B., Blewett, D.T., Buratti, B.J., Carsenty, U., Denevi, B.W., De Sanctis, M.C., Garry, W.B., Keller, H.U., Kersten, E., Krohn, K., Li, J.-Y., Marchi, S., Matz, K.D., McCord, T.B., McSween, H.Y., Mest, S.C., Mittlefehldt, D.W., Mottola, S., Nathues, A., Neukum, G., O'Brien, D.P., Pieters, C.M., Prettyman, T.H., Raymond, C.A., Roatsch, T., Russell, C.T., Schenk, P., Schmidt, B.E., Scholten, F., Stephan, K., Sykes, M.V., Tricarico, P., Wagner, R., Zuber, M.T., Sierks, H.: Vesta's shape and morphology. *Science* **336**, 687–690 (2012)
- Jewitt, D., Luu, J.: Physical nature of the Kuiper belt. In: Mannings, V., Boss, A.P., Russell, S.S. (eds.) *Protostars and Planets IV*, pp. 1201–1229. University of Arizona Press, Tucson, AZ (2000)
- Jewitt, D., Agarwal, J., Weaver, H., Mutchler, M., Larson, S.: The extraordinary multi-tailed Main-Belt Comet P/2013 P5. *Astrophys. J. Letters* **778**: L21 (4pp) (2013)
- Joy, K.H., Crawford, I.A., Russell, S.S., Swinyard, B., Kellett, B., Grande, M.: Lunar Regolith Breccias MET01210, PCA02007 and DAG400: their importance in understanding the lunar surface and implications for the scientific analysis of D-CIXS data. *Lunar Planet. Sci.* **37**(1274 Suppl), 5221 (2006)
- Karlsson, H.R., Clayton, R.N., Gibson Jr., E.K., Mayeda, T.K.: Water in SNC meteorites: evidence for a Martian hydrosphere. *Science* **255**, 1409–1411 (1992)
- Karttunen, H., Kroger, P., Oja, H., Poutanen, M., Donner, K.J. (eds.): *Fundamental Astronomy*. Springer, Berlin (2003)
- Kelley, D.H., Milone, E.F.: *Exploring Ancient Skies*, 2nd edn. Springer, New York (2011)
- Kirsten, T.: Time and the solar system. In: Dermott, S.F. (ed.) *Origin of the Solar System*, pp. 267–346. Wiley, New York (1978)

- Lindblad, B.A., Southworth, R.B.: A study of asteroid families and streams by computer techniques. In: Gehrels, T. (ed.) *Physical Studies of Minor Planets*, pp. 338–352. NASA SP 267, Washington, DC (1971)
- Liu, Y., Nyquist, L., Wiesmann, H., Shih, C., Schwandt, C., Takeda, H.: Internal Rb-Sr age and initial $^{87}\text{Sr}/^{86}\text{Sr}$ of a silicate inclusion from the Campo Del Cielo iron meteorite. *Lunar Planet. Sci.* **XXXIV** (2003)
- Marti, K., Kim, J.S., Thakur, A.N., McCoy, T.J., Keil, K.: Signatures of the Martian atmosphere in glass of the Zagami meteorite. *Science* **267**, 1981–1984 (1995)
- Matsumura, S., Pudritz, R.E., Thommes, E.W.: Saving planetary systems: dead zones and planetary migration. *Astrophys. J.* **660**, 1609–1623 (2007)
- Meaburn, J.: An extended high-speed flow from a compact, ionized knot in the Orion Nebula (M42). *Month. Notice. R. Astronom. Soc.* **233**, 791–800 (1988)
- Milone, E.F., Wilson, W.J.F.: *Solar System Astrophysics: Background Science and the Inner Solar System*, 2nd edn. Springer, New York (2014)
- Morbidelli, A., Brown, M.E.: The Kuiper belt and the primordial evolution of the solar system. In: Festou, M.C., Keller, H.U., Weaver, H.A. (eds.) *Comets II*, pp. 175–191. University of Arizona Press, Tucson, AZ (2004)
- Morbidelli, A., Bottke Jr., W.F., Froeschlé, C., Michel, P.: Origin and evolution of near-Earth objects. In: Bottke Jr., W.F., Cellino, A., Paolicchi, P., Binzel, R.P. (eds.) *Asteroids III*, pp. 409–422. University of Arizona Press, Tucson, AZ (2002)
- Moser, D.E., Chamberlain, K.R., Tait, K.T., Shmitt, A.K., Darling, J.R., Barker, J.R., Hyde, B.C.: Solving the Martian meteorite age conundrum using micro-baddeleyite and launch-generated zircon. *Nature* **499** doi:10.1038/nature12341 (2013)
- O'Dell, C.R., Wen, Z.: Postrefurbishment mission Hubble Space Telescope images of the Orion Nebula: proplyds, Herbig-Haro objects, and measurement of a circumstellar disk. *Astrophys. J.* **436**, 194–202 (1994)
- Pinson Jr., W.H., Schnetzler, C.C., Beiser, E., Fairbairn, H.W., Hurley, P.M.: Rb-Sr age of stony meteorites. *Geochim. Cosmochim. Acta* **29**, 455–466 (1965)
- Righter, K., Gruener, J.: *The Lunar Meteorite Compendium* (2012). <http://www-curator.jsc.nasa.gov/antmet/lmc/index.cfm>
- Russell, C.T., Raymond, C.A., Coradini, A., McSween, H.Y., Zuber, M.T., Nathues, A., De Sanctis, M.C., Jaumann, R., Konopliv, A.S., Preusker, F., Asmar, S.W., Park, R.S., Gaskell, R., Keller, H.U., Mottola, S., Roatsch, T., Scully, J.E.C., Smith, D.E., Tricarico, P., Toplis, M. J., Christensen, U.R., Feldman, W.C., Lawrence, D.J., McCoy, T.J., Prettyman, T.H., Reedy, R.C., Sykes, M.E., Titus, T.N.: Dawn at Vesta: testing the protoplanetary paradigm. *Science* **336**, 684–686 (2012)
- Sears, D.W.G., Dodd, R.T.: *Meteorites and the Early Solar System*. University of Arizona Press, Tucson, AZ (1988)
- Shimoda, G., Nakamura, N., Kimura, M., Kami, T., Nohda, S., Yamamoto, K.: Evidence from the Rb-Sr system for 4.4 Ga alteration of chondrules in the Allende (CV3) parent body. *Meteorit. Planet. Sci.* **40**(Nr 7), 1059–1072 (2005)
- Smith, B.A., Terrie, R.J.: A circumstellar disk around Beta Pictoris. *Science* **226**, 1421–1424 (1984)
- Tatsumoto, M., Unruh, D.M., Desborough, G.A.: U-Th-Pb and Rb-Sr systematics of Allende and U-Th-Pb systematics of Orgueil. *Geochim. Cosmochim. Acta* **40**, 617–634 (1976)
- Taylor, S.R.: *Solar System Evolution: A New Perspective*. University Press, Cambridge (1992)
- Taylor, A.D., Baggaley, W.J., Steel, D.I.: Discovery of interstellar dust entering the Earth's atmosphere. *Nature* **380**, 323–325 (1996)
- Tholen, D.J.: Asteroid taxonomic classifications. In: Binzel, R.P., Gehrels, T., Matthews, M.S. (eds.) *Asteroids II*, pp. 1139–1150. University of Arizona Press, Tucson, AZ (1989)
- Treiman, A.H., Gleason, J.D., Bogard, D.D.: The SNC meteorites are from Mars. *Planet. Space Sci.* **48**, 1213–1230 (2000)

- Tsiganis, K., Gomes, R., Morbidelli, A., Levison, H.F.: Origin of the orbital architecture of the giant planets of the Solar System. *Nature* **435**, 459–461 (2005)
- Urey, H.C., Craig, H.: The composition of stone meteorites and the origin of the meteorites. *Geochim. Cosmochim. Acta* **4**, 36–82 (1953)
- Van Schmus, W.R., Wood, J.A.: A chemical-petrologic classification for the chondritic meteorites. *Geochim. Cosmochim. Acta* **31**, 747–765 (1967)
- Wasson, J.T.: Meteorites: Their Record of Early Solar System History. Freeman, New York (1985)
- Wetherill, G.W., Chapman, C.R.: Asteroids and meteorites. In: Kerridge, J.F., Matthews, M.S. (eds.) *Meteorites and the Early Solar System*, pp. 35–67. The University of Arizona Press, Tucson, AZ (1988)
- Williams, J.P., Cieza, L.A.: Protoplanetary disks and their evolution. *Annu. Rev. Astronom. Astrophys.* **49**, 67–117 (2011)
- Wlotzka, F.: A weathering scale for the ordinary chondrites. *Meteoritics* **28**, 460 (1993)
- Wood, J.A.: Meteorites and the Origin of Planets. McGraw-Hill, New York (1968)
- Wood, J.A.: Meteorites. In: Beatty, J.K., Chaikin, A. (eds) *The New Solar System*, 3rd ed., pp. 241–250. Sky, Cambridge, MA; Press Syndicate of University of Cambridge, Cambridge, UK (1990)
- Zappalà, V., Cellino, A., Farinella, P., Knezevic, Z.: Asteroid families. I. Identification by hierarchical clustering and reliability assessment. *Astronom. J.* **100**, 2030–2046 (1990)
- Zeigler, R.A., Korotev, R.L., Jolliff, B.L., Haskin, L.A.: Petrography of lunar meteorite MET 01210. *Lunar and Planetary Science*, **XXXVI**, Abstract No. 2385 (2005)
- Zeilik, M., Gregory, S.A.: *Introductory Astronomy and Astrophysics*. Saunders College Publishing, Fort Worth, TX (1998)

Chapter 16

Extra-Solar Planetary Systems

16.1 Historical Perspective

Our solar system can no longer be considered unique! Planets are common among stars like the Sun, especially those richer in metals¹ and they are not absent near other types of stars, such as sub-giants, giants, a certain type of pulsar, and around very cool, low-mass late K and M dwarfs. In fact, it appears that the latter types of stars may harbor the greatest number of extrasolar planets. Such stars are so common that recent estimates suggest that there are as many planets as stars in the galaxy. We suspect they may be even more numerous.

Toroidal circumstellar disks have been discovered around main sequence stars through detection of extended infrared regions around young main sequence stars and through direct visual imaging with an occulting disk blocking the light of the star. The first star about which a disk was detected with the coronagraphic technique, as the latter is called, was β Pictoris. Beginning in 1995, planetary discoveries have increased monthly. Virtually every issue of the major journals now contains papers on circumstellar disks, disk remnants, or extra-solar planets. The history of pursuit of such planets did not start in 1995, however.

From the 1960s on, Peter Van de Kamp (1963, 1975 and references therein), of the Sproul Observatory claimed to discover one or possibly two Jupiter mass companions for Barnard's Star on the basis of proper motions. This study has not been replicated and the planets remain in doubt. Moreover a lengthy radial velocity study by Choi et al. (2013) has placed strong limitations on any planets around Barnard's Star, by finding no periodic signals above 2 m/s. This rules out planets with masses above $10 M_E$ ($0.03 M_J$) in orbits with periods of 2 years and less, unless the orbits lie much closer to the plane of the sky than Van de Kamp thought.

Other early searches for planets in orbit around stars included that by Campbell and Walker (1979), and Campbell et al. (1988) using a spectrograph at the

¹ The term “metals” in astrophysics frequently, as here, refers to all elements heavier than hydrogen and helium.

Canada–France–Hawaii Telescope. At those times the precision achievable with the technique that they employed was almost sensitive enough to reveal the radial velocity variations of the star in its absolute orbit with planetary objects.

In 1992, planets were detected around a pulsar (Wolszczan and Frail 1992). Although some claimed detections of planetary-sized masses around such an object have been found to be due to artifacts of the observing and data reduction processes, in the case of PSR 1257+12, the claim has thus far survived all scrutiny. Since then, other planet-bearing pulsar system candidates have been found; e.g., PSR B1620-26. We discuss these systems later. In 1995, the discovery of a planet around a main sequence star, 51 Pegasi, was announced by Michel Mayor at Geneva (Mayor and Queloz 1995). Confirmation of the planetary nature of this object, and the discovery of about a dozen other candidates, were announced in short order by a team headed by Geoffrey Marcy (see the Marcy and Butler 1998 review). In these cases, radial velocity variations of the stars indicated the presence of massive Jupiter-like planets.

The kinds of methods that can be used to find planets around other stars are described in Sect. 16.2; each is limited in particular ways, but all have proven productive. For nearly two decades, one method (spectroscopy) was the most successful (Sect. 16.2.1). Many suspected planets have been detected by this method. However, other methods are yielding more and more detections. The first planet to be observed by photometric transits (Sect. 16.2.2) of the surface of a star, HD 209458b (discussed in detail in Sect. 16.4.1) had been discovered previously through radial velocity variations of the star. By 2013, a number of ground-based campaigns and two space-based missions (CoRoT and Kepler) have revealed thousands of candidate transiting planets, most of them yet to be confirmed. Increasing numbers of other candidate planets are being discovered by photometric as well as radial velocity and astrometric techniques, and most of these have been or are in the process of being confirmed with a variety of techniques.

As of mid-November, 2013, there were 1039 confirmed planets in 787 planetary systems listed on the Extrasolar Planet Encyclopedia site, <http://voparis-exoplanet-new.obspm.fr> and another 3455 unconfirmed Kepler-mission candidates listed on the exoplanet.org interactive website.

Table 16.1 lists a subset of the stars with known planetary systems and Table 16.2 is a list of the confirmed planets of these stars. The comprehensive website maintained by Jean Schneider (CNRS-LUTH, Paris Observatory), <http://exoplanet.eu/catalog> and that maintained by the extra-solar planet finding group, <http://exoplanets.org> (Wright et al. 2011), have proven invaluable for compiling these tables, and should be consulted for updates and for details on other systems. Table 16.1 includes data from the Bright Star Catalogue, from the SIMBAD database accessed through: <http://simbad.u-strasbg.fr/Simbad>, and from other sources in the literature, some of which are identified in the comments column of Table 16.2. The data are arranged according to right ascension and are thus suitable for observational use. The observable quantities are emphasized, but some absolute parameters, such as the true size of the orbit, the planetary radius, and the

mass, when known, are also given. The columns of Table 16.1 give: the most familiar designations (1, 2); the position in 2000.0 coordinates (3–8); the spectral type (9); the V (or other, as indicated) magnitude (10); the (B-V) color index (11); the star’s parallax (12) and uncertainty in it (13) in units of milliarc-sec; the corresponding distance (14), and lower and upper bounds (15, 16), respectively; the radial velocity (17); and the proper motion in RA and Dec, rounded to the nearest milliarc-sec per year (18, 19); finally, the number of planets discovered in that system to date (20). We have not entered several types of data which would be useful to know, namely the mass, radius, effective temperature, rotational velocity indicator ($v \sin i$, where i is the inclination of the star’s rotation pole to the line of sight), and an indication of chemical composition ([Fe/H]). These quantities tend to be model specific, so we refer the reader to the references in Table 16.2 for relevant sets of these data.

The planets are listed in Table 16.2, and are placed in the same order as their host stars in Table 16.1. The columns of Table 16.2 display: the name of the system (1–2); the component (3; the star itself is component “a”, and companions usually are designated “b” for the first discovered, “c” for the second, and so on); the period of the system and the uncertainty in it (4, 5); the semi-major axis, and its uncertainty, in au (6, 7); the eccentricity and its uncertainty (8, 9); the projected mass (or the actual mass if the inclination is derived through a non-spectroscopic method) and its uncertainty, given in units of Jupiter’s mass (10, 11); the inclination and its uncertainty in degrees (12, 13); the radius and its uncertainty in terms of Jupiter’s radius (14, 15); an epoch, T_0 , usually a moment of periastron passage, and its uncertainty (16, 17), in modified Julian Day numbers (JDN-24 400 000); a predicted moment of transit, T_t , and its uncertainty (18, 19); and two columns of comments (20, 21). Abbreviated references are given in the last column and usually not listed in the end of chapter References list to save space; double asterisks mark short references placed at the end of the table. Again, space limitations prevent us from including still more data, such as the argument of periastron, that would be useful in carrying out analytical studies.

Some of the RV-detected planets in this list may actually be brown dwarfs or, perhaps, members of some intermediate but not yet recognized class. This is the case because the inclinations, i , of their orbits are not usually known and spectroscopic analysis yields only the projected masses, $M \sin i$. Where the companion may be a brown dwarf, we designate the system with a “BD?” in column 20, and provide references for these cases in column 21. Column 20 also indicates if the planet has been detected astrometrically (“A”), photometrically through a transit eclipse of its star (“T”), eclipse or pulsation timings (and in pulsars, pulse timings) (“V”), through gravitational lensing events (“G”), by direct imaging (“I”), or by indirect means (“In”). In most of these techniques, the masses obtained are not projected, whereas those determined through the radial velocity method, namely $M \sin i$, are lower limits to M . When known, the full masses are indicated in column 10.

Wherever possible, we have extracted the data from the original papers in preference to the on-line compilations. It is important to note, however, that the Schneider et al. (2011) and Wright et al. (2011) on-line sites may have more recent

Table 16.1 A selected list of stars with planets

Henry Draper Catalog Number	Names Bayer/Flamsteed/HR/Hipparcos/ Other Designation	Position (2000.0)						Spectral Type
		RA h	RA m	RA s	Dec Deg	Dec '	Dec "	
HD 142	HR 6, HIP 522	00	06	19.2	-49	04	31	G1 IV
HD 1461	BD -08 38, LTT 149	00	18	41.6	-08	03	10	G0 V
-	HIP 5158, CD -23 395	01	06	01.9	-22	27	10	K5 V
HD 7449	HIP 5806	01	14	29.4	-05	02	49	F9.5 V
HD 9446	HIP 7245	01	33	20.1	+29	15	55	G5
HD 9826	50 epsilon And, HR 458, HIP 7513	01	36	47.8	+41	24	20	F8 V
HD 10180	HIP 7599	01	37	53.6	-60	30	42	G1 V
HD 11506	BD -20 219, HIP 8770	01	52	50.5	-19	30	24	G0 V
HD 11964	HIP 9094	01	57	09.6	-10	14	33	G5
HD 12661	HIP 9683	02	04	34.3	+25	24	52	G6 V/K0 III/K0 V
HD 12929	alpha Ari, HR 617	02	07	10.3	+23	27	46	K2 III
HD 13808	HIP 10301	02	12	42.9	-53	44	38	K2 V
-	HIP 13044, CD -36 1052	02	47	37.4	-36	06	27	F2, HB
HD 20003	HIP 14530	03	07	37.9	-72	19	19	G8 V
-	HIP 14810, BD +20 518	03	11	14.2	+21	05	50	G5
HD 20794	82 e Eri, HR 1008, HIP 15510	03	19	55.6	-43	04	11	G8 V
HD 20781	HIP 15526, CD -29 1229	03	20	02.9	-28	47	02	G9.5 V
HD 21693	HIP 16184	03	27	12.5	-58	19	25	G9 IV-V
HD 22049	18 epsilon Eri, HR 1084, HIP 16537	03	32	55.8	-09	27	30	K2 V
-	Gl 163, HIP 19394	04	09	15.7	-53	22	25	M3.5d
HD 27442	epsilon Ret, HR 1355, HIP 19921	04	16	29.0	-59	18	08	K2 IVA/gK5
HD 28305	epsilon Tau, HR 1409	04	28	36.9	+19	10	50	K0 III
HD 31527	HIP 22905	04	55	38.4	-23	14	31	G0 V
HD 37124	HIP 26381	05	37	02.5	+20	43	51	G4 V/IV-V
HD 37605	HIP 26664	05	40	01.7	+06	03	38	K0 V
HD 39194	HIP 27080	05	44	31.9	-70	08	37	K0 V
HD 38529	HIP 27253	05	46	34.9	+01	10	05	G4 IV/G4 V
HD 39060	beta Pic, HR 2020	05	47	17.1	-51	03	59	A6 V
-	BD -06 1339, HIP 27803	05	53	00.3	-05	59	41	K7 V/M0 V
HD 40307	HIP 27887	05	54	04.2	-60	01	24	K2.5 V
HD 41004A	HIP 28393, HDS 814(A), WDS J05598-4814A	05	59	49.7	-48	14	23	K1 V
HD 44627	AB Pic	06	19	12.9	-58	03	16	K2 V
HD 45364	HIP 30579	06	25	38.4	-31	28	51	K0 V
-	WASP-12, 2MASS J063032.79+294020.4	06	30	32.8	+29	40	20	G0d
HD 47186	HIP 31540	06	36	08.8	-27	37	20	G5 V
HD 47536	HR 2447, HIP 31688	06	37	47.6	-32	20	23	K0 III-K2 III
-	CoRoT-7, 2MASS 06434947-0103468	06	43	49.5	-01	03	47	K0 V
HD 51608	HIP 33229	06	54	51.3	-55	15	34	K0 IV-V
HD 60532	HR 2906, HIP 36795	07	34	03.2	-22	17	46	F6 IV-V
-	NGC 2423 No. 3, BD -13 2130, 2MASS J07370922-1354239	07	37	09.2	-13	54	24	G IV-V
HD 62509	Pollux, 78 beta Gem, HR 2990, NSV3712	07	45	19.0	+28	01	34	K0 IIIb
-	XO-2, GSC -3413-00005	07	48	06.5	+50	13	33	K0 V
HD 65216	HIP 38558	07	53	41.3	-63	38	50	G5 V
HD 69830	HIP 36616	08	08	23.9	-12	37	56	G8 V/K0 V
HD 73526	HIP 42214	08	37	16.5	-41	19	09	G6 V
-	HAT-P-13, 2MASS J08393180+4721073	08	39	31.8	+47	21	07	G4
HD 74156	HIP 42723	08	42	25.1	+04	34	41	G0 V
HD 75732	55 rho ¹ Cnc, HR 3522, HIP 43587	08	52	35.8	+28	19	51	G8 V
HD 80606	NSV 4463, IDS 09158+5102B, HIP 45982	09	22	37.6	+50	36	13	G5
HD 82943	HIP 47007	09	34	50.7	-12	07	46	G0 V

(continued)

Table 16.1 (continued)

Stellar Properties				d error				PM		
V	B-V	p mas	p error mas	d pc	-	+	Vr km/s	RA mas	Dec	No of planets
5.70	0.52	39.00	0.64	25.64	-0.41	0.43	+2.60	+575	-40	2
7.14	0.67	43.02	0.51	23.25	-0.27	0.28	-10.7	+417	-144	3
10.21	1.08	24.28	2.14	41.19	-3.34	3.98	+14.91	+203	-107	2
7.48	0.60	25.69	0.48	38.93	-0.71	0.74	-19.9	-161	-139	2
8.35	0.68	19.10	1.06	52.36	-2.75	3.08	+20.2	+192	-54	2
4.09	0.54	74.25	0.72	13.47	-0.13	0.13	-28.30	-173	-381	4
7.32	0.63	25.63	0.38	39.02	-0.57	0.59	+35.2	-14.6	+6.5	7 or 9
7.51	0.60	19.34	0.58	51.71	-1.51	1.60	-8.1	+23	-99	2
6.42	0.83	29.43	0.91	33.98	-1.02	1.08	-6.90	-368	-243	2
7.44	0.72	26.91	0.83	37.16	-1.11	1.18	-47.27	-108	+75	2
1.996	1.16	49.56	0.25	20.18	-0.10	0.10	-14.51	+189	-148	1
8.38	0.85	34.91	0.67	28.65	-0.54	0.56	+40.4	-108	+31	2
9.98	0.44	0.17	0.04	5900	-	-	+306	+3.6	+10.4	1
8.37	0.77	22.83	0.65	43.80	-1.21	1.28	-16.5	+73	-9	2
8.51	0.75	18.91	1.45	52.88	-3.77	4.39	-5.3	-3	-54	3
4.255	0.715	165.47	0.19	6.04	-0.01	0.01	+87.3	+3038	+727	3
8.60	1.01	28.27	1.08	35.37	-1.30	1.41	+40.14	+349	-57	2
7.94	0.775	30.88	0.49	32.38	-0.51	0.52	+39.1	+250	+94	2
3.73	0.88	310.74	0.85	3.22	-0.01	0.01	+15.50	-976	+18	1
11.811	1.491	66.69	1.82	14.99	-0.40	0.42	+36.9	+1041	+583	2
4.44	1.08	54.84	0.50	18.23	-0.16	0.17	+29.30	-48	-168	1
3.5	1.01	22.24	0.25	44.96	-0.50	0.51	+38.36	+106	-38	1
7.484	0.587	25.93	0.60	38.57	-0.87	0.91	+25.6	-66	+130	3
7.68	0.67	30.08	1.15	33.24	-1.22	1.32	-12.00	-80	-420	3
8.69	0.83	23.32	1.31	42.88	-2.28	2.55	-22.05	+199	-13	2
8.075	0.766	38.61	0.65	25.90	-0.43	0.44	-8	-309	+1238	3
5.94	0.75	23.57	0.92	42.43	-1.59	1.72	+28.90	-80	-142	2
3.861	0.168	51.44	0.12	19.44	-0.05	0.05	+20	+5	+83	1
9.693	1.348	49.23	1.65	20.31	-0.66	0.70	+26.0	-1	-346	2
7.147	0.95	76.95	0.37	13.00	-0.06	0.06	+30.4	-53	-60	6
8.65	0.84	23.24	1.02	43.03	-1.81	1.98	+42.20	-42	+65	1
9.19	0.84	21.97	0.82	45.52	-1.64	1.76	+22.20	+14	+45	1
8.1	0.72	30.59	0.68	32.69	-0.71	0.74	+15.9	+53	-15	2
11.57	0.57	-	-	-	-	-	-	-0.7	-7.8	1
7.6	0.71	25.26	0.65	39.59	-0.99	1.05	+3.8	+21	-263	2
5.26	1.19	8.24	0.56	121.36	-7.72	8.85	+78.80	+109	+64	1
11.73	1.05	-	-	-	-	-	-	+13	-4	3
8.17	0.78	28.71	0.51	34.83	-0.61	0.63	+40.1	-26	-160	2
4.39	0.55	39.53	0.27	25.30	-0.17	0.17	+61.1	-40	+47	2
9.45	1.21	-	-	766	-	-	+18.2	+1.9	-5.4	1
1.15	1.00	96.74	0.87	10.34	-0.09	0.09	+3.30	-626	-46	1
11.18	0.82	-	-	150	-2.00	4	+47.4	-35	-154	1
7.98	0.64	28.10	0.69	35.59	-0.85	0.90	+42.30	-122	+146	2
5.95	0.79	79.48	0.77	12.58	-0.12	0.12	+44.30	-69	-208	3
9.00	0.69	10.57	1.01	94.61	-8.25	10.00	+26.10	-60	+162	2
10.6	0.73	-	-	-	-	-	-	-25	-28	2
7.62	0.54	15.49	1.10	64.56	4.28	4.93	+3.70	+25	-200	2
5.95	0.87	79.80	0.84	12.53	0.13	0.13	+26.60	-484	-234	5
8.93	0.72	17.13	5.79	58.38	14.75	29.81	+3.30	+47	+7	1
6.54	0.59	36.42	0.84	27.46	0.62	0.65	+8.10	+2	-174	2

(continued)

Table 16.1 (continued)

Henry Draper Catalog Number	Names Bayer/Flamsteed/HR/Hipparcos/ Other Designation	Position (2000.0)						Spectral Type
		RA h	RA m	RA s	Deg	'	"	
-	BD -08 2823, LTT 3669	10	00	47.9	-09	31	00	K3 V
-	BD +20 2457, 2MASS J10164485+1953290	10	16	44.9	+19	53	29	K2 II
HD 89484	41 gamma Leo A, HR 4057, HIP 50583, ADS 7724AB	10	19	58.2	+19	50	31	K0 III
HD 90043	24 Sex, HIP 50887	10	23	28.3	+00	54	08	G5
HD 93385	HIP 52676	10	46	15.1	-41	27	52	G2/G3 V
HD 95128	47 UMa, HR 4277, HIP 53721	10	59	28.0	+40	25	49	G0 V
HD 96700	HIP 54400	11	07	54.4	-30	10	28	G0 V
-	DP Leo, IRXS J111715.2+175733	11	17	16.0	+17	54	41	AM Her, pulsar
HD 99492	83 Leo B, Wolf 394, HIP 55848	11	26	46.3	+03	00	23	K2 V
-	GJ 433, HIP 56528, 2MASS J11352695-3232232	11	35	27.0	-32	32	16	M1 V
-	GJ 436, HIP 57087	11	42	11.1	+26	42	24	M2.5
-	HIP 57274, 2MASS J11444095+3057339	11	44	41.0	+30	57	37	K5 V
HD 102272	HIP 57428	11	46	23.5	+14	07	26	K0
HD 108874	HIP 61028	12	30	26.9	+22	52	47	G5
HD 109271	HIP 61300	12	33	35.6	-11	37	19	G5d
-	HW Vir, HIP 62157	12	44	20.2	-08	40	17	sdB + dM
-	PSR B1257+12, PSR J1300+1240	13	00	03.6	+12	40	56	-
-	DT Vir, Ross 458AB, HIP 63510	13	00	46.6	+12	22	33	M2 Ve
IID 115617	61 Vir, IIR 5019, IIIP 64924	13	18	25.0	-18	18	31	G5 V
HD 117176	70 Vir, HR 5072, HIP 65721	13	28	25.8	+13	46	44	G2.5 Va/G5 V
-	NY Vir, 2MASS J13384814-0201491	13	38	48.2	-02	01	49	sdB + dM
HD 120136	4 tau Boo, HR 5185, HIP 67275	13	47	15.7	+17	27	25	F6 IV/F7 V
HD 125612	HIP 70123	14	20	53.5	-17	28	53	G3 V
HD 128311	HIP 71395	14	36	00.6	+09	44	47	K0 III
IID 128621	alpha Cen B, IIR 5460, IIIP 71681	14	39	39.4	-60	50	22	K1 V
HD 134060	HR 5632, HIP 74273	15	10	44.7	-61	25	20	G0 V
HD 134987	23 Lib, HR 5657, HIP 74500	15	13	28.7	-25	18	34	dG4/G5 V
HD 134606	HIP 74653	15	15	15.0	-70	31	11	G6 IV
-	GJ 581, HO Lib, Wolf 562, HIP 74995	15	19	26.8	-07	43	20	M3
HD 136352	HR 5699, HIP 75181	15	21	48.2	-48	19	03	G4 V
-	GQ Lup	15	49	12.1	-35	39	04	K7e V
-	NN Ser, 2MASS J15525613+1254446	15	52	56.1	+12	54	45	DAOI(WD) + M4
HD 143107	eps Crb, HR 5947, HIP 78159	15	57	35.3	+26	52	41	K2 III
-	WASP-17, 2MASS J15595095-2803422	15	59	50.9	-28	03	42	F6 V
HD 143761	15 rho Crb, HR 5968., HIP 78459	16	01	02.7	+33	18	13	G2 V/G0 Va
-	XO-1, GSC 02041-01657	16	02	11.8	+28	10	10	-
-	UScoCTIO 108	16	05	53.9	-18	18	42.7	M7, Brown dwarf
-	1RSXs 160929, IRXS J160929.1-210524	16	09	30.3	-21	04	59	K7 V/M0
HD 147018	HIP 80250	16	23	00.1	-61	41	20	G9 V
-	PSR B1620-26, NGC 6121 IRF 1030	16	23	38.1	-26	31	53	-
HD 155358	HIP 83949	17	09	34.8	+31	21	23	G0
-	PSR J1719-14, PSR J1719-1438	17	19	10.1	-14	38	01	-
-	OGLE-2012-BLG-0026L	17	34	18.7	-27	08	34	-
HD 159868	HIP 86375	17	38	59.5	+43	08	44	G5 V
HD 160691	mu Arae, HR 6585, HIP 86796	17	44	08.7	-51	50	03	G3 IV-V/G5 V
-	MOA-2009-BLG-266L	17	48	06.0	-35	00	19	-
-	OGLE 05-071L, EWS 2005-BUL-071L	17	50	09.0	-34	40	23	-
-	OGLE-Tr 10, V5125 Sgr	17	51	28.3	-29	52	35	G2 V
-	OGLE-2006-BLG-109L, OGLE BUL-SC37 381991	17	52	34.6	-30	05	16	-
HD 163607	HIP 87601, 2MASS J17534049+5623309	17	53	40.6	+56	23	30	G5 IV
-	OGLE 2005-BLG-390L	17	54	19.2	-30	22	38	-
-	OGLE 2003-BLG-235L, MOA 2003-BLG-53, EWS 2003-BUL-235	18	05	16.4	-28	53	42	G/K V
HD 168443	HIP 89844	18	20	03.9	-09	35	45	G5 IV
HD 169830	HR 6907, HIP 90485	18	27	49.5	-29	49	01	G0 V/F9 V
-	KOI 250, Kepler 26, 2MASS J18594583+4633595	18	59	45.8	+46	34	00	-
-	KOI 904, Kepler 55, 2MASS J19004040+4401352	19	00	40.4	+44	01	35	K5

(continued)

Table 16.1 (continued)

Stellar Properties				PM					
V	B-V	p mas	p error mas	d pc	d error		RA mas	Dec mas	No of planets
					-	+			
9.86	1.08	23.53	1.56	42.50	2.64	3.02	+8.10	-376	+27 2
9.74	1.25	-	-	-	-	-	-	-37	-31 2
1.98	1.15	25.07	0.52	39.89	0.81	0.84	-35.65	+304	-154 1
6.441	0.959	12.91	0.38	77.46	2.21	2.35	+7.08	+66	-35 2
7.486	0.94	23.70	0.69	42.19	1.19	1.27	+47.3	-48	-54 2
5.10	0.56	71.04	0.66	14.08	0.13	0.13	+12.60	-316	+55 3
6.503	0.607	38.98	0.47	25.65	0.31	0.31	+12.7	-505	-131 2
17.5	-	-	-	-	-	0	-	-	1
7.57	1.01	55.59	3.31	17.99	1.01	1.14	+1.70	-730	+191 1
9.813	1.51	112.58	1.44	8.88	0.11	0.12	-	-73	-852 2
10.68	1.52	97.73	2.27	10.23	0.23	0.24	+10.00	+896	-814 1
8.96	1.13	38.58	1.00	25.92	0.65	0.69	+28.6	-26	-381 3
8.71	1.00	4.10	0.97	243.90	46.66	75.59	-	-6.5	+6.2 2
8.76	0.71	14.59	1.24	68.54	5.37	6.37	-30.70	+129	-89 2
8.05	0.66	16.21	0.75	61.69	2.73	2.99	-5.40	-170	+81 2
10.61	-0.20	2.03	2.01	492.61	-245.09	-	+42	+7.5	-14 1
-	-	-	-	-	-	-	-	-	3
9.76	1.473	85.54	1.53	11.69	0.21	0.21	-13.56	-616	-14 1
4.74	0.70	116.89	0.22	8.56	0.02	0.02	-8.5	-1070	-1064 3
5.00	0.69	55.22	7.30	18.11	2.11	2.76	+4.90	-235	-576 1
13.30	0.30	-	-	-	-	-	-	-	1
4.50	0.48	64.12	0.70	15.60	0.17	0.17	-15.60	-480	+54 1
8.32	0.61	18.45	1.09	54.20	3.02	3.40	-18.45	-61	-68 3
7.51	0.99	60.35	0.99	16.57	0.27	0.28	-9.60	+205	-250 2
1.33	0.88	747.10	1.20	1.339	-0.002	0.002	-20.7	-3614	+803 1
6.285	0.625	41.32	0.45	24.20	0.26	0.27	+38.3	-185	-11 2
6.45	0.70	38.98	0.98	25.65	0.63	0.66	+3.40	-399	-75 2
6.854	0.756	37.74	0.54	26.50	-0.37	0.38	-	-178	-165 3
10.61	1.15	159.52	2.27	6.27	0.09	0.09	-9.50	-1225	-100 4
5.649	0.63	67.51	0.39	14.81	0.09	0.09	-69.4	-1623	-276 3
11.40	0.96	-	-	140:	50:	50:	-	-27	-14 1
16.67	-0.67	-	-	-	-	-	-	-	2
4.13	1.23	14.73	0.21	67.89	0.95	0.98	-30.92	-77	-61 1
11.79	0.24	-	-	-	-	-	-	-8	-11 1
5.40	0.61	57.38	0.71	17.43	0.21	0.22	+ 18.40	-197	-773 1
11.19	0.66	-	-	200	20	20	-	-20	+15 1
-	-	-	-	145	2	2	-	-	1
I=11.0	B=13.7	-	-	-	-	-	-	-11	-22 1
8.30	0.77	23.28	0.86	42.96	1.53	1.65	-27.9	-178	-315 2
22.01	-	-	-	-	-	-	-	-	1
7.270	0.52	22.67	0.48	44.11	0.91	0.95	-9.2	-222	-216 2
-	-	-	-	-	-	-	-	-	1
-	-	-	-	4080	300	-	-	-	2
7.24	0.72	17.04	0.76	58.69	2.51	2.74	-23.5	-232	-167 2
5.15	0.70	65.46	0.80	15.28	0.18	0.19	-9.00	-15	-191 4
15.86	V-I=1.82	-	-	3040	330	330	-	-	1
I = 19.5	-	-	-	2900	-	-	-	-	1
15.78	V-I=0.85-	-	-	1500	-	-	-	-	1
19.04	V-I=2.39-	-	-	-	-	-	-	-	2
7.979	0.783	14.53	0.46	68.82	2.11	2.25	-	-76	+120 2
I=15.7	-	-	-	6500	1000	1000	-	-	1
I=21.4	-	-	-	5200	2900	200	-	-	1
6.92	0.70	26.40	0.85	37.88	1.18	1.26	-48.85	-92	-224 1
5.91	0.48	27.53	0.91	36.32	1.16	1.24	-17.40	-84	+15 2
J=13.41	J-K=0.78-	-	-	-	-	-	-	-	2
J=13.97	J-K=0.68-	-	-	-	-	-	-	-	2

(continued)

Table 16.1 (continued)

Henry Draper Catalog Number	Names Bayer/Flamsteed/HR/Hipparcos/ Other Designation	Position (2000.0)							Spectral Type	
		RA		Dec						
		h	m	s	Deg	,	"	"		
–	KOI 806, Kepler 30, 2MASS J19010807+3856502	19	01	08.1	+47	29	28	–		
–	KOI 377, Kepler 9	19	02	17.8	+38	24	03	G2		
–	KOI 72, Kepler 10	19	02	43.1	+50	14	29	G3		
–	TrES 1, GSC 02625-01324	19	04	09.8	+36	37	58	K0 V		
HD 177830	HIP 93746	19	05	20.8	+25	55	14	dK2/K0		
–	KOI 244, Kepler 25, 2MASS J19063321+3929164	19	06	33.2	+39	29	16	–		
–	KOI 775, Kepler 52, 2MASS J19065712+4958327	19	06	57.1	+49	58	32	–		
–	KOI 1529, Kepler 59, 2MASS J19080948+4638244	19	08	09.5	+46	38	24	–		
–	KOI 70, Kepler 20, 2MASS J19104752+4220194	19	10	47.5	+42	20	19	–		
–	KOI 262, Kepler 50, 2MASS J19122420+5002013	19	12	24.2	+50	02	01	–		
–	KOI 2086, Kepler 60, 2MASS J19155069+4215540	19	15	50.7	+42	15	54	–		
–	KOI 707, Kepler 33, 2MASS J19161861+4600187	19	16	18.6	+46	00	18	–		
–	KOI 872, Kepler 46, 2MASS J19170449+4236150	19	17	04.5	+42	36	15	–		
–	KOI 1102, Kepler 24, 2MASS J19213918+3820375	19	21	39.2	+38	20	37	–		
–	KOI 829, Kepler 53, 2MASS J19215082+4033448	19	21	50.8	+40	33	45	–		
–	KOI 277, Kepler 36, 2MASS J19250004+4913545	19	25	00.0	+49	13	55	–		
HD 181433	HIP 95467, GJ 756.1	19	25	09.9	-66	28	10	K3 III-IV		
HD 183263	HIP 95740	19	28	24.6	+08	21	29	G2 IV		
–	KOI 870, Kepler 28, 2MASS J19283288+4225459	19	28	32.9	+42	25	45	–		
–	KOI 961, Kepler 42, 2MASS J19285255+4437096	19	28	52.6	+44	37	10	M3 V		
–	KOI 841, Kepler 27, 2MASS J19285682+4105091	19	28	56.8	+41	05	09	–		
–	KOI 248, Kepler 49, 2MASS J19291070+4035304	19	29	10.7	+40	35	30	–		
–	KOI 1270, Kepler 57, 2MASS J19343390+4439253	19	34	33.9	+44	39	25	–		
–	KOI 1241, Kepler 56, 2MASS J19350200+4152187	19	35	02.0	+41	52	18	–		
–	KOI 935, Kepler 31, 2MASS J19360552+4551110	19	36	05.5	+45	51	11	–		
–	KOI 168, Kepler 23, 2MASS J19365254+4928452	19	36	52.6	+49	28	45	–		
–	KOI 886, Kepler 54, 2MASS J19390574+4303226	19	39	05.8	+43	03	22	–		
–	KOI 3154, Kepler 47, 2MASS J19411149+4655136	19	41	11.5	+46	55	14	–		
HD 186427	16 CygB, HR 7504, ADS 12815 B, HIP 96901	19	41	52.0	+50	31	05	G3 V		
–	KOI 1336, Kepler 58, 2MASS J19452607+3906546	19	45	26.1	+39	06	54	–		
–	KOI 620, Kepler 51, 2MASS J19455514+4956156	19	45	26.1	+49	56	15	–		
HD 187123	HIP 97336	19	46	58.1	+34	25	10	G5 IV		
–	KOI 157, Kepler 11, 2MASS J19482762+4154328	19	48	27.6	+41	54	33	G 5 V		
–	KOI 952, Kepler 32, 2MASS J19512217+4634273	19	51	22.2	+46	34	27	M1 V		
–	KOI 137, Kepler 18, 2MASS J19521906+4444467	19	52	19.1	+44	44	47	–		
–	KOI 738, Kepler 29, 2MASS J19532359+4729284	19	53	23.6	+42	29	28	–		
–	KOI 148, Kepler 48, 2MASS J19563341+4056564	19	56	33.4	+40	56	56	–		
HD 189733A	V452 Vul, HIP 98505, GJ 4130, Wolf 864	20	00	43.7	+22	42	39	G5 V		
HD 190360	GJ 777A, HR 7670, HIP 98767	20	03	37.4	+29	53	49	G6 IV		
HD 192263	ADS 13547 A, HIP 99711	20	13	59.8	-00	52	01	K2 V		
HD 195019	ADS 13886 AB, HIP 100970	20	28	18.6	+18	46	10	G3 IV-V		
–	NSVS 1425 (AB), 2MASS J20200405+0437564	20	20	00.5	+04	37	57	sdOB+dM		
HD 200964	2MASS J21063983-0348110	21	06	39.8	+03	48	11	K0		
HD 202206	HIP 104903	21	14	57.8	-20	47	21	G5 IV/G6 V		
HD 204313	HIP 106006	21	28	12.2	-21	43	32	G5 V		
–	HAT P-17, 2MASS J21380873+3029193	21	38	08.7	+30	29	19	G0d		
HD 206860	HN Peg, HR 8314	21	44	31.2	+14	46	20	G0 V		
HD 207832	2MASS J21523626-2601352	21	52	36.3	-26	01	34	G5 V		
HD 209458	V376 Peg, HIP 108859	22	03	10.8	+18	53	04	F8 V		
–	V391 Peg, GSC 02212-01369	22	04	12.2	+26	25	08	sdB		
HD 215152	HIP 112190, GJ 4291	22	43	21.3	-06	24	03	K0		
HD 215456	HR 8658, HIP 112414	22	46	08.0	-48	58	44	G0.5 V		
HD 215497	HIP 112441	22	46	36.8	-56	35	58	K3 V		
–	GJ 876, IL Agr, HIP 113020	22	53	16.7	-14	15	49	M5.0 V		
HD 217014	51 Peg, HR 8729, NSV 14374, HIP 113357	22	57	28.0	+20	46	08	G2.5 IVa		

(continued)

Table 16.1 (continued)

Stellar Properties				PM								
V	B-V	p mas	p error mas	d pc/s		d error		Vr km/s	RA		Dec	
				-	+	-	+		mas	mas	No of planets	
J=14.00	J-K=0.42	-	-	-	-	-	-	-	-1.5	-2.1	3	
13.90	J-K=0.37	-	-	-	-	-	-	+5.6	-13	3		
J=9.89	J-K=0.39	-	-	-	-	-	-	-19.0	+43	2		
11.30	0.90	-	-	156	6	6	-	-40	-22	1		
7.18	1.09	16.94	0.76	59.03	2.53	2.77	-74.00	-41	-52	2		
10.77	0.55	-	-	-	-	-	-	+16	+6.8	2		
J=13.15	J-K=0.79	-	-	-	-	-	-	-	-	2		
J=13.25	J-K=0.33	-	-	-	-	-	-	-	-	2		
12.51	0.90	-	-	-	-	-	-	-4.2	-26	5		
10.54	0.48	-	-	-	-	-	-	+1.5	-5.3	2		
J=12.80	J-K=0.29	-	-	-	-	-	-	-	-	3		
13.74	0.65	-	-	-	-	-	-	-0.39	-15	5		
J=13.81	J-K=0.47	-	-	-	-	-	-	-	-	2		
J=13.76	J-K=0.39	-	-	-	-	-	-	-	-	2		
J=14.25	J-K=0.44	-	-	-	-	-	-	-	-	2		
11.94	0.72	-	-	-	-	-	-	-	-	2		
8.38	1.04	37.37	1.13	26.76	0.79	0.83	+37.9	-231	+235	3		
7.86	0.63	18.93	1.06	52.83	2.80	3.13	-50.70	-18	-33	2		
J=13.33	J-K=0.62	-	-	-	-	-	-	-	-	2		
J=12.18	J-K=0.71	-	-	-	-	-	-	+84	-423	3		
J=14.48	J-K=0.36	-	-	-	-	-	-	-	-	2		
J=13.18	J-K=0.80	-	-	-	-	-	-	-	-	2		
J=13.44	J-K=0.54	-	-	-	-	-	-	-	-	2		
J=10.81	J-K=0.59	-	-	-	-	-	-	-	-	2		
J=14.23	J-K=0.36	-	-	-	-	-	-	-	-	2		
J=12.35	J-K=0.36	-	-	-	-	-	-	-	-	2		
J=13.51	J-K=0.86	-	-	-	-	-	-	-	-	2		
J=13.97	J-K=0.43	-	-	-	-	-	-	-	-	2		
6.20	0.66	47.14	0.27	21.21	0.12	0.12	-27.4	-135	-164	1		
J=13.64	J-K=0.36	-	-	-	-	-	-	-	-	2		
J=13.56	J-K=0.36	-	-	-	-	-	-	-	-	2		
7.86	0.61	20.87	0.71	47.92	1.58	1.69	-17.60	+143	-123	2		
J=12.54	J-K=0.37	-	-	610:	-	-	-	-	-	6		
J=13.61	J-K=0.86	-	-	303	14	14	-32.5	-	-	2		
J=12.19	J-K=0.43	-	-	-	-	-	-	-	-	3		
J=14.13	J-K=0.47	-	-	-	-	-	-	-	-	2		
J=11.70	J-K=0.48	-	-	-	-	-	-	-	-	2		
7.68	V-K=2.14	51.41	0.69	19.45	0.26	0.26	-2.38	-2.5	-251	1		
5.71	0.73	62.92	0.62	15.89	0.16	0.16	-43.30	+683	-524	2		
7.79	0.94	50.27	1.13	19.89	0.44	0.46	-11.30	-63	+262	1		
6.91	0.64	26.77	0.89	37.36	1.20	1.28	-92.70	+349	-57	1		
J=13.66	J-K=-0.29	-	-	-	-	-	-	+9.0	0.0	2		
6.487	0.892	13.85	0.52	72.20	2.61	2.82	-71.84	+95	+50	2		
8.08	0.69	21.58	1.14	46.34	2.33	2.58	-	-38	-120	2		
8.02	0.69	21.11	0.62	47.37	1.35	1.43	-10.1	+43	-272	3		
10.38	0.95	-	-	-	-	-	-	-77	-125	2		
5.95	0.58	55.91	0.45	17.89	0.14	0.15	-18.9	+230	-113	1		
8.79	0.69	18.37	0.92	54.44	2.60	2.87	-17.0	+132	-143	2		
7.65	0.53	21.12	0.72	47.35	1.56	1.67	-14.80	+29	-18	1		
B=13.6	-	-	-	-	-	-	-	-	-	1		
8.13	0.99	46.47	0.90	21.52	0.41	0.43	-13.81	-156	-291	2		
6.630	0.63	26.30	0.46	38.02	0.65	0.68	-18.8	+209	-48	2		
8.95	0.97	22.94	1.09	43.59	1.98	2.17	-	-54	-60	2		
10.17	1.56	213.28	2.12	4.69	0.05	0.05	+8.70	+960	-675	4		
5.49	0.67	65.10	0.76	15.36	0.18	0.18	-31.20	+208	+61	1		

(continued)

Table 16.1 (continued)

Henry Draper Catalog Number	Names Bayer/Flamsteed/HR/Hipparcos/ Other Designation	Position (2000.0)							Spectral Type	
		RA			Dec					
		h	m	s	Deg	'	"			
HD 216956	24 beta PsA, Fomalhaut, HR 8728	22	57	39.0	-29	37	20	A3 V		
HD 217107	HR 8734, HIP 113421	22	58	15.5	-02	23	43	G5/G8 IV		
HD 218396	V342 Peg, HR 8799	23	07	28.6	+21	08	04	A5 V, γ Dor var.		
HD 222404	5 gamma Cep, HR 8974, NSV 14656, HIP 116727	23	39	20.8	+77	37	56	K III-IV/K I V		
HD 222439	kappa And, HR 8976	23	40	24.4	+44	20	02	B9 IV		

(continued)

orbital parameters following further modeling, with more data, especially if another planet has been added to the system beyond those in the sources we have cited.

An interesting fact to emerge from Table 16.2 is the number of cases where the eccentricity is large. If all planets formed within a disk and with coplanar, concentric orbits, how could such eccentricities arise? In some cases a large inferred eccentricity is not real, but arises in the modeling when another still undetected planet is present in a nearby orbit. When both planets are included in the modelling, the orbits may display significantly lower eccentricities. Often the high eccentricities are real, however, as shown by later analyses with longer base-line data. Whether they are in close orbits or not, resonances among orbiting bodies can play an important role in determining this orbital parameter as well as the argument of perihelion. One suggestion is that some higher eccentricities may arise through the *Kozai mechanism* (Kozai 1962), where angular momentum exchanges with a distant companion star in a high-inclination orbit give rise to long-period oscillations in the eccentricity and inclination of the planet. A fuller discussion can be found in Takeda and Rasio (2005). If the Kozai mechanism applies, the period of oscillation of the eccentricity can be shown to be (Mazeh and Shaham 1979; Ford et al. 2000; Takeda and Rasio 2005),

$$P_{\text{Kozai}} = P_p \left[(M_p + M_1)/M_2 \right] \left(a_{12}/a_p \right)^3 \left(1 - e_{12}^2 \right)^{3/2} \quad (16.1)$$

where P_p and a_p are the period and semimajor axis of the planet, M_1 and M_2 are the masses of the primary and secondary components of the binary, and a_{12} and e_{12} are the semimajor axis and eccentricity of the binary, respectively. For the inner pair of objects, we take the planet and primary star, à la Marmier et al. (2013), or, more specifically, Takeda and Rasio (2005). If this period is shorter than the age of the system and of such other dynamic timescales as the apsidal motion due to stellar oblateness or general relativity effects (see Milone and Wilson 2014, Sect. 9.1.2), it could well apply. Most stars with planetary systems are not known to be binary stars (although some certainly are). Interactions among planets, both detected and undetected, and with objects in the equivalent of an Edgeworth-Kuiper Belt or within a disk, may be responsible in other cases.

Despite the question of their true masses, the RV-detected objects in Tables 16.1 and 16.2 cannot *all* be brown dwarfs, because a plot of the distribution of projected masses with semi-major axis indicates a dearth of more massive objects; an increase in numbers at this end of the scale would be expected if they were brown dwarfs (Mayor et al. 1998).

Table 16.1 (continued)

Stellar Properties				PM			
V	B–V	<i>p</i> mas	<i>p</i> error mas	<i>d</i> error		RA mas	Dec mas
				–	+		
1.16	0.09	129.81	0.47	7.70	0.03	0.03	+6.5
6.18	0.72	50.71	0.75	19.72	0.29	0.30	-14.00
6.0	0.26	25.38	0.70	39.40	-1.06	1.12	-11.5
3.23	1.03	72.50	0.52	13.79	0.10	0.10	-42.40
4.137	-0.061	19.37	0.19	51.63	0.50	0.51	-9.
							+81
							-19
							1

Table 16.3 lists a number of confirmed brown dwarfs. The table is characteristic only; no attempt has been made to make it complete.

Column 3 indicates if the substellar companion is isolated (I) or found in combination (C) with one or more stars. Among the non-RV studied brown dwarfs, the comments indicate the cluster or other details of combination, and the basis for the brown dwarf identification (AO = adaptive optics; BD = brown dwarf; bin = binary; CI = color index, i.e., in color-magnitude diagrams; CS = circumstellar; DA = dynamical analysis; EB = eclipsing binary; IR = infrared observations; Li = presence of lithium or CH₄ = methane in spectra; phot = photometry; PM = detected in proper motion survey; SB2 = double-lined spectroscopic binary; WD = white dwarf). Other surveys identified by acronyms: 2MASS, DENIS-P, HIPP. = HIPPARCOS, SDSS (Sloan Digital Sky Survey). A colon suffix indicates uncertainty.

Where the object is in a binary system, some estimated orbital properties are given. The HD 168443 system, with a main sequence star and a likely brown dwarf, also harbors a possible planet with $M_J \sin i = 7.7$ (Udry et al. 2002).

The uncertainties are such that objects recorded here as brown dwarfs near the planetary cut-off limit may actually be planets. Similarly, some labeled sub-stellar objects may be low-mass stars.

Analyses of the light- and RV curves of the eclipsing system 2MASS J0535-0546 provide precise and accurate radii for this pair of brown dwarfs: 0.67 and 0.515 R_{\odot} , for components *a* and *b*, respectively; in addition, the ratio of temperatures is deduced to be $T_2/T_1 = 1.054$, so that the lower mass object is hotter (Stassun et al. 2006), an effect attributable to extensive star spot activity on the more massive component (Stassun et al. 2007).

Despite the example of HD 168443, cited above, brown dwarfs have been said to be absent in binary combinations with stars, a circumstance referred to in the literature as the “brown dwarf desert.” The 2MASS, DENIS, and SDSS surveys show that they are present in the field and in combination with other low-mass, low-luminosity objects. The view that the deficiency in brown dwarf companions of normal stars in binary star systems might be, as Basri (2000) put it, merely a brown-dwarf “desert island,” partly attributable to the faintness and extreme redness (due to their low temperatures) of the objects, waxes and wanes. For example, at large separations the frequency of occurrence is higher (Gizis et al. 2001) and this may be true for very small separations also. However, the deficit continues to be apparent as more and more planets, including objects suspected of being “free-floating planets,” continue to be discovered, whereas brown dwarf numbers in binary systems are being discovered at much lower rates.

Table 16.2 A selected list of extrasolar planets

Planet Designation	Bayer/Flamsteed/HIP/ Gliese/other Designation	Com Period (d)	P error (d)	α au	error (au)	e	e error	M/M ($\sin i$) [*] (M _J)	M^* (M _J)	i deg	err deg
HD 142	HIP 522	b	349.7	1.2	1.02	0.03	0.17	0.06	1.25	0.15	...
HD 142	HIP 522	c	6005	477	5.3	0.7	0.21	0.07	5.3	0.07	...
HD 1461	BD-08 38	b	5.7718	0.0001	0.063431	0.000008	0	...	0.024	0.002	...
HD 1461	BD-08 38	c	446	9	1.151	0.016	0	...	0.088	0.015	...
HD 1461	BD-08 38	d	5017	1171	5.78	0.82	0	...	0.27	0.16	...
...	HIP 5158, CD-23 395	b	345.63	1.99	0.89	0.01	0.54	0.04	1.44	0.14	...
...	HIP 5158, CD-23 395	c	9018	3181	7.70	1.88	0.14	0.10	15.04	10.55	...
HD 7449	HIP 5806	b	1275	15	2.340	0.04	0.820	0.06	1.11	+0.37,-0.27	...
HD 7449	HIP 5806	c	4046	366	4.96	0.3	0.53	0.08	2.0	+0.54,-0.36	...
HD 9446	HIP 7245	b	30.052	0.027	0.189	0.006	0.20	0.06	0.7	0.06	...
HD 9446	HIP 7245	c	192.9	0.9	0.654	0.022	0.06	0.06	1.82	0.17	...
HD 9826	ups And, HIP 7513	b	4.617136	0.000047	0.0595	0.0034	0.013	0.016	0.672	0.056	...
IID 9826	ups And, HIP 7513	c	241.33	0.20	0.832	0.048	0.224	0.021	1.92	0.16	...
IID 9826	ups And, HIP 7513	d	1278.1	2.9	2.53	0.15	0.267	0.021	4.13	0.35	...
HD 9826	ups And, HIP 7513	e	3848.86	0.74	5.2456	0.0007	0.00540.0004	0.0059	0.028
IID 10180	HIP 7599	b	1.17765	0.00018	0.02225	0.00038	0.0	...	0.00437	0.00082	90
HD 10180	HIP 7599	c	5.75962	0.00028	0.0641	0.0011	0.077	0.033	0.0414	0.002	90
HD 10180	HIP 7599	d	16.3567	0.0043	0.1285	0.0022	0.143	0.058	0.0376	0.0024	90
HD 10180	HIP 7599	e	49.747	0.024	0.2699	0.0045	0.065	0.035	0.0799	0.0044	90
IID 10180	HIP 7599	f	112.72	0.20	0.4928	0.0083	0.133	0.066	0.0743	0.0053	90
HD 10180	HIP 7599	g	602.	11	1.423	0.030	0	...	0.0673	0.0094	90
HD 10180	HIP 7599	h	2248	+102,-106	3.42	+0.12,-0.13	0.151	0.072	0.2055	0.0145	90
IID 10180	HIP 7599	i	9.66	-0.02,+0.07	0.090	-0.005,+0.004	0.05	-0.05,+0.23	0.006	-0.0003,+0.0110	90
HD 10180	HIP 7599	j	67.55	-0.88,+0.68	0.330	-0.016,+0.017	0.07	-0.07,+0.12	0.016	-0.010,+0.042	90
HD 11506	BD-20 219, HIP 8770	b	1270	-95,+194	2.43	-0.12,+0.24	0.22	-0.12,+0.25	3.44	-0.47,+0.90	...
IID 11506	BD-20 219, HIP 8770	c	170.6	-6.2,+3.3	0.639	-0.017,+0.007	0.42	-0.42,+0.20	0.82	-0.50,+0.31	...
HD 11964	HIP 9094	b	1945	26	3.16	0.19	0.041	0.47	0.622	0.056	...
HD 11964	HIP 9094	c	37.91	0.04	0.229	0.013	0.30	0.17	0.0788	0.01	...
IID 12661	HIP 9683	b	262.71	0.08	0.83	0.05	0.377	0.008	2.3	0.19	...
IID 12661	HIP 9683	c	1708	14	2.90	0.17	0.031	0.022	1.92	0.16	...
HD 12929	alpha Ari, HR 617	b	380.8	0.3	1.2	0.25	0.03	1.8	0.2
HD 13808	HIP 10301	b	14.182	0.005	0.102	0.002	0.17	0.07	0.033	0.003	...
HD 13808	HIP 10301	c	53.83	0.11	0.248	0.004	0.43	0.20	0.363	0.005	...
...	HIP 13044, CD -36 1052	b	16.2	0.3	0.116	0.01	0.25	0.05	1.25	0.05	...
HD 20003	HIP 14530	b	11.849	0.003	0.097	.002	0.40	0.08	0.038	0.003	...
HD 20003	HIP 14530	c	33.823	0.065	0.196	.003	0.16	0.09	0.042	0.004	...
...	HIP 14810, BD +20 518	b	6.67386	0.00002	0.069	0.004	0.14270.0009	3.88	0.32
...	HIP 14810, BD +20 518	c	147.73	0.07	0.55	0.03	0.16	0.01	1.28	0.10	...
HD 20781	HIP 14810, BD +20 518	d	952	15	1.89	0.11	0.17	0.03	0.57	0.05	...
HD 20781	BD +00 571	b	29.15	0.02	0.169	0.003	0.11	0.06	0.038	0.004	...
HD 20781	BD +00 571	c	85.13	0.12	0.346	0.006	0.28	0.09	0.050	0.004	...
HD 20794	82 c Eri, HR 1008	b	18.3150	0.0088	0.121	0.002	0	...	0.0085	0.0009	90
HD 20794	82 e Eri, HR 1008	c	40.114	0.053	0.204	0.003	0	...	0.0076	0.0013	90
HD 20794	82 e Eri, HR 1008	d	90.31	0.18	0.3498	0	...	0.0151	0.0019	90	...
HD 21693	HIP 16184	b	22.656	0.024	0.148	0.002	0.26	0.17	0.032	0.005	...
HD 22049	eps Eri, HIP 16537	b	2502	10	3.39	0.36	0.25	0.23	1.55	0.24	30.1 3.2
...	GI 163, HIP 19394	b	0.63	0.001	0.0607	0.0001	0.354	0.002	...
...	GI 163, HIP 19394	c	25.63	0.02	0.1254	0.0001	0.226	0.003	...
HD 27442	eps Ret, HIP 19921	b	428.1	1.1	1.271	0.073	0.060	0.043	1.56	0.14	...

(continued)

Table 16.2 (continued)

R $R(R_J)$	T_0 (mod. JDN)	T_f (mod. JDN)	T_f err (d)	Comment/ Method*	Comments/reference
...	12683	26	...	RV	Wittenmyer 2012 ApJ, 753, 169
...	15954	223	...	RV	Wittenmyer 2012 ApJ, 753, 169
...	10366.52	RV	Rivera et al. 2010 ApJ, 708, 1492-1499
...	RV	Rivera et al. 2010 ApJ, 708, 1492-1499
...	RV	Rivera et al. 2010 ApJ, 708, 1492-1499
...	RV	Feroz et al. 2011 MNRAS, 416, L104-L108
...	RV	Feroz et al. 2011 MNRAS, 416, L104-L108; possible 3rd p w P=108 d
...	15298.	22	...	RV	Dumusque et al. 2011 A&A, 535, 55
...	15883.	172	...	RV	Dumusque et al. 2011 A&A, 535, 55
...	14854.4	2	...	RV	Hébrard 2010 A&A 513, 373-378
...	14510	70	...	RV	Hébrard 2010 A&A 513, 373-378
...	14425.02	0.64	11802.966	0.033	RV
...	14265.57	0.64	10063.9	3.8	RV
...	13937.73	0.64	8127	39	RV
...	RV	Wright et al. 2009 ApJ, 693, 1084-1099
...	13999.51	RV, 7-pl fit	Lovis et al. 2011 A&A, 528, A112; but see Tuomi 2012
...	14001.5	RV, 7-pl fit	Lovis et al. 2011 A&A, 528, A112; but see Tuomi 2012
...	14005.38	RV, 7-pl fit	Lovis et al. 2011 A&A, 528, A112; but see Tuomi 2012
...	14008.79	RV, 7-pl fit	Lovis et al. 2011 A&A, 528, A112; but see Tuomi 2012
...	14027.55	RV, 7-pl fit	Lovis et al. 2011 A&A, 528, A112; but see Tuomi 2012
...	14042.58	RV, 7-pl fit	Lovis et al. 2011 A&A, 528, A112; but see Tuomi 2012
...	13619.17	RV, 7-pl fit	Lovis et al. 2011 A&A, 528, A112; but see Tuomi 2012
...	RV	Tuomi 2012 A&A, 543, 152
...	RV	Tuomi 2012 A&A, 543, 152
...	RV	Tuomi&Kotiranta 2009 A&A, 496, L13-L16; Fischer et al.** 2007
...	RV	Tuomi&Kotiranta 2009 A&A, 496, L13-L16; Fischer et al.** 2007
...	14170	380	...	RV	Wright et al. 2009 ApJ, 693, 1084-1099
...	14370	380	...	RV	Wright et al. 2009 ApJ, 693, 1084-1099
...	14152.75	0.9	...	RV	Wright et al. 2009 ApJ, 693, 1084-1099
...	16153.42	0.9	...	RV	Wright et al. 2009 ApJ, 693, 1084-1099
...	11213.5	7.4	...	RV	Lee et al. 2011 A&A, 529, A34
...	RV	Mayor et al. 2011
...	RV	Mayor et al. 2011
...	15109.78	0.02	...	RV	Setiawan et al. 2010 Science, 330, 1642-1644
...	RV	Mayor et al. 2011
...	RV	Mayor et al. 2011
...	13694.598	0.007	...	RV	Wright et al. 2009 ApJ, 699, L97-L101
...	14672.240	0.007	...	RV	Wright et al. 2009 ApJ, 699, L97-L101
...	14317.198	0.007	...	RV	Wright et al. 2009 ApJ, 699, L97-L101
...	RV	Mayor et al. 2011
...	RV	Mayor et al. 2011
...	14774.81	RV	Pepe et al. 2011 A&A, 534, 443-458
...	14766.8	RV	Pepe et al. 2011 A&A, 534, 443-458
...	14779.3	RV	Pepe et al. 2011 A&A, 534, 443-458
...	RV	Mayor et al. 2011
...	14207	7	9330	200	A, In, RV
					Benedict et al. 2006 AJ, 132, 2206-2218; Baines & Armstrong 2012 ApJ, 714, A138; Butler et al. 2006, Hatzes et al. 2000; mass funct.= $5.9(+/-1.0)\times 10^{-10}$
...	RV	Extrasolar Planet Encyclopedias
...	10836	55	10692.2	8.6	RV
					Butler et al. 2006 ApJ, 646, 505-522

(continued)

Table 16.2 (continued)

Planet Designation	Bayer/Flamsteed/HIP/ Gliese/other Designation	Com Period (d)	P error (d)	a au	a error (au)	e	e error	M/M ($\sin i$)*	M^* (M_J)	i err (M_J)
HD 28305	eps Tau, IIR 1409	b	594.9	5.3	1.93	0.03	0.151	0.023	7.6	0.2
HD 31527	HIP 22905	b	16.546	0.007	0.1253	0.0020	0.13	0.05	0.0363	0.0025
HD 31527	HIP 22905	c	51.28	0.09	0.2665	0.0044	0.11	0.07	0.0498	0.0035
HD 31527	HIP 22905	d	274.5	7.8	0.818	0.020	0.38	0.25	0.052	0.003
HD 37124	HIP 26381	b	154.378	0.089	0.5336	0.0002	0.054	0.028	0.675	0.017
HD 37124	HIP 26381	c	885.5	5.1	1.710	0.007	0.125	0.055	0.652	0.052
HD 37124	HIP 26381	d	1862	38	2.807	0.038	0.16	0.14	0.696	0.059
HD 37605	HIP 26664	b	55.0131	0.0006	0.2831	0.0016	0.67670.0019	2.802	0.011	...
HD 37605	HIP 26664	c	2720.	57	3.814	0.058	0.013	0.015	3.366	0.072
HD 39194	HIP 27080	b	5.6363	0.0008	0.0519	0.0008	0.20	0.10	0.0117	0.0010
HD 39194	HIP 27080	c	14.025	0.005	0.0954	0.0016	0.11	0.06	0.0187	0.0015
HD 39194	HIP 27080	d	33.941	0.035	0.1720	0.0029	0.20	0.16	0.0162	0.0021
HD 38529	HIP 27253	b	14.3102	0.0008	0.1313	0.0076	0.244	0.028	0.856	0.074
HD 38529	HIP 27253	c	2146.1	5.5	3.72	0.21	0.35510.0074	13.1	1.1	...
HD 39060	beta Pic, HR 2020	b	19.6:	...	8.8:	...	0.021:	88.5: 1.7
HD 39060	beta Pic, HR 2020	b	28.3:	...	11.2:	...	0.16	88.8: ...
HD 39060	beta Pic, HR 2020	b	8:	...	0.05:	...	7-11	...
...	BD -06 1339	b	3.8728	0.0004	0.0428	0.0007	0	...	0.027	0.004
...	BD -06 1339	c	125.94	0.44	0.435	0.007	0	...	0.17	0.03
HD 40307	HIP 27887	b	4.312	0.001	0.047	0.002	0.20	-0.16,+0.14	0.013	0.002
HD 40307	HIP 27887	c	9.618	0.005	0.081	0.005	0.06	-0.06,+0.11	0.0208	0.003
HD 40307	HIP 27887	d	20.43	0.02	0.132	0.008	0.07	-0.07,+0.09	0.0299	0.005
HD 40307	HIP 27887	e	34.6	0.2	0.19	0.01	0.15	-0.15,+0.12	0.011	0.004
HD 40307	HIP 27887	f	51.8	0.5	0.25	-0.02,+0.01	0.02	-0.02,+0.20	0.016	0.005
HD 40307	HIP 27887	g	198	-9,+6	0.60	0.03	0.29	-0.29,+0.31	0.022	0.008
HD 41004 A	HIP 28393	b	963	38	0.0059	0.0018	0.74	0.20	2.54	0.74
HD 41004 B	HIP 28393	b	1.3283	0.000012	0.000744	8.6E-06	0.081	0.012	18.37	0.22
HD 44627	Af Pic	b	260	13.5 (10-14)	...
HD 45364	HIP 30579	b	226.93	0.37	0.6813	...	0.168	0.019	0.1872	...
HD 45364	HIP 30579	c	342.85	0.28	0.8972	...	0.097	0.012	0.659	...
...	WASP-12	b	1.091423	0.000003	0.0229	0.0008	0.049	0.015	1.41	0.1
HD 47186	HIP 31540	b	4.0845	0.0002	0.050	...	0.038	0.020	0.07167	...
HD 47186	HIP 31540	c	1353.6	57.1	2.395	...	0.249	0.073	0.35061	...
HD 47536	HIP 31688	b	712.13	0.31	1.613	0.093	0.200	0.080	5.2	0.99
...	CoRoT-7	b	0.853585	0.00024	0.0172	0.0002	0	...	0.02335	0.0038
...	CoRoT-7	c	3.697	0.019	0.045	...	0	...	0.04153	0.0129
...	CoRoT-7	d:	9.021	0.019	0.080	...	0	0.05	0.0525	0.0013
HD 51608	HIP 33229	b	14.070	0.004	0.1059	0.0017	0.15	0.06	0.0413	0.0031
HD 51608	HIP 33229	c	95.42	0.39	0.379	0.006	0.41	0.18	0.0565	0.0082
HD	HR 2906, HIP 36795	b	201.30	0.60	0.759	0.044	0.28	0.03	1.03	0.16
IID 60532	IIR 2906, IIIP 36795	c	604	9	1.580	0.093	0.02	0.02	2.46	0.36
...	NGC 2413 No. 3, BD-13	b	714.3	5.3	2.10	...	0.21	0.07	10.6	...
...	2130									
HD 62509	Pollux, 78 beta Gem, HR	b	589.64	0.81	1.64	0.27	0.02	0.03	2.30	0.45
...	2990									
...	XO-2	b	2.615857	0.000005	0.0368	0.0004	0	...	0.566	0.055
HD 65216	HIP 38558	b	613.1	11	1.374	0.082	0.410	0.060	1.216	0.19
HD 69830	HIP 36616	b	8.667	0.030	0.0782	...	0.100	0.04	0.0316	...
HD 69830	HIP 36616	c	31.56	0.040	0.1851	...	0.130	0.06	0.0368	...
HD 69830	HIP 36616	d	197	3	0.627	...	0.070	0.07	0.0563	...
HD 73526	HIP 42282	b	187.50	0.03	0.651	0.038	0.390	0.054	2.04	0.29
HD 73526	HIP 42282	c	376.88	0.09	1.037	0.060	0.400	0.054	2.26	0.27

(continued)

Table 16.2 (continued)

R err $R(R_1)$	T_0 err (mod. JDN)	T_t err (mod. JDN)	T_t err (d)	Comment/ Method*	Comments/reference	
...	12879	12	...	RV	Sato et al. 2007 ApJ 661, 527-531	
...	RV	Mayor et al. 2011	
...	RV	Mayor et al. 2011	
...	RV	Mayor et al. 2011	
...	10305	11	...	RV	Wright et al. 2011 ApJ, 730, 93	
...	9534	11	...	RV	Wright et al. 2011 ApJ, 730, 93	
...	8558	11	...	RV	Wright et al. 2011 ApJ, 730, 93	
...	13378.241	0.02	15901.361	0.069	RV	Wang et al. 2012 ApJ, 761, 46
...	14840.	581	...	RV	Wang et al. 2012 ApJ, 761, 46	
...	Mayor et al. 2011	
...	Mayor et al. 2011	
...	Mayor et al. 2011	
...	14384.8	8.7	9991.56	0.17	...	Wright et al. 2009 ApJ, 693, 1084-1099
...	12255.9	8.4	10319	13	...	Wright et al. 2009 ApJ, 693, 1084-1099
...	[2006.3]:	I, T ² ; Bayesian analysis	Chauvin et al. 2012 A&A, 542, A41; Lecavalier des Etangs et al. 1995, A&A, 299, 557	
...	[2013.3]:	I; Damped LS analysis	Chauvin et al. 2012 A&A, 542, A41	
...	I	Bonnefoy et al. 2011 A&A, 528, 357-362; Ks=12.6(I), Ks-L'=1.4(2)	
...	15220.5	0.10	...	RV	LoCurto et al. 2013 A&A, 551, A59	
...	15265.2	17.6	...	RV	LoCurto et al. 2013 A&A, 551, A59	
...	14562.77	0.08	...	RV	Tuomi et al. 2013 A&A, 549 A48; Wright et al. 2009; Mayor et al. 2009 A&A 493, 639	
...	14551.53	0.15	...	RV	Tuomi et al. 2013 A&A, 549 A48; Wright et al. 2009; Mayor et al. 2009 A&A 493, 639	
...	14532.42	0.29	...	RV	Tuomi et al. 2013 A&A, 549 A48; Wright et al. 2009; Mayor et al. 2009 A&A 493, 639	
...	RV	Tuomi et al. 2013 A&A, 549 A48; Mayor et al. 2009 A&A 493, 639	
...	RV	Tuomi et al. 2013 A&A, 549 A48; Mayor et al. 2009 A&A 493, 639	
...	RV	Tuomi et al. 2013 A&A, 549 A48; Mayor et al. 2009 A&A 493, 639	
...	12425	37	...	RV	Zucker et al. 2004 A&A, 426, 695; Raghavan et al. 2006 ApJ, 646, 523	
...	12434.88	0.029	...	RV; BD?	Zucker et al. 2004 A&A, 426, 695; Raghavan et al. 2006 ApJ, 646, 523	
...	I	Bonnefoy et al. 2010 A&A, 512, 398-400; Chauvin et al. 2005	
...	13500.00	RV	Correia et al. 2009 A&A, 496, 521-526	
...	13500.00	RV	Correia et al. 2009 A&A, 496, 521-526	
1.79	0.09	14508.9761	0.0002	T, RV	Hibb et al. 2009 ApJ, 693, 1920-1928	
...	...	14566.95	0.36	...	Bouchy et al. 2009 A&A, 496, 527	
...	...	12010	180	...	RV	
...	...	11599	22	...	RV	
0.004970.00031	[14899.761]	T, RV	Butler et al. 2006 ApJ, 644, 505-522; Setiawan et al. 2003 Hatzes et al. 2011 ApJ, 743, 75-85; Queloz et al. 2009 A&A 506, 303-309; Bruntt 2010 A&A, 519, 467-478; also see Pont et al. 2011 MNRAS 411, 1953-1962	
...	...	14899.2	0.7	...	RV	
...	...	14446.16	0.09	...	RV	
...	RV	Boisse et al. 2011 A&A, 528, A44; Hatzes et al. 2010 A&A, 520, A93; Queloz et al. 2009 A&A, 506, 303-319	
...	...	13987.0	2.0	...	RV	
...	...	13730,	160	...	RV	
...	...	13213	21	...	RV	
...	...	7739.02	4.5	...	RV	
0.983	0.029	T, RV	Hatzes et al. 2006; Reffert et al. 2006 ApJ, 652, 661	
...	...	10762	25	...	RV	
...	...	13496.8	0.6	...	RV	
...	...	13469.6	2.8	...	RV	
...	...	13358	34	...	RV	
...	...	10038	15	...	RV, kinematic	
...	...	10184.5	8.6	...	RV, kinematic	

(continued)

Table 16.2 (continued)

Planet	Bayer/Flamsteed/HIP/ Gliese/other Designation	Com. Designation	Period (d)	P error (d)	α au	error (au)	e	e error	M/M ($\sin i$) [*]	M^* err (M _J)	i deg	i err deg	
HD 73526	HIP 42282	b	188.3	0.9	0.19	0.05	2.9	0.2	
HD 73526	HIP 42282	c	377.8	2.4	0.14	0.09	2.5	0.3	
...	HAT-P-13	b	2.9162	0.0000	0.04383	0.00053	0.0133		0.906	0.024	81.93	0.26	
...	HAT-P-13	c	446.22	0.27	1.226				0.66160.0052				
HD 74156	HIP 42723	b	51.638	0.004	0.29169	0.00001	0.63	0.01	1.78	0.04	
HD 74156	HIP 42723	c	2520	15	3.9	0.02	0.38	0.02	8.2	0.2	
HD 75732	rho1 Cnc, 55 Cnc, HIP 43587	b	14.651	0.0001	0.1134	0.006	0.004	0.003	0.801	0.012	
HD 75732	"	c	44.38	0.007	0.2373	0.0013	0.07	0.02	0.1646	0.0054	
HD 75732	"	d	4909	30	5.47	0.06	0.02	0.008	3.53	0.08	
HD 75732	"	e	0.736546	0.00003	0.01544	...	0	...	0.0263	0.0012	82.5	...	
HD 75732	rho1 Cnc, 55 Cnc, HIP 43587	f	261.2	0.4	0.774	0.005	0.32	0.05	0.172	0.008	
HD 80606	HIP 45982	b	111.4367	0.0004	0.455	0.008	0.933	0.0005	4.08	0.14	89.269	0.018	
HD 82943	HIP 47007	b	439.2	1.8	1.18	0.069	0.022	0.098	1.72	0.19	
HD 82943	HIP 47007	c	219.5	0.13	0.74	0.043	0.36	0.26	1.99	0.21	
...	BD-08 2823	b	5.6	0.02	0.0558	0.002	0.15	0.15	0.045	0.007	
...	BD-08 2823	c	237.6	1.5	0.68	0.02	0.19	0.09	0.33	0.03	
...	BD+20 2457	b	379.63	2.01	1.45	...	0.15	0.03	21.42	
...	BD+20 2457	c	621.99	10.2	2.01	...	0.18	0.06	12.47	
...	gamma 1 Lco	b	428.5	1.25	1.195	0.02	0.144	0.046	8.78	1	
HD 90043	24 Sex	b	455.2	3.2	1.338	0.024	0.184	0.029	1.6	0.2	
HD 90043	24 Sex	c	910	21	2.123	0.049	0.412	0.064	1.4	0.2	
HD 90043	24 Sex	b	452.8	-4.5,+2.1	1.333	-0.009,-0.0040.09	-0.06,+0.14	1.99	-0.38,+0.26
HD 90043	24 Sex	c	883	-13.8,+32.4	2.05	-0.02,-0.05	0.29	-0.09,+0.16	0.86	-0.22,+0.35	
HD 93385	HIP 52676	b	13.186	0.006	0.1116	0.0018	0.15	0.11	0.0263	0.0028	
HD 93385	HIP 52676	c	46.025	0.073	0.257	0.0043	0.24	0.18	0.0318	0.0046	
HD 95128	47 UMa, HIP 53721	b	1078	2	2.1	0.02	0.032	0.014	2.53	-0.6,+0.7	
HD 95128	47 UMa, HIP 53721	c	2391	-87,+100	3.6	0.1	0.098	-0.06,+0.047	0.54	-0.73,+0.06	
HD 95128	47 UMa, HIP 53721	d	14002	-5095,+4018	11.6	-2.9,+2.1	0.16	-16,+0.9	1.64	-48,+29	
HD 96700	HIP 54400	b	8.1256	0.0013	0.0774	0.0012	0.1	0.05	0.0284	0.002	
HD 96700	HIP 54400	c	103.49	0.58	0.422	0.007	0.37	0.19	0.0402	0.0051	
...	DP Leo	b	10230	730	8.19	0.39	0.39	0.13	6.05	0.47	
HD 99492	83 Leo B, HIP 55848	b	17.054	0.003	0.12186	0.00002	0.13	0.07	0.087	0.006	
HD 99492	83 Leo B, HIP 55848	c	4970	744	5.4	0.5	0.1	0.2	0.36	0.06	
...	GJ 433	b	7.3709	0.0008	0.05804	...	0.08	0.08	0.0182	
...	GJ 433	c	3693	253	3.6	...	0.17	0.09	44.6	
...	GJ 436, HIP 57087	b	2.64385	0.000084	0.02872	0.00029	0.16	0.052	0.0729	0.0025	86.36	0.17	
...	HIP 57274	b	8.1352	0.004	0.07	...	0.19	0.01	0.0365	0.004	
...	HIP 57274	c	32.03	0.02	0.178	...	0.05	0.02	0.409	0.009	
...	HIP 57274	d	431.7	8.5	1.01	...	0.27	0.05	0.527	0.025	
HD 102272	HIP 57428	b	127.58	0.3	0.614	0.001	0.05	0.04	5.9	0.2	
HD 102272	HIP 57428	c	520	26	1.57	0.05	0.68	0.06	2.6	0.4	
HD 107383	11 Com, HR 4697	b	326.03	0.32	1.29	0.05	0.231	0.005	19.4	1.5	
...	NGC 4349 No 127	b	677.8	6.2	2.38	...	0.19	0.07	19.8	
HD 108874	HIP 61028	b	394.48	0.6	1.053	0.061	0.128	0.022	1.34	0.12	
HD 108874	HIP 61028	c	1680	24	2.77	0.16	0.273	0.04	1.06	0.1	
HD 109271	HIP 61300	b	7.8543	0.0009	0.079	0.001	0.25	0.08	0.054	0.004	
HD 109271	HIP 61300	c	30.93	0.02	0.196	0.003	0.15	0.09	0.076	0.007	
...	HW Vir	b	5.3	0.23	0.1551	0.0054	0.46	0.05	19.23	0.24	
...	HW Vir	c	3.62	0.52	0.0468	0.0066	0.31	0.15	8.47	0.42	
...	PSR B1257+12, PSR J1300+1240	b	25.262	0.0001	0.19	...	0	...	0.00006	0.00006	

(continued)

Table 16.2 (continued)

$R(R_J)$	T_0 err (mod. R_J)	T_0 err (JDN)	T_t err (mod. JDN)	T_t err (d)	Comment/ Method*	Comments/reference
...	RV, dynamic	Tinney et al. 2006 ApJ 647, 594-599; 2:1 resonance
...	RV, dynamic	Tinney et al. 2006 ApJ 647, 594-599; 2:1 resonance
1.487	0.038	14777.98	14779.93	...	T, V	Southworth et al. 2012, MNRAS, 420, 2580-2587; Winn 2010
		15335.45	T, V	Southworth et al. 2012, MNRAS, 420, 2580-2587; Winn 2010
...	...	10793.3	0.2	...	RV	Meschiari et al. 2011ApJ, 727, 117
...	...	8416	33	...	RV	Meschiari et al. 2011ApJ, 727, 117
...	...	130350	2.2	...	RV	Endl et al. 2012 ApJ, 759, #19
...	...	13083	3.3	...	RV	Endl et al. 2012 ApJ, 759, #19
...	...	13490	437	...	RV	Endl et al. 2012 ApJ, 759, #19
0.194	0.009	15568.01	0.0001	15568.011 0.008	RV, T	Endl et al. 2012 ApJ, 759, #19
...	...	11878	5	...	RV	Endl et al. 2012 ApJ, 759, #19
0.981	0.023	15204.92	0.004	15210.64 0.001	T, RV	Hébrard et al. 2012 A&A, 516, 567-583; Wynn et al. 2009 ApJ 703, 2091; Moutou et al. 2009 A&A, 498, L5-L8
...	...	10931.41	RV	Lee et al. 2006, Mayor et al. 2004; Butler et al. reverse b and c
...	...	10969.87	RV	Lee et al. 2006, Mayor et al. 2004; Butler et al. reverse b and c
...	...	14637.7	1.6	...	RV	Hébrard et al. 2010a A&A 512, 1724-1733
...	...	14193	13	...	RV	Hébrard et al. 2010a A&A 512, 1724-1733
...	...	14677.03	28.19	...	RV; BD?	Niedzielski et al. 2009 ApJ 707, 768-777; 3:2 MMR
...	...	13866.95	27.99	...	RV; BD?	Niedzielski et al. 2009 ApJ 707, 768-777; 3:2 MMR
...	...	11236	13.5	...	RV	Han et al. 2010 A&A 509, 423-432
...	...	14758	30	...	RV, non-int. soln	Johnson et al. 2011 AJ 141, 16; Wittenmyer et al. 2012 ApJ, 761, 165
...	...	14941	30	...	RV, non-int. soln	Johnson et al. 2011 AJ 141, 16; Wittenmyer et al. 2012 ApJ, 761, 165
...	...	14762	-172,+67	...	RV, n-body soln.	Johnson et al. 2011 AJ 141, 16
...	...	14930	-97,+210	...	RV, n-body soln.	Johnson et al. 2011 AJ 141, 16
...	RV	Mayor et al. 2011
...	RV	Mayor et al. 2011
...	...	11917	-76,+63	Gregory & Fischer 2010 MNRAS 403, 731-747
...	...	12441	-825,+628	Gregory & Fischer 2010 MNRAS 403, 731-747
...	...	11736	-5051,+6783	Gregory & Fischer 2010 MNRAS 403, 731-747
...	RV	Mayor et al. 2011
...	RV	Mayor et al. 2011
...	...	13025	500	...	V	Beuermann et al. 2010, A&A, 526, A53; pulsar planet
...	...	10449	2	...	RV	Meschiari et al. 2011 ApJ, 727, 117
...	...	9636	2210	...	RV	Meschiari et al. 2011 ApJ, 727, 117
...	...	54287	RV	Delfosse et al. 2012 A&A, A&A 553 A8(15)
...	...	54287	1	...	RV	Delfosse et al. 2012 A&A, A&A 553 A8(15)
0.377	0.009	11551.72	0.11	14415.62 0.068	T, RV	Torres et al. 2008 ApJ, 677, 1324-1342; Maness et al. 2007 PASP, 119, 90; high e, small a;Beust et al. 2012 A&A, 545, A88
...	...	14801	1.3	15801.78 0.271	RV	Fischer et al. 2012 ApJ, 745, 21
...	...	15785.2	9.5	15793.04 0.176	RV	Fischer et al. 2012 ApJ, 745, 21
...	...	15108	14	...	RV	Fischer et al. 2012 ApJ, 745, 21
...	...	12146	64	...	RV	Niedzielski et al. 2009 ApJ, 693, 276
...	...	14135	260	...	RV	Niedzielski et al. 2009 ApJ, 693, 276
...	...	12899.6	1.6	...	RV, BD	Liu et al. 2008 ApJ, 672, 553-557
...	...	14114	34	...	RV	Lovis & Mayor 2007 A&A, 472, 657-664
...	...	14045	49	...	RV	Wright et al. 2009 ApJ, 693, 1084-1099; Gozdziewski et al. 2006 ApJ, 645, 688-703
...	...	12797	49	...	RV	Wright et al. 2009 ApJ, 693, 1084-1099; Gozdziewski et al. 2006 ApJ, 645, 688-703
...	...	55719	4	...	RV	Lo Curto 2013 A&A 551 A59(7)
...	...	55733	8	...	RV	Lo Curto 2013 A&A 551 A59(7)
...	...	14500	39	...	V	Lee et al. 2009 AJ, 137, 3181-3190; Kilkenny et al. 2003 The Observatory, 123, 31-36
...	...	9840	63	...	V	Lee et al. 2009 AJ, 137, 3181-3190
...	...	9765.1	0.2	...	V	Konacki et al. 2003 ApJL, 591, L147-L150; Wolszczan 1994 Science 264, 538-542

(continued)

Table 16.2 (continued)

Planet Designation	Bayer/Flamsteed/HIP/ Gliese/other Designation	Com	Period (d)	P error (d)	a au	a error (au)	e	e error	M/M^* ($\sin i$) [*] (M _J)	M^* err (M _J)	i deg	i err deg
...	PSR B1257+12, PSR J1300+1240	c	66.5419	0.0001	0.36	...	0.0186	0.0002	0.0135	0.0006
...	PSR B1257+12, PSR J1300+1240	d	98.2114	0.0002	0.46	...	0.0252	0.0002	0.0123	0.0006
...	DT Vir, Ross 458AB	c/C	...	50,000y	1100	< 6.3-11
HD 113585	HIP 63833, GJ 9425	b	263.3	2.3	0.71	0.01	0.61	0.11	0.27	0.08
HD 113585	HIP 63833, GJ 9425	c	1657	48	2.43	0.06	0.32	0.06	0.71	0.06
HD 115617	61 Vir	b	4.215	0.0006	0.050201	0.000005	0.12	0.11	0.016	0.002
HD 115617	61 Vir	c	38.021	0.034	0.2175	0.0001	0.14	0.06	0.0573	0.0035
HD 115617	61 Vir	d	123.01	0.55	0.476	0.001	0.35	0.09	0.0721	0.0082
HD 117176	70 Vir, HR 5072	b	116.6884	0.0044	0.484	0.028	0.4007	0.0035	7.44	0.61	16.1	...
...	NY Vir	b	2900	...	3.3	2.3	0.3
HD 120136	Tau Boo, HIP 67275	b	3.312463	0.000014	0.0481	0.0028	0.023	0.015	4.14	0.34
HD 120136	Tau Boo, HIP 67275	b	3.312	0	...	5.95	0.28	44.5	1.5
HD 125612	HIP 70123	c	4.1547	0.0005	0.05	...	0.27	0.12	0.058
HD 125612	HIP 70123	d	3008	202	4.2	...	0.28	0.12	7.2
HD 125612	HIP 70123	b	559.4	1.3	1.37	...	0.46	0.01	3
HD 128311	HIP 71395	b	454.2	1.6	1.086	0.008	0.345	0.049	1.45	0.13
HD 128311	HIP 71395	c	923.8	5.3	1.745	0.017	0.23	0.058	3.24	0.1
HD 128621	alpha Cen B, HR 5460	b	3.2357	0.0008	0.04185	...	0	...	0.00356	0.00028
HD 134060	HR 5632, HIP 74273	b	3.27	0.0002	0.0444	0.0007	0.4	0.04	0.0351	0.0021
HD 134060	HR 5632, HIP 74273	c	1161	27	2.226	0.051	0.75	0.19	0.151	0.071
HD 134987	23 Lib, HIP 74500	b	258.19	0.07	0.81	0.02	0.233	0.002	1.59	0.02
HD 134987	23 Lib, HIP 74500	c	5000	400	5.8	0.5	0.12	0.02	0.82	0.03
HD 134606	HIP 74653	b	12.083	0.01	0.1023	0.0017	0.15	0.1	0.0292	0.0003
HD 134606	HIP 74653	c	59.52	0.17	1.157	0.024	0.29	0.2	0.0382	0.0053
HD 134606	HIP 74653	d	459.3	8.3	1.157	0.024	0.46	0.09	0.1212	0.013
...	GJ 581	b	5.3685	0.0004	0.041	0.003	0.007	-0.07,+0.44	0.0494	0.007	>40	...
...	GJ 581	c	12.92	0.02	0.07	0.01	0.09	-0.09,+0.20	0.017	0.004	>40	...
...	GJ 581	d	66.9	-0.0,-+,9	0.22	0.02	0.39	-0.39,+0.28	0.014	0.007	>40	...
...	GJ 581	e	3.149	0.002	0.028	0.02	0.08	-0.08,+0.35	0.006	0.0023	>40	...
HD 136352	HR 5699, HIP 75181	b	11.577	0.006	0.0933	0.0015	0.18	0.14	0.0166	0.002
HD 136352	HR 5699, HIP 75181	c	27.582	0.023	0.1665	0.0028	0.16	0.07	0.0358	0.0003
HD 136352	HR 5699, HIP 75181	d	106.72	1.03	0.411	0.007	0.43	0.24	0.0317	0.0059
...	GO Lup	b	103	37	21.5	20.5
...	NN Ser	b	5571	67	5.32	0.28	0.22:	0.06:	6.71	0.41	>28	...
...	NN Ser	c	2605	124	3.20:	0.42:	0.05	0.02	4.00:	0.62:	>9	...
HD 143107	epsilon CrB, HR 5947	b	417.9	0.5	1.307	...	0.11	0.03	6.76	0.3
...	WASP-17	b	3.735442	7.3E-06	0.0501	0.0018	0.129	-0.068,+0.106	0.49	-0.056,+0.059	87.8	-1.0,+2.0
HD 143761	rho CrB, HIP 78459	b	39.845	0.0063	0.229	0.013	0.057	0.028	1.04	0.098	...	0.5?
...	XO-1, GSC 02041-01657	b	3.941534	0.000027	0.0493	0.0009	0	...	0.918	0.08	88.81	1.2
...	UScoCTIO 108	b	650	14	-8,+2
...	IRSSX 160929, 1RXS J160929-2110524	b	311	8.5	2.5
HD 147018	HIP 80250	b	44.236	0.008	0.2388	0.0039	0.4686	0.0081	2.12	0.07
HD 147018	HIP 80250	c	1008	18	1.922	0.039	0.133	0.011	6.56	0.32
...	PSR B1620-26, NGC 6121 IRF 1030	b	23	2.5	1
HD 155358	HIP 83949	b	194.3	0.3	0.64	0.01	0.17	0.03	0.85	0.05
HD 155358	HIP 83949	c	391.9	1	1.02	0.02	0.16	0.1	0.82	0.07
...	PSR 1719-14, PSR J1719-b-1438	b	0.090706	2E-10	545.3 km	0.03 km	<0.06	...	1.2
...	OGLE-2012-BLG-0026L	b	3.82	0.3	0.11	0.02
...	OGLE-2012-BLG-0026L	c	4.63	0.37	0.68	0.1
HD 159868	HIP 86375	b	1178.4	8.8	2.25	0.03	0.01	0.03	2.25	0.03

(continued)

Table 16.2 (continued)

R err $R(R_J)$ (R_J)	T_0 (mod. JDN)	T_0 err (d)	T_t (mod. JDN)	T_t err (d)	Comment/ Method*	Comments/reference	
...	9768.1	0.1	V	Konacki et al. 2003 ApJL, 591, L147-L150; Wolszczan 1994 Science 264, 538-542	
...	9766.5	0.1	V	Konacki et al. 2003 ApJL, 591, L147-L150; Wolszczan 1994 Science 264, 538-542	
1.25	I, BD?	Sp. Type T8.5; Burgasser et al. 2010 ApJ, 725, 1405-1420; Rodriguez et al. 2011 ApJ, 732, L29; largest known planetary orbit	
...	14950	8.5	RV	Moutou et al. 2011 A&A, 527A, 63	
...	16110	515	RV	Moutou et al. 2011 A&A, 527A, 63	
...	Vogt et al. 2010 ApJ, 708, 1366-1375	
...	Vogt et al. 2010 ApJ, 708, 1366-1375	
...	Vogt et al. 2010 ApJ, 708, 1366-1375	
...	7239.82	0.21	7138.27	0.21	...	Marcy & Butler 1996, ApJL, 464, L147-L151; Butler et al 2006, Nacif et al. 2004	
...	V	Qian et al. 2012 ApJL, 745, L23	
...	6957.81	0.54	6956.916	0.028	RV	Butler et al. 2006 ApJ, 646, 505-522; Butler et al. 1997 ApJ, 474, L115-118	
...	RV (CO line)	Brogi et al. 2012 Nature, 486, 502	
...	14420.17	0.23	RV	Lo Curto et al. 2010 A&A, 512, 168-183	
...	17174	-17,+396	RV	Lo Curto et al. 2010 A&A, 512, 168-183	
...	14894.9	2.5	RV	Lo Curto et al. 2010 A&A, 512, 168-183; Fischer et al. 2007	
...	13835	11	RV	Wittenmyer et al. 2009 ApJS, 182, 97-119	
...	16987	41	RV	Wittenmyer et al. 2009 ApJS, 182, 97-119	
...	15280.17	0.17	RV	Dumusque et al. 2012 Nature, 491, 207-211	
...	RV	Mayor et al. 2011	
...	RV	Mayor et al. 2011	
...	10071	0.8	10119.4	1.8	RV	Jones et al. 2010 MNRAS, 403, 1703-1713	
...	11100	600	RV	Jones et al. 2010 MNRAS, 403, 1703-1713	
...	RV	Mayor et al. 2011	
...	RV	Mayor et al. 2011	
...	RV	Mayor et al. 2011	
...	14753.95	RV	Tuomi 2011 A&A, 528, L5; Bonfils et al. 2013 A&A, 549, A109; Mayor et al. 2009	
...	14763	RV	Tuomi 2011 A&A, 528, L5; Bonfils et al. 2013 A&A, 549, A109; Mayor et al. 2009	
...	RV	Tuomi 2011 A&A, 528, L5; Bonfils et al. 2013 A&A, 549, A109; Mayor et al. 2009	
...	14750.31	RV	Tuomi 2011 A&A, 528, L5; Bonfils et al. 2013 A&A, 549, A109; Mayor et al. 2009	
...	RV	Mayor et al. 2011	
...	RV	Mayor et al. 2011	
...	RV	Mayor et al. 2011	
3.7	I, BD?	Guenther et al. 2005 AN 326, 958-963; star is a T Tau variable; Sp late M, early L.	
...	13155	217	V	Beuermann et al. 2010 A&A, 521,L13-L16; Horner 2012 MNRAS, 425, 719; stable 2:1 resonance	
...	18029	173	V	Beuermann et al. 2010 A&A, 521,L13-L16; Horner 2012 MNRAS, 425, 719; stable 2:1 resonance	
...	11235.3	39.7	RV	Lee et al. 2012 A&A, 546, 5L	
1.99	0.08	14559.18	0.0003	14559.18	0.0003	T, RV	Anderson 2010 ApJ 709, 159-167, 2011 MNRAS 416, 2108-2122; Triaud et al. 2010 A&A, 524, 25T; orbital and star eq planes misaligned; very low-density
...	10563.2	4.1	10539.58	0.35	RV	Butler et al. 2006; Noyes et al. 1997 ApJ, 483, L111-L116; but see Gatewood et al. 2001 ApJ, 548, L61-1.63.	
1.206	-0.042,+0.047	13808.92	...	13808.92	0.0011	T	Torres et al. 2008 ApJ, 677, 1324-1342; McCullough et al. 2006; Holman et al. 2006 get R=1.8R _J ; f=89.3
...	I, BD?	Bejar et al. 2008 ApJL, 673, L185-189; host is BD
...	I	Ireland 2011 ApJ, 726, #113; Lafreniere 2010 ApJL, 689, L153; Neuhauser and Schmidt 2012; Sc-Cen OB assn	
...	14459.49	0.1	RV	Segransan et al. 2010 A&A, 511, A45	
...	15301	22	RV	Segransan et al. 2010 A&A, 511, A45	
...	V	Sigurdsson et al. 2006 Science, 301, 193	
...	11224.8	6	RV	Robertson et al. 2012 AJ, 749, 39; [Fe/H]=-0.68	
...	15345.4	28	RV	Robertson et al. 2012 AJ, 749, 39; [Fe/H]=-0.68	
...	15235.52	V	High-density stellar remnant; Bailes et al. 2011 Science 333, 1717-1720	
...	GLensing	Han et al. 2013 ApJL, 762, L28-L33	
...	GLensing	Han et al. 2013 ApJL, 762, L28-L33	
...	13435	56	RV	Wittenmyer 2012 ApJ, 753, #169; OToole et al. 2007 ApJ, 660, 1636-1641	

(continued)

Table 16.2 (continued)

Planet	Bayer/Flamsteed/HIP/ Designation Gliese/other Designation	Com	Period (d)	P error (d)	α au	α error (au)	e	e error	M/M ($\sin i$) [*]	M^* (M_J)	i deg	i err deg
HD 159868	HIP 86375	c	352.3	1.3	1	0.01	0.15	0.05	0.73	0.05
HD 160691	mu Arae, HIP 86796	b	643.25	0.9	1.497	...	0.128	0.017	1.676
HD 160691	mu Arae, HIP 86796	c(e)	4205.8	758.9	5.235	...	0.099	0.063	1.814
HD 160691	mu Arae, HIP 86796	c(d)	9.6386	0.0015	0.0909	...	0.172	0.04	0.03321
HD 160691	mu Arae, HIP 86796	d(e)	310.55	0.83	0.921	...	0.067	0.012	0.5219
...	MOA-2009-BLG-266L	b	7.6	+7.7,-1.5	3.2	+1.9,-0.5	0.0327	0.0054
...	OGLE 2005-BLG 071	b	1692	215	3.6	0.2	3.8	0.4
...	V5125 Sgr, OGLE-TR-10	b	3.101269	0.00004	0.0434	0.0014	0	...	0.62	0.14	84.5	0.6
...	OGLE 2006-BLG 109L	b	4.9y	-1.5,+1.6	2.3	0.5	0.73	0.06	64:00:00	...
...	OGLE 2006-BLG 109L	c	13.5y	-4.8,+9.7	4.5	+1.0,+1.9	0.15	-0.10,+0.17	0.27	0.02	64	+4,-7
HD 163607	HIP 87601, 2MASS J17534049+5623309	b	75.29	0.02	0.36	0.01	0.73	0.02	0.77	0.04
HD 163607	HIP 87601, 2MASS J17534049+5623309	c	1314	8	2.42	0.16	0.12	0.06	2.29	0.16
...	OGLE 2005-BLG-390L	b	2.6	+1.5,-0.6	0.017	+0.017,-0.009
HD 163917	64 nu Oph, HR 6698, HIP 88048	b	530.32	0.35	0.013853	0.0009	0.1256	0.0065	24
HD 163917	64 nu Oph, HR 6698, HIP 88048	c	3186	14	0.05213	0.00085	0.165	0.013	27
...	OGLE 2003-BLG-235L, MOA 2003-BLG-53, EWS 2003-BUL-235	3	-1.7,+0.1	1.5	-1.2,+0.1
HD 168443	HIP 168443	b	58.11247	0.00086	0.2938	0.017	0.529	0.0032	7.7	0.65
HD 169830	HIP 90485	b	225.62	0.22	0.817	0.047	0.31	0.01	2.92	0.25
HD 169830	HIP 90485	c	2100	260	3.62	0.42	0.33	0.02	4.1	0.41
...	KOI 250, Kepler 26	b	12.2829	...	0.085	...	0	...	0.38
...	KOI 250, Kepler 26	c	17.2513	...	0.107	...	0	...	0.375
...	KOI 904, Kepler 55	b	27.94814	0.00024	0.1557
...	KOI 904, Kepler 55	c	42.15164	0.00053	0.2021
...	KOI 806, Kepler 30	b	29.334	0.008	0.1855	...	0.042	0.003	0.0356	0.0044	89.82	0.16
...	KOI 806, Kepler 30	c	60.321	0.0002	0.3	...	0.0111	0.001	2.01	0.16	89.68	0.03
...	KOI 806, Kepler 30	d	143.343	0.009	0.534	...	0.022	0.005	0.0727	0.0085	89.84	0.02
...	KOI 377, Kepler 9	b	19.24316	...	0.14	0.001	0.151	...	0.252	0.013	88.55	...
...	KOI 377, Kepler 9	c	38.90861	...	0.225	0.001	0.133	...	0.171	0.013	88.12	...
...	KOI 377, Kepler 9	d	1.592851	0.000045	0.0273	0.00043	0
...	KOI 72, Kepler 10	b	0.837495	...	0.1676	...	0	...	0.0142	...	84.4	...
...	KOI 72, Kepler 10	c	42.29485	-0.0076,+0.000650.241	-0.005,+.004	<0.199	0.005	89.65	-12.+,09	...
...	TrES 1, GSC 02652-01324	b	3.030065	0.000008	0.0393	0.0006	0	...	0.752	0.047	90	-1.1,+0
HD 177830	HIP 93746	b	406.6	0.4	1.2218	0.0008	0.009	0.004	1.49	0.03
HD 177830	HIP 93746	c	110.9	0.1	0.5137	0.0003	0.3	0.1	0.15	0.02
...	KOI 244, Kepler 25	b	6.2385	...	0.068	...	0	...	12.7
...	KOI 244, Kepler 25	c	12.7204	...	0.11	...	0	...	4.16
...	KOI 775, Kepler 52	b	7.877357	0.000038	0.0631
...	KOI 775, Kepler 52	c	16.385	0.00014	0.1028
...	KOI 1529, Kepler 59	b	11.86817	0.00036	0.1931
...	KOI 1529, Kepler 59	c	17.98012	0.0003	0.1361
...	KOI 70, Kepler 20	b	3.696122	...	0.04537	...	0	...	0.0266	...	86.5	...
...	KOI 70, Kepler 20	c	10.85409	...	0.093	...	0	...	0.049	...	88.39	...
...	KOI 70, Kepler 20	d	77.61184	...	0.3453	...	0	...	0.024	...	89.57	...
...	KOI 70, Kepler 20	e	6.098493	0.000065	0.0634	<0.28	...	<0.012,>...	87.5	-34.,+33
...	KOI 70, Kepler 20	f	19.57706	0.00052	0.1379	<0.32	...	<0.021,>...	88.68	-17.,+14
...	KOI 262, Kepler50	b	7.812512	0.000052	0.0826
...	KOI 262, Kepler50	c	9.376137	0.000056	0.0932
...	KOI 2086, Kepler 60	b	7.131619	0.000093	0.0751	0.0751
...	KOI 2086, Kepler 60	c	8.91935	0.00011	0.0872	0.0872
...	KOI 2086, Kepler 60	d	11.90162	0.0002	0.1056	0.1056
...	KOI 707, Kepler 33	b	5.66793	0.00012	0.0677	0.0014	0	86.39	1.17	...

(continued)

Table 16.2 (continued)

R $R(R_J)$	T_0 (mod. JDN)	T_0 (d)	T_i (mod. JDN)	T_i err (d)	Comment/ Method*	Comments/reference
...	13239	21	RV	Wittenmyer 2012 ApJ, 753, 169; OToole et al. 2007 ApJ, 660, 1636-1641
...	12365.6	12.6	RV	Pepe et al. 2007, A&A, 462, 769-776
...	12955.2	521.8	RV	Pepe et al. 2007, A&A, 462, 769-776; xsp cat assigns "c"
...	12991.1	0.04	RV	Pepe et al. 2007, A&A, 462, 769-776; xsp cat assigns "d"
...	12708.7	8.3	RV	Pepe et al. 2007, A&A, 462, 769-776; xsp cat. assigns "c"
...	GLensing	Muraki et al. 2012 ApJ 741, #20
...	GLensing	Dong et al. 2009 ApJ 695, 970-987; Udaishi et al. 2005; q = 0.0071; wider of two orbit models chosen.
1.25	-0.12,+0.14	12070.22	...	12070.22	0.0008	T
...	GLensing	Torres et al. 2008 ApJ, 677, 1324-1342
...	GLensing	Bennett, et al. 2010 ApJ, 713, 837-855
...	14185	0.24	15841.59	0.24	RV	Bennett, et al. 2010 ApJ, 713, 837-855
...	RV	Giguere et al. 2012 ApJ, 744, 4-12; tr prob: 0.08
...	15085	880	17074	15	RV	Giguere et al. 2012 ApJ, 744, 4-12
...	GLensing	Beaulieu et al. 2006 Nature 439, 437-440
...	12034.2	6.6	RV, BD	Sato et al. 2012 PASJ
...	13038	38	RV, BD	Sato et al. 2012 PASJ
...	GLensing	Bond et al. 2004 ApJL, 606, L155-L158
...	15626.2	0.034	10042.92	0.043	RV	Pilyavsky et al. 2011 ApJ, 743, 162
...	11923	1	Wright 2009 ApJ, 693, 1084-1099; Mayor et al. 2004
...	12516	25	Wright 2009 ApJ, 693, 1084-1099; Mayor et al. 2004
0.32	14978.83	...	14978.83	...	T	Steffen et al. 2012 MNRAS, 421, 2342-2354
0.32	14982.89	...	14982.89	...	T	Steffen et al. 2012 MNRAS, 421, 2342-2354
0.217	15011.8	0.0031	T	Steffen et al. 2013 MNRAS, 428, 1077-1087
0.197	14971.99	0.0045	T	Steffen et al. 2013 MNRAS, 428, 1077-1087
0.348	0.018	15237.13	15246.65	0.04	T	Sanchez-Ojeda et al. 2012 Nature, 487, 449-453
1.096	0.036	15334.7	15357.89	0.0005	T	Sanchez-Ojeda et al. 2012 Nature, 487, 449-453
0.785	0.044	15171.8	15273.53	0.01	T	Sanchez-Ojeda et al. 2012 Nature, 487, 449-453
0.842	0.069	...	15073.43	...	T, RV	Holman et al. 2010 Science, 330, 51
0.823	0.067	...	15164.18	...	T	Holman et al. 2010 Science, 330, 51
0.146	-0.012,+0.077	...	15015.09	-0.0033,+0.0018	T	Torres et al. 2011 ApJ, 727, 24-41
0.1263	...	14964.57	14964.57	...	T	Batalha et al. 2011 ApJ, 729, 27-47
0.1987	0.005	...	14971.68	-0.0025,-0.0020	T, RV	Fressin et al. 2011 ApJS, 197, 5
1.067	0.022	...	13186.81	0.0002	T,RV	Torres et al. 2008 ApJ, 677, 1324-1342; Alonso et al. 2004
...	10154	42	10154	35	RV	Meschiari et al. 2010 ApJ, 727, 117-128
...	10179	7	RV	Meschiari et al. 2010 ApJ, 727, 117-128
0.23	14973.51	0.32	T	Steffen et al. 2012 MNRAS 421, 2342-2354
0.4	14986.09	0.32	T	Steffen et al. 2012 MNRAS 421, 2342-2354
0.187	15009.38	0.0015	T	Steffen et al. 2013 MNRAS 428, 1077-1087
0.164	15005.73	0.0027	T	Steffen et al. 2013 MNRAS 428, 1077-1087
0.098	14970.75	0.011	T	Steffen et al. 2013 MNRAS 428, 1077-1087
0.177	14980.7	0.0065	T	Steffen et al. 2013 MNRAS 428, 1077-1087
0.17	-0.019,+0.011	14966.3	14967.5	...	T	Gautier et al. 2012 ApJ, 749, 15-33
0.274	-0.028,+0.018	14963	14971.61	...	T	Gautier et al. 2012 ApJ, 749, 15-33
0.245	-0.027,+0.015	14955	14997.73	...	T	Gautier et al. 2012 ApJ, 749, 15-33
0.0774	-0.0086,+0.0066	14968.93	14968.93	0.0039	T	Fressin et al. 2012 Nature, 482, 195-198
0.092	-0.0116,+0.0089	14968.22	14968.22	0.011	T	Fressin et al. 2012 Nature, 482, 195-198
0.196	15005.63	0.0022	T	Steffen et al. 2013 MNRAS 428, 1077-1087
0.249	14969.97	0.0022	T	Steffen et al. 2013 MNRAS 428, 1077-1087
0.203	14969.04	0.0047	T	Steffen et al. 2013 MNRAS 428, 1077-1087
0.22	14973.07	0.0047	T	Steffen et al. 2013 MNRAS 428, 1077-1087
0.228	14966.25	0.0063	T	Steffen et al. 2013 MNRAS 428, 1077-1087
0.155	0.016	...	14964.9	0.0075	T	Lissauer et al. 2012 ApJ, 750, #112

(continued)

Table 16.2 (continued)

Planet	Bayer/Flamsteed/HIP/ Gliese/other Designation	Com.	Period (d)	P error (d)	a au	α error (au)	e	M/M ($\sin i$) [*]	M^* (M_J)	i deg	i err deg
...	KOI 707, Kepler 33	c	13.17562	0.00014	0.1189	0.0025	0	88.19	0.72
...	KOI 707, Kepler 33	d	21.77596	0.00011	0.1662	0.0035	0	88.71	0.51
...	KOI 707, Kepler 33	e	31.7844	0.00039	0.2138	0.0045	0	88.94	0.37
...	KOI 707, Kepler 33	f	41.02902	0.00042	0.2535	0.0054	0	89.17	0.34
...	KOI 872, Kepler 46	b	33.60134	0.00021	0.197	0.003	0.01	0.01	...	89.04	0.07
...	KOI 872, Kepler 46	c	57.011	-.061,+.051	0.28	0.004	0.0146	0.0035	...	87.4	-1.0,+1.6
...	KOI 872.03 (Kepler 46:)	d:	6.7667	0.0008	0.0679	0.0035	0	88.55	-.69,.49
...	KOI 1102, Kepler 24	b	8.1453	...	0.08	...	0
...	KOI 1102, Kepler 24	c	12.3318	...	0.1055	...	0
...	KOI 829, Kepler 53	b	18.64895	0.00016	0.1367
...	KOI 829, Kepler 53	c	38.5583	0.00041	0.2219
...	KOI 277, Kepler 36	b	13.83989	-.0600,+.0082	0.1153	0.0015	0	0.014	0.001	89.52	...
...	KOI 277, Kepler 36	c	16.23855	-.0544,+.0038	0.1283	0.0016	0	0.025	0.002	89.76	...
HD 181433	HIP 95467, Gl 756.1	b	9.3743	0.0019	0.08	...	0.396	0.062	0.024
HD 181433	HIP 95467, Gl 756.1	c	962	15	1.76	...	0.28	0.02	0.64
HD 181433	HIP 95467, Gl 756.1	d	2172	158	3	...	0.48	0.05	0.535
HD 183263	HIP 95740	b	626.5	1.1	1.51	0.087	0.3567	0.009	3.67	0.3	...
HD 183263	HIP 95740	c	3070	110	4.35	0.28	0.239	0.064	3.57	0.55	...
...	KOI 870, Kepler 28	b	5.9123	...	0.062	...	0	...	1.51
...	KOI 870, Kepler 28	c	8.9858	...	0.081	...	0	...	1.36
...	KOI 961.01, Kepler 42	b	1.213767	4.6E-06	0.0116
...	KOI 961.02, Kepler 42	c	0.453285	9.7E-07	0.0006
...	KOI 961.03, Kepler 42	d	1.865169	0.000014	0.0154
...	KOI 841, Kepler 27	b	15.3348	...	0.118	...	0	...	9.11
...	KOI 841, Kepler 27	c	31.3309	...	0.191	...	0	...	13.8
...	KOI 248, Kepler 49	b	7.203794	0.000022	0.05981
...	KOI 248, Kepler 49	c	10.91293	0.000069	0.0789
...	KOI 1270, Kepler 57	b	5.72932	0.000018	0.05889
...	KOI 1270, Kepler 57	c	11.60926	0.000086	0.0943
...	KOI 1241, Kepler 56	b	10.50343	0.000025	0.1042
...	KOI 1241, Kepler 56	c	21.40505	0.000036	0.1676
...	KOI 935, Kepler 31	b	20.8613	0.0002	0.16	...	0
...	KOI 935, Kepler 31	c	42.6318	0.0005	0.26	...	0
...	KOI 168, Kepler 23	b	7.1073	...	0.0987	...	0
...	KOI 168, Kepler 23	c	10.7421	...	0.0766	...	0
...	KOI 886, Kepler 54	b	8.010943	0.000069	0.0626
...	KOI 886, Kepler 54	c	12.07172	0.00029	0.0823
...	KOI 3154, Kepler 47	b	49.514	0.04	0.2956	0.0047	<0.035	89.59	0.5
...	KOI 3154, Kepler 47	c	303.158	0.072	0.989	0.016	<0.411	89.826	0.01
HD 186408	16 Cyg B, HR 7504, HIP 96901	b	798.5	1	1.681	0.097	0.681	0.017	1.64	0.15	...
...	KOI 1336, Kepler 58	b	10.2185	0.00015	0.0906
...	KOI 1336, Kepler 58	c	15.57416	0.00027	0.12
...	KOI 620, Kepler 51	b	45.1555	0.000072	0.2482
...	KOI 620, Kepler 51	c	85.31287	0.000096	0.3793
HD 187123	HIP 97336	b	3.096583	0.000078	0.0426	0.0025	0.0103	0.0059	0.523	0.043	...
HD 187123	HIP 97336	c	3810	420	4.89	0.53	0.252	0.033	1.99	0.25	...
...	KOI 157, Kepler 11	b	10.30375	0.00016	0.091	0.003	0	...	0.013	-.006,+.007	88.5
...	KOI 157, Kepler 11	c	13.02502	0.00008	0.106	0.004	0	...	0.042	-.019,+.015	89
...	KOI 157, Kepler 11	d	22.6872	0.0002	0.159	0.005	0	...	0.019	-.005,+.010	89.3
...	KOI 157, Kepler 11	e	31.9959	0.0003	0.194	0.007	0	...	0.026	-.006,+.008	88.8

(continued)

Table 16.2 (continued)

R $R(R_J)$	T_0 err (mod. JDN)	T_0 err (d)	T_i err (mod. JDN)	T_i err (d)	Comment/ Method*	Comments/reference
0.285	0.027	...	14976.68	0.0042	T	Lissauer et al. 2012 ApJ, 750, #112
0.477	0.044	...	15022.63	0.0018	T	Lissauer et al. 2012 ApJ, 750, #112
0.359	0.034	...	14968.87	0.0048	T	Lissauer et al. 2012 ApJ, 750, #112
0.398	0.037	...	15005.58	0.004	T	Lissauer et al. 2012 ApJ, 750, #112
0.808	0.043	...	15053.28	0.0014	T	Nesvorný et al. 2012 Science, 336, 1133-1136
...	T	Nesvorný et al. 2012 Science, 336, 1133-1136
0.151	0.009	...	15255.26	0.0032	T	Nesvorný et al. 2012 Science, 336, 1133-1136
0.21	14973.57	...	T, V	Ford et al. 2012 ApJ, 750, #113
0.25	14970.59	...	T, V	Ford et al. 2012 ApJ, 750, #113; + two more transiting objects.
0.256	15007.78	0.0029	T	Steffen et al. 2013 MNRAS 428, 1077-1087
0.283	14996.85	0.0038	T	Steffen et al. 2013 MNRAS 428, 1077-1087
0.13260.0031	14960.98	0.006	T, V	Carter et al. 2012 Science, 337, 556-559
0.32820.0048	14955.91	0.001	T, V	Carter et al. 2012 Science, 337, 556-559
...	14542	0.26			T	Bouchy et al. 2009 A&A, 496, 527-531
...	13235	7.3			T	Bouchy et al. 2009 A&A, 496, 527-531
...	12150	194			T	Bouchy et al. 2009 A&A, 496, 527-531
...	12111.7	3	11910	11911	RV	Wright et al. 2009 ApJ, 693, 1084-1099
...	11971	94			RV	Wright et al. 2009 ApJ, 693, 1084-1099
0.32	...	14975.62	...	14975.62	...	T
0.3	...	14981.73	...	14981.73	...	T
0.07	0.012	...	15003.48	0.0054	T	Muirhead et al. 2012 ApJ, 747, 144-159
0.065	0.018	...	14966.87	0.0042	T	Muirhead et al. 2012 ApJ, 747, 144-159
0.051	0.016	...	14966.78	0.0013	T	Muirhead et al. 2012 ApJ, 747, 144-159
0.36	...	14991.67	...	14991.67	...	T
0.44	...	14986.43	...	14986.43	...	T
0.243	15003.29	0.001	T	Steffen et al. 2012 MNRAS, 421, 2342-2354
0.228	15002.85	0.0022	T	Steffen et al. 2012 MNRAS, 421, 2342-2354
0.195	14971.56	0.001	T	Steffen et al. 2013 MNRAS 428, 1077-1087
0.138	14966.99	0.0027	T	Steffen et al. 2013 MNRAS 428, 1077-1087
0.343	14968.56	0.0088	T	Steffen et al. 2013 MNRAS 428, 1077-1087
0.7	14980.09	0.0061	T	Steffen et al. 2013 MNRAS 428, 1077-1087
0.49	0.1	...	14992.14	0.006	T	Fabrycky et al. 2012 ApJ, 750, 114-130
0.47	0.1	...	14974.19	0.007	T	Fabrycky et al. 2012 ApJ, 750, 114-130; +2 more transit signals in lc
0.17	14971.3	...	T	Ford 2012 ApJ, 750, #113
0.29	14966.29	...	T	Ford 2012 ApJ, 750, #113; + 1 more transit signal
0.187	15003.21	0.0029	T	Steffen et al. 2013 MNRAS 428, 1077-1087
0.11	14976.45	0.0091	T	Steffen et al. 2013 MNRAS 428, 1077-1087; +1 more transit signal
0.266	0.011	T circumbinary	Orosz et al. 2012 Science, 337, 1511-1514
0.411	0.018	T circumbinary	Orosz et al. 2012 Science, 337, 1511-1514
...	...	6549.1	6.6	6546.3	6.4	RV
Butler et al 2006						
0.249	14969.87	0.0056	T	Steffen et al. 2013 MNRAS 428, 1077-1087
0.255	14965.43	0.0066	T	Steffen et al. 2013 MNRAS 428, 1077-1087
0.629	14992.1	0.00062	T	Steffen et al. 2013 MNRAS 428, 1077-1087
0.509	15128.32	0.0022	T	Steffen et al. 2013 MNRAS 428, 1077-1087
...	...	14343.12	0.31	10807.56	0.016	RV
Wright et al. 2009 ApJ, 693, 1084-1099						
...	...	13580.04	0.3		RV	Wright et al. 2009 ApJ, 693, 1084-1099
0.176	0.017	...	14971.51	0.0077	T	Lissauer et al. 2011 Nature, 470, 53-58
0.281	0.027	...	14971.17	0.0031	T	Lissauer et al. 2011 Nature, 470, 53-58
0.306	0.029	...	14981.46	0.0044	T	Lissauer et al. 2011 Nature, 470, 53-58
0.403	0.038	...	14987.16	0.0037	T	Lissauer et al. 2011 Nature, 470, 53-58

(continued)

Table 16.2 (continued)

Planet	Bayer/Flamsteed/HIP/ Gliese/other Designation	Com. Designation	Period (d)	P error (d)	α au	α error (au)	e	e error	M/M ($\sin i$) [*] (M_J)	M^* (M_J)	i deg	i err deg
...	KOI 157, Kepler 11	f	46.6888	0.0007	0.25	0.009	0	...	0.0072	-.0037,+.0069	89.4	-0.2,+0.3
...	KOI 157, Kepler 11	g	118.3777	0.0011	0.462	0.016	0	...	<0.94	...	89.8	0.02
...	KOI 952, Kepler 32	b	5.90124	0.00010	0.0519	0.0008	0	...	0.010:
...	KOI 952, Kepler 32	c	8.7522	0.0003	0.067	0.001	0	...	0.011:
...	KOI 952, Kepler 32	d	22.7802	0.0005	0.128	0.002
...	KOI 952, Kepler 32	e	2.8960	0.0003	0.0323	0.0005
...	KOI 952, Kepler 32	f	0.74296	0.00007	0.0130	0.0002
...	KOI 137, Kepler 18	b	3.504725	0.000028	0.0447	0.0006	0	...	0.022	0.011	84.92	0.26
...	KOI 137, Kepler 18	c	7.64159	0.00003	0.075	0.001	0.00034...	...	0.054	0.006	87.68	0.22
...	KOI 137, Kepler 18	d	14.85888	0.00004	0.117	0.002	0.00052...	...	0.052	0.004	88.07	0.1
...	KOI 738, Kepler 29	b	10.3376	0.0002	0.09	...	0
...	KOI 738, Kepler 29	c	13.2907	0.0004	0.11	...	0
...	KOI 148, Kepler 48	b	4.77798	0.00001	0.0534
...	KOI 148, Kepler 48	c	9.673928	0.00002	0.0855
HD 189733	GJ 4130, Wolf 864	b	2.218573	0.000020	0.031	1.15	0.04	85.79	0.24
HD 190360	GJ 777 A, HIP 98767	b	2915	2916	4.01	0.23	0.313	0.019	1.56	0.13
HD 190360	GJ 777 A, HIP 98767	c	17.111	0.0048	0.1304	0.0075	0.237	0.082	0.06	0.0076
HD 192263	HIP 99711	b	24.3587	0.0022	0.15312	0.00095	0.008	0.014	0.733	0.015
HD 195019	HIP 100970	b	18.20132	0.00039	0.1388	0.008	0.0138	0.0044	3.69	0.3
...	NSVS 14256825 AB	b:	6.86	0.45	2.9	0.7	0.52	0.08	8	1.5
...	NSVS 14256825 AB	c:	3.49	0.38	1.9	0.8	0	0.08	2.9	0.4
HD 200964	2MASS J2063983+0348110	b	613.8	-1.4,+1.3	1.601	0.002	0.04	-0.02,+0.04	1.84	-0.08,+.14
HD 200964	2MASS J2063983+0348110	c	825	-3.1,+5.1	1.944	0.041	0.181	-0.058,+.024	0.895	-0.063,+.123
HD 202206	HIP 104903	b	256.389	0.044	0.8053	...	0.431	0.001	16.59	...	90	...
HD 202206	HIP 104903	c	1397.4	19.1	2.4832	...	0.104	0.024	2.179	...	90	...
HD 204313	HIP 106006	b	1920.1	25	3.04	0.06	0.23	0.04	3.55	0.2
HD 204313	HIP 106006	c	34.873	0.039	0.2103	0.0035	0.17	0.09	0.054	0.0054
HD 204313	HIP 106006	d	2831.6	150	3.93	0.14	0.28	0.09	1.7	0.3
...	HAT-P-17	b	10.33852	0.00009	0.0882	0.0014	0.342	0.006	0.534	0.018	89.2	-0.1,+0.2
...	HAT-P-17	c	1610	20	2.555	0.041	0.086	-0.67,+0.099	1.31	+0.18,-0.15
HD 206860	51 Peg, HR 8314	b	795	12-28
HD 207832	2MASS J21523626-2601352	b	161.97	-78,+97	0.57	0.002	0.13	-0.05,+1.18	0.56	-0.03,+.06
HD 207832	2MASS J21523626-2601352	c	1156	-37,+72	2.11	-0.05,+.09	0.27	-0.10,+.22	0.73	-0.05,+.18
HD 209458	V376 Peg, HIP 108859	b	3.524746	...	0.04707	0.00047	0	...	0.685	0.015	86.71	0.05
...	V391 Peg, GSC 02212-01369	b	1170	44	1.7	0.1	0	...	3.2	0.7
HD 215152	HIP 112190, GJ 4291	b	7.283	0.006	0.0652	0.001	0.34	0.27	0.0088	0.0014
HD 215152	HIP 112190, GJ 4291	c	10.866	0.014	0.0852	0.0014	0.38	0.23	0.0098	0.0015
HD 215456	HR 8658, HIP 112414	b	191.99	0.73	0.652	0.011	0.15	0.1	0.1013	0.0092
HD 215456	HR 8658, HIP 112414	c	2277	67	3.394	0.088	0.19	0.11	0.2466	0.0279
HD 215497	HIP 112441	b	3.93404	0.00066	0.047	...	0.16	0.09	0.02
HD 215497	HIP 112441	c	567.94	2.7	1.282	...	0.49	0.04	0.33
...	GJ 876, HIP 113020	b	60.990	0.007	0.211063	0.000001	0.0328	0.0013	2.377	0.042	56.1	1.5
...	GJ 876, HIP 113020	c	30.183	0.006	0.13173	0.00002	0.2498	0.0028	0.747	0.013	56.1	1.5
...	GJ 876, HIP 113020	d	1.93789	0.00002	0.0211063 1E-06	0.178	0.044	0.022	0.001	56.1	1.5	...
...	GJ 876, HIP 113020	e	124.5	0.5	0.3396	0.0009	0.008	0.027	0.048	0.005	56.1	1.5
HD 217014	51 Peg, HIP 113357	b	4.230785	0.000036	0.05211	0.003	0.013	0.012	0.461	0.039
HD 216956	24 beta PsA, Fomalhaut, HR 8728	b	2000y	...	170	<1?
HD 217107	HIP 113431	b	7.12682	0.00004	0.0748	0.0043	0.1267	0.0052	1.39	0.11
HD 217107	HIP 113431	c	4270	220	5.32	0.38	0.517	0.033	2.6	0.15
HD 218396	V342 Peg, HR 8799	b	450y	...	68	>0,<30	...
HD 218396	V342 Peg, HR 8799	c	190y	...	38	>0,<30	...
HD 218396	V342 Peg, HR 8799	d	100	...	24	>0,<30	...
IID 218396	V342 Peg, IIR 8799	e	50y	...	14.5	0.4	10-Jul	3	>0,<30	...
HD 222404	gamma Cep, HIP 116727	b	902.8	3.5	1.94	0.06	0.113	0.058	1.43	0.13
HD 222439	kappa And, HR 8976	b	61	-20,+50	12.8	-1.0,+2.0

* Columns 9 and 10 contain projected masses, i.e., $M \sin i$, unless column 19 indicates that the planet has been detected through transit (T), gravitational lensing (G) or direct imaging (I) observations

** Fischer et al. 2007 ApJ 669, 1336-1344 ; Mugrauer et al. 2007 MNRAS 378, 1328-1334;

(continued)

Table 16.2 (continued)

R err $R(R_*)$	T_0 (mod. JDN)	T_0 (d)	T_i (mod. JDN)	T_i err (d)	Comment/ Method*	Comments/reference
0.233 0.022	14964.65	0.0059	T	Lissauer et al. 2011 <i>Nature</i> , 470, 53-58
0.327 0.031	15120.29	0.0022	T	Lissauer et al. 2011 <i>Nature</i> , 470, 53-58
0.20 0.01	14974.902	0.008	T,V	Fabrycky et al. 2012 <i>ApJ</i> , 750, #114; + 2 more transit signals; Swift et al. 2012
0.18 0.02	14977.378	0.013	T,V	Fabrycky et al. 2012 <i>ApJ</i> , 750, #114; + 2 more transit signals; Swift et al. 2012
0.24 0.01	14988.211	0.011	T,V	Swift et al. 2012
0.13 0.01	14966.61	0.03	T,V	Swift et al. 2012
0.072 0.004	14965.54	0.04	T,V	Swift et al. 2012
0.178 0.009	14966.51	0.0021	T	Cochran et al. 2011 <i>ApJS</i> , 197, #7
0.49 0.023	15167.09	0.0023	T	Cochran et al. 2011 <i>ApJS</i> , 197, #7
0.623 0.029	15169.18	0.0013	T	Cochran et al. 2011 <i>ApJS</i> , 197, #7
0.32 0.04	14982.75	0.009	T,V	Fabrycky et al. 2012 <i>ApJ</i> , 750, 114-130
0.26 0.04	14978.47	0.016	T,V	Fabrycky et al. 2012 <i>ApJ</i> , 750, 114-130
0.191	14957.06	0.001	T	Steffen et al. 2013 <i>MNRAS</i> 428, 1077-1087
0.28	14958.34	0.00077	T	Steffen et al. 2013 <i>MNRAS</i> 428, 1077-1087
1.154 0.033	2453629.3942	0.0002	RV,T	Bouchy et al. 2005; Bakos et al. 2006, Companion B at 216 au
...	13542	31	RV	Wright et al. 2009 <i>ApJ</i> , 693, 1084-1099
...	14390	31	RV	Wright et al. 2009 <i>ApJ</i> , 693, 1084-1099
...	11796.9	6.8	[10986.74]	[0.21]	RV	Dragomir et al. 2012 <i>ApJ</i> , 754, #37; Butler et al. 2006, Santos et al. 2003,
...	11015.5	1.1	11008.45	0.04	RV	Butler et al. 2006
...	12643	110	V	Almeida, Jablonski, & Rodrigues 2013 <i>ApJ</i> 766, 11
...	11513	95	V	Almeida, Jablonski, & Rodrigues 2013 <i>ApJ</i> 766, 11
...	14916	30	RV	Wittenmyer et al. 2012 <i>ApJ</i> , 761, #165; Johnson et al. 2011 <i>AJ</i> , 141, 19-25
...	15029	130	RV	Wittenmyer et al. 2012 <i>ApJ</i> , 761, #165; Johnson et al. 2011 <i>AJ</i> , 141, 19-25
...	RV	Coedic et al. 2010 <i>A&A</i> , 519, A10;Correia et al. 2005
...	RV	Coedic et al. 2010 <i>A&A</i> , 519, A10;Correia et al. 2005
...	12112.6	28	RV	Robertson et al. 2012 <i>ApJ</i> , 754, 50-58; Mayor et al. 2011 in press; Ségransan 2010 <i>A&A</i> 511 A45(6pp)
...	RV	Mayor et al. 2011 <i>A&A</i> in press; Ségransan 2010 <i>A&A</i> 511 A45(6pp)
...	16376.9	176	RV	Robertson et al. 2012 <i>ApJ</i> , 754, 50-58
1.01 0.029	14801.17	0.0002	T, RV	Howard et al. 2012 <i>ApJ</i> , 749, 134-145; 1 sigma confid. levels
...	12456.35	-176.55,-335.66	[12820.0]	[17.7]	RV	Howard et al. 2012 <i>ApJ</i> , 749, 134-145; 2 sigma confid. levels
0.98- 1.30	I, BD	Leggett et al. 2008, <i>ApJ</i> , 682, 1256-1263; Luhman et al. 2007, <i>ApJ</i> , 651, 1166, G0V+T2.5, Mass debs on age
...	13191.07	RV	Haghhighipour et al. 2012 <i>ApJ</i> , 756, 91-97
...	13191.07	RV	Haghhighipour et al. 2012 <i>ApJ</i> , 756, 91-97
1.359 -0.019,+0.016	12826.63	...	12826.63	...	RV, T	Torres et al. 2008 <i>ApJ</i> , 677, 1324-1342
...	12418	96	V	Silvotti et al. 2007 <i>Nature</i> , 449, 189-191; Silvotti et al. 2010 <i>AN</i> , arXiv: 1005.2840, 2 pulsation periods.
...	RV	Mayor et al. 2011 arXiv:1109.2497
...	RV	'Mayor et al. 2011 arXiv:1109.2497
...	RV	'Mayor et al. 2011 arXiv:1109.2497
...	RV	'Mayor et al. 2011 arXiv:1109.2497
...	14858.95	0.37	RV	Lo Curto et al. 2010 <i>A&A</i> , 512, 48-53
...	15003.48	5.15	RV	Lo Curto et al. 2010 <i>A&A</i> , 512, 48-53
...	12000	RV	Baluev 2011 <i>Cel Mechs & Dynam Astr</i> , 111, 235-266; Rivera et al. 2010 <i>ApJ</i> , 719, 890-899; Laplace commensurabilities
...	12000	RV	Baluev 2011 <i>Cel Mechs & Dynam Astr</i> , 111, 235-266; Rivera et al. 2010 <i>ApJ</i> , 719, 890-899; Laplace commensurabilities
...	12000	RV	Baluev 2011 <i>Cel Mechs & Dynam Astr</i> , 111, 235-266; Rivera et al. 2010 <i>ApJ</i> , 719, 890-899; Laplace commensurabilities
...	12000	RV	Baluev 2011 <i>Cel Mechs & Dynam Astr</i> , 111, 235-266; Rivera et al. 2010 <i>ApJ</i> , 719, 890-899; Laplace commensurabilities
...	10001.51	0.61	[10001.881]	[0.018]	RV	Butler et al. 2006, Naef et al. 2004 <i>A&A</i> , 414, 351-360
...	I	Gaibacher et al. 2013 <i>ApJ</i> 769, 421(12pp); nature unclear - dust/debris clou around planet?
...	14396	39	RV	Wright et al. 2009 <i>ApJ</i> , 693, 1084-1099
...	11106	39	RV	Wright et al. 2009 <i>ApJ</i> , 693, 1084-1099
...	I	Marois et al. 2008 <i>Science</i> , 322, 1348; Sudol & Haghhighipour 2012 <i>ApJ</i> , 755, #38
...	I	Marois et al. 2008 <i>Science</i> , 322, 1348; Sudol & Haghhighipour 2012 <i>ApJ</i> , 755, #38
...	13146	72	RV	Torres et al. 2007, <i>ApJ</i> , 654, 1095-110; Hatzes et al. 2003 <i>ApJ</i> , 599, 1383-1394
...	I	Carson et al. 2013 <i>ApJL</i> 763, L32(6pp)

Table 16.3 Brown dwarfs—isolates or companions

HD Number	Names Bayer/Flamsteed/HR/Hipparcos/ Other Designation	I or C	Position (2000.0)							Properties		
			RA			Dec				Spectral Type, T	m(WL) magn	m(WL) magn
			h	m	s	Deg	°	'	"			
...	ULAS J003402.77-005206.7 B NLTT 5306 B, SDSS J013532.98+144555.8 B	I C C	00 01 02	34 35 57	02.7 33.0 13.1	-00 +14 -24	52 45 58	08 56 30	550-600 L5.5(1.5)
HD 18445b	HIP 13769b:	C	02	57	13.1	-24	58	30
HD 23514 B	Melotte 22 HII 1132 B	C:	03	46	38.4	+22	55	11	M7(I)/2600(100)	15.9(J)	14.9(Ks)	
...	Teide 1	I	03	47	17.9	+24	22	31.7	M8.0(5)/2584(100)	19.26(I)	15.10(K)	
...	PPL 15, Melotte 22 IPMBD 23	I	03	48	04.7	+23	39	30	M6.5	17.82(I)	14.16(K)	
...	Roque 25	I	03	48	30.8	+22	44	50	L0.1	17.71(J)	16.25(K)	
...	PIZ 1	I	03	48	31.4	+24	34	37.7	M9	19.64(I)	15.5(K)	
...	Calar 3	I	03	51	25.6	+23	45	21.3	M8.0(5)/2584(100)	16.08(J)	15.01(K)	
...	BRB 29	I	03	54	01.4	+23	49	58	L4.5(I)/1735(190)	18.7(J)	17.0(K)	
...	2MASSW J035541.9+225702	I	03	55	42.0	+22	57	01	L3	16.11(J)	14.80(K*)	
...	DH Tau B, HAT-6a B	C	04	29	41.6	+26	32	58	T8	14.96(H)	14.19(K)	
...	GG Tau Bb, Koku GG Tau c, WDS J04325+1732Bb	C	04	32	30.3	+17	31	41	M8	
HD 283750b	V833 Tau b, HIP 21482b	C	04	36	48.2	+27	07	56	
HD 29587b	HIP 21832b	C	04	41	46.3	+42	07	07	
...	2MASS J05352184-0546085	C	05	35	21.8	-05	46	09	M6.5; T=2715(100)	
...	2MASS J05352184-0546085	C	05	35	21.8	-05	46	09	M6.5; T=2820(105)	
...	S Ori 47, 2MASS J05381462-0240154	I	05	38	14.6	-02	40	15	L1.5(0.5)	20.53(I)	16.2(H)	
HD 38529b	HR 1988b, HIP 27253b	C	05	46	34.9	+01	10	06	
HD 41004Bb	HDS 814Bb	C	05	59	49.7	-48	14	23	
...	GJ 337C	C	09	12	14.7	+14	59	40	L8	16.3(J)	14.8(K)	
...	GJ 337D	C	09	12	14.7	+14	59	40	L8/T	16.3(J)	14.8(K)	
...	2MASS J09373487+2931409	I	09	37	34.9	+29	31	41	T6.0p	14.7(J)	14.7(H)	
...	BD+20 2457b	C	10	16	44.9	+19	53	29	
HD 89707b	HIP 50671b	C	10	20	50.0	-15	28	48	
...	WISE J104915.57-531906A	C	10	49	15.6	-53	19	06	L8(I)	11.51(J)	9.56(Ks)	
...	WISE J104915.57-531906B	C	10	49	15.6	-53	19	06	T1(2)	11.29(J)	9.77(Ks)	
...	Cha Halpha 1	I	11	07	16.7	+77	35	53	M7.75	12.42(Ks)	...	
HD 98230b	53 UMa Bb, HR 8374b, SDSS J121209.31+013627.7 B	C	11	18	11.0	+31	31	46	
HD 107383b	11 Com b, HR 5697b, HIP 60202b	C	12	20	43.1	+17	47	34	
...	NGC 4349 No. 127b	C	12	24	35.5	-61	49	12	
...	HW VirABb, HIP 62157b	C	12	44	20.2	-08	40	17	
...	HW VirABe, HIP 62157e	C	12	44	20.2	-08	40	17	
HD 112758b	HIP 63366b	C	12	56	01.6	-09	50	03	

(continued)

Table 16.3 (continued)

d pc	M/M _{sin} J/Sun	Properties				P d/yr	e	Method	Comments, References
		+/- dM J/Sun	R J/Sun	+/- dR J/Sun	a/asini J/Sun				
12.6(6) 71(4)	16.5J 56J	3.5J 3J	...	0.04J	0.566(5)R _{sun}	101.88(2)min	...	I RV,phot	T type brown dwarf; Smart et al. 2010 C: WD; Steele et al. 2013
26.1	39J	0.9	554.67d	0.54	RV	C: K2V; Zucker & Mazeh 2001 find 0.17Msun from Hipparcos data.
135(10)	0.06Sun	0.01Sun	~360	I	in the Pleiades; dust ring 0.25au from C: F6V; Rodriguez et al. 2012
~133	0.052Sun	I	in the Pleiades; Rebolo et al. 1996
~133	80J	10J	I	in the Pleiades; Rebolo et al.
~133	37.5J	2.5J	I	in the Pleiades; Bihain et al. 2010
134.9	0.048Sun	I	in the Pleiades; Cossburn et al. 1997.
~133	0.054Sun	I	in the Pleiades; Rebolo et al. 1996
~133	0.024	I	in the Pleiades; Rebolo et al. 1996
37.6(16)	I	in the Hyades; Hogan et al. 2008
...	40J	10J	330	6000y:	...	I	C: T Tau star, in Taurus molecular cloud; Itoh et al. 2005; H2O
140:	55J/0.044S	5J/0.006S	~207 AU:	I	C: T Tau quad system; GG Tau Aa+Ab: Mo-e-M2.0eV, GG Tau Ba: M6.Li; White et al. 1999
18.0(5)	50J	0.04	1.79	0.02	RV	C: K7V, BY Dra variable; Zucker & Mazeh 2001
27.57	57J	7J	19.6	1475d	0.33(15)	RV	C: G2V; Mazeh et al. 1996; Zucker & Mazeh 2001
456(34)	0.057Sun	0.005Sun	0.674Sun	0.023Sun	0.041(1)	9.77956(2)	0.328(3)	RV, phot	SB2EB; i=89.2(2); prob. magnetically active, P rot=3.3d; Stassun et al. 2007
456(34)	0.036Sun	0.003Sun	0.485Sun	0.018Sun	0.041(1)	9.77956(2)	0.328(3)	RV, phot	SB2EB; i=89.2(2); Stassun et al. 2007
380(18)	0.015Sun	0.005Sun	I	in sigma Orionis cluster; Zapatero-Osorio et al. 1999
39.28	12.8J	3.38	5.95y	0.36	RV	planet?; C: G4IV/V; Sahlmann et al. 2011
43.03	18.37J	0.02	1.3283d	0.081	RV	C: M2V; binary sep: 21.5 au; Zucker et al. 2003; Zucker et al. 2004
20.8(5)	~0.04Sun	10.9(6)	140-180	...	I	C: GJ 337AB (G8V+K1V), a (AB- CD)=880pc; Burgasser et al. 2005
20.8(5)	~0.04Sun	10.9(6)	140-180	...	I	C: GJ 337AB (G8V+K1V), a (AB- CD)=880pc; Burgasser et al. 2005
6.1	I	Burgasser et al. 2002
200:	21.42J	1.45	380(2)	0.15(3)	RV	C: K2II; [Fe/H]=-1.0; Niedzielski et al. 2009.
32.73	54J	198.25d	0.95	RV	C: G4IV; Sahlmann et al. 2011
2.02(+16,-14)	0.045Sun	0.005Sun	I	Closest BDs; Kniazev et al. 2013; Luhmann et al. 2013
2.25	0.04Sun	0.01Sun	I	Closest BDs; Kniazev et al. 2013; Luhmann et al. 2013
...	45J	I	in Cha dark cloud asson I; Ahmic et al. 2007; Joergens & Muller 2007.
8.83	37J	0.06	3.98d	0.00	RV	C: SB, P=3.98d; F8 5V; Wright 2013
120	88.4min	...	I	C:13MG, DA WD; Burleigh et al. 2006
111(+21,-10)	19.4J	1.5J	1.29(5)	326.0(3)d	0.231(5)	RV	C: G2-3III; [Fe/H]=-0.35(9); Liu et al. 2008.
2200	19.8J	2.38	678(6)d	0.19(7)	RV	C: G8III; [Fe/H]=-0.12(4); Lovis & Mayor 2007.
181(20)	14.3J	1.0J	4.69(06)	12.7(2)y	0.40(10)	ET,DA	planet?; C: EB: sdB+dM; Beuermann et al. 2012 A&A; Lee et al. 2009
181(20)	65J:	15J	12.8(2)	55:y	0.05	ET,DA	planet? (Lee et al. 2009 give 8.5Mj); C: EB: sdB+dM; Beuermann et al. 2012 A&A, in press; Lee et al. 2009.
20.9(4)	35J	0.35	103.2d	0.16	RV	C: G9V; low-mass star acc. to Reffert &Quirrenbach 2011.

(continued)

Table 16.3 (continued)

HD Number	Names Bayer/Flamsteed/HR/Hipparcos/ Other Designation	I or C	Position (2000.0)							Properties	
			RA			Dec				Spectral Type, T	m(WL) magn
			h	m	s	Deg	'	"	
...	Kelu-1Aa, V421 Hya Aa	C	13	05	40.2	-25	41	06	L0.5(0.5)
...	Kelu-1Ab, V421 Hya Ab	C	13	05	40.2	-25	41	06	T7.5(I)
...	Kelu-1B, V421 Hya B	C	13	05	40.2	-25	41	06	L3(1.5)	13.44(II)	12.73(Ks)
HD 114762b	HIP 64426b SDSS J1416+1348A	C	13	12	19.7	+17	31	02
...	SDSS J1416+1348B	C	14	16	23.9	+13	48	36	T7.5(0.5)	17.35(J)	17.58(H)
HD 127506b	HIP 70950b LSPM 1159+0857 B, ULAS 1459+0857	C	14	30	45.0	+35	27	14
...	UScoCTIO 108 A	C	14	59	32.1	+08	51	28	T4.5(0.5)	17.93(J)	17.92(K)
HD 131664b	HIP 73408	C	15	00	06.1	-73	32	07	T
HD 137510b	HR 5740b, HIP 75535b	C	15	25	53.3	+19	28	51
...	GQ Lup b/B, 2MASS J15491210- 3539051 b/B	C	15	49	12.1	-35	39	04	I,1.5/2650(100)	13.4(K)	...
...	UScoCTIO 108 B	C	16	05	53.9	-18	18	42.7	M7	15.7(I)	13.4(J)
...	UScoCTIO 108 B	C	16	05	53.9	-18	18	42.7	M9.5	19.9(I)	16.5(J)
...	GY92 141	I	16	26	51.3	-24	32	42	M8.5	15.06(J)	13.86(Ks)
...	CFHTWIR-Oph 33	I	16	26	39.7	-24	22	06	L4	18.16(J)	15.68(Ks)
HD 163917b	64 nu Oph b, HR 6698b, HIP 88048b	C	17	59	01.6	-09	46	25
HD 163917c	64 nu Oph c, HR 6698b, HIP 88048b	C	17	59	01.6	-09	46	25
HD 168443c	HIP 89844c WISEP J1828+2650	C	18	20	03.9	-09	35	47
...	WISEP J1828+2650	I	18	28	31.0	+26	50	38	>Y0:275-300	23.6(J)	22.9(H)
...	SCR J 1845-6357 B	C	18	45	05.1	-63	57	47	T5.5(1.0)	15.2(II)	...
...	CoRoT-3b	C	19	28	13.3	+00	07	19
HD 202206b	HIP 104903b	C	21	14	57.8	-20	47	21
HD 206869b	HN Peg b, HR8314b	C	21	44	31.3	+14	46	19	T2.5-T3
...	Wolf 940 B, ULAS J214638.83- 001038.7	C	21	46	38.4	-00	10	34	T8.5 (570(25))	18.16(J)	18.77(II)
HD 209100a	epsilon Indi Ba, HIP 108870 a	C	22	04	10.5	-56	46	58	T0.5	24.12(V)	11.6(H)
HD 209100b	epsilon Indi Bb, HIP 108870 b	C	22	04	10.5	-56	46	58	T6.0	>26.6(V)	13.4(H)
HD 217580b	HIP 113718b	C	23	01	51.5	-03	50	55

(continued)

The “brown dwarf desert” is well illustrated in Fig. 16.1, taken from Grether and Lineweaver (2006). To the present, extra-solar planets have been detected primarily through low-amplitude radial velocity surveys and through transit detections, conducted in the visual region of the spectrum, whereas brown dwarfs have been uncovered through long-wavelength photometric surveys and through direct visual and infrared imaging. Therefore, there may yet be room for systematic effects leading the statistics in these cases. One direct infrared imaging search for widely-separated companions of late-type, low-luminosity stars failed to find any (Allen et al. 2007), but others have been more successful. In a survey of the solar neighborhood (Dieterich et al. 2012), the multiplicity fraction of M dwarfs and L and T companions was found to be only $2.3^{+5.0}_{-0.7}\%$ for separations between 14 and 70 au.

In studies of very young clusters and associations, disks have been discovered around T dwarfs which are also brown dwarfs. So, sometimes brown dwarfs appear

Table 16.3 (continued)

d pcs	Properties						Method	Comments, References
	M/Msini J/Sun	+/- dM J/Sun	R J/Sun	+/- dR J/Sun	a/asini J/Sun	P d/yr		
18.7(7)	I	C: compB; Brown Dwarf; M(ABC) = 177MJ; Stumpf et al. 2013, Gelino et al. 2006
18.7(7)	I	C: compB; Brown Dwarf; Stumpf et al. 2013.
18.7(7)	6.4(+2.4,-1.3)	38(+8,-6)y	0.82(1)	I C: compA; Brown Dwarf binary; i = 84.9(2); Stumpf et al. 2013.
39(1) 7.9(1.7)	11..0J	0.1J	0.353(1)	83.915(3)d	0.333(5)	RV
7.9(1.7)	75:	I planet? C: F8V; Kane et al. 2011, H ₂ O, FeH; Bowler et al. 2010; Scholz 2010; Schmidt et al. 2010.
10.6(-3.0,-2.8)	30J	75:	I H ₂ O, CH ₄ , NIB; Burgasser et al. 2010; Scholz 2010.
22.7(6) 43-69	36 0.067	20J 0.007	0.154 16,500-26,000	2599d ...	0.72 ...	RV C: K3; Reffert & Quirrenbach 2011 C: WD; range due to single or double T-dwarf; Day-Jones et al. 2011.
55.43	18.15J	0.35J	3.17	1951(41)d	0.64(2)	A, RV C: G3V; i = 55(12) deg.; Sozzetti & Desidera 2010
41.8(2)	27J	2J	1.88(6)	798.2(14)	0.399(7)	RV C: GOIV-V/F9, [Fe/H] = -0.38(13); Diaz et al. 2012; Endl et al. 2004.
139(45)	20J	+16, -15J	3.0J	0.5J	112:	I C: T'Tau, K7V; A: eq. i = 27(5); Neuhauser et al. 2008; Broeg et al. 2007.
145(2)	60J	20J	670:	I in Upper Sco assn; C: M9.5 planet/BD; Bejar et al. 2008.
145 -160	14J ...	+2, -8J	670:	I C: M7 BD; Bejar et al. 2008. in the rho Oph Dark Cloud; Alves deOliveira 2012 in press; Luhmann et al. 1997; Alves deOliveira 2012
~160	I in the rho Oph Dark Cloud; Alves deOliveira 2012 in press.
46.2(6)	24J	1.9	530.3(4)d	0.1256(65)	RV C: G9III, [Fe/H] = -0.13(5); Sato et al. 2012; Quirrenbach et al. 2011.
46.2(6)	27J	6.1	3186d	0.165(13)	RV C: G9III, [Fe/H] = +0.13(5); Sato et al. 2012; Quirrenbach et al. 2011.
37.4(1)	18.1J	2.9(2)	1748.2(10)d	0.212(2)	RV C: G6V; Wright et al. 2009.
...	I NH3 abs. band?; Cushing et al. 2011
3.85(2)	45J	5J	4.5	I C: M8.5V; Biller et al. 2006
680(160)	21.7	1.0	1.01J	0.07	0.057	4.25680(1)d	0.0	T, RV superplanet?; C: F3V; i = 85.9, [Fe/H] = -0.02; Deleuil et al. 2008
45.3(17)	17.3J	2.4J	0.82(5)	225.87(6)d	0.435(1)	RV C: G5 IV/G6 V, + planet; Wright et al. 2009
17.9(1)	16J	9J	1.10J	0.06J	795:	I C: G0V, BY Dra var, in Her-Lyr Assn; Leggett et al. 2008
12.5(7)	26J	6J	0.094Sun	0.004Sun	400(22):	14000y:	...	I C: Wolf 490A, M4V; Burningham et al. 2009
3.622(4)	47J	I C: eps Ind A K5V, [Fe/H] = -0.23(6); King et al. 2010; McCaughean et al. 2004
3.622(4)	27J	I C: eps Ind A K5V, [Fe/H] = -0.23(6); King et al. 2010; McCaughean et al. 2004
157(+28,+20)	60	1	454.66	0.52	RV C: K2.5V; Reffert & Quirrenbach 2011

to have star-like origins, but not always. In Sect. 16.3 we discuss the boundaries separating stars, brown dwarfs, and planets, and in Sect. 16.5 the origins of the brown dwarfs and planets.

Individual properties of a selection of brown dwarfs are given in Table 16.3, where we list some of the objects identified as brown dwarfs in the exoplanet websites and in the literature. There has been no attempt to ensure that the list is complete (the topic is just beyond our mandate, here, after all!), but should be taken as illustrative of the properties of these objects, as currently understood. The on-line dwarf catalog <http://spider.ipac.caltech.edu/staff/davy/ARCHIVE/index.shtml> contains charts, spectra, and photometric details for 536 M dwarfs, and 1,281 L, T, and Y dwarfs, at present writing; many of these are brown dwarfs.

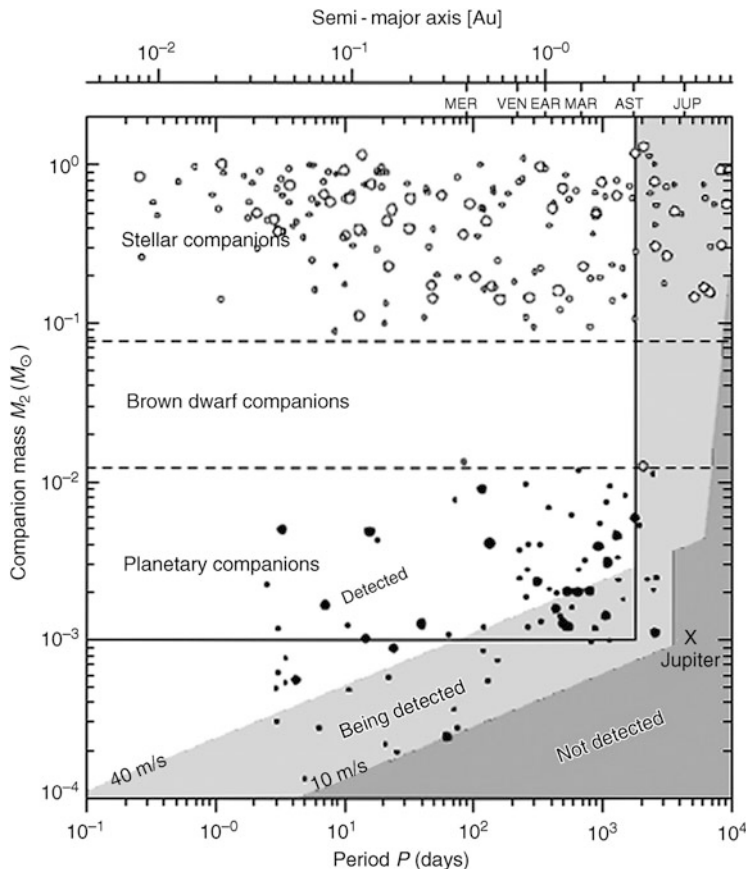


Fig. 16.1 The brown dwarf desert as illustrated in the survey of objects within 25 pc (*large symbols*) and 50 pc (*small symbols*) of the Sun. The figure, taken from Grether and Lineweaver (2006) and reproduced here by permission of the AAS, plots the masses of the companions to objects of stellar mass against the period of the binary systems. The *dashed lines* indicate the approximate dividing lines between stars and brown dwarfs ($80 M_J = 0.076 M_\odot$), and planets ($13 M_J = 0.0124 M_\odot$). The *solid line* indicates the regime where masses are greater than $10^{-3} M_\odot$ and periods less than 5 years. The *dark gray region* in the *lower right* indicates the regime where objects had not at that time been detected. Note the dearth of companions in the brown dwarf companion regime. Since publication of this plot the “not detected” zone has shrunk further, and a still small but increasing number of objects are appearing in the “Brown dwarf companions” region. Courtesy D. Grether and C. H. Lineweaver

16.2 Methods to Find “Small”-Mass Companions

There are more or less six direct and a few indirect methods to detect the presence of a brown dwarf or of a planet near a star:

- Radial velocity variations
- Transit eclipses

- Astrometric variations
- Direct imaging/spectroscopy
- Gravitational lensing
- Timings (of minima or maxima in periodic variable stars, variations in transit timings, or time delays for pulsar planets)
- Indirect effects (e.g., stability analyses for already known planetary systems)

We now discuss each of these methods in turn.

16.2.1 *Radial Velocity Variations of the Visible Component*

Periodic variations in the Doppler shift of the star as seen in its spectrum are a dead giveaway for something pulling the star around. Because masses of planets are much smaller than those of stars, the orbital motion of the star around the common center of mass is correspondingly smaller.

Therefore, high accuracy and precision are required. The technique usually involves a comparison with a high-resolution spectrum of a source, such as the absorption spectrum of an iodine vapor cell placed in the beam from the telescope. The absorption spectrum is superimposed on the observed stellar spectrum at the same high dispersion and resolution. The technique is well described by Butler et al. (1996), who discuss the use of an echelle spectrograph (see the solar spectrum produced by an echelle spectrograph in Fig. 4.10, Milone and Wilson 2014, Sect. 4.6) and cross-disperser to separate out many highly resolved spectral orders. The European exoplanet teams use the ELODIE and CORALIE spectrographs, also equipped with echelle gratings and cross-dispersing elements, and a thorium lamp or other calibrating device.

Detection of planets through stellar radial velocity variations has been the major method of detection thus far. The situation is comparable to that of a single-lined spectroscopic binary where the spectrum of the secondary component cannot be seen because the spectral radiance of the primary component overwhelms that of the less luminous companion. This is the case for all planets detected by this technique, except those that can also be detected by transit eclipses (such as HD 209458b; see Charbonneau et al. 2000) or imaged directly (and therefore capable of revealing its own orbital motions). Technical improvements in spectrograph stability, in spectral comparison techniques, and in analysis methods have lowered the uncertainties to less than 1 m/s. In addition to detection improvement, long-term averaging of data is beginning to yield long-period, low-amplitude effects in the radial velocity signatures of the parent stars—the effects of planets several astronomical units or more from the star—in other words, the searches have begun to probe the region occupied by giant planets in our own solar system, and may improve even further as described in the comprehensive review given by Perryman (2011).

Achievement of improvements to $\lesssim 1$ m/s or greater means that investigators have had to enter a realm dominated by noise effects in the atmospheres of the stars. Solar-like activity generates localized velocity variations that are modulated by

both stellar rotation and magnetic activity cycle intervals. The separation of these effects from the effects of multiple low-amplitude planetary periodicities is a major problem, but it is not insurmountable, given enough time and dedication, as the possible (though disputed) detection of a planet around α Centauri B demonstrates (see Sect. 16.4.11 below). For instance, the rotation period of the star may be obtained through the modeling of line profiles produced by high-resolution spectroscopy. The stellar activity (or starspot) cycle on the star is not strictly periodic, but rather cyclic, as in the Sun, in the sense that the amplitudes of the variations fluctuate in a more stochastic way rather than with strictly periodic variations due to planetary gravitational influences. This having been said, it may take decades rather than years to find the effects of low-mass planets. In the case of planets that are very distant from their stars, the orbital motion may be negligible over intervals of only a few years, even if their masses approach the brown dwarf boundary, which is discussed in Sect. 16.3. In this case, some other technique, such as eclipse timings, direct imaging, or microlensing may be successful sooner.

The method of finding the mass of a sub-stellar object from the radial velocity variation of the star is analogous to the determination of the mass of the unseen component in a single-line spectroscopic binary. The method is as follows.

Because only one set of spectral lines is visible in the spectrum, the mass of each component is not directly obtainable. Instead one finds a function of the masses. From Kepler's third law (Milone and Wilson 2014, Eq. 3.38),

$$\kappa(M_1 + M_2)P^2 = a^3 \quad (16.2)$$

where P is the period of the orbit, M_1 and M_2 are the masses of the star and the (invisible) second component and the constant $\kappa = G/4\pi^2$ disappears if the units for M , P , and a are solar masses, years, and au , respectively.

However, radial velocity measurements provide only the foreshortened quantity: $a \sin i$. Rewriting (16.2) with the appropriate units, we have

$$(M_1 + M_2)P^2 \sin^3 i = (a \sin i)^3 \quad (16.3)$$

The masses and semi-major axes are related through the definition of the center of mass by

$$M_1/M_2 = a_2/a_1 \quad (16.4)$$

where a_1 and a_2 are the (average) separations of M_1 and M_2 from the center of mass, and $a = a_1 + a_2$. Now note that

$$a^3 = a_1^3(1 + a_2/a_1)^3 = a_1^3(1 + M_1/M_2)^3 \quad (16.5)$$

so that (16.3) may be written as

$$(M_1 + M_2)P^2 \sin^3 i = a_1^3(1 + M_1/M_2)^3 \sin^3 i \\ = a_1^3(M_2 + M_1)^3 \sin^3 i / M_2^3 \quad (16.6)$$

from which we get the *mass function* for a single-line spectroscopic system:

$$f(M) = (M_2 \sin i)^3 / (M_2 + M_1)^2 = a_1^3 \sin^3 i / P^2 \quad (16.7)$$

However, the right hand side can be written more conveniently. From the radial velocity curve, supposing that the orbits are circular,

$$v_1 = 2\pi a_1/P \text{ and } v_2 = 2\pi a_2/P \quad (16.8)$$

where $v_{1,2}$ are expressed in units of au/y. Substituting for a_1 from (16.8) in (16.7), we obtain:

$$f(M) = (M_2 \sin i)^3 / (M_2 + M_1)^2 = P v_1^3 \sin^3 i / (2\pi)^3 \quad (16.9)$$

To convert to v in km/s, substitute

$$v(\text{au/y}) = v(\text{km/s}) (1/1.496 \times 10^8) (\text{au/km}) \times (3.156 \times 10^7 \text{ s/y}) \\ = 0.2110 v(\text{km/s})$$

and divide by $(2\pi)^3 = 248.050$. Then we arrive at an expression for the mass function in terms of the known quantities P and $v_1 \sin i$, even though neither v_1 nor i is known separately:

$$f(M) = M_2^3 \sin^3 i / (M_2 + M_1)^2 = 3.785 \times 10^{-5} P v_1^3 \sin^3 i \quad (16.9a)$$

so $f(M)$ or, as it is sometimes written, $f(M_1)$, is computable from $v_1 \sin i$ and where P is in years, v_1 is in km/s, and the masses are in solar masses. From (16.9a),

$$M_2 = \left[f(M_1) (M_1 + M_2)^2 \right]^{1/3} / \sin i \quad (16.10)$$

Therefore, if M_1 is known, the projected mass of the other component, $M_2 \sin i$, can be determined directly if $M_2 \ll M_1$, because $M_1 + M_2 \approx M_1$. This is typically the case if M_2 is a planet and M_1 is a star.

More generally (for elliptical orbits) the amplitude of the radial velocity curve, K_1 , is used:

$$K_1 = (v_1 \sin i)_{\max} \quad (16.11)$$

(we actually observe only the projected velocity in any case). The mass function for a single-line spectroscopic binary (SB1) becomes:

$$f(M) = (M_2 \sin i)^3 / (M_1 + M_2)^2 = 1.036 \times 10^{-7} K_1^3 P (1 - e^2)^{1.5} \quad (16.12)$$

where K_1 is in km/s, P is in days, e is the eccentricity, and M is in solar masses. The eccentricity is determinable from a highly precise radial velocity curve, so all quantities on the far right hand side of (16.12) are known.

Under special circumstances, M_2 may be found even if it is not small compared to M_1 . In the case of β Lyrae, for example, even though the companion appears to be obscured by a thick disk of material, eclipses are seen, so the inclination must be close to 90° , and M_2 can be found by iteration.

When both components are observable, in a double-lined spectroscopic binary (SB2), we have:

$$\left. \begin{aligned} M_1 \sin^3 i &= 1.036 \times 10^{-7} (K_1 + K_2)^2 K_2 P (1 - e^2)^{1.5} \\ M_2 \sin^3 i &= 1.036 \times 10^{-7} (K_1 + K_2)^2 K_1 P (1 - e^2)^{1.5} \end{aligned} \right\} \quad (16.13)$$

Note that without the inclination from a visual or an eclipsing binary analysis, only *lower limits* on the masses are obtainable. Further discussion is beyond our mandate here, but for a fuller discussion of the benefits and limitations of eclipsing and spectroscopic binary analyses, see, for example, Kallrath and Milone (2009). For planetary work, (16.9a)–(16.12) are the operative equations.

The expressions used by (for example) Butler et al. (2006) to define the projected mass and semi-major axis which they tabulate [their equations (1) and (2)] are:

$$M_{\text{planet}} \sin i = K_{\text{star}} (1 - e^2)^{1/2} \left[P (M_{\text{star}} + M_{\text{planet}} \sin i)^2 / 2\pi G \right]^{1/3} \quad (1)$$

$$(a/au)^3 = [(M_{\text{star}} + M_{\text{planet}} \sin i)/M_\odot] (P/y)^2 \quad (2)$$

where we have added the subscripts to the masses in the numerator for clarity. They are written this way instead of what is expected from (16.5 or 16.6) because $\sin i$ is not known in these cases and because the stellar mass is not a measured quantity; the quantities K_{star} and a_{star} are small compared to K_{planet} and a_{planet} , but the end result is that both a and $M_{\text{planet}} \sin i$ will be underestimated, by the factors $r = (M_{\text{star}} + M_{\text{planet}} \sin i)/(M_{\text{star}} + M_{\text{planet}})$ for expression (2) and $r^{2/3}$ for (1). We prefer not to redefine well-established quantities by approximations to those quantities, no matter how close the approximation. Nevertheless, we reproduce the values quoted by Butler et al. (2006) and other authors, because the uncertainties are probably greater than the error introduced by the approximations.

For the special case of a planet revolving around a pulsar, PSR J1719-1438, discussed below, the mass function $f(m_{\text{planet}})$ was found to be $7.85(1) \times 10^{-10} M_\odot$. Bailes et al. (2011) assumed the mass of the pulsar to be $1.4 M_\odot$ to find a minimum mass for the “planet” of $1.15 \times 10^{-3} M_\odot = 1.20 M_J$.

16.2.2 Transit Eclipses

In 1999, radial velocity variations detected with the 1.5-m telescope at the Harvard College Observatory revealed a planetary candidate around the field star HD 209458. Charbonneau monitored the star for photometric eclipses and, with the help of observers at Texas and Hawaii, succeeded in observing one (Charbonneau et al. 2000; Henry et al. 2000). A transit was subsequently observed with the HST (Brown et al. 2001). The integrated spectral data were so precise that limits were established on perturbations due to moons and rings (none have been seen). Subsequent investigation revealed transits in HIPPARCOS satellite data also. A careful analysis of the HST data set revealed the spectral signature of sodium from the absorption of the starlight as it passed through the planet’s atmosphere (Charbonneau et al. 2002). This was the first such identification of the composition of an extra-solar planet. Subsequently, Vidal-Madjar et al. (2004) showed that the planet is outgassing at an enormous rate, and may well appear in some wavelengths as a giant comet. See Figs. 16.2 and 16.3 for the modeling of the HST-integrated light photometry and the radial velocity light curves, from Williams’s (2001) MSc thesis, probably containing the best analysis, to that date and somewhat later, of the HST and other transit light curves of HD 209458. Figure 16.4 depicts the expected L light curve of the occultation of the planet. In Table 16.2, however, we have entered more recent results from Torres et al. (2008).

The unprecedented precision of the spectrally integrated HST light allowed an extraordinary degree of precision in the parameter modeling (Sect. 16.4.1); both stellar and planetary radii were extracted, but the single-lined radial velocity curve, shown in Fig. 16.3, did not permit unique determinations of the mass of both star and planet.

The detections of the secondary (less deep) occultation eclipses in TrES-1, HD 209458, and HD 189733 were later reported by Charbonneau et al. (2005) and Deming et al. (2005, 2006), who used the infrared spectrometer on the Spitzer Space Telescope. In TrES-1, Charbonneau et al. (2005) found eclipse depths of 0.00066 ± 0.00013 at $4.5 \mu\text{m}$ and 0.00225 ± 0.00036 at $8 \mu\text{m}$, from which they infer a blackbody temperature of $1,060 \text{ K} \pm 50 \text{ K}$ for the planet and a Bond albedo $A = 0.31 \pm 0.14$. For HD 209458, Deming et al. (2005) found a depth of 0.0026 ± 0.0005 at $24 \mu\text{m}$, and a planetary flux of $55 \pm 10 \mu\text{Jy}$, from which they obtain a brightness temperature of $1,130 \pm 150 \text{ K}$. For HD 189733, they found a depth of 0.0055 ± 0.0003 at $16 \mu\text{m}$, from which they derived a heated face brightness temperature of $1,117 \pm 42 \text{ K}$. Demory et al. (2012) have observed the occultation of the planet 55 Cancri e, again with the Spitzer Space Telescope, and deduced a temperature of the star-facing disk of this $2R_J$ planet: 2,360 K.

The OGLE lensing survey has revealed an increasing number of potential transit-like events of very low depth, that are repeating, suggesting planetary transits. It is not always clear if these are caused by transits by planets or grazing eclipses by stars. Several of the discoveries have been followed up with radial velocities studies on large telescopes. Four that have proven to be planetary transits are: OGLE-TR 56b, TR 111b, TR 113b, and TR 132b (see Konacki et al. 2004). The planets in these

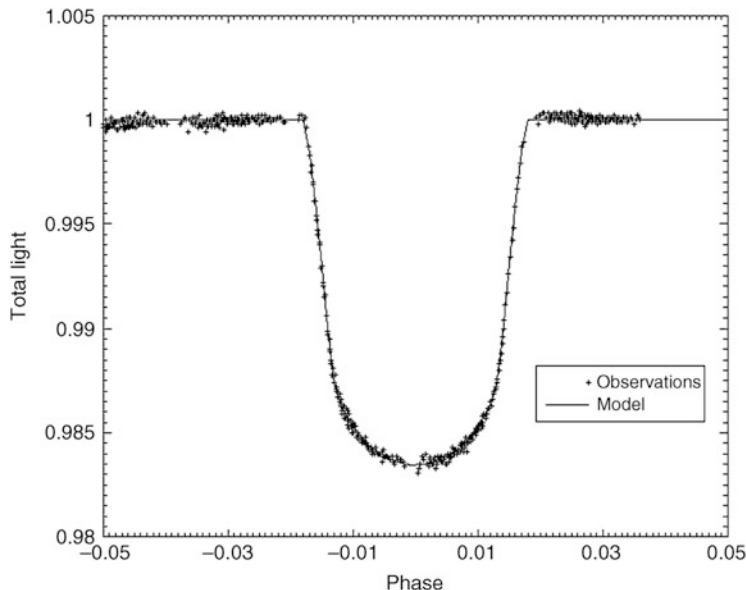


Fig. 16.2 HD 209458 HST observations from Charbonneau et al. (2000) modeled with the University of Calgary version of the Wilson-Devinney program, wd95k93h, as modified by Williams (2001) to handle the small grid sizes needed to model planetary transits. Courtesy, Michael D. Williams

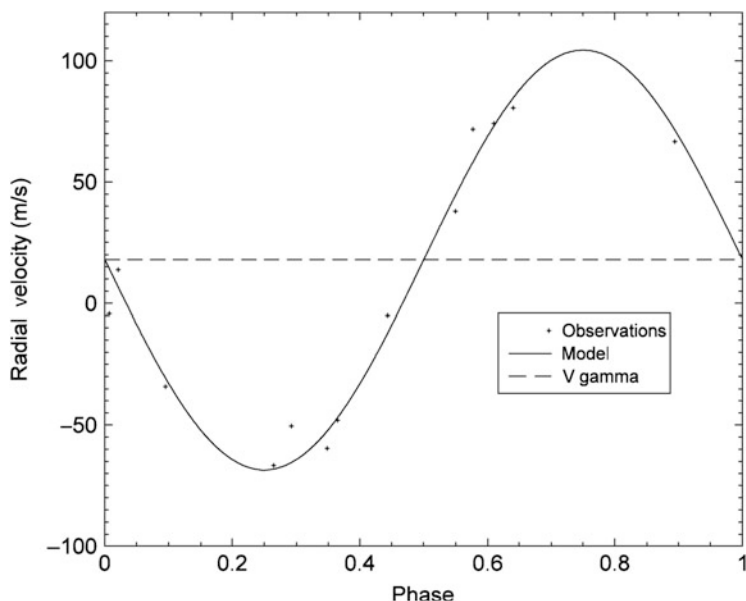


Fig. 16.3 The preliminary HD 209458 single-lined radial velocity curve subsequently published forwarded by D. Charbonneau and later greatly enhanced by Mazeh et al. (2000) with the global solution obtained with the wd98k93h light curve modeling code by Williams (2001). The derived system parameters are listed in Sect. 16.4.1. Courtesy, Michael D. Williams

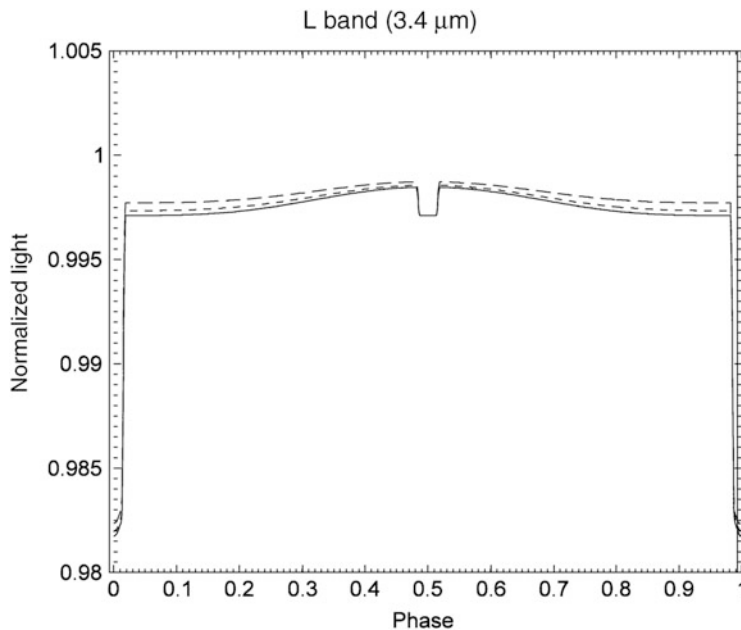


Fig. 16.4 The expected L passband light curves of HD 209458 for several different effective temperatures of the planet as modeled by Williams (2001) with wd98k93h. The occultation eclipse is shown centered, at phase 0.5. The only way to find the temperature difference between star and planet is to observe both eclipses, and this is possible only in the thermal infrared, where the planet has detectable brightness. Nevertheless, the secondary, occultation eclipse is extremely shallow. Courtesy, Michael D. Williams

systems are even closer to their stars than the previously found “hot Jupiters.” The host stars of these objects are typically low-mass stars located between 1 and 8 kpc from us; therefore they are very faint and require very large telescopes to investigate further. For these four systems, the host stars’ brightnesses are between 16th and 17th magnitude in V. Analyses by Southworth (2012) highlight the need for highly precise light curves to obtain precise determinations of the parameters.

TrES-1b, the first planet to be detected by transit in large-field surveys of brighter stars, was announced by Alonso et al. (2004). It was found to have an orbit similar to that of HD 209458b, and similar mass, but smaller radius ($\sim 1.08 R_J$).

Other transit surveys have been eclipsed now by the massive number of transit discoveries of the Kepler mission (Borucki et al. 2010). Hundreds of planetary transits have been confirmed and thousands more await confirmation, and all this from a fixed and limited region of the sky, 115 square degrees, less than 0.3 % of the total area of the sky.

The basic method to investigate the properties of the planet from a transit eclipse are well known from eclipsing binary studies (see Kallrath and Milone 2009, for detailed discussions of the methods). The analysis of an optical transit light curve is simpler because the secondary, occultation eclipse of the planet produces very little

measurable decrease in light of the system. In a highly precise light curve obtained in the intermediate infrared (say in a modern variation of Johnson's L, M or N passbands), however, it is possible and planetary occultation eclipses have been detected in several cases.

Both the depth of the eclipse and the shape can reveal the relative radii of the star and planet. The ratio of the radii is given by $k = r_s/r_g$, where r is the radius and subscripts s and g refer to the smaller and greater objects, respectively, in the notation of Henry Norris Russell (for the most complete description of this method see Russell and Merrill 1952, but for a summary of this and detail on more accurate and robust methods, see Kallrath and Milone 2009). In the simplest case, for central eclipses, the light of the system during transit is:

$$\ell = L_g(1-f) + L_s \quad (16.14)$$

where L_g is the light of the star, L_s that of the planet, normalized so that $L_g + L_s = 1$, and $f = k^2$ is the light lost during the transit. For optical wavelengths, the planet is expected to contribute almost nothing to the light of the system, so $L_s \approx 0$. Modifications are required in the more realistic case that the star is limb-darkened (see Milone and Wilson 2014, Sect. 4.5.2), and a contribution for the light of the planet may be required for infrared light curves. If the planet is not small compared to the star itself (as in a massive Jovian planet around a red or brown dwarf), the contribution of the planet to the light is important, and the shape of the shoulders of the minimum must be modeled. For non-central eclipses, $a \sin i$ is present and i must be optimized. For further modeling details, see Kallrath and Milone (2009).

Twenty-three of the known transiting exoplanets and their stars are depicted to scale in Fig. 16.5 from Torres et al. (2008), nicely illustrating the effects that a planet's traversal chord and disk size relative to the star have on the transit light curve.

The old treatment of Russell and Merrill (1952) is adequate for the case of a purely spherical star and planet, but the modern light curve codes can provide improved fitting, as well as allow for the appropriate limb-darkened effects of the star's atmosphere. Similar comments have been made by Gimenez (2006), but his assertion that programs such as that of Wilson-Devinney program are unsuitable for these analyses was patently wrong, as the work done by Williams (2001) demonstrated (cf. Sect. 16.4.1). The correct physics for the intensity distribution of the light across the disk of the star is provided in the most modern codes; it was not in the coding of the purely geometrical models of Russell-Merrill and successor programs that failed to consider the correct radiative and, for interactive stars, even the correct geometric properties of the stars. The distinctions are addressed in Kallrath and Milone (2009).

16.2.3 Astrometric Variations

Proper motions are secular angular motions in the plane of the sky, usually expressed in units of arc s/y in coordinates such as right ascension and declination. They indicate slight changes in the direction of the star as seen from the Sun.

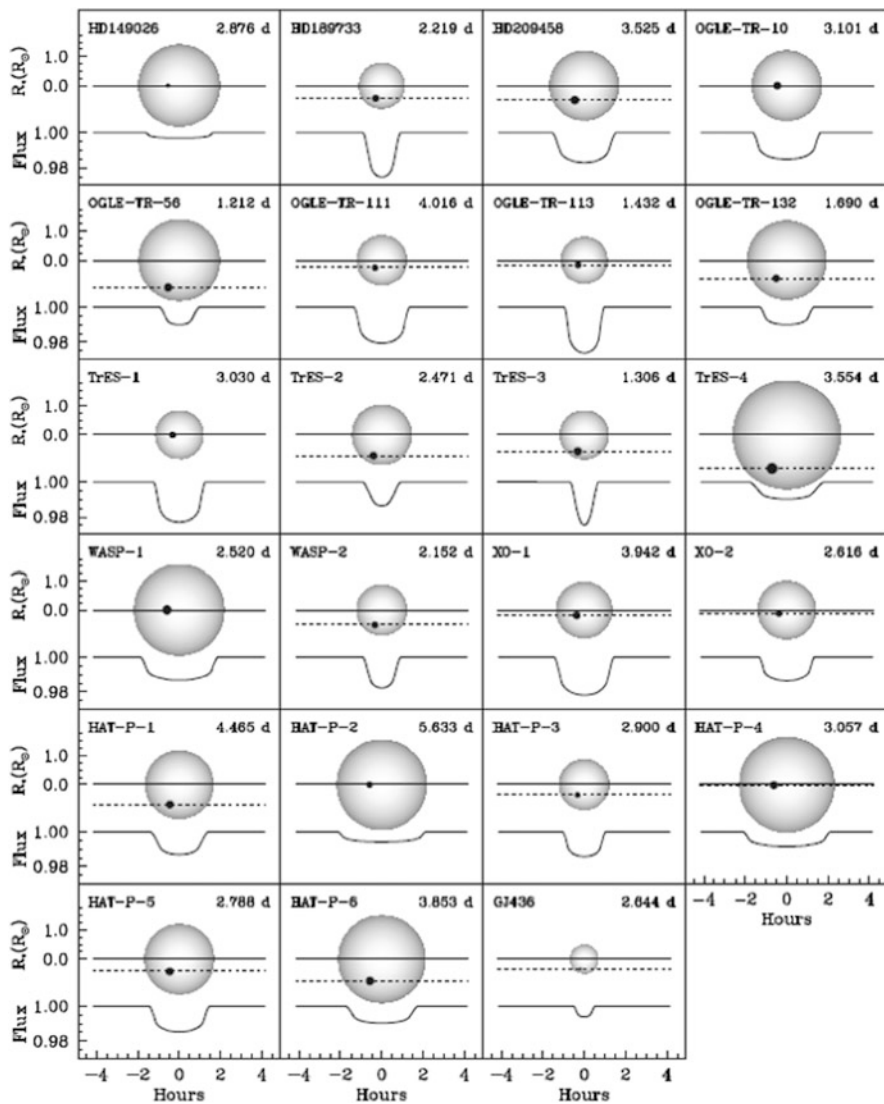


Fig. 16.5 A “portrait gallery” of transiting exoplanets drawn to scale, demonstrating the effects of the transit chord, and the sizes of both planet and star, on the light curve. Reproduced from Fig. 8, p. 1335 of Torres et al. (2008), courtesy of Dr. Guillermo Torres, and with the permission of the American Astronomical Society

The size of this motion depends on the object’s distance as well as the object’s linear motion across the line of sight. Periodic variation in the proper motion of a star is a sign of binarity. Astrometric binaries are binary star systems where only one star is visible, yet a sinusoidal variation in proper motion is seen. The amplitude of the variation depends on the ratio of the masses of the stars, which is inversely

proportional to the separation of the two stars from the center of mass of the system. If the mass of the visible star is known, for example, through a well-calibrated mass-luminosity relation (determined through binary star studies), the mass of the second star can be determined. One such procedure is demonstrated here:

Begin with Kepler's third law, (Milone and Wilson 2014, Eq. 3.38),

$$G(M_1 + M_2)P^2 = 4\pi^2(a_1 + a_2)^3 \quad (16.15)$$

where P is the period of the orbit, M_1 and M_2 are the masses of the visible and non-visible component, and a_1 and a_2 are the (average) separations of M_1 and M_2 from the center of mass. Their sum is the semi-major axis of the relative orbit: $a = a_1 + a_2$. From the definition of the center of mass, setting the origin to the center of mass,

$$M_1a_1 - M_2a_2 = 0 \quad (16.16)$$

From the latter, we get:

$$M_2 = M_1(a_1/a_2) \quad (16.17)$$

and

$$a_2 = a_1(M_1/M_2) \quad (16.18)$$

We assume that P , M_1 , and a_1 are known (i.e., that the absolute visual orbit of the visible star is known and the orbital elements have been derived). We begin with a guess for M_2 . From (16.18), we find a_2 . Then, we solve for M_2 from (16.15), and return to (16.18) to find a_2 . Iteration continues until successive iteration values of M_2 are in agreement.

The method is applicable to any low-mass companions, and so to brown dwarfs and planets as well as stars.

Advanced astrometry space missions, following up the HIPPARCOS-Tycho mission, may be capable of finding some variations due to precise and frequent astrometric measurements. NASA discontinued its sponsorship of SIM (Space Interferometry Mission) at the end of 2010, but ESA's GAIA mission was to be launched imminently, at present writing. These missions were planned to achieve several microarc-sec of positional precision. Both proper motions and parallaxes were to be determined, providing distance and kinematic detail to any discoveries. Although each was to have high-precision astrometry capabilities, SIM was to have been a pointed mission, whereas GAIA will be a survey instrument. In addition, GAIA will be equipped with a radial velocity spectrometer to provide RVs as well as spectrophotometry from which passband photometry will be replicated. Although the GAIA spectrometer's resolution ($\sim 11,200$) will not be high enough to detect variations due to planets in stellar spectra, astrometric and photometric effects most likely will be seen (see below).

The systems Lalande 21185 and ε Eri were studied by Gatewood (1996); however, the claimed planetary discoveries in these systems required confirmation; this seems to have been provided for ε Eri (see below and Sect. 16.4), but not, thus far, for Lalande 21185.

Benedict et al. (2002) have made astrometric measurements of a star perturbed by an orbiting planet previously detected from radial velocities of stellar reflective motions, Gliese 876, an M4 dwarf, also known as Ross 780. The measurements were made using the Fine Guidance Sensor on the Hubble Space Telescope. They yielded an unprojected mass of $1.89 \pm 0.34M_{\odot}$ for the planet, Gliese 876b. Further radial velocity work has yielded three planets in this system; this system, too, is discussed further, in Sect. 16.4.

Reffert and Quirrenbach (2011) examined the Hipparcos revised astrometric data (Van Leeuwen 2007) to seek restraints on the orbital inclination and longitude of the ascending node of planets discovered through radial velocity searches. They were able to confirm the planets: β Gem b, ε Eri b, ε Ret b, μ Ara b, ν And c and d, 47 UMa b, HD 10647 b, and HD 147513 b, and as brown dwarfs: HD 137510 B and HD 168443 C, by placing 3σ lower limits on the inclinations, and corresponding upper limits on the masses. They also were able to derive astrometric orbits for the planets ι Dra b (cf. Frink et al. 2002) and HD 87833 b (Fischer et al. 2009) and for eight brown dwarf companions.

16.2.4 Gravitational Lensing

Among the many useful descriptions of extrasolar planet detections in the literature, we find those of Perryman (2000, 2011), whose exposition on microlensing we follow here, especially clear; but for a more recent update and additional detail on planetary gravitational lensing, we recommend Gaudi (2012).

Einstein predicted that the gravitational field of a star could cause light from more distant objects to be bent. Thus the star acts as a lens. The passage of a single star (lens) in front of a more distant one causes varying brightness resulting in two detectable sources. Usually, the brightness of the more refracted ray is too low to be measurable due to scattering effects. An exact alignment will produce the “Einstein ring” phenomenon. Most often, however, only one varying peak is seen. From the first detection in 1993 to the present, hundreds of events have been seen.

In this lensing context, the effective radius of the lensing object is known as the *Schwarzschild* or *gravitational radius*,

$$R_g = 2GM_L/c^2 \quad (16.19)$$

where M_L is the mass of the lens and c is the speed of light. In gravitational theory the radius of an object is $2M$, and the constant term G/c^2 provides the conversion factor from mass to length units (Misner et al. 1973, pp. 35ff). The source object undergoes distortion as the lens moves in front of it, resulting in a perfect ring when

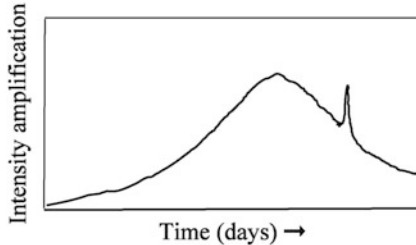


Fig. 16.6 The amplification of signal of a distant source due to microlensing by a star (*broad variation*) and planet (*spike*) as the lensing system passes in front of the source. The example shown is very similar to the lensing object OGLE-2005-BLG-390Lb (Beaulieu et al. 2006)

the foreground lens and background source objects are in the line of sight. The radius of this ring is the *Einstein radius*,

$$R_E = (2R_g \Delta r d)^{\frac{1}{2}} \quad (16.20)$$

where $\Delta r = (r_s - r_L)$ is the difference in distance to the source and lens respectively, and $d = r_L/r_s$, is the distance ratio. The apparent or angular Einstein radius is then given by

$$\Theta_E = R_E/r_L \quad (16.21)$$

which depends implicitly on the square root of M_L , inversely on the square root of r_L , and on the square root of the factor $(1 - d)$.

Usually there is no consensus of the distance of the star that is acting as the lens, but when the lens turns out to be a binary star, the additional lensing action of the second star and an assumption about the motion of the lensing system in the plane of the sky, permit a distance estimate to be made. The time scale is given by

$$t_E = R_E/v_L \quad (16.22)$$

where v_L is the transverse speed. This is the time of crossing by the *caustic* (named after a surface of maximum brightness created by spherical aberration in a spherical lens/mirror) and it may last for several tens of days for a massive object such as a star or cluster, or hours for a planet. Gaudi (2012) reports a median length for microlensing events of 20 days. If there is a planet in the lensing system, a sharp spike will be seen, in addition to the star's broader amplification effect (see Fig. 16.6).

The ground-based OGLE (for Optical Gravitational Lensing Experiment) survey of the galactic bulge region of the galaxy has detected many planetary candidates through light curves, but not directly through lensing. A few of the confirmed or strongly suspected cases (at present writing) are included in Tables 16.1 and 16.2.

Gaudi (2012) stated that 14 planetary lensing cases had been confirmed to that time. Since then, another 2-planet lensing system has been discovered: OGLE-2012-BLG-0026Lb, bringing the number of lensing planets to 16 as of May, 2013. The earliest three reported were: that of OGLE-2003-BLG-235Lb; OGLE-2005-BLG-071Lb; and OGLE-2005-BLG-390Lb. The most recent (at this writing) are: OGLE-2005-BLG-05-169Lb (Gaudi et al. 2005; Gould et al. 2006), OGLE-MOA-2011-BLG-266Lb (Muraki et al. 2011), and the two planets OGLE-2012-BLG-0026Lb,c (Han et al. 2013). For these systems, the estimated planet masses are 1.5(12), 3.8(4), 0.017(17), 0.033(5), 0.11(2), and 0.68(10) M_J , respectively.

Figure 3 of Gould et al. (2006) implies that of all the techniques for finding planets, gravitational microlensing from space will be the only one capable of detecting objects significantly smaller than an Earth mass. This, however, has been proven not quite correct by the Kepler mission; Kepler 37b, with $\sim 1/3 M_E$, was discovered in a 3-planet system (Barclay et al. 2013). Nevertheless, the (ground-based) technique is finding low-mass planets beyond the “snow-line,” which in the solar system is in the asteroid belt, and where the solid ices are thought to enable more rapid accretion than inside this distance, r_{SL} , which is assumed to scale with stellar mass: $r_{SL} = 2.7 \times (M/M_\odot)$. The existence of large numbers of “super-Earths” outside the snow-line is not a prediction of the core-accretion theory (see Sect. 16.5). These “super-Earths” are, in effect, “failed Jupiters.”

16.2.5 Direct Imaging and Spectroscopy

In both optical and infrared spectral regions, one can look for faint companions to nearby stars, but true planets (at least the “hot Jupiters,” located far closer to the star than Mercury is to the Sun in our system) are not likely to be luminous enough to be seen directly. It would be even more difficult to obtain any kind of spectral resolution to discern identifying features in the spectrum of any such candidate objects. Because of the overwhelming light of the parent star, it has not been possible to separate the flux of the known planets from their stars, for these types of planets, thus far, but coronographic (Lyot 1933) and diffraction techniques have already been successful in finding more distant planetary companions. New generation space telescopes are an obvious answer to this need, but high-resolution techniques on existing telescopes may permit detection sooner.

Candidate planets and brown dwarfs are being detected, both very near and, more surprisingly, relatively far from their parents. For example, there is an object with mass $5 \pm 2 M_J$, 41 au from the M8, $25 M_J$ brown dwarf 2MASSW J1207334-393254 (Chauvin et al. 2004). The object itself has a spectral type in the range L5–L9.5. A second candidate orbits the faint, red, T Tauri type variable star GQ Lupi with spectral type K7e V (Neuhäuser et al. 2005). The companion is much fainter but appears to have the same proper motion as the star on the plane of the sky. The object is located at 103 ± 37 au from the variable star. Therefore its

orbital motion over the few years it has been observed is very small, and so far, unobserved. Seifahrt et al. (2007) find a radius $3.5^{+1.5}_{-1.0} R_{\odot}$ and likely mass $<36 M_{\text{J}}$. The companion to the K2 V star AB Pic is another candidate with spectral type L0–L1 and a mass $13.5 \pm 0.5 M_{\text{J}}$, right at the boundary between planets and brown dwarfs, at a projected separation of 260 au from the star (Bonnefoy et al. 2010).

Although the natures of these objects are hardly clearcut, the three cases raise questions about the prerequisite environments for planetary development.

Infrared surveys, and imaging in methane and ammonia bands are turning up very red and faint objects, and many of these have been confirmed to be brown dwarfs through subsequent spectroscopy. Some very red objects in clusters have also turned out to be sub-stellar objects (see Basri 2000 for an early but still useful summary), and some have disks. Cha 110913-773444, located in the Chameleon I star-forming region, which is 165 pc from the Sun, was discovered by Luhman et al. (2005). It is estimated to have a mass of $8^{+7}_{-3} M_{\text{J}}$ as determined from a mass-luminosity relation derived for similar objects, it has a disk, and is estimated to have an age between 0.5 and 10 My. There are several stages in this determination that require further scrutiny, but the possibility of the formation of an isolated object of approximately planetary mass is indeed intriguing (see the discussion of proplyds in Chap. 15 for the possibility of the formation of even lower mass objects in star-forming regions).

16.2.6 Pulsar Timings

Whereas the radial velocity technique has been carried out in the visual part of the spectrum, and the photometry, direct imagery, and lensing monitoring in visual and infrared light, pulsar timings have been carried out at radio frequencies. The work on the rapidly rotating (millisecond!) pulsar PSR 1257+12 by Wolszczan and collaborators (e.g., Wolszczan and Frail 1992; Wolszczan 1996; Wolszczan et al. 2000a, b; Konacki and Wolszczan 2003) has provided convincing evidence of the existence of planets around this object. Unless there was a complicated history of migrations, one would expect the three reasonably certain components (b, c, and d, which Wolszczan and colleagues refer to as planets A, B, and C) to have been *inside* the super-giant star that preceded the supernova of which the pulsar is the remnant core. Presumably, therefore, the existing planets accreted from the debris disk produced in the eruption, perhaps from the interaction with a companion star. The latter may have contributed to the tremendous spin-up of the pulsar.

The detection involves periodic shifts in the pulse beams emitted by the pulsar, which is thought to be a dual beamed, rotating neutron star. As the sharply collimated beams rotate into the line of sight, the system briefly brightens and quickly fades. The time delay in the pulses indicates the reflex motion of the pulsar around the center of mass in the same way that the motion of a star reveals the reflex motion of a planet in other systems. The variation in arrival time of the pulses is periodic due to the increased and decreased distance to the observer of the pulsar.

Table 16.4 Millisecond-pulsar planets

Pulsar system	a (au)	P (d/y)	e	i	ω	Ω	$M[\sin i]$ (M_J or M_E)
PSR B1257+12	0.1885	25 ^d 262	0.0	50°	0.0	0.00	0.019 M_E
	0.35952	66 ^d 5419	0.0186	53°	250.4	0.00	4.250 M_E
	0.46604	98 ^d 2114	0.0252	47°	108.3	3.26	3.873 M_E
PSR B1620-26 b	23	100 y	–	55°	–	–	2.5 M_J
PSR J1719-14 b	545 km	0 ^d 090706	<0.06	–	–	–	1.2 M_J

The discovery of a planet around PSR 1257+12, reported by Wolszczan and Frail (1992), was arguably the first valid detection of an extra-solar planetary system. At present, three planets are known, one of which (b) is only ~50 % more massive than the Moon. Thus far, this is the smallest known exoplanet. The data in Table 16.4 are from Goździewski et al. (2005) and Konacki and Wolszczan (2003). Note that the ratio of the periods of planets b and c is ~2:3, so the planets are locked in a mean motion ratio of ~3:2. An alternate model has $i = 127^\circ$ and 133° for orbits of c and d, respectively. Significant gravitational perturbations are observed.

In addition to the planets of the pulsar PSR 1257+12, two pulsar candidate planets are listed in Table 16.4. Pulsar planets are rare, so the environments of these systems are important to study. PSR B1257+12b is a field pulsar. PSR B1620-26 is located in the globular cluster M4, otherwise known as NGC 6121. The planet-mass object is revolving about a binary consisting of a neutron star and a white dwarf. PSR J1719-14 is a millisecond field pulsar, and the planetary-mass object is in a very tight orbit around the neutron star.

The pulsar PSR B1620-26 system is located near the edge of the core of a globular cluster, M4. It is a binary star consisting of the pulsar and a white dwarf. The inclination of the orbit is 55°. Fregau et al. (2006) conclude that the system is most likely the result of an exchange encounter of the binary with a planet-bearing main-sequence star; the encounter left the planet around the binary. Many such exchange systems have been found in the dense environment of globular clusters.

The 5.7 ms pulsar PSR J1719-1438 has what appears to be a very low-mass ($M \sin i = 1.2 M_J$) stellar remnant in close proximity to a rapidly rotating neutron star; if the “planet” is constrained by its *Roche* lobe (the inner Lagrangian surface around both stars on which Lagrangian point L₁ is located, as depicted in Milone and Wilson 2014, Fig. 3.3), the radius is ~0.4 R_J ; the density may be as great as 23,000 kg/m³ (Bailes et al. 2011). The exotic, diamond-like “planet” in PSR J1719-1438 may be the result of ablation of a companion star.

16.2.7 Indirect Effects

These include O–C (for *Observed–Computed* instants of mid-eclipse) or eclipse timing curves, and various effects on stellar disks: warps, gaps, and clumps.

E. F. Guinan et al. (1998) claimed detection of one or more planets in the CM Draconis system, an eclipsing M-dwarf binary, but found only one photometric

event (disputed by Deeg et al. (2000), who claimed their own marginally significant evidence for a planet). Both groups have studied the timing of the mutual eclipses and compiled O–C curves of the eclipsing system, which furnishes evidence of the gravitational effect on the orbits of the two stars. Deeg et al. (2000) found that a common proper motion white dwarf companion is not the cause of the timing variation reported earlier, but provide no further evidence for a planet in the system. At present, a planet in this system remains unconfirmed.

Proto-planetary disks have been seen around several stars, including β Pictoris and Vega, and remnants of disks have been seen around older stars. Gaps and warping have been attributed to the presence of planets or proto-planets in some of these systems.

Gorkavyi et al. (2004) summarize the case for a $10M_J$ planet orbiting β Pictoris, the first star discovered to have a disk around it. There are now other known cases of candidate planets around stars with remnant disks, such as ε Eridani and GQ Lupi. Clumpings of material in the disks of ε Eri and Vega have been interpreted as evidence of mean motion resonances (see Milone and Wilson 2014, Chap. 3 for a discussion of commensurabilities) involving planets. However, few details about the planets can be obtained through this method, should it prove to be reliable.

Before we close this section on techniques, we need to mention the analytic approaches that have been applied to date. From 1995 to \sim 2005, much of the work done on the evaluation of planetary transits in the literature appears to have been carried out by people who had little previous experience analyzing such light curves, and who did not discuss the details of their methods in doing so. Therefore, if more recent work has not appeared, we report their results here as they reported them, but in most cases further work will have to be performed to verify them and perhaps to optimize the determinations. Currently more rigorous analyses and methods are being applied and optimization procedures are being described in the literature (as, e.g., by Foreman-Mackay et al. 2013). Curiously, however, many of the planetary investigation teams seem to have adopted a particular optimization approach: the Markov Chain Monte Carlo method frequently coupled to Bayesian inference techniques (see Ford 2005, 2006). Although this approach seems to be successful, given its random walk nature it is not clear that any group has in fact conducted a rigorous search for the most robust and efficient modeling algorithms. These remarks apply to all types (RV, lensing, etc.) of exoplanet studies.

Having now discussed the methods by which planets may be discovered, we turn to a thorny but essential issue: the definition of a planet.

16.3 Definitions of Planets and Brown Dwarfs

It is a great irony that although the planets have been studied as long as they have borne their identifying characteristic of wandering among the stars, until 2006 planetary scientists had failed to agree as to exactly what it is that makes a planet a planet.

Until now naming controversies have raged only at the low mass and diameter end of the scale, where the distinction among moon-sized bodies, asteroids, and planets has become more difficult with increasing discoveries. The various factors underlying the controversy are reviewed by Basri and Brown (2006). As far as we are concerned, the term “minor planet” could well have been used to distinguish objects that are smaller and less massive than the largest planetary moon, whether or not they happen to be currently locked in an orbital resonance. However, it is up to the International Astronomical Union (IAU) to adjudicate matters of astronomical nomenclature, and a definition was adopted at the IAU General Assembly meeting in Prague in 2006:

A planet is a celestial body that is

- (a) in orbit about the Sun,
- (b) has sufficient mass for its self-gravity to overcome rigid body forces so that it assumes a hydrostatic equilibrium (nearly round) shape, and
- (c) has cleared the neighborhood around its orbit.

Thus the asteroid (433) Eros, described in Chap. 15, fails to meet criterion (b). With these definitions, there are now eight planets, because Pluto fails the “clearing” criterion, (c). Instead, Pluto is relegated to a class known as *dwarf planets*, defined, in the same IAU resolution, as celestial bodies that fulfill planetary criteria (a) and (b) but fail (c), and are not satellites. The main belt asteroid (1) Ceres, and the Edgeworth-Kuiper Belt object Eris, initially designated (2003-UB313), are also dwarf planets. Pluto is, however, the prototype of the trans-Neptunian objects (TNOs, a group to be given another name at some future date—recently *Plutooids* has been suggested as a name for TNO dwarf planets), and the eponymous prototype of a subgroup of the TNOs, the *Plutinos*, which are icy bodies locked in a 3:2 mean motion resonance with Neptune. Interestingly, the barycenter of Pluto and its principal moon Charon is outside Pluto’s radius. This makes the Pluto-Charon system a double dwarf planet, with four small moons orbiting in nearly the same plane—see Chap. 13. Most asteroids clearly do not qualify as dwarf planets; thus, no asteroid (or planetoid or minor planet, as these objects have been called) and no Edgeworth-Kuiper Belt object, can be reassigned to dwarf planet status unless it has been determined to be round. All objects not in the planet or dwarf planet categories and not satellites are simply called “Small Solar System Bodies,” with disputed cases to be handled in some way by the IAU. The definitions are likely to be challenged, and probably will be further refined, in practice, if not by writ, but in any case, no one can now claim that astronomers have not provided some leadership in offering a definition of a planet!

At the high mass end of planetary definitions, there is somewhat less disagreement, probably because we have not enough clear-cut examples of objects in the transition region. Theoretical work done so far suggests that deuterium burning begins at a mass $\sim 13M_J$ providing a convenient dividing line between planets and other low mass objects (Saumon et al. 1996). Sub-stellar objects above this mass are assumed to be brown dwarfs. Objects at the brown dwarf-star interface are

considered to be stars if their masses are greater than $\sim 75M_J$ (or $0.072 M_\odot$), if they have solar composition. For stars with no metals, this limit increases to $90M_J$.

As a practical matter, in at least some cases, one may be able to distinguish a planet from a brown dwarf, and a brown dwarf from a low-mass star, through observational means: brightness, color and/or spectral characteristics. One possible criterion is the presence of lithium (Li), which is easily destroyed in stars through large-scale convection. According to Basri (2000, p. 494), any object of spectral class later than M7, and having lithium, must be sub-stellar. According to Chabrier and Baraffe (2000), the characteristic spectral sequence features for ranges of temperature at the cool end of the spectral sequence (with examples of brown dwarfs added) can be summarized as follows:

$\lesssim 4,000$ K	M dwarfs. Most of the hydrogen is in the form of H ₂ and most of the carbon in CO. O is bound mostly in TiO, VO, and H ₂ O, some in OH and in monatomic O, and metal oxides. Metal hydrides (e.g., CaH, FeH, MgH) are also present. In optical spectra, TiO and VO dominate; in the IR, H ₂ O and CO features are seen. E.g.: 2MASS J0535-0546A,B, M6.5; Teide 1, M8.
$\lesssim 2,800$ K	O-rich compounds condense in the atmosphere and may go into perovskite (CaTiO ₃).
$\lesssim 2,000$ K	The realm of the <i>L dwarfs</i> (example: GD 165B, L4). Some TiO remains, but metal oxides and hydrides disappear from the spectra. Alkali metals are present in atomic form. Some methane may be seen.
$\lesssim 1,800$ K	Refractory elements (e.g., Al, Ca, Ti, Fe, V) condense into grains. Corundum (Al ₂ O ₃), perovskite condense. Depending on the pressure, rock-forming elements such as Mg, Si, Fe may condense as metallic iron, forsterite (Mg ₂ SiO ₄), or enstatite (MgSiO ₄).
1,700 to ~600 K	Region of cross-over to <i>T dwarfs</i> , also known as <i>methane dwarfs</i> (example: Gliese 229B, T6.5). Methane absorption is strong in the infrared broad passbands H (1.7 μm), K (2.4 μm), and L (3.3 μm), giving rise to a steep spectrum at shorter wavelengths, with J-K $\lesssim 0$, but with I-J $\gtrsim 5$. Possible cross-over to “Y dwarfs.”

A planetary temperature is typically less than $\sim 1,200$ K, but this depends on the surface temperature of the star, the proximity to it, and the planet’s albedo. Moreover, as we shall note later, this assumes that the planet is in thermal equilibrium. There are substantial reasons to doubt the validity of this assumption for at least some of the lower mass planets in very close proximity to their stars, for example in HD 209458b, which is detectably outgassing (see the discussion below).

As with stellar characteristics, the observed properties of brown dwarfs will change with time. Figure 16.7 demonstrates the changes in absolute K passband magnitude vs. temperature expected for objects of various masses between one and five My. Note the changes in position of lower mass objects in the course of time between the isochrones. In a group of brown dwarfs of identical age, the more massive will be brighter in a particular IR passband; for brown dwarfs of the same mass, the younger will tend to appear brighter.

All simulations suggest that the lower temperature brown dwarfs would have clouds and other atmospheric features usually associated with gaseous planets. Planetary modeling of hot Jupiters indicates equilibrium temperatures to be, very roughly, $\sim 1,000$ K. Williams (2001) estimated the temperature of HD 209458b to

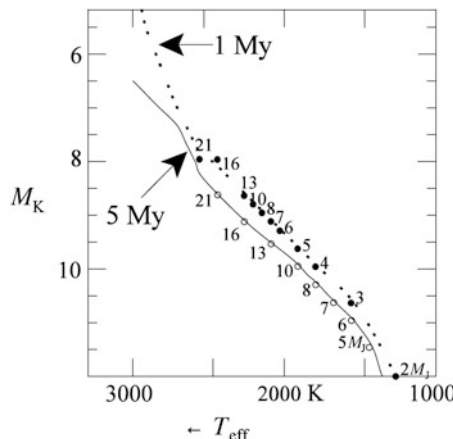


Fig. 16.7 A form of a Hertzsprung-Russell diagram for planets and brown dwarfs. The isochrones (lines of constants ages) for objects of 1 and 5 Myr ages; the masses (in M_J) of the objects along the isochrones are indicated. Diagram adapted from that in Jayawardhana and Ivanov (2006) from models of Baraffe et al. (2002) and Chabrier et al. (2000). Reproduced and modified by permission of the authors and the American Astronomical Society

be ~ 915 K, assuming no significant internal energy sources. Charbonneau et al. (2005) found from Spitzer observations that the temperature of HD 209458b is 1,350 K. This is hotter than many of the brown dwarfs that have been observed, as deduced from their infrared colors. Presumably as more of these objects are studied, criteria will become more definitive. See Reid et al. (2006) for a catalog of L dwarfs, Burgasser et al. (2006) for a list of T dwarfs and a discussion of objects at the L/T boundary, and Cushing et al. (2011) for suggestions about the ultra-cool Y dwarfs.

Notwithstanding that the origins of all planets are not known with certainty, Burgasser et al. (2010) were reluctant to classify Ross 458 ABb as a planet even though its mass ($\sim 0.006 M_\odot = 6M_J$) and radius ($\sim 1.2R_J$) suggest it is, and its T8 spectral type and low temperature (600–800 K) are consistent with such an assignment, because it is very far from the M0.5 + M7V binary about which it orbits: a whopping projected distance of 1,100 au. However, planet formation at or migration to such a separation requires rare and unusual circumstances, hence they referred to it as Ross 458C, a suitable designation only for a star or brown dwarf companion.

16.4 Extra-Solar Planets Detected or Awaiting Confirmation

As of mid-November, 2013 well over 4,000 confirmed/suspected extra-solar planets had been discovered. Of these, ~ 730 had reliably computed orbital elements; another 26 candidate planets were detected by imaging and microlensing. Table 16.1 is a selected position-ordered list of stars which are known or strongly suspected to

have planets. Only confirmed Kepler candidates as well as those found by RV and astrometric techniques at the time of compilation were included, however. Table 16.2 is ordered in the same way, with the planets in each system listed together. The sub-stellar entries on each line are arranged in increasing distance from the star. These are mainly objects with $M \sin i$ values less than $13M_J$ but there are exceptions. Because the mass is a lower limit for the RV-studied systems (one of the exceptions is HD 209458b, among those which have been studied with more than one technique), some of these may turn out to exceed this critical mass which has been used to divide brown dwarfs from planets.

Note the large number of “hot Jupiters,” large planets with small distances from their stars. Although many of these have low eccentricities, as expected because circularization effects operate in close binary star systems over time scales of millions or tens of millions of years, some do not. The latter can be interpreted as the result of recent migration into these orbits or of planetary interactions in a multi-planet system. Thus the presence of “hot Jupiters,” especially with sizable eccentricities, may imply dynamically active systems.

The metallicities of most stars with confirmed planets appear to be greater than for the Sun. This also points to a relatively young stellar environment. This conclusion is further enhanced by a failure to see any evidence of planetary transits in more than 8 days of continual monitoring of more than 50,000 stars in core and peripheral HST frames of the globular cluster 47 Tucanae (Gilliland et al. 2000). In such cases, planetary deficiency could be explained by intra-system dynamical and extra-system tidal effects to which the planets would have been subjected over the great age of the globular cluster (~13 Gy). A ground-based study of 47 Tuc by Weldrake et al. (2005) that concentrated on the outlying fields of 47 Tuc, confirmed the apparent absence of planets in that cluster. Simulations of planetary systems in globular cluster environments led Fregau (2006) to conclude that the close-in planets targeted in the Gililand experiment would have survived dynamical encounters over the age of the cluster; they therefore attributed the absence of these planets to the cluster’s low metallicity ($[Fe/H] = -0.76$). Notwithstanding this result, no planets have been found in the metal-rich ($[Fe/H] = +0.32$), dense open cluster NGC 6791, either, to our knowledge. Even in sparser clusters orbiting planets seem to be rare. One planet has been found in the Hyades, orbiting the red giant star ϵ Tauri (Sato et al. 2007). Additionally, Zuckerman et al. (2013) argue that the Hyades white dwarf, LP 475-242, has a planetary system because its spectrum contains Ca lines. A white dwarf is not expected to have metals on its surface because the gravitational field strength is so great that heavy elements diffuse downward rapidly (see, e.g., Zuckerman (2003)), so the Ca lines may be evidence of contamination by planetary material having fallen into the white dwarf. Two planets have been found in Praesepe, the “Manger” or “Beehive” or M44: Pr0201b and Pr0211b (Quinn et al. 2012). Both clusters are ~600 My old and metal-rich. On the whole, these cases suggest that stellar number density and age, as well as metallicity, are key environmental factors in determining the existence of giant, short-period planets (surveys tend to be biased toward this group, but as the time-line increases, the bias against long-period, and lower mass objects is being reduced).

The tidal radius of a star becomes a critical matter in planetary systems in dense clusters. If planets tend to be formed further out than 5 au, and if the mean free path through the dense portion of a cluster is small enough, some planets may be stripped from their parent stars and left to be “free-floating”. The discovery of such objects probably requires the very large mid-infrared space telescopes planned for the future, and gravitational lensing (Gaudi 2012).

To complement Table 16.2, Table 16.3 lists some of the newly found brown dwarfs. See Basri (2000) for a review of the observational properties and Chabrier and Baraffe (2000) for the theory of these objects. In addition to these low mass objects, the planetary or planet-like objects around three pulsars are listed in Table 16.4. The planets of PSR 1257+12 are among the lowest mass sub-stellar objects detected. Wang et al. (2006) have identified the infrared signature of a supernova “fallback” disk around a young neutron star, 4U 0142+61, in which planet formation may occur. They estimate the total mass of the disk to be $\sim 10^{-5} M_{\odot}$, comparable to the total mass of the PSR 1257+12 planets. Such disks seem to be rare around intermediate and older pulsars, likely the result of disk destruction by x-ray winds and other mechanisms. Wang et al. (2006) conclude that in the case of 4U 0142+61, the disk should outlast the spin-down, perhaps aiding the process through magnetic coupling, and, possibly, permitting planet formation.

There is an increasing number of multi-planet systems being found where two or more planets are orbiting a star. As of May 1, 2013, 131 systems were known to have at least two confirmed planets, and 31 systems had at least three planets each. Three systems are known to have at least six planets each: HD 10180, HD 40307, and Kepler 11.

Another growing group of planets are those detected through planetary transits. These include the Kepler-, Corot-, HAT-, WASP-, and TrES-systems, and a steadily increasing number found in the course of the gravitational lens survey of the galactic bulge, such as: OGLE-TR-10b, -56b, -109b (though probably a brown dwarf), -111b, -113b, and -132b (cf. Santos et al. 2006 for all but -109b, -132b; Fernandez et al. 2006 for -109b; and Gillon et al. 2007 for -132b). These are important because they provide independent values for the radius, and, in combination with radial velocity data, the true masses, because careful photometric analysis can yield orbital inclinations. Other planets have been found to transit after they were discovered through radial velocity variations. These include HD 209458b (Sect. 16.4.1), HD 149026b (Sato et al. 2005), HD 189733b (Bakos et al. 2006), and 55 Cnc e (Sect. 16.4.3).

If only a transit eclipse is observed, the relative radii (the radius of each object divided by the semi-major axis) are obtainable, and unless the star is not very large compared with the planet and/or the eclipse is central, so that all four contact points can be observed, the planetary radius determination depends on the assumed radius for the star. In a transit eclipse, however, the darkened limb of the star results in a gradual decrease in light during the beginning of the transit, though the limb-darkening coefficients must be determined or known for a star with similar characteristics. When a radial velocity curve becomes available, even though single-lined, the absolute radii are obtainable, because the transit can be

modeled to obtain an optimum inclination (which, in any case, will likely not be too different from 90°). The planetary mass depends on the assumed mass of the star, as noted in Sect. 16.2.1, because basically only the mass function is known from analyses of a single-lined RV curve. Therefore, in discussing what is known about extra-solar planets, the stellar radii and masses are often included in full discussions. Consequently, we include them in our descriptions of some of the more interesting systems of Table 16.2 in the sections to follow. References for mass, radius, and chemical composition for many of the stars of Table 16.1 can be found in Butler et al. (2006) and from the online extra-solar planets encyclopedia and exoplanets websites mentioned above, as well as from the Simbad website: <http://simbad.u-strasbg.fr/Simbad>.

16.4.1 HD 209458b

This is the first extra-solar planet to have been observed transiting its star and consequently to have its radius measured and the first to have had a constituent of its atmosphere detected. The excellent Keck radial velocity data (kindly supplied by G.W. Marcy), and the HST observations, in particular, have been so precise that both extensive rings and satellites of this object can be ruled out. The HST and previous light curves were analyzed with the light curve analysis programs in use at the University of Calgary. The best fit parameters to both light curve and RV curves (RV, Marcy 2000; y&b, Henry et al. 2000; VB $R_C I_C$, Jha et al. 2000; HST R_C , Brown et al. 2001; and R_J , Charbonneau et al. (2000, 2005)) of that study, by Williams (2001), are summarized in Table 16.5. The Brown et al. light curve permitted the limb-darkening coefficient to be derived: $x(R_C)^* = 0.510 \pm 0.008$ (the parameters that Williams computed are marked with an asterisk).

Thanks to the transit observations, the radius of this planet was determined to be $R_p^* = 1.37 \pm 0.01 R_J$, so that the density can be found: $330 \pm 10 \text{ kg/m}^3$. The epoch of mid-eclipse is $t_e^* = 2451254.587 \pm 0.002$. The orbit appears to be circular to high precision, with $a = 10.06 R_\odot$ (assumed). The spectroscopic properties of the star were taken from Mazeh et al. (2000).

The movement of the planet across the limbs of the star during the transit produces a slight distortion in the profile of a spectral line which leads to a distortion in the derived radial velocity curve (commonly known as the *Rossiter effect* or sometimes, the *Rossiter-McLaughlin effect*).² From an analysis of the

² Rossiter (1924); McLaughlin (1924). During the 2012 transit of Venus, Molaro et al. (2013) succeeded in detecting the Rossiter-McLaughlin effect as Venus transited the Sun's disk. They used the HARPS spectrograph on the 3.6-m ESO telescope. They observed the partial Venus eclipse in the light of the Sun reflected in the Moon. The transit of Venus across the receding solar hemisphere produced a modulation in the radial velocity with a negative amplitude of $\approx -1 \text{ m s}^{-1}$, in agreement with the theoretical model. The change in RV is comparable to the solar jitter and $\lesssim 1/2$ that detected in the RV profiles of hot Neptunes, for example.

Table 16.5 The HD 209458 planetary system

Planet	Period*	T_0^* (JD-2450000)	e^*	ω^*	K (m/s)	M_p/M_J^*	R/R_J	i^*	a (au)
b	3 ^d 52478(5)	1245.587(2)	0.0000(3)	–	70.2	0.69(1)	1.36(2)	86 ^d 54(2)	0.0467
Star	γ^*	$v \sin i$	Sp. type	$M (M_\odot)$	$\mathfrak{R}/\mathfrak{R}_\odot^*$	V	r (pc)	[Fe/H]	T
a	18(8) m/s	4.49 m/s	F8V	1.09(1)	1.145(3)	7.65	47.4(1.7)	0.00(2)	6,000(50) K

effect in HD 209458, Winn et al. (2005) derived a $v \sin i$ value of 4.7 km/s, similar to that found in line profile analyses. Williams (2001) also found no evidence for period variation ($\dot{P}^* = 0 \pm 2 \times 10^{-7} \text{ d/d}$).

It is instructive to compare the above results with that from later work. From the solutions based on new Elodie and Coralie radial velocity measurements and an analysis by Naef et al. (2004):

$$\begin{aligned} a &= 0.048 \text{ au}; \quad M_p \sin i = 0.699 \pm 0.007 M_J; \quad R_p = 1.27 \pm 0.02 R_J; \\ P &= 3.5246 \pm 0.0001 \text{ d}; \quad T_{\text{periapse}} = 2452765.790 \pm 0.021; \\ T_t &= 2452618.66774 \pm 0.007; \quad \gamma = 14.741 \pm 0.002. \end{aligned}$$

The projected mass that they derive is based on a mass of the star of $1.15 M_\odot$. With the inclination given in Table 16.5, this yields a mass of precisely $0.700 M_J$.

And, from the values of parameters and elements from the newer analyses of Torres et al. (2008): $i = 86.71 \pm 0.05$; $a = 0.0471 \pm 0.0005$ au; $M_p = 0.685 \pm 0.015 M_J$; $R_p = 1.36 \pm 0.02 R_J$; $\rho_p = 338 \pm 15 \text{ kg/m}^3$. The comparisons demonstrate that modern eclipsing binary curve analysis code is quite capable of yielding precise and accurate results from planetary transit photometry and single-line RV curves.

The radius of HD 209458b is larger than one would expect for a planet less massive than Jupiter, especially when compared to the radii of other “hot Jupiters.” A larger size for such a planet (relative to *our* Jupiter) is expected because of its proximity to its star, which would increase the equilibrium temperature ($1,449 \pm 12$ K, as tabulated in Torres et al. 2008, most likely computed for the 1:1 spin-orbit coupled “slow rotator” case) and therefore increase the pressure scale height of the atmosphere; but the radius of HD 209458b exceeds predictions of models that take this into account. With a mean density of $330 \pm 10 \text{ kg/m}^3$ (Williams 2001), less than half that of Saturn, the result is not in doubt: the atmosphere is distended! In this, however, HD 209458 is not alone; many such distended planets are known.

Subsequent observations by Vidal-Madjar et al. (2004) have shown evidence for a trailing cloud of hydrogen, carbon, and oxygen, indicating hydrodynamic loss of atmosphere from this planet. The group refers to the planet as Osiris, after the Egyptian god who was killed and dismembered by Seth (see Kelley and Milone 2011, Chap. 8.1.2). Vidal-Madjar et al. suggest that planets older and closer to their parent stars than HD 209458b may have been deprived of their atmospheric envelopes and become a new class of planets (*chthonian*).

Excess H absorption has been confirmed by Ballester et al. (2007), and Ehrenreich et al. (2008), among others. That there are high-velocity carbon ions (CII) well off the disk of the planet was confirmed by Linsky et al. (2010), who also detected absorption in Si III, implying outflow rates of $8\text{--}40 \times 10^6 \text{ kg/s}$. The velocities cannot be explained by thermal speeds alone, so the star's x-ray and XUV radiation, and stellar winds appear necessary. Similar extended outflows have been detected in other exoplanet systems as well: HD 189733b (Bourrier et al. 2013 and references therein); WASP-12b (Fossati et al. 2010); HAT-P-6b (Hébrard et al. 2011); and in the planet of an M dwarf, GJ 436b (Ehrenreich et al. 2011). Ehrenreich and Désert (2011) consider the x-ray and XUV energy deposited in a planetary atmosphere and gravitational potential energy to predict outflow rates of $10^6\text{--}10^{13} \text{ kg/s}$.

Bourrier et al. (2013) and Lecavelier des Etangs et al. (2012) discuss the transient evaporation of H as seen in Lyman alpha in HD 189733b, possibly due to a major flare recorded by Swift 8 h before the transit event. The high velocities and high altitudes imply a loss rate of neutral H of $\sim 10^6 \text{ kg/s}$ and a stellar wind of $\sim 190 \text{ km/s}$.

The confirmed OGLE planets constitute a closer and therefore even hotter class of hot Jupiters, but their sizes appear to be smaller than HD 209458b. Work on the evolution of hot Jupiters by Baraffe et al. (2004) suggests that for objects lower than a given mass at a particular distance from the star, the initial hydrogen envelope evaporates, after which the icy and rocky components will expand and evaporate also. The time scale depends greatly on the XUV radiation from the star. These authors investigated the varying fluxes of solar-type stars at different ages for the orbital radii of HD 209458b (0.046 au) and OGLE-TR-56b (0.023 au) and found that the planets in the mass range of $0.5\text{--}5 M_J$ have evaporation rates varying from $10^{-8} M_J/\text{y}$ at young ages, to $\sim 10^{-12}$ for ages greater than 5 Gy.

From Spitzer Space Telescope data, infrared observations obtained during secondary eclipse imply a temperature for the planet on its heated face of $T = 1,130 \pm 150 \text{ K}$ (Deming et al. 2005). This result is very close to that found for the transiting planet HD 189733b by Deming et al. (2006), namely $T = 1,117 \pm 17 \text{ K}$, observed in a more sensitive mode and to higher precision than previous planetary occultation observations. Therefore, in the lower density planets, such as HD 209458b, we may be witnessing a more evolved state of hot Jupiters. Observations to detect sodium in the atmosphere have been made (e.g., by Charbonneau et al. 2002). Most have been successful, but less has been seen than expected, possibly due to clouds or condensation of sodium on the night side (see also Sect. 16.4.9, below). Since then other elements have been detected in the atmospheres of exoplanets, including carbon, magnesium, oxygen, and silicon, and compounds such as CO, H₂O and CH₄, have also been detected. A recent example is the detection of a Mg-absorbing disk or thick torus around WASP-12b (Haswell et al. 2012).

Table 16.6 *v* Andromedae planetary system

Planet	Period	T_{peri} (JD-2450000)	e	ω	K (m/s)	$M_J \sin i$	a (au)
<i>v</i> And b	4 ^d 61710	2.093	0.012	73°	70.2	0.69	0.059
<i>v</i> And c	241 ^d 5	160.5	0.28	250°	53.9	1.89	0.829
<i>v</i> And d	1284 ^d	64	0.27	260°	61.1	3.75	2.53
Star	P (rotn)	Sp. type	Mass (M_\odot)	V	r (pc)	[Fe/H]	
<i>v</i> And a	10 ^d 2	F8V		1.32	4.09	12.47	0.15

16.4.2 The Multi-planet System of *v* Andromedae

This was the first multi-planet system discovered. Data provided by Marcy's California & Carnegie Planet Search Team, as of September 24, 2002 are summarized in Table 16.6.

One, two, and finally, three-planet fittings to the radial velocity data show successively smaller residuals. Note the 'hot Jupiter', *v* And b, with a low eccentricity orbit, is close to the star while *v* And c, although still fairly close to *v* And a, has a much higher eccentricity. Modeling studies of the orbital behavior of hot Jupiters in multiple planet systems reveal that the interactions among planets can induce oscillations in such orbital parameters as the eccentricity, semi-major axis, and inclination, just as has been found for asteroids and for irregular moons of the gas giants in our solar system (Sect. 13.3.5).

16.4.3 The Multi-planet System of 55 Cancri

The 55 Cnc = ρ^1 Cnc system is one a growing number of planetary systems with as many as five detected planets (McArthur et al. 2004; Butler et al. 2006; Fischer et al. 2008). This is typical of the results of extended monitoring as the velocity residuals over longer and longer intervals of time reveal additional periodicities. The innermost planet, e, was found by Dawson and Fabrycky (2010) to have a period of 0.7365d, rather than 2.80d obtained earlier (Fischer et al. 2008) and identified 55 Cnc e as having a high transit probability; subsequently, transits were discovered by Winn et al. (2010) and Demory et al. (2011). The parameters in Tables 16.2 and 16.7 are based on new analyses of a significantly larger RV data set and of 55 Cnc e, in particular, by Endl et al. (2012). The inclination of 55 Cnc e is 82°5, giving an unprojected mass of $M = 8.37 \pm 0.38 M_E = 0.026 \pm 0.001 M_J$. The radius, $R = 2.17 \pm 0.10 R_E$, is from Gillon et al. (2012); whence the density $\rho = 4,500 \pm 200 \text{ kg/m}^3$. Endl et al. (2012) find a faint but insignificant signal at 131 d, but speculate that there could be still more planets in this system between planets f and d. The star itself has a common proper motion companion 7 magnitudes fainter, 85 arc s away.

Table 16.7 The 55 Cancri planetary system

Planet	Period	T _{per}	ε	ω	K	M sin i	a
	days	(JD-2450000)		degs	m/s	M _J	au
e	0.736546(3)	5568.011(8)	0 (fixed)	90 (fixed)	6.30(21)	0.026(1)*	0.01544
b	14.651(0)	3035(2)	0.004(3)	110(54)	71.1(2)	0.80(1)	0.1134(6)
c	44.38(1)	3083(3)	0.07(2)	356(22)	10.1(2)	0.165(5)	0.237(1)
f	261.2(4)	1878(5)	0.32(5)	139(8)	6.2(3)	0.172(8)	0.77(1)
d	4909(30)	3490(437)	0.02(1)	254(32)	45.2(4)	3.53(8)	5.47(6)
Star	V sin i	V	B - V	SpT	T	R	M
	km/s	magn	magn		K	R _{sun}	M _{sun}
a	2.46	5.95(5)	0.87	G8V	5196	0.943	0.905
							+0.29
							...
							12.53(13)

* The mass for planet e is unprojected.

Table 16.8 The Kepler 11 planetary system

Planet	Period	Duration	Depth	i	a	R	M	T _{transit}
	days	hours	mmags	degs	au	R _E	M _E	-2440000
b	10.30376(2)	4.02(8)	0.31(1)	88.5(+10,-6)	0.091(3)	1.97(19)	4.3(+22,-20)	14971.5052
c	13.02502(8)	4.62(4)	0.82(1)	89.9(+10,-6)	0.106(4)	3.15(30)	13.5(+48,-61)	14971.1748
d	22.6872(2)	5.58(6)	0.80(2)	89.3(+6,-4)	0.159(5)	3.43(32)	6.1(+31,-17)	14981.4550
e	31.9959 (3)	4.33(7)	1.49(2)	88.8(+2,-2)	0.194(7)	4.52(43)	8.4(+25,-19)	14987.1590
f	46.6888(7)	6.54(14)	0.55(2)	89.4(+3,-2)	0.250(9)	2.61(25)	2.3(+22,-19)	14964.6487
g	118.378 (1)	9.60(13)	1.15(3)	89.8(+2,-2)	0.46(2)	3.66(35)	<300	15120.2901
Star	V sin i	Kepler	V	SpT	T	R	M	[Fe/H]
	Km/s	magn	magn		K	R _{sun}	M _{sun}	
a	0.4(5)	13.7	14.2	GV	5680(100)	1.1(1)	0.95(10)	0.0(1)
								...
								610

16.4.4 The Multi-planet System of Kepler 11

This system was discovered via transits observed during the Kepler mission. The data in Table 16.8 are from Lissauer et al. (2011). The uncertainties are indicated by parentheses following each quantity, in units of the last decimal place given. Thus the orbit of planet b has an inclination $i = 88.5_{-0.6}^{+1.0}$ degrees and a mass $M = 4.3_{-2.0}^{+2.2} M_E$, where M_E is the mass of the Earth.

Lissauer et al. (2011) carried out high-resolution spectroscopy of Kepler 11a and found a solar composition ($[\text{Fe}/\text{H}] \approx 0$) and a gravitational acceleration, $g \approx 200_{-70}^{+120} \text{ m/s}^2$, roughly similar to the solar value: $g = 273.98 \pm 0.04 \text{ m/s}^2$ (Milone and Wilson 2014, Sect. 4.2). Kepler 11a is seen to be a solar analog star but slightly larger, less massive, and somewhat less dense than the Sun. Both the size and mass of the host star are needed in order to determine the planetary sizes and masses. Note the shallowness of the transit eclipses (the units of the depth below maximum level are milli-magnitudes). The total decrease in light during transit eclipse is proportional to the square of the ratio of the radii of planet and star. The long intervals

Table 16.9 The HD 69830 planetary system

Planet	Period	T_{peri} (JD-245000)	e	ω	K (m/s)	$M_J \sin i$	a (au)
b	8 ^d 667	3496.80	0.10	340°	3.5	0.032	0.079
c	31 ^d 56	3469.6	0.13	221°	2.7	0.037	0.19
d	197 ^d 0	3358.	0.07	224°	2.2	0.057	0.633
Star	P (rotn)		Sp. Type	M/M_{\odot}	V	r (pc)	[Fe/H]
a	25 ^d		G8/K0 V	0.86	5.95	12.58	-0.05

between transits provides the orbital period. The differences between the instants of the four contacts (t_1 and t_4 , the two external contacts when the star and planet are side-by-side; and t_2 and t_3 , the two internal contacts when the planet is just within the disk of the star) provide the radii of the star and planet in terms of a , the semi-major axis; thus, $t_2 - t_1 = t_4 - t_3 \propto 2R_p$; $t_3 - t_1 = t_4 - t_2 \propto 2R_s$. The modeling of the transit duration and shape can provide also the stellar limb-darkening, and the inclination, which depends on the length and orientation of the chord across the disk, for each planet. See Kallrath and Milone (2009) for a fuller discussion of the extraction of properties from transit (and occultation) eclipses.

The Kepler 11 planets are all larger than the Earth, and their radii approach or exceed that of Uranus ($\sim 4R_E$), the masses are relatively more uncertain but are also greater than Earth's. The corresponding densities range from ~ 0.1 to ~ 0.6 that of the Earth, or ~ 0.4 to ~ 2.3 times that of Jupiter. The orbits are all crammed into a tiny volume close to their star; all but planet g would fall within Mercury's orbit if transported to the solar system. Planet g is less well characterized than are the other planets, but the analysis team performed a Bayesian analysis and concluded that the chances of a false positive for its transit signature were extremely low. All of the eccentricities are poorly constrained, however. Planets c and b are roughly in a 5:4 orbital period resonance (1.26). Finally, Lissauer et al. (2011) carried out dynamical analyses to assess the stability of this tightly packed system over an interval of 2.5×10^8 years, and cautiously concluded that the interactions are weak enough between planets b and c and the other planets to allow long-term stability.

16.4.5 The Multi-planet System of HD 69830

This is an interesting triple planet system, analyzed by Lovis et al. (2006). The properties of the system are shown in Table 16.9. Unless the inclinations of these planets turn out to be significantly different from 90°, these objects are in the Uranus ($0.046M_J$)-Neptune ($0.054M_J$) class of planets. Note, however, even though they may be lesser giants, all three orbits are crammed within an astronomical unit of their star.

The system has been found to emit strong infrared radiation attributed to silicate grains at a temperature ~ 400 K, possibly from a debris disk due to an *asteroid mill* (replenishment of an asteroid belt by collisions), a source of grains in the solar system (Lovis et al. 2005).

Table 16.10 The Gliese J 876 planetary system

Planet	Period	T_0 (JD-2450000)	e	ω	K (m/s)	M_J	a (au)
b	60 ^d 990(7)	–	0.033(1)	249(3) ^o	213.2(3)	2.37(4)	0.21102(2)
c	30 ^d 183(6)	2000.	0.250(3)	252(1) ^o	84.7(4)	0.75(1)	0.1313(2)
d	1 ^d 93789(2)	–	0.18(4)	224(16)	6.2(3)	0.022(1)	0.0211063(1)
e	124.5(5)	2000.	0.01(3)	181(77)	3.4(3)	0.048(5)	0.3396(9)
Star	Sp. type	M/M_\odot	$\mathfrak{R}/\mathfrak{R}_\odot$	V	B-V	r (pc)	[Fe/H]
a	M4 V	0.32	0.3	10.192(2)	1.54	4.69(5)	0.02

Perhaps one of their most interesting findings is that the outer planet is in the *habitable zone*, a region where an object with sufficiently great surface gravitational acceleration can retain water in liquid phase on its surface.

16.4.6 The Multi-planet System of Gliese J 876

This four-planet system (Baluev 2011; Rivera et al. 2010) may be the closest known planetary system to Earth. There appears to be very little RV jitter in this star, a faint, red dwarf variable star, IL Aquarii. It is one of a growing number of M dwarfs that have been discovered to harbor planets (Bonfils et al. 2013; others are: GJ 436, GJ 674, and GJ 581 with three planets). The properties of the system are summarized in Table 16.10. Assuming the planets are coplanar, Baluev (2011) finds an optimized inclination of 56° 1 and unprojected masses for planets b, c, d, and e of 2.38, 0.747, 0.022 M_J ($= 6.9 M_\oplus$), and 0.048 M_J , respectively. Planet d is among the lowest mass objects found through the radial velocity technique. Rivera et al. (2010) and Baluev (2011) also explored non-coplanar solutions.

Initially, the large masses of two of these planets were unexpected around such a low-mass star, because the time scale of formation of such planets exceeds that of the disk from which planets are expected to form. This provided difficulties for both the core-accretion theory and the gravitational instabilities theory of planet formation. Moreover, the estimate of metals in this star is relatively low. This seemed to compound the problem of how these planets were formed, because stars with metallicities higher than that of the Sun are found to be more likely to have planets, indicating that the dust in the planetary disk plays a key role in the formation of planets. However, many systems with even less metallicity than the Sun have been found to have giant planets, so the mystery remains.

16.4.7 The ϵ Eridani System

This is an interesting system for a number of reasons. First, the star is of a late spectral type, and it demonstrates the large velocity jitter due to strong photospheric effects that are expected in late-type stars. The “jitter” is caused by distortions in

Table 16.11 The ε Eridani planetary system

Planet	Period	T_{peri} (JD-2450000)	e	ω	K (m/s)	$M_J \sin i$	a (au)
b	2500 ^d	8940.	0.25	6°	18.6	1.06	3.38
Star	$v \sin i$	Sp. type	M/M_\odot	$\mathfrak{R}/\mathfrak{R}_\odot$	V	r (pc)	[Fe/H]
a	1.7 km/s	K2 V	0.82	0.76	3.73	3.22	–

spectral line profiles as the star's active regions literally highlight the radial velocities of the matter in those regions across the disk. The distortions complicate the Doppler shift measurement that is needed to obtain the star's radial velocity. The star is also known to possess spotted regions (see, for example, Frey et al. (1991)). Nevertheless, radial velocity variations have been reported as due to a planet (Hatzes et al. 2000). Table 16.11 summarizes the properties of this interesting system. Butler et al. (2006) also list only one planet, with period $2,500 \pm 350$ d, $T_{\text{peri}} = 8940 \pm 520$, $e = 0.25 \pm 0.23$, $\omega = 6^\circ$, $K = 18.6 \pm 2.9$ m/s, $M \sin i = 1.06 \pm 0.16 M_J$, and $a = 3.38 \pm 0.43$ au. Other planets have been proposed as well. Clumps of material peaking in brightness at ~ 18 arc s from the star (~ 60 au) and extending to 35 arc s from the star, have been interpreted as remnants of a disk, seen nearly pole-on (Greaves et al. 1998). Given that the age of ε Eri is estimated as 1 Gy, the disk cannot be the remainder of a protoplanetary disk, which would have disappeared long ago, but is interpreted as a *debris disk*, a dust-filled region of collisional debris. Other studies of the disk and attempts to observe planets through direct imaging are summarized by Marengo et al. (2006), who report three possible objects seen in their Spitzer Space Telescope data at $3.6 \mu\text{m}$, but no evidence of objects with the expected colors and fluxes appropriate for masses as low as $\sim 2 M_J$ within the disc, or $1 M_J$ outside it. Lower mass objects could not be the cause of resonant clumpings within the disk (a hypothesis advanced by Quillen and Thorndike 2002). Nevertheless, spot modeling of long series of observations made with the MOST satellite suggests an inclination of $30 \pm 3^\circ$ (Croll et al. 2006) of the rotation axis to the line of sight. This work also confirmed differential rotation from the tracking of two spot regions and, based on an assumed radius of $0.76 R_\odot$, produced an equatorial rotation period of $11^{\text{d}}20$ and an equatorial rotation rate of 3.42 km/s (from which the entry $v \sin i = 1.7$ km/s is derived).

From HST fine guidance sensor astrometric data, Benedict et al. (2006) found $i = 30.1 \pm 3.8$ and a mass of $1.55 \pm 0.24 M_J$ and, from Hipparcos data, Reffert and Quirrenbach (2011) derived $i = 23 \pm 5$ and a mass of $2.4 \pm 1.1 M_J$, values that agree within the errors. So, there is at least one real planet in the system, and it is either in or close to the plane of the disk.

16.4.8 The TrES-1 System

This is one of the transit systems discovered with a small, wide-field camera, and subsequently studied spectroscopically to determine the mass. The system is described by Alonso et al. (2004) and reanalyze by Torres et al. (2008), whose

Table 16.12 The TrES-1 planetary system

Planet	Period	T_{tr} (JD-2450000)	e	ω	$R (R_J)$	M/M_J	i	$a (\text{au})$
b	3 ^d 030065(8)	3186.806	0	–	1.07(2)	0.75(5)	90(1) [°]	0.0393(6)
Star	$v \sin i$	Sp. type	M/M_\odot	$\mathfrak{R}/\mathfrak{R}_\odot$	V	$r (\text{pc})$	[Fe/H]	T
a	10.359 m/s	K0 V	0.88(4)	0.82(1)	11.76(1)	152(7)	0.02(5)	5,230(50) K

Table 16.13 The WASP-17 planetary system

Planet	Period	T_{tr} (JD-2454500)	e	ω	$R (R_S)$	M/M_J	i	$a (\text{au})$
b	3 ^d 735438(7)	77.8581(3)	0.028(18)	-82.6^{+15}_{-3}	1.99(8)	0.49(3)	86.8(6)	0.0515(3)
Star	$v \sin i$ (km/s)	Sp. type	M/M_\odot	$\mathfrak{R}/\mathfrak{R}_\odot$	V	$r (\text{pc})$	[Fe/H]	T
a	10.1(9)	F6 V	1.31(3)	1.57(6)	11.6	400(6)	-0.19(9)	6,650(80) K

results are included in the properties of the TrES-1 system listed in Table 16.12. Sozzetti et al. (2004, 2006) discuss the host star. The density is $769^{+69}_{-64} \text{ kg m}^{-3}$, slightly more than Saturn's, but about twice that of HD 209548b. Charbonneau et al. (2005) succeeded in observing the secondary eclipse (occultation of TrES-1b by the host star, TrES-1a), enabling the flux with and without the planet to be measured in the infrared with the Spitzer Space Telescope. Assuming thermal equilibrium, they derived $T = 1,060 \pm 50 \text{ K}$ and a Bond Albedo, $A = 0.31 \pm 0.14$, the first such determination for an extra-solar planet.

16.4.9 The WASP-17 System

Discovered by Anderson et al. (2010), in a transit survey, and more recently analyzed with Monte Carlo Markov chain algorithm software by Anderson et al. (2011), WASP-17b (Table 16.13) was shown to have two distinctive properties. It has nearly twice the radius of Jupiter yet only half its mass, thus a density of $\sim 1/16$ of Jupiter, more precisely $0.0616 \pm 0.0080 \rho_J$ or $83(11) \text{ kg m}^{-3}$, the lowest density of any planet found to date. Moreover, it is revolving retrograde to its star's rotation. This was determined through the Rossiter-McLaughlin effect, discussed in Sect. 16.4.1. (Anderson et al. 2011; Bayliss et al. 2010). Triaud et al. (2010) confirmed the retrograde motion of WASP-17b and found two other planets in other systems with similar motions: WASP-2b and WASP-15b. They remark, however, that mismatches between the orbital plane and the stellar equator are common in hot Jupiters. The consensus is that an explanation for this misalignment involves interactions with either the star or another planet. Presumably the planet originated in a protostellar disk beyond the snow line and migrated

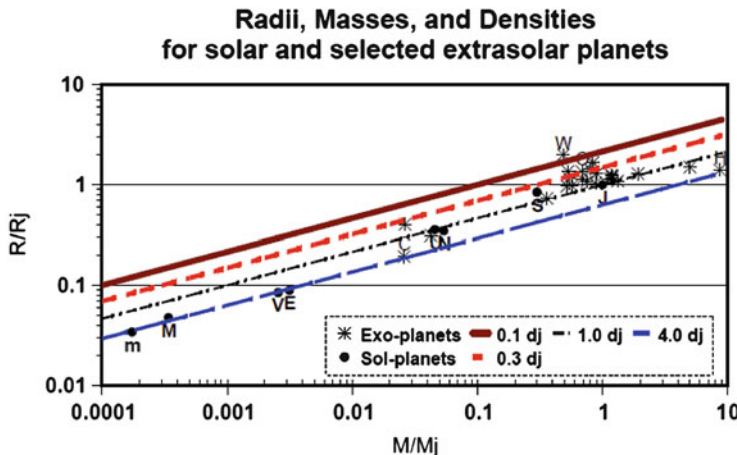


Fig. 16.8 The log radius vs. log mass relation for selected exoplanets, amid lines of constant density relative to Jupiter. The solar system's major planets are also shown for comparison (m = Mercury, M = Mars, etc.). Identifications: C = 55 Cnc e; H = HAT-P2b; O = HD 209458b; W = WASP-17b

inward, but, as it did so, it interacted tidally with its star and, possibly, with another planet, as yet undetected, resulting, via the Kozai mechanism and/or other resonance phenomena, in a varying-eccentricity, varying-inclination orbit. The circularization that sets in with eccentric orbits around stars can result in internal heating, which can cause the planet to bloat. The proximity to an earlier type star than is the case for most other hot Jupiters contributes to greater heating at similar stellar distances. However, current models cannot fully account for the huge bloating in WASP-17b.

Moreover, the low mass and large radius have another consequence. Because of an extremely low gravitational acceleration [$g = 2.448(42)$, cgs], the pressure scale height of the atmosphere is also the largest of any known planet. To take advantage of the long path lengths over which atmospheric constituents may be measured, transmission spectroscopy was carried out on this planet. Consequently, sodium was detected in WASP-17b's atmosphere by Wood et al. (2011) and confirmed by Zhou and Bayliss (2012). Observing with the Very Large Telescope (VLT), Wood et al. (2011) found a scale height of 2,090–2,570 km, compared with ~500 km for HD 209458b. They found a small amount of narrow Na absorption, stronger than that seen in HD 209458; in both planets, however, this was less than expected. They found an even stronger depletion in wider passbands, which they attributed both to clouds in the lower atmosphere, where the higher pressure affects the absorption in the wings of the sodium lines, and to a real depletion due to condensation of the sodium on the cool night side of the planet. Zhou and Bayliss (2012), observing with the Magellan 6.5-m telescope, confirmed the detection.

The equilibrium temperature of the planet for the rapid rotation case is $1,771 \pm 35$ K, and for the slow rotation case, $2,106 \pm 41$ K, assuming an albedo of 0.

Table 16.14 The Kepler 32 planetary system

Planet	Period	T _{tr}	depth	T _{dur}	a	R	M	T _{eq}		
K32	days	-2454900.	mmag	day	au	R _E	M _E	K		
Star	V _r	Kepler	V	SpT	T	R	M	[Fe/H]	P _{rot}	r
	km/s	magn	magn		K	R _○	M _○		days	pc
a	-32.5(5)	15.80	16.45	M1V	3793(80)	0.53(2)	0.54(2)	-0.01(9)	37.8(12)	303(14)
b	5.9012(1)	74.902(8)	1.79	0.088(5)	0.0519(8)	2.2(1)	3.4:	530		
c	8.7522(3)	77.378(4)	1.58	0.097(10)	0.067(1)	2.0(2)	3.8:	470		
(d)	22.7802(5)	88.211(11)	2.37	0.124(3)	0.128(2)	2.7(1)	...	340		
(e)	2.8960 (3)	66.61(3)	0.728	0.053(4)	0.0323(5)	1.5(1)	...	680		
(f)	0.74296(7)	65.54(4)	0.243	0.039(4)	0.0130(2)	0.81(5)	...	1100		

Figure 16.8 provides a graphical illustration involving only some of the known planets. The mass and radius and thus the mean density of extrasolar planets is seen to vary widely.

16.4.10 The Closely Packed Planetary System of Kepler 32

This system was discovered via transits observed during the Kepler mission and announced by Fabrycky et al. (2012). The data in Table 16.14 are from Swift et al. (2012). As for other tables, the uncertainties are indicated by parentheses following each quantity, in units of the last decimal place given. According to Swift et al.’s adopted values, Kepler 32a has a solar composition ([Fe/H] = −0.01(9), roughly half the Sun’s mass, 0.54(2) M_{\odot} and radius, 0.53(2) R_{\odot} , with a much cooler temperature, 3793^{+80}_{-74} K. These properties indicate it to be an M1 dwarf, with an estimated age of more than 2 Gy. As noted previously, both the size and mass of the host star are needed in order to determine the planetary sizes and masses. The rotation period of the star, from a spot modulation analysis by Fabrycky et al. (2012), is 37^d8.

Planets Kepler 32 *b* and *c* are considered confirmed; but the other planets were considered by Fabrycky et al. (2012) to be strong candidates only, retaining the KOI (for *Kepler Object of Interest*), namely KOI-952.03, .04, and .05. However, Swift et al. (2012) estimate the false positive probability (FPP) be less than 0.3 % for all of them. The depths of eclipse in milli-magnitudes were computed from the part-per-million values listed in Fabrycky et al. (2012) by the relation $\Delta m = 1.0857 \Delta P/P$.

All but one of the planets are slightly larger than the Earth, and that one (*f*) is slightly smaller. Their radii range from 0.8 R_{E} to 2.7 R_{E} , the masses are uncertain because no radial velocities have been obtained, and are based on transit timing variations (TTV) which place an upper limit on the masses of 6.6 and 8.4 M_{E} (Fabrycky et al. 2012). Swift et al. (2012) apply corrections to the TTV to obtain the masses listed in Table 16.14, but they must be considered highly uncertain. An empirical relation found for the solar system: $M \propto R^{\gamma}$, where $\gamma = 2.06$ has been applied in some

Table 16.15 The (unconfirmed) α Centauri B system

Planet	Period (days)	$T_{(RV\ max)}$ (JD-2450000)	e	ω	K (cm/s)	$M \sin i$ (M_E)	i (deg)	a (au)		
b	2.2357(8)	280.17(17)	0	–	51(4)	1.13(9)	–	0.04		
Star	$v \sin i$ (km/s)	V (magn)	$B-V$	Sp. type	T (K)	$\mathfrak{R}/\mathfrak{R}_\odot$	M/M_\odot	[Fe/H]	P_{rot} (days)	r (pc)
a	1.0(6)	1.33	0.88	K1 V	5,146(56)	0.844(5)	$0.934(6)+0.30(7)$		38.7	1.255(4)

analyses of Kepler systems, and from their estimated masses for planets b and c, Swift et al. (2012) note that γ is in the range 1.5–1.9. In any case, the planets are crammed into a tiny volume close to their star; all five planets would fall within a *third* of Mercury’s orbit if transported to the solar system. The proximity raises the questions of tidal effects on the planetary dynamics. Swift et al. (2012) assume initial spin periods of 10 h, a tidal dissipation factor, $Q = 100$, a rigidity factor of 3×10^{11} . Adopting a density profile such that the moment of inertia obeys the relation, $I = 0.5MR^2$, they find a tidal-locking timescale to be ~ 1 My or less, so the rotations of all the planets should be tidally locked. For $Q < 10^4$ they note that the eccentricities are likely to be damped for the inner planets. However Lithwick et al. (2012) find from TTV phase analyses that the eccentricities of planet b and c, although small (<0.01), are not zero, implying a high Q value for at least these two planets.

Swift et al. (2012) carried out dynamical analyses to assess the stability of this tightly packed system over an interval of 30 My (500 million revolutions of the outermost detected planet), and found no variations in eccentricity large enough to affect long-term stability. Planets b and c are just short of a 2:1 resonance and planet b is roughly in a 2:1 resonance with e.

Swift et al. (2012) propose that the system formed beyond the snow line for this system and migrated through interactions with the dusty disk when the system was young.

The planetary system of this M dwarf may be typical of the largest number of planetary systems in the galaxy, because this is the most common type of star (Bonfils et al. 2013).

16.4.11 Approaching Another Milestone in Extrasolar Planet Research: The Search for α Cen Bb

The announcement of evidence for a planet in orbit around a star of the closest star system to the Sun late in 2012 was exciting. The discovery announced by Dumusque et al. (2012) was noteworthy for the extremely small planetary-like signal detected in the radial velocity of the star, α Centauri B, one of the components of the triple star system α Centauri. The precision required to detect this signal is ~ 10 cm/s. If accurately assessed, this marks a new level of improvement in the RV technique, and is a credit to the HARPS instrument used on the 3.6-m telescope of ESO on La Silla in Chile. The careful evaluation of the critical sources of

instrumental, environmental, and stellar noise in the signal is, however, critical to the determination. We discuss this further, below. The details of both the star and the candidate planet and are given in Table 16.15. The stellar data are taken from the tabulations of Bruntt et al. (2010).

α centauri B is slightly smaller than the Sun, is cooler and thus redder than the Sun, and demonstrates spot activity. Ca II H and K emission is seen in the spectrum, and the H & K II activity index, $\log(R'_{HK})$ varied between -5.00 and -4.82 over the 4-year interval the object was observed. The modulation is seen in the light curve in the form of partial sinusoids with varying amplitude, as one would expect from numbers of transient spots distributed over the surface, and having cycle lengths across three seasons of 39.76, 37.8, and 36.71 days, respectively, the sort of behavior expected in a star with differential rotation and spot migration from higher to lower latitudes during the course of an activity cycle (see Milone and Wilson 2014, Sect. 4.5.5). The presence of a strong RV signal in a periodogram was assumed by Dumusque et al. (2012) to be the star's rotation period: 38.7 d. The stellar activity contributed on average a jitter of 1.51 m/s to the radial velocity measurements, which therefore dwarfed the signal; additional sources of noise that were accounted for were instrumental noise (0.7 m/s) stellar granulation (0.6 m/s), and stellar oscillations (\sim 4 cm/s over periods of up to 5 min). Finally, the light of α Cen A, which is only 21 arc s away from α Cen B, and is brighter ($V = -0.01$), has to be correctly subtracted or contamination can result, adding additional noise to the signal. In total, the amplitudes of the several noise contributions dwarf the cadenced purported planetary signal. It is therefore not too surprising that a reanalysis of the data by Hatzes (2013) demonstrated that the planetary signal is not fully robust and seems to depend on the noise filtering procedure. Consequently, additional observations are essential, not only to confirm the Dumusque et al. (2012) determination and, if confirmed, to seek additional planets. Sufficient data now exist to state that \sim 70 % of lower main sequence stars that have been found to have a planet have more than one. The present planet candidate has a minimum mass similar to Earth's, but the orbital inclination is unknown so the true mass could be considerably larger. Longer-period objects will take longer to find through RV monitoring, but direct imaging could be successful sooner, if, indeed, planets do exist around this star. But they are worth searching for, especially in the habitable zone of the star (\sim 0.7 au in this case).

This concludes our brief examination of some individual planetary systems. We now discuss briefly the origins of the planets and their more massive cousins, the brown dwarfs, and conclude with a still briefer discussion of the meaning of "habitable zones," around the Sun and other stars.

16.5 Origins of Brown Dwarfs and Planets

The nature of the planetary discoveries since 1995 has demonstrated the variety of planetary systems that can exist around stars, both near to us, and quite distant. As we have noted often, the masses of the great majority of the planets discovered

through radial velocity variations of their stars are underestimated; therefore at least a few of the objects in Table 16.2 are brown dwarfs. This is also the case for some of the objects discovered through direct imaging, if the 13 Jovian mass limit for planets turns out to be correct generally (for example, for all chemical compositions). Unless and until the existence of “free-floating” field planets can be verified, one must suppose that they are all born within a disk surrounding a proto-star, or, perhaps, a proto-brown dwarf, as we discussed in Chap. 15. Yet some of them are very far from the star or brown dwarf primaries. Were they captured during dynamical encounters in the stellar association in which they formed? Whatever the origin of those lonesome planets, work by Muench et al. (2001) points quite clearly to an origin for brown dwarfs similar to that of stars (and therefore different from that of planets), and this seems to be generally accepted.

The implications of planets at small distances from the star, yet possessing discernible eccentricities, raises interesting questions about how long such planets could have remained in such configurations. The results of much modeling in the multi-planet systems have shown that the dynamic interactions among planets are such as to render the orbits non-Keplerian and in some cases chaotic. The result is variation in orbital elements. The likelihood is that planets migrate from their initial birthplaces in response to the viscous environment from which they formed, but that some circumstances, such as fortuitous locations of low viscosity “dead zones” (Matsumura and Pudritz 2003; Matsumura et al. 2007) may enable some of them to escape tumbling into the star. Outward migrations of some planets, induced by perturbations of large gas giants, may also occur, as has been suggested for Uranus and Neptune. One of the more interesting extra-solar cases is that of HD 188753Ab (cf. Portegies Zwart & McMillan 2005). The star is in a triple system, with a short-period spectroscopic binary. The planet orbits the single star, but it is located only at 0.046 au from it. Clearly, hierarchical systems exist. Planets have also been found around M dwarfs and around K giant stars. Moreover, it is quite likely that planets exist around hotter non-solar type stars, such as Vega; at least, the hypothesis has been put forward that clumpy features observed in the infrared are due to the trapping of disk material in mean motion resonances of a Neptune-mass planet in an orbit 65 au from the star (Marsh et al. 2006).

Brown dwarfs, on the other hand, seem to be found less frequently in the company of normal stars (see Fig. 16.1). Yet, the evidence seems to suggest that they are born like stars, from a fragmenting molecular cloud. If so, why is there a “brown dwarf desert?” In fact, there seem to be “brown dwarf deserts”: there is a paucity also of wide substellar binaries (Allen et al. 2007). The “deserts” can be understood if brown dwarfs do form in clusters, as stars do. Preferential ejections (with probability $P \propto M^{-3}$ according to Anosova 1986) of low-mass objects occur through collisions. Hence, solitary substellar objects should be the rule and pairs of them exceptions. Such a “dynamical bias” was found by Clarke (1996) in simulations, and later used by Reipurth and Clarke (2001) to support a hypothesis that brown dwarfs result through dynamical disruption by collisions of possibly late-forming protostellar embryos before they could accrete sufficient mass to become stars, and so are “ejected stellar embryos.” Consequently, evidence for disk

truncation of such embryos has been sought. Scholz et al. (2006) found, however, that 25 % of brown dwarfs in Taurus have disks that extend to distances greater than 10 au. Moreover, interrupted systems might be expected to have lower incidence of binarity, especially of widely separated systems. However, such binaries are being discovered in number, and this would seem to pose a challenge to the ejection hypothesis (Ahmic et al. 2007).

The origins of at least some types of planets are also somewhat uncertain at present. A birth within a disk around a proto-star appears very likely, but is this due to core-accretion, where accretion through collisions results in objects sufficiently massive to attract large amounts of gas, or is it due to the onset of gravitational instabilities (where the thermal gas pressure is unable to prevent the collapse of material into gravitationally viable clumps), as suggested by Boss (1997)? The latter mechanism may occur in the cooler, outer portions of the disk, and over short time scales, \sim 1,000 years or less, while core-accretion may take \sim 8 My to form a Jupiter-mass planet.

Because the lifetime of proto-planetary disks is believed to be less than \sim 10 My at best, and may be less than a million years in high-mass star forming regions, the rapid time scale promised by gravitational instability seems to be required in at least some systems. Further work by Boss (2002, for example) suggests that the clumps formed in realistic simulations satisfy Jeans mass and length criteria (they are massive enough so that gravity triumphs over thermal dissipation), and that at least some of them can survive to continue to accrete material and grow as the disk dissipates. Core-accretion, which is favored by some observations (Fischer and Valenti 2005) and by some theoretical work (Rafikov 2004, 2005), may occur under certain circumstances, quickly enough (Thommes et al. 2007). If the core of a star is formed in cold conditions—sufficiently cold that volatile gases can condense—at the “snow-line,” $2 < a < 4$ au in the solar system—the addition of ice to the dust will accelerate accretion. As the mass continues to grow, at some critical core mass, it attracts the still volatile gas (namely, H and He) if it is as massive as Jupiter or Saturn, until the disk dissipates (Pollack et al. 1996). The rate of accretion of planetesimals depends inversely on the core mass, with ice giants taking \sim 8 \times longer than Jupiter. As a result there is less time for gas accretion, resulting in a less massive giant. In core accretion, hot super-Earths are a prediction, cold super-Earths are not—yet lensing is finding both types. Disk instability is fast, and, if it exists, can produce the cold super-Earths as well as cold Neptunes and Jupiters. In any case, if a gas giant is in an external orbit, a super-Earth may be forced to migrate to a region where it lacks material to grow further. Then it appears that terrestrial planets and objects as large as Neptune can be formed through accretion. Future studies of disks and disk structures may clarify if the instability does occur. At the moment it seems not far-fetched to suggest that either mechanism might operate, given optimal circumstances.

Modeling of the evolution of brown dwarfs (and planetary objects—see Fig. 16.8) suggests that they are initially bright, and dim as they cool with age. Similarly, their rotational velocities initially speed up (presumably corresponding to gravitational contraction, in conservation of angular momentum), and then slow

down with age. Planets must follow a similar path, although presumably with no internal nuclear energy source.

The detection and study of the orbits of extra-solar planets has led to a closer look at the stability of the solar system. The evidence for migration of Saturn, Uranus and Neptune outward, where they perturbed some of the Edgeworth-Kuiper Belt objects into a scattered population, and the inward migration of Jupiter seems very strong (see Sect. 15.10). We appear to be living at the right time and place to be able to contemplate such things, because the simulations suggest that the solar system may be only marginally dynamically stable. The probability is not high, but the interactions between Mars and the Earth and between Mercury, Venus, and Jupiter, can cause increases in the eccentricities. In some simulations, and, with just slight changes in initial positions, Mercury is ejected; in others, Mars is ejected, and in still others, collisions occur—signs of chaotic behavior. If a free-floating planet should encounter the solar system, major perturbations would ensue. Of course, as far as we know, this has not happened in the past 6 eons.

This is where the research clues have led us thus far from the list of solar system facts in the first chapter of the first volume. But grand mysteries yet remain to be unraveled. Is there life elsewhere in the solar system or beyond it? One of the closest Earth analogs detected thus far may be Gl 581c with $m \sin i = 5.0 M_{\oplus}$ at 0.073 au, on the hot end of the star's *habitable zone* (Udry et al. 2007). There are programs to seek terrestrial planets within their stars' habitable zones, and then to look for the signatures of biological activity. The next generation of space missions may provide the answers. For now, we comment on "habitable zones" as follows.

The habitable zone for any star is the range of distances from the star within which life may exist on a planet or large moon. We include here the usual (but perhaps not necessary!)³ restriction to carbon-based life forms that require liquid water (i.e., similar to life on the Earth), and also to life on the planetary surface, including surface oceans. The latter restriction excludes some regions of a planetary system where life may in fact be possible, such as subsurface oceans on Europa, Ganymede, Callisto and Enceladus, or within the cryovolcanoes of Titan, all dependent on non-solar sources of heat. For example, phyllosilicates have been detected on the surface of Europa, and are interpreted as having been deposited by a cometary impact (Shirley et al. 2013). Small solar system bodies with phyllosilicates often also contain organic compounds. Observed indications of mixing between the surface and the subsurface ocean on Europa then suggest a pathway by which organics could have been delivered to the ocean.

We locate the inner and outer boundaries of the habitable zone at those distances for which the mean equilibrium temperature is, respectively, 373 and 273 K, the boiling and freezing points of water. As defined in Sect. 10.1, the mean equilibrium temperature of a planet is the blackbody temperature the planet must have (in the

³ Lunine (2005, p. 88) makes a strong case that because of its multivalent nature, carbon can be involved in many more structures and varieties of structures than other relevant elements that it is far more suitable as a basis for biochemistry than, say, silicon.

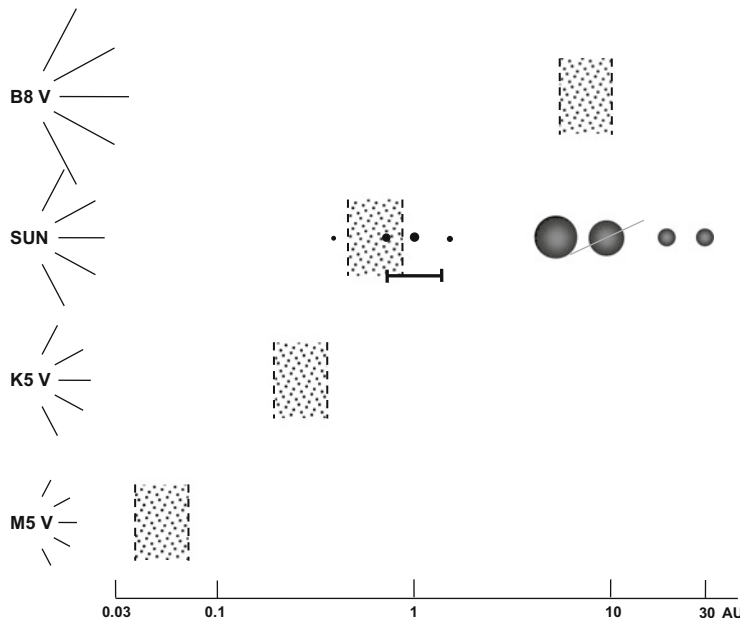


Fig. 16.9 Habitable zones around the Sun (spectral type G2V) and three other main sequence stars: B8V, K5V and M5V. The inner and outer edges of the habitable zones were calculated for airless, quickly-rotating planets of mean equilibrium temperatures 100 °C at the inner edge of the zone and 0 °C at the outer edge, and an assumed Bond (bolometric) albedo of 0.306 for a “typical” terrestrial planet (the Earth). These criteria place the Earth outside the Sun’s habitable zone, because the equilibrium temperature for a planet at 1 au is ~254 K. However, the mean temperature of the Earth is ~288 K, at least in part because of the thermal effects of the atmosphere. With such an atmosphere, the habitable zone is located further from the Sun, as indicated by the bracketed line. Similar effects could be expected of exo-planetary systems also, but the amount of shift for other planets depends critically on the abundance of greenhouse gases (e.g., methane, carbon dioxide, and water vapor) in the planets’ atmospheres

absence of internal sources of heat) in order to radiate the same total energy per second that it receives from the star. As such, it should be identical to the mean bolometric temperature as observed from space, and is the same (when the mean is taken over the entire planet) for any planet of a given albedo placed at that distance from the star.

The rapid-rotator case discussed in Milone and Wilson (2014), Sects. 6.3, and 10.1 in the present volume gives this temperature directly.

Figure 16.9 shows the habitable zones for a planetary albedo equal to that of the Earth, for four stars, including the Sun, characterized by the following effective temperatures and radii, according to data tabulated in Cox (2000): for B8V, 11,400 K, $3.0 R_{\odot}$; K5V, 4,410 K, $0.72 R_{\odot}$; M5V, 3,170 K, $0.27 R_{\odot}$. For the Sun, we took $T_{\text{eff}} = 5,770$ K and $R_{\odot} = 6.955 \times 10^8$ m. The radial distance to the habitable zone increases as the square root of both the stellar luminosity and the absorptivity, $1-A$ (where A is the albedo) by Milone and Wilson (2014) Eq. 6.31 or

the unnumbered equation below (10.6), if we replace the solar luminosity by the stellar luminosity. From Milone and Wilson (2014) Example 6.1, the Earth's equilibrium temperature is 254 K, which, as Fig. 16.8 shows, places the Earth outside the Sun's habitable zone by the definitions used here. However, the existence of life does not depend (directly) on the mean bolometric temperature, but on the actual surface temperature of the planet, and the latter can be strongly influenced by atmospheric and oceanic circulations and the greenhouse effect. We retain the definitions used here because the latter effects can vary markedly from planet to planet (note Venus!!) and are difficult to predict. In Fig. 16.8, the bracketed line indicates where the habitable zone would be located if it were centered on the Earth, where the mean surface temperature is 288 K instead of 323 K. One must be cautious in interpreting the boundaries of the zone in this case, because if the Earth were arbitrarily moved to a location elsewhere within this zone, particularly near the boundaries, atmospheric and oceanic feedback mechanisms (e.g., runaway greenhouse effect) might in fact result in the Earth becoming uninhabitable. Similarly, it may be an inconvenient truth that altering the composition of the Earth's atmosphere is equivalent, in its effect on Earth's future habitability, to hypothetically moving the Earth's orbit.

Potential niches for life, in the solar system (caves of Mars, interior of Titan, subsurface oceans of Europa and Enceladus to name only a few), or beyond, may prove to be viable, but for all practical purposes, it is prudent to consider the Earth the only habitable world and to treat it accordingly.

Challenges

- [16.1] Plot the eccentricities of the objects in Table 16.2 vs. their semi-major axes. What can you conclude about the process of orbital circularization for these systems?
- [16.2] Now perform the same test for the objects in Table 16.3. What can you conclude about the process of orbit circularization for *these* systems? Can you account for the differences between the plots?
- [16.3] Examine the spectral types associated with each star in Table 16.1 with one or more planets. Can you draw any conclusions about the type(s) of star likely to have planets? Justify your response.
- [16.4] Compute the Roche limit and the synchronous orbit radius for the three closest planets in Table 16.2. You may need to look up data and make assumptions to do the computation, so name all sources and state all assumptions. Are these planets stable against tidal disruption at present or in the foreseeable future?
- [16.5] Compute the equilibrium temperature of HD 209458b and calculate the expected pressure scale height of its upper atmosphere; compare these values to those of Jupiter. Again, you may need to look up data and make

- assumptions to do the computation, so name all sources and state all assumptions.
- [16.6] For the case of HD 209458b, compute the true and Table 16.2 values of $M \sin i$ and a (see Sects. 16.2.1 and 16.4).
 - [16.7] From the methods you have learned in the course of reading Solar System Astrophysics, and the data given in this chapter, calculate the brightness of the proposed planet in the alpha Centauri B system in, say, V magnitude, and suggest how it could be imaged.
 - [16.8] Compute the “Hill radius”, the distance from a planet beyond which a satellite would be dominated by the star, for the “hot Jupiter” in the HD 209458 system. Compare the Hill radius with the Roche limit of the planet, to determine if such a planet could retain a moon.

References

- Ahmic, M., Jayawardhana, R., Brandeker, A., Scholz, A., van Kerkwijk, M.H., Delgade-Donati, E., Froebrich, D.: Multiplicity among young brown dwarfs and very low mass stars. *Astrophys. J.* **671**, 2074–2081 (2007)
- Allen, P.R., Koerner, D.W., McElwain, M.W., Cruz, K.L., Reid, I.N.: A new brown dwarf desert? A scarcity of wide ultracool binaries. *Astron. J.* **133**, 971–978 (2007)
- Alves de Oliveira, C., Moraux, E., Bouvier, J., Bouy, H.: Spectroscopy of new brown dwarf members of ρ Ophiuchi and an updated initial mass function. *Astron. Astrophys.* **531**, 1 (2012). arXiv:1201.1912v2
- Alonso, R., Brown, T.M., Torres, G., Latham, D.W., Sozzetti, A., Mandushev, G., Belmonte, J.A., Charbonneau, D., Deeg, H.J., Dunham, E.W., O’Donovan, F.T., Stefanik, R.P.: TrES-1: the transiting planet of a bright K0 V star. *Astrophys. J.* **613**, L153–L156 (2004)
- Anderson, D.R., Hellier, C., Gillon, M., Triaud, A.H.M.J., Smalley, B., Hebb, L., Collier Cameron, A., Maxted, P.F.L., Queloz, D., West, R.G., Bentley, S.J., Enoch, B., Horne, K., Lister, T.A., Mayor, M., Parley, N.R., Pepe, F., Pollacco, D., Ségransan, D., Udry, S., Wilson, D.M.: WASP-17b: an ultra-low density planet in a probable retrograde orbit. *Astrophys. J.* **709**, 159–167 (2010)
- Anderson, D.R., Smith, A.M.S., Lanotte, A., Barman, T.S., Collier Cameron, A., Campo, C.J., Gillon, M., Harrington, J., Hellier, C., Maxted, P.F.L., Queloz, D., Triaud, A.H.M.J., Wheatley, P.J.: Thermal emission at 4.5 and 8 μm of WASP-17b, an extremely large planet in a slightly eccentric orbit. *Mon. Not. R. Astron. Soc.* **416**, 2108–2122 (2011)
- Anosova, J.P.: Dynamical evolution of triple systems. *Astrophys. Space Sci.* **124**, 217–241 (1986)
- Bailes, M., Bates, S.D., Bhalerao, V., Bhat, N.D., Burgay, M., Burke-Spolaor, S., D’Amico, N., Johnston, S., Leith, M.J., Kramer, M., Kulkarni, S.R., Levin, L., Lyne, A.G., Milia, S., Possenti, A., Spitler, L., Stappers, B., van Straten, W.: Transformation of a star into a planet in a millisecond pulsar binary. *Science* **333**, 1717–1721 (2011)
- Bakos, G.Á., Knutson, H., Pont, F., Moutou, C., Charbonneau, D., Shporer, A., Bouchy, F., Everett, M., Hergenrother, C., Latham, D.W., Mayor, M., Mazeh, T., Noyes, R.W., Queloz, D., Pál, A., Udry, S.: Refined parameters of the planet orbiting HD 189733. *Astrophys. J.* **650**, 1160–1171 (2006)
- Ballester, G.E., Sing, D.K., Herbert, F.: The signature of hot hydrogen in the atmosphere of the extrasolar planet HD 209458. *Nature* **445**, 511–514 (2007)
- Baluev, R.V.: Orbital structure of the GJ876 extrasolar planetary system based on the latest Keck and HARPS radial velocity data. *Celest. Mech. Dyn. Astron.* **111**, 235–266 (2011)

- Baraffe, I., Chabrier, G., Allard, F., Hauschildt, P.H.: Evolutionary models for low-mass stars and brown dwarfs: uncertainties and limits at very young ages. *Astron. Astrophys.* **382**, 563–572 (2002)
- Baraffe, I., Selsis, F., Chabrier, G., Barman, T.S., Allard, F., Hauschildt, P.H., Lammer, H.: The effect of evaporation on the evolution of close-in giant planets. *Astron. Astrophys.* **419**, L13–L16 (2004)
- Barclay, T., Rowe, J.F., Lissauer, J.J., Huber, D., Fressin, F., Howell, S.B., Bryson, S.T., Chaplin, W.J., et al.: A sub-mercury-sized exoplanet. *Nature* **494**, 452–454 (2013)
- Basri, G.: Observations of brown dwarfs. In: Burbidge, G., Sandage, A., Shu, F.H. (eds.) *Annual Review of Astronomy and Astrophysics*, vol. 38, pp. 485–519. Annual Reviews Inc., Palo Alto, CA (2000)
- Basri, G., Brown, M.E.: Planetesimals to brown dwarfs: what is a planet? *Annu. Rev. Earth Planet. Sci.* **34**, 193–216 (2006)
- Bayliss, D.D.R., Winn, J.N., Mardling, R.A., Sackett, P.D.: Confirmation of a retrograde orbit for exoplanet WASP-17b. *Astrophys. J.* **722**, L224 (2010)
- Beaulieu, J.-P., et al.: Discovery of a cool planet of 5.5 Earth masses through gravitational microlensing. *Nature* **439**, 437–440 (2006)
- Béjar, V.J.S., Zapatero Osorio, M.R., Pérez-Garrido, A., Álvarez, C., Martín, E.L., Rebolo, R., Villó-Pérez, I., Díaz-Sánchez, A.: Discovery of a wide companion near the deuterium-burning mass limit in the Upper Scorpius association. *Astrophys. J.* **673**, L185–L189 (2008)
- Benedict, G.F., McArthur, B.E., Forveille, T., Delfosse, X., Nelan, E., Butler, R.P., Spiesman, W., Marcy, G., Goldman, B., Perrier, C., Jeffreys, W.H., Mayor, M.: A mass for the extrasolar planet Gliese 876b determined from *Hubble Space Telescope* fine guidance sensor 3 astrometry and high-precision radial velocities. *Astrophys. J.* **581**, L115–L118 (2002)
- Benedict, G.F., Barbara E. McArthur, B.E., Gatewood, G., Nelan, E., William, D., Cochran, W.D., Hatzes, A., Endl, M., Wittenmyer, R., Sallie, L., Baliunas, S.L., Gordon, A. H., Walker, G.A.H., Yang, S., Kurster, M., Els, S., Paulson, D.B.: The extrasolar planet ϵ Eridani b: orbit and mass. *Astron. J.* **132**, 2206–2218 (2006)
- Beuermann, K., Dreizler, S., Hessman, F.V., Deller, J.: The quest for companions to post-common envelope binaries III. A reexamination of HW Virginis. *Astron. Astrophys.* **543**, A138 (2012). arXiv:1206.3080v1
- Bihain, G., Rebolo, R., Zapatero-Osorio, M.R., Béjar, V.J.S., Caballero, J.A.: Near-infrared low-resolution spectroscopy of Pleiades L-type brown dwarfs. *Astron. Astrophys.* **519**, 543–572 (2010)
- Biller, B.A., Kasper, M., Close, L.M., Brandner, W., Kellner, S.: Discovery of a brown dwarf very close to the sun: a methane-rich brown dwarf companion to the low-mass star SCR 1845-6357. *Astrophys. J.* **641**, L141–L144 (2006)
- Bond, I., et al.: OGLE 2003 BLG-235/MOA 2003-BLG-53: a planetary microlensing event. *Astrophys. J.* **606**, L155–L158 (2004)
- Bonfils, X., Delfosse, X., Udry, S., Forveille, T., Mayor, M., Perrier, C., Bouchy, F., Gillon, M., Lovis, C., Pepe, F., Queloz, D., Santos, N.C., Segransan, D., Betaux, J.-L.: The HARPS search for southern extra-solar planets. XXXI. The M-dwarf sample. *Astron. Astrophys.* **549**, A109 (2013)
- Bonnefoy, M., Chauvin, G., Rojo, P., Allard, F., Lagrange, A.-M., Homeier, D., Dumas, C., Beuzit, J.-L.: Near-infrared integral-field spectra of the planet/brown dwarf companion AB Pictoris b. *Astron. Astrophys.* **512**, 398–404 (2010)
- Borucki, W.J., Koch, D., et al.: Kepler planet-detection mission: introduction and first results. *Science* **327**, 977–980 (2010)
- Boss, A.P.: Giant planet formation by gravitational instability. *Science* **276**, 1836–1839 (1997)
- Boss, A.P.: Evolution of the solar nebula. V. Disk instabilities with varied thermodynamics. *Astrophys. J.* **576**, 462–472 (2002)
- Bouchy, F., Udry, S., Mayor, M., Moutou, C., Pont, F., Iribarne, N., da Silva, R., Illovaisky, S., Queloz, D., Santos, N.C., Segransan, D., Zucker, S.: ELODIE metallicity-biased search for

- transiting hot Jupiters: II. A very hot Jupiter transiting the bright star HD 189733. *Astron. Astrophys.* **444**, L15–L19 (2005)
- Bourrier, V., Lecavelier des Etangs, A., Dupuy, H., Ehrenreich, D., Vidal-Madjar, S., Hébrard, G., Ballester, G.E., Desert, J.M., Ferlet, R., Sing, D.K., Wheatley, P.J.: Atmospheric escape from HD 189733b in HI Lyman- α detailed analysis of HST/STIS September 2011 observations. *Astron. Astrophys.* **551**, A63 (2013)
- Bowler, B.P., Liu, M.C., Dupuy, T.J.: SDSS J141624.08 + 134826.7: a nearby blue L dwarf from the Sloan Digital Sky Survey. *Astrophys. J.* **710**, 45–50 (2010)
- Broeg, C., Schmidt, T.O.B., Guenther, E., Bedalov, A., Neuhäuser, R., Walter, F.M.: Rotational period of GQ lupi. *Astron. Astrophys.* **468**, 1039–1044 (2007)
- Brown, T.M., Charbonneau, D., Gilliland, R.L., Noyes, R.W., Burrows, A.: Hubble Space Telescope time-series photometry of the transiting planet of HD 209458. *Astrophys. J.* **552**, 699–709 (2001)
- Bruntt, H., Bedding, T.R., Quirio, P.-O., Lo Curto, G., Carrier, F., Smalley, B., Dall, T.H., Arentoft, T., Bazot, M., Butler, R.P.: Accurate fundamental parameters for 23 bright solar-type stars. *Mon. Not. R. Astron. Soc.* **405**, 1907–1923 (2010)
- Burgasser, A.J., Kirkpatrick, J.D., Lowrance, P.J.: Multiplicity among widely separated brown dwarf companions to nearby stars: Gliese 337D. *Astron. J.* **129**, 2849–2855 (2005)
- Burgasser, A.J., Kirkpatrick, J.D., Brown, M.E., Reid, I.N., Burrows, A., Liebert, J., Matthews, K., Gizis, J.E., Dahn, C.C., Monet, D.G., Cutri, R.M., Skrutskie, M.F.: The spectra of T dwarfs. I. Near-infrared data and spectral classification. *Astrophys. J.* **564**, 421–451 (2002)
- Burgasser, A.J., Kirkpatrick, J.D., Cruz, K.L., Reid, I.N., Leggett, S.K., Liebert, J., Burrows, A., Brown, M.E.: Hubble Space Telescope NICMOS observations of T dwarfs: brown dwarf multiplicity and new probes of the L/T transition. *Astrophys. J.* **166**, 585–612 (2006)
- Burgasser, A.J., Simcoe, R.A., Bochanski, J.J., Saumon, D., Mamajek, E.E., Cushing, M.C., Marley, M.S., McMurtry, C., Pipher, J.L., Forrest, W.J.: Clouds in the coldest brown dwarfs: FIRE spectroscopy of Ross 458C. *Astrophys. J.* **725**, 1405–1420 (2010)
- Burke, C.J., et al.: XO-2b: transiting hot Jupiter in a metal-rich common proper motion binary. *Astrophys. J.* **671**(2), 2115–2128 (2007)
- Burleigh, M.R., Marsh, T.R., Gänsicke, B.T., Goad, M.R., Dhillon, V.S., Littlefair, S.P., Wells, M., Bannister, N.P., Hurkett, C.P., Martindale, A., Dobbie, P.D., Casewell, S.L., Baker, D.E. A., Duke, J., Farihi, J., Irwin, M.J., Hewett, P.C., Roche, P., Lewis, F.: The nature of the close magnetic white dwarf + probable brown dwarf binary SDSS J121209.31 + 013627.7. *Mon. Not. R. Astron. Soc.* **373**, 1416–1422 (2006)
- Burningham, B., Pinfield, D.J., Leggett, S.K., Tinney, C.G., Liu, M.C., Homeier, D., West, A.A., Day-Jones, A., Huelamo, N., Dupuy, T.J., Zhang, Z., Murray, D.N., Lodieu, N., Barrado y Navascués, D., Folkes, S., Galvez-Ortiz, M.C., Jones, H.R.A., Lucas, P.W., Morales Calderon, M., Tamura, M.: The discovery of an M4 + T8.5 binary system. *Mon. Not. R. Astron. Soc.* **395**, 1237–1248 (2009)
- Butler, R.P., Marcy, G.W., Williams, E., McCarthy, C., Dosanjh, P., Vogt, S.S.: Attaining Doppler precision of 3 ms $^{-1}$. *Publ. Astron. Soc. Pac.* **108**, 500–509 (1996)
- Butler, R.P., Wright, J.T., Marcy, G.W., Fischer, D.A., Vogt, S.S., Tinney, C.G., Jones, H.R.A., Carter, B.D., Johnson, J.A., McCarthy, C., Penny, A.J.: Catalog of nearby exoplanets. *Astrophys. J.* **646**, 505–522 (2006)
- Campbell, B., Walker, G.A.H.: Precision radial velocities with an absorption cell. *Publ. Astron. Soc. Pac.* **91**, 540–545 (1979)
- Campbell, B., Walker, G., Yang, S.: A search for substellar companions to solar-type stars. *Astrophys. J.* **331**, 902–921 (1988)
- Chabrier, G., Baraffe, I.: Theory of low-mass stars and substellar objects. In: Burbidge, G., Sandage, A., Shu, F.H. (eds.) Annual Review of Astronomy and Astrophysics, vol. 38, pp. 337–377. Annual Review Inc., Palo Alto, CA (2000)
- Chabrier, G., Baraffe, I., Allard, F., Hauschildt, P.: Evolutionary models for very low-mass stars and brown dwarfs with dusty atmospheres. *Astrophys. J.* **542**, 464–472 (2000)

- Charbonneau, D., Brown, T., Noyes, R., Gilliland, R.: Detection of an extrasolar planet atmosphere. *Astrophys. J.* **568**, 377–384 (2002)
- Charbonneau, D., Brown, T., Latham, D., Mayor, M., Mazeh, T.: Detection of planetary transits across a sun-like star. *Astrophys. J.* **529**, L45–L48 (2000)
- Charbonneau, D., Allen, L.E., Megeath, S.T., Torres, G., Alonso, R., Brown, T.M., Gilliland, R.L., Latham, D.W., Mandushev, G., O'Donovan, F.T., Sozzetti, A.: Detection of thermal emission from an extrasolar planet. *Astrophys. J.* **626**, 523–529 (2005)
- Chauvin, G., Lagrange, A.M., Dumas, C., Zuckerman, B., Mouillet, D., Song, I., Beuzit, J.-L., Lowrance, P.: A giant planet candidate near a young brown dwarf: direct VLT/NACO observations using IR wavefront sensing. *Astron. Astrophys.* **425**, L29–L32 (2004)
- Chauvin, G., Lagrange, A.M., Zuckerman, B., Dumas, C., Mouillet, D., Song, I., Beuzit, J.-L., Lowrance, P., Bessell, M.S.: A companion to AB Pic at the planet/brown dwarf boundary. *Astron. Astrophys.* **438**, L29–L32 (2005)
- Choi, J., McCarthy, C., Marcy, G.M., Howard, A.W., Fischer, D.A., Johnson, J.A., Isaacson, H., Wright, J.T.: Precise Doppler monitoring of Barnard's star. *Astrophys. J.* **764**, 131 (12pp) (2013)
- Clarke, C.J.: The formation of binaries in small N clusters. In: Milone, E.F., Mermilliod, J.-C. (eds.) *The Origin, Evolution, and Destinies of Binary Stars in Clusters*. ASP Conference Series, vol. 90, pp. 242–251. ASP, San Francisco, CA (1996)
- Correia, A.C.M., Udry, S., Mayor, M., Laskar, J., Naef, D., Pepe, F., Queloz, D., Santos, N.C.: The CORALIE survey for southern extra-solar planets. XIII. A pair of planets around HD 202206 or a circumbinary planet? *Astron. Astrophys.* **440**, 751–758 (2005)
- Cossburn, M.R., Hodgkin, S.T., Jameson, R.F., Pinfield, D.J.: Discovery of the lowest-mass brown dwarf in the Pleiades. *Mon. Not. R. Astron. Soc.* **288**, L23–L27 (1997)
- Cox, A.N. (ed.): *Allen's Astrophysical Quantities*, 4th edn. Springer, New York (2000)
- Croll, B., Walker, G.A.H., Kuschnig, R., Matthews, J.M., Rowe, J.F., Walker, A., Rucinski, S.M., Hatzes, A.P., Cochran, W.D., Robb, R.M., Guenther, D.B., Moffat, A.F.J., Sasselov, D., Weiss, W.W.: Differential rotation of ϵ Eridani detected by MOST. *Astrophys. J.* **648**, 607–613 (2006)
- Cushing, M.C., Kirkpatrick, J.D., Gelino, C.R., Griffith, R.L., Skrutskie, M.F., Mainzer, A., Marsh, K.A., Beichman, C.A., Burgasser, A.J., Prato, L.A., Simcoe, R.A., Marley, M.S., Saumon, D., Freedman, R.S., Eisenhardt, P.R., Wright, E.L.: The discovery of Y dwarfs using data from the *Wide-Field Infrared Survey Explorer (WISE)*. *Astrophys. J.* **743**, 50 (2011) (11pp)
- Dawson, R.I., Fabrycky, D.C.: Radial velocity planets de-aliased: a new, short period for super-Earth 55 Cnc e. *Astrophys. J.* **722**, 937–953 (2010)
- Day-Jones, A.C., Pinfield, D.J., Ruiz, M.T., Burningham, B., Gallardo, J., Gianninas, A., Napiwotzki, R., Jenkins, J.S., Zhang, Z.H., Murray, D.N., Catalán, S., Gomes, J.: Discovery of a T dwarf + white dwarf binary system. *Mon. Not. R. Astron. Soc.* **410**, 705–716 (2011)
- Deeg, H.J., Doyle, L.R., Kozhevnikov, V.P., Blue, J.E., Martín, E.L., Schneider, J.: A search for Jovian-mass planets around CM Draconis using eclipse minima timing. *Astron. Astrophys.* **358**, L5–L8 (2000)
- Deleuil, M., Deeg, H.J., Alonso, R., Bouchy, F., Rouan, D., Auvergne, M., Baglin, A., Aigrain, S., Almenara, J.M., Barbieri, M., Barge, P., Bruntt, H., Bordé, P., Collier Cameron, A., Csizmadia, S., De la Reza, R., Dvorak, R., Erikson, A., Fridlund, M., Gandolfi, D., Gillon, M., Guenther, E., Guillot, T., Hatzes, A., Hébrard, G., Jorda, L., Lammer, H., Léger, A., Llebaria, A., Loeillet, B., Mayor, M., Loutou, C., Ollivier, M., Pätzold, M., Pont, F., Queloz, D., Rauer, H., Schneider, J., Shporer, A., Zucker, S.: Transiting exoplanets from CoRoT space mission VI. CoRoT-Exo-3b: the first secure inhabitant of the brown-dwarf desert. *Astron. Astrophys.* **491**, 889–897 (2008)
- Deming, D., Seager, S., Richardson, L.J., Harrington, J.: Infrared radiation from an extrasolar planet. *Nature* **434**, 740–742 (2005)
- Deming, D., Harrington, J., Seager, S., Richardson, L.J.: Strong infrared emission from the extrasolar planet HD 189733. *Astrophys. J.* **644**, 560–564 (2006)

- Demory, B.-O., Gillon, M., Deming, D., Valencia, D., Seager, S., Benneke, B., Lovis, C., Harrington, J., Stevenson, K.B., Mayor, M., Pepe, F., Queloz, D., Ségransan, D., Udry, S.: Detection of a transit of the super-Earth 55 Cancri with warm Spitzer. *Astron. Astrophys.* **533**, (7pp) (2011)
- Demory, B.O., Gillon, M., Seager, S., Benneke, E., Deming, D., Jackson, B.: Detection of thermal emission from a super-earth. *Astrophys. J.* **751**, L28–L34 (2012)
- Díaz, R.F., Santerne, A., Sahlmann, J., Hébrard, G., Eggenberger, A., Santos, N.C., Moutou, C., Arnold, L., Boisse, I., Bonfils, X., Bouchy, F., Delfosse, X., Desort, M., Ehrenreich, D., Forveille, T., Lagrange, A.-M., Lovis, C., Pepe, F., Perrier, C., Queloz, D., Ségransan, D., Udry, S., Vidal-Madjar, A.: The SOPHIE search for northern extrasolar planets IV. Massive companions in the planet-brown dwarf boundary. *Astron. Astrophys.* **538**, A113 (2012)
- Dieterich, S.B., Henry, T.J., Golimowski, D.A., Krist, J.E., Tanner, A.M.: The solar neighborhood XXVII: the multiplicity fraction of nearby stars from 5 to 70 AU and the brown dwarf desert around M dwarfs. *Astron. J.* **144**, 64–82 (2012)
- Dumusque, X., Pepe, F., Lovis, C., Ségransan, D., Sahlmann, J., Benz, W., Bouchy, F., Mayor, M., Queloz, D., Santos, N., Udry, S.: An earth-mass planet orbiting α Centauri B. *Nature* **491**, 207–211 (2012)
- Ehrenreich, D., Lecavelier des Etangs, A., Delfosse, X.: New observations of the extended hydrogen exosphere of the extrasolar planet HD 209458. *Astron. Astrophys.* **483**, 933–937 (2008)
- Ehrenreich, D., Désert, J.-M.: Mass-loss rates for transiting exoplanets. *Astron. Astrophys.* **529**, L4–L14 (2011)
- Ehrenreich, D., Lecavelier des Etangs, A., Delfosse, X.: Lyman- α observations of the quiet M dwarf GJ 436. *Astron. Astrophys.* **529**, 511–518 (2011)
- Endl, M., Cochran, W.D., Wittenmyer, R.A., Hatzes, A.P.: Determination of the orbits of the planetary companion to the metal-rich star HD 45350. *Astron. J.* **131**, 3131–3134 (2006)
- Endl, M., Hatzes, A.P., Cochran, W.D., McArthur, B., Allende Prieto, C., Paulson, D.B., Guenther, E., Bedalov, A.: HD 137510: an oasis in the brown dwarf desert. *Astrophys. J.* **611**, 1121–1124 (2004)
- Endl, M., Robertson, P., Cochran, W.D., MacQueen, P.J., Brugamyer, E.J., Caldwell, C., Wittenmyer, R.A., Barnes, S.I., Kevin Gullikson, K.: Revisiting ρ Cancri e: a new mass determination of the transiting super-Earth. *Astrophys. J.* **759**, (7pp) (2012)
- Fabrycky, D.C., Ford, E.B., Steffen, J.H., Rowe, J.F., Carter, J.A., Moorhead, A.V., Batalha, N.M., Borucki, W.J., Bryson, S., Buchhave, L.A., Christiansen, J.L., Ciardi, D.R., Cochran, W.D., Endl, M., Fanelli, M.N., Fischer, D., Fressin, F., Geary, J., Haas, M.R., Hall, J.R., Holman, M. J., Jenkins, J.M., Koch, D.G., Latham, D.W., Li, J., Lissauer, J., Lucas, P., Marcy, G.W., Mazeh, T., McCauliff, S., Quinn, S., Ragozzine, D., Sasselov, D., Shporer, A.: Transit timing observations from Kepler: IV. Confirmation of 2 multiple planet systems by simple physical models. *Astrophys. J.* **750**(2), 114 (2012). arXiv: 1201.5415v2
- Fernandez, J.M., Minniti, D., Pietrzynski, G., Gieren, W., Ruiz, M.T., Zoccali, M., Udalski, A., Szeifert, T.: Millimagnitude optical photometry for the transiting planetary candidate OGLE-TR-109. *Astrophys. J.* **647**, 587–593 (2006)
- Fischer, D.A., Marcy, G.W., Butler, R.P., Vogt, S.S., Laughlin, G., Henry, G.W., Abouav, D., Peek, K.M.G., Wright, J.T., Johnson, J.A., McCarthy, C., Isaacson, H.: Five planets orbiting 55 Cancri. *Astrophys. J.* **675**, 790–801 (2008)
- Fischer, D., Driscoll, P., Isaacson, H., Giguere, M., Marcy, G.W., Valenti, J., Wright, J.T., Henry, G.W., Johnson, J.A., Howard, A., Peek, K., McCarthy, C.: Five planets and an independent confirmation of HD 196885Ab from Lick Observatory. *Astrophys. J.* **703**, 1545–1556 (2009).
- Foreman-Mackay, D., Hogg, D.W., Lang, D., Goodman, J.: emcee: The MCMC hammer. *Publ. Astron. Soc. Pac.* **925**, 306–312 (2013)
- Ford, E.B.: Quantifying the uncertainties in the orbits of extrasolar planets. *Astron. J.* **129**, 1706–1717 (2005)

- Ford, E.B.: Improving the efficiency of Markov chain Monte Carlo for analyzing the orbits of extrasolar planets. *Astrophys. J.* **642**, 505–522 (2006)
- Ford, E.B., Kozinsky, B., Rasio, F.A.: Secular evolution of hierarchical triple star systems. *Astrophys. J.* **535**, 385–401 (2000)
- Fossati, L., Haswell, C.A., Froning, C.S., Hebb, L., Holmes, S., Kolb, U., Helling, C., Carter, A., Wheatley, P., Cameron, A.C., Loeillet, B., Pollaco, D., Street, R., Stempels, H.C., Simpson, E., Udry, S., Joshi, Y.C., West, R.G., Skillen, I., Wilson, D.: Metals in the exosphere of the highly irradiated planet WASP-12b. *Astrophys. J.* **714**, L222–L227 (2010)
- Fregau, L., Chatterjee, S., Rasio, F.: Dynamical interactions of planetary systems in dense stellar environments. *Astrophys. J.* **640**, 1086–1098 (2006)
- Frey, G.J., Grim, B., Hall, D.S., Mattingly, P., Robb, S., Zeigler, K.: The rotation period of ϵ Eri from photometry of starspots. *Astron. J.* **102**, 1813–1815 (1991)
- Frink, S., Mirell, D.S., Quirrenbach, A., Fischer, D.A., Marcy, G.W., Butler, R.P.: Discovery of a substellar companion to the K2 III Giant τ Draconis. *Astrophys. J.* **576**, 478–484 (2002)
- Gatewood, G.: Lalande 21185. *Bull. Am. Astron. Soc.* **28**, 885 (1996)
- Gaudi, R.S.: Microlensing surveys for exoplanets. *Annu. Rev. Astron. Astrophys.* **50**, 411–453 (2012)
- Gaudi, B.S., Gould, A., Udalski, A., An, D., Bennett, D., Zhou, A., Dong, S., Rattenbury, N.J., Yock, P.C., Bond, I.A., Christie, G.W., Horne, K., Anderson, J., Stanek, K.Z., MicroFUN Collaboration, OGLE Collaboration, RobotNet Collaboration: Microlens OGLE-2005-BLG-169 implies cool Neptune-like planets are common. *Bull. Am. Astron. Soc.* **38**, 88 (2005)
- Gelino, C.R., Kulkarni, S.R., Stephens, D.C.: Evidence of orbital motion in the binary brown dwarf Kelu-1AB. *Publ. Astron. Soc. Pac.* **118**, 611–616 (2006)
- Gilliland, R.L., Brown, T.M., Guhathakurta, P., Sarajedini, A., Milone, E.F., Albrow, M.D., Baliber, N.R., Bruntt, H., Burrows, A., Charbonneau, D., Choi, P., Cochran, W.D., Edmunds, P.D., Frandsen, S., Howell, J.H., Lin, D.N.C., Marcy, G.W., Mayor, M., Naef, D., Sigurdsson, S., Stagg, C.R., Vandenberg, D.A., Vogt, S.S., Williams, M.D.: A lack of planets in 47 tucanae from a Hubble Space Telescope search. *Astrophys. J.* **545**, L47–L51 (2000)
- Gillon, M., Pont, F., Moutou, C., Santos, N.C., Bouchy, F., Hartman, J.D., Mayor, M., Melo, C., Queloz, D., Udry, S., Magain, P.: The transiting planet OGLE-TR-132b revisited with new spectroscopy and deconvolution photometry. *Astron. Astrophys.* **466**, 743–748 (2007)
- Gillon, M., Demory, B.-O., Benneke, B., Valencia, D., Deming, D., Seager, S., Lovis, Ch., Mayor, M., Pepe, F., Queloz, D., Ségransan, D., Udry, S.: Improved precision on the radius of the nearby super-Earth 55 Cnc e. *Astron. Astroph.* **539**, (7pp) (2012)
- Gimenez, A.: Equations for the analysis of the light curves of extra-solar planetary transits. *Astron. Astrophys.* **450**, 1231–1237 (2006)
- Gizis, J.E., Kirkpatrick, J.D., Burgasser, A., Reid, I.N., Monet, D.G., Liebert, J., Wilson, J.C.: Substellar companions to main sequence stars: no brown dwarf desert at large separations. *Astrophys. J.* **551**, L163–L166 (2001)
- Goździewski, K., Konacki, M., Wolszczan, A.: Long-term stability and dynamic environment of the PSR 1258 + 12 planetary system. *Astrophys. J.* **619**, 1084–1097 (2005)
- Gorkavyi, N., Heap, S., Ozernoy, L., Taidakova, T., Mather, J.: Indicator of exo-solar planet(s) in the circumstellar disk around β Pictoris. In: Penny, A.J., Artymowicz, P., Lagrange, A.M., Russell, S.S. (eds.). *Planetary Systems in the Universe—Observation, Formation, and Evolution*, Procs., IAU Symposium No. 202, pp. 331–334. ASP: San Francisco, CA (2004)
- Gould, A., et al.: Microlens OGLE-2005-BLG-169 implies that cool Neptune-like planets are common. *Astrophys. J.* **644**, L37–L40 (2006)
- Greaves, J.S., Holland, W.S., Moriarty-Schieven, G., Jenness, T., Dent, W.R.F., Zuckerman, B., McCarthy, C., Webb, R.A., Butner, H.M., Gear, W.K., Walker, H.J.: A dust ring around ϵ Eridani: analog to the young solar system. *Astrophys. J.* **506**, L133–L137 (1998)
- Grether, D., Lineweaver, C.H.: How dry is the brown dwarf desert: quantifying the relative number of planets, brown dwarfs, and stellar companions around nearby sun-like stars. *Astrophys. J.* **640**, 1051–1062 (2006)

- Guenther, E.W., Neuhauser, R., Wuchterl, G., Mugrauer, M., Bedalov, A., Hauschildt, P.H.: The low-mass companion of GQ Lupi. *Astron. Nachr.* **326**, 958–963 (2005)
- Guinan, E.F., Bradstreet, D.H., Ribas, I., Wolf, M., McCook, G.: IAUC 6864 (1998)
- Han, C., Ugalski, A., Choi, J.-Y., Yee, J.C., Gould, A., Christie, G., Tan, T.-G., Syzmański, M.K., Kubiac, M., Soszyński, I., Pietrzynski, G., Poleski, R., Ulaczyk, K., Pietrukowicz, P., Kozłowski, S., Skowron, J., Wyrzykowski, Ł., (The Ogle Collaboration); Almeida, L.A., Batista, V., Depoy, D.L., Dong, S., Drummond, J., Gaudi, B.S., Hwang, K.-H., Jablonski, F., Jung, Y.-K., Lee, C.-U., Koo, J.-R., McCormick, J., Monard, L.A.G., Natusch, T., Ngan, H., Park, H., Pogge, R.W., Porritt, I., Shin, I.-G., (the µFUN Collaboration): The second multiple-planet system discovered by microlensing: OGLE-2012-BLG-0026Lb,c – a pair of Jovian planets beyond the snow line. *Astrophys. J. Lett.* **762**, L28 (6pp) (2013)
- Haswell, C.A., Fossati, L., Ayres, T., France, K., Froning, C.S., Holmes, S., Kolb, U.C., Busutil, R., Street, R.A., Hebb, L., Collier Cameron, A., Enoch, B., Burwitz, V., Rodriguez, J., West, R. G., Pollacco, D., Wheatley, P.J., Carter, A.: Near-ultraviolet absorption, chromospheric activity, and star-planet interactions in the WASP-12 system. *Astrophys. J.* **760**, 79 (2012) (23pp)
- Hatzes, A.P.: Radial velocity detection of earth mass planets in the presence of activity noise: the case of α Centauri Bb. *Astrophys. J.* **770**(2), 133 (2013). arXiv:1305.4960v1
- Hatzes, A.P., Cochran, W.D., McArthur, B., Baliunas, S.L., Walker, G.A.H., Campbell, B., Irwin, A.W., Yang, S., Kurster, M., Endl, M., Els, S., Butler, R.P., Marcy, G.W.: Evidence of a long-period planet orbiting ϵ Eridani. *Astrophys. J.* **544**, L145–L148 (2000)
- Hatzes, A.P., Cochran, W.D., Endl, M., McArthur, B., Paulson, D., Walker, G.A.H., Campbell, B., Yang, S.: A planetary companion to γ Cephei A. *Astrophys. J.* **599**, 1383–1394 (2003)
- Hatzes, A.P., Cochran, W.D., Endl, M., Guenther, E.W., Saar, S.H., Walker, G.A.H., Yang, S., Hartmann, M., Esposito, M., Paulson, D.B., Doollinger, M.P.: Confirmation of the planet hypothesis for the long-period radial velocity variations of β Geminorum. *Astron. Astrophys.* **457**, 335–342 (2006)
- Hébrard, G., Ehrenreich, D., Bouchy, F., Delfosse, X., Moutou, C., Arnold, L., Boisse, I., Bonfils, X., Díaz, R.F., Eggenberger, A., Forveille, T., Lagrange, A.-M., Lovis, C., Pepe, F., Perrier, C., Queloz, D., Santerne, A., Santos, N.C., Ségransan, D., Udry, S., Vidal-Madjar, A.: The retrograde orbit of the HAT-P-6b exoplanet. *Astron. Astrophys.* **527**, 373–374 (2011)
- Henry, G., Marcy, G., Butler, P., Vogt, S.: A transiting 51 Peg-like planet. *Astrophys. J.* **529**, L41–L44 (2000)
- Hogan, E., Jameson, R.F., Casewell, S.L., Osbourne, S.L., Hambly, N.C.: L dwarfs in the Hyades. *Mon. Not. R. Astron. Soc.* **388**, 495–499 (2008)
- Holman, M.J., Winn, J.N., Latham, D.W., O'Donovan, F.T., Charbonneau, D., Bakos, G.A., Esquerdo, G.A., Hergenrother, C., Everett, M.E., Pal, A.: The Transit Light Curve (TLC) project. I. Four consecutive transits of the exoplanet XO-1b. *Astrophys. J.* **652**, 1715–1723 (2006)
- Itoh, Y., Hayashi, M., Tamura, M., Tsuji, T., Oasa, Y., Fukagawa, M., Hayashi, S.S., Naoi, T., Ishii, M., Mayama, S., Morino, J.-I., Yamashita, T., Pyo, T.-S., Nishikawa, T., Usuda, T., Murakawa, K., Suto, H., Oya, S., Takato, N., Ando, H., Miyama, S.M., Kobayashi, M., Kaifu, N.: A young brown dwarf companion to DH Tauri. *Astrophys. J.* **620**, 984–993 (2005)
- Jayawardhana, R., Ivanov, V.: Spectroscopy of young planetary mass candidates with disks. *Astrophys. J.* **647**, L167–L170 (2006)
- Jha, S., Charbonneau, D., Garnavich, P.M., Sullivan, D.J., Sullivan, T., Brown, T.M., Tonry, J.L.: Multicolor observations of a planetary transit of HD 209458. *Astroph. J.* **540**, L45–L48 (2000)
- Joergens, V., Muller, A.: 16–20 M_{Jup} Radial velocity companion orbiting the brown dwarf candidate Cha H α 8. *Astrophys. J.* **666**, L113–L116 (2007)
- Kallrath, J., Milone, E.F.: *Eclipsing Binary Stars: Modeling and Analysis*, 2nd edn. Springer, New York (2009)
- Kane, S.R., Henry, G.W., Dragomir, D., Fischer, D.A., Howard, A.W., Wang, X., Wright, J.T.: Revised orbit and transit exclusion for HD 114762b. *Astrophys. J. Lett.* **735**, L41 (2011) (5pp)

- Kelley, D.H., Milone, E.F.: Exploring Ancient Skies: Survey of Ancient and Cultural Astronomy, 2nd edn. Springer, New York (2011)
- King, R.R., McCaughean, M.J., Homeier, D., Allard, F., Scholz, R.-D., Lodieu, N.: ε Indi Ba, Bb: a detailed study of the nearest known brown dwarfs. *Astron. Astrophys.* **510**, A99 (2010). doi:[10.1051/0004-6361/200912981](https://doi.org/10.1051/0004-6361/200912981)
- Kniazev, A.Y., Vaisanen, P., Mužić, K., Mehner, A., Boffin, H.M.J., Kutev, R., Melo, C., Ivanov, V.D., Girard, J., Mawet, D., Schmidtobreick, L., Huelamo, N., Borissova, J., Minniti, D., Ishibashi, K., Potter, S.B., Beletsky, Y., Buckley, D.A.H., Crawford, S., Gulbis, A.A.S., Kotze, P., Miszalski, B., Pickering, T.E., Romero Colmenero, E., Williams, T.B.: Characterization of the nearby L/T binary brown dwarf WISEJ104915.57-531906.1 at 2 parsecs from the sun. *Astrophys. J.* **770**(2), 124 (2013). arXiv.1303.7171v2
- Konacki, M., Wolszczan, A.: Masses and orbital inclinations of planets of the PSR B 1257+12 system. *Astrophys. J.* **591**, L147–L150 (2003)
- Konacki, M., Torres, G., Sasselov, D.D., Pietrzynski, G., Udalski, A., Jha, S., Ruiz, M.T., Gieren, W., Minniti, D.: The transiting extrasolar giant planet around the star OGLE-TR-113. *Astrophys. J.* **609**, L37–L40 (2004)
- Kozai, Y.: Secular perturbations of asteroids with high inclination and eccentricity. *Astron. J.* **67**, 591–598 (1962)
- Lecavelier des Etangs, A., Bourrier, V., Wheatley, P.J., Dupuy, H., Ehrenreich, D., Vidal-Madjar, A., Hébrard, G., Ballester, G.E., Désert, J.-M., R. Ferlet, R., Sing, D.K.: Temporal variations in the evaporating atmosphere of the exoplanet HD 189733b. *Astron. Astrophys.* **543**, 4pp, DOI: 10.1051/0004-6361/201219363 (2012)
- Lee, M.H., Butler, R.P., Fischer, D.A., Marcy, G.W., Vogt, S.S.: On the 2:1 orbital resonance in the HD 82943 planetary system. *Astrophys. J.* **641**, 1178–1187 (2006)
- Lee, J.W., Kim, S.-E., Kim, C.-H., Koch, R.H., Lee, C.-U., Kim, H.-I., Park, J.-H.: The sdB + M eclipsing system HW Virginis and its circumbinary planets. *Astron. J.* **137**, 3181–3190 (2009)
- Leggett, S.K., Saumon, D., Albert, L., Cushing, M.C., Liu, M.C., Luhman, K.L., Marley, M.S., Kirkpatrick, J.D., Roellig, T.L., Allers, K.N.: HN Peg B: a test of models of the L to T dwarf transition. *Astrophys. J.* **682**, 1256–1263 (2008)
- Linsky, J.L., Yang, H., France, K., Froning, C.S., Green, J.C., Stocke, J.T., Osterman, S.N.: Observations of mass loss from the transiting exoplanet HD 209458. *Astrophys. J.* **717**, 1291–1299 (2010)
- Lissauer, J.J., Fabrycky, D.C., Ford, E.B., Borucki, W.J., Fressin, F., Marcy, G.W., Orosz, J.A., Rowe, J.F., Torres, G., Welsh, W.F., Batalha, N.M., Bryson, S.T., Buchhave, L.A., Caldwell, D.A., Carter, J.A., Charbonneau, D., Christiansen, J.L., Cochran, W.D., Desert, J.-M., Dunham, E.W., Fanelli, M.N., Fortney, J.J., Gautier III, T.N., Geary, J.C., Gilliland, R.L., Haas, M.R., Hall, J.R., Holman, M.J., Koch, D.G., Latham, D.W., Lopez, E., McCauliff, S., Miller, N., Morehead, R.C., Quintana, E.V., Ragozzine, D., Sasselov, D., Short, D.R., Steffen, J.H.: A closely packed system of low-mass, low-density planets transiting Kepler-11. *Nature* **470**, 53–58 (2011)
- Lithwick, Y., Xie, J., Wu, Y.: Extracting planet masses and eccentricity from TTV data. *Astrophys. J.* **761** (11 pp). arXiv:1207.4192v2 (2012)
- Liu, Y.-J., Sato, B., Zhao, G., Noguchi, K., Wang, H., Kambe, E., Ando, H., Izumiura, H., Chen, Y.-Q., Okada, N., Toyota, E., Omiya, M., Masuda, S., Takeda, Y., Murata, D., Itoh, Y., Yoshida, M., Kokubo, E., Ida, S.: A substellar companion to the intermediate-mass giant 11 Comae. *Astrophys. J.* **672**, 553–557 (2008)
- Lovis, C., Mayor, M., Bouchy, F., Pepe, F., Queloz, D., Santos, N.C., Udry, S., Benz, W., Bertaux, J.-L., Mordasini, C., Sivan, J.-P.: The HARPS search for southern extra-solar planets. III. Three Saturn-mass planets around HD 93083, HD 101930 and HD 102117. *Astron. Astrophys.* **437**, 1121–1126 (2005)
- Lovis, C., Mayor, M.: Planets around evolved intermediate-mass stars I. Two substellar companions in the open clusters NGC 2423 and NGC 4349. *Astron. Astrophys.* **472**, 657–664 (2007). arXiv:0706.2174v1

- Lovis, C., Mayor, M., Pepe, F., Alibert, Y., Benz, W., Bouchy, F., Correia, A.C.M., Laskar, J., Mordasini, C., Queloz, D., Santos, N.C., Udry, S., Bertaux, J.-L., Sivan, J.-P.: An extrasolar planetary system with three Neptune-mass planets. *Nature* **441**, 305–309 (2006)
- Luhman, K.L.: Discovery of a binary brown dwarf at 2 parsecs from the sun. *Astrophys. J. Let.* (in press) arXiv.org/pdf/1303.2401v2.pdf (2013)
- Luhmann, K.L., Liebert, J., Rieke, G.H.: Spectroscopy of a young brown dwarf in the ρ Ophiuchi Cluster. *Astrophys J.* **489**, L165–L168 (1997)
- Luhman, K.L., Adame, L., d’Alessio, P., Calvet, N., Hartmann, L., Megeath, S.T., Fazio, G.G.: Discovery of a planetary-mass brown dwarf with a circumstellar disk. *Astrophys. J.* **635**, L93–L96 (2005)
- Lunine, J.I.: *Astrobiology: A Multidisciplinary Approach*, Addison Wesley (Pearson Education), San Francisco (2005)
- Lyot, B. (tr. Marschall, R. K.): The study of the solar corona without an eclipse. *J. R. Astron. Soc. Can.* **27**, 225–234; 265–280 (1933)
- Marcy, G.W.: Personal communication to M.D. Williams (2000)
- Marcy, G.W., Butler, R.P.: Detection of extrasolar giant planets. *Annu. Rev. Astron. Astrophys.* **36**, 57–97 (1998)
- Marengo, M., Megeath, S.T., Fazio, G.G., Stapelfeldt, K.R., Werner, M.W., Backman, D.E.: A Spitzer IRAC search for substellar companions of the debris disk star ϵ Eridani. *Astrophys. J.* **647**, 1437–1451 (2006)
- Marmier, M., Ségransan, D., Udry, S., Mayor, M., Pepe, F., Queloz, D., Lovis, C., Naef, D., Santos, N.C., Alonso, R., Alves, S., Berthet, S., Chazelas, B., Demory, B.-O., Dumusque, X., Eggenberger, A., Figueira, P., Gillon, M., Hagelberg, J., Lendl, M., Mardling, R.A., Mégevand, D., Neveu, M., Sahlmann, J., Sosnowska, D., Tewes, M., Triaud, A.H.M.J.: The CORALIE survey for southern extrasolar planets. XVII. New and updated long period and massive planets. *Astron. & Astrophys.* **551**, A90. <http://dx.doi.org/10.1051/0004-6361/201219639> (2013)
- Marsh, K.A., Dowell, C.D., Velusamy, T., Grogan, K., Beichman, C.A.: Images of the Vega dust ring at 350 and 450 μ m: new clues to the trapping of multiple-sized dust particles in planetary resonances. *Astrophys. J.* **646**, L77–L80 (2006)
- Martin, E.L., Delfosse, X., Basri, G., Goldman, B., Forveille, T., Zapatero Osorio, M.R.: Spectroscopic classification of late-M and L field dwarfs. *Astron. J.* **118**, 2466–2482 (1999)
- Matsumura, S., Pudritz, R.E.: The origin of Jovian planets in protostellar disks: the role of dead zones. *Astrophys. J.* **598**, 645–656 (2003)
- Matsumura, S., Pudritz, R.E., Thomas, E.W.: Saving planetary systems: dead zones and planetary migration. *Astrophys. J.* **660**, 1609–1623 (2007)
- Mayor, M., Queloz, D., Udry, S.: Mass function and orbital distribution of substellar companions. In: Rebolo, R., Martin, E.L., Zapatero Osorio, M.R. (eds.) *Brown Dwarfs and Extrasolar Planets*. ASP Conf. Series, vol. 134, pp. 140–151. ASP, San Francisco, CA (1998)
- Mayor, M., Udry, S., Naef, D., Pepe, F., Queloz, D., Santos, N.C., Burnet, M.: The CORALIE survey for southern extra-solar planets. XII. Orbital solutions for 16 extra-solar planets discovered with CORALIE. *Astron. Astrophys.* **415**, 391–402 (2004)
- Mazeh, T., Shaham, J.: The orbital evolution of close triple systems—the binary eccentricity. *Astron. Astrophys.* **77**, 145–151 (1979)
- Mazeh, T., et al.: The spectroscopic orbit of the planetary companion transiting HD 209458. *Astrophys. J.* **532**, L55–L58 (2000)
- McArthur, B.E., Endl, M., Cochran, W.D., Benedict, G.F., Fischer, D.A., Marcy, G.W., Butler, R. P., Naef, D., Mayor, M., Queloz, D., Udry, S., Harrison, T.E.: Detection of a Neptune-mass planet in the ρ^1 Cancri system using the Hobby-Eberly Telescope. *Astrophys. J.* **614**, L81–L84 (2004)
- McCaughrean, M.J., Close, L.M., Scholz, R.-D., Lenzen, R., Biller, B., Brandner, W., Hartung, M., Lodieu, N.: ϵ Indi Ba, Bb: the nearest binary brown dwarf. *Astron. Astrophys.* **413**, 1029–1036 (2004)

- McCullough, P.R., Sty, J.E., Valenti, J.A., Johns-Krull, C.M., Janes, K.A., Heasley, J.N., Bye, B.A., Dodd, C., Fleming, S.W., Pinnick, A., Bissinger, R., Gary, B.L., Howell, P.J., Vanmunster, T.: A transiting planet of a sun-like star. *Astrophys. J.* **648**, 1228–1238 (2006)
- McLaughlin, D.B.: Some results of a spectrographic study of the Algol system. *Astrophys. J.* **60**, 22–31 (1924)
- Milone, E.F., Wilson, W.J.F.: Solar System Astrophysics: Background Science and the Inner Solar System, 2nd edn. Springer, New York (2014)
- Misner, C.W., Thorne, K.S., Wheeler, J.A.: Gravitation. Freeman, San Francisco, CA (1973)
- Mitchell, D.S., Frink, S., Quirrenbach, A., Fischer, D.A., Marcy, G.W., Butler, R.P.: Four substellar companions found around K giant stars. *Bull. Am. Astron. Soc.* **35**, 1234 (2003)
- Molaro, P., Monaco, L., Barbieri, M., Zaggia, S.: Detection of the Rossiter–McLaughlin effect in the 2012 June 6 Venus transit. *Mon. Not. R. Astron. Soc.* **429**, L79–L83 (2013)
- Muraki, Y., Han, C., Bennett, D.P. et al. (130 authors): Discovery and mass measurements of a cold, 10 Earth mass planet and its host star. *Astrophys. J.* **742**, 22 (15pp) (2011)
- Muench, A.A., Alves, J., Lada, C.J., Lada, E.A.: Evidence for circumstellar disks around young brown dwarfs in the trapezium cluster. *Astrophys. J.* **558**, L51–L54 (2001)
- Naef, D., Mayor, M., Beuzit, J.L., Perrier, C., Queloz, D., Sivan, J.P., Udry, S.: The ELODIE survey for northern extra-solar planets. III. Three planetary candidates detected with ELODIE. *Astron. Astrophys.* **414**, 351–359 (2004)
- Neuhäuser, R., Schmidt, T.O.B.: Direct imaging of extra-solar planets — Homogeneous comparison of detected planets and candidates. Chapter 3 In: Tyson, R.K. (ed.) Topics in Adaptive Optics, InTech (2012)
- Neuhäuser, R., Guenther, E.W., Wuchterl, G., Mugrauer, M., Bedalov, A., Hauschildt, P.H.: Evidence for a co-moving sub-stellar component to GQ Lupi. *Astron. Astrophys.* **345**, L13–L16 (2005)
- Neuhäuser, R., Mugrauer, M., Seifahrt, A., Schmidt, T.O.B., Vogt, N.: Astrometric and photometric monitoring of GQ Lup and its sub-stellar companion. *Astron. Astrophys.* **484**(1), 281–291 (2008). arXiv:0801.2287.pdf
- Niedzielski, A., Nowak, G., Adamów, M., Wolszczan, A.: Substellar-mass companions to the K-dwarf BD+14 4559 and the K-giants HD 240210 and BD+20 2457. *Astrophys. J.* **707**, 768–777 (2009)
- Noyes, R.W., Jha, S., Korzennik, S.G., Krockenberger, M., Nisenson, P., Brown, T.M., Kennelly, E.J., Horner, S.D.: A planet orbiting the star ρ Coronae Borealis. *Astrophys. J.* **483**, L111–L114 (1997)
- Pepe, F., Correia, A.C.M., Mayor, M., Tamuz, O., Couetdic, J., Benz, W., Bertaux, J.L., Bouchy, F., Laskar, J., Lovis, C., Naef, D., Queloz, D., Santos, N.C., Sivan, J.-P., Sosnowska, D., Udry, S.: The HARPS search for southern extra-solar planets. VIII. μ Arae, a system with four planets. *Astron. Astrophys.* **462**, 769–776 (2007)
- Perryman, M.A.C.: Extra-solar planets. *Rep. Prog. Phys.* **63**, 1209–1272 (2000)
- Perryman, M.A.C.: The Extrasolar Planet Handbook. Cambridge University Press, Cambridge (2011)
- Pollack, J.B., Hubickyi, O., Bodenheimer, P., Lissauer, J.J., Podolak, M., Greenzweig, Y.: Formation of the Giant Planets by Concurrent Accretion of Solids and Gas. *Icarus* **124**, 62–85 (1996)
- Portegies Zwart, S.F., McMillan, S.L.W.: Planets in triple star systems: the case of HD 188753. *Astrophys. J.* **633**, L141–L144 (2005)
- Quillen, A.C., Thorndike, S.: Structure in the ϵ Eridani dusty disk caused by mean motion resonances with a 0.3 eccentricity planet at periastron. *Astrophys. J.* **578**, L149–L152 (2002)
- Quinn, S.N., White, R.J., Latham, D.J., Buchhave, L.A., Cantrell, J.R., Dahm, S.E., Fűrész, G., Szenthgyorgyi, A.H., Geary, J.C., Torres, G., Bieryla, A., Berlind, P., Calkins, M.C., Esquerdo, G.A., and Stefanik, R.P.: Two “b”s in the Beehive: The discovery of the first hot Jupiters in an open cluster. *Astrophys. J.* **756**, L33–37 (2012)

- Quirrenbach, A., Reffert, S., Bergmann, C.: Planets around giant stars. In: Planetary Systems beyond the Main Sequence, AIP Conference Proceedings, vol. 1331, pp. 102–109. (2011)
- Rafikov, R.R.: Fast accretion of small planetesimals by protoplanetary cores. *Astron. J.* **128**, 1348–1363 (2004)
- Rafikov, R.R.: Can giant planets form by direct gravitational instability? *Astrophys. J.* **621**, L69–L72 (2005)
- Raghavan, D., Henry, T.J., Mason, B.D., Subasavage, J.P., Jao, W.-C., Beaulieu, T.D., Hambly, N. C.: Two suns in the sky: stellar multiplicity in exoplanet systems. *Astrophys. J.* **646**, 523–542 (2006)
- Rebolo, R., Martín, E.L., Basri, G., Marcy, G.W., Zapatero-Osorio, M.R.: Brown dwarfs in the Pleiades cluster confirmed by the lithium test. *Astrophys. J.* **469**, L53–L56 (1996)
- Reffert, S., Quirrenbach, A.: Mass constraints on substellar companion candidates from the reduced Hipparcos intermediate astrometric data: nine confirmed planets and two confirmed brown dwarfs. *Astron. Astrophys.* **527**, A140 (2011). doi:[10.1051/0004-6361/201015861](https://doi.org/10.1051/0004-6361/201015861)
- Reid, I.N., Lewitus, E., Allen, P.R., Cruz, K.L., Burgasser, A.J.: A search for binary systems among the nearest L dwarfs. *Astron. J.* **132**, 891–901 (2006)
- Rivera, E.J., Laughlin, G., Butler, R.P., Vogt, S.S., Haghighipour, N., Meschiari, S.: The Lick-Carnegie Exoplanet Survey: a Uranus-mass fourth planet for GJ 876 in an extrasolar Laplace configuration. *Astrophys. J.* **719**, 890–899 (2010)
- Reipurth, B., Clarke, C.: The formation of brown dwarfs as ejected stellar embryos. *Astron. J.* **122**, 432–439 (2001)
- Rodriguez, D.R., Marois, C., Zuckerman, B., Macintosh, B., Melis, C.: A substellar companion to the dusty Pleiades star HD 23514. *Astrophys. J.* **748**, 30 (2012)
- Rossiter, R.A.: On the detection of an effect of rotation during eclipse in the velocity of the brighter component of β Lyr, and on the constancy of velocity of this system. *Astrophys. J.* **60**, 15–21 (1924)
- Russell, H.N., Merrill, J.E.: The Determination of the Elements of Eclipsing Binaries. Princeton University Observatory Contributions, vol. 26. Princeton University Observatory, Princeton, NJ (1952)
- Sahlmann, J., Ségransan, D., Queloz, D., Udry, S., Santos, N.C., Marmier, M., Mayor, M., Naef, D., Pepe, F., Zucker, S.: Search for brown-dwarf companions of stars. *Astron. Astrophys.* **525**, A95 (2011)
- Santos, N.C., Israelian, G., Mayor, M., Rebolo, R., Udry, S.: Statistical properties of exoplanets. II. Metallicity, orbital parameters, and space velocities. *Astron. Astrophys.* **398**, 363–376 (2003)
- Santos, N.C., Pont, E., Melo, C., Israelian, G., Bouchy, F., Mayor, M., Moutou, C., Queloz, D., Udry, S., Guillot, T.: High resolution spectroscopy of stars with transiting planets: the cases of OGLE-TR-10, 56, 111, 113, and TrES-1. *Astron. Astrophys.* **450**, 825–831 (2006)
- Sato, B., Omiya, M., Harakawa, H., Izumiura, H., Kambe, E., Takeda, Y., Yoshida, M., Itoh, Y., Ando, H., Kokubo, E., Ida, S.: Substellar companions to seven evolved intermediate-mass stars. *Pub. Astron. Soc. Jpn.* **64**(6), 135 (2012). arXiv:1207.3141v1
- Sato, B., Izumieura, H., Toyoya, E., Kambe, E., Takeda, Y., Masuda, S., Omiya, M., Murata, D., Itoh, Y., Ando, H., Yoshida, M., Ikoma, M., Kokubo, E., Ida, S.: A planetary companion to the Hyades giant ϵ Tauri. *Astrophys. J.* **661**, 527–531 (2007)
- Sato, B., et al.: The N2K consortium II. A transiting hot Saturn around HD 149026 with a large dense core. *Astrophys. J.* **633**, 465–473 (2005)
- Saumon, D., Hubbard, W.B., Burrows, A., Guillot, T., Lunine, J.I., Chabrier, G.: A theory of extrasolar giant planets *Astrophys. J.* **460**, 993–1018 (1996)
- Schmidt, S.J., West, A.A., Burgasser, A.J., Bochanski, J.J., Hawley, S.L.: Discovery of an unusually blue L dwarf within 10 pc of the sun. *Astron. J.* **139**, 1045–1050 (2010)
- Schneider, J., Delieu, C., Le Sidaner, P., Savalle, R., Zolotukhin, I.: Defining and cataloging exoplanets: the exoplanet.eu database. *Astron. Astrophys.* **532**, L27–L56 (2011)
- Scholz, A., Jayawardhana, R., Wood, K.: Exploring brown dwarf disks: a 1.3 mm survey in Taurus. *Astrophys. J.* **645**, 1498–1508 (2006)

- Scholz, R.-D.: ULAS J141623.94+134836.3—a faint common proper motion companion of a nearby L dwarf. *Astron. Astrophys.* **510**, L8 (2010)
- Seifahrt, A., Neuhauser, R., Hauschildt, P.H.: Near-infrared integral-field spectroscopy of the companion to GQ Lupi. *Astron. Astrophys.* **463**, 309–313 (2007)
- Setiawan, J., et al.: Planets around evolved stars. In: *Toward Other Earths: DARWIN/TPF and the Search for Extrasolar Terrestrial Planets*. (ESA SP-539), pp. 595–598 (2003)
- Shirley, J.H., Kamp, L.W., Dalton, J.B.: Phyllosilicates and cometary impacts on the surface of Europa. Abstract P54A-07, AGU Fall Meeting, San Francisco, 9–13 December, 2013
- Smart, R.L., Jones, H.R.A., Lattanzi, M.G., Leggett, S.K., Warren, S.J., Adamson, A.J., Casali, M., Evans, D.W., Irwin, M.J., Pinfield, D.: The distance to the cool T9 brown dwarf ULAS J003402.77-005206.7. *Astron. Astrophys.* **511**, 421–439 (2010)
- Southworth, J.: Homogeneous studies of transiting extrasolar planets – V. New results for 38 planets. *Mon. Not. R. Astron. Soc.* **426**, 1291–1323 (2012)
- Sozzetti, A., Yong, D., Torres, G., Charbonneau, D., Latham, D.W., Allende Prieto, C., Brown, T. M., Carney, B.W., Laird, J.B.: High-resolution spectroscopy of the transiting planet host star TrES-1. *Astrophys. J.* **616**, L167–L170 (2004)
- Sozzetti, A., Yong, D., Carney, B.W., Laird, J.B., Latham, D.W., Torres, G.: Chemical composition of the planet-harboring star TrES-1. *Astron. J.* **131**, 2274–2289 (2006)
- Sozzetti, A., Torres, G., Charbonneau, D., Latham, D.W., Holman, M.J., Winn, J.N., Laird, J.B., O’Donovan, F.T.: Improving stellar and planetary parameters of transiting planet systems: the case of TrES-2. *Astrophys. J.* **664**, 1190–1198 (2007)
- Sozzetti, A., Desidera, S.: Hipparcos preliminary astrometric masses for the two close-in companions to HD 131664 and HD 43848: a brown dwarf and a low-mass star. *Astron. Astrophys.* **509**, A103 (2010)
- Stassun, K., Mathieu, R.D., Valenti, J.A.: Discovery of two young brown dwarfs in an eclipsing binary system. *Nature* **441**, 305–309 (2006)
- Stassun, K., Mathieu, R.D., Valenti, J.A.: A surprising reversal of temperatures in the brown dwarf eclipsing binary 2MASS J05352184-0546085. *Astrophys. J.* **664**, 1154–1166 (2007)
- Steele, P.R., Saglia, R.P., Burleigh, M.R., Marsh, T.R., Gänsicke, B.T., Lawrie, K., Cappetta, M., Girven, J., Napiwotzki, R.: NLTT 5306: the shortest period detached white dwarf + brown dwarf binary. *Mon. Not. R. Astron. Soc.* **429**, 3492–3500 (2013)
- Stumpf, M.B., Brandner, W., Henning, Th., Bouy, H., Köhler, R., Hormuth, F., Joergens, V., Kasper, M.: Kelu-1 AB—A possible brown dwarf triple system: First resolved spectra and dynamical mass estimates. *Astronomy and Astrophysics*, ms. No. Kelu1'AB (2013)
- Swift, J.J., Johnson, J.A., Morton, T.D., Crepp, J.R., Montet, B.T., Fabrycky, D.C., Muirhead, P.S.: Characterizing the cool KOIs IV: Kepler-32 as a prototype for the formation of compact planetary systems throughout the galaxy. *Astrophys. J.* **764**, 105 (2012). arXiv: 1301.0023v1
- Takeda, G., Rasio, F.: High orbital eccentricities of extrasolar planets induced by the Kozai mechanism. *Astrophys. J.* **627**, 1001–1010 (2005)
- Thommes, E.W., Nilsson, L., Murray, N.: Overcoming migration during giant planet formation. *Astrophys. J.* **616**, L25–L28 (2007)
- Tinney, C.G., Butler, R.P., Marcy, G.W., Jones, H.R.A., Laughlin, G., Carter, B.D., Bailey, J.A., O’Toole, S.: The 2:1 resonant exoplanetary system orbiting HD 73526. *Astrophys. J.* **647**, 594–599 (2006)
- Torres, G., Winn, J.N., Holman, M.J.: Improved parameters for extrasolar transiting planets. *Astrophys. J.* **677**, 1324–1342 (2008)
- Triaud, A.H.M.J., Collier Cameron, A., Queloz, A., Anderson, D.R., Gillon, M., Hebb, L., Hellier, C., Loeillet, B., Maxted, P.F.L., Mayor, M., Pepe, F., Pollacco, D., Ségransan, D., Smalley, B., Udry, S., West, R.G., Wheatley, P.J.: Spin-orbit angle measurements for six southern transiting planets. *Astron. Astrophys.* **524**, A25 (2010)
- Udalski, A., Paczyński, B., Zebrun, K., Szymański, M., Kubiak, M., Soszyński, I., Szewczyk, O., Wyrzykowski, L., Pietrzyński, G.: The optical gravitational lensing experiment. Search for planetary and low-luminosity object transits in the galactic disk. Results of 2001 campaign. *Acta Astron.* **52**, 1–19 (2002) (astro-ph/0202320)

- Udalski, A., et al.: A jovian-mass planet in microlensing event OGLE-2005-BLG-071. *Astrophys. J.* **628**, L109–L112 (2005)
- Udry, S., Mayor, M., Naef, D., Queloz, D., Santos, N.C., Burenat, M.: The CORALIE survey for southern extra-solar planets. VIII. The very low-mass companions of HD 141937, HD 168443 and HD 202206: brown dwarfs or “superplanets?” *Astron. Astrophys.* **390**, 267–279 (2002)
- Udry, S., Bonfils, X., Delfosse, X., Forveille, T., Mayor, M., Perrier, C., Bouchy, F., Lovis, C., Pepe, F., Queloz, D., Beraux, J.-L.: The HARPS search for southern extra-solar planets. XI. Super-earths (5 and 8 M_{\oplus}) in a 3-planet system. *Astron. Astrophys.* **469**, L43–L47 (2007)
- Udry, S., Mayor, M., Clausen, J.V., Freyhammer, L.M., Helt, B.E., Lovis, C., Naef, D., Olsen, E. H., Pepe, F., Queloz, D., Santos, N.C.: The CORALIE survey for southern extra-solar planets. X. A hot Jupiter orbiting HD 73256. *Astron. Astrophys.* **407**, 679–684 (2003b)
- van de Kamp, P.: Astrometric study of Barnard’s star from plates taken with the 24-inch Sproul refractor. *Astron. J.* **68**, 515–521 (1963)
- van de Kamp, P.: Astrometric study of Barnard’s star from plates taken with the Sproul 61-cm refractor. *Astron. J.* **80**, 658–661 (1975)
- van Leeuwen, F.: Hipparcos, the New Reduction of the Raw Data. ASSL, Springer, Dordrecht (2007)
- Vidal-Madjar, A., Désert, J.-M., Lecavelier des Étangs, A., Hébrard, G., Ballester, G., Ehrenreich, D., Ferlet, R., McConnell, J.C., Mayor, M., Parkinson, C.D.: Detection of oxygen and carbon in the hydrodynamically escaping atmosphere of the extrasolar planet HD209458b. *Astrophys. J.* **604**, L69–L72 (2004)
- Wang, Z., Chakrabarty, D., Kaplan, D.L.: A debris disk around an isolated young neutron star. *Nature* **440**, 772–775 (2006)
- Weldrake, D.T.F., Sackett, P.D., Bridges, T.J., Freeman, K.C.: An absence of hot Jupiter planets in 47 Tucanae: results of a wide-field transit search. *Astrophys. J.* **620**, 1043–1051 (2005)
- White, R.J., Ghez, A.M., Reid, I.N., Schultz, G.: A test of pre-main-sequence evolutionary models across the stellar/substellar boundary on spectra of the young quadruple GG Tauri. *Astrophys. J.* **520**, 811–821 (1999)
- Williams, M.D.: In the shadows of unseen companions: modeling the transits of extra-solar planets. M.Sc. Thesis, University of Calgary (2001)
- Winn, J.N., Noyes, R.W., Holman, M.J., Charbonneau, D., Ohta, Y., Taruya, A., Suto, Y., Narita, N., Turner, E.L., Johnson, J.A., Marcy, G.W., Butler, R.P., Vogt, S.S.: Measurement of spin-orbit alignment in an extrasolar planetary system. *Astrophys. J.* **631**, 1215–1226 (2005)
- Wolszczan, A.: Further observations of the planets pulsar. In: Johnston, S., Walker, M.A., Bailes, M. (eds.) *Pulsars: Problems and Progress*. ASP Conf. Series, vol. 105, pp. 91–94. ASP, San Francisco, CA (1996)
- Wolszczan, A., Frail, D.: A planetary system around the millisecond pulsar PSR 1257+12. *Nature* **355**, 145–147 (1992)
- Wolszczan, A., Hoffman, I.M., Konacki, M., Anderson, S.B., Xilouris, K.M.: A 25.3 day periodicity in the timing of the pulsar PSR B1257+12: a planet or a heliospheric propagation effect? *Astrophys. J.* **540**, L41–L44 (2000a)
- Wolszczan, A., Doroshenko, O., Konacki, M., Kramer, M., Jessner, A., Wielebinski, R., Camilo, F., Nice, D.J., Taylor, J.H.: Timing observations of four millisecond pulsars with the Arecibo and Effelsberg radiotelescopes. *Astrophys. J.* **528**, 907–912 (2000b)
- Wood, P.L., Maxted, P.F.L., Smalley, B., Iro, N.: Transmission spectroscopy of the sodium ‘D’ doublet in WASP-17b with the VLT. *Mon. Not. R. Astron. Soc.* **412**, 2376–2382 (2011)
- Wright, J.T., Fakhouri, O., Marcy, G.W., Han, E., Feng, Y., Johnson, J.A., Howard, A.W., Fischer, D.A., Valenti, J.A., Anderson, J., Piskunov, N.: The exoplanet orbit database. *Publ. Astron. Soc. Pac.* **123**, 412–422 (2011)
- Wright, J.T., Upadhyay, S., Marcy, G.W., Fischer, D.A., Ford, E.B., Johnson, J.A.: Ten new and updated multiplanet systems and a survey of exoplanetary systems. *Astrophys. J.* **693**, 1084–1099 (2009)

- Wright, E.L., Skrutskie, M.F., Kirkpatrick, J.D., Gelino, C.R., Griffith, R.L., Marsh, K.A., Jarrett, T., Nelson, M.J., Borish, H.J., Mace, G., Mainzer, A.K., Eisenhardt, P.R., McLean, I.S., Tobin, J.J., Cushing, M.C.: A T8.5 brown dwarf member of the ζ Ursae Majoris system. *Astron. J.* **145**, 84 (2013) (8pp)
- Zapatero-Osorio, M.R., Béjar, V.J.S., Rebolo, R., Martín, E.L., Basri, G.: An L-type substellar object in Orion: reaching the mass boundary between brown dwarfs and giant planets. *Astrophys. J.* **524**, L115–L118 (1999)
- Zhou, G., Bayliss, D.D.R.: Detection of sodium absorption in WASP-17b with Magellan. *Mon. Not. R. Astron. Soc.* **426**, 2483–2488 (2012)
- Zucker, S., Mazeh, T.: Analysis of the Hipparcos observations of the extrasolar planets and the brown dwarf candidates. *Astron. J.* **562**, 549–557 (2001)
- Zucker, S., Mazeh, T., Santos, N.C., Udry, S., Mayor, M.: Multi-order TODCOR: application to observations taken with the CORALIE echelle spectrograph. I. The system HD 41004. *Astron. Astrophys.* **404**, 775–781 (2003)
- Zucker, S., Mazeh, T., Santos, N.C., Udry, S., Mayor, M.: Multi-order TODCOR: application to observations taken with the CORALIE echelle spectrograph. II. A planet in the system HD 41004. *Astron. Astrophys.* **426**, 695–698 (2004)
- Zuckerman, B., Koester, D., Reid, I.N., Hunsch, M.: Metal lines in DA white dwarfs. *Astrophys. J.* **96**, 477–495 (2003)
- Zuckerman, B., Xu, S., Klein, B., Jura, M.: The Hyades cluster: identification of a planetary system and escaping white dwarfs. *Astrophys. J.* **770**, 140–147 (2013)

Index

A

- Absorptivity, 642, 682
Abundance(s), 339, 388, 389, 408, 410, 484, 485, 491, 509, 541, 560, 561, 616, 619, 621, 648, 654, 658–661, 665, 667, 668, 670, 673, 676, 780
Acetonitrile (CH_3CN), 561, 619
Acetylene (C_2H_2), 559, 560, 562
Adams, J.C., 492, 493, 582
Adams-Williamson equation, 494
Adiabatic
 convection, 344, 345
 lapse rate, 348, 368, 369, 375, 385
 pressure-density relation, 344
 processes, 345
Adoration of Magi, 610, 612
Adrastea (satellite, Jupiter XV), 524, 529, 572
Airy, G.B., 492
Albedo
 bolometric, 338, 477, 636, 642, 687, 780
 bond, 477, 516, 627, 747, 772, 780
 geometric (visual), 477, 564, 581
Alfvén waves, 460
Aluminum isotopes, 694
Alvarez, L., 668
Amalthea (satellite, Jupiter V), 355, 529, 537, 572
Ambipolar diffusion, 402, 703
American Meteor Society, 637, 638
Amidogen radical (NH_2),
Ammonia (NH_3), 348, 391, 480, 481, 483, 485, 512, 558, 560, 619, 625, 627, 756
Ammonium hydrosulfide (NH_4SH), 481, 483
Anaxagoras of Clazomenae, 598
Angular
 diameter(s), 493, 686
momentum, 354, 383–385, 443–445, 475, 479, 510, 589, 607, 681, 701, 778
resolution, 686
velocity/velocities, 349, 350, 354, 570, 605
Apollonius of Myndus, 598
Aquinus, T., 598
Archaeomagnetic data, 423
Ariel (satellite, Uranus I), 523, 527, 532, 533, 564
 albedo, 564
Aristotle, 598, 599
Artemis, 648
Asteroid(s) (general)
 albedo(s), 683, 686–688, 696, 700
 densities, 639, 689–690
 dimension(s), 686–690
 double, 689
 inner solar system plot, 678, 681, 690
 masses, 686–690
 nomenclature, 648–649, 677–681
 orbital properties
 families, 681–685
 Kirkwood gaps, 582, 678, 695, 697
 outer solar system plot, 588–590, 603
 radii, 688
 rotations, 688, 700
 thermal emissions, 697
Asteroid mill, 639, 676, 769
Asteroids (individual)
 (2101) Adonis, 683
 (1221) Amor, 681, 690
 (3554) Amun, 683
 (1943) Anteros, 681
 (2061) Anza, 681
 (1862) Apollo, 683, 684, 698
 (197) Ariete, 689
 (2062) Aten, 683

- Asteroids (individual) (*cont.*)

 (1865) Cerberus, 683

 (1) Ceres, 676–677, 689

 (2060) Chiron, 627, 684

 (1864) Daedalus, 683

 (136199) Eris, 528, 690

 (433) Eros, 681, 683, 690, 691, 698

 (951) Gaspra, 689

 (2340) Hathor, 683

 (624) Hektor (Hector), 689

 (2212) Hephaistos, 683

 (944) Hidalgo, 627, 684, 699

 (1566) Icarus, 683

 (243) Ida, 689

 (3) Juno, 690, 691

 (2) Pallas, 677, 678, 687, 689–691, 698

 1989 PB,

 (3200) Phaethon, 631, 683

 (5145) Pholus, 627, 685

 (1915) Quetzalcoatl, 681

 (5381) Sekhemet, 681

 (2608) Seneca, 681

 2004 VB61, 681

 (4) Vesta, 653, 689–696

 2004 WC1, 683

 2004 WS2, 683
- Asteroids (types)

 Amor(s), 681, 690

 Apollo(s), 683, 684, 698

 Aten(s), 683

 Centaur(s), 589, 609, 627, 680

 Cubewano(s), 681

 excited/hot objects, 685

 Flora family, 681, 682

 Hilda family, 679, 681, 684, 698

 Koronis family, 681, 682, 689

 Kuiper Belt objects (KBOs)

 classical/cold, 685

 excited/hot, 685

 main belt, 642, 678, 679, 681, 690, 693, 697, 759

 Plutino(s), 568, 589, 680, 681, 685, 759

 scattered population, 626, 628, 685, 779

 trans-Neptunian object(s) (TNOs), 568, 589, 685, 690, 759

 eccentricities *vs.* semi-major axes, 685

 Trojan(s) & Greek(s), 548, 677, 679, 681, 684, 690, 699

 Astronomical unit (au), 339, 601, 609, 769

 Atlas (satellite, Saturn XV), 526, 530, 576

 Atmosphere/atmospheric

 air mass(es), 364, 365

 circulation(s)
- eddy/eddies, 363–365, 384

 Ferrel cell(s), 362–363, 378, 385

 global, 360–367

 Hadley cell(s), 361–362, 378–380, 384, 480, 555, 558

 meridional, 363–366, 378–381, 384, 555, 556

 parasitic cell(s), 363

 polar cell(s), 362–363

 thermal, 357–358, 362

 wave motion(s), 365

 zonal, 365, 366, 380–385, 555

 constituent(s), 337–340, 371, 372, 479, 560, 764, 773

 comparative, 387

 convection, 344, 345, 369, 388, 483

 diffusion, 386–389, 484, 496

 diffusion time, 388, 496

 diffusive equilibrium, 388

 Earth

 average lapse rate, 368

 circulation, 357, 361, 377, 378, 555

 composition, 387, 781

 cyclones, 383, 384

 diffusion time, 388

 dry adiabatic lapse rate (DALR), 368, 375

 escape mechanisms, 411–416

 exosphere, 371, 411, 415, 467, 545

 heterosphere, 389

 homosphere, 389

 hurricane(s), 354, 375, 385

 lapse rate, 372

 mesopause, 370, 389

 mesosphere, 369–370

 mixing time, 388, 389

 ozone, 367

 pressure scale height, 357, 371, 372, 449

 Rossby number, 377, 378, 383

 saturated adiabatic lapse rate (SALR), 369

 stratosphere, 369–370

 superrotation, 384, 385

 thermal structure, 368

 thermosphere, 370, 371, 373, 376

 tropopause, 365

 troposphere, 367–369, 372, 386, 393, 556

 winds, 361, 365, 372, 380, 382, 384, 385, 413, 416, 423, 424, 440, 448, 455, 464, 467, 480, 503, 509, 510, 512, 555, 558

- eddy/eddies, 356, 363–364, 380, 384
 effects on heat transport, 363, 365
 escape mechanisms, 411–416
 exobase, 411–413, 446, 467, 547
 heterosphere, 389
 homopause, 389
 homosphere, 389
 isobars, 356, 359
 isotherm(s), 357, 358, 360, 380, 381
 jet stream(s), 365–367, 374, 380, 480
Jupiter
 belts, 480, 482, 582, 678, 679, 681,
 695, 779
 brown barges, 480, 481
 Great Red Spot (GRS), 480–482, 485, 493
 helium deficiency, 496
 mean molecular weight, 343, 478, 479
 pressure scale height, 765
 white spot(s), 538
 winds, 480, 481, 500, 503, 509–511, 514
 zones, 480–483, 487, 503, 509, 543,
 587, 628
- Mars**
 averaged temperatures, 381
 circulation, 377, 378, 380–381, 385
 composition, 387, 653, 666
 dust devils, 372, 373
 homopause, 389
 ionosphere, 409–410, 467
 lapse rate, 372, 373
 mixing rate,
 mixing ratio(s), 349, 407
 Rossby number, 377, 378
 stratomesosphere, 371
 thermal structure, 368, 371
 thermosphere, 371, 373, 376
 troposphere, 371–373, 375, 407
 meridional cross-section(s), 365, 366
 mixing, 386–389
 mixing ratio, 349, 391, 407
 mixing time, 388, 389
 Neptune, 395, 483, 492–494
 pressure
 baroclinic instabilities, 363
 gradient(s), 342, 353–357, 359, 360,
 376, 382, 383, 479
 high/low, 356, 358, 359, 362, 364,
 383, 481
 refractive index, 344, 418, 421, 423
Saturn
 features, 487, 490
 structure, 486–489, 497, 515, 582
 winds, 488, 509, 513, 515
- seeing, 686
 structure, 340–349, 368, 371, 375, 478,
 483–486, 490, 497
 subtropical fronts, 365, 366
 thermal inertia, 371, 375, 378, 385–386
 tides, 439, 586, 648
 total density scale height, 412
 Uranus, 483, 485, 490–491, 493, 496
Venus
 circulation, 377, 378, 381–385
 composition, 387
 cryosphere, 376, 412
 cyclostrophic balance, 382–384, 555
 exobase altitude, 412
 haze layer, 374, 381
 homopause, 389
 lapse rate, 372, 375
 mesosphere, 375, 376, 555
 Rossby number, 380, 382
 stratomesosphere,
 superrotation, 381–382, 384, 385
 temperature, 349, 367, 372, 375, 376,
 386, 393, 394, 412–414, 463, 555
 thermal structure, 368, 375
 thermosphere, 375–377
 troposphere, 375, 556
 Aurora(e), 434–436, 441, 449, 452, 454, 456,
 469, 485, 488, 503, 504
 Auroral oval, 416, 449, 450, 452–454, 456,
 488, 503, 504, 507, 515, 584
 Avogadro's number, 343, 346
- B**
- Bacon, R., 598
 Baroclinic instability, 363
 Bayeaux tapestry, 610, 612
 Benzene (C_6H_6), 562
 Bessel, F.W., 601
 Bielids, 631
 Bipolar outflow(s), 701, 703
 Birkeland currents, 453, 454
 Bode, J.E., 676
 Bolide(s), 631, 632, 635, 637, 638, 647, 659
 Bolometer, 688
 Boltzmann constant, 337, 338, 411, 702
 Borelli, G., 600
 Boundary current, 440, 441, 448, 451, 462,
 464, 510
 Bradley, J., 490
 Brahe,T., 598–600
 Breccia(s)
 anorthositic, 666

- Breccia(s) (*cont.*)
 basaltic, 666
 genomict, 663
 monomict, 655, 663
 polymict, 655, 663
 regolith, 663, 664, 666
- Bright Star Catalog, 714
- Brown dwarf desert, 723, 740, 742, 777
- Brown dwarf(s), general
 definition, 758–761
 detection techniques, 723, 743, 744, 755
 evolution, 778
 origins, 776–781
 spectral characteristics, 650, 681, 693, 695, 760
- Brown dwarf(s), individual
 AB Pic B, 756
 Cha 110913-773444, 756
 GD 165 B, 760
 Gliese 229 B, 760
 GQ Lupi B, 322
 HD 137510 B, 753
 HD 168443 C, 753
 2MASS J0535-0546 A, 760
 2MASS J1207-3932 a, 755
 OGLE-TR-109B, 763
 Ross 458 C, 761
- Brownlee particles, 620, 639
- Brunt-Väisälä frequency, 386
- C**
- Calcium-aluminum inclusion(s) (CAI), 620, 640, 657–660, 662, 676
- Callisto (satellite, Jupiter IV)
 atmosphere, 545, 547
 domed crater(s), 543, 547
 interior, 555
 magnetic field, 545
 moment of inertia, 545, 553
 ringed plain(s), 541, 545
 sub-surface ocean, 555, 779
 surface feature(s), 358, 539
 Valhalla (ringed plain), 545, 546
- Campbell, W.W., 575
- Capture mechanisms, 535
- Carbon black, 627
- Carbon dioxide (CO₂), 348, 367, 370, 372, 373, 375, 376, 378, 387, 389–391, 393, 407, 408, 410, 411, 413, 469, 512, 547, 550, 552, 560, 565, 568, 619, 621, 780
- Carbon monosulfide (CS), 619
- Carbon monoxide (CO), 347, 372, 387, 407, 408, 412, 483, 547, 560, 565, 568, 619, 620, 651, 653, 657, 659, 661, 698, 760, 766
- Cardan, Jerome (Cardano, Girolamo), 598
- Cassini/Cassini's Division, 575, 576, 585
- Cassini, J.-D., 575
- Cassini state, 489
- Catalog of Meteorites, 649
- Centaurs, 589, 609, 627, 680, 684, 685
- Ceres (asteroid dwarf planet), 522, 568, 589, 759
- Chaeeremon the Stoic, 597
- Chalcophilic elements, 658
- Challis, J., 492
- Chaotic variation, 627, 697
- Chapman-Ferraro current, 440, 462
- Charge-exchange reactions, 467, 506, 514
- Charon (satellite, Pluto I)
 atmosphere, 528, 533, 568, 570
 composition, 478
 discovery, 528, 568, 589
 orbit/orbital
 elements, 477, 528, 549, 627
 properties, 475, 535, 570, 706, 723
 spin-orbit resonance, 568
- Chinook, 395
- Chiron (asteroid), 589, 609, 625, 627, 684, 685
- Chladni, E.F.F., 647
- Chondrites. *See under* Meteorites
- Chondrules
 composition, 652, 657, 658, 660
 origin, 658
- CHON particles, 620
- CH radical, 562
- Circulation
 Ferrel cell(s), 362–363
 global, 360–367
 Hadley cell(s), 361–363, 378
 parasitic cell(s), 363
 polar cell(s), 362–363
- Clairaut, A.-C., 601
- CN radical, 614
- Coefficient
 ablation, 635
 drag, 634
- Comet(s)/cometary
 attrition, 628
 coma, 613, 615, 616, 622, 685
 cometopause, 624
 composition, 614–622
 demise, 628–629

- dust, 608, 614, 617, 620, 622, 625, 628, 629, 639, 640
envelope, 613, 614
Halley group, 615, 626
Jupiter family, 604, 615, 626, 628
Kracht group, 604
Kreutz group, 604
lost, 608
Marsden group, 604
Meyer group, 604
nucleus, 612, 614, 615, 620, 622–625, 627
orbital elements, 608, 609
orbit computation, 602, 605, 608
origin, 535, 605, 625–628, 639
parabolic (or long-period), 600, 603, 605, 614, 624, 626, 627, 700
periodic, 600, 602, 603, 609, 610, 680
probability of approach, 625–627
specific angular momentum, 607
structure, 612–614, 624
surface ice, 547, 565, 568
tail(s)
dust, 611, 614, 617, 622, 629
ion, 617, 618, 621, 623
virgin, 610, 617
- Comet of
1577, 598–600, 609
1680, 600
1772, 601, 610
371 B.C., 598, 601
the century, 604
- Comets (individual)
C/1996 B2 (Hyakutake), 616
C/1973 E1 (Kohoutek), 610
C/1980 E1 (Bowell), 605
C/1999 H1 (Lee), 617
C/1995 O1 (Hale-Bopp), 611, 613, 627
C/1997 P2 (Spacewatch), 605
C/2006 P7 (SOHO), 604
C/2004 Q2 (Machholz), 622
C/1908 R1 (Morehouse), 621
C/1961 R1 (Humason), 621
C/1577 V1 (Comet of 1577), 598–600, 609
C/2002 V1 (NEAT), 613
C/1996 Y1 (SOHO-6), 604
3D/Biel, 610, 631
3D/Biel (Biel's Comet of 1772), 601
D/ 1992 F2 (Shoemaker-Levy 9), 488
19P/Borrelly, 614
23P/Brorsen-Metcalf, 617, 618
95P/Chiron, 609
67P/Churyumov-Gerasimenko, 615
79P/du Toit-Hartley, 609
2P/Encke, 603, 609, 610, 615, 631
21P/Giacobini-Zinner, 610, 615, 631
26P/Grigg-Skjellerup, 609, 615
1P/Halley, 602, 603, 610–612, 614–616, 619, 620, 631
103P/Hartley, 615
153P/Ikeya-Zhang, 617
13P/Olbers, 609, 610
29P/Schwassmann-Wachmann, 609
73P/Schwassmann-Wachmann 3, 628
109P/Swift-Tuttle, 609–611, 631
9P/Tempel 1, 608, 609, 613, 615, 616, 618, 619
55P/Tempel-Tuttle, 610, 631
81P/Wild2, 614, 615, 640
107P/Wilson-Harrington, 609
Condensation sequence, 658, 701
Conservation of angular momentum, 354, 383, 443, 701, 778
Copernicus, N., 600
Cordelia (satellite, Uranus VI), 527, 532, 578, 579
Core accretion, 496, 497, 755, 770, 778
Coriolis
force, 349–354, 356–360, 362, 363, 377–378, 380, 382, 383, 461, 479
parameter, 479
Coriolis, G.G., 362
Coronal
holes, 417, 449
mass ejection, 436, 449, 613
Cosmic rays, 370, 404, 444, 515, 545, 619, 669, 673, 694, 700
albedo neutron decay (CRAND), 515
Cosmogenic nuclei, 673
Counterglow, 640
Crater(s)
impact, 536, 539, 541, 551, 558, 566
volcanic, 536
Cretaceous-Tertiary interface, 668
Critical
frequency, 422, 498, 515
orbital radius, 570, 587
Cryo-volcanoes, 558, 566, 567, 779
Curie point, 423, 468, 544, 694
Curvature drift, 437–439, 447, 448, 460, 510
Cyanogen(C_2N_2), 560
Cyclostrophic
balance, 382–384, 555
winds, 383
Cyclotron
frequency, 498
motion, 428
radius, 428

D

- Dactyl (243 Ida 1), 588, 689
DALR. *See* Dry adiabatic lapse rate (DALR)
 Daörffel, G.S., 600
 Daphnis (satellite, Saturn XXXV), 526, 531, 576, 577
 d'Arrest, Heinrich Louis (Ludwig), 492
 Darwin, G.H., 586
 de Laplace, Pierre Simon, 492
 Dead zone(s), 706, 777
 Debris disk(s), 704–706, 756, 769, 771
 4U 0142+61, 763
 Deimos (satellite, Mars II), 522, 524, 529, 533–535, 590, 690
 Del values, 655, 656, 674, 676
 Democritus, 598
 Descartes, René,
 Despina (Satellite, Neptune V), 527, 532, 582
 Deuterium, 412, 496, 639, 662, 676, 759
 Deuterium/hydrogen ratio (D/H), 662, 676, 700
 Diacetylene (C_4H_2), 561
 Diamagnetism, 430–431
 Diapir(s), 546
 Diffusion time, 388, 389, 496
 Diffusive equilibrium, 388
 Dione (satellite, Saturn IV), 525, 530
 plasma wake, 553
 Disk(s)
 dead zone, 706
 debris/remnant, 704–706, 756, 769, 771
 Dispersion relation, 420
 Dissociative recombination, 401, 404, 405, 410, 414, 469, 547, 548
 Doldrums, 361
 Doppler ranging, 688
 Dry adiabatic lapse rate (DALR), 368, 375
 Dungey cycle, 457–459, 510
 Dunham, D.W., 687, 691
 Dunham, J.B., 687
 Dust
 composition, 505, 675
 destinies, 640–642
 Dust devils, 372, 373
 Dysnomia (satellite, Eris I), 528, 533, 589

E

- Earth
 atmosphere/atmospheric tides, 339, 340, 349, 365–367, 384, 390, 391, 393, 439, 470, 553, 599781
 aurora(e)/auroral oval, 416, 449, 450, 452–454, 456, 488, 503, 504

Caspian Sea, 556

- cycles
 carbon, 389–390
 nitrogen, 391, 392
 oxygen, 390–391
 sulfur, 391–393
 dipolar magnetic field, 423
 electrojets, 450, 454
 geocorona, 449
 geosynchronous orbit, 586
 ion
 loss mechanisms, 401, 403, 404
 molecular, 401, 404, 507
 production mechanisms, 400, 403, 405, 409–410
 ionosphere/ionospheric
 Birkeland current, 453, 454
 charge separation, 402
 D layer, 399, 404–406
 dominant ions, 409, 410
 dynamo, 439–440
 E layer, 403, 404
 electro jet(s), 453, 454
 electron density, 399, 400, 464
 exobase altitude, 412
 field-aligned current, 453, 459
 F layer, 399, 406
 Hall current, 453, 454
 joule heating, 434, 435, 452
 Pedersen current, 507
 Lake Ontario, 556, 557
 lower atmosphere properties, 371, 372
 lunar quiet current system, 440
 magnetic
 crustal anomalies, 468
 field, 402, 424, 433, 439, 440, 448–449, 456
 reconnection, 455–457, 459, 465, 469, 624
 storm(s), 441, 448–449, 452, 454
 substorm(s), 454–455
 magnetopause, 424, 440, 449, 452, 458–462
 magnetosheath, 424
 magnetosphere/magnetospheric
 Birkeland currents, 453, 454
 Chapman-Ferraro boundary current, 440
 convection, 449–450, 453, 460
 cross-tail current, 451, 455, 456, 465, 514
 diamagnetic ring current, 460
 magnetotail(s), 337, 424, 441, 449–450, 455–458, 460, 465, 502

- mass, 510, 511
neutral point, 441
neutral sheet, 424, 451
plasma sheet, 451, 455–457,
 459, 460
plasmoids, 456, 459, 465
polar cusp, 402, 416, 441, 452, 459
radius, 339
reconnection(s), 455–457, 459, 465,
 469, 624
ring current, 441–449, 452, 456, 460,
 510, 511, 513, 514
ring prospect,
solar disturbed current system, 452
solar quiet current system, 439
solar constant, 367, 372
Van Allen radiation belts
 mirror points, 444, 460
 pitch angles, 444
 precipitation, 444
 ring current, 447
Edgeworth, K., 680
Edgeworth-Kuiper Belt/Cloud, 489, 568,
 615, 626, 680, 681, 685, 700, 722,
 759, 779
 shape and size, 626
Effective gravity (gravitational
 acceleration), 352
Einstein radius, 754
Einstein ring, 753
Elsasser number, 461
Enceladus (satellite, Saturn II)
 plumes, 512, 522, 550
 tiger stripes, 512, 550
Encke gap, 549, 576, 577, 582, 585
Encke, J.F., 601
Energy budget, 394
Enstatite (MgSiO_3), 651, 660, 664, 698, 760
Ephorus of Cyme, 598
Epimetheus (satellite, Saturn XI), 525, 530
Equation
 Adams-Williamson, 494
 of hydrostatic equilibrium, 342, 494, 759
Equation(s) of state, 342, 346, 494
Equatorial, 353, 363, 461, 480–482, 486,
 487, 499, 501, 503, 510, 511, 514,
 533, 544, 551, 560, 575, 578, 590,
 703, 771
 bulge, 353
Equilibrium
 hydrostatic, 340, 342, 494, 759
 mechanical, 341
 temperature, 337, 338
Eris (dwarf planet)
 albedo, 589
 comparison with Pluto radius, 568
 satellite, 527, 528
 temperature, 589
Escape velocity, 337, 479, 605, 628, 671
Ethane (C_2H_6), 553–556, 559, 560, 562,
 616, 619
Ethanol ($\text{C}_2\text{H}_5\text{OH}$),
Ethylene (C_2H_4), 560–562
Ethyl radical(s) (C_2H_5), 561, 562
Ethynyl radical (C_2H), 562
Europa (satellite, Jupiter II)
 atmosphere, 540
 cratering density, 522
 magnetic field, 540
 mean density, 539
 ocean, 539–541, 779
 surface feature(s)
 chaotic terrain, 539, 540
 cracks, 539, 540
 ice rafts, 539
 lenticulae (dark spots), 540
 linea, 540, 542
 mountains, 539
 ringed plains, 540, 541
 wrinkle ridges, 539
Eutectic mixture(s), 539
Exobase, 371, 411–413, 446, 467, 547, 548
Extra-ordinary ray(s), 498
Extra-solar planet(s) (general)
 chthonian, 765
 detection techniques
 astrometric, 743, 750–753
 direct imaging, 755–756
 gravitational lensing, 715, 743,
 753–755, 763
 pulsar timings, 756–757
 radial velocity variations, 714, 743–746,
 756, 770
 transit photometry, 747–750, 765
 direct imaging candidates, 755–756
 free-floating, 723, 763, 777, 779
 habitable zone, 770, 776, 779–781
 host stars, 749
 L-band simulated light curve, 749
 multi-planet systems, 763
 O-C analyzes, 757
 occultation observations, 766
 outgassing evidence, 560
 sodium detection, 766
 spectroscopy, 521
 transit observations, 764

Extra-solar planet(s) (individual systems)
 AB Pictoris, 756
 ν Andromedae, 767
 μ Arae, 753
 55 Cancri, 747, 767–768
 α Centauri B, 744, 775, 776
 Cha 110913-773444, 756
 ι Draconis, 757
 ε Eridani, 704, 758, 770–771
 β Geminorum, 753
 GJ 436, 766
 GJ 674, 770
 GJ 876, 770
 Gl 581, 779
 HAT P-1, 763
 HD 10180, 763
 HD 10647, 753
 HD 37124,
 HD 40307, 763
 HD 69830, 769–770
 HD 74156,
 HD 87833, 753
 HD 147513, 753
 HD 149026, 763
 HD 168443, 723, 753
 HD 188753A, 777
 HD 189733, 747, 763, 766
 HD 209458
 L-band simulated light curve, 749
 O-C analyses, 757
 occultation observations, 547, 766
 outgassing evidence, 560
 sodium detection, 766
 transit observations, 747, 764
 IL Aquarii, 770
 Kepler 347, 763, 768–769
 Kepler 368, 774–775
 2MASSW J1207334-393254, 755
 MOA-2003-BLG-53 (*see* OGLE-2003-BLG-235)
 OGLE-2003-BLG-235L, 755
 OGLE-2005-BLG-071L, 755
 OGLE-2005-BLG-169L, 755
 OGLE-2005-BLG-390L, 754, 755
 OGLE-2012-BLG-0026L, 755
 OGLE-MOA-2011-BLG-266L, 755
 OGLE-TR-10, 763
 OGLE-TR-56, 766
 OGLE-TR-109, 763
 OGLE-TR-111, 763
 OGLE-TR-113, 747
 OGLE-TR-132, 763
 51 Pegasi, 714

PSR 1257+12, 714, 756, 757, 763
 PSR 1719-1438, 746
 PSR B1620-26, 714, 757
 ε Tauri, 762
 TrES-1, 747, 749, 771–772
 47 Ursae Majoris,
 WASP-1, 763
 WASP-17, 772–774
 XO-1,

F
 Fayalite (Fe_2SiO_4), 621, 653
 Ferrel cell(s), 363, 378
 Field-aligned currents, 431–433, 453, 455, 456, 459, 469, 507, 508, 511, 514
 Flamsteed, J., 490
 Föhn, 395
 Force(s)
 apparent, 349, 351
 centrifugal, 349–353
 centripetal, 428, 438, 570, 571
 Coriolis, 349–354, 356–360, 362, 363, 377–378, 380, 382, 383, 461, 479
 disruptive differential, 571
 electric, 425, 427, 450
 fictitious, 349, 352
 friction, 355, 356, 377
 gravitational, 352, 427, 440, 570, 574, 641
 Lorentz, 425–426, 441, 461
 pressure gradient, 353–360, 376, 382, 383
 tidal, 550, 551, 570
 virtual, 349
 Formaldehyde (H_2CO), 619
 Forsterite (Mg_2SiO_4), 538, 620, 621, 760
 Frame(s) of reference, 349, 350
 Fugacity, 674

G
 Galatea (Satellite, Neptune VI), 527, 532, 582
 Galilean satellites, 522, 523, 583
 Galilei, G., 599
 Galle, J.G., 492
 Ganymede (satellite, Jupiter II)
 atmosphere, 543
 crater(s)
 Achelaous, 543
 Gula, 543
 cratering densities, 522
 Galileo Regio, 542
 ice polymorph(s), 543
 magnetic field, 543

- mantle, 544
mean density, 476, 479, 495, 533, 538, 539, 543, 553
moment of inertia, 538, 539, 543, 545, 553, 675
sub-surface ocean, 555, 779
surface features
 cratered plains, 542, 545
 grooved terrain, 542, 544
 palimpsest(s), 542, 543
 penepalimpsest(s), 542, 543
 ringed plain(s), 540, 541, 545
 strike-slip faults, 540
 sulcus/sulci, 542
- Gas(es)
 chemically active, 348
 monatomic, 347, 348, 760
 polyatomic, 348
- Gas giants
 albedos, 496
 densities, 505
 heat fluxes, 496
 ionospheres, 497–498
 pressure(s)
 central, 463, 495
 internal, 494–495
 properties
 orbital, 475, 535, 570
 physical, 475, 529, 564, 568
 temperature(s), 701
 winds, 605
- Gauss, K.F., 677
- Gauss's law, 419
- Gegenschein, 640
- Geminids, 631
- Georgium Sidus (Uranus), 490
- Geostrophic
 balance, 356–358, 382, 556
 winds, 356–357
- Germane (GeV_4), 483
- Gradient drift, 437–438
- Gram-molecular weight, 346
- Gravitational constant, 412
- Gravitational contraction, 778
- Gravitational instability/instabilities, 497, 770, 778
- Gravitational radius, 753
- Greenhouse
 effect, 394, 395, 494
 runaway, 781
 gases, 780
- Guiding center, 429–430, 433, 436, 437, 441
- Gulliver's Travels*, 528
- Gyration frequency, 442
- Gyromotion, 428–430, 433, 441–444, 508, 509
- Gyroradius, 428, 429, 437, 442, 443
- H**
- Habitable zone, 770, 776, 779–781
- Hadley cell(s), 361–363, 377–380, 480, 555, 556
- Hadley, G., 362
- Hagecius, T., 599
- Half-life/lives, 658, 670, 673
- Hall, A., 533
- Hall current, 434, 435, 453, 454, 507
- Halley, E., 600
- Harding, K.L., 677
- HCN. *See* Hydrogen cyanide (HCN)
- Heat capacity/capacities, 345, 347, 358, 363
- Heat of ablation, 635
- Helium, 339, 395, 479, 483–485, 488, 491, 496, 561, 673, 713
 source, 496
- Helium rain, 395, 484, 496
- Herschel, C., 610
- Herschel, J., 601, 610
- Herschel, W., 490, 677
- Hertzsprung-Russell diagram, 761
 for planets and brown dwarfs, 760
- Hevel, J., 600
- Hill, G.W., 362, 596
- Hirayama, K., 681, 682
- Hohmann orbital transfer, 570
- Horse latitudes, 361
- Horseshoe-shaped orbits, 549
- Hot Jupiters, 497, 749, 755, 760, 762, 765–767, 772, 773
- Hurricane(s), 354, 375, 385
 Wilma, 354, 355
- Huygens, C., 553
- Hydrazine (N_2H_4), 483
- Hydrodynamic outflow, 413
- Hydrogen, 339, 412, 413, 449, 466, 469, 479, 483–486, 491, 500, 502, 509, 540, 559, 560, 563, 613, 614, 662, 676, 702, 713, 760, 765, 766
- Hydrogen cyanide (HCN), 559, 560, 619
- Hydrogen sulfide (H_2S), 391, 392, 480, 483, 619
- Hydrostatic equilibrium, 340–342, 494, 759
- Hydroxyl radical (OH), 407, 408
- Hyperion (satellite, Saturn XVIII), 525, 530, 551, 552
- moments of inertia, 552

I

Iapetus (satellite, Saturn VIII), 523, 530, 551
 terrain, dark, 551

Ice(s)

 polymorph (s), 543
 water, 379, 385, 542, 543, 566, 569, 577,
 583, 588, 616
 phase diagram, 545

Ice giants, 706, 778

Interplanetary magnetic field (IMF), 416, 424,
 454–457, 459, 463–469, 492, 542,
 623, 624, 694

Interstellar medium, 619, 620, 662, 676, 703

Inter-tropical convergence zone, 361

Io (satellite, Jupiter I) atmosphere

 composition, 478
 cratering density, 522
 interior, 507, 535
 loss mechanisms
 hydrodynamic outflow, 505
 Jeans escape, 506
 sputtering, 506
 volcanism, 504, 506, 522

mean density, 538

orbit(al), 501, 504, 507, 524, 535, 538

 elements, 504, 524

physical properties, 529, 535

plasma torus, 505, 507, 510

plumes, 504, 506, 537, 538, 550

pressure scale height, 510

sodium D-line emission,

volatiles, 410

volcano(es)

 Pele, 537

 Pillan Patera, 537

 Prometheus, 537

 Tvashtar Catena, 538

Ionosphere(s)/ionospheric

 critical frequency, 422, 498, 515

 field-aligned current(s), 453

 index of refraction, 497

 loss mechanisms, 410

 plasma frequency, 422, 497, 498

 production mechanisms, 409–410

 reflection, 406

 refraction, 406, 421, 497

Iron

 Curie point, 423

 meteorites (q. v.), 647–650, 652, 656, 657,
 660, 661, 663, 667–669, 671, 673,
 693, 699

Isobaric processes, 346

Isobars, 356–360, 379, 380

Isochoric processes, 346

Isotherms, 357, 358, 360, 380, 381

J

Jacobi's integral, 607

Janus (satellite, Saturn X), 492, 525, 530,
 552, 577, 585

Jeans

 escape mechanism, 411–413

 length, 778

 mass, 778

 parameter, 411

Jeans, J., 340, 778

Jefferson, T., 647

Jet streams, 365–367, 380

Joule heating, 434, 435, 452

Junge layer, 393

Jupiter

 age, 479, 484

 albedo, 477

 atmosphere

 belts, 480, 482, 582, 678, 679, 681,

 695, 779

 blue-grey regions, 482

 brown barges, 480, 481

 color interpretation, 558

 composition, 478, 479

 Great Red Spot, 480–482, 485, 493

 Hadley cell interpretation, 480

 mean molecular weight, 343, 478, 479

 photochemical products, 483

 scale height, 478, 485

 structure, 483–486

 UV photolysis, 480

 white ovals, 480, 481

 winds, 480, 481, 500, 503, 509, 510, 514

 zones, 480–483, 487, 503, 509, 543,

 587, 628

 aurorae(e), 485, 488

 circulation, 479, 480, 483, 486

 composition, 478

 core, 483, 489, 496

 Coriolis parameter, 479

 density, 479

 escape velocity, 479

 flattening, 479

 global oscillations, 496

 gravitational acceleration, 479

 helium content, 479, 483–485

 internal structure, 483–485

 Io footprint, 507

 lightning, 482, 485

- liquid hydrogen layer, 483
 Lorentz resonance, 574
 magnetic field
 compared to Earth's, 485
 dynamo, 500
 quasi-dipolar, 500
 magnetodisk, 502
 magnetosphere
 corotational enforcement current, 511
 inner, 485
 interaction with Io, 503–511
 outer, 483
 Vasyliūnas cycle, 510–511
 magnetotail, 502
 mass, 484, 485
 mean density, 479
 metallic hydrogen, 483, 485, 486
 migration, 779
 nuclear reactions, 496
 occultation, 478
 orbit, 475, 482
 plasmoids, 510
 pressure(s)
 central, 495
 internal, 494–495
 scale height, 496
 radiation
 belts, 514–515
 decametric (DAM), 498, 508–509
 decimetric (DIM), 500
 excess, 496–497
 synchrotron, 500
 radius, 765
 resonance, 535, 609, 678, 681, 684, 695,
 697, 706
 ring(s)
 Amalthea, 524, 537, 575
 Gossamer, 541, 574, 575
 Halo, 573, 574
 Thebe, 524, 529, 573–575
 Rossby number, 479
 rotation periods, 479
 satellites
 direct, 478, 535, 626
 Galilean, 478, 522, 535, 536, 583
 orbits, 535, 536
 physical properties, 535
 retrograde, 535, 549
 temperature(s), 479, 496, 497
- K**
 Kamacite crystals, 667
 Keeler gap, 576, 577
- Keeler, J.E., 575
 Kepler, J., 533, 600, 601, 612, 677, 714, 744,
 752, 755, 762, 763, 768–769,
 774–775, 777
 Kirkwood gaps, 582, 678, 695, 697
 Kozai mechanism, 722, 773
 Kreutz, H.C.F., 604, 628
 Kronos (Saturn), 486
 Kuiper Belt. *See* Edgeworth-Kuiper Belt/Cloud
 Kuiper, G.P., 478, 564, 680
 Kursk magnetic anomaly, 468
- L**
 Lagrangian points, 475, 684, 757
 Lalande, J.-J., 490, 493
 Lapse rate
 adiabatic
 dry adiabatic lapse rate (DALR),
 368, 375
 saturated adiabatic lapse rate
 (SALR), 369
 environmental, 369
 Latent heat, 369, 385
 Law(s)
 Gauss's, 419
 Kepler's 3rd, 601, 744, 752
 Newton's 2nd, 419–421
 Newton's 3rd, 615, 634
 Titius-Bode, 493, 676, 677
 L dwarf(s), 760, 761
 GD 165B, 760
 Least squares computational scheme, 677
 Lemonnier, P.C., 490
 Leonids, 630, 631
 Le Verrier/Leverrier, Urbain-Jean-Joseph,
 492, 493
 Light curve modeling, 748, 749
 Russell-Merrill model, 750
 Wilson-Devinney program,
 748, 750
 Lithophilic elements, 658
 Lorentz force, 425–426, 441, 461
 Lorentz resonance, 574
- M**
 Mab (satellite, Uranus XXVI), 527, 532,
 564, 580
 water ice absorption, 564
 Maestlin (Mästlin), Michael, 599
 Magnetic
 bottle(s), 442, 444–446
 loss cone, 446

- Magnetic (*cont.*)

bow shock, 424, 457, 459, 465, 466, 503, 623, 624, 633

field(s)

boundary current, 440–441, 448, 451, 462, 464, 510

crustal, 461, 468, 469

curvature drift, 437–439, 447, 448, 460, 510

diamagnetic currents, 431, 440, 441, 460, 464, 465

dipolar, 423, 458, 500, 512, 514

dynamo model, 423, 458, 461, 462, 468, 544, 694

 $E \times B$ drifts, 402, 431–435, 451, 460, 470, 471

field-aligned current(s), 431–433, 452, 453, 456, 507, 508, 511, 514

gradient drift, 437–439, 447, 448, 460, 510

north/south-seeking poles, 424, 450, 458, 499

pressure, 464, 624

quasi-dipolar, 500

mirror(s)

pitch angle, 429, 444–447, 470, 501

point, 444, 445, 470

ratio, 446, 470

moment, 443, 462

ring current, 441–448, 511

storms, 441, 448–449, 452, 454–458

tail(s), 444, 455, 466

Magnetism, remanent, 461, 468, 544, 694

Magnetopause, 424, 440, 449, 452, 453, 457, 459, 460, 462, 466, 469, 502, 503, 511–514, 544, 614

Magnetopause nose, 459

Magnetosphere, 339, 395, 399–471, 475, 478, 486, 488, 494, 496, 498–516, 535, 540, 543, 547, 552, 584, 614, 622–624

Magnetotactic bacteria, 665

Marcy, G., 714, 764, 767

Mars

Argyre basin, 468

atmosphere, 349, 367, 368, 371–374, 376–381, 385–387, 389, 391, 407–408

aurora(e), 469

core, 462, 468, 469, 544

dust devils, 372, 373, 379

Hellas basin, 468

hydrosphere, 674

ice cap, 470

impact basins, 468, 692, 693

ionosphere

dominant ions, 409, 410

loss mechanisms, 410

production mechanisms, 409–410

iron content, 468, 544

lower atmosphere properties, 371, 372

magnetic field

crustal anomalies, 468

dynamo, 468, 469

global dipole moment, 467

global upper limit, 467

reconnection, 469

strengths, 468

magnetism, remanent, 468

magnetosphere, 467–469

induced, 468, 469

north-south dichotomy, 468

regolith oxidation, 469

satellites, 522, 524–525, 528–535, 568, 587, 677

spiders,

suprathermal atoms and ions, 414

water, 385, 407, 408, 470

Marsden, B.G., 533, 601, 603, 604, 608–610

Mass function, 635, 647, 714, 715, 764

Ma Tuan-Lin, 597

Maxwellian distribution, 340, 411, 412, 414

Maxwell, J.C., 575

Maxwell's equations, 417–420

Mayer, T., 490

Mayor, M., 714, 722

Mean free path, 340, 371, 412, 763

Medicean satellites (Galilean satellites, q.v.), 498, 501, 522, 523, 535, 583

Mercury

Elsasser number, 461

Lorentz force, 461

magnetic field

axial tilt, 458

dipole moment, 458, 461

dipole offset, 458

models, 461

origin, 653, 665

quadrupole term, 458

reconnection, 458

magnetopause, 457–460, 462, 466

magnetosphere, 458–462

bow shock, 457, 465

molten core,

“Metals,” in stellar astrophysics, 713

- Meteor(s)
ablation rate, 635
bolide(s) (fireballs), 631, 632, 637, 647, 659
brightness distribution, 639
brightness variation, 636
fast vs. slow, 635, 636
fragmentation, 625, 636, 673
ionization probability, 636
luminous efficiency, 635
shower, 630–632
sporadic, 632, 633, 637, 647
visibility, 632, 633, 636, 637
- Meteor crater(s), Ries, 667
- Meteorite(s) (individual)
Abee (EH4), 661
ALH 84001 (SNC), 649, 665, 666
ALH A77005 (SNC), 664
Allende (CV3, 2), 651, 659, 660, 671, 672, 675, 798
Bruderheim (L3), 651, 661
Chassigny (SNC), 651, 652, 664
EET A79001 (SNC), 664
Governador Valadares (SNC), 665
Henbury (IIAB), 651, 668
Lafayette (SNC), 668
MET 01210 (lunar), 666
Millarville (IVA), 649
Nakhla (SNC), 651, 664, 665, 671
NWA 7325 (Mercury), 667
QUE 94201 (SNC), 674
Shergotty (SNC), 651, 652, 661, 664, 674
Sikhote-Alin (IIAB), 668, 669
Zagami (SNC basaltic shergottite), 665, 666, 673, 674
- Meteorite Hills Antarctica, 653, 664, 666
- Meteorites (general)
age(s)
cosmic ray exposure, 669, 673, 694
crystallization, 674
differentiation, 674
ejection, 666, 674
formation, 674
gas retention, 669, 672–673
mean isochron, 672
radiogenic, 653, 669, 673
terrestrial, 673
breccia(s) (q.v.), 652, 655, 663, 664, 666, 671
calcium-aluminum inclusions (CAI), 620, 640, 657–660, 662, 676
chondrule(s), 639, 640, 651, 654, 658–660, 662, 675, 703
classification, 648, 650–652
- deuterium/hydrogen ratio, 662, 676
equilibration, 661
falls and finds, 649, 653, 670
isochrones, 671, 761
kamacite bands, 667
nomenclature, 648–649
origin(s), 661, 665, 669–672
petrographic/petrologic properties, 650–651
shock stages, 648
strewn field, 659
weathering grade, 648
- Meteorites (groups/classes/clans/ types)
acapulcoites, 663, 675
achondrites, 651–653, 659, 661–663, 665, 671, 675, 694, 698
aerolites (stony), 648
angrites, 651, 663, 675
Antarctic, 648, 666
ataxites, 656, 668
aubrites, 656, 664
brachinites, 663, 675
carbonaceous chondrites
CH (High-Fe), 659
CI (Ivuna), 659, 698
CK (Karoonda), 659
CM (Migei), 659
CO (Ormans), 659
CR (Renazzo), 659
CV (Vigrano), 659
chassignite(s), 652, 665, 698
chondrites
carbonaceous (v.s.), 533, 651, 657, 659–661, 672, 674, 675, 696–699
enstatite (v.i.), 651, 660, 698
ordinary (v.i.), 651, 660, 671, 675, 684, 698
Rumurutiite (R), 661
differentiated, 650–656, 662
origin, 652, 653
differentiated silicate-rich (DSR), 650–652, 655, 662–667, 674, 701
diogenites, 651–653, 655, 663, 665, 675, 694
enstatite(s)
EH (high iron), 651, 660, 661, 671
EL (low iron), 651, 660, 664
eucrites, 651–653, 655, 663, 675, 694
HED, 653, 663, 694–696
hexahedrites, 653, 656, 667
howardites, 651–653, 655, 663, 675, 694, 696
IAB, 651, 656, 661, 663, 668

- Meteorites (groups/classes/clans/ types) (*cont.*)
- IIAB, 651, 656, 663, 668, 669
 - IIIAB, 651, 656, 663, 668
 - IIICD, 651, 656, 661, 668
 - IVA, 651, 656
 - igneous, 650–652, 654, 663–666, 698
 - iron(s), 648–653, 656–661, 663, 664, 666–669, 671–674, 693
 - cooling rates, 658, 668
 - lodranites, 663, 675
 - lunar, 649, 651, 653, 666, 675
 - Martian (SNC), 665, 666, 673–675
 - mesosiderites, 651, 652, 655–557, 663, 664, 671, 675
 - microbreccias, 652
 - minichondrule, 651, 659
 - moldavite, 667
 - nakhrites, 652, 664, 671, 675
 - non-differentiated, 650
 - octahedrites, 653, 667, 668
 - plessitic, 656, 668
 - ordinary chondrites
 - H (high iron), 660
 - L (low iron), 660
 - LL (low iron, metal), 651, 653, 660, 662
 - orthopyroxenite, 665
 - pallasites, 651, 652, 655–657, 663, 664, 698
 - plessites, 668
 - primitive achondrites (IAB clan), 661
 - refractory-rich, 651, 658, 659
 - shergottites, 652, 664, 665, 671, 675
 - Shergotty-nakhla-chassigny (SNC), 651, 652, 663–666, 671, 673–675
 - siderites (irons), 648
 - siderolites (stony-irons), 648
 - tektite(s), 667, 675
 - ureilites, 652, 655, 664, 675
 - very-low-titanium (VLT) basalt, 666
 - volatile-rich, 651, 659
 - winonaites, 663, 675
 - Meteoritical Bulletin*, 649
 - Meteoroid, 370, 513, 552, 570, 573, 583, 584, 632–635, 638, 639, 648, 673, 676, 696
 - Meteor shower(s), 629–632, 637, 647, 669
 - radiant(s), 630–633
 - Methane (CH_4), 348, 395, 482, 483, 491, 493, 494, 550, 553–556, 558–561, 567, 569, 619, 625, 723, 756, 760, 780
 - clathrate hydrate, 560
 - Methanol (CH_3OH), 619, 627
 - Methylacetylene ($\text{CH}_3\text{C}_2\text{H}$), 660, 662
 - Methylene (CH_2), 561
 - Methylidyne (CH), 661
 - Methyl radical(s) (CH_3), 559–563
 - Metis (satellite, Jupiter XVI), 524, 529, 573
 - Micrometeorites
 - asteroidal/cometary dust ratio, 640
 - Brownlee particles
 - chondritic porous (CP), 639
 - chondritic smooth (CS), 639
 - destinies,
 - origins, 639
 - Milankovic cycles, 380
 - Millisecond pulsars, 756, 757
 - Mimas (Saturn I), 512, 523, 525, 530, 585
 - Minerals
 - anhydrous, 675
 - anthracene, 621
 - augite, 664, 665
 - enstatite, 664
 - feldspar, 664
 - ferrosilite, 621
 - forsterite, 538, 621, 760
 - hibonite, 658
 - kamacite, 654, 667, 668, 694
 - magnesite, 621
 - magnetite, 421, 544, 639, 664, 665
 - maskelynite, 664, 674
 - melilite, 658
 - nontronite, 621
 - olivine, 620, 621, 627, 651, 653, 655, 661, 663–665
 - orthopyroxene, 620, 655, 661, 663, 665
 - perovskite, 658, 760
 - pigeonite, 655, 664
 - plagioclase, 663–665, 667
 - siderite, 621, 648
 - smectite, 621
 - spinel, 658
 - taenite, 668
 - Minor Planet Center, 609, 628, 679, 680, 685, 687
 - Minor planets. *See* Asteroids
 - Miranda (satellite, Uranus V)
 - corona(e), 521
 - the “racetrack,” 563
 - scarp(s), 563
 - scissor fault, 563
 - Mission(s)
 - Cassini
 - Huygens probe, 475, 521, 553, 554, 556, 558, 563
 - orbiter, 480, 482, 486, 487, 512, 521, 549–553, 576–579, 583, 584
 - CoRoT, 714, 763

- Deep Impact, 608, 618–620
extended mission (EPOXI), 615
- Deep Space 337, 614
- Friendship, 371
- GAIA, 752
- Galileo
orbiter, 523, 537, 539, 541, 571, 573, 574
Probe, 374, 483, 484
thermal imagers, 536
- Giotto, 614
- Herschel Space Observatory, 627
- HIPPARCOS, 686, 723, 752, 753, 771
- Hubble Space Telescope (HST), 371, 374, 478, 488, 491, 504, 541, 569, 580, 581, 583, 584, 704, 747, 748, 753, 764, 771
- International Comet Explorer (ICE), 615
- International Space Station, 371, 435, 436
- Juno, 475, 482, 677, 690, 691
- Kepler, 714, 744, 749, 755, 768, 774
- Long Duration Exposure Facility
satellite, 639
- Magellan, 462, 773
- Mariner(s), 361, 458
- Mars Express, 412
- Mars Global Surveyor (MGS), 467, 469
- Mars Opportunity Rover, 649
- Mars Spirit Rover, 649
- Messenger, 458, 460
- MOST, 771
- NEAR Shoemaker, 683, 690
- New Horizons, 475, 482, 570, 573, 582
- Pathfinder, 468
- Phobos, 522, 524, 529, 533–535, 590, 690
- Pioneer(s)
Pioneer 10, 475, 482
Pioneer 11, 475, 482, 488, 499, 511
Pioneer Venus, 375, 385, 464, 466
- Rosetta, 615
- Solar Dynamics Observatory, 621
- Space Interferometry (SIM), 752
- Spitzer Space telescope, 551, 620, 627–629, 747, 766, 771, 772
- Stardust, 614, 640
- Stardust NExT, 614
- Suisei, 615
- Ulysses, 475, 482, 624
- Vega, 615, 620, 704, 758, 777
- Venera, 375, 383, 385
- Venus Express, 376, 465, 466
- Viking(s),
Orbiter(s),
- Vostok, 371
- Voyager(s)
Voyager 1, 475, 482, 487, 488, 546
Voyager 2, 475, 485, 490, 491, 493, 494, 511, 563–567, 578, 580–583
- Mixing
lines, 675
ratio, 349, 391, 407
time, 388, 389
- Moldavite, tektites, 667
- Molecular
charge transfer, 400–403, 410, 411, 623
dissociation, 401, 507
ionization, 404
ions, 401, 404, 507
photodissociation, 369, 393, 399, 403, 404, 407, 413, 415, 513, 548, 561
photoexcitation, 395
thermal speeds, 506
viscosity, 356
weight, 337, 338, 342–344, 346, 352, 372, 388, 478, 479
- Molecular cloud(s)
density, 639, 702, 703, 715
mass, 704, 715
radius, 702, 703, 715
- Monatomic gas(es), 347, 348
- The Moon, 440, 461, 478, 503, 504, 515, 521–523, 528–563, 567, 572, 580, 582, 585–591, 598, 599, 649, 659, 700, 706, 757, 764
orbital evolution, 586
- Müller, Johann (Regiomontanus), 598
- N
Naiad (satellite, Neptune III), 527, 532, 581
- Natural Satellite Data Center,
Neptune
angular diameter, 493
atmosphere
Great Blue/Dark Spot, 493, 494
the scooter, 494
composition, 395, 478, 493
discovery, 156, 492, 493, 523
electrolytic sea, 494
excess radiation, 394, 496–497
greenhouse effect, 394, 395, 494
magnetic field, 494
magnetosphere, 494
mean density, 476, 493
pressure(s)
central, 463, 495
internal, 494, 495
properties, 499

- Neptune (*cont.*)

 rings

 arcs, 771

 clumpiness, 771

 satellites

 orbits, 475, 489, 492, 493

 physical properties, 475

 winds, 494

Nereid (satellite, Neptune II)

 orbital elements, 523, 527, 532

 orbital properties, 528, 565

Neutral point, 441

Newton, I., 600

Newton's 2nd law, 419, 427, 428

Nice model, 706

Nitrogen (N, N₂)

 sublimation, 565, 568

 triple point, 566

Noise, 498, 686, 743, 776

 improvement, 686, 743, 775

Nuremberg Chronicles, 612
- O**
- Oberon (satellite, Uranus IV), 527, 532, 587

Observatories

 Harvard college, 747

 Paris, 714

 Sprout, 713

Occultation(s), 343, 344, 478, 487, 533, 547, 552, 568, 578, 581, 583, 588, 627, 686, 747, 749, 750, 766, 769, 772

OGLE. *See* Optical Gravitational Lensing Experiment (OGLE)

OGLE-2003-BLG-235, 755

Ohmic losses, 434

Olbers, H.W.M., 677

Olivine, 461, 620, 621, 627, 651, 653–655, 661, 663–665, 693, 694, 698

Oort cloud

 inner, 625, 626, 700, 701

 outer, 625, 626, 700, 701

 population, 626, 700

 radius, 626

Oort, J., 610, 615, 626, 700

Ophelia (satellite, Uranus VII), 527, 532, 578, 579

Optical depth, 344, 578, 584, 704

Optical Gravitational Lensing Experiment (OGLE), 747, 754, 755, 763, 766

Optics

 active, 686

 adaptive, 689, 723

Ordinary ray(s), 498

Origen, 597

Orthopyroxene, 620, 655, 661, 663, 665, 675, 694

Osculating orbits, 609

Osiris, 765

Oxygen, 371, 387, 390–391, 393, 399, 407, 412, 415, 466, 469, 502, 506, 507, 509, 513, 552, 621, 658, 660, 663–665, 674, 675

Oxygen ions, 502, 507

Oxygen isotopes, 660, 663–665, 675

Ozone (O₃)

 concentration, 370

 production, 369, 370
- P**
- Palaeomagnetic data, 423

Pan (satellite, Saturn XVIII), 526, 531, 576

Pandora (satellite, Saturn XVII), 526, 531, 577

Parker spiral, 465

Particle precipitation, 444, 446, 449, 460

Paul of Tarsus (St. Paul), 648

Pedersen current, 434, 435, 453, 454

Perfect gas law, 342, 344

Perseids, 630–632

Petrography, 650, 665

Petrologic classes, 652, 654, 659, 661, 663, 675

Petrology, 650, 694

Phobos (satellite, Mars I), 524, 529, 533–535

 decaying orbit, 534, 535

Phoebe (satellite, Saturn IX), 525, 530, 551, 578, 587

Phosphine (PH₃), 483

Phosphorescence, 395

Photodissociation, 369, 393, 399, 403, 404, 407, 413, 415, 513, 548, 561

Photolysis, 393, 399, 407, 408, 480, 540, 547, 556, 559, 560, 616

Piazzi, G., 676

Planet/planetary

 definition(s), 351, 384, 588, 589, 758–761, 781

 distinction from brown dwarfs, 652, 656, 715, 722, 723, 740, 741, 758–761

 evolution, 484, 489, 492, 705

 migration, 489, 706, 756, 761

 origins

 core-accretion, 755, 770, 778

 gravitational instability, 497, 778

Plasma frequency, 417–423, 497, 498

Plasmoids, 456, 459, 465

Plessite(s), 668

Pliny the Elder, 598

- Plutino(s), 568, 589, 680, 681, 685, 759
Pluto (dwarf planet)
 albedo markings, 569
 atmosphere, 569
 comparison with Eris, 568, 589
 comparison with Triton, 568–570, 587, 589
 discovery, 568
 interior, 568
 orbit/orbital
 elements, 570
 properties, 568, 570
 resonance with Neptune, 568
 satellites, 568–570
 seasons, 568–570
 spin-orbit coupling, 568
 temperature(s), 569
Plutoid, 680, 759
Polar cusp, 402, 416, 425, 441, 452, 459
Polarization drift, 435–437
Polarized waves, 420–423
Polyacetylene(s), 562
Polycyclic aromatic hydrocarbon (PAH), 621, 665
Portia (satellite, Uranus XII), 527, 532, 580, 581
Posidonius, 598
Poynting–Robertson drag, 642
Poynting–Robertson effect, 640, 642, 700
Pressure
 density relation, 342, 344
 equation, 342
 gradient, 342, 355, 357
 force, 353–360, 376, 382, 383, 479
 high/low, 356, 358–360, 362–364, 481, 560, 773
 partial, 387, 388, 517, 565
 radiation, 573, 613, 640–642, 697, 701
 scale height, 343, 344, 357, 371, 372, 376, 402, 412, 449
Prometheus (satellite, Saturn XVI), 526, 531, 537, 576, 577
Propane (C_3H_8), 559, 560, 562
Propylene (C_3H_6), 562
Proteus (satellite, Neptune VIII), 523, 527, 532
Proto-planetary disks (proplyds)
 dead zone, 706
 detection techniques, 757
 coronographic, 713
 heterogeneity, 675
 lifetime, 778
 mass, 681, 701, 706
 model, 705, 706
Orion, 704
Puck (satellite, Uranus XV), 527, 532, 581
Pulsar timings, 756–757
- Q**
Quadrans muralis, 631
Quasi-trapped particles, 460
Quenching, 394, 395
- R**
Radiants, 362, 367, 630–631, 633
Radiation
 coefficient, 477, 642
 excess, 394–395, 496–497
 pressure, 573, 613, 640–642, 697, 701
Radioactive isotopes
 aluminum 26 (^{26}Al), 658, 694
 argon 39 (^{39}Ar), 561, 673
 rubidium 87 (^{87}Rb), 669–673
 uranium 238 (^{238}U), 672
Radioactivity, 522, 523
Radio AM band, 406
Radio wave reflection, 406
Ratio of specific heats, 345, 347
Red giant wind, 703
Refraction, 344, 406, 420–22, 497, 498, 585
Refractivity scale height, 344
Refractory material, 658, 701
Regiomontanus (Johann Müller), 598
Rhea (satellite, Saturn V), 523, 525, 530, 549, 552, 553, 577, 578
 atmosphere, 552, 553
Ries crater, 667
Right-hand rule, 351–353, 425, 430, 432, 433, 438–440, 511
Ring/ring structures
 albedos, 496, 564, 581, 683, 688, 696
 current, 441–449, 452, 456, 460, 510, 511, 513, 514
 Jupiter, 572–575, 582, 583
 Neptune, 574, 581–582, 586
 origin, 570–572, 582–586, 663, 701
 particle sizes, 574
 resonances, 574, 585
 Rhea, 552, 578
 Saturn, 486–489, 496, 511–515, 551, 552, 576, 577, 582–584
 scattering function, 585
 spiral waves, 585
 Uranus, 491, 563, 578, 579, 583, 586
 vertical oscillations, 585
Roche limit, 570–572, 586

- Rosalind (satellite, Uranus XIII), 527, 532, 580, 581
- Rossby number (R_o), 377, 378, 380, 382, 383, 479, 480
- Rossiter/Rossiter-McLaughlin effect, 764, 772
- Rotational flattening, 353
- Rothmann, C., 599
- Russell, H.N., 750
- S**
- Sallamu, 601
- Saturated adiabatic lapse rate (SALR), 369
- Saturn
- albedos, 496, 564
 - atmosphere/atmospheric
 - belts, 444, 479, 481, 487, 493, 514
 - storms, 487
 - velocities, 575
 - zones, 487
 - aurora(e), 488
 - color index, 715, 723
 - cosmic ray albedo neutron decay (CRAND), 515
 - electroglow, 488, 491
 - excess radiation, 394–395, 496, 497
 - helium abundance, 484–485
 - helium rain, 395, 496
 - magnetic field
 - dipole offset, 458, 499
 - quadrupole term, 458
 - magnetodisk, 512–514
 - magnetosphere, 511–515
 - mass, 489
 - metallic hydrogen, 485
 - obliquity, 489
 - period(s)
 - revolution, 680
 - rotational, 511, 515
 - plasma disk, 487
 - poles, 488
 - precessions, 489, 695
 - pressure(s)
 - central, 495
 - internals, 495
 - radiation, 394, 496
 - kilometric (SKR), 515
 - radiation belts, 515
 - radius, 476, 477, 511, 551
 - resonance, 489, 585, 695, 706
 - ring(s)
 - A ring, 548, 551, 576, 582
 - associated satellites, 573
- B ring, 585
- Cassini Division, 575, 585
- composition, 583
- C ring, 576, 585
- discovery, 548, 585
- Encke gap, 549, 576, 577, 582
- E ring, 512
- F ring, 576, 577, 582
- G ring, 576
- Keeler gap, 576, 577
- kinked, 582
- Maxwell gap, 576
- Phoebe, 551, 578
- resonances, 489
- spokes, 578, 584
- temperatures, 578
- satellites
 - co-orbital, 549
 - orbits, 475, 489, 512
 - physical properties, 530–531
 - propeller-shaped moonlets, 548
 - temperature(s), 484, 494
- Scattered disk, 626, 685
- Schwarzschild radius, 753
- Seneca, 598, 681
- Shepherding satellites, 577, 579–582
- Siderophilic elements, 657
- Silica (SiO_2), 635, 657
- Silicate emission, 620
- Silicates, 372, 504, 566, 620, 621, 625, 639, 652, 655, 661, 664, 667, 769
- SIMBAD database, 714
- Sirocco, 395–396
- Snell's law, 421
- The snow line, 625, 662, 755, 772, 775, 778
- Sodium (Na), 460, 503–506, 509, 512, 536, 619–620, 633, 657, 658, 747, 766, 767, 773
- Sodium chloride (NaCl), 505–507
- Solar apex, 625
- Solar constant(s), 367, 372
- Solar wind, 415–417, 423–425, 440, 441, 448–450, 454, 455, 458–460, 462–469, 500, 503, 510, 512–515, 545, 614, 617–619, 623, 624, 640, 662, 663, 697, 701
- Spallation products, 673
- Specific angular momentum, 607
- Specific heat(s)
 - capacity, 347
 - per unit mass, 347, 348
- Spectrograph(s)/spectrographic
 - CORALIE, 743

- echelle, 743
- ELodie, 743
 - precision, 686, 743, 752, 764
- Spectroscopic, 745, 764
 - binaries, 723, 743, 744, 746, 777
- Sputtering, 415, 466, 469, 506, 513, 540, 545, 547, 552, 553, 574
- Stable isotopes
 - argon, 674
 - oxygen,
 - strontium,
- Standard mean ocean water (SMOW), 674
- Star clusters
 - Hyades, 762
 - NGC 6791, 762
 - Praesep (M44), 762
 - 47 Tuc, 762
- Star of Bethlehem, 597, 612
- Stars (classes)
 - brown dwarfs (q.v.), 722, 723, 740, 741, 750, 752, 758, 759, 762, 763, 777
 - double-line (SB2), 723, 746
 - K-stars, 756
 - L dwarfs, 760, 761
 - methane dwarf, 760
 - M-stars, 745
 - neutron stars, 756, 763
 - red dwarfs, 770
 - red giants, 703
 - single-line (SB1), 743–745
 - solar-like, 743
 - spectroscopic binaries, 745–746
 - T dwarfs, 740, 760, 761
 - white dwarfs, 723, 757, 758, 762
- Stars (individual)
 - AB Pictoris, 755
 - ν Andromedae, 676
 - Barnard's Star, 713
 - 55 Cancri, 747, 767–768
 - α Centauri B, 744, 775
 - Cha 110913-773444, 756
 - CM Draconis, 756
 - ε Eridani, 704, 758, 770–771
 - Gliese 876, 753
 - GQ Lupi, 755
 - HD 69830, 769–770
 - HD 168443, 723, 753
 - HD 189733, 747, 763, 766
 - HD 209458, 714, 747–750, 760, 761, 764–767, 773
 - Kepler 11, 763, 768–769
 - Kepler 32, 774–775
 - Lalande 21185, 753
 - LP 475-242, 762
- α Lyrae (Vega),
- β Lyrae, 677, 746
- 2MASSW J1207334-393254, 755
- OGLE-TR-10, 763
- 51 Pegasi, 649, 714
- β Pictoris, 704, 713, 758
- α Piscium Austrini (Fomalhaut), 631, 704
- PSR 1257+12, 714, 756, 763
- PSR B1620-26, 714, 757
- PSR J1719-14, 746, 757
- Ross 458, 761
- Ross 780, 753
- SCR J1845-6357, 783,
- SN 1572, 598
- 34 Tauri(Uranus), 490
- ε Tauri, 762
- TrES-1, 747, 771–722
- 4U 0142+61, 763
- XO-1, 788,
- Star(s)/stellar (general)
 - limb-darkening, 763, 764
 - line profiles, 744, 771
 - magnetic activity cycles, 744
 - metallicity/metallicities, 762, 770
 - rotation, 744, 772, 774, 776
 - spectral types, 650, 755, 761, 770, 780
- Sulfur, 391–394, 409, 483, 502, 504, 507, 536, 537, 544, 661
 - boiling point, 536
- Sulfur dioxide (SO_2), 372, 387, 391, 505, 506, 512, 537, 619
- Sulfur oxide (SO), 504
- Sung-shih annals, 602
- Sun/solar
 - apex, 625
 - corona(e), 416, 614, 639
 - F-corona, 639
 - disturbed current(s), 452
 - flare(s), 404, 406, 417, 439, 448, 662
 - flux, 372, 441, 448, 641
 - luminosity, 338, 641, 687, 781
 - nebula, 489, 583, 621, 625, 657, 660, 661, 672, 674, 675, 694, 700–703
 - photon momentum, 640
 - quiet current(s), 439
 - wind, 415–417, 423–425, 440, 441, 448–450, 454, 455, 458–460, 463–469, 500, 503, 509–515, 545, 614, 616–618, 623, 624, 640, 662, 663, 697, 701
- Supernova, 600, 703, 756, 763
- Survey(s), 490, 537, 569, 600, 690, 723, 740, 742, 747, 749, 752, 754, 756, 762, 763, 772

Survey(s) (*cont.*)

optical gravitational lensing experiment (OGLE), 747, 754, 755, 764, 766

Swift, J., 528, 774, 775
Szebehely, V., 586, 587

T

Taenite crystal(s), 667
Taylor instability, 481
T dwarf(s), 740, 760, 761
 Gliese 229B, 324

Tektite(s), 667, 675

Telescopes

 Canada–France–Hawaii (CFHT), 714
 Frederick C. Gillette (Gemini North), 620
 Hubble space (HST), 371, 374, 478, 488,
 491, 504, 569, 580, 581, 704, 747,
 748, 753, 762, 764, 771
 Keck, 581, 764
 Spitzer Space, 551, 620, 627–629, 747, 766,
 771, 772

 Subaru, 620

Temperature(s)

 effective, 477, 496, 497, 715, 749
 equilibrium, 337, 338, 367, 491, 496, 536,
 568, 688, 760, 765, 773, 779, 780

Tethys (satellite, Saturn III), 512, 514, 523,
 525, 530, 548, 549, 553, 575,
 577, 583

Tetraacetylene (C_8H_2), 562

Thalassa (Satellite, Neptune IV), 527, 532, 581

Thebe (satellite, Jupiter XIV), 524, 529,
 573–575

Thermal

 circulation, 357–358, 362
 inertia, 371, 375, 378, 385–386
 wind, 358–360, 380

Tholins, 627

Tide(s)/tidal

 action, 522, 628
 bulge, 572, 586
 critical density, 571
 critical distance, 570, 571, 587
 disruption criteria, 570, 572
 friction, 572, 586
 instability, 570
 raising force, 570, 586

 Roche limit, 570–572, 586

Tisserand, F.F., 608, 627

Tisserand invariant/parameter, 608, 627

Tisserand's criterion, 608

Titan (satellite, Saturn VI)

atmosphere

 aerosols, 559
 chemistry, 562
 cloud(s), 554, 556
 composition, 560
 Hadley cells, 555
 polar storms, 556, 559
 primordial, 560
 superrotation, 555
 thermosphere, 555, 563

cat scratches, 558

crustal material, 541

cryovolcano, 779

dendritic channels, 556

hydrogen torus, 563

hydrological cycle, 555, 559

Kraken Mare, 556

lake(s), 555–559

Ligeia Mare, 556, 557

Love number, 555

Menrva Crater, 558

methane cycle, 558–559

obliquity, 555

Ontario Lacus, 556

orbit/orbital

 elements, 525

 properties, 530, 558

panoramic view, 554

polar lakes, 558

rotation period, 555

sand seas, 558

seasons, 555, 556

Sotra Facula, 558

subsurface ocean, 555, 557

surface images, 553–559, 563

temperature(s), 555, 563

tide(s)/tidal, 553

 heating, 583

water retention, 560, 563

Titania (satellite, Uranus III), 521, 523,

 527, 532

Titius von Wittenberg, Johann Daniel, 676

Toscanelli, P., 598

Triacetylene (C_6H_2), 562

Triton (satellite, Neptune I)

 atmosphere/atmospheric

 cloud(s), 566

 composition, 690

 pressure, 565

 thermosphere, 566

 cantaloupe terrain, 567

 color, 565, 567

 cryovolcano(s), 566, 567

- geyser(s), 566, 567
impact crater(s), 566
 Mazomba, 566
mean density, 566
nitrogen geyser(s), 566
orbit/orbital
 elements, 527
 precession, 565
 properties, 532
seasons, 565
 Rauch Planitia, 567
surface relief, 566
synchronous rotation, 567
- Trochoid, 432, 437
- T Tauri stage, 662, 697
- T'ung-k'ao annals, 602
- Twain, Mark (Samuel Clemens), 611
- U**
- Umbriel (satellite, Uranus II), 523, 527, 532
 albedo, 564
- Units
 astronomical unit (au), 339, 367, 417, 476,
 490, 502, 601, 603, 604, 609, 610,
 613, 622–628, 641, 662, 676–681,
 683, 685, 686, 690, 694, 695,
 698–700, 703, 704, 715, 744, 745,
 755, 757, 761, 763, 765–767,
 769–774, 776–780
 mho (conductance), 459
 siemens (conductance), 459
- Universal gas constant, 343
- Uranus
 angular size, 490
 atmosphere, 490, 491
 brightness (opposition magnitude), 490
 color,
 composition, 583
 density profiles, 490
 discovery, 490, 676
 electroglow, 491
 He/H ratio, 490
 helium abundance, 491
 internal pressure, 485, 495
 lightning, 491
 magnetic field, 491
 magnetosphere, 395, 496, 499, 500
 ring(s)
 discovery, 491, 578, 581
 smoke, 583
 variation, 491
 rotation, 490, 491
- satellites
 orbits, 490
 physical properties, 532
seasons, 490
superheated water, 491
- V**
- Van de Kamp, P., 713
- Vector, 341, 342, 349–351, 354, 355, 360,
 418–420, 425–429, 461, 471, 489,
 511, 607
cross-product, 350, 428
- The Venerable Bede, 598
- Venus
 atmosphere/atmospheric, 464
 loss, 466–467
 cycles, 409
 sulfur, 393, 394
 dominant ions, 410
 exosphere, 467
 heat flux, 468, 484, 496, 536
 induced magnetosphere, 463–466
 ionopause, 464, 465
 ionosphere/ionospheric
 diamagnetic current, 464
 dominant ions, 410
 electron density, 464
 loss mechanisms, 410–411
 plasma pressure, 464
 processes, 463
 production mechanisms, 410–411
 solar wind interaction, 463
 limit on magnetic dipole moment, 462
 lower atmosphere properties, 371, 372
 magnetic field pressure, 463
 magnetocavity, 465
 magnetospheric bow shock, 465, 466
 rotation, 463, 465
 surface cratering, 522
- Vesta (asteroid), 653, 677, 684, 689–698
- Virial theorem, 702
- Volatile substance, 658
- Volcano(es), 391, 505, 506, 536, 558, 566, 620
- von Purbach, G., 598
- Von Zach, Baron Franz Xaver
 (János Ferenc), 676
- W**
- Water
 ice, 379, 385, 540, 542, 543, 545, 553, 565,
 566, 568, 577, 583, 588, 616, 627

- Water (*cont.*)
 vapor, 349, 367, 379, 385, 413, 485, 512,
 627, 780
- Whipple, F., 614
- Widmanstätten figures, 667
- Wildt, R., 483, 490
- Winds
 Chinook, 395
 Coriolis parameter, 479
 cyclostrophic, 382–384, 555
 easterlies, 362, 365, 480
 Föhn, 395
 geostrophic, 356–360, 385, 479
 Sirocco, 395
 solar, 415–417, 423–425, 439, 441,
 448–451, 454, 455, 458–460,
 463–469, 500, 503, 509–515, 545,
 614, 616–618, 623, 624, 640,
 661–663, 697, 701
 thermal, 358–360, 380
 trade, 360–362, 365, 384, 385, 480
 westerlies, 360–365, 385, 480
 zonally averaged distribution, 366
- Y**
Yarkovsky effect, 695, 697, 700
Yarkovsky force, 700
- Z**
Zodiacal light, 639